

A Quantum Chemical Approach to Singlet and Triplet Excitation Energy Transfer

Inaugural-Dissertation

zur Erlangung des Doktorgrades
der Mathematisch-Naturwissenschaftlichen Fakultät
der Heinrich-Heine-Universität Düsseldorf

vorgelegt von

Simon Metz
aus Düsseldorf

Düsseldorf, Februar 2025

aus dem Institut für Theoretische Chemie und Computerchemie
der Heinrich-Heine-Universität Düsseldorf

Gedruckt mit der Genehmigung der
Mathematisch-Naturwissenschaftlichen Fakultät der
Heinrich-Heine-Universität Düsseldorf

Berichterstattende:

1. Prof. Dr. Christel M. Marian
2. Prof. Dr. Shirin Faraji
3. Prof. Dr. Reinhold F. Fink

Tag der mündlichen Prüfung: 03.07.2025

Eidesstattliche Erklärung

Ich versichere an Eides Statt, dass die Dissertation von mir selbständig und ohne unzulässige fremde Hilfe unter Beachtung der Grundsätze zur Sicherung guter wissenschaftlicher Praxis an der Heinrich-Heine-Universität Düsseldorf erstellt worden ist. Die Dissertation wurde in der vorliegenden oder in ähnlicher Form noch bei keiner anderen Prüfungsbehörde eingereicht. Es wurden keine früheren erfolglosen Promotionsversuche unternommen.

Düsseldorf, den

Danksagung

Zuerst möchte ich meiner Doktormutter, Frau Prof. Dr. Christel Marian, meinen tiefsten Dank aussprechen. Sie hat nicht nur diese Promotion ermöglicht, sondern bereits meine Bachelor- und Masterarbeit betreut. Über all diese Jahre hinweg stand Sie mir jederzeit hilfreich zur Seite und unterstützte mich stets mit wertvollen und konstruktiven Ratschlägen.

Ebenso danke ich herzlich Frau Prof. Dr. Shirin Faraji für die Übernahme des Zweitgutachtens.

Ein großes Dankeschön geht auch an alle aktuellen und ehemaligen Kolleginnen und Kollegen im TC-Arbeitskreis. Die angenehme Arbeitsatmosphäre, die konstruktiven Diskussionen, die freundschaftliche Zusammenarbeit sowie die zahlreichen gemeinsamen Veranstaltungen – sei es innerhalb oder außerhalb des Instituts – haben die gemeinsame Zeit bis zum Abschluss dieser Arbeit zu einer unvergesslichen Erfahrung gemacht. Besonders bei meinem mich seit Studienanfängen begleitenden Bürokollegen Jeremy Kaminski möchte ich für seine Unterstützung und den produktiven Austausch bedanken. Ebenso danke ich ihm und Tobias Böhmer für das Korrekturlesen dieser Arbeit.

Nicht zuletzt geht ein besonderer Dank an meine Familie, allen voran meinen Eltern. Sie haben mich in jeder erdenklichen Hinsicht unterstützt und mir stets den Rücken freigehalten, sodass ich mich ganz meiner wissenschaftlichen Arbeit widmen konnte. Ohne ihre Geduld und ihr Verständnis wäre diese Promotion weitaus schwieriger gewesen.

Abschließend danke ich allen Mitgliedern des Graduiertenkolleg ModISC. Die gemeinsamen Veranstaltungen waren nicht nur wissenschaftlich bereichernd, sondern auch immer von guter Laune und einem inspirierenden Gemeinschaftsgeist geprägt.

Der Deutschen Forschungsgesellschaft (DFG) möchte ich für die finanzielle Unterstützung dieser Promotion durch das Graduiertenkolleg ModISC (Projektnummer 396890929/GRK 2482) danken.

Abstract

Excitation Energy Transfer (EET) is a widely used process in biomolecular structure analysis. Recent studies have proposed EET as a mechanism to improve the stability, efficiency, and color properties of fluorescent and phosphorescent organic light-emitting diodes (OLEDs). This mechanism involves the generation of excitons on a dopant followed by Förster resonance energy transfer (FRET) to a highly fluorescent emitter molecule. In order to study the EET properties of a donor–acceptor system from a quantum chemical point of view, it is necessary to calculate the photophysical processes in the individual molecules. For this purpose, the semiempirical DFT/MRCI method was employed to compute the excited state properties.

In addition to the desired long-range FRET process, also other transfer mechanisms such as the short-range Dexter energy transfer can play an important role. Therefore, in this work, the triplet–triplet EET extension of the singlet–triplet excitation energy transfer (STrEET) program was tested for the first time. However, the Dexter energy transfer in the chosen spiran-linked anthrone-naphthalene molecule is symmetry forbidden. Consequently, non-adiabatic coupling matrix elements were calculated, yielding EET time constants in very good agreement with the experiment. Despite the unsuccessful test of the EET software, a new excited state energy dissipation pathway for this molecule was proposed.

At short intermolecular distances charge-transfer mediated EET can occur. To account for this effect, Dyson orbitals, the overlap between wave functions with different number of electrons, were implemented. An evaluation of the implementation showed that the energies of the charged states and thus the EET couplings are very unreliable. However, Dyson norms were successfully used to reproduce experimentally observed ionization probabilities in a series of oligophenylenes.

In another study, the STrEET program was utilized to calculate energy transfer properties in a hyperfluorescent OLED. The excitonic coupling matrix elements (ECMEs) were computed using the ideal dipole approximation (IDA) and monomer transition density (MTD) approaches. Both methods show good overall agreement and yield EET rate constants that are close to experimental values.

In addition, a new extension for triplet–singlet EET has been implemented to the STrEET program. Again, the ECMEs obtained with the IDA and MTD approaches agree very well for a system of smaller size molecules. This extension can also be applied for larger molecular systems, making it available for the calculation of phosphor-sensitized OLEDs.

Zusammenfassung

Anregungsenergietransfer (EET) ist eine weit verbreitete Methode in der biomolekularen Strukturanalyse und als Mechanismus vorgeschlagen, um die Stabilität, Effizienz und Farbeigenschaften von organischen Leuchtdioden (OLEDs) zu verbessern. Dabei werden Exzitonen an einem Dotierstoff erzeugt, gefolgt von einem Förster-Resonanz-Energietransfer (FRET) auf ein stark fluoreszierendes Molekül. Um die EET Eigenschaften mit quantenchemischen Rechnungen zu untersuchen, ist es notwendig, die photophysikalischen Prozesse in den einzelnen Molekülen zu berechnen. Zu diesem Zweck wurde die semi-empirische DFT/MRCI Methode verwendet, um die Eigenschaften der angeregten Zustände zu berechnen. Neben dem gewünschten langreichweitigen FRET-Prozess können auch andere Mechanismen, wie der kurzreichweitige Dexter-Energietransfer, eine wichtige Rolle spielen. In der vorliegenden Arbeit wurde erstmalig die Triplett-Triplett-EET-Erweiterung des Singulett-Triplett-Anregungsenergietransfer-Programms (STrEET) getestet. In dem gewählten spiro-verknüpften Anthron-Naphthalin-Molekül ist der Dexter-Energietransfer allerdings aus Symmetriegründen verboten. Daher wurden nicht-adiabatische Kopplungsmatrixelemente berechnet. Die daraus resultierenden EET-Zeitkonstanten zeigen eine sehr gute Übereinstimmung mit dem Experiment. Trotz des erfolglosen Tests der EET-Software wurde ein neuer Mechanismus der Energiedissipation dieses Moleküls vorgeschlagen.

Bei kurzen Abständen kann EET auch über ionische Übergangszustände ablaufen. Um diesen Effekt zu berücksichtigen, erfolgte die Implementierung von Dyson-Orbitalen, definiert als Überlapp zwischen Wellenfunktionen mit unterschiedlicher Anzahl an Elektronen. Ein Test der Implementierung zeigte, dass die Energien der geladenen Zustände und damit die EET-Kopplungen unzuverlässig sind. Die Dyson-Normen wurden jedoch erfolgreich zur Reproduktion experimenteller Ionisierungswahrscheinlichkeiten in einer Reihe von Oligophenylenen verwendet.

In einer anderen Studie wurde das STrEET-Programm zum ersten Mal zur Berechnung der Energietransfereigenschaften in einer hyperfluoreszierenden OLED eingesetzt. Die exzitonenischen Kopplungsmatrixelemente (ECMEs) wurden mithilfe der idealen Dipolnäherung (IDA) und der Monomerübergangsdichte (MTD) berechnet. Es konnte festgestellt werden, dass beide Methoden eine gute Übereinstimmung aufweisen und EET-Ratenkonstanten liefern, die nahe an den experimentellen Werten liegen.

Darüber hinaus wurde eine neue Erweiterung für Triplett-Singulett-EET in das STrEET-Programm implementiert. Auch hier zeigen die mit den IDA- und MTD-Ansätzen erhaltenen ECMEs eine sehr gute Übereinstimmung für ein System mit kleineren Molekülen. Diese Erweiterung kann auch für größere Molekülsysteme angewendet werden, sodass sie für die Berechnung von phosphorsensibilisierten OLEDs geeignet ist.

List of Publications

Included in this thesis:

1. Intersystem crossing and intramolecular triplet excitation energy transfer in spiro[9,10-dihydro-9-oxoanthracene-10,2'-5',6'-benzindan] investigated by DFT/MRCI methods
Can. J. Chem., **101**, 633–640 (2023)
Simon Metz, Tobias Böhmer, Ben Raunitschke, Christel M. Marian

Contribution: All quantum chemical calculations; preparation of all figures; writing first draft; revision of the manuscript

2. Electron affinities and lowest triplet and singlet state properties of para-oligophenylenes (n=3–5): Theory and experiment
J. Phys. Chem. A, **127**, 8073–8082 (2023)
Timo Schulz, Paul Konieczny, Dennis R. Dombrowski, Simon Metz, Christel M. Marian, Rainer Weinkauff

Contribution: Implementation of Dyson orbitals and their respective norms (DENSOMAT); writing part about Dyson orbitals; revision of the manuscript

3. Excitonic Coupling of a TADF Assistant Dopant and a Multi-Resonance TADF Emitter
Adv. Opt. Mater., 2402241 (2024)
Simon Metz, Christel M. Marian

Contribution: All quantum chemical calculations; preparation of all figures; writing and revision of manuscript

4. Computational Approach to Phosphor-Sensitized Fluorescence Based on Monomer Transition Densities

J. Chem. Theory Comput., **21**, 2569-2581 (2024)

Simon Metz, Christel M. Marian

Contribution: Implementation of triplet–singlet EET (STrEET); All quantum chemical calculations; preparation of all figures; writing first draft; revision of manuscript

Not included in this thesis:

1. Modulation of intersystem crossing by chemical composition and solvent effects: Benzophenone, anthrone, fluorenone

ChemPhotoChem, **6**, e202200098 (2022)

Simon Metz, Christel M. Marian

Contribution: All quantum chemical calculations; preparation of all figures; revision of manuscript

Contents

1	Introduction	1
2	Theory	7
2.1	Density Functional Theory	7
2.2	Time-Dependent Density Functional Theory	8
2.3	Solvation Effects	10
2.4	DFT/MRCI	10
2.5	Spin-Orbit Coupling	13
2.6	Rate Constants	15
2.6.1	Non-radiative Rate Constants	15
2.6.2	Radiative Rate Constants	20
2.7	Vibronic Transitions	21
2.8	Excitation Energy Transfer	21
2.8.1	Ideal Dipole Approximation	22
2.8.2	Monomer Transition Density Approach	23
3	The STReET Program	29
4	Results	33
4.1	Intramolecular Triplet-Triplet Excitation Energy Transfer	33
4.2	Charge-Transfer Contributions to Excitation Energy Transfer	36
4.2.1	Dyson Norms as Ionization Probabilities	38
4.3	Singlet-Singlet Excitation Energy Transfer	42
4.4	Triplet-Singlet Excitation Energy Transfer	47
5	Conclusion	55
A	List of Abbreviations	I
B	Appendix	V
C	Included Publications	XV

1 Introduction

Excitation energy transfer (EET) is a photophysical process that occurs in nature and is frequently employed in biomolecular imaging and in organic electronic applications. It represents a pivotal stage in the process of photosynthesis in plants. Following the absorption of light by the light-harvesting complexes, the excitation energy is transferred to the photosynthetic reaction center. Subsequently, the light energy is converted into chemical energy.^[1] In biomolecular applications, EET can be employed to determine the interaction of proteins, for example the conformational dynamics of DNA or RNA, in vitro or in a living system.^[2] Furthermore, EET can be used in organic solar cells and organic light-emitting diodes (OLEDs). Before going into detail about OLEDs and the application and benefits of EET in them, a more detailed introduction to EET will follow.

Excitation Energy Transfer

EET is defined as the non-radiative transfer of an exciton between two interacting systems. Although it is typically observed for distinct molecules, energy transfer can also occur between units of a polymer or between two moieties of a single molecule. The initial situation starts with the EET donor in an excited state and the acceptor in its electronic ground state. Two well-know mechanisms are used to describe the energy transfer. The first mechanism was extensively elaborated by Förster in the 1940s and is therefore named Förster resonance energy transfer (FRET) (sometimes incorrectly named fluorescence resonance energy transfer^[3]). It is based on a Coulomb interaction between an excited donor molecule (\mathbf{D}^*) and an acceptor (\mathbf{A}), where a simultaneous de-excitation of the donor and an excitation of the acceptor occurs:



In the simplest model, FRET can be described as a concurrent transition from the highest occupied molecular orbital (HOMO) to the lowest unoccupied molecular orbital (LUMO) of the acceptor and vice versa for the donor (Fig. 1.1a). The

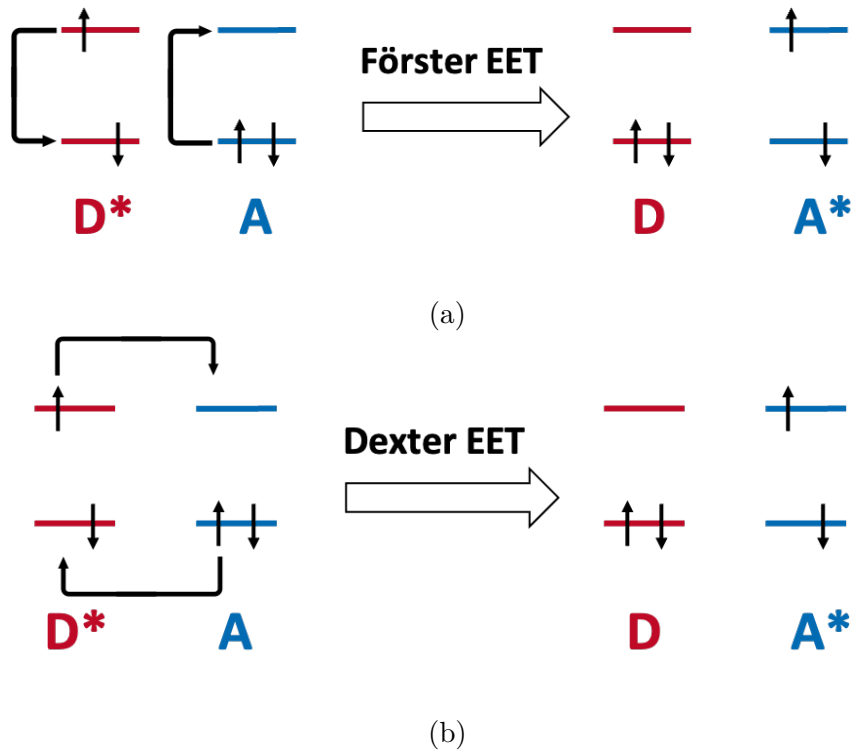


Figure 1.1: Schematic representation of Förster and Dexter energy transfer in a four-electron-four-orbital model.

efficiency of the FRET process (η_{FRET}) is given by:

$$\eta_{\text{FRET}} = \frac{k_{\text{FRET}}}{k_{\text{FRET}} + k_{\text{rad,D}} + k_{\text{nr,D}}} \quad (1.2)$$

where k_{FRET} is the rate of the energy transfer process, $k_{\text{rad,D}}$ is the radiative rate and $k_{\text{nr,D}}$ is the non-radiative rate of the donor. In Förster theory k_{FRET} is given by:

$$k_{\text{FRET}} = \frac{1}{\tau_{\text{D}}} \left(\frac{R_{\text{F}}}{r} \right)^6 \quad (1.3)$$

where τ_{D} is the lifetime of the excited donor state, leading to a proportionality of k_{FRET} and k_{rad} . Therefore, to facilitate efficient energy transfer it is imperative that the radiative rate exceeds that of non-radiative deactivation processes within the donor molecule. The Förster radius (R_{F}), the distance at which FRET efficiency is 50%, measures the efficiency of a donor–acceptor system. According to Förster’s early studies, the energy transfer is only possible if both transitions are allowed. Consequently, the prevailing view is that FRET occurs exclusively between two singlet states. However, it is important to note that spin–orbit coupling (SOC) has the potential to make formally forbidden processes allowed, thereby enabling triplet–singlet excitation energy transfer (TSEET). Such triplet–singlet energy

transfer may be slow but still can be effective, because competing intramolecular de-excitation processes on the donor are forbidden as well.^[4] This mechanism was first observed in small organic molecules during the early 1960s.^[5,6]

The second EET mechanism was elaborated by Dexter who suggested EET as an exchange interaction. Here, an overlap between the molecular orbitals (MOs) of the two interacting states is required, making it a short-range process. It is essentially a simultaneous electron transfer between the HOMOs and LUMOs of donor and acceptor (Fig. 1.1b). It thereby preserves the spin symmetry of the donor–acceptor pair and is responsible for triplet–triplet excitation energy transfer (TTEET). At short intermolecular distances, intermediate charge-transfer (CT) states can facilitate the energy transfer process, where separate electron transfer processes lead to ionic bridging states.^[7]

Organic light emitting diodes

OLEDs play a crucial role in the modern display market, offering a number of advantages over alternative display technologies, such as liquid crystal displays (LCDs). The processing of OLEDs allows for the manufacturing of displays that are both thinner and lighter in weight.^[8] Furthermore, they are more energy-efficient, as they do not require a white backlight. The first OLED was reported in 1987 by Tang and VanSlyke, which consisted of four distinct layers.^[9] The bottom of the device was a glass coated with a transparent anode. Additionally, a hole transport layer, a luminescence layer, and the cathode were present. In modern OLEDs, more layers, such as electron transport layers, are incorporated to enhance the performance.^[10] This thesis primarily focuses on the emitter molecules in the luminescence layer. Here, electrons and holes recombine to form excitons, in accordance with spin-statistics. 25% of these excitons are singlets and 75% are triplets.^[9,11]

The luminescent layer in OLED displays can be constructed in different ways. For smaller displays, such as mobile phones, individual red, green and blue sub-pixels are used. Because of scaling issues in the production, large displays (*e.g.*, TVs) use a white backlight with subtractive color filters. The latest technology uses a blue backlight and additive fluorescent filters for the red and green sub-pixels.^[12] In the first-generation OLEDs, purely organic fluorescent dyes are utilized as emitters. These dyes exhibit excellent emission characteristics, high color purity due to narrow emission bands and good operational stability owing to rapid radiative decay of the dyes (nanosecond regime).^[13] However, the inherent limitation of these types of OLED devices is the restricted internal quantum efficiency (IQE),

1 Introduction

as only the singlet excitons can be harvested for luminescence, which ultimately limits the maximum achievable IQE to 25%.

To achieve an IQE of 100%, the generated triplet excitons must be integrated into the light-emitting process. One method for achieving this goal is the utilization of phosphorescent dyes.^[14] The use of organometallic complexes with heavy metal cores (predominantly Ir and Pt) facilitates high SOC, thereby enabling these molecules to harvest singlet excitons through rapid intersystem crossing (ISC).^[15] Through this mechanism an IQE of up to 100% can be obtained. The main limitation of these devices is the comparatively long radiative lifetime (microsecond regime) of the emitter, which induces undesirable side effects, namely quenching processes and bleaching reactions. Especially, in blue emitters these reactions result in diminished operational stability of the OLED devices. Furthermore, the use of heavy metal atoms gives rise to additional concerns, namely those pertaining to the environment and the high cost of the complexes themselves.^[16,17] Current industrial OLED displays are made with red and green phosphorescent emitters, while efficient blue emitters are realized by utilizing triplet–triplet annihilation (TTA).^[18] This process requires a sensitizer that rapidly undergoes ISC to the triplet manifold, populating the TTA emitter’s triplet state via TTEET. Two triplet excitons of this emitter then recombine to form a singlet ground state and an excited singlet state to emit fluorescence. This process has a maximum IQE of 62.5%.^[19,20]

The third generation of OLEDs exhibits a maximum IQE of 100% without the use of heavy metals. The mechanism utilized is known as thermally activated delayed fluorescence (TADF). This mechanism involves the upconversion of triplet excitons into the singlet manifold through reverse intersystem crossing (rISC). One of the prerequisites for this upconversion to occur is a small energy gap between the lowest-lying singlet state and lowest-lying triplet state (ΔE_{ST}).^[21] To realize such small energy gaps, typical TADF emitters comprise metal-free organic donor–acceptor systems or coinage metal CT complexes.^[22,23] However, there are two main disadvantages: the rather low radiative rate and the breadth of the CT emission bands, which is unfavorable for application in displays. Multi-resonance TADF emitters improve these properties, while the ΔE_{ST} remains small. The HOMO and LUMO of these molecules have alternating wave function amplitudes on neighboring atoms.^[24,25] They are often planar polycyclic molecules containing boron and nitrogen.^[18] However, TADF OLEDs still suffer from low efficiencies and degradation, due to long exciton lifetimes.^[12]

The latest generation of OLEDs is trying to improve the efficiency of the devices even further. One concept is to utilize TADF molecules as assistant dopants in

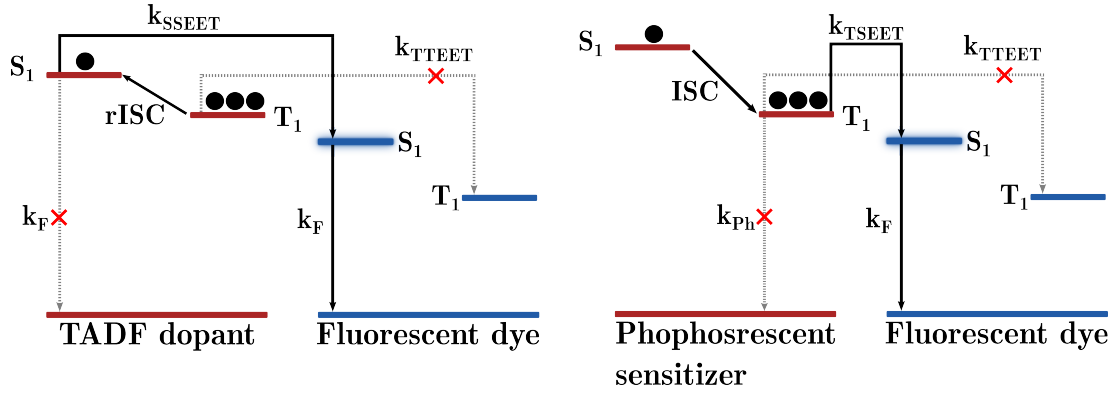


Figure 1.2: Schematic view of hyperfluorescence (left) and phosphor-sensitized fluorescence (right).

conjunction with a fluorescent emitter, which is often called hyperfluorescence or thermally assisted fluorescence (TAF). The primary exciton formation occurs on the TADF molecules, which upconverts the triplet excitons to the lowest singlet state. Subsequently, the excitons are transferred to the lowest excited singlet state on the fluorescent emitter via FRET (Fig. 1.2). The efficient rISC of the TADF assistant dopant enables an IQE of up to 100%, while the emission properties of the fluorescent emitter leads to a high color purity and high stability of the devices. The energy transfer process is strongly dependent on the orientation and the distance between the two interacting molecules. A shorter distance facilitates a faster FRET process, but also increases the likelihood of unwanted processes occurring at shorter distances, such as TTEET. The population of the triplet state of the fluorescent emitter is undesirable due to its non-emissive nature, which can lead to the degradation of the dye. Accordingly, the assistant dopant and the fluorescent emitter have to be incorporated into a host material in low concentrations.^[12,26] The key requirements for the TADF sensitizer are different from those for TADF emitters, as slower rate constants for ISC and fluorescence can still lead to an efficient FRET process.^[27] Instead of using a host material and a sensitizer, TADF type exciplexes can be employed. These exciplexes are formed by complexation of an electron-donating and electron-accepting molecule.^[28-30] Another approach uses phosphorescent molecules as auxiliary dopants, similar to hyperfluorescence. This concept is based on the transfer of energy from a triplet state on the assistant dopant to a singlet state on the fluorescent dye.^[13] By analogy with singlet-singlet excitation energy transfer (SSEET), this mechanism is sometimes referred to as hyperphosphorescence, although this term was also used as an early name for radioactivity.^[31] The term used in this work is therefore phosphor-sensitized fluorescence.

2 Theory

2.1 Density Functional Theory

The majority of the calculations presented in this work are based on the density functional theory (DFT). Similarly to wave function theory (WFT), it is based on solving the time-independent non-relativistic Schrödinger equation of an n -electron system:

$$\left[\sum_{i=1}^n \left(-\frac{\hbar^2}{2m} \nabla_i^2 \right) + \sum_{i=1}^n V(\mathbf{r}_i) + \sum_{i=1}^n \sum_{j<i}^n U(\mathbf{r}_i, \mathbf{r}_j) \right] \psi = E\psi \quad (2.1)$$

where the first term in the square brackets represents the kinetic energy of each electron, the second term the interaction energy between each electron and the collection of atomic nuclei, and the last one the interaction energy between different electrons.^[32] In contrast to wave function based methods, which require the solution of a $3n$ -dimensional equation, DFT separates the problem into n individual 3-dimensional ones by utilizing the electron density.^[33] Using electron density in electronic structure calculations was known earlier^[34], but its practical implementation became feasible only after Hohenberg and Kohn proposed their theorems.^[35] In the approach subsequently developed by Kohn and Sham, the exact electron density can, in theory, be determined by solving an equation for each electron. The Kohn-Sham equations are analogous to Eq. 2.1:

$$\left[\left(-\frac{\hbar^2}{2m} \nabla^2 \right) + V(\mathbf{r}) + V_H(\mathbf{r}) + V_{XC}(\mathbf{r}) \right] \psi_i(\mathbf{r}) = \epsilon_i \psi_i(\mathbf{r}) \quad (2.2)$$

with the first potential in this equation being identical to that in Eq. 2.1. The second potential defines the Coulomb repulsion between the electron and the electron density $\rho(\mathbf{r})$:

$$V_H(\mathbf{r}) = e^2 \int \frac{\rho(\mathbf{r}')}{|\mathbf{r} - \mathbf{r}'|} d^3\mathbf{r}' \quad (2.3)$$

As the electron itself is also part of the electron density, this term includes the so-called self-interaction. The last potential describes exchange (X) and correlation (C) contributions and, among other things, attempts to correct the

self-interaction:

$$V_{XC}(\mathbf{r}) = \frac{\delta E_{XC}(\mathbf{r})}{\delta \rho(\mathbf{r})} \quad (2.4)$$

However, this potential is very difficult to define and requires approximations. The energy of the exchange-correlation term (E_{XC}) is approximately less than 10% of the total energy, yet it remains a crucial factor in determining material properties, such as the formation of covalent bonds.^[33] It follows that the quality of a DFT calculation is dependent on the XC approximation. There are a number of approximations for the density functional of the XC energy. In the local density approximation (LDA), the complex electron density is divided into a number of discrete regions of uniform electron density. Subsequently, the energies of these local elements are summed up to get the total energy. This approach is relatively straightforward but also has certain limitations. In the generalized gradient approximation (GGA) the energy density and its gradient at a given point are employed to improve the LDA. They can be further enhanced by mixing non-local Hartree-Fock (HF) exchange energy into the functionals:

$$E_{XC} = cE_X^{\text{HF}} + (1 - c)E_X^{\text{GGA}} + E_C^{\text{GGA}} \quad (2.5)$$

Additionally, a correction can be incorporated to include long-range electron-electron exchange interactions. Hybrid methods that employ long-range corrections utilize 100% HF exchange for the long-range component of the interelectron repulsion operator, a semilocal exchange density functional for the complementary short-range operator, and a semilocal correlation density functional. A parameter, ω , is often defined to control the mixing, with the degree of mixing varying depending on the interelectron distance.^[36]

The calculations included in this thesis were performed using the following density functionals: BH-LYP^[37], PBE0^[38], and LC- ω HPBE^[39,40].

2.2 Time-Dependent Density Functional Theory

Since DFT is only valid for the electronic ground state, its basic idea has been extended to time-dependent density functional theory (TDDFT) to describe excited states. It is based on the statement that the time-dependent density can unambiguously describe a molecule under a time-dependent perturbation.^[41] The foundation for modern TDDFT was laid by Runge and Gross and their theorems^[42], which have similarities to those of Hohenberg and Kohn. The

starting point is again the Schrödinger equation but in its time-dependent form:

$$i \frac{\delta}{\delta t} \psi(\{\mathbf{r}\}, t) = \hat{H}(\{\mathbf{r}\}, t) \psi(\{\mathbf{r}\}, t) \quad (2.6)$$

In a very similar Kohn-Sham approach for the ground state DFT one can formulate time-dependent Kohn-Sham equations:

$$i \frac{\delta}{\delta t} \phi_i(\mathbf{r}, t) = \hat{H}_{KS}(\mathbf{r}, t) \phi_i(\mathbf{r}, t) \quad (2.7)$$

with the time-dependent Kohn-Sham orbitals $\phi_i(\mathbf{r}, t)$ and the Kohn-Sham Hamiltonian defined as:

$$\hat{H}_{KS}(\mathbf{r}, t) = -\frac{\nabla^2}{2} + v_{ext}(\mathbf{r}, t) + v_H[\rho](\mathbf{r}, t) + v_{XC}[\rho](\mathbf{r}, t) \quad (2.8)$$

The XC potential is a collection of all non-trivial many-body effects and needs to be approximated. This is, similar to ground state DFT, the only fundamental approximation in TDDFT.

Because the total energy is not a conserved quantity in a time-dependent system the variational principle can not be based on the total energy. However, the variational principle can be applied to the quantum mechanical action.^[43] For weak external perturbations, the time-dependent equations can be solved using linear response theory. This leads to a non-Hermitian eigenvalue equation often written in matrix form:^[44]

$$\begin{bmatrix} \mathbf{A} & \mathbf{B} \\ \mathbf{B}^* & \mathbf{A}^* \end{bmatrix} \begin{pmatrix} \vec{X} \\ \vec{Y} \end{pmatrix} = \omega \begin{bmatrix} \mathbf{1} & \mathbf{0} \\ \mathbf{0} & -\mathbf{1} \end{bmatrix} \begin{pmatrix} \vec{X} \\ \vec{Y} \end{pmatrix} \quad (2.9)$$

where ω is the excitation (de-excitation) energy and the elements of the matrices \mathbf{A} and \mathbf{B} are defined as:^[45]

$$\begin{aligned} A_{ia,jb} &= \delta_{ij} \delta_{ab} (\epsilon_a - \epsilon_i) + K_{ia,jb} \\ B_{ia,jb} &= K_{ia,bj} \end{aligned} \quad (2.10)$$

The indices i, j are occupied, a, b unoccupied MOs and ϵ their respective energies. The coupling matrix $K_{ia,jb}$ is defined as:

$$K_{ia,jb} = (ia|jb) + (ia|f_{XC}|jb) + K_{ia,jb}^{\text{HF}} \quad (2.11)$$

Here, $K_{ia,jb}^{\text{HF}}$ is the mixed HF exchange integral term, which is 0 in case of pure functionals and is:

$$K_{ia,jb}^{\text{HF}} = c_x (ja|ib) \quad (2.12)$$

for hybrid functionals, with the constant mixing rate c_x . Additionally, long-range corrected exchange functionals also exhibit non-zero terms.^[45]

The Tamm-Dancoff approximation (TDA) often produces similar results as standard TDDFT and can cut computational cost and reduces triplet instabilities. In this approximation, the occupied virtual elements and therefore the \mathbf{B} matrix is neglected, which leads to a Hermitian eigenvalue equation:^[46]

$$\mathbf{A}\vec{X} = \omega\vec{X} \tag{2.13}$$

2.3 Solvation Effects

Accurately describing solvation effects on molecules is an important step in the computation of photophysical processes. The influence on photophysical processes stems from different charge distributions in the ground and excited states. This difference can lead to stabilization or destabilization of excited states and thus to shifts of the emission energies and changes in the energetic order of excited states. One way of including solvent effects into quantum mechanical calculations are explicit solvent molecules, placed around the solute. While it offers a high degree of accuracy, this method can be computationally demanding due to the increased number of atoms and the need for extensive sampling to account for solvent fluctuations.^[47] In contrast, implicit solvation models treat the solvent as a continuous medium characterized by its dielectric constant, without explicitly modeling individual solvent molecules. This approach greatly reduces computational cost while providing a satisfactory approximation of solvation effects, particularly for systems where specific solute-solvent interactions are not dominant. The polarizable continuum model (PCM) is one of the most widely used implicit solvation models. Here, the interaction between the solute and the solvent is characterized by the polarization of the solvent continuum in response to the solute’s electric field. In this work, the integral equation formalism (IEFPCM) was used.^[48,49]

2.4 DFT/MRCI

The semiempirical DFT/MRCI method is a combination of the DFT and the multireference configuration interaction (MRCI) methods. During this work it was used to calculate vertical excited state properties and is the foundation of subsequent energy transfer calculations. One of advantages of the DFT/MRCI method is the balanced description of correlation effects. The dynamic correlation

is well described by DFT while the static correlation is accounted for by the MRCI method. Because some dynamic correlation is also provided by MRCI, a correction in the Hamiltonian is needed to avoid double counting. In DFT/MRCI, the MRCI wave function is constructed from a one-electron basis of Kohn-Sham (KS) orbitals and a closed or single open-shell anchor configuration.

The spin-independent electronic Hamiltonian in second quantization can be written as:^[50]

$$\hat{\mathcal{H}} = \sum_{ij} h_{ij} \hat{E}_i^j + \frac{1}{2} \sum_{ijkl} V_{ijkl} (\hat{E}_i^j \hat{E}_k^l - \delta_{jk} \hat{E}_i^l) \quad (2.14)$$

where h_{ij} is a one-electron integral, \hat{E}_i^j a one-electron excitation operator that annihilates an electron in orbital j and creates one in orbital i and V_{ijkl} is a two-electron integral. Following Wetmore and Segal^[51,52] this can be reformulated to:

$$\begin{aligned} \hat{\mathcal{H}}^{CI} = & E^{\text{SCF}} - \sum_i F_{ii} \bar{w}_i + \frac{1}{2} \sum_{ij} \left(V_{ijij} - \frac{1}{2} V_{ijji} \right) \bar{w}_i \bar{w}_j \\ & + \sum_{ij} F_{ij} \hat{E}_i^j - \sum_{ijk} \left(V_{ikjk} - \frac{1}{2} V_{ikkj} \right) \bar{w}_k \hat{E}_i^j \\ & + \frac{1}{2} \sum_{ijkl} V_{ijkl} (\hat{E}_i^j \hat{E}_k^l - \delta_{jk} \hat{E}_i^l) \end{aligned} \quad (2.15)$$

where \bar{w}_i is the occupation of the orbital i and F_{ij} are elements of the Fock matrix:

$$F_{ij} = h_{ij} + \sum_k \bar{w}_k \left(V_{ikjk} - \frac{1}{2} V_{ikkj} \right) \quad (2.16)$$

The diagonal elements F_{ii} of the Fock matrix are the MO energies. Eq. 2.15 is the starting point of the original DFT/MRCI modifications of Grimme and Waletzke.^[53] The Hamilton matrix elements are divided into diagonal and off-diagonal contributions of one- and two-electron differences. The diagonal matrix elements in the DFT/MRCI Hamiltonian can be written as:

$$\begin{aligned} \langle \omega w | \hat{\mathcal{H}}^{\text{DFT}} - E^{\text{DFT}} | \omega w \rangle = & \langle \omega w | \hat{\mathcal{H}} - E^{\text{HF}} | \omega w \rangle - \sum_{i \in c}^{n_{exc}} (F_{ii}^{\text{HF}} - F_{ii}^{\text{KS}}) \\ & + \sum_{i \in a}^{n_{exc}} (F_{ii}^{\text{HF}} - F_{ii}^{\text{KS}}) + \Delta E_{\text{coul}} - \Delta E_{\text{exch}} \end{aligned} \quad (2.17)$$

Here, E^{DFT} is the total KS energy of the anchor configuration, n_{exc} is the number of excitations and c and a represent created and annihilated electrons. F_{ii}^{HF} is an effective one-electron matrix element build up in a HF-like manner from the given KS orbital basis. Therefore, E^{HF} is not the total HF energy but can be expressed

2 Theory

as:

$$E^{\text{HF}} = \sum_i \bar{w}_i F_{ii}^{\text{HF}} - \frac{1}{2} \sum_{ik} \bar{w}_i \bar{w}_k \left(V_{ikik} - \frac{1}{2} V_{ikki} \right) \quad (2.18)$$

with \bar{w}_i being the occupation number. The two-electron contributions ΔE_{coul} and ΔE_{exch} are corrected by parameters fitted to match the energy of small organic molecules. In the original Hamiltonian of Grimme and Waletzke^[53] the fitted parameters are dependent of the spin multiplicity. The redesigned Hamiltonian of Lyskov^[54] (R2016) has multiplicity-independent parameters to better describe photoexcited dimers. It is formulated only for a closed-shell anchor and was extended by Heil^[55] for systems with an open-shell configuration (R2017).

In contrast to the diagonal elements, off-diagonal elements with same spatial occupation are not scaled in the original Hamiltonian. In the redesigned Hamiltonians an exchange correction parameter is introduced, leading to:

$$\langle \omega w | \hat{\mathcal{H}}^{\text{DFT}} | \omega' w \rangle = \langle \omega w | (1 - p_X) \hat{\mathcal{H}}^{\text{CI}} | \omega' w \rangle \quad (2.19)$$

Scaling of off-diagonal elements with unequal spatial occupation is crucial in the DFT/MRCI method, since double (and higher) excitations into energetically high-lying orbitals introduce dynamic correlation in an *ab initio* CI treatment. But in DFT/MRCI, this type of correlation is already taken care of by the DFT exchange correlation functional. In order to avoid double counting, the contributions of these excitations have to be scaled down. In the original Hamiltonian an exponential damping function is used, while in the redesigned Hamiltonian R2016 and R2017 a different function is used:

$$\langle \omega w | \hat{\mathcal{H}}^{\text{DFT}} | \omega' w \rangle = \langle \omega w | \hat{\mathcal{H}}^{\text{CI}} | \omega' w \rangle \frac{p_1}{1 + (p_2 \Delta E_{\omega w'})^5 \arctan(p_2 \Delta E_{\omega w'})^5} \quad (2.20)$$

Because these Hamiltonians have problems to accurately describe 3d elements, another redesigned Hamiltonian was introduced by Heil^[56] (R2018) with a damping function similar to that of the original Hamiltonian:

$$\langle \omega w | \hat{\mathcal{H}}^{\text{DFT}} | \omega' w \rangle = \langle \omega w | \hat{\mathcal{H}}^{\text{CI}} | \omega' w \rangle p_1 e^{-p_2 \Delta E_{\omega w'}^6} \quad (2.21)$$

Recently, a new modification of the Hamiltonian (R2022) was published to improve the description of doubly excited and degenerate states.^[57] Here, the diagonal correction is separated for double excitations depending on whether the two electrons are from the same or from different orbitals.

In this work the redesigned Hamiltonians R2016, R2017 and R2018 were used for the calculation of excited state properties.

2.5 Spin–Orbit Coupling

Spin–orbit coupling is a relativistic effect and is the main reason for the zero field splitting (ZFS) of electronic spin multiplets. In addition, it can also couple states of different spin multiplicities, which leads to measurable phosphorescence and ISC rate constants even in purely organic molecules.^[58]

Spin–orbit effects can be calculated with the help of spin–orbit Hamiltonians. One of the most commonly used ones is the one- and two-electron Breit-Pauli Hamiltonian:

$$\hat{\mathcal{H}}_{\text{SO}}^{\text{BP}} = \frac{e^2}{2m_e^2 c^2} \left(\hat{h}_{\text{SO}}^{\text{BP}}(1) + \hat{\mathcal{H}}_{\text{SO}}^{\text{BP}}(1, 2) \right) \quad (2.22)$$

Here, e and m_e are the charge and mass of an electron and c is the speed of light. The one-electron part $\hat{h}_{\text{SO}}^{\text{BP}}(1)$ is determined by the interaction of the spin magnetic moment of an electron i with the magnetic moment caused by orbiting in the field of the nucleus I with its charge Z_I :

$$\hat{h}_{\text{SO}}^{\text{BP}}(1) = \sum_i \left(-\nabla_i \left(\sum_I \frac{Z_I}{\hat{r}_{iI}} \right) \times \hat{p}_i \right) \cdot \hat{s}_i \quad (2.23)$$

The two-electron term consists of a spin-same-orbit term where the spin and orbital magnetic moments are from the same electron and two spin-other-orbit terms in which the momenta belong to different electrons:^[59]

$$\begin{aligned} \hat{\mathcal{H}}_{\text{SO}}^{\text{BP}}(1, 2) = & \sum_i \sum_{j \neq i} \left(\nabla_i \left(\frac{1}{\hat{r}_{ij}} \right) \times \hat{p}_i \right) \cdot \hat{s}_i \\ & + \sum_i \sum_{j \neq i} \left(\nabla_j \left(\frac{1}{\hat{r}_{ij}} \right) \times \hat{p}_j \right) \cdot \hat{s}_i \\ & + \sum_j \sum_{i \neq j} \left(\nabla_i \left(\frac{1}{\hat{r}_{ji}} \right) \times \hat{p}_i \right) \cdot \hat{s}_j \end{aligned} \quad (2.24)$$

To reduce computational cost, a spin–orbit mean field (SOMF) Hamiltonian based on the Breit-Pauli Hamiltonian is used. Thereby, the screening by other electrons is done in a HF-like mean field approach to get an effective one-electron operator. Utilizing this SOMF Hamiltonian, a resulting matrix element is given by:^[60]

$$\begin{aligned} \langle i(1) | \hat{\mathcal{H}}_{\text{SO}}^{\text{mf}} | j(1) \rangle = & \langle i(1) | \hat{h}_{\text{SO}}^{\text{BP}} | j(1) \rangle \\ & + \frac{1}{2} \sum_k n_k \{ 2 \langle i(1)k(2) | \hat{\mathcal{H}}_{\text{SO}}^{\text{BP}}(1, 2) | j(1)k(2) \rangle \\ & - 3 \langle k(1)i(2) | \hat{\mathcal{H}}_{\text{SO}}^{\text{BP}}(1, 2) | j(1)k(2) \rangle \\ & - 3 \langle k(1)i(2) | \hat{\mathcal{H}}_{\text{SO}}^{\text{BP}}(1, 2) | k(1)j(2) \rangle \} \end{aligned} \quad (2.25)$$

2 Theory

In order to further reduce the computational effort, the multicenter spin-orbit integrals are neglected, resulting in a sum of atomic mean fields. In this case, the index k runs over all spatial atomic orbitals, with n_k being their occupation number.^[60] The spin-orbit coupling matrix elements (SOCMEs), calculated with the SOMF operator, are involved in the determination of ISC rate constants (see Sec. 2.6.1). For the computation of phosphorescence rate constants and excitonic coupling matrix elements (ECMEs) in phosphor-sensitized fluorescence systems, mixed spin wave functions are needed. A computationally cheap method to obtain them is the spin-orbit coupling quasi-degenerate perturbation theory (SOCQDPT). Unfortunately, SOCQDPT is known to converge very slowly for phosphorescence rate constants.^[61] The more sophisticated method used in this work is the combined method of DFT and multireference spin-orbit configuration interaction (MRSOCI). Here, the DFT/MRCI pure-spin wave functions and the SOCMEs are used as a start. After a Davidson diagonalization of the complex-valued Hamiltonian matrix, the mixed spin wave functions are obtained. The MRSOCI wave function $|A\rangle$ can be written as a linear combination of configuration state functions (CSFs):^[60]

$$|A\rangle = \sum_{S=S_{\min}}^{S_{\max}} \sum_{M_S=-S}^S \sum_{\{\Gamma\}} \sum_{\{\mathbf{n}\}} \sum_{\omega(\mathbf{n})} a_{S,M_S,\Gamma,\mathbf{n},\omega(\mathbf{n})} |S, M_S, \Gamma, \mathbf{n}, \omega(\mathbf{n})\rangle \quad (2.26)$$

where S and M_S are the spin quantum numbers, Γ the irreducible representations, \mathbf{n} the configurations and $\omega(\mathbf{n})$ the associated CSF indices. Using a similar notation for $|B\rangle$ and the (spin-free) η coefficients of Wetmore and Segal^[51], the elements ρ_{ij}^{BA} of the reduced one-particle transition density matrix (1-RTDM) can be expressed as:

$$\begin{aligned} \rho_{ij}^{BA} = & \sum_{S=S_{\min}}^{S_{\max}} \sum_{M_S=-S}^S \sum_{\{\Gamma\}} \sum_{\{\mathbf{n}\}} \sum_{\omega(\mathbf{n})} \eta(S, \mathbf{n}, \omega(\mathbf{n}), \mathbf{n}', \omega'(\mathbf{n}')) \\ & \times \sum_{M_S=-S}^S a_{S,M_S,\Gamma,\mathbf{n},\omega(\mathbf{n})}^* b_{S,M_S,\Gamma',\mathbf{n}',\omega'(\mathbf{n}')} \end{aligned} \quad (2.27)$$

In contrast to spin-orbit-free MRCI wave functions, a summation over the spin quantum numbers is performed. Additionally, the 1-RTDMs are complex-valued for the MRSOCI case.

2.6 Rate Constants

2.6.1 Non-radiative Rate Constants

Fermi's Golden Rule

Fermi's golden rule can be used to calculate rate constants when an initial state is weakly coupled to a continuum of final states. The starting point is a system described by a Hamiltonian:^[62–65]

$$\mathcal{H}\psi = i\hbar \frac{\partial}{\partial t} \psi \quad (2.28)$$

with \mathcal{H} being:

$$\mathcal{H} = \mathcal{H}_0 + \mathcal{H}' \quad (2.29)$$

Here, \mathcal{H}_0 is a time-independent operator, while \mathcal{H}' is a time-dependent perturbation. The eigenfunctions ϕ_n of the unperturbed Hamiltonian are orthonormal and fulfill the condition:

$$\mathcal{H}_0\phi_n = E_n\phi_n \quad (2.30)$$

The eigenfunctions $\psi_n(t)$ of the time-dependent Schrödinger equation are split into a time-independent term, equivalent to the eigenfunctions of \mathcal{H}_0 , and a time-dependent imaginary exponential function:

$$\psi_n(t) = \phi_n e^{-iE_n t/\hbar} \quad (2.31)$$

The wave function of the perturbed system can be expressed as a linear combination of the unperturbed wave functions, where the coefficients $a_n(t)$ are time-dependent:

$$\psi(t) = \sum_n a_n(t) \phi_n e^{-iE_n t/\hbar} \quad (2.32)$$

Inserting Eq. 2.32 into Eq. 2.28 one obtains:

$$\sum_n a_n(t) \mathcal{H}_0 \phi_n e^{-iE_n t/\hbar} + \sum_n a_n(t) \mathcal{H}' \phi_n e^{-iE_n t/\hbar} = \frac{\partial}{\partial t} i\hbar \sum_n a_n(t) \phi_n e^{-iE_n t/\hbar} \quad (2.33)$$

Using Eq. 2.30 and the product rule for the derivative on the right side the expression becomes:

$$\begin{aligned} \sum_n a_n(t) E_n \phi_n e^{-iE_n t/\hbar} + \sum_n a_n(t) \mathcal{H}' \phi_n e^{-iE_n t/\hbar} \\ = i\hbar \sum_n \frac{\partial}{\partial t} a_n(t) \phi_n e^{-iE_n t/\hbar} + \sum_n a_n(t) E_n e^{-iE_n t/\hbar} \end{aligned} \quad (2.34)$$

2 Theory

where the outer terms cancel each other:

$$\sum_n a_n(t) \mathcal{H}' \phi_n e^{-iE_n t/\hbar} = i\hbar \sum_n \frac{\partial}{\partial t} a_n(t) \phi_n e^{-iE_n t/\hbar} \quad (2.35)$$

Multiplying with ϕ_k from the left using the orthogonality ($\langle \phi_k | \phi_n \rangle = \delta_{kn}$) and the matrix element $\mathcal{H}'_{kn} = \langle \phi_k | \mathcal{H}' | \phi_n \rangle$ yields the following expression:

$$\sum_n a_n(t) \mathcal{H}'_{kn} e^{-iE_n t/\hbar} = i\hbar \frac{\partial}{\partial t} a_k(t) e^{-iE_k t/\hbar} \quad (2.36)$$

Rearranging to isolate $\frac{\partial}{\partial t} a_k(t)$ leads to:

$$\frac{\partial}{\partial t} a_k(t) = \frac{1}{i\hbar} \sum_n a_n(t) \mathcal{H}'_{kn} e^{i\omega_{kn} t} \quad (2.37)$$

where:

$$\omega_{kn} = \frac{E_k - E_n}{\hbar} \quad (2.38)$$

For small systems, such as two-level systems, Eq. 2.37 can be solved explicitly. In cases of bigger systems a perturbation expansion is needed to solve it approximately. The approximation of order $(p+1)$ is found from the solution of order (p) by:^[64]

$$\frac{\partial}{\partial t} a_k^{(p+1)}(t) = \frac{1}{i\hbar} \sum_n a_n^{(p)}(t) \mathcal{H}'_{kn} e^{i\omega_{kn} t} \quad (2.39)$$

In zeroth order there is no perturbation, so the system would not get out of the initial state m , so that:

$$a_n^{(0)}(t) = \delta_{nm} \quad (2.40)$$

Inserting this into Eq. 2.39 yields the first-order approximation:

$$\frac{\partial}{\partial t} a_k^{(1)}(t) = \frac{1}{i\hbar} \mathcal{H}'_{km} e^{i\omega_{km} t} \quad (2.41)$$

Assuming that the perturbation is starting at $t = 0$ and that \mathcal{H}'_{km} is time-independent, the equation can be solved by integrating:

$$a_k^{(1)}(t) = \frac{1}{i\hbar} \mathcal{H}'_{km} \int_0^t e^{i\omega_{km} t} \quad (2.42)$$

$$= \frac{1}{i\hbar} \mathcal{H}'_{km} \left(\frac{e^{i\omega_{km} t} - 1}{i\omega_{km}} \right) \quad (2.43)$$

$$= \frac{2}{i\hbar} \mathcal{H}'_{km} e^{i\omega_{km} t/2} \frac{\sin(\omega_{km} t/2)}{\omega_{km}} \quad (2.44)$$

The perturbation expansion is truncated after the first-order term, which leads to $a_k(t) \approx a_k^{(1)}(t)$. The transition probability $P_k(t)$ is the probability of finding the system with the initial state m at time t in the state k and is defined as:

$$P_k(t) = |a_k(t)|^2 \approx \frac{4}{\hbar^2} |\mathcal{H}'_{km}|^2 \frac{\sin^2(\omega_{km}t/2)}{\omega_{km}^2} \quad (2.45)$$

Here, the exponential function vanishes because the absolute value of a complex exponential function is 1. The mean rate for the transition is given by the probability per time ($P_{m \rightarrow k}(t)/t$). Seeing that $\frac{\sin^2(\omega_{km}t/2)}{\omega_{km}^2}$ is strongly peaking near $\omega_{km} = 0$ means that in order for a transition to occur the states need to be close in energy ($w_{km} \approx 0$). Since there will be a number of states (dn) fulfilling this condition, the possible transition states are written as:

$$dn = \rho(k)dE_k \quad (2.46)$$

where $\rho(k)$ is the ‘density of states’ per unit energy interval near E_k . In order to get the total transition rate constant to states near k :

$$k_{km} = \frac{1}{t} \sum_{k' \text{ near } k} P_{k'}(t) \quad (2.47)$$

the summation is solved by an integration over dE_k :

$$\begin{aligned} k_{km} &= \frac{1}{t} \int P_{k'}(t) \rho(k') dE_{k'} \\ &= \int \frac{4}{\hbar^2} |\mathcal{H}'_{km}|^2 \frac{1}{t} \frac{\sin^2(\omega_{km}t/2)}{\omega_{km}^2} \rho(k) dE_k \end{aligned} \quad (2.48)$$

Using the relation $E = \omega\hbar$ between the energy E and the angular frequency ω , the expression can be written as:

$$k_{km} = \frac{4}{\hbar^2} |\mathcal{H}'_{km}|^2 \rho(k) \int_{-\infty}^{\infty} \frac{1}{t} \frac{\sin^2(\omega_{km}t/2)}{\omega_{km}^2} d\omega \quad (2.49)$$

where the last integral has the value $\pi/2$ and the expression becomes the famous ‘Golden Rule’ of Fermi:

$$k_{km} = \frac{2\pi}{\hbar^2} |\mathcal{H}'_{km}|^2 \rho(k) \quad (2.50)$$

Intersystem Crossing

Rate constants for ISC can be calculated with Fermi’s golden rule if the spin–orbit interaction between the two interacting states is small compared to their adiabatic energy difference and the density of final states is high at the energy of the

2 Theory

initial state. In case of pure-spin Born-Oppenheimer states, the ISC rate constant between the singlet state S_a and the triplet state T_b^α with fine-structure levels α can be expressed as: [59,66]

$$k_{\text{ISC}} = \frac{2\pi}{\hbar} \left| \sum_k \sum_\alpha \langle v_{bk}, \Psi_{T_b^\alpha} | \hat{\mathcal{H}}_{\text{SO}} | \Psi_{S_a}, v_{aj} \rangle \right|^2 \delta(E_{aj} - E_{bk}) \quad (2.51)$$

where Ψ and v are the electronic and vibrational wave functions, respectively. In Condon approximation, *i.e.*, assuming that the coupling strength does not change upon nuclear distortion, the electronic and vibrational contributions can be separated:

$$k_{\text{ISC}}^{\text{FC}} = \frac{2\pi}{\hbar} \sum_\alpha |\langle \Psi_{T_b^\alpha} | \hat{\mathcal{H}}_{\text{SO}} | \Psi_{S_a} \rangle|_{Q_0}^2 \sum_k |\langle v_{bk} | v_{aj} \rangle|^2 \delta(E_{aj} - E_{bk}) \quad (2.52)$$

Here, Q_0 is the reference point which is often chosen as the minimum geometry of the initial state. The last two terms are the overlap of the vibrational wave functions and are called the Frank-Condon weighted density of states (FCWDOS). For initial states that are spatially degenerate or of higher multiplicity, individual rate constants for every component are determined and then averaged. This is relevant for the rISC process, where the starting point is a triplet state and a factor of 1/3 is used in the equation. Additionally, rISC is oftentimes an uphill process, so temperature effects need to be included. In a thermal equilibrium with the environment, the rate constant can be determined as an ensemble average. To this end, the probability of occupation of the initial vibronic level [67]:

$$p(E_{aj}) = \frac{e^{-\frac{E_{aj}}{k_B T}}}{\sum_j e^{-\frac{E_{aj}}{k_B T}}} = \frac{e^{-\frac{E_{aj}}{k_B T}}}{Z} \quad (2.53)$$

with the Boltzmann constant k_B and the temperature T , is multiplied with Eq. 2.51 and summed up over all initial vibronic levels to get:

$$k_{\text{ISC}}^{\text{FC}} = \frac{2\pi}{\hbar Z} \sum_\alpha |\langle \Psi_{T_b^\alpha} | \hat{\mathcal{H}}_{\text{SO}} | \Psi_{S_a} \rangle|_{Q_0}^2 \sum_{j,k} e^{-\frac{E_{aj}}{k_B T}} |\langle v_{bk} | v_{aj} \rangle|^2 \delta(E_{aj} - E_{bk}) \quad (2.54)$$

where Z can be extracted from the sum over j because it is constant for all vibronic levels.

In some cases, nuclear motion has a large impact on the ISC rate constant, and it is necessary to go beyond the Condon approximation. Then the electronic and vibrational parts of the wave functions can not be separated anymore. For these cases, the Herzberg-Teller (HT) approach can be employed, where two terms are

added to Eq. 2.54:^[68]

$$k_{\text{ISC}}^{\text{FC/HT}} = \frac{4\pi}{\hbar Z} \sum_{\alpha} \langle \Psi_{T_b^{\alpha}} | \hat{\mathcal{H}}_{\text{SO}} | \Psi_{S_a} \rangle \Big|_{Q_0} \quad (2.55)$$

$$\times \sum_{j,k} e^{\frac{-E_{aj}}{k_B T}} \langle v_{bk} | v_{aj} \rangle \langle v_{bk} | \mathbf{b}^{\dagger} \mathbf{Q}_S | v_{aj} \rangle \delta(E_{aj} - E_{bk})$$

$$k_{\text{ISC}}^{\text{HT}} = \frac{2\pi}{\hbar Z} \sum_{j,k} e^{\frac{-E_{aj}}{k_B T}} \left| \langle v_{bk} | \mathbf{b}^{\dagger} \mathbf{Q}_S | v_{aj} \rangle \right|^2 \delta(E_{aj} - E_{bk}) \quad (2.56)$$

where \mathbf{Q}_S contains the normal mode coordinates of the initial state and \mathbf{b} contains the first-order derivatives of the electronic coupling:

$$b_k = \frac{\partial \langle \Psi_{T_b^{\alpha}} | \hat{\mathcal{H}}_{\text{SO}} | \Psi_{S_a} \rangle}{\partial (Q_S)_k} \Big|_{Q_0} \quad (2.57)$$

In order to cut the computational cost that comes from the summation over all final vibrational states, Fermi's golden rule can be transformed into the Heisenberg picture. The FCWDOS is then obtained by performing an integration of a correlation function (see Sec. 2.7).^[69]

There are some qualitative rules for estimating the size of ISC rate constants. The El-Sayed rule states that the SOC, and therefore the ISC rate, is relatively large if the transition involves a change of orbital type.^[3,70] In addition, there are four other conditions. The leading configurations must be singly excited with respect to each other, and the excited orbitals must have electron density distributions on the same atoms. The angular momentum of the orbitals must also be conserved, and their magnetic quantum number must not change by more than 1. Finally, the spin multiplicities have to differ by 2.^[66] According to this rule, $^1\pi\pi^* \rightsquigarrow ^3\text{n}\pi^*$ and $^1\text{n}\pi^* \rightsquigarrow ^3\pi\pi^*$ are faster than $^1\pi\pi^* \rightsquigarrow ^3\pi\pi^*$ and $^1\text{n}\pi^* \rightsquigarrow ^3\text{n}\pi^*$ in typical organic molecules.

The second qualitative rule, which is separated into two cases, concerns the vibrational contributions to the ISC rate constant. The weak coupling limit describes the radiationless transition between states with small geometric displacements. Here, the FCWDOS decreases exponentially with increasing adiabatic energy separation of the two potential energy surfaces (PESs). For states with large geometrical displacements, the strong coupling case, a Gaussian-shaped dependency on the energy gap is observed.^[66]

Internal Conversion

The determination of internal conversion (IC) rate constants is reliant on the derivative couplings, also called non-adiabatic coupling matrix elements (NACMEs):

$$V_{ab}^{\text{IC}} = \langle \Psi_{b,S',M'_S} \{v_{bk}\} | \nabla_{Q_a}^\dagger \nabla_{Q_a} | \Psi_{a,S,M_S} \{v_{aj}\} \rangle \delta_{S,S'} \delta_{M_S,M'_S} \quad (2.58)$$

$$\approx \sum_k^{3N-6} \left\langle \{v_{bk}\} \left| \left\langle \Psi_b \left| \frac{\partial}{\partial Q_{ak}} \right| \Psi_a \right\rangle \frac{\partial}{\partial Q_{ak}} \right| \{v_{aj}\} \right\rangle \quad (2.59)$$

$$= \sum_k^{3N-6} \left\langle \{v_{bk}\} \left| f_{ab}(k) \frac{\partial}{\partial Q_{ak}} \right| \{v_{aj}\} \right\rangle \quad (2.60)$$

The spin selection rules $\delta_{S,S'}$ and δ_{M_S,M'_S} ensure that IC only occurs between states with same spin quantum numbers. In this work, these NACMEs are computed as finite differences of wave function overlaps.^[71,72] The straightforward calculation of these NACMEs is computationally very expensive, because the overlap between every Slater determinant of the initial state with every determinant of the final state has to be evaluated. To cut computation time, the number of overlapping determinants can be reduced, for example, by making use of symmetry selection rules and truncating the CI expansion.^[72]

2.6.2 Radiative Rate Constants

Radiative rate constants can also be expressed through Fermi's golden rule:

$$k_{\text{rad}} = \frac{4e^2}{3c^3\hbar^4} |\langle \Psi_0 | \hat{\mu}_{el} | \Psi_I \rangle|^2 \Delta E_{I0}^3 \quad (2.61)$$

Here, $\langle \Psi_0 | \hat{\mu}_{el} | \Psi_I \rangle$ is the electronic transition dipole moment and ΔE_{I0} the energy gap between the initial state Ψ_I and the ground state Ψ_0 . For the phosphorescence, the rate constant has to be computed for every triplet sublevel (α, β, γ) . At high temperatures and a small ZFS the total rate constant can be described by an average:

$$k_{\text{Ph}} = \frac{1}{3} (k_{\text{rad},\alpha} + k_{\text{rad},\beta} + k_{\text{rad},\gamma}) \quad (2.62)$$

If these conditions are not fulfilled the rate constant is calculated considering the Boltzmann population of each state:^[73]

$$k_{\text{Ph}} = \frac{k_\alpha + k_\beta e^{\Delta E_{\alpha,\beta}/k_B T} + k_\gamma e^{\Delta E_{\alpha,\gamma}/k_B T}}{1 + e^{\Delta E_{\alpha,\beta}/k_B T} + e^{\Delta E_{\alpha,\gamma}/k_B T}} \quad (2.63)$$

2.7 Vibronic Transitions

The determination of vibrationally resolved emission and absorption spectra, as well as the ISC rate constant, is contingent upon the calculation of vibronic transitions, which combine electronic and vibrational transitions. There are two approaches to compute vibronic transitions. The time-independent approach demands significant computational effort, because each vibrational transition is calculated individually. Therefore, this approach is not suitable for the size of the molecules discussed in this thesis, even if the computational effort can be reduced by discarding selected vibrational levels.

In the time-dependent approach, the calculation of all vibronic transitions is performed simultaneously through the utilization of a generating function or time-correlation formalism. The expression for the ISC rate constant in Condon approximation can then be expressed as follows:^[74]

$$k_{\text{ISC}}^{\text{FC}} = \frac{1}{Z} |\langle \Psi_S | \hat{H}_{\text{SO}} | \Psi_T \rangle|^2 \int_{-\infty}^{\infty} G(t) e^{\frac{it}{\hbar} \Delta E_{ST}^0} dt \quad (2.64)$$

where $G(t)$ denotes the correlation function between the harmonic oscillator eigenfunctions for the singlet and triplet states, and the time-integration is done numerically.

In both approaches, knowledge of the PES associated with the electronic states involved in the transition is required. In the adiabatic Hessian (AH) model, the PES is described by a harmonic function at the minimum structures of both involved electronic states. This approach yields good results for rigid systems, for which the harmonic approximation holds. However, in certain instances, the calculation of the stationary point of the final state can be challenging due to crossing of PESs. In such cases, the vertical Hessian (VH) method can be employed, as it only necessitates the knowledge of the equilibrium geometry of the initial state. The PES of the final state is then extrapolated by the Hessian matrix and gradients at this Franck-Condon point. The VH method provides favorable outcomes for peak maxima and short-time spectra, where nuclei have not yet fully adapted to the electronic potential of the final state.^[74,75]

2.8 Excitation Energy Transfer

In the weak coupling regime, the EET rate constant between the donor (D) and the acceptor (A) follows Fermi's golden rule expression:^[76]

$$k_{\text{EET}} = \frac{2\pi}{\hbar} |V_{\text{DA}}|^2 \rho(E) \quad (2.65)$$

2 Theory

where $\rho(E)$ is the FCWDOS and V_{DA} is the ECME. The FCWDOS is often approximated with the spectral overlap integral:^[77]

$$k_{\text{EET}} = \frac{2\pi}{\hbar} |V_{\text{DA}}|^2 \int_0^\infty E_{\text{D}}(\omega) A_{\text{A}}(\omega) d\omega \quad (2.66)$$

For the spectral overlap integral the product function of the normalized donor emission ($E_{\text{D}}(\omega)$) and normalized acceptor absorption ($A_{\text{A}}(\omega)$) spectra has to be integrated.

In a two-state system of a homo dimer, the ECME can be expressed as half the energy difference between the two interacting states:

$$V_{\text{DA}} = \frac{\Delta E}{2} \quad (2.67)$$

This splitting is often called Davydov splitting. Given that the two-state model frequently proves inadequate, even for small molecules such as the ethylene dimer, it is evident that alternative approaches are necessary.^[78] Diabatization schemes are capable of calculating the coupling for hetero dimers, by rotating the adiabatic states into a set of diabatic states. The ECME is then determined with the help of a mixing angle (θ):^[79]

$$V_{\text{DA}} = \frac{1}{2} \sin(2\theta) (\epsilon_2 - \epsilon_1) \quad (2.68)$$

The mixing angle can be computed by finding a rotation matrix connecting the adiabatic and diabatic states. The rotation matrix is determined by maximizing different localizing functions.^[79,80]

As diabatization requires the calculation of the full system, there is a need for computational methods that are more efficient in calculating the ECME. Two such methods will be discussed in the following sections.

2.8.1 Ideal Dipole Approximation

The ideal dipole approximation (IDA) rests on a dipole-dipole Coulomb interaction between donor and acceptor. This approximation is applicable if the spatial extension of both transition densities is small compared to the intermolecular distance \vec{R}_{DA} . Then, the ECME can be expressed as:

$$V_{\text{DA}} = \kappa \frac{|\vec{\mu}_{\text{D}}| |\vec{\mu}_{\text{A}}^*|}{n |\vec{R}_{\text{DA}}|^3} \quad (2.69)$$

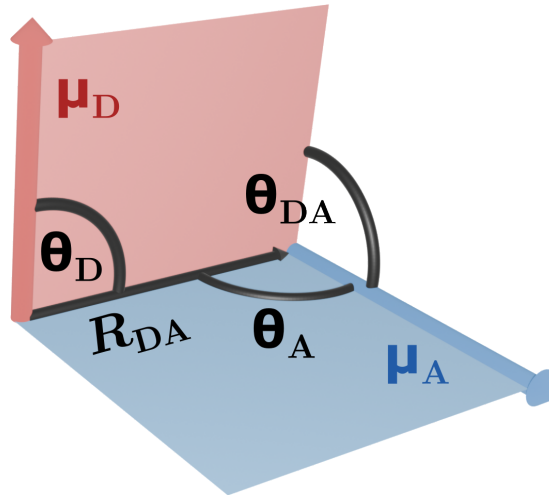


Figure 2.1: Graphical representation of values used in the determination of the orientation factor (κ^2).

where n is the refractive index of the surrounding medium and $\vec{\mu}_D$ and $\vec{\mu}_A$ are the electric transition dipole moments of donor and acceptor, respectively. The orientation factor (κ^2) depends on the relative orientation of the molecules and can be expressed in terms of the unit vectors of $\vec{\mu}$ (\vec{n}) and \vec{R}_{DA} (\vec{e}_{DA}):

$$\kappa^2 = (\vec{n}_D \vec{n}_A - 3(\vec{e}_{DA} \vec{n}_D)(\vec{e}_{DA} \vec{n}_A))^2 \quad (2.70)$$

or using the angle between transition dipole moments (θ_{DA}) and the angles between the dipole moments and the vector connecting the interacting molecules (Fig. 2.1):

$$\kappa^2 = (\cos(\theta_{DA}) - 3 \cos(\theta_D) \cos(\theta_A))^2 \quad (2.71)$$

The orientation factor can adopt values in the range of 0 for a perfectly perpendicular orientation of the transition dipole moment vectors (TDMVs) to 4 for a collinear arrangement of the TDMVs. Note, however, that different orientations can lead to the same κ^2 values. In case of two freely movable and rotatable molecules, κ^2 is often approximated to $2/3$.^[81] For random but rigid orientations, its average is estimated to be lower ($\kappa^2 = 0.476$).^[82]

Since IDA neglects exchange interaction between the molecules, it can not describe Dexter EET, leading to a failure of this approach at close donor–acceptor distances.^[83]

2.8.2 Monomer Transition Density Approach

In the monomer transition density (MTD) approach, the ECMEs are computed with the help of 1-RTDMs. As the name suggests, it is a fragmentation-based

2 Theory

method, where the antisymmetrization of the wave functions of the fragments is neglected. This results in a significant reduction in computational cost compared to full system calculations, such as diabaticization approaches. For molecular aggregates, the electronic Hamiltonian can be expressed as the Hamiltonian of the individual molecules and a coupling operator for each pair of molecules. In the case of a donor–acceptor system like in EET, the Hamiltonian has the form:^[77,84]

$$\hat{\mathcal{H}}_{\text{DA}} = \hat{\mathcal{H}}_{\text{D}} + \hat{\mathcal{H}}_{\text{A}} + \hat{\mathcal{V}}_{\text{DA}} \quad (2.72)$$

For the energy transfer process, a two-level system is assumed in order to solve the Schrödinger equation of the supermolecular system:

$$\hat{\mathcal{H}}\Psi = E\Psi \quad (2.73)$$

where the wave function is written as a linear combination of locally excited states:

$$\Psi = C_1\psi_{\text{D}^*\text{A}} + C_2\psi_{\text{DA}^*} \quad (2.74)$$

This leads to a matrix equation for the expansion coefficients $C_{1,2}$:

$$\begin{pmatrix} \langle \psi_{\text{D}^*\text{A}} | \hat{\mathcal{H}}_{\text{DA}} | \psi_{\text{D}^*\text{A}} \rangle - E & \langle \psi_{\text{D}^*\text{A}} | \hat{\mathcal{H}}_{\text{DA}} | \psi_{\text{DA}^*} \rangle \\ \langle \psi_{\text{DA}^*} | \hat{\mathcal{H}}_{\text{DA}} | \psi_{\text{D}^*\text{A}} \rangle & \langle \psi_{\text{DA}^*} | \hat{\mathcal{H}}_{\text{DA}} | \psi_{\text{DA}^*} \rangle - E \end{pmatrix} \begin{pmatrix} C_1 \\ C_2 \end{pmatrix} = E \begin{pmatrix} C_1 \\ C_2 \end{pmatrix} \quad (2.75)$$

The energies E of the dimer states are then obtained by the secular equation:

$$\begin{vmatrix} \langle \psi_{\text{D}^*\text{A}} | \hat{\mathcal{H}}_{\text{DA}} | \psi_{\text{D}^*\text{A}} \rangle - E & \langle \psi_{\text{D}^*\text{A}} | \hat{\mathcal{H}}_{\text{DA}} | \psi_{\text{DA}^*} \rangle \\ \langle \psi_{\text{DA}^*} | \hat{\mathcal{H}}_{\text{DA}} | \psi_{\text{D}^*\text{A}} \rangle & \langle \psi_{\text{DA}^*} | \hat{\mathcal{H}}_{\text{DA}} | \psi_{\text{DA}^*} \rangle - E \end{vmatrix} = 0 \quad (2.76)$$

Solving this equation yields:

$$\begin{aligned} E_{\pm} = & \frac{1}{2} \{ \langle \psi_{\text{D}^*\text{A}} | \hat{\mathcal{H}}_{\text{DA}} | \psi_{\text{D}^*\text{A}} \rangle + \langle \psi_{\text{DA}^*} | \hat{\mathcal{H}}_{\text{DA}} | \psi_{\text{DA}^*} \rangle \\ & \pm \sqrt{(\langle \psi_{\text{D}^*\text{A}} | \hat{\mathcal{H}}_{\text{DA}} | \psi_{\text{D}^*\text{A}} \rangle - \langle \psi_{\text{DA}^*} | \hat{\mathcal{H}}_{\text{DA}} | \psi_{\text{DA}^*} \rangle)^2 + 4 \langle \psi_{\text{DA}^*} | \hat{\mathcal{H}}_{\text{DA}} | \psi_{\text{D}^*\text{A}} \rangle^2} \} \end{aligned} \quad (2.77)$$

It is assumed that the electronic overlap between the molecules is small, so that the wave function of the aggregate can be written as a product of the monomer functions:

$$\begin{aligned} \psi_{\text{D}^*\text{A}} &= \psi_{\text{D}^*}\psi_{\text{A}} \\ \psi_{\text{DA}^*} &= \psi_{\text{D}}\psi_{\text{A}^*} \end{aligned} \quad (2.78)$$

This leads to the following diagonal matrix elements:

$$\begin{aligned}
 \langle \psi_{D^*A} | \hat{\mathcal{H}}_{DA} | \psi_{D^*A} \rangle &= \langle \psi_{D^*A} | \hat{\mathcal{H}}_D + \hat{\mathcal{H}}_A + \hat{\mathcal{V}}_{DA} | \psi_{D^*A} \rangle \\
 &= \langle \psi_{D^*} \psi_A | \hat{\mathcal{H}}_D | \psi_{D^*} \psi_A \rangle + \langle \psi_{D^*} \psi_A | \hat{\mathcal{H}}_A | \psi_{D^*} \psi_A \rangle \\
 &\quad + \langle \psi_{D^*} \psi_A | \hat{\mathcal{V}}_{DA} | \psi_{D^*} \psi_A \rangle \\
 &= \langle \psi_{D^*} | \hat{\mathcal{H}}_D | \psi_{D^*} \rangle \langle \psi_A | \psi_A \rangle + \langle \psi_{D^*} | \psi_{D^*} \rangle \langle \psi_A | \hat{\mathcal{H}}_A | \psi_A \rangle \\
 &\quad + \langle \psi_{D^*A} | \hat{\mathcal{V}}_{DA} | \psi_{D^*A} \rangle \\
 &= \epsilon_{D^*} + \epsilon_A + V_{vdW}^{D^*A}
 \end{aligned} \tag{2.79}$$

$$\langle \psi_{DA^*} | \hat{\mathcal{H}}_{DA} | \psi_{DA^*} \rangle = \epsilon_D + \epsilon_{A^*} + V_{vdW}^{DA^*} \tag{2.80}$$

where $V_{vdW}^{DA^*}$ is a van der Waals interaction energy, lowering the total energy. The off-diagonal term is:

$$\begin{aligned}
 \langle \psi_{DA^*} | \hat{\mathcal{H}}_{DA} | \psi_{D^*A} \rangle &= \langle \psi_{DA^*} | \hat{\mathcal{H}}_D + \hat{\mathcal{H}}_A + \hat{\mathcal{V}}_{DA} | \psi_{D^*A} \rangle \\
 &= \langle \psi_D \psi_{A^*} | \hat{\mathcal{H}}_D | \psi_{D^*} \psi_A \rangle + \langle \psi_D \psi_{A^*} | \hat{\mathcal{H}}_A | \psi_{D^*} \psi_A \rangle \\
 &\quad + \langle \psi_D \psi_{A^*} | \hat{\mathcal{V}}_{DA} | \psi_{D^*} \psi_A \rangle \\
 &= \langle \psi_D | \hat{\mathcal{H}}_D | \psi_{D^*} \rangle \langle \psi_{A^*} | \psi_A \rangle + \langle \psi_D | \psi_{D^*} \rangle \langle \psi_{A^*} | \hat{\mathcal{H}}_A | \psi_A \rangle \\
 &\quad + \langle \psi_{DA^*} | \hat{\mathcal{V}}_{DA} | \psi_{D^*A} \rangle \\
 &= \langle \psi_{DA^*} | \hat{\mathcal{V}}_{DA} | \psi_{D^*A} \rangle \\
 &= V_{DA}
 \end{aligned} \tag{2.81}$$

Here, $\langle \psi_{DA^*} | \hat{\mathcal{V}}_{DA} | \psi_{D^*A} \rangle$ is defined as the ECME (V_{DA}). In the original version of the MTD approach, antisymmetrization is neglected and therefore V_{DA} is reduced to the Coulomb contributions.^[85,86] Later it was extended to also include exchange interactions.^[87] For an energy transfer between two singlet states, V_{DA} is defined in terms of 1-RTDMs (ρ) as:

$$V_{DA}^{SS} = \sum_{ijkl} \rho_{ij}^{S_{D^*} \rightarrow S_D} \rho_{kl}^{S_A \rightarrow S_{A^*}} \left[(\phi_i \phi_j | \phi_k \phi_l) - \frac{1}{2} (\phi_i \phi_l | \phi_k \phi_j) \right] \tag{2.82}$$

where the summation runs over all occupied and virtual MOs (ϕ) of donor and acceptor. The two-electron Coulomb and exchange integrals are calculated employing a resolution-of-identity (RI) approximation:

$$(\phi_i \phi_l | \phi_k \phi_j) \approx \sum_{P,Q} (\phi_i \phi_l | P) (Q | P)^{-1} (Q | \phi_k \phi_j) \tag{2.83}$$

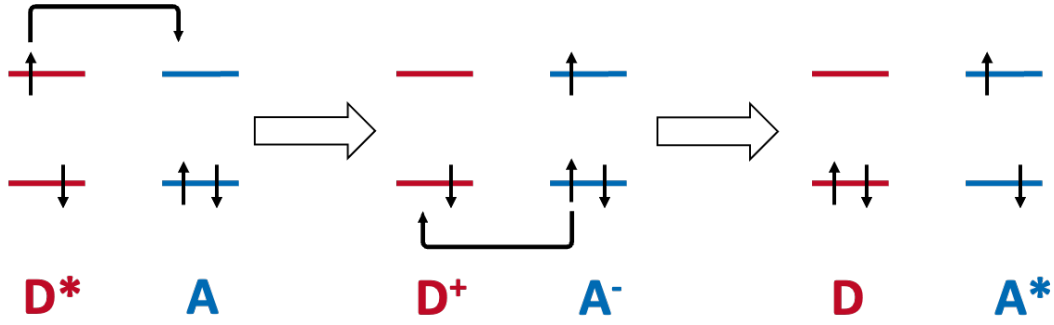


Figure 2.2: Schematic view of an intermediate charge transfer state in an EET process.

where P and Q are auxiliary basis functions.

The TTEET is connected with spin flip excitations. This means that dipole-dipole terms are neglected and only exchange-type integrals contribute. However, the transition density terms are separated according to the three triplet components, where the transfer is considered only for components with the same magnetic spin quantum number:^[88]

$$V_{DA}^{TT} = - \sum_{ijkl} \left[\rho_{ij}^{T_{D^*},+ \rightarrow S_D} \rho_{kl}^{S_A \rightarrow T_{A^*},+} + \rho_{ij}^{T_{D^*},- \rightarrow S_D} \rho_{kl}^{S_A \rightarrow T_{A^*},-} + \frac{1}{2} \rho_{ij}^{T_{D^*},0 \rightarrow S_D} \rho_{kl}^{S_A \rightarrow T_{A^*},0} \right] (\phi_i \phi_l | \phi_k \phi_j) \quad (2.84)$$

Here, +, - and 0 denominate the $M_S = +1$, $M_S = -1$ and $M_S = 0$ sublevels of the respective triplet states.

Charge-Transfer Contributions

At short distances between the donor and acceptor molecules it is known that not only the exchange mechanism plays a crucial role, but also intermediate charge transfer states.^[7,89–92] Through two sequential electron transfer processes, intermediate ionic states are formed. Although the process of an electron transfer from the donor followed by a hole transfer from the acceptor is more likely (Fig. 2.2), it is also possible to start with the hole transfer from the acceptor to the donor. The contributions from these intermediate states can be included with a perturbation treatment. The interacting wave functions of the initial (Ψ_I) and final (Ψ_F) states are mixtures of the locally excited configurations (ψ_{D^*A} and

ψ_{DA^*}) and the charge transfer configurations ($\psi_{D^+A^-}$ and $\psi_{D^-A^+}$):^[93]

$$\begin{aligned}\Psi_I &= \psi_{D^*A} + \lambda_I \psi_{D^+A^-} + \mu_I \psi_{D^-A^+} \\ \Psi_F &= \psi_{DA^*} + \lambda_F \psi_{D^+A^-} + \mu_F \psi_{D^-A^+}\end{aligned}\tag{2.85}$$

For the calculation of the ECME, all substates of the initial state have to be coupled with all substates of the final state. The resulting ECME is given by:

$$\begin{aligned}V_{DA} &= \langle \psi_{DA^*} | \hat{\mathcal{H}} | \psi_{D^*A} \rangle - \frac{\langle \psi_{DA^*} | \hat{\mathcal{H}} | \psi_{D^+A^-} \rangle \langle \psi_{D^+A^-} | \hat{\mathcal{H}} | \psi_{D^*A} \rangle}{E_{D^+A^-} - E_{DA^*}} \\ &\quad - \frac{\langle \psi_{DA^*} | \hat{\mathcal{H}} | \psi_{D^-A^+} \rangle \langle \psi_{D^-A^+} | \hat{\mathcal{H}} | \psi_{D^*A} \rangle}{E_{D^-A^+} - E_{DA^*}}\end{aligned}\tag{2.86}$$

where the first term is the direct coupling between the locally excited configurations and the last two terms are the contributions from the charge transfer states, which are scaled by an energy difference. The coupling terms involving an interaction between the charge transfer states is neglected as they are small. Fujimoto developed a method to treat these integrals within the Koopman's theorem applying a HOMO-LUMO approximation.^[91] A closely related method was developed by Spiegel *et al.*, which is not restricted to a four-orbital–four-electron model, but requires the calculation of the full system.^[78]

3 The STrEET Program

The software utilized in this work to calculate the EET properties is unified in the singlet–triplet excitation energy transfer (STrEET) program. The predecessor of this program was a collection of Fortran scripts written by Dominik Spiegel.^[94] This fragmentation into different programs made it cumbersome to use. Furthermore, the implementation was limited to singlet–singlet EET. Subsequently, these scripts were rewritten in C++ code and unified into the STrEET program by Fabian Meitza.^[95] The program was then extended to encompass the calculation of TTEET.

In this work, three distinct calculation modes of the STrEET program were utilized in order to determine the EET rate constants. Following Eq. 2.66, the calculation of the rate constant is separated into two parts: the determination of the spectral overlap integral, and the computation of the ECME. For the computation of the ECME, different methods are available. The two used in this work are the IDA and MTD approach. The values in question were calculated using their respective calculation types in the STrEET program, which are executed with distinct input files. The following commands can be used to generate them:

```
1 street -g [type]
2 street --generateInput [type]
3 [type] can be: [IDA, MTD, SPECTRALOVERLAP]
```

The appendix contains a set of example inputs (Listings B.1, B.2, B.3).

In the spectral overlap mode, the program utilizes polynomial splines to align the grids of the donor emission and acceptor absorption spectra. These splines are then multiplied to obtain the product spectrum. This spectrum is subsequently integrated between a specified start and end point to determine the spectral overlap integral.

The computation of the ECME in the IDA mode utilizes Eq. 2.69. This calculation type requires the TDMV of the donor and acceptor molecule, the distance between their barycenters, and the refractive index of the surrounding medium. If a value is not supplied in the input, the orientation factor, κ^2 , is computed from the TDMVs. In this work, the IDA mode was expanded to allow an alignment of the input structure to a reference structure employing a quaternion approach^[96],

3 The STrEET Program

followed by the subsequent rotation of the TDMV.

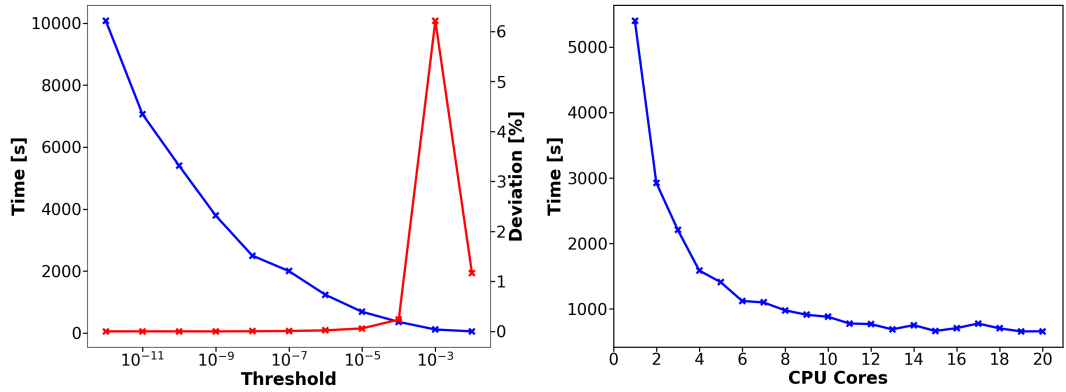
The initial step in the MTD mode is the construction of a dimer from the donor and acceptor molecule, thereby enabling the calculation of the two-electron integrals. Consequently, the Turbomole files, *control*, *basis*, *auxbasis*, *mos*, and *coord*, from both molecules are combined. Analogous to the IDA mode, the molecules can undergo rotation and alignment to a reference structure beforehand. After a rotation of a molecule, the MOs and 1-RTDM must undergo rotation in a congruent manner to circumvent recalculation. If the two-electron integrals are calculated successfully, the integrals are contracted with the 1-RTDMs of the two molecules to obtain the ECME according to Eq. 2.82 or 2.84.

Furthermore, the STrEET program was expanded to include the calculation of TSEET. Given that this process involves a spin-flip process on the donor, the utilization of spin-orbit mixed wave functions is needed. In the extension of the MTD approach the DFT/MRSOCI wave functions (Eq. 2.26) and the 1-RTDMs (Eq. 2.27) between them are employed to calculate ECMEs for each triplet fine-structure level (*a*):

$$V_{DA}^{T_aS} \approx \sum_{ijkl} \rho_{ij}^{T_{D^*,a} \rightarrow S_D} \rho_{kl}^{S_A \rightarrow S_{A^*}} \left[(\phi_i \phi_j | \phi_k \phi_l) - \frac{1}{2} (\phi_i \phi_l | \phi_k \phi_j) \right] \quad (3.1)$$

In order to calculate the EET rate constant, it is necessary to average the three couplings. The contributions of the individual fine-structure levels are dependent upon their population. In the case of a DFT/MRSOCI calculation, the 1-RTDMs are complex-valued and consequently, the coupling matrix element ($V_{DA}^{T_aS}$) is also complex-valued. As part of this work, a new interface was developed for importing the complex-valued 1-RTDMs. Since the STrEET program was already able to handle complex numbers, the triplet-singlet excitation energy transfer can then internally be handled like a SSEET calculation.

A typical step to reduce the computational cost in the calculation of the two-electron integrals is to freeze MOs with energies below $-3 E_h$ and above $2 E_h$. To validate this step in the MTD approach, calculations were performed with and without the frozen core. The result obtained from these calculations revealed no significant differences between the two setups, validating the approximation and accelerating the computational process (see Tab. B.1). Furthermore, the STrEET program utilizes a threshold, wherein all entries of the 1-RTDM that fall below the threshold are excluded from the integral contraction, to speed up the MTD calculations. A series of calculations with different thresholds for the system discussed in Sec. 4.3 were conducted to assess the impact on the time and the accuracy of the computation (Fig. 3.1a). It is observed that as the number of



(a) The time of integral contraction (blue) for different thresholds and the deviation of the ECME to the one calculated with the highest threshold (red). (b) The time of computation for different number of cores.

Figure 3.1: Test calculations for the STREET program.

entries in the 1-RTDMs decreases (Fig. B.6 and Fig. B.7), the calculation time exhibits a fast decline. Notably, the ECME retained its high degree of accuracy for thresholds lower than 10^{-7} .

Additionally, a series of calculations was conducted to assess the parallelization capabilities of the program. Fig. 3.1b illustrates the runtime of an ECME calculation performed on varying number of CPU cores. It should be noted that this test was not carried out on dedicated hardware, which might explain the small observed deviations. Nevertheless, a discernible trend is obtained. These tests demonstrate ways for accelerating the calculation of the ECME. However, it is crucial to acknowledge that these tests were carried out using preexisting files for the two-electron integrals. The generation of these integrals necessitates a substantially larger amount of time and can only run on a single core.

4 Results

4.1 Intramolecular Triplet–Triplet Excitation Energy Transfer

Intersystem crossing and intramolecular triplet excitation energy transfer in spiro[9,10-dihydro-9-oxoanthracene-10,2'-5',6'-benzindan] investigated by DFT/MRCI methods (Paper 1)^[97]

The initial project of this work was to test the reworked EET program, which had been previously developed. A novel feature of the program was the ability to compute TTEET with the MTD approach. The search for an appropriate test system led to the spiran-linked anthrone (**A**)-naphthalene (**N**) molecule (**AN**) (Fig. 4.1). In this system, the experimental observation of intramolecular TTEET from the anthrone to the naphthalene moiety was achieved through the observation of phosphorescence from the naphthalene moiety following direct excitation of a singlet state on the anthrone in a butyronitrile (BuCN) solution.^[98] The given excited-state dissipation pathway included an ISC process between the lowest singlet and triplet state on the anthrone unit, which were reportedly both of $n\pi^*$ character.

To investigate the processes in this molecule the geometry of five different electronic states (S_0 , $^1n\pi^*(\mathbf{A})$, $^3n\pi^*(\mathbf{A})$, $^3\pi\pi^*(\mathbf{A})$, $^3\pi\pi^*(\mathbf{N})$) were optimized in vacuum and BuCN. Except for the $^3\pi\pi^*(\mathbf{N})$ geometry, which has C_{2v} symmetry, the (TD)DFT

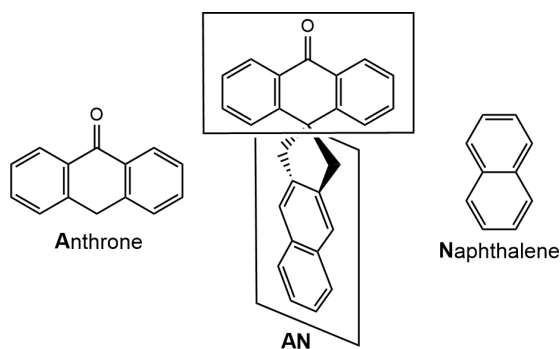


Figure 4.1: Chemical structure of anthrone (**A**), naphthalene (**N**) and spiro[9,10-dihydro-9-oxoanthracene-10,2'-5',6'-benzindan] (**AN**)

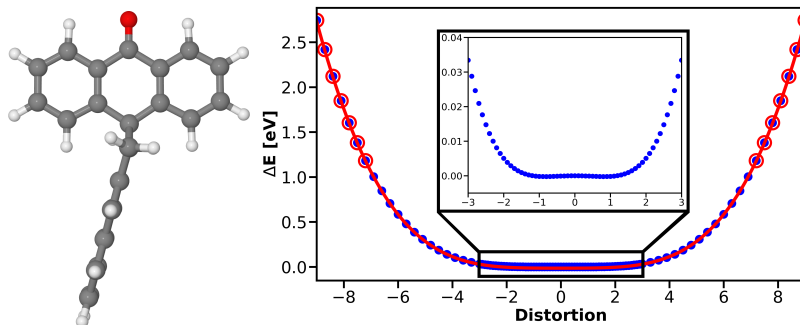


Figure 4.2: Scan along the dimensionless normal coordinate of the imaginary vibrational mode at the C_{2v} -symmetric ground state geometry in vacuum. The energy profile of the DFT (PBE0/def2-TZVP) calculations show a shallow double minimum structure. Red encircled points are used for the fit of the harmonic potential (red line).

minima were symmetry-broken. After further investigation with the DFT/MRCI method it was found that all of these states have a true minimum in C_{2v} symmetry, while they exhibit an imaginary frequency at the (TD)DFT level of theory. In order to get a real-valued frequency for subsequent rate constant calculations, the molecule was distorted along the corresponding normal mode and the curvature of the outer energy profile was used to fit a harmonic potential (Fig. 4.2). The evaluation of the adiabatic energies of the excited states revealed that the lowest triplet state on the anthrone moiety is of $n\pi^*$ character in vacuum, whereas it has $\pi\pi^*$ character in a polar environment (BuCN). Given that the lowest excited singlet state of **AN** is the $^1n\pi^*(\mathbf{A})$ state, the ISC to $^3n\pi^*(\mathbf{A})$ is, in accordance with El-Sayed’s rule (see Sec. 2.6.1), a very slow process in Condon approximation. Incorporating spin-vibrational effects into the calculations results in an ISC rate constant that falls within the range of 10^{10} s^{-1} , making it an efficient de-excitation pathway. However, this value remains over ten times slower than that computed for the $^1n\pi^*(\mathbf{A}) \rightsquigarrow ^3\pi\pi^*(\mathbf{A})$ transition, irrespective of the solvent environment. This is a first indication that the $^3\pi\pi^*(\mathbf{A})$ state is involved in the deactivation process. For an unambiguous assignment of the intermediate triplet state, the calculated excited state absorption (ESA) spectra of the states located on the anthrone moiety are compared to an experimental spectrum recorded after short delay time (Fig. 4.3a). The best agreement to the experiment has the spectrum of $^3\pi\pi^*(\mathbf{A})$, which further corroborates the assumption that this state is involved in the excited state dissipation pathway. For the investigation of the TTEET process, the MTD approach (see Sec. 2.8.2) was chosen. In Eq. 2.84 the 1-RTDMs of the triplet states are multiplied with the electronic repulsion integral:

$$(\phi_i\phi_l|\phi_k\phi_j) \equiv \left\langle \phi_i(r_1)\phi_k(r_2) \left| \frac{1}{r_{12}} \right| \phi_l(r_1)\phi_j(r_2) \right\rangle \quad (4.1)$$

4.1 Intramolecular Triplet–Triplet Excitation Energy Transfer

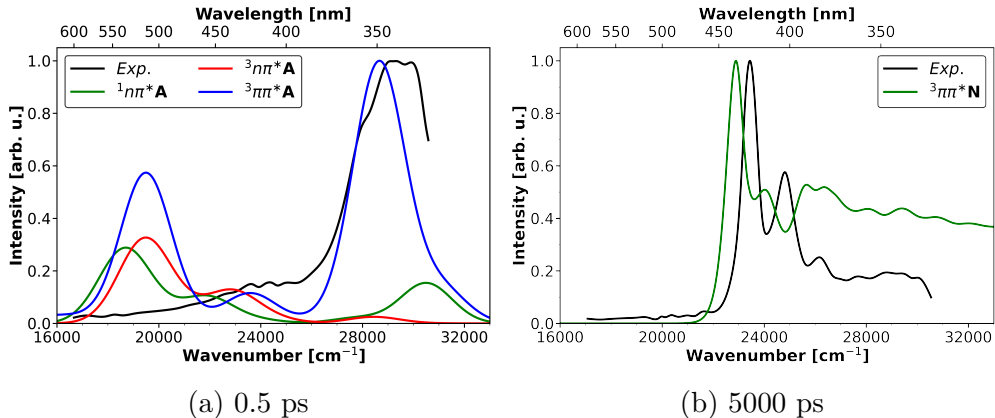


Figure 4.3: Calculated ESA spectra in BuCN compared to experimental spectra recorded after short (0.5 ps) and long (5000 ps) delay times. The computed short-time line spectra were normalized with respect to the intensity of the highest peak of the ${}^3\pi\pi^*(\mathbf{A})$ ESA spectrum and were broadened by Gaussian functions with a full width at half maximum (FWHM) of 2360 cm^{-1} . For the ${}^3\pi\pi^*(\mathbf{N})$ a vibrationally resolved ESA spectrum computed with the VH method is shown.

Here, ϕ_i and ϕ_j represent MOs of the donor molecule, while ϕ_k and ϕ_l correspond to those of the acceptor molecule. Given that the molecule exhibits C_{2v} symmetry, it follows that these integrals can only yield a non-zero value if the direct product of the four irreducible representations (irreps) contain the totally symmetric representation a_1 . In order to see whether the transition from the ${}^3n\pi^*(\mathbf{A})$ or ${}^3\pi\pi^*(\mathbf{A})$ to the ${}^3\pi\pi^*(\mathbf{N})$ adopt values that differ from zero, an examination of the leading configurations of the respective wave function expansion is done. The involved MOs for the acceptor state (${}^3\pi\pi^*(\mathbf{N})$) transform according to the a_2 and b_1 irrep, respectively. In case of ${}^3n\pi^*(\mathbf{A})$ being the donor state, the MOs ϕ_i and ϕ_j transform according to b_2 and b_1 , leading to the direct product:

$$b_2 \otimes b_1 \otimes a_2 \otimes b_1 = b_1 \quad (4.2)$$

For the ${}^3\pi\pi^*(\mathbf{A})$ as donor state, with MOs both transforming according to b_1 , the direct product becomes:

$$b_1 \otimes b_1 \otimes a_2 \otimes b_1 = b_2 \quad (4.3)$$

In both of these cases, the electronic repulsion integral vanishes, resulting in TTEET rate constant of zero. Even in the distorted C_s geometries, the Dexter energy transfer from ${}^3\pi\pi^*(\mathbf{A}) \rightsquigarrow {}^3\pi\pi^*(\mathbf{N})$ is symmetry forbidden. Therefore, it is mandatory to go beyond the Condon approximation. Instead of a Herzberg-Teller like expansion for the ECME, the transition rate constants were computed using NACMEs. The calculations revealed a rate constant two orders of magnitude faster

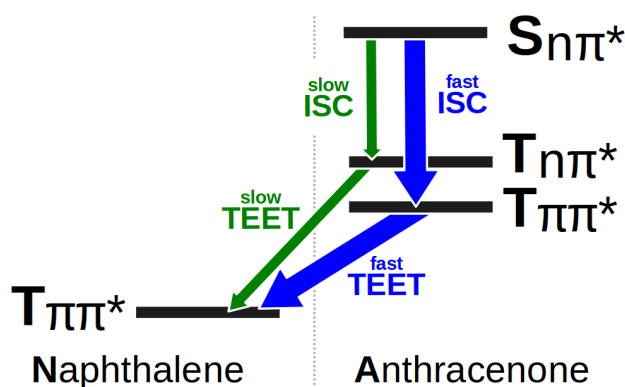


Figure 4.4: Schematic excited state dissipation pathway of AN in BuCN.

for the ${}^3\pi\pi^*(\mathbf{A}) \rightsquigarrow {}^3\pi\pi^*(\mathbf{N})$ transition than for that of the ${}^3n\pi^*(\mathbf{A}) \rightsquigarrow {}^3\pi\pi^*(\mathbf{N})$ process in BuCN. In vacuum, the ${}^3\pi\pi^*(\mathbf{A}) \rightsquigarrow {}^3\pi\pi^*(\mathbf{N})$ process slows down significantly, but remains approximately three times faster than its counterpart. The population of ${}^3\pi\pi^*(\mathbf{N})$ can be verified by the ESA at long delay times. The experimental spectrum exhibits multiple distinct peaks, which could be attributed to vibrational transitions of a single electronic state based on our calculations. Confirmation of this assignment is provided by a vibrationally resolved spectrum computed using the Vertical Hessian method, which shows very good agreement with the experimental spectrum (Fig. 4.3b).

It can be concluded that the consecutive ${}^1n\pi^*(\mathbf{A}) \rightsquigarrow {}^3\pi\pi^*\mathbf{A}$ ISC and ${}^3\pi\pi^*(\mathbf{A}) \rightsquigarrow {}^3\pi\pi^*(\mathbf{N})$ TTEET processes represents the only pathway whose time constant falls within the experimentally determined rise time of the ${}^3\pi\pi^*(\mathbf{N})$ ESA (Fig. 4.4). The fact that the two moieties are held relatively rigidly at right angles to each other by spiran linkage was believed to be beneficial for the MTD calculation because of fixed distance and orientation between TTEET donor and acceptor. As it turns out, this fixed arrangement in the C_{2v} symmetric geometries led to the Dexter energy transfer being symmetry forbidden.

4.2 Charge-Transfer Contributions to Excitation Energy Transfer

The approach proposed by Fujimoto to include CT contributions to EET is limited to HOMO-LUMO excitations and relies on Koopmans' theorem (see Sec. 2.8.2).^[91] Consequently, there is need for improvement. A first step is to incorporate a sum

4.2 Charge-Transfer Contributions to Excitation Energy Transfer

over CT states (m):

$$V_{\text{CT}} = \sum_m \left(- \frac{\langle \psi_{DA^*} | \hat{\mathcal{H}} | \psi_{D^+A^-,m} \rangle \langle \psi_{D^+A^-,m} | \hat{\mathcal{H}} | \psi_{D^*A} \rangle}{E_{D^+A^-,m} - E_{DA^*}} \right. \\ \left. - \frac{\langle \psi_{DA^*} | \hat{\mathcal{H}} | \psi_{D^-A^+,m} \rangle \langle \psi_{D^-A^+,m} | \hat{\mathcal{H}} | \psi_{D^*A} \rangle}{E_{D^-A^+,m} - E_{DA^*}} \right) \quad (4.4)$$

Here, the energy E_{DA^*} consists of two components: the excitation energy of the locally excited state on the acceptor, and the polarization effects from the donor molecule. In addition, the energies of the CT states include the Coulomb interactions between the two molecules. In a manner analogous to the MTD approach (see Sec. 2.8.2), a product approach can be applied to obtain the dimer wave functions ($\psi_{D^+A^-,m}$ and $\psi_{D^-A^+,m}$). The wave functions of the charged monomer states are constructed by removing or adding an electron from the uncharged monomers. This process can be written in terms of Dyson orbitals, which are the overlap between wave functions with different number of electrons:

$$\phi_{IF}^{\text{Dyson}}(x_1) = \sqrt{N} \int \Psi_F^{N-1}(x_2, x_3, \dots, x_N) \\ \Psi_I^N(x_1, x_2, x_3, \dots, x_N) dx_2, dx_3, \dots, dx_N \quad (4.5)$$

They can also be written as a linear combination of the MO set of the initial wave function $\{\phi_p\}$:

$$\phi_{IF}^{\text{Dyson}}(x_1) = \sum_p \gamma_p \phi_p(x_1) \quad (4.6)$$

where the expansion coefficients, also called Dyson amplitudes, are defined as:

$$\gamma_p = \langle \Psi_F^{N-1} | a_p | \Psi_I^N \rangle \quad (4.7)$$

For the calculation of the Dyson orbitals, the density operators $\hat{D}^A = \hat{a}^\dagger$ and $\hat{D}^C = \hat{a}$ were implemented in the DENSITYENGINE, which is part of the DENSOMAT program developed by Fabian Meitza during his PhD.^[95] Starting from the already existing density operators:

$$\hat{S} = \hat{a}_\alpha^\dagger \hat{a}_\alpha + \hat{a}_\beta^\dagger \hat{a}_\beta \quad (4.8)$$

$$\hat{T}_{+1} = \hat{a}_\alpha^\dagger \hat{a}_\beta \quad (4.9)$$

$$\hat{T}_0 = \hat{a}_\alpha^\dagger \hat{a}_\alpha - \hat{a}_\beta^\dagger \hat{a}_\beta \quad (4.10)$$

$$\hat{T}_{-1} = \hat{a}_\beta^\dagger \hat{a}_\alpha \quad (4.11)$$

$$(4.12)$$

4 Results

only small changes were needed. In addition to addressing various minor software issues, the new modifications included the incorporation of a novel variable that stores the charge of the wave function. Furthermore, a mechanism has been integrated to verify the excitation order difference, thereby facilitating the coupling of wave functions with different numbers of electrons.

Using the Dyson orbitals gives rise to the following expressions for the transition densities:

$$\begin{aligned}\langle \psi_{DA^*} | \hat{E}_i^j | \psi_{D^+A^-,m} \rangle &= \langle \psi_D \psi_{A^*} | \hat{a}_i^\dagger \hat{a}_j | \psi_{D_m^+} \psi_{A_m^-} \rangle \\ &= \langle \psi_D | \hat{a}_i^\dagger | \psi_{D_m^+} \rangle + \langle \psi_{A^*} | \hat{a}_j | \psi_{A_m^-} \rangle\end{aligned}\quad (4.13)$$

$$\begin{aligned}\langle \psi_{D^+A^-,m} | \hat{E}_i^j | \psi_{DA^*} \rangle &= \langle \psi_{D_m^+} \psi_{A_m^-} | \hat{a}_i^\dagger \hat{a}_j | \psi_D \psi_{A^*} \rangle \\ &= \langle \psi_{D_m^+} | \hat{a}_j | \psi_D \rangle + \langle \psi_{A_m^-} | \hat{a}_i^\dagger | \psi_{A^*} \rangle\end{aligned}\quad (4.14)$$

$$\begin{aligned}\langle \psi_{DA^*} | \hat{E}_i^j | \psi_{D^-A^+,m} \rangle &= \langle \psi_D \psi_{A^*} | \hat{a}_i^\dagger \hat{a}_j | \psi_{D_m^-} \psi_{A_m^+} \rangle \\ &= \langle \psi_D | \hat{a}_j | \psi_{D_m^-} \rangle + \langle \psi_{A^*} | \hat{a}_i^\dagger | \psi_{A_m^+} \rangle\end{aligned}\quad (4.15)$$

$$\begin{aligned}\langle \psi_{D^-A^+,m} | \hat{E}_i^j | \psi_{DA^*} \rangle &= \langle \psi_{D_m^-} \psi_{A_m^+} | \hat{a}_i^\dagger \hat{a}_j | \psi_D \psi_{A^*} \rangle \\ &= \langle \psi_{D_m^-} | \hat{a}_i^\dagger | \psi_D \rangle + \langle \psi_{A_m^+} | \hat{a}_j | \psi_{A^*} \rangle\end{aligned}\quad (4.16)$$

To avoid the use of non-orthogonal orbital sets, the unchanged MO basis of the neutral states is used for the charged monomer states. This approximation makes it impossible, however, to find good estimates for the energies in the denominator in Eq. 4.4. Comparisons of electron affinities and ionization energies yielded large and unsystematic deviations from the experiment. Given that the current implementation of the Dyson orbitals only allows the use of the same basis for the neutral and ionic states, the resulting couplings are inherently unreliable. Nevertheless, to assess the implementation of the Dyson orbitals, they can be employed to approximate ionization probabilities.

4.2.1 Dyson Norms as Ionization Probabilities

Dyson orbitals and their respective norms are often employed as an approximation for ionization probabilities, assuming that the overlap between the outgoing electron and the ionization continuum state can be disregarded.^[99–102] The squared

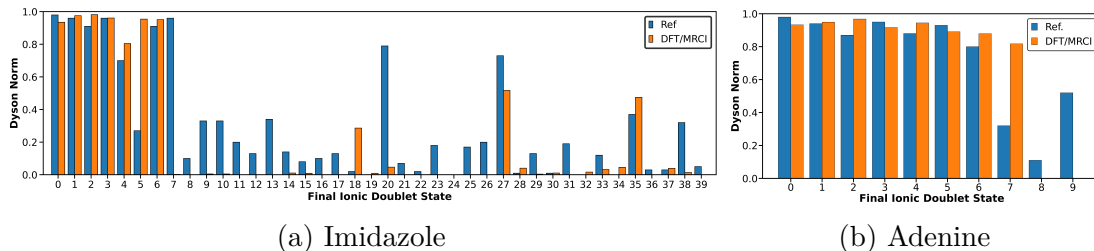


Figure 4.5: Dyson norms between the neutral ground state and cationic states calculated with DFT/MRCI wave functions (R2017/BH-LYP/aug-cc-pVDZ) compared to TDDFT literature values (CAM-B3LYP/aug-cc-pVDZ) for imidazole and adenine.^[99]

Dyson norm can be written as the sum over the squared Dyson amplitudes γ_p :

$$\sigma_{IF} = \|\phi_{IF}^{\text{Dyson}}\|^2 = \sum_p \gamma_p^2 \quad (4.17)$$

These Dyson norms can adopt values between 0 for states that cannot be described by a one-electron transition and 1 for two states that differ exactly in the occupation of one spin orbital.

For a test of the implementation, the ionization probabilities calculated with DFT/MRCI wave functions are compared to reference values from the literature. Arbelo-González *et al.* simulated the steady photoelectron spectra of adenine and imidazole.^[99] They employed TDDFT, in conjunction with the CAM-B3LYP functional and the aug-cc-pVDZ basis set to calculate Dyson orbitals and their respective norms for the transition of the electronic ground state to cationic states. For imidazole, they calculated the first 40 cationic states, while for adenine, they calculated the first 10 cationic states. To make a fair comparison, the electronic ground state of imidazole and adenine were optimized with the B3LYP functional and the aug-cc-pVDZ basis set. Subsequently, DFT/MRCI calculations for the singlet and cationic doublet roots were performed with the R2017 Hamiltonian.^[55] Fig. 4.5 shows the literature Dyson norms compared to the values calculated with the DFT/MRCI method. In the case of adenine, a very good agreement for the first 7 cationic states can be seen. While some difference cannot be explained without knowledge of the TDDFT configurations, the discrepancy between the last two cationic states can be attributed to the fact that these states exhibit predominantly double excitation character in the DFT/MRCI method, whereas the TDDFT approach considers only single excitations. It is not possible for double excitations with respect to the doublet ground state to couple with the neutral ground state, given that there is at least a difference between two spin orbitals (Fig. B.1). The same reason is responsible for the difference in the high

4 Results

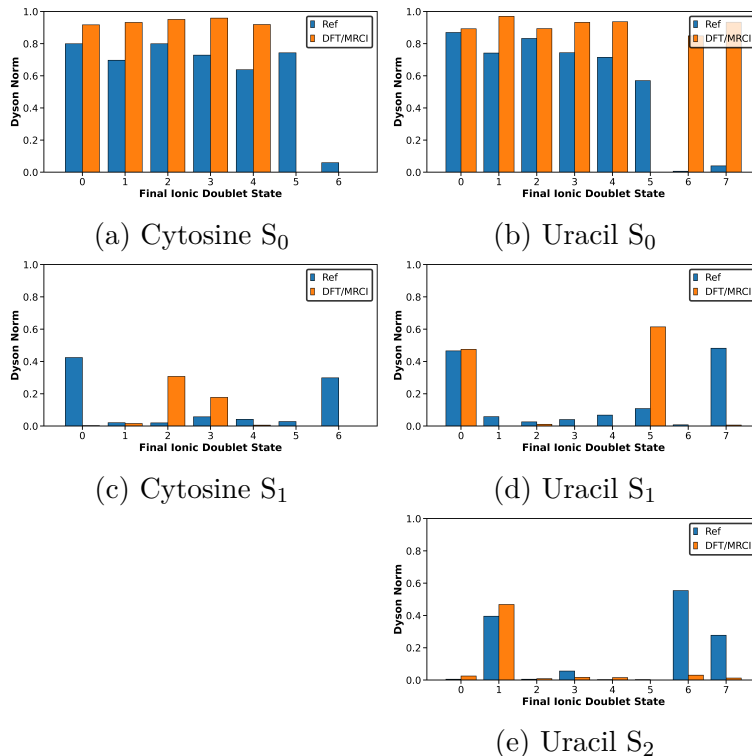


Figure 4.6: Dyson norms calculated with DFT/MRCI wave functions (R2017/BH-LYP/aug-cc-pVDZ) compared to MCSCF literature values (aug-cc-pVDZ) for cytosine and uracil.^[100]

excited states of imidazole, while an overall satisfactory agreement is still in place. In a separate study, Spanner *et al.* investigated the extreme-ultraviolet ionization of cytosine and uracil through multiconfiguration self-consistent field (MCSCF) calculations.^[100] They calculated the Dyson norms for the transition from the electronic ground state and first excited singlet state into the first seven cationic states of cytosine. Additionally, for uracil, they calculated the second excited singlet state and one cationic state more. Overall the agreement between the Dyson norms calculated with the DFT/MRCI and the MCSCF method is excellent (Fig. 4.6). The discrepancies between the two methods can be attributed to different dominant configurations in the wave functions. For example, the dominant configuration of the first cytosine doublet state has a singly occupied HOMO in the reference, whereas the singly occupied orbital is the HOMO-2 in the DFT/MRCI for this state. The configuration with the HOMO as the singly occupied orbital mixes into the third and fourth ionic states of the DFT/MRCI wave function. Therefore, the Dyson norm for the S₁ state, which is a HOMO→LUMO+1 transition, is partitioned between these two states and is zero for the first ionic state. For a schematic representation of the leading configurations in these two molecules, see Fig. B.2 and Fig. B.3.

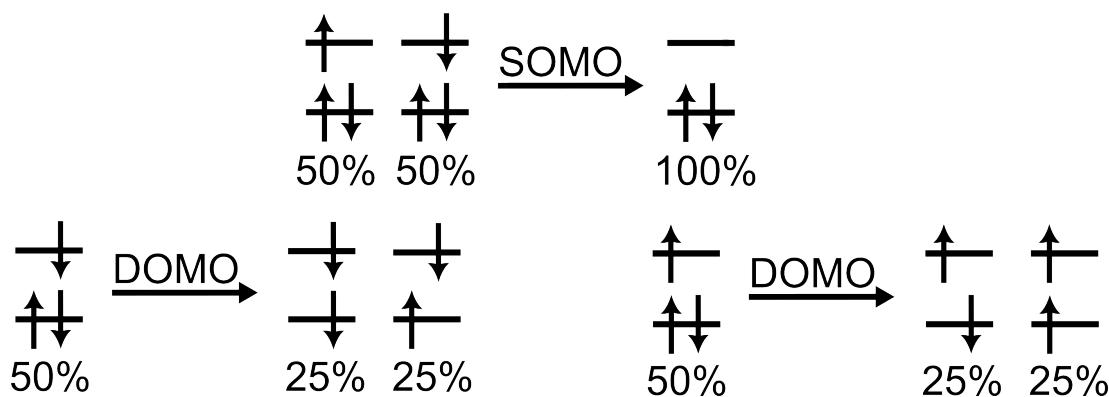


Figure 4.7: A one-electron detachment from a doublet state might only yield a Dyson norm of 1 if the detachment is from a SOMO (top). Otherwise, the detachment gives a singlet or triplet configuration with a probability of $\frac{1}{2}$, respectively (bottom). Note that in the generation of the anion no spin arrangement is preferred and the probability of alpha or beta occupation in the SOMO is exactly one half.

Electron affinities and lowest triplet and singlet state properties of *para*-oligophenylenes (n=3-5): Theory and experiment (Paper 2)^[103]

In this publication, Dyson norms were used to study the ionization probability in photodetachment-photoelectron (PD-PE) spectroscopy of *para*-terphenyl (p3P), *para*-quaterphenyl (p4P) and *para*-quinquephenyl (p5P). For this spectroscopy, radical anions of the investigated molecules are generated. By means of laser excitation, an electron is detached, and the kinetic energy of the removed electron is subsequently measured. This approach enables the direct spectroscopy of otherwise inaccessible states, such as triplet states. The assignment of the measured peaks heavily relies on quantum chemical calculations. In addition to energies, Dyson norms can play an instrumental role in this process, by providing intensity ratios. During the investigation of these molecules, it was discovered that the Dyson norm between an initial anionic state and a final singlet state can only attain a value of 1 if the electron is annihilated from a singly occupied molecular orbital (SOMO). Conversely, if the electron is detached from a doubly occupied molecular orbital (DOMO), a singlet or triplet configuration is generated with a probability of $\frac{1}{2}$, respectively (Fig. 4.7).

Fig. 4.8 shows the experimental and calculated PD-PE spectra of p3P. Although the T_3 state is omitted from the calculated spectrum because its minimum structure could not be found, Dyson norms provide an intensity ratio between T_3 and T_2 in a qualitative agreement with the experimental observed intensity of the peak structure above the T_2 . Also, despite the near-degeneracy of the T_4 and S_1 states in terms of energy, the Dyson norms indicate that the peaks of the T_4 is obscured

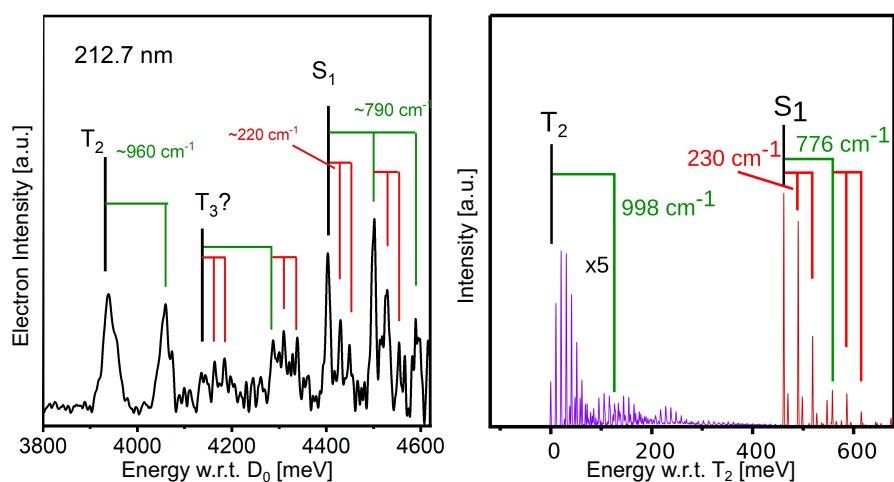


Figure 4.8: Experimental (left side) and calculated (right side) PD-PE spectra of p3P. Note that the T_3 state was omitted from the calculated spectrum because its origin position was not found.

by the S_1 spectrum. A similar analysis was conducted for the other two molecules, where the Dyson norms were also helpful in the assignment of experimental peaks.

4.3 Singlet–Singlet Excitation Energy Transfer

Excitonic Coupling of a TADF Assistant Dopant and a Multi-resonance TADF Emitter (Paper 3)^[104]

In this study, the MTD approach was employed for the first time to calculate the excitonic couplings between two molecules utilized in a hyperfluorescence OLED. These molecules are typically quite large, necessitating substantial computational effort. The assistant dopant of the hyperfluorescence system is a reported TADF molecule with a dihydrobenzothieno-indolo-carbazol (BTICz) donor and an oxygen-bridged boron (DBA) acceptor moiety (DBA-BTICz, Fig. 4.9a). The fluorescent emitter is a widely utilized multi-resonance TADF molecule (ν -DABNA, Fig. 4.9b) that exhibits a very narrow emission band within the blue region. In an attempt to reduce the computational cost associated with the MTD calculations, a smaller derivative, the h -DABNA (Fig. B.4), was examined. However, due to the smaller π -system, the characteristics of the excited states are markedly different. The absorption of the first excited singlet states is strongly blue-shifted (Fig. B.5), and the transition dipole moment of this transition is also more than halved compared to the full molecule. Both properties have a significant influence on the magnitude of the energy transfer, consequently leading to a reduction in the EET rate constant. It was therefore deemed necessary to consider the full

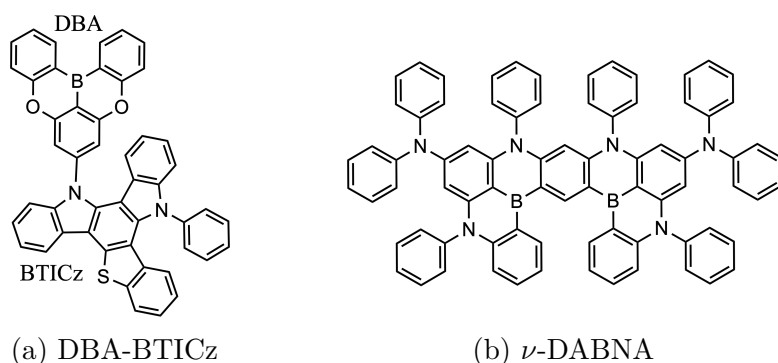


Figure 4.9: Chemical structures of the FRET donor DBA-BTICz and the FRET acceptor ν -DABNA.

molecule in the MTD calculations.

In the MTD approach, the molecules are calculated as isolated monomers in an implicit toluene solution. Interestingly, for the assistant dopant DBA-BTICz, two conformers were identified, differing in the relative orientation of the two moieties. These conformers are designated as the left and right conformers, as shown in Fig. 4.10. Despite the significant geometric disparities between the minimum ground state structures, the energy difference (< 1 kJ/mol) and the barrier (ca. 10 kJ/mol) are found to be remarkably low. Furthermore, the absorption features exhibited by these conformers are strikingly similar, impeding the ability to determine the favored conformation in the experiment.

To elucidate the EET capabilities, the lowest excited states were optimized. In both conformers, three triplet states are found to be energetically below the first excited singlet state. For the two locally excited (LE) triplet states (T_{BTICz} and T_{DBA}), a minimum structure could be determined. However, due to crossings in the PES, the minimum of the T_{CT} could not be found. The lowest excited singlet state of both conformers is of CT character, and they also exhibit very similar adiabatic energies (3.23 eV). The calculated fluorescence spectra are also similar and reproduce the experimental spectrum (Fig. 4.10b) very well. Despite these similarities, the TDMVs strength and direction vary, originating from different shapes of the HOMO. For a more detailed analysis, please refer to Paper 3. The different TDMV strength results in a fluorescence rate constant for the left conformer (6×10^7 s $^{-1}$) that is one order of magnitude higher than for the right conformer (6×10^6 s $^{-1}$). In both conformers, the lowest triplet state has predominantly LE character on the BTICz moiety (T_{BTICz}). While the adiabatic ΔE_{ST} in the right conformer is 0.40 eV, the triplet state in the left conformer lies lower, leading to a ΔE_{ST} of 0.51 eV. These values are considerably higher than the onset difference of experimental room-temperature and low-temperature

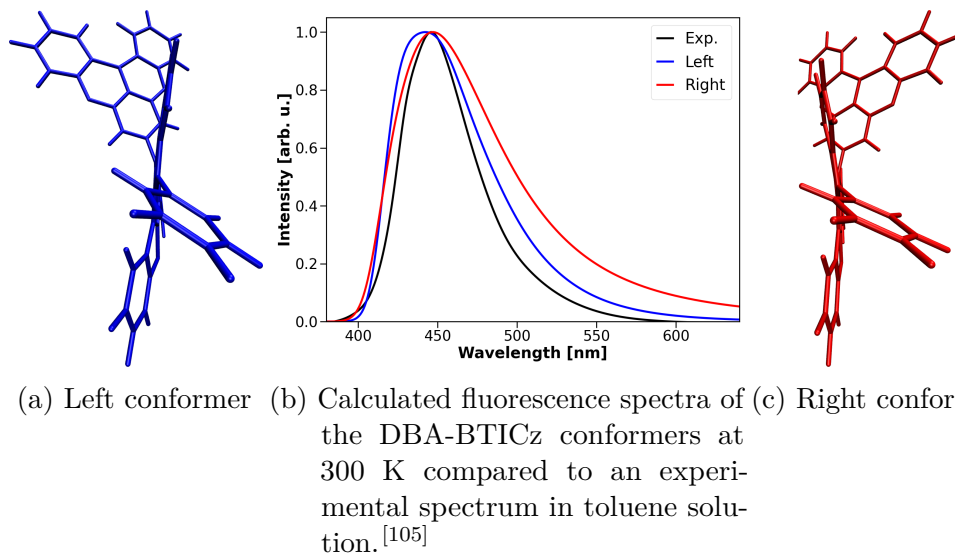


Figure 4.10

luminescence spectra (0.29 eV).^[105] Given that the ISC rate constant represents a non-radiative dissipation pathway of the S_{CT} state, it is important to take this shift into consideration when accessing the FRET efficiency (Eq. 1.2). Therefore, the rate constants were computed using the calculated adiabatic ΔE_{ST} and by shifting the potentials to match the experimental value. Utilizing the calculated energy gap, the $S_{CT} \rightsquigarrow T_{BTICz}$ rate constant for the left conformer is ($9 \times 10^7 \text{ s}^{-1}$) is one order of magnitude higher than that of the right conformer ($4 \times 10^6 \text{ s}^{-1}$). For both conformers employing the lower experimental energy gap results in a lower rate constant, as the geometries of the involved states are markedly different, leading to a strong coupling case (see Sec. 2.6.1). Furthermore, the ISC to the second LE triplet state (T_{DBA}), which exhibits rate constants analogous to the $S_{CT} \rightsquigarrow T_{BTICz}$ transition, results in an ISC process that is as fast or even faster than the fluorescence. However, the calculated rate constant for the reverse $S_{CT} \leftarrow T_{BTICz}$ process is found to be considerably lower than necessary for the observed TADF properties, even when the lower experimental energy gap is employed. To achieve a more comprehensive understanding, it is necessary to incorporate spin-vibronic interactions involving the intermediate triplet states (T_{DBA} , T_{CT}). However, this investigation falls outside the scope of this thesis due to the substantial computational cost associated with such an analysis.

The fluorescence emitter of the hyperfluorescence system, ν -DABNA, is a multiresonance TADF molecule. The core of the molecule consists of five benzene rings connected by boron and nitrogen atoms, thereby introducing the multiresonance character. Two diphenylamino substituents and further phenyl rings ensure sterical protection. The ground state and all optimized excited state geometries (S_1 , S_2 ,

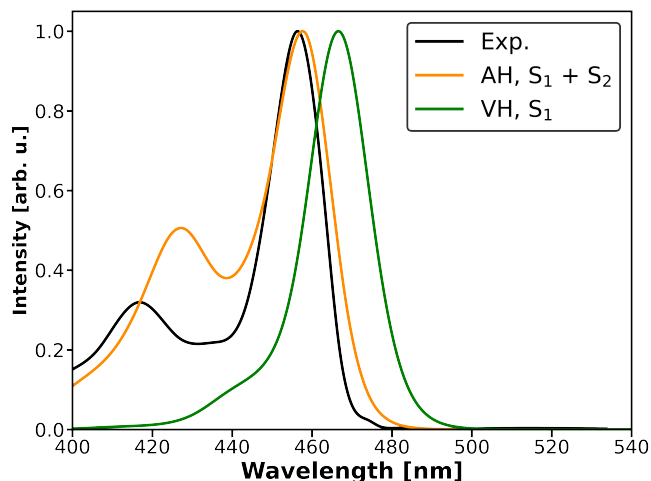


Figure 4.11: Experimental absorption spectrum of ν -DABNA in toluene^[106] compared to the VH spectrum of the S_1 state and the combined AH spectra of the S_1 and S_2 states.

T_1 , T_2) exhibit C_2 symmetry. In the experimental absorption spectrum in toluene, two distinct peaks are visible between 400 and 480 nm, which are attributed to the B -symmetric S_1 and the A -symmetric S_2 state.^[106] The combined calculated adiabatic absorption spectra of the S_1 and S_2 states shows a nearly perfect fit to the experimental spectrum, with the S_2 state exhibiting a slight red shift and an overestimated relative intensity. The absorption spectrum computed with the VH approach of the S_1 state is also slightly red shifted compared to the experimental and adiabatic spectra.

The first two triplet states are energetically lower than the first excited singlet state. The T_1 is the B -symmetric state that corresponds to the S_1 state. With an adiabatic $\Delta E_{S_1-T_1}$ value of approximately 200 meV, the computed energy gap overestimates the experimental ΔE_{ST} of 70–120 meV.^[106,107] However, the T_2 state, which is the A -symmetric state corresponding to the S_2 state, is about 120 meV lower in energy than the S_1 state and is likely to play a very important role in the (r)ISC processes in this molecule.^[106,107] Therefore, the rISC rate constants were computed. The calculated rISC rate constants of $2 \times 10^{-1} \text{ s}^{-1}$ ($T_1 \leftarrow S_1$) and $6 \times 10^2 \text{ s}^{-1}$ ($T_2 \leftarrow S_1$) are considerably lower than the experimental rate of $3 - 6 \times 10^5 \text{ s}^{-1}$ and thus inadequate to explain any TADF properties of ν -DABNA. As in the rISC process in DBA-BTICz, spin-vibronic interactions will have a large impact, but are too costly to investigate.

The main effort in this study went into the investigation of various effects on the EET rate constants. At first, numerous spectral overlap integrals calculations were conducted to investigate the influence of the VH and AH method. For both DBA-BTICz conformers, the VH emission spectrum was utilized and subsequently

4 Results

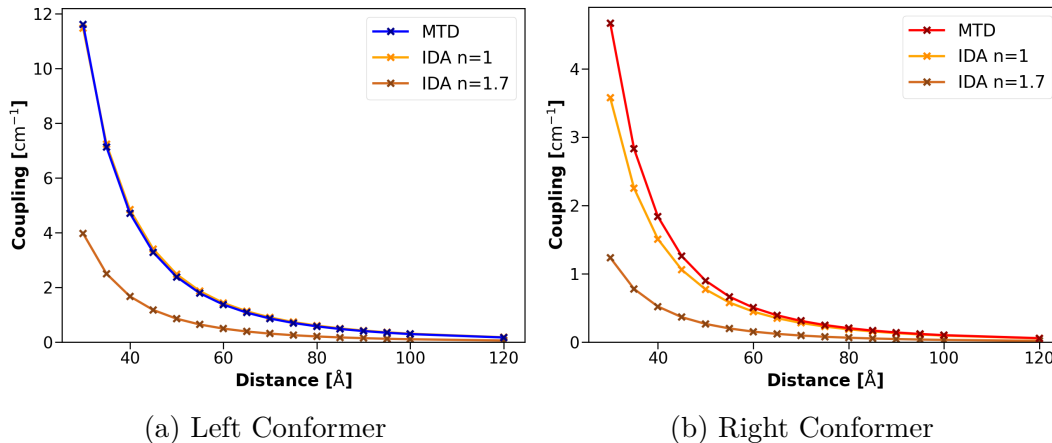


Figure 4.12: Distance dependency of the ECME obtained with the MTD and IDA approach for the inline orientation of the TDMV.

multiplied with the AH and VH absorption spectrum of the S_1 state of ν -DABNA. The calculated spectral overlap integral values for these four combinations range from $2\text{-}2.4 \times 10^{-4}$ cm (inverse wavenumber units). Furthermore, the integral was computed utilizing the experimental spectra. In this case, the emission spectra of DBA-BTICz in toluene solution and in a film were compared, which differ by a red shift of the emission maximum in the film. Notably, both spectral overlap integral values are found to be one order of magnitude lower than those obtained from the computed spectra, despite the fact that they individually show great resemblance. This finding underscores the sensitivity of the spectral overlap integral to even minor variations in the spectral width.

While the spectral overlap integral is not contingent on external influences, the ECME is dependent on numerous factors. In order to study the orientation dependency, the left conformer of DBA-BTICz and the ν -DABNA were aligned to obtain different orientation factor (κ^2) values at a given barycenter distance. In case of the maximal orientation factor ($\kappa^2=4$), a study of the distance dependency was conducted for both conformers with a series of calculations in the range between 30 and 120 Å. To assess the validity of the IDA approach in this system, the ECME was calculated with both the MTD and the IDA. As illustrated in Fig. 4.12, the two approaches exhibit nearly perfect agreement for the left conformer. However, for the right conformer, a substantial discrepancy becomes evident for distances less than 60 Å.

A further factor that exerts a substantial influence on the electronic coupling is the damping effect of the surrounding medium. This effect is approximated in the IDA by dividing the ECME by the square of the refractive index of the medium (Eq. 2.69). In Fig. 4.12, the damping of the IDA ECME by a refractive index of 1.7

is depicted, which corresponds to the measured value for the DBFPO host matrix utilized in the experimental setup.^[105] A critical aspect that necessitates careful scrutiny when comparing the computed EET rate constant to the experimental one is the uncertainty associated with the orientation between the donor and acceptor in an OLED. In Förster theory, an orientation factor of 2/3 is frequently employed for freely movable and rotatable molecules. However, this approximation is not applicable to molecules within a matrix. Consequently, the orientation factor is adjusted to 0.476 as proposed for randomly aligned donor and acceptor molecules in the solid state.^[82] Considering these factors and utilizing the spectral overlap integral of the computed spectra, rate constants of $9 \times 10^7 \text{ s}^{-1}$ for the left conformer and $1 \times 10^7 \text{ s}^{-1}$ for the right conformer are obtained at an intermolecular distance of 40 Å. These values are in excellent agreement with the experimental rate constant of $7.5 \times 10^7 \text{ s}^{-1}$.

Furthermore, the Förster radius (R_F) was calculated by comparing the sum of the fluorescence and ISC rate constant to the EET rate constant at varying distances, taking into account damping and random orientation. Intriguingly, the Förster radius of the right conformer (40–45 Å) exceeds that of the left conformer (30–35 Å), despite the lower EET rate constant. This observation can be attributed to the higher fluorescence and ISC rate constant of the left conformer, consequently lowering the FRET efficiency (see Eq. 1.2).

4.4 Triplet–Singlet Excitation Energy Transfer

Computational Approach to Phosphor-Sensitized Fluorescence Based on Monomer Transition Densities (Paper 4)^[108]

As written in Sec. 1, the TSEET constitutes a novel methodology for enhancing the efficiencies and operational stability of OLEDs. The conventional phosphorescent molecules in an OLED are often very large iridium complexes. Consequently, for a preliminary application of the extension to triplet–singlet EET of the STRREET program (see Chapter 3), a more compact system was selected. Here, the energy transfer properties between a platinum complex and a fluorescein derivative is computed. This system was experimentally investigated with a focus on their characteristics pertaining to phosphorescence lifetime imaging microscopy (PLIM).^[109] Luminescence lifetime imaging can be utilized to determine changes for example in temperature, viscosity and pH in living cells.^[110–112]

The Pt^{II}-complex (AG97 – Fig. 4.13a) under investigation bears triphenylphosphine on one side and a tridentate ligand, comprising two trifluoromethylpyrazoles

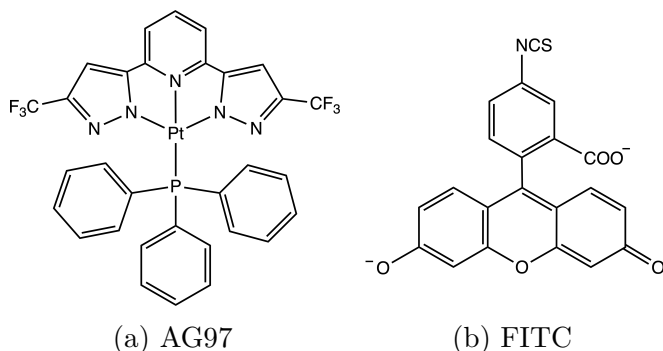


Figure 4.13: Chemical structures of the phosphorescent Pt^{II} -complex AG97 and the dianionic fluorescent label fluorescein isothiocyanate (FITC).

and a pyridine, on the other. The planarity of the tridentate ligand results in a quasi-square-planar coordination of the platinum center. The experiment reveals that the luminescence of the AG97 is almost completely quenched in solutions of dichloromethane (DCM) and dimethylsulfoxide (DMSO). However, phosphorescence is observable in phosphate-buffered saline (PBS) buffer, where aggregates are formed. Notably, these aggregates exhibit the emission properties of the monomeric species, contrasting with the typical red shift of aggregate emission.^[109] The ground state minimum structure was optimized in vacuum, DCM and DMSO. In all cases, the results showed good agreement with the experimental crystal structure, except for the rotation of the phenyl groups of the triphenylphosphine ligand. Additionally, the vertical excitation energies of the first three excited states (S_1 , T_1 , T_2) at these geometries are relatively similar. This is attributable to the predominant ligand-centered (LC) character of these states, accompanied by minor metal-to-ligand charge transfer (MLCT) character mixed into the wave functions.

In order to gain a better understanding of the photophysical processes of this molecule, the geometries of the three aforementioned excited states were optimized in DCM. It was observed that, at the S_1 geometry, the S_1 and T_1 states are both dominated by transitions from the HOMO to the LUMO, resulting in nearly identical difference densities (Fig. 4.14) and a low SOCME between these states (Tab. 4.1). The most important change in the wave function of the T_2 state is the contribution of a different d -orbital leading to a large SOCME with the S_1 state (Tab. 4.1). Due to the crossing in the T_2 PES with the T_1 PES, the T_2 minimum structure could not be located. Consequentially, the ISC rate constants were computed employing the VH method, which requires only the equilibrium geometry of the initial state. It has been demonstrated that the SOCME for the $S_1 \rightsquigarrow T_2$ process is considerably larger than for the $S_1 \rightsquigarrow T_1$ transition. Furthermore, the FCWDOS for both transitions are nearly identical. Consequently, the ISC

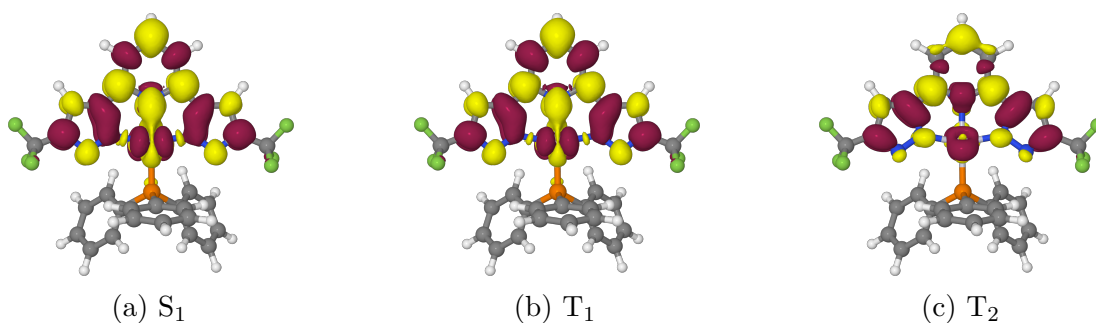


Figure 4.14: Difference densities of AG97 at the S₁ geometry in DCM (isovalue ± 0.001). Red-colored areas indicate a loss, yellow-colored areas a gain of electron density in the excited state.

Table 4.1: ISC rate constants k_{ISC} determined at the S₁ geometry of AG97 in DCM.

Transition	$\sum \text{SOCMEs}^2$ [cm ⁻²]	FCWDOS [cm ² s ⁻¹]	k_{ISC} [s ⁻¹]
S ₁ \rightsquigarrow T ₁	1.93	2.0×10^7	3.8×10^7
S ₁ \rightsquigarrow T ₂	305777.67	1.4×10^7	4.3×10^{12}

process into the T₂ state is considerably faster (Tab. 4.1). These rate constants lead to the assumption that after absorption, the T₂ state is populated via ISC and then transfers its population to the T₁ state via IC.

In contrast to the S₁ structure, the T₁ geometry is not symmetrical with respect to the central Pt-N bond. This change in geometry results in a localization of the differences densities of the T₁ and T₂ states on different sides of the tridentate ligand. Furthermore, the phenyl rings of the triphenylphosphine and the CF₃ groups exhibit larger rotation with respect to the ground state geometry. These structural differences lead to overestimation of the intensity in the lower energy parts of the computed phosphorescence spectra compared to the experimental emission spectra at room temperature in DCM and in a mixture of methanol (MeOH) and DCM at 77 K (Fig. 4.15). However, the computed radiative lifetime of 33 μs fits very well with the reported luminescence decay time of 19 μs .^[109] As previously discussed, the ECME has to be calculated for each triplet fine-structure level of the phosphorescent sensitizer. On the DFT/MRSOCI level of theory, the three sublevels (T_a, T_b, T_c) are energetically very close together (ZFS of 44 cm⁻¹), but show distinct features of their TDMVs. While the length of the TDMV of T_a is one order of magnitude smaller than the other two, it exhibits a nearly identical orientation to that of the TDMV of T_b. Both TDMVs are almost perpendicular to the plane of the tridentate ligand, while the TDMV of T_c lies in the plane of the ligand.

4 Results

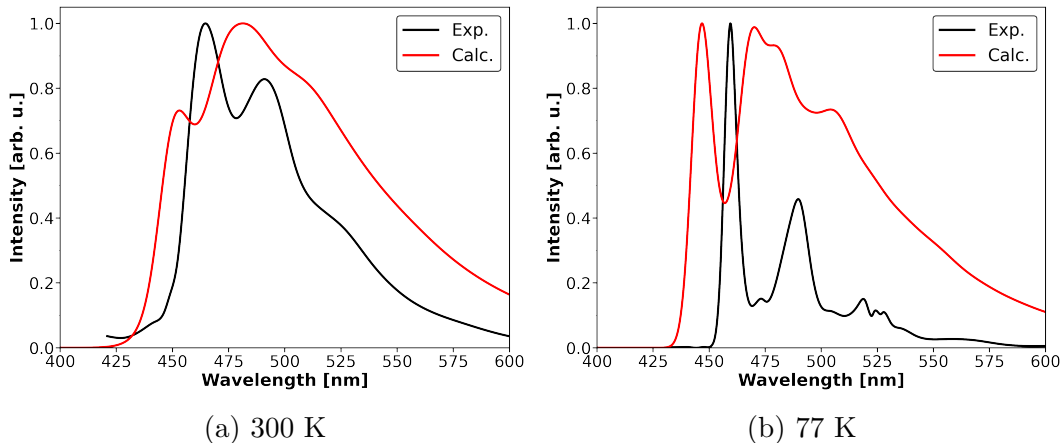
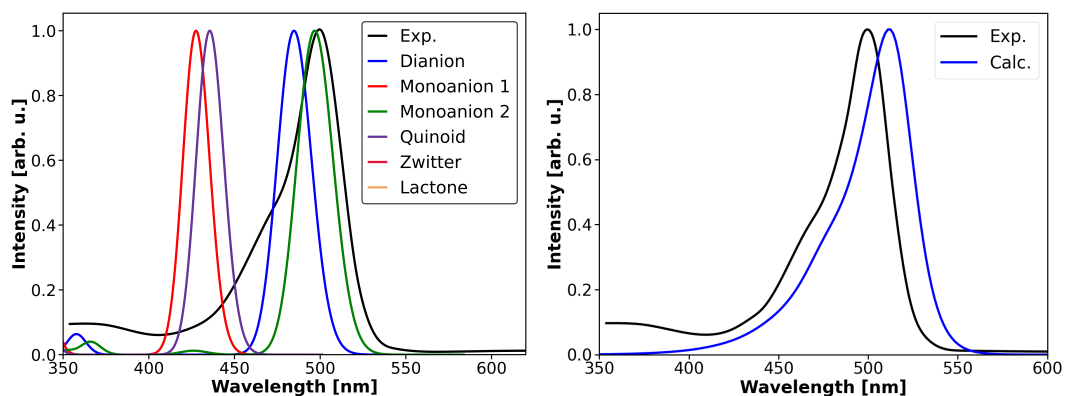


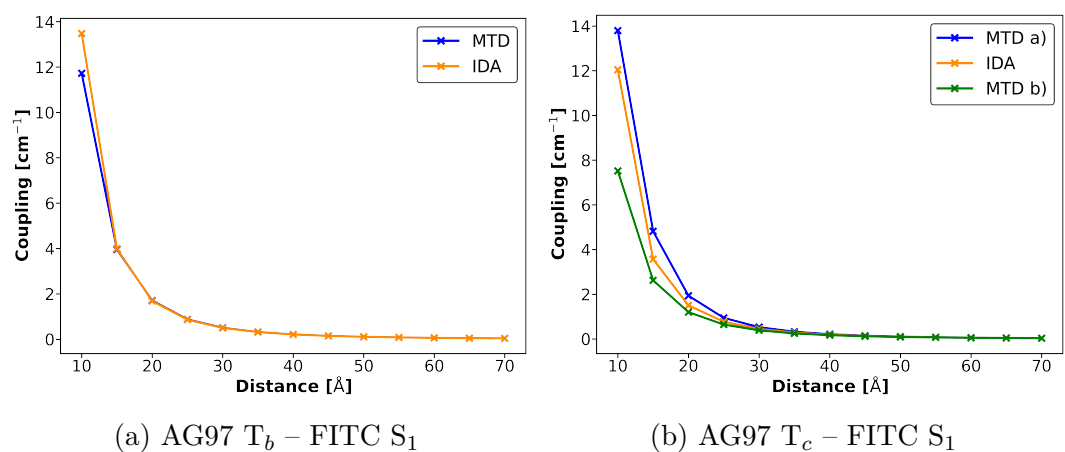
Figure 4.15: Calculated phosphorescence spectrum of AG97 in DCM at 300 K and 77 K compared to the experimental emission spectra in deaerated DCM at room temperature and in a mix of MeOH and DCM at 77 K.^[109]

The fluorescent probe in the experimental setup was fluorescein isothiocyanate (FITC), which, depending on the pH value, can exist in different tautomeric and prototropic forms. The known neutral tautomeric forms of fluorescein are a lactone, a zwitterion and a quinoid-like structure, which also has two monoanionic and a dianionic form (Fig. B.9).^[113] For each of these forms, the ground state structure was optimized in an implicit water environment, and the absorption spectrum was calculated based on the Gaussian broadened DFT/MRCI oscillator strengths (Fig. 4.16a). The analysis of these results suggest the presence of the monoanionic and dianionic species. A comparison of the experimental absorption spectrum of BSAFITC in PBS buffer solution with experiments in varying pH values suggests that the dianion is the dominant species in this setting.^[109,113] Therefore, the vibrational resolved absorption spectrum of the S_1 of the dianion, which is characterized by a $\pi\pi^*$ excitation located on the xanthone unit, was calculated with the VH method. This calculated spectrum exhibits an exceptional resemblance to the experimental BSAFITC absorption spectrum (Fig. 4.16b).^[109] The TDMV of this S_1 state is oriented along the long axis of the xanthone core. The initial step in the computational analysis of the EET process entailed the calculation of the spectral overlap integral. Despite the considerable discrepancy between the spectral envelopes of the calculated phosphorescence spectrum of AG97 and the experimental emission spectrum, the spectral overlap integral yielded very similar results for the usage of computed and experimental spectra. In a similar procedure as discussed in Sec. 4.3 the distance dependency of the ECME was calculated using the IDA and MTD approach for the inline orientation between each triplet fine-structure level of AG97 and FITC. The two methods



(a) Gaussian broadened absorption spectra (FWHM of 1000 cm^{-1}) of all tautomeric and prototropic forms of FITC. The zwitterion and the lactone form absorb only below 350 nm. (b) VH spectrum of the dianionic form of FITC.

Figure 4.16: Absorption spectra computed in an implicit water environment compared to the experimental spectrum of BSAFITC in PBS puffer.^[109]



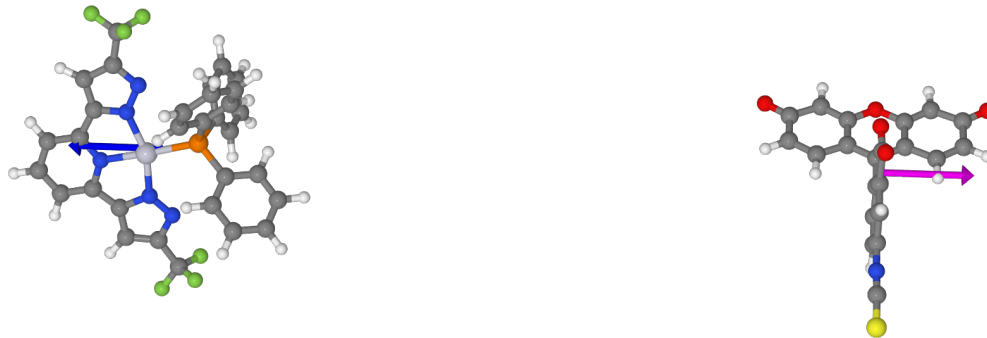
(a) AG97 T_b – FITC S_1

(b) AG97 T_c – FITC S_1

Figure 4.17: Distance dependency of the ECME between AG97 and FITC calculated with the IDA and MTD approach for the inline orientation of the respective TDMVs.



(a) Subcase a: Tridentate ligand and FITC on the same sides of the AG97 barycenter.



(b) Subcase b: Tridentate ligand and FITC on opposite sides of the AG97 barycenter.

Figure 4.18: Donor–acceptor arrangements in which the TDMV of the T_b sublevel of AG97 is aligned inline with the singlet TDMV (pink) of FITC.

demonstrate a strong similarity, particularly in the case of the T_b , as illustrated in Fig. 4.17a. For this particular orientation, the difference is only significant when the barycenter distances drops below 20 Å. Two cases can be established with regard to the coupling between the T_c and FITC. In the first case (Fig. 4.18a), the FITC is aligned on the same side of the platinum atom as the tridentate ligand. In the other case (Fig. 4.18b), the FITC is aligned on the opposite side of the platinum atom. The IDA method utilizes the distance between the two centers of masses, resulting in the same coupling for both orientations. The distance dependence of the MTD approach is attributed to the two-electron integrals, and given the predominance of the transition density matrix on the tridentate ligand, the two cases result in different ECMEs. Specifically, in the former case, the MTD ECME exceeds the IDA value, while in the latter case, the ECME is smaller than the IDA value (Fig. 4.17b) even for longer distances. The findings indicate that the distance between the center masses is not always a reliable metric for assessing the dipole-dipole coupling.

An analysis of the coupling of the three AG97 sublevels to FITC for the inline orientation of T_a reveals that, despite the very similar TDMV orientation, the ECME for T_b is three times larger than for T_a , in accordance with the length of

the TDMVs. Additionally, due to the nearly orthogonal orientation between the TDMVs of T_a and T_c , the ECME for the latter one is nearly vanishing. A similar outcome is obtained for the optimal orientation of T_b . Correspondingly, if the TDMV of the T_c is aligned collinearly with the TDMV of FITC, the ECMEs of T_a and T_b are negligible. Due to the nearly perpendicular arrangement of the TDMV of T_c and the other two sublevels, there are only a few molecular orientations that result in a vanishing coupling of all three sublevels. Additionally, the small ZFS and the subsequent thermal accessibility of all three sublevels enable energy transfer for a wide range of every molecular arrangement.

As previously discussed, the ECME and EET rate are dependent on the distance and orientation between the donor and acceptor molecules. Because the experiment does not allow for the determination of the orientation, the EET rate constant is computed with an averaged orientation factor (κ^2). In the case of freely rotating molecules, an average κ^2 -value of $2/3$ is obtained, while for random but rigid orientations, $\kappa^2 = 0.476$ is derived.^[82] The EET rate is further influenced by the refractive index of the surrounding medium, which enters the denominator of the rate equation in fourth power. For fluorescein in water, the refractive index is 1.34, resulting in a damping factor of approximately 3.22. These factors must be considered when determining the rate constant of each triplet sublevel of AG97. The resulting EET rate constant values are then averaged, given the estimation of an equal population for each, due to the low ZFS. In order to get an estimate for the Förster radius, the resulting rate constant is then compared to the averaged phosphorescence rate constant. This is done under the assumption that no other deactivation pathway of the donor has to be considered. With a value of $2/3$ for the orientation factor, the Förster radius is between 55 and 60 Å. For a κ^2 -value of 0.476 the Förster radius is approximately 55 Å. The experiments of Delcanale *et al.*^[109] revealed a photoluminescence quantum yield of 0.05 for the aggregates of AG97 in PBS buffer at room temperature. This finding suggests that non-radiative deactivations are predominant in this molecule, thereby diminishing the Förster radius. When the quantum yield of 5% is taken into account, the calculated Förster radius is reduced to 35 Å.

5 Conclusion

The objective of this work was to assess and extend the quantum chemical approach to excitation energy transfer, with the aim of computing systems that are suitable to OLEDs. In this context, energy transfer can play a pivotal role in enhancing the stability and color purity of these devices. The software utilized for the calculation of the EET rate constants was reworked and extended to triplet–triplet excitation energy transfer in a previous thesis.^[95] As a first test for the extension to triplet–triplet EET, the intramolecular energy transfer process in a spiran-linked anthrone-naphthalene molecule was examined. The investigation of the low-lying excited states revealed that, in contrast to an energy scheme proposed in the literature, a $^3\pi\pi^*$ state on the anthrone subunit is the lowest triplet state on this moiety in BuCN. Furthermore, the computations of the ISC rate constants suggest that this state is readily populated from the $^1n\pi^*$ on the anthrone. However, the Dexter energy transfer between the triplet states on the anthrone subunit and the first triplet state on the naphthalene moiety are forbidden in C_{2v} symmetry. Consequently, it is mandatory to go beyond the Condon approximation to model this process. To this end, NACMEs were computed, yielding time constants in very good agreement with the experiment. Despite the unsuccessful testing of the EET software, the proposed excited state energy dissipation pathway has elucidated certain inconsistencies in the extant literature.

It has been well established that, in addition to Dexter couplings, CT mediated energy transfer plays a pivotal role at short distances between donor and acceptor. In an effort to incorporate the effect of the bridging ionic states, Dyson orbitals were implemented into the DENSOMAT software. To test the implementation, Dyson norms were compared to literature values of small organic molecules, resulting in very good agreements. The observed deviations in these tests can be attributed to the utilization of different methods for computing the electronic wave functions. Furthermore, the calculation of Dyson norms was employed to reproduce experimentally observed ionization probabilities in a series of oligophenylenes. This approach enabled the identification of the states involved in photodetachment-photoelectron spectra, thereby substantiating the efficacy of the implementation of the Dyson orbitals. However, it was found that the energies of the charged

5 Conclusion

states are very unreliable when the same basis for neutral and charged states are used, which is required for the calculation of the Dyson orbitals. Consequently, the reliability of the couplings for the CT mediated energy transfer is questionable, given the role these energies play in their determination.

In another study, the STrEET program was utilized for the first time to calculate energy transfer properties in a hyperfluorescent OLED. Despite the size of the FRET donor and acceptor, excitation energies and transition dipole moments in accordance with the experimental values were obtained with the DFT/MRCI method. The calculation of emission spectra by means of a VH approach yields band shapes that exhibit a high degree of similarity to the experimental ones. For both molecules, two conformers were found. While the energetic difference in the conformers of the acceptor is negligible, the two conformers of the donor molecule exhibit distinct properties. This is evidenced by the substantial change in excitation energies, transition dipole moment strengths, and direction. These differences have a considerable impact on the EET properties of these conformers. The excitonic coupling matrix elements were computed using the IDA and MTD approach. In a series of calculations with varying donor–acceptor distances, the two methods demonstrated excellent agreement for one of the two donor conformers, while substantial deviations were observed for the other. When comparing with experimental findings, the most crucial factors are the spectral overlap integral and the relative orientation between the donor and acceptor. The spectral overlap integral can be calculated from the experimental spectra if available. However, determining the orientation in experiments is not possible, necessitating the use of average values for the orientation factor. Utilizing these average values and the damping from the medium, EET rate constants are derived that exhibit strong agreement with the experimental values. It is noteworthy that the conformer with the higher TDMV strength exhibits a lower Förster radius, attributable to the significantly larger ISC rate constant for this conformer.

Furthermore, the STrEET program was extended during this work to calculate triplet–singlet excitation energy transfer with the MTD approach. This extension was then applied to a PLIM system with smaller sized molecules. Similar to the hyperfluorescent system discussed above, DFT/MRCI excitation energies and transition dipole moments are in good agreement with the experimental values. Additionally, analogous studies regarding the distance and orientation dependence have been conducted with similar results. The ECMEs obtained with the IDA and MTD approach match very well. One advantage of the triplet–singlet EET compared to the singlet–singlet EET is the fact that the TDMVs of the individual triplet sublevels can face in different directions. Therefore, they cover

a larger angular range since fewer alignments yield vanishing ECMEs. However, the general smaller radiative rate constants of phosphorescent molecules lead to stronger competition with non-radiative deactivation processes of the EET rate constant. Since the computational effort is comparable to the singlet–singlet EET, this extension can also be employed for larger molecular systems, making it available for the calculation of phosphor-sensitized OLEDs.

Bibliography

- [1] F. Laquai, Y. Park, J. Kim, and T. Basché, “Excitation Energy Transfer in Organic Materials: From Fundamentals to Optoelectronic Devices,” *Macromol. Rapid Commun.*, vol. 30, pp. 1203–1231, 2009.
- [2] A. Periasamy, N. Mazumder, Y. Sun, K. G. Christopher, and R. N. Day, “FRET Microscopy: Basics, Issues and Advantages of FLIM-FRET Imaging,” in *Advanced Time-Correlated Single Photon Counting Applications*, pp. 249–276, Springer International Publishing, 2015.
- [3] S. E. Braslavsky, “Glossary of terms used in photochemistry, 3rd edition (IUPAC Recommendations 2006),” *Pure Appl. Chem.*, vol. 79, pp. 293–465, 2007.
- [4] R. O. Bennett and R. E. Kellogg, “MECHANISMS AND RATES OF RADIATIONLESS ENERGY TRANSFER,” *Photochem. Photobiol.*, vol. 7, pp. 571–581, 1968.
- [5] V. L. Ermolaev and E. B. Sveshnikova, “Inductive-resonance transfer of energy from aromatic molecules in the triplet state,” *So. Phys. Dokl.*, pp. 373–376, 1963.
- [6] R. G. Bennett, R. P. Schwenker, and R. E. Kellogg, “Radiationless Intermolecular Energy Transfer. II. Triplet→Singlet Transfer,” *J. Chem. Phys.*, vol. 41, pp. 3040–3041, Nov. 1964.
- [7] V. May, “Beyond the Förster theory of excitation energy transfer: importance of higher-order processes in supramolecular antenna systems,” *Dalton Trans.*, p. 10086, 2009.
- [8] H.-W. Chen, J.-H. Lee, B.-Y. Lin, S. Chen, and S.-T. Wu, “Liquid crystal display and organic light-emitting diode display: present status and future perspectives,” *Light Sci. Appl.*, vol. 7, pp. 17168–17168, 2018.
- [9] C. W. Tang and S. A. VanSlyke, “Organic electroluminescent diodes,” *Appl. Phys. Lett.*, vol. 51, pp. 913–915, 1987.

Bibliography

- [10] J. Wang, H. Pang, Z. Cui, X. Chen, R. Zheng, R. Kwong, and S. Xia, “Stack design of OLEDs with high performance and simplified device structures,” *J. Soc. Inf. Disp.*, vol. 30, pp. 495–504, 2021.
- [11] M. A. Baldo, D. F. O’Brien, M. E. Thompson, and S. R. Forrest, “Excitonic singlet-triplet ratio in a semiconducting organic thin film,” *Phys. Rev. B*, vol. 60, pp. 14422–14428, 1999.
- [12] A. Monkman, “Why Do We Still Need a Stable Long Lifetime Deep Blue OLED Emitter?,” *ACS Appl. Mater. Interfaces*, vol. 14, pp. 20463–20467, 2022.
- [13] G. Hong, X. Gan, C. Leonhardt, Z. Zhang, J. Seibert, J. M. Busch, and S. Bräse, “A Brief History of OLEDs—Emitter Development and Industry Milestones,” *Adv. Mater.*, vol. 33, 2021.
- [14] M. A. Baldo, D. F. O’Brien, Y. You, A. Shoustikov, S. Sibley, M. E. Thompson, and S. R. Forrest, “Highly efficient phosphorescent emission from organic electroluminescent devices,” *Nature*, vol. 395, pp. 151–154, 1998.
- [15] W. C. H. Choy, W. K. Chan, and Y. Yuan, “Recent Advances in Transition Metal Complexes and Light-Management Engineering in Organic Optoelectronic Devices,” *Adv. Mater.*, vol. 26, pp. 5368–5399, 2014.
- [16] D. Volz, M. Wallesch, C. Fléchon, M. Danz, A. Verma, J. M. Navarro, D. M. Zink, S. Bräse, and T. Baumann, “From iridium and platinum to copper and carbon: new avenues for more sustainability in organic light-emitting diodes,” *Green Chem.*, vol. 17, pp. 1988–2011, 2015.
- [17] J.-H. Lee, C.-H. Chen, P.-H. Lee, H.-Y. Lin, M.-k. Leung, T.-L. Chiu, and C.-F. Lin, “Blue organic light-emitting diodes: current status, challenges, and future outlook,” *J. Mater. Chem. C*, vol. 7, pp. 5874–5888, 2019.
- [18] E. Tankelevičiūtė, I. D. W. Samuel, and E. Zysman-Colman, “The Blue Problem: OLED Stability and Degradation Mechanisms,” *J. Phys. Chem. Lett.*, vol. 15, pp. 1034–1047, 2024.
- [19] D. Y. Kondakov, “Triplet–triplet annihilation in highly efficient fluorescent organic light-emitting diodes: current state and future outlook,” *Philos. Trans. R. Soc. A*, vol. 373, p. 20140321, 2015.

- [20] C. Chen, N. T. Tierce, M. Leung, T. Chiu, C. Lin, C. J. Bardeen, and J. Lee, “Efficient Triplet–Triplet Annihilation Upconversion in an Electroluminescence Device with a Fluorescent Sensitizer and a Triplet-Diffusion Singlet-Blocking Layer,” *Adv. Mater.*, vol. 30, 2018.
- [21] A. Endo, K. Sato, K. Yoshimura, T. Kai, A. Kawada, H. Miyazaki, and C. Adachi, “Efficient up-conversion of triplet excitons into a singlet state and its application for organic light emitting diodes,” *Appl. Phys. Lett.*, vol. 98, 2011.
- [22] H. Yersin, *Highly Efficient OLEDs: Materials Based on Thermally Activated Delayed Fluorescence*. Wiley, 2018.
- [23] E. Cariati, E. Lucenti, C. Botta, U. Giovanella, D. Marinotto, and S. Righetto, “Cu(I) hybrid inorganic–organic materials with intriguing stimuli responsive and optoelectronic properties,” *Coord. Chem. Rev.*, vol. 306, pp. 566–614, 2016.
- [24] T. Hatakeyama, K. Shiren, K. Nakajima, S. Nomura, S. Nakatsuka, K. Kinoshita, J. Ni, Y. Ono, and T. Ikuta, “Ultrapure Blue Thermally Activated Delayed Fluorescence Molecules: Efficient HOMO–LUMO Separation by the Multiple Resonance Effect,” *Adv. Mater.*, vol. 28, pp. 2777–2781, 2016.
- [25] H. Jiang, J. Jin, and W. Wong, “High-Performance Multi-Resonance Thermally Activated Delayed Fluorescence Emitters for Narrowband Organic Light-Emitting Diodes,” *Advanced Functional Materials*, vol. 33, 2023.
- [26] S. Gottardi, M. Barbry, R. Coehoorn, and H. van Eersel, “Efficiency loss processes in hyperfluorescent OLEDs: A kinetic Monte Carlo study,” *Appl. Phys. Lett.*, vol. 114, 2019.
- [27] K. Stavrou, L. G. Franca, A. Danos, and A. P. Monkman, “Key requirements for ultraefficient sensitization in hyperfluorescence organic light-emitting diodes,” *Nat. Photonics*, vol. 18, pp. 554–561, 2024.
- [28] S. Y. Byeon, D. R. Lee, K. S. Yook, and J. Y. Lee, “Recent Progress of Singlet-Exciton-Harvesting Fluorescent Organic Light-Emitting Diodes by Energy Transfer Processes,” *Adv. Mater.*, no. 34, 2019.
- [29] K. H. Lee and J. Y. Lee, “High External Quantum Efficiency in Fluorescent OLED by Cascade Singlet Harvesting Mechanism,” *Adv. Opt. Mater.*, vol. 8, 2020.

Bibliography

- [30] M. Zhang, C.-J. Zheng, H. Lin, and S.-L. Tao, “Thermally activated delayed fluorescence exciplex emitters for high-performance organic light-emitting diodes,” *Mater. Horiz.*, no. 2, pp. 401–425, 2021.
- [31] S. P. Thompson, “V. On hyperphosphorescence,” *London Edinburgh Dublin Philos. Mag. & J. Sci.*, vol. 42, pp. 103–107, 1896.
- [32] D. S. Sholl and J. A. Steckel, *Density Functional Theory: A Practical Introduction*. John Wiley & Sons, 2022.
- [33] W. Kohn and L. J. Sham, “Density functional theory,” in *Conference Proceedings-Italian Physical Society*, vol. 49, pp. 561–572, 1996.
- [34] P. A. M. Dirac, “Note on Exchange Phenomena in the Thomas Atom,” *Math. Proc. Camb. Philos. Soc.*, vol. 26, pp. 376–385, 1930.
- [35] P. Hohenberg and W. Kohn, “Inhomogeneous Electron Gas,” *Phys. Rev.*, vol. 136, pp. B864–B871, 1964.
- [36] Y.-S. Lin, G.-D. Li, S.-P. Mao, and J.-D. Chai, “Long-Range Corrected Hybrid Density Functionals with Improved Dispersion Corrections,” *J. Chem. Theory Comput.*, vol. 9, pp. 263–272, 2012.
- [37] A. D. Becke, “A new mixing of Hartree–Fock and local density-functional theories,” *J. Chem. Phys.*, vol. 98, pp. 1372–1377, 1993.
- [38] C. Adamo and V. Barone, “Toward reliable density functional methods without adjustable parameters: The PBE0 model,” *J. Chem. Phys.*, vol. 110, pp. 6158–6170, 1999.
- [39] O. A. Vydrov and G. E. Scuseria, “Assessment of a long-range corrected hybrid functional,” *J. Chem. Phys.*, vol. 125, 2006.
- [40] T. M. Henderson, A. F. Izmaylov, G. Scalmani, and G. E. Scuseria, “Can short-range hybrids describe long-range-dependent properties?,” *J. Chem. Phys.*, vol. 131, 2009.
- [41] M. Huix-Rotllant, N. Ferré, and M. Barbatti, “Time-Dependent Density Functional Theory,” in *Quantum Chemistry and Dynamics of Excited States*, ch. 2, pp. 13–46, John Wiley and Sons, Ltd, 2020.
- [42] E. Runge and E. K. U. Gross, “Density-Functional Theory for Time-Dependent Systems,” *Phys. Rev. Lett.*, vol. 52, pp. 997–1000, 1984.

- [43] M. Marques and E. Gross, “Time-Dependent Density Functional Theory,” *Annu. Rev. Phys. Chem.*, vol. 55, pp. 427–455, 2004.
- [44] M. Casida and M. Huix-Rotllant, “Progress in Time-Dependent Density-Functional Theory,” *Annu. Rev. Phys. Chem.*, vol. 63, pp. 287–323, 2012.
- [45] Y. Tawada, T. Tsuneda, S. Yanagisawa, T. Yanai, and K. Hirao, “A long-range-corrected time-dependent density functional theory,” *J. Chem. Phys.*, vol. 120, pp. 8425–8433, 2004.
- [46] A. Dreuw and M. Head-Gordon, “Single-Reference ab Initio Methods for the Calculation of Excited States of Large Molecules,” *Chemical Reviews*, vol. 105, pp. 4009–4037, 2005.
- [47] C. J. Cramer and D. G. Truhlar, “Implicit Solvation Models: Equilibria, Structure, Spectra, and Dynamics,” *Chem. Rev.*, no. 8, pp. 2161–2200, 1999.
- [48] E. Cancès, B. Mennucci, and J. Tomasi, “A new integral equation formalism for the polarizable continuum model: Theoretical background and applications to isotropic and anisotropic dielectrics,” *J. Chem. Phys.*, vol. 107, pp. 3032–3041, 1997.
- [49] J. Tomasi, B. Mennucci, and R. Cammi, “Quantum Mechanical Continuum Solvation Models,” *Chem. Rev.*, vol. 105, pp. 2999–3094, 2005.
- [50] C. M. Marian, A. Heil, and M. Kleinschmidt, “The DFT/MRCI method,” *WIREs Comput. Mol. Sci.*, vol. 9, 2018.
- [51] R. W. Wetmore and G. A. Segal, “Efficient generation of configuration interaction matrix elements,” *Chem. Phys. Lett.*, vol. 36, pp. 478–483, 1975.
- [52] G. A. Segal, R. W. Wetmore, and K. Wolf, “Efficient methods for configuration interaction calculations,” *Chem. Phys.*, vol. 30, pp. 269–297, 1978.
- [53] S. Grimme and M. Waletzke, “A combination of Kohn–Sham density functional theory and multi-reference configuration interaction methods,” *J. Chem. Phys.*, vol. 111, pp. 5645–5655, 1999.
- [54] I. Lyskov, M. Kleinschmidt, and C. M. Marian, “Redesign of the DFT/MRCI Hamiltonian,” *J. Chem. Phys.*, vol. 144, 2016.
- [55] A. Heil and C. M. Marian, “DFT/MRCI Hamiltonian for odd and even numbers of electrons,” *J. Chem. Phys.*, vol. 147, 2017.

Bibliography

- [56] A. Heil, M. Kleinschmidt, and C. M. Marian, “On the performance of DFT/MRCI Hamiltonians for electronic excitations in transition metal complexes: The role of the damping function,” *J. Chem. Phys.*, vol. 149, 2018.
- [57] D. R. Dombrowski, T. Schulz, M. Kleinschmidt, and C. M. Marian, “R2022: A DFT/MRCI Ansatz with Improved Performance for Double Excitations,” *J. Phys. Chem. A*, vol. 127, pp. 2011–2025, 2023.
- [58] C. M. Marian, “Spin-Orbit Coupling in Molecules,” in *Reviews in Computational Chemistry*, vol. 17, pp. 99–204, New York: Wiley, 2001.
- [59] C. M. Marian, “Spin-orbit coupling and intersystem crossing in molecules,” *WIREs Comput. Mol. Sci.*, vol. 2, pp. 187–203, 2011.
- [60] M. Kleinschmidt, J. Tatchen, and C. M. Marian, “SPOCK.CI: A multireference spin-orbit configuration interaction method for large molecules,” *J. Chem. Phys.*, vol. 124, 2006.
- [61] M. Kleinschmidt, J. Tatchen, and C. M. Marian, “Spin-Orbit Coupling of DFT/MRCI Wavefunctions: Method, Test Calculations, and Application to Thiophene,” *Journal of Computational Chemistry*, vol. 23, pp. 824–833, 2002.
- [62] L. J. Brillson, *Surfaces and Interfaces of Electronic Materials*. Wiley, 2010.
- [63] L. C. Feldman and J. W. Mayer, *Fundamentals of Surface and Thin Film Analysis*. Prentice Hall, 1986.
- [64] R. F. Schwitters, “Scattering and decays from Fermi’s golden rule including all the \hbar ’s and c ’s.” University of Texas: PHY362L Supplementary Note, 2004.
- [65] D. J. Griffiths, *Introduction to Quantum Mechanics*. Prentice Hall, 1995.
- [66] C. M. Marian, “Understanding and Controlling Intersystem Crossing in Molecules,” *Annu. Rev. Phys. Chem.*, vol. 72, pp. 617–640, 2021.
- [67] M. Etinski, J. Tatchen, and C. M. Marian, “Thermal and solvent effects on the triplet formation in cinnoline,” *Phys. Chem. Chem. Phys.*, vol. 16, p. 4740, 2014.
- [68] M. Etinski, V. Rai-Constapel, and C. M. Marian, “Time-dependent approach to spin-vibronic coupling: Implementation and assessment,” *J. Chem. Phys.*, vol. 140, 2014.

- [69] M. Etinski, “The role of Duschinsky rotation in intersystem crossing: A case study of uracil,” *J. Serb. Chem. Soc.*, vol. 76, pp. 1649–1660, 2011.
- [70] M. El-Sayed, D. Tinti, and D. Owens, “Spectroscopic determination of the most probable intersystem crossing route in phosphorescing molecules,” *Chem. Phys. Lett.*, vol. 3, pp. 339–342, 1969.
- [71] F. Plasser, M. Ruckebauer, S. Mai, M. Oettel, P. Marquetand, and L. González, “Efficient and Flexible Computation of Many-Electron Wave Function Overlaps,” *J. Chem. Theory Comput.*, vol. 12, pp. 1207–1219, 2016.
- [72] M. Bracker, C. M. Marian, and M. Kleinschmidt, “Internal conversion of singlet and triplet states employing numerical DFT/MRCI derivative couplings: Implementation, tests, and application to xanthone,” *J. Chem. Phys.*, vol. 155, 2021.
- [73] B. de Souza, G. Farias, F. Neese, and R. Izsák, “Predicting Phosphorescence Rates of Light Organic Molecules Using Time-Dependent Density Functional Theory and the Path Integral Approach to Dynamics,” *J. Chem. Theory Comput.*, no. 3, pp. 1896–1904, 2019.
- [74] T. Böhmer, M. Kleinschmidt, and C. M. Marian, “Toward the improvement of vibronic spectra and non-radiative rate constants using the vertical Hessian method,” *J. Chem. Phys.*, vol. 161, 2024.
- [75] A. Hazra, H. H. Chang, and M. Nooijen, “First principles simulation of the UV absorption spectrum of ethylene using the vertical Franck-Condon approach,” *The Journal of Chemical Physics*, vol. 121, pp. 2125–2136, 2004.
- [76] E. Hennebicq, G. Pourtois, G. D. Scholes, L. M. Herz, D. M. Russell, C. Silva, S. Setayesh, A. C. Grimsdale, K. Müllen, J.-L. Brédas, and D. Beljonne, “Exciton Migration in Rigid-Rod Conjugated Polymers: An Improved Förster Model,” *J. Am. Chem. Soc.*, vol. 127, pp. 4744–4762, 2005.
- [77] V. May and O. Kühn, *Charge and Energy Transfer Dynamics in Molecular Systems*. John Wiley & Sons, Incorporated, 3rd ed., 2011.
- [78] J. D. Spiegel, I. Lyskov, M. Kleinschmidt, and C. M. Marian, “Charge-transfer contributions to the excitonic coupling matrix element in BODIPY-based energy transfer cassettes,” *Chem. Phys.*, vol. 482, 2017.

Bibliography

- [79] J. E. Subotnik, J. Vura-Weis, A. J. Sodt, and M. A. Ratner, “Predicting Accurate Electronic Excitation Transfer Rates via Marcus Theory with Boys or Edmiston-Ruedenberg Localized Diabatization,” *J. Phys. Chem. A*, vol. 114, pp. 8665–8675, 2010.
- [80] J. E. Subotnik, R. J. Cave, R. P. Steele, and N. Shenvi, “The initial and final states of electron and energy transfer processes: Diabatization as motivated by system-solvent interactions,” *J. Chem. Phys.*, vol. 130, 2009.
- [81] T. Förster, “Zwischenmolekulare Energiewanderung und Fluoreszenz,” *Ann. Phys.*, vol. 437, pp. 55–75, 1948.
- [82] M. Z. Maksimov and I. M. Rozman, “On Energy Transfer in Solid Solutions,” *Opt. Spectrosc.*, vol. 12, p. 337, 1962.
- [83] J. D. Spiegel, S. Fulle, M. Kleinschmidt, H. Gohlke, and C. M. Marian, “Failure of the IDA in FRET Systems at Close Inter-Dye Distances Is Moderated by Frequent Low κ^2 Values,” *J. Phys. Chem. B*, vol. 120, pp. 8845–8862, 2016.
- [84] M. Kasha, H. R. Rawls, and M. Ashraf El-Bayoumi, “The exciton model in molecular spectroscopy,” *Pure Appl. Chem.*, vol. 11, pp. 371–392, 1965.
- [85] R. F. Fink, J. Pfister, A. Schneider, H. M. Zhao, and B. Engels, “Ab initio configuration interaction description of excitation energy transfer between closely packed molecules,” *Chem. Phys.*, vol. 343, pp. 353–361, 2008.
- [86] R. F. Fink, J. Pfister, H. M. Zhao, and B. Engels, “Assessment of quantum chemical methods and basis sets for excitation energy transfer,” *Chem. Phys.*, vol. 346, pp. 275–285, 2008.
- [87] J. D. Spiegel, M. Kleinschmidt, A. Larbig, J. Tatchen, and C. M. Marian, “Quantum-Chemical Studies on Excitation Energy Transfer Processes in BODIPY-Based Donor–Acceptor Systems,” *J. Chem. Theory Comput.*, vol. 11, pp. 4316–4327, 2015.
- [88] H. Nagae, T. Kakitani, T. Katoh, and M. Mimuro, “Calculation of the excitation transfer matrix elements between the S_2 or S_1 state of carotenoid and the S_2 or S_1 state of bacteriochlorophyll,” *J. Chem. Phys.*, vol. 98, pp. 8012–8023, 1993.
- [89] R. D. Harcourt, G. D. Scholes, and K. P. Ghiggino, “Rate expressions for excitation transfer. II. Electronic considerations of direct and

- through-configuration exciton resonance interactions,” *J. Chem. Phys.*, vol. 101, pp. 10521–10525, 1994.
- [90] G. D. Scholes, “Long-Range Resonance Energy Transfer in Molecular Systems,” *Annu. Rev. Phys. Chem.*, vol. 54, pp. 57–87, 2003.
- [91] K. J. Fujimoto, “Transition-density-fragment interaction combined with transfer integral approach for excitation-energy transfer via charge-transfer states,” *J. Chem. Phys.*, vol. 137, 2012.
- [92] L. M. Thompson, E. M. Kempfer-Robertson, S. Saha, S. Parmar, and P. M. Kozlowski, “Nonorthogonal Multireference Wave Function Description of Triplet–Triplet Energy Transfer Couplings,” *J. Chem. Theory Comput.*, vol. 19, pp. 7685–7694, 2023.
- [93] R. D. Harcourt, K. P. Ghiggino, G. D. Scholes, and S. Speiser, “On the origin of matrix elements for electronic excitation (energy) transfer,” *J. Chem. Phys.*, vol. 105, pp. 1897–1901, 1996.
- [94] J. D. Spiegel, *Singlet excitation energy transfer in covalently bridged and non-bridged bichromophoric systems*. PhD thesis, Heinrich Heine University, Düsseldorf, Germany, 2016. Available at <https://docserv.uni-duesseldorf.de/servlets/DocumentServlet?id=40442>.
- [95] F. Meitza, *Electronic Matrix Elements and Their Derivatives for Radiative and Non-Radiative Rate Constants: Development and Applications*. PhD thesis, Heinrich Heine University, Düsseldorf, Germany, 2023. Available at <https://docserv.uni-duesseldorf.de/servlets/DocumentServlet?id=62953>.
- [96] E. A. Coutias, C. Seok, and K. A. Dill, “Using quaternions to calculate RMSD,” *J. Comput. Chem.*, vol. 25, pp. 1849–1857, 2004.
- [97] S. Metz, T. Böhmer, B. Raunitschke, and C. M. Marian, “Intersystem crossing and intramolecular triplet excitation energy transfer in spiro[9,10-dihydro-9-oxoanthracene-10,2'-5',6'-benzindan] investigated by DFT/MRCI methods,” *Can. J. Chem.*, vol. 101, pp. 633–640, 2023.
- [98] J. Dobkowski, A. Gorski, M. Kijak, M. Pietrzak, K. Redeckas, and M. Vengris, “Combined Picosecond Time-Resolved UV–Vis and NMR Techniques Used for Investigation of the Excited State Intramolecular Triplet–Triplet Energy Transfer,” *J. Phys. Chem. A*, vol. 123, pp. 6978–6985, 2019.

Bibliography

- [99] W. Arbelo-González, R. Crespo-Otero, and M. Barbatti, “Steady and Time-Resolved Photoelectron Spectra Based on Nuclear Ensembles,” *J. Chem. Theory Comput.*, vol. 12, pp. 5037–5049, 2016.
- [100] M. Spanner, S. Patchkovskii, C. Zhou, S. Matsika, M. Kotur, and T. C. Weinacht, “Dyson norms in XUV and strong-field ionization of polyatomics: Cytosine and uracil,” *Phys. Rev. A*, vol. 86, p. 053406, 2012.
- [101] M. L. Vidal, A. I. Krylov, and S. Coriani, “Dyson orbitals within the fc-CVS-EOM-CCSD framework: theory and application to X-ray photoelectron spectroscopy of ground and excited states,” *Phys. Chem. Chem. Phys.*, vol. 22, pp. 2693–2703, 2020.
- [102] B. N. C. Tenorio, A. Ponzi, S. Coriani, and P. Decleva, “Photoionization Observables from Multi-Reference Dyson Orbitals Coupled to B-Spline DFT and TD-DFT Continuum,” *Molecules*, vol. 27, p. 1203, 2022.
- [103] T. Schulz, P. Konieczny, D. R. Dombrowski, S. Metz, C. M. Marian, and R. Weinkauff, “Electron affinities and lowest triplet and singlet state properties of para-oligophenylenes ($n = 3-5$): theory and experiment,” *Phys. Chem. Chem. Phys.*, vol. 25, pp. 29850–29866, 2023.
- [104] S. Metz and C. M. Marian, “Excitonic Coupling of a TADF Assistant Dopant and a Multi-Resonance TADF Emitter,” *Adv. Opt. Mater.*, 2024.
- [105] R. Braveenth, H. Lee, J. D. Park, K. J. Yang, S. J. Hwang, K. R. Naveen, R. Lampande, and J. H. Kwon, “Achieving Narrow FWHM and High EQE Over 38% in Blue OLEDs Using Rigid Heteroatom-Based Deep Blue TADF Sensitized Host,” *Adv. Func. Mater.*, vol. 31, 2021.
- [106] K. Stavrou, A. Danos, T. Hama, T. Hatakeyama, and A. Monkman, “Hot Vibrational States in a High-Performance Multiple Resonance Emitter and the Effect of Excimer Quenching on Organic Light-Emitting Diodes,” *ACS Appl. Mater. Interfaces*, vol. 13, pp. 8643–8655, 2021.
- [107] Y. Kondo, K. Yoshiura, S. Kitera, H. Nishi, S. Oda, H. Gotoh, Y. Sasada, M. Yanai, and T. Hatakeyama, “Narrowband deep-blue organic light-emitting diode featuring an organoboron-based emitter,” *Nat. Photonics*, vol. 13, pp. 678–682, July 2019.
- [108] S. Metz and C. M. Marian, “Computational Approach to Phosphor-Sensitized Fluorescence Based on Monomer Transition Densities,” *J. Chem. Theory Comput.*, vol. 21, pp. 2569–2581, 2024.

- [109] P. Delcanale, A. Galstyan, C. G. Daniliuc, H. E. Grecco, S. Abbruzzetti, A. Faust, C. Viappiani, and C. A. Strassert, “Oxygen-Insensitive Aggregates of Pt(II) Complexes as Phosphorescent Labels of Proteins with Luminescence Lifetime-Based Readouts,” *ACS Appl. Mater. Interfaces*, vol. 10, pp. 24361–24369, 2018.
- [110] P. I. Bastiaens and R. Pepperkok, “Observing proteins in their natural habitat: the living cell,” *Trends Biochem. Sci.*, vol. 25, pp. 631–637, 2000.
- [111] F. S. Wouters, P. J. Verveer, and P. I. Bastiaens, “Imaging biochemistry inside cells,” *Trends Cell Biol.*, vol. 11, pp. 203–211, 2001.
- [112] R. Datta, T. M. Heaster, J. T. Sharick, A. A. Gillette, and M. C. Skala, “Fluorescence lifetime imaging microscopy: fundamentals and advances in instrumentation, analysis, and applications,” *J. Biomed. Opt.*, vol. 25, p. 1, 2020.
- [113] M. A. Gerasimova, F. N. Tomilin, E. Y. Malyar, S. A. Varganov, D. G. Fedorov, S. G. Ovchinnikov, and E. A. Slyusareva, “Fluorescence and photoinduced proton transfer in the protolytic forms of fluorescein: Experimental and computational study,” *Dyes Pigm.*, vol. 173, p. 107851, 2020.

A List of Abbreviations

AH	adiabatic Hessian
BuCN	butyronitrile
CSF	configuration state function
CT	charge-transfer
DCM	dichlormethane
DFT	density functional theory
DMSO	dimethylsulfoxide
DOMO	doubly occupied molecular orbital
ECME	excitonic coupling matrix element
EET	excitation energy transfer
ESA	excited state absorption
FCWDOS	Frank-Condon weighted density of states
FRET	Förster resonance energy transfer
FWHM	full width at half maximum
GGA	generalized gradient approximation
HF	Hartree-Fock
HOMO	highest occupied molecular orbital
HT	Herzberg-Teller
IC	internal conversion
IDA	ideal dipole approximation
irrep	irreducible representation
IQE	internal quantum efficiency
ISC	intersystem crossing
KS	Kohn-Sham
LC	ligand-centered

A List of Abbreviations

LCD	liquid crystal display
LDA	local density approximation
LE	locally excited
LUMO	lowest unoccupied molecular orbital
MeOH	methanol
MLCT	metal-to-ligand charge transfer
MO	molecular orbital
MRCI	multireference configuration interaction
MRSOCI	multireference spin-orbit configuration interaction
MTD	monomer transition density
NACME	non-adiabatic coupling matrix element
OLED	organic light-emitting diode
PBS	phosphate-buffered saline
PCM	polarizable continuum model
PES	potential energy surface
PD-PE	photodetachment-photoelectron
PLIM	phosphorescence lifetime imaging microscopy
RI	resolution-of-identity
rISC	reverse intersystem crossing
1-RTDM	reduced one-particle transition density matrix
SOC	spin-orbit coupling
SOCME	spin-orbit coupling matrix element
SOCQDPT	spin-orbit coupling quasi-degenerate perturbation theory
SOMF	spin-orbit mean field
SOMO	singly occupied molecular orbital
SSEET	singlet-singlet excitation energy transfer
STrEET	singlet-triplet excitation energy transfer
TADF	thermally activated delayed fluorescence
TAF	thermally assisted fluorescence
TDA	Tamm-Dancoff approximation

TDDFT	time-dependent density functional theory
TDMV	transition dipole moment vector
TSEET	triplet–singlet excitation energy transfer
TTA	triplet–triplet annihilation
TTEET	triplet–triplet excitation energy transfer
VH	vertical Hessian
WFT	wave function theory
ZFS	zero field splitting

B Appendix

```
1 #===== EET Input File =====#
2 #Please keep Key-Value Pairs in this format: 'Key : Value'
3
4 #===== CALCULATION TYPE =====#
5 # type can be: [IDA, MTD, SPECTRALOVERLAP]
6     CALCULATION_TYPE : IDA
7
8 #===== Donor Properties =====#
9
10 #=== Donor Geometry ===#
11     DONOR-SOURCE : TURBOMOLE
12     DONOR-PATH : /psycopath/
13     #DONOR_ALIGNMENT_PATH : /psycopath/
14
15 #=== Donor Transition Dipole Moment ===#
16     DONOR_X_TDM : 0.0
17     DONOR_Y_TDM : 0.0
18     DONOR_Z_TDM : 0.0
19
20 #=== Donor Rotation before Dimer Construction ===#
21     DONOR_X_ROTATION : 0.0
22     DONOR_Y_ROTATION : 0.0
23     DONOR_Z_ROTATION : 0.0
24     DONOR_ROTATION_ORDER : XYZ
25
26
27 #===== Acceptor Properties =====#
28
29 #=== Acceptor Geometry ===#
30     ACCEPTOR-SOURCE : TURBOMOLE
31     ACCEPTOR-PATH : /sociopath/
32     #ACCEPTOR_ALIGNMENT_PATH : /sociopath/
33
34 #=== Acceptor Transition Dipole Moment ===#
35     ACCEPTOR_X_TDM : 0.0
36     ACCEPTOR_Y_TDM : 0.0
37     ACCEPTOR_Z_TDM : 0.0
```

B Appendix

```
38
39 #=== Acceptor Rotation before Dimer Construction ===#
40     ACCEPTOR_X_ROTATION : 0.0
41     ACCEPTOR_Y_ROTATION : 0.0
42     ACCEPTOR_Z_ROTATION : 0.0
43     ACCEPTOR_ROTATION_ORDER : XYZ
44
45
46 #===== Dimer Properties =====#
47
48 #=== Distance between Donor and Acceptor Center of Masses ===#
49     DIMER_X_DISTANCE : 0.0
50     DIMER_Y_DISTANCE : 0.0
51     DIMER_Z_DISTANCE : 0.0
52
53 #=== Kappa (-2,...,2) ===#
54 #Overrides any defined Rotation
55     KAPPA : 0.0
56
57 #=== Refractive Index ===#
58     REFRACTIVE_INDEX : 1.0
```

Listing B.1: Input file for a IDA calculation

```

1 #===== EET Input File =====#
2 #Please keep Key-Value Pairs in this format: 'Key : Value'
3
4 #===== CALCULATION TYPE =====#
5 # type can be: [IDA, MTD, SPECTRALOVERLAP]
6     CALCULATION_TYPE : MTD
7
8 #===== DIMER PARAMETERS =====#
9 # distance in Angstroem, angles in degree
10
11 #=== DONOR ===#
12     DONOR_PATH : /sociopath/
13     DONOR_FORMAT : TURBOMOLE
14 #DONOR_ALIGNMENT_PATH : /sociopath/
15     DONOR_X_ROTATION : 0.0
16     DONOR_Y_ROTATION : 0.0
17     DONOR_Z_ROTATION : 0.0
18     DONOR_ROTATION_ORDER : xyz
19
20 #=== ACCEPTOR ===#
21     ACCEPTOR_PATH : /psychopath/
22     ACCEPTOR_FORMAT : TURBOMOLE
23 #ACCEPTOR_ALIGNMENT_PATH : /psychopath/
24     ACCEPTOR_X_ROTATION : 0.0
25     ACCEPTOR_Y_ROTATION : 0.0
26     ACCEPTOR_Z_ROTATION : 0.0
27     ACCEPTOR_ROTATION_ORDER : xyz
28
29 #=== DIMER ===#
30     DIMER_X_DISTANCE : 0.0
31     DIMER_Y_DISTANCE : 0.0
32     DIMER_Z_DISTANCE : 0.0
33     DIMER_X_ROTATION : 0.0
34     DIMER_Y_ROTATION : 0.0
35     DIMER_Z_ROTATION : 0.0
36     DIMER_ROTATION_ORDER : xyz
37
38
39 #===== SEET PARAMETERS =====#
40 # density format can be: [DENSOMAT, DFTMRCI, SPOCKCI]
41     SEET : ON
42
43 #=== SEET DONOR ===#
44     SEET_DONOR_DENSITY_FORMAT : DENSOMAT
45     SEET_DONOR_TRANSITION_DENSITY_PATH : /sociopath/
46     SEET_DONOR_FINAL_STATE : 1

```

B Appendix

```
47 SEET_DONOR_INITIAL_STATE : 2
48
49 #=== SEET ACCEPTOR ===#
50 SEET_ACCEPTOR_DENSITY_FORMAT : DENSOMAT
51 SEET_ACCEPTOR_TRANSITION_DENSITY_PATH : /psychopath/
52 SEET_ACCEPTOR_FINAL_STATE : 2
53 SEET_ACCEPTOR_INITIAL_STATE : 1
54
55 #===== TEET PARAMETERS =====#
56 # density format can be: [DENSOMAT, DFTMRCI, SPOCKCI]
57 TEET : OFF
58
59 #===TEET DONOR ===#
60 TEET_DONOR_DENSITY_FORMAT : DENSOMAT
61 TEET_DONOR_TRANSITION_DENSITY_PATH : /sociopath/
62 # Final Singlet State
63 TEET_DONOR_FINAL_STATE : 1
64 # Initial Triplet State
65 TEET_DONOR_INITIAL_STATE : 1
66
67 #===TEET ACCEPTOR ===#
68 TEET_ACCEPTOR_DENSITY_FORMAT : DENSOMAT
69 TEET_ACCEPTOR_TRANSITION_DENSITY_PATH : /psychopath/
70 # Final Triplet State
71 TEET_ACCEPTOR_FINAL_STATE : 1
72 # Initial Singlet State
73 TEET_ACCEPTOR_INITIAL_STATE : 1
74
75 #===== ORTHOGONALIZATION CORRECTIONS =====#
76 #only possible without a Freeze!
77 ORTHOGONALISE : OFF
78
79 #===== DENSITY SCREENING =====#
80 # threshold to omit density contributions
81 DENSITY_SCREENING : 1.0E-10
```

Listing B.2: Input file for a MTD calculation

```

1 #===== EET Input File =====#
2 #Please keep Key-Value Pairs in this format: 'Key : Value'
3
4 #===== CALCULATION TYPE =====#
5 # type can be: [IDA, MTD, SPECTRALOVERLAP]
6     CALCULATION_TYPE : SPECTRALOVERLAP
7
8 #===== Donor Spectrum Properties =====#
9 #Path to Donor Emission Spectrum in Wavenumbers (X-Y Plot)
10    DONOR-PATH : /path/
11
12 #=== Spline Fit Parameters ===#
13    DONOR-NRMSD : 0.0001
14    DONOR-ITERATIONS : 100
15
16 #===== Acceptor Spectrum Properties =====#
17 #Path to Acceptor Absorption Spectrum in Wavenumbers (X-Y Plot)
18    ACCEPTOR-PATH : /path/
19
20 #=== Spline Fit Parameters ===#
21    ACCEPTOR-NRMSD : 0.0001
22    ACCEPTOR-ITERATIONS : 100
23
24 #===== Product Spectrum Properties =====#
25
26 #=== Spline Fit Parameters ===#
27    PRODUCT-NRMSD : 0.0001
28    PRODUCT-ITERATIONS : 100
29
30 #=== Grid Properties ===#
31 #start and end of integration in Wavenumbers
32    GRID-START : 15000
33    GRID-END : 25000
34    GRID-INCREMENT : 0.25

```

Listing B.3: Input file for a Spectral Overlap calculation

Table B.1: Comparison of MTD calculations with and without a frozen core.

	ECME	Computation time	Number of Orbitals	Memory
TDMV of T_a (AG97) and S_1 (FITC) collinear - 10 Å				
Freeze	3.574801	1h 50m 40s	792	4.7 Gb
NoFreeze	3.574816	3h 8m 57s	1179	11 Gb
TDMV of T_b (AG97) and S_1 (FITC) collinear - 10 Å				
Freeze	11.721456	1h 48m 49s	792	4.7 Gb
NoFreeze	11.721534	3h 8m 51s	1179	11 Gb
TDMV of T_c (AG97 - case a) and S_1 (FITC) collinear - 10 Å				
Freeze	13.798273	2h 0m 27s	792	4.7 Gb
NoFreeze	13.798277	3h 14m 26s	1179	11 Gb
TDMV of T_c (AG97 - case b) and S_1 (FITC) collinear - 10 Å				
Freeze	7.517651	2h 0m 44s	792	4.7 Gb
NoFreeze	7.517666	3h 16m 48s	1179	11 Gb
TDMV of S_1 (DBA-BTICz) and S_1 (ν -DABNA) collinear - 35 Å				
Freeze	1.656531	10h 17m 2s	1513	
NoFreeze	1.673928	17h 12m 25s	2126	

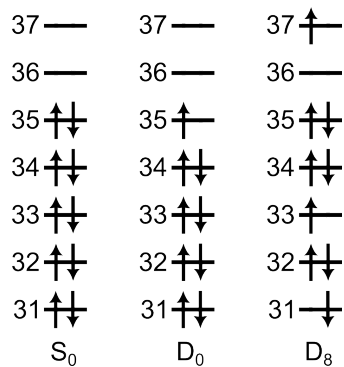


Figure B.1: Leading configurations of the DFT/MRCI wave functions of adenine in the electronic ground state (S_0), cationic ground state (D_0) and the 9th cationic state (D_8).

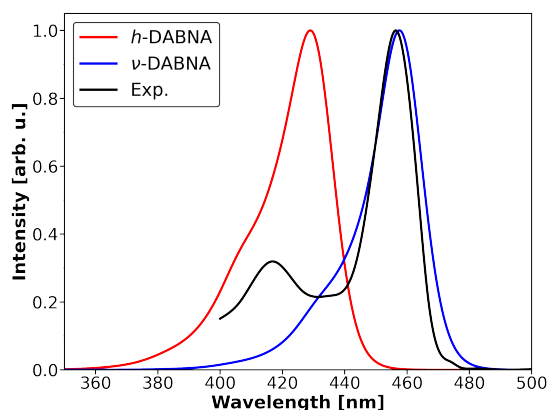


Figure B.5: Calculated absorption spectra of h -DABNA and ν -DABNA with the AH model compared to an experimental absorption spectrum of ν -DABNA in toluene.

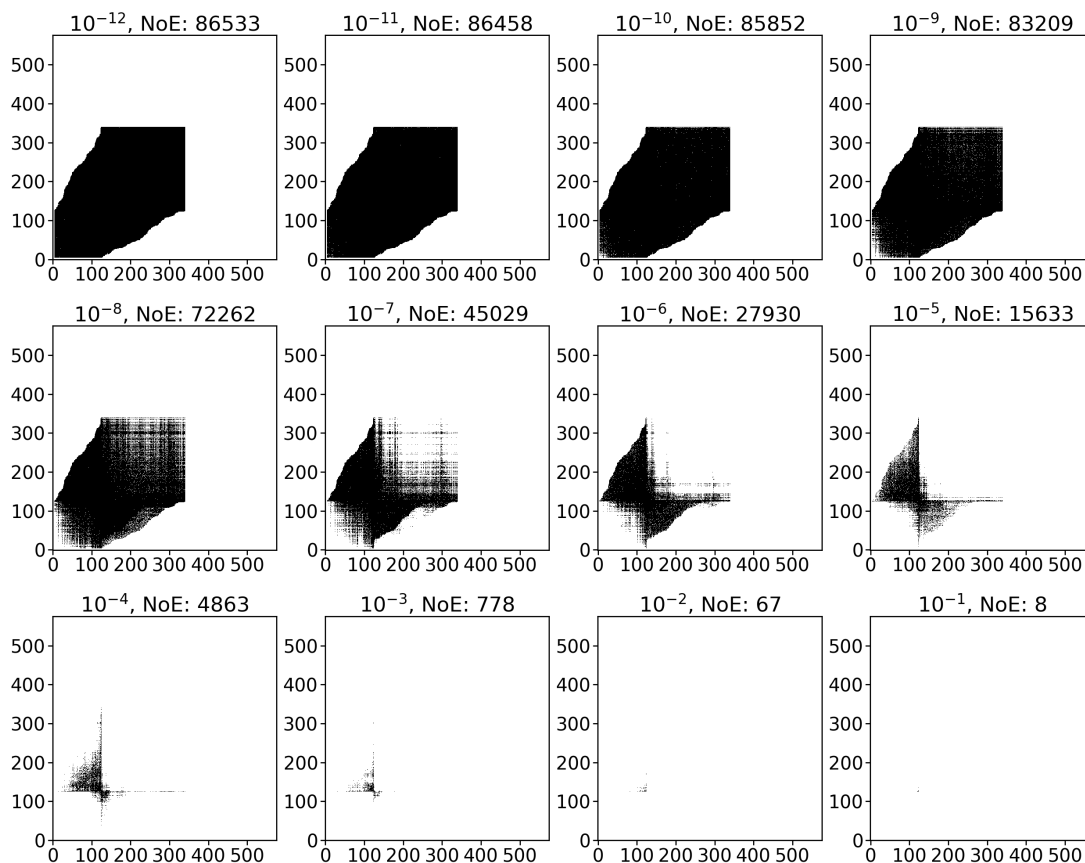


Figure B.6: Entries larger than the given threshold for the $S_0 \leftarrow S_1$ 1-RTDM of the left DBA-BTICz conformer. The number of entries (NoE) are given in the caption.

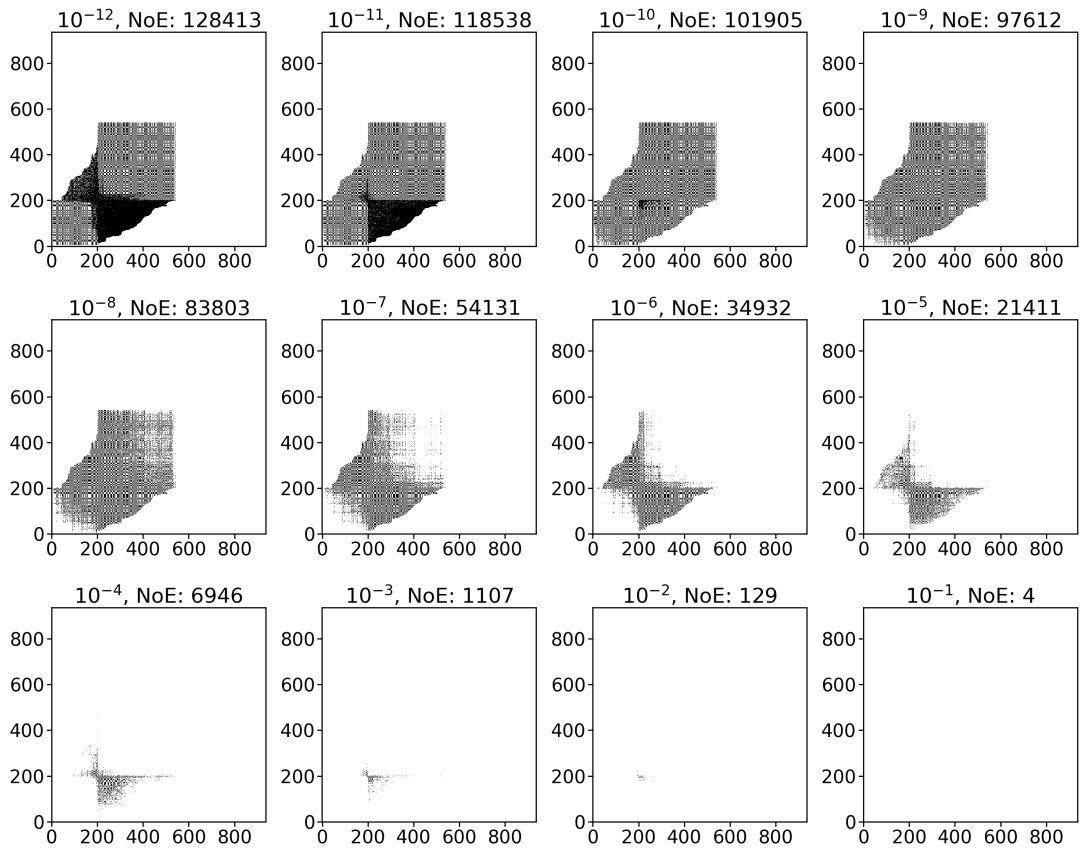


Figure B.7: Entries larger than the given threshold for the $S_0 \rightarrow S_1$ 1-RTDM of ν -DABNA. The number of entries (NoE) are given in the caption.

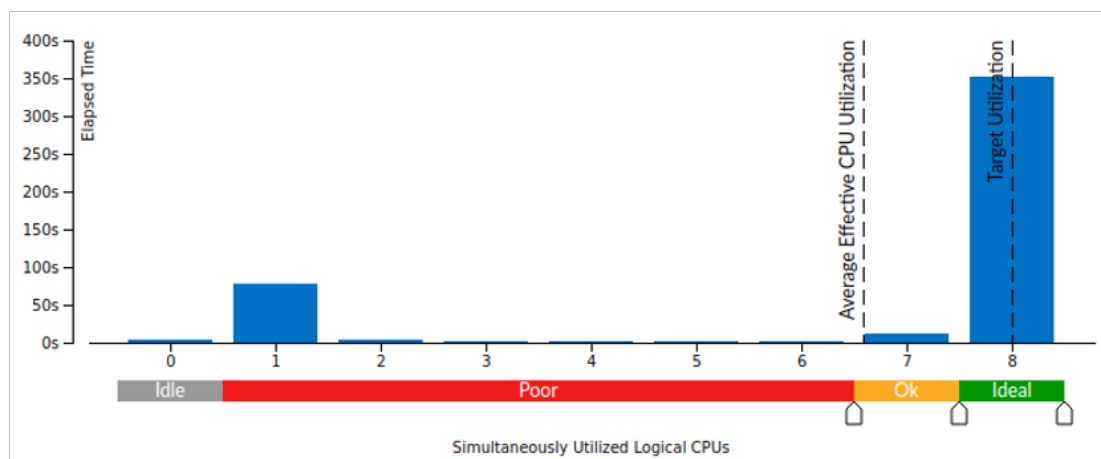


Figure B.8: The duration of the ECME calculation in relation to the number of cores utilized. Analysis done with the Intel Vtune Profiler.

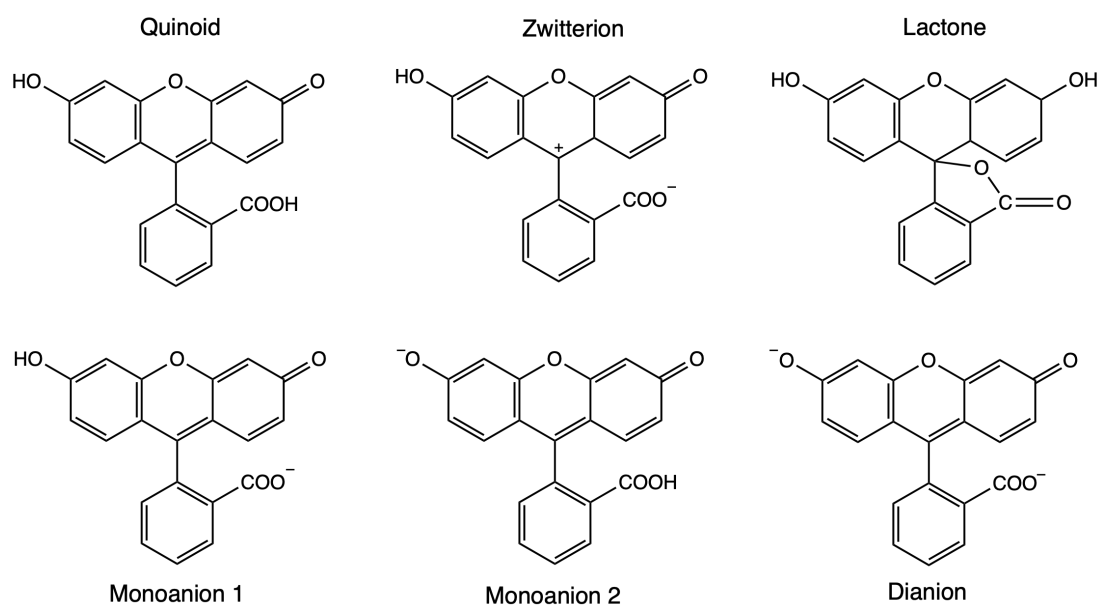


Figure B.9: Fluorescein tautomers.

C Included Publications

Paper 1

Intersystem crossing and intramolecular triplet excitation energy transfer in spiro[9,10-dihydro-9-oxoanthracene-10,2'-5',6'-benzindan] investigated by DFT/MRCI methods

Can. J. Chem., **101**, 633–640 (2023)

Simon Metz, Tobias Böhmer, Ben Raunischke, Christel M. Marian

Contribution: All quantum chemical calculations; preparation of all figures; writing first draft; revision of the manuscript

Intersystem crossing and intramolecular triplet excitation energy transfer in spiro[9,10-dihydro-9-oxoanthracene-10,2'-5',6'-benzindan] investigated by DFT/MRCI methods

Simon Metz, Tobias Böhmer, Ben Raunischke, and Christel M. Marian 

Institute of Theoretical and Computational Chemistry, Heinrich Heine University Düsseldorf, Universitätsstr. 1, Düsseldorf, 40225, Germany

Corresponding author: Christel M. Marian (email: christel.marian@hhu.de)

Abstract

Recent experimental studies of a spiro-linked anthracenone (A)–naphthalene (N) compound (AN) in butyronitrile (BuCN) solution (Dobkowski et al., *J. Phys. Chem. A* **2019**, *123*, 6978) proposed an excited-state energy dissipation pathway [$^1\pi\pi^*(\text{N}) + ^1\pi\pi^*(\text{A}) \rightsquigarrow ^1n\pi^*(\text{A}) \rightsquigarrow ^3n\pi^*(\text{A}) \rightsquigarrow ^3\pi\pi^*(\text{N})$]. However, a detailed theoretical study employing combined density functional theory and multireference configuration interaction methods, performed in the present work, suggests that the photoexcitation decay follows a different pathway. In BuCN solution, the intersystem crossing (ISC) follows the well-established El-Sayed rule and involves the $^3\pi\pi^*(\text{A})$ state which is found to be the lowest excited triplet state localized on the anthracenone moiety. Because the Dexter triplet excitation energy transfer (TEET) to the first excited triplet state of the naphthalene subunit is forbidden in C_{2v} symmetry, it is mandatory to go beyond the Condon approximation in modeling this process. Nonadiabatic coupling matrix elements were computed to obtain a TEET rate different from zero. Our calculations yield time constants of 5 ps for the $^1n\pi^*(\text{A}) \rightsquigarrow ^3\pi\pi^*(\text{A})$ ISC and of 3 ps for the subsequent $^3\pi\pi^*(\text{A}) \rightsquigarrow ^3\pi\pi^*(\text{N})$ TEET in BuCN whereas the energy dissipation involving the $^3n\pi^*(\text{A})$ state as an intermediate occurs on a much longer time scale.

Key words: multireference methods, intersystem crossing, nonadiabatic coupling, intramolecular triplet energy transfer, solvent effects

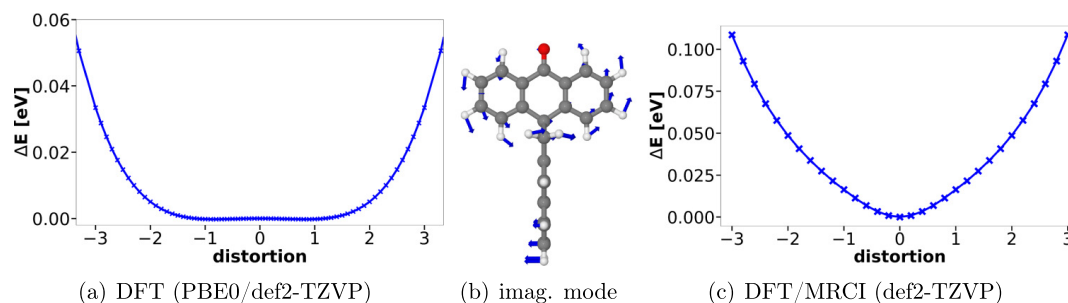
1. Introduction

Excitation energy transfer (EET) between a triplet sensitizer and a triplet acceptor is a common chemical process used to photoinitiate radical reactions¹ or triplet–triplet annihilation upconversion.² To be less dependent on accidental encounters between the donor and acceptor molecules, covalently linked photosensitizers undergoing intramolecular triplet EET (TEET) on the nanosecond or even picosecond time scale have been devised.^{3–9} The donor fragments of these compounds typically comprise aromatic ketones with triplet quantum yields close to unity. Their first-order spin-orbit coupling (SOC) originates from interactions between electrons occupying the lone-pair n and the p_π orbitals of the carbonyl oxygen, in agreement with El-Sayed's rules.^{10,11} Owing to the weaker exchange interaction of the open shells in $n\pi^*$ states as compared to $\pi\pi^*$ states, the first excited singlet (S_1) states of aromatic ketones typically exhibit $n\pi^*$ electronic structure whereas the first excited triplet (T_1) state may have $\pi\pi^*$ or $n\pi^*$ characteristics, depending on the chemical composition of the aromatic ketone and the solvent polarity.¹¹ In any case, aromatic ketones possess small to medium-sized

singlet–triplet energy gaps with close-lying $^1n\pi^*$, $^3n\pi^*$, and $^3\pi\pi^*$ states. With regard to the conditions promoting efficient intramolecular TEET,⁵ the combination of an aromatic ketone, playing the role of the singlet acceptor and triplet donor, and a conjugated hydrocarbon fragment, acting as a singlet donor and triplet acceptor, appears ideal. In contrast to aromatic ketones, oligoacenes exhibit large S_1 – T_1 energy gaps.^{12,13} The chances are, therefore, high that the $S_1 \leftarrow S_0$ transition of the acene is located energetically above the $S_1 \rightarrow S_0$ transition of the ketone. In this way, quenching of the excited-state population on the ketone moiety by singlet EET is prevented. The energetically low-lying triplet acceptor T_1 state on the other hand increases the likelihood that the TEET from the ketone to the oligoacene is irreversible.

In this paper, we report extensive quantum chemical calculations on spiro[9,10-dihydro-9-oxoanthracene-10,2'-5',6'-benzindan] (AN) (Chart 1) which is composed of an anthracenone (A) and a naphthalene (N) subunit, held relatively rigidly at right angles to each other by a spiran linkage. When the molecule is excited with 312 nm radiation in toluene¹⁴ or 308 nm radiation in butyronitrile (BuCN)

Fig. 1. Scan along the dimensionless normal coordinate of the imaginary vibrational mode at the C_{2v} -symmetric ground-state geometry in vacuum. The energy profile of the DFT (PBE0/def2-TZVP) calculations show a shallow double minimum structure whereas the DFT/MRCI energy profile has a minimum at the symmetry point.



solution,¹⁵ the fluorescence of the N moiety is quenched, while phosphorescence characteristic of N is observed with a relatively large quantum yield. Direct excitation of the $S_1(A) \leftarrow S_0$ transition at 362 nm leads to phosphorescence from the $T_1(N)$ state as well,¹⁴ clearly suggesting that AN undergoes intramolecular triplet(A)–triplet(N) energy transfer. Less clear is the nature of the involved triplet(A) state. Based on the results of combined experimental and computational studies of AN in BuCN solution, Dobkowski et al.¹⁵ proposed an excited-state energy dissipation path [$^1\pi\pi^*(N) + ^1\pi\pi^*(A) \rightsquigarrow ^1n\pi^*(A) \rightsquigarrow ^3n\pi^*(A) \rightsquigarrow ^3\pi\pi^*(N)$]. The first step was associated with a time constant of 1.6 ± 0.2 ps. The second and third steps occur within 35 ± 3 ps, but τ_{ISC} and τ_{TEET} could not be temporally resolved. The kinetic scheme suggests that the $^1n\pi^*(A) \rightsquigarrow ^3n\pi^*(A)$ intersystem crossing (ISC) proceeds at a rate constant of $3 \times 10^{10} \text{ s}^{-1}$ or more which is surprising in view of El-Sayed's rules,^{10,11} which require a change of orbital character for fast and efficient ISC. A recent quantum chemical study of the ISC processes in the isolated A molecule¹⁶ has shown that the El-Sayed-forbidden direct $S_1(^1n\pi^*) \rightsquigarrow T_1(^3n\pi^*)$ passage is comparatively slow ($k_{ISC}^{HT} = 4 \times 10^9 \text{ s}^{-1}$ including spin-vibronic interactions in Herzberg–Teller (HT) approximation) and cannot compete against the much faster El-Sayed-allowed $S_1(^1n\pi^*) \rightsquigarrow T_2(^3\pi\pi^*)$ transition which proceeds with a rate constant of $k_{ISC}^{HT} = 5 \times 10^{11} \text{ s}^{-1}$. The exact energetic location of the $T_2(\pi\pi^*)$ state of the A molecule is not known experimentally, but it is reasonable to assume that it is almost isoenergetic to the S_1 state in nonpolar solvents and below S_1 in polar environments.¹⁷ Earlier experiments on AN in *n*-hexane found a longer rise time of the triplet excited-state absorption (ESA) of 80 ± 20 ps.¹⁴ Polar solvents such as BuCN cause the $\pi\pi^*$ states of aromatic ketones to shift bathochromically with respect to apolar environments whereas the $n\pi^*$ states are shifted hypsochromically. Therefore the question arises whether the larger time constant in the older work by Maki et al.¹⁴ is just a consequence of the lower temporal resolution of their apparatus, as supposed by Dobkowski et al.,¹⁵ or whether AN follows different photoexcitation decay paths in apolar (*n*-hexane) and polar (BuCN) environments.

Although no evidence of an El-Sayed-allowed two-step mechanism $^1n\pi^*(A) \rightsquigarrow ^3\pi\pi^*(A) \rightsquigarrow ^3n\pi^*(A)$ was reported for AN, one may wonder where the $^3\pi\pi^*(A)$ state of AN is located energetically in relation to the $^3n\pi^*(A)$ state and whether it plays a mediating role in the fast $^1n\pi^*(A) \rightsquigarrow ^3n\pi^*(A)$ ISC process. Alternatively, if the $^3\pi\pi^*(A)$ state turns out to be the lower one of the two triplet (A) states in polar solvents, the question arises whether the $^3n\pi^*(A)$ state is involved at all in the energy dissipation pathway of AN. Further, it is interesting to know which of the two processes, ISC or TEET, is the slower one and thus the rate-determining step for the build-up of the ESA signal of the N moiety. Finally, since Dexter EET from the $^3n\pi^*(A)$ and $^3\pi\pi^*(A)$ states to the first excited $^3\pi\pi^*(N)$ state is symmetry forbidden in first order (vide infra), the question arises why TEET is so efficient in AN and which vibrational modes promote the TEET between the A and N moieties. Our present theoretical study strives to answer these questions based on extensive quantum chemical computations of energy schemes, spectral properties and rate constants of intramolecular transitions employing combined density functional theory (DFT) and multireference configuration interaction (MRCI) methods.

2. Computational methods

The Gaussian 16 program package¹⁸ was used for all geometry optimizations and vibrational frequency analyses. The ground-state equilibrium structure was determined using Kohn–Sham density functional theory (KS-DFT) in conjunction with the PBE0 hybrid functional^{19,20} and the def2-TZVP basis set.²¹ Solvent–solute interactions were included through the polarizable continuum model.²² For the optimization of the excited singlet states, time-dependent DFT (TDDFT) was used while the Tamm–Dancoff approximation (TDA) to TDDFT was applied for locating the triplet minima. The normal mode frequencies and coordinates were further utilized to generate Franck–Condon (FC) factors and FC-weighted densities of states (FCWDOS) for determining spectral profiles and rate constants.

Two general routes have been implemented into the VIBES source code^{23,24} and were used to compute vibronic spectra.

The phosphorescence spectra were computed using the Adiabatic Hessian approach whereas for the vibrationally resolved triplet absorption spectra the Vertical Hessian (VH) method was used. The latter is suitable to describe the vibronic transitions around the FC region without the requirement of effectively computing the final state's equilibrium geometry.^{25,26} For the VH method, the gradients and Hessian matrix of the respective final state are calculated at the optimized geometry of the initial state. This information is utilized to extrapolate the potential energy surface (PES) from the nonstationary point. The derivatives are used to generate the frequencies and normal modes at the extrapolated equilibrium geometry of the final state. Modes with an imaginary frequency are eliminated for both electronic states. The omission is valid as long as the modes that are expected to affect the spectral shape the most are still included.²⁶ The reorganization energy was estimated based on the vertical excitation energies to determine the offset of the spectrum according to the following equation.²⁷

$$(1) \quad E_v = E_{ad} + \frac{1}{2} \mathbf{K}^T \overline{\overline{\Omega}}^{-2} \mathbf{J}^T \mathbf{K}$$

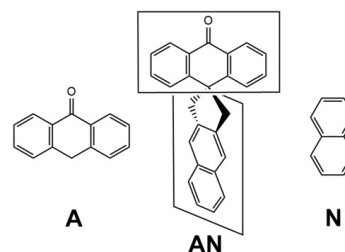
Here, \mathbf{K} is the displacement vector, \mathbf{J} the Duschinsky rotation matrix, and $\overline{\overline{\Omega}}$ the diagonal frequency matrix of the final state. Vertical (E_v) and adiabatic (E_{ad}) excitation energies were calculated employing the R2016 Hamiltonian²⁸ of the DFT/MRCI method^{29,30} and a configuration selection threshold of 1.0 E_h . Herein, Kohn–Sham BH-LYP^{31,32} molecular orbitals (MOs) of the closed-shell ground-state determinant served as one-particle basis set. To take account of solute–solvent interactions in the KS-DFT MO optimization, the point charges from the preceding Gaussian 16 calculations were imported into Turbomole.³³ The cbas auxiliary basis sets from the Turbomole library³⁴ were utilized to construct the two-electron integrals in the resolution-of-the-identity approximation. Fragment-based analyses of the DFT/MRCI wavefunctions were performed with Theodore.³⁵ Electronic spin–orbit coupling matrix elements and component-averaged phosphorescence lifetimes were obtained with the SPOCK program.^{36,37} ISC and internal conversion (IC) rate constants were determined for a temperature of 300 K via a fast Fourier transformation ansatz employing the VIBES program.^{24,38} The derivatives with respect to the normal coordinates, required for the HT expansion of the SOC, and the nonadiabatic coupling matrix elements (NACMEs) of the triplet states, promoting the IC, were computed at the DFT/MRCI level using finite difference techniques.^{38,39} Further computational details may be found in the Supplementary Material (SM).

3. Results and discussion

3.1. Molecular symmetry

Before we present our theoretical results on AN in detail, a short discussion of the molecular symmetry properties appears appropriate. Using DFT (B3LYP/6-311+G(d,p)), Dobkowski et al.¹⁵ determined a double minimum structure

Chart 1: Chemical structures of anthracenone (A), naphthalene (N) and spiro[9,10-dihydro-9-oxoanthracene-10,2'-5',6'-benzindan] (AN).



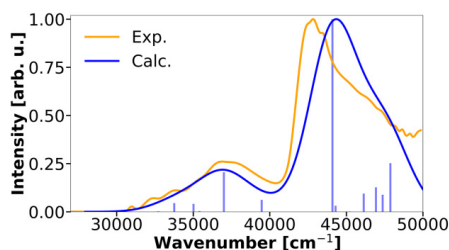
for AN in the electronic ground state in which the N unit is tilted by ca. $\pm 15^\circ$ with respect to the mirror plane perpendicular to the A molecular plane and including the C=O bond. We found a similar nuclear arrangement in our DFT (PBE0/def2-TZVP) calculations (Fig. S1a of the SM). While the TDDFT-TDA optimization of the lowest locally excited (LE) triplet state on the N part yielded a C_{2v} symmetrical minimum, symmetry-broken solutions were obtained for the lowest excited singlet state and two triplet LE states on the A part of the molecule (see Fig. S2a of the SM for the ${}^3\pi\pi^*$ (A) state). Subsequent DFT/MRCI calculations suggest, however, that the true minima of these states have C_{2v} -symmetric structures (Fig. 1, and Fig. S2c).

The tilt of N unit in the electronic ground state has only a minor effect on the computed $S_n \leftarrow S_0$ line spectrum (Fig. S3 of the SM). Its comparison with the measured static absorption spectrum can therefore not be used to probe the true equilibrium structure of the compound. In contrast to the electronic line spectra, the vibrational fine-structure of the phosphorescence emission depends heavily on the choice of the ground-state potential. While the FC factors of the C_{2v} -symmetric T_1 and S_0 potentials represent the intensity distribution in the experimental phosphorescence spectrum almost perfectly, the symmetry-broken solutions produce too intense vibrational transitions in the low-energy part of the spectrum (Fig. S4 of the SM), thus nourishing our suspicion that the symmetry-broken solutions are artifacts of the (TD)DFT treatment. Such artifacts have been encountered earlier in other heteroaromatic compounds whose geometrical structures are well known.^{40,41} In the following sections, therefore mainly the properties determined at the C_{2v} symmetric geometries will be discussed. For being able to compute meaningful FC spectra and nonradiative rate constants, the negative eigenvalue of the Hessian has to be corrected. To this end, the curvature of the PBE0/def2-TZVP energy profile at larger displacements was used to fit a harmonic frequency. For more details see the SM (Fig. S1b).

3.2. The Franck–Condon region

Most of the low-lying excited states possess wavefunction expansions with more than one leading term (Tables S1 and S2 of the SM). For their further categorization, a fragmentation-based analysis was performed (Fig. S6 of the

Fig. 2. Renormalized absorption spectrum of AN in BuCN. The computed line spectrum was broadened by Gaussians with 1500 cm^{-1} FWHM. In orange, a digitized experimental stationary absorption spectrum¹⁵ in BuCN at room temperature is shown.



SM). The calculated normalized absorption spectrum in BuCN solution fits well with the experimental room temperature stationary absorption spectrum (Fig. 2). Both show their first intense band with a maximum at about 37000 cm^{-1} which originates from a LE $\pi\pi^*$ on the A moiety and a very intense peak at about $43000\text{--}44000\text{ cm}^{-1}$ which stems from a multiconfigurational LE state on the N subunit, correlating with the bright 1B_b state of N in Platt's nomenclature.⁴² For the interpretation of the experimental transient absorption (TA) spectra, which was recorded with an excitation wavelength of 308 nm (32500 cm^{-1}) by Dobkowski et al.,¹⁵ the high-energy part of the static absorption spectrum is of no relevance, however.

The S_1 state has a vertical excitation energy of about 29900 cm^{-1} in BuCN solution and corresponds to an optically dark $n\pi^*$ LE on the A part of the molecule. Even the next two singlet transitions at ca. 32700 and 32800 cm^{-1} , respectively, are barely visible in the computed spectrum (Fig. 2). S_2 is a state of mixed charge-transfer $N\rightarrow A$ and LE(A) character. S_3 a multiconfigurational LE state correlating with the very weak 1L_b transition of N. The shoulder around 34000 cm^{-1} is assigned to the lowest ${}^1\pi\pi^*$ excitation on A and the shoulder around 35000 cm^{-1} to the 1L_a transition of N.

The T_1 state, located about 6000 cm^{-1} below S_1 , is a LE ${}^3\pi\pi^*$ (N) state. Like in the isolated N molecule,⁴³ it is not the counterpart of the lowest lying ${}^1\pi\pi^*$ state but shares the electronic structure with the 1L_a state. The next two triplet states are both local excitations on the A moiety. In the isolated molecule, which may serve as a proxy for the photophysical properties of AN in an apolar solvent such as *n*-hexane, the T_2 state is the triplet counterpart of the S_1 state with $n\pi^*$ excitation character, while a triplet state stemming from a local $\pi\pi^*$ excitation on the A part forms the T_3 state. A BuCN environment reverses the order of these two triplet states in comparison to vacuum conditions. As we will see below, the close energetic proximity of the ${}^3\pi\pi^*$ (A) and ${}^3n\pi^*$ (A) states has a large impact on the ISC and TEET kinetics of AN in different media.

Fig. 3. Difference densities of the excited states at their respective minimum geometries in BuCN. Red areas lose electron density in comparison to the ground state, whereas yellow areas gain electron density.

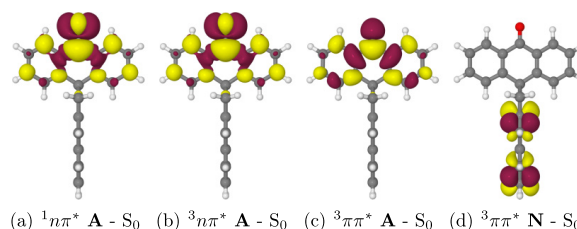


Table 1. ZPVE-corrected DFT/MRCI adiabatic energies of the low-lying excited states of AN in vacuum and BuCN.

State	Vacuum (cm^{-1})	BuCN (cm^{-1})
${}^1n\pi^*$ (A)	25 295	26 496
${}^3n\pi^*$ (A)	23 320	25 267
${}^3\pi\pi^*$ (A)	24 587	24 137
${}^3\pi\pi^*$ (N)	19 972	19 903

3.3. Excited-state properties

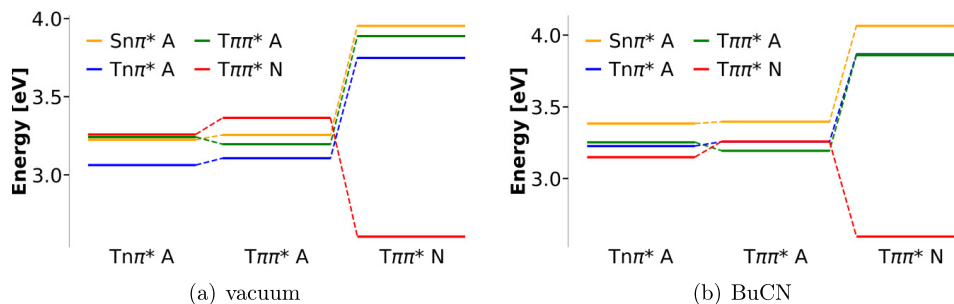
Difference densities of the excited states at their respective C_{2v} -symmetric minimum geometries (Fig. 3) reveal that the S_1 , T_1 , T_2 , and T_3 states have LE character. Their adiabatic excitation energies in vacuum and BuCN, corrected for zero-point vibrational energies (ZPVEs), are listed in Table 1. While PES crossings between the ${}^1n\pi^*$ (A) state and the ${}^3\pi\pi^*$ (A) and ${}^3\pi\pi^*$ (N) states can be made out in vacuum (Fig. 4a), the ${}^1n\pi^*$ (A) state is located energetically above the three triplet states at all considered geometries in BuCN (Fig. 4b). In contrast, several intersections between the triplet potentials are observed in the latter medium. Here, the ${}^3\pi\pi^*$ (N) state clearly is the lowest among the triplet states in the FC region and at the optimized ${}^3\pi\pi^*$ (N) geometry, but it is located very close to the ${}^3n\pi^*$ (A) state at the ${}^1n\pi^*$ (A) and ${}^3n\pi^*$ (A) minimum geometries and even crosses the ${}^3\pi\pi^*$ (A) potential on the path connecting the ${}^3n\pi^*$ (A) and ${}^3\pi\pi^*$ (A) minima (Fig. 4b). As will be seen below, the close energetic proximity of the T_1 , T_2 , and T_3 states at the ${}^3n\pi^*$ (A) and ${}^3\pi\pi^*$ (A) minimum structures facilitates the TEET.

3.4. Photoexcitation decay pathways

While the spectral position of the ${}^3\pi\pi^*$ (N) state is nearly unaffected by a solvent environment, solvent-solute interactions stabilize the ${}^3\pi\pi^*$ (A) state whereas they destabilize the ${}^3n\pi^*$ (A) state with the effect that the adiabatic order of the two triplet LE(A) states is reversed. Therefore, it may well be that the relaxation of AN after photoexcitation in *n*-hexane and BuCN follows different pathways.

According to Dobkowski et al.,¹⁵ the ISC in AN proceeds along the ${}^1n\pi^*$ (A) \rightarrow ${}^3n\pi^*$ (A) pathway with a time constant τ_{ISC} smaller than 35 ps in BuCN. Maki et al.¹⁴ found a longer rise time of about $80 \pm 20\text{ ps}$ for the $T_n \leftarrow T_1$ absorption in *n*-hexane. Our calculations yield a high rate constant of $7.8 \times$

Fig. 4. DFT/MRCI energies of the low-lying excited states of AN at the optimized triplet geometries relative to the C_{2v} -symmetric electronic ground state minimum in (a) vacuum and (b) BuCN.



10^{11} s^{-1} ($\tau \approx 1 \text{ ps}$) for the El-Sayed-allowed $^1n\pi^*(A) \rightarrow ^3\pi\pi^*(A)$ process in the isolated AN. In BuCN solution, this rate constant decreases to $2.2 \times 10^{11} \text{ s}^{-1}$, but with a time constant of about $\tau_{\text{ISC}} \approx 5 \text{ ps}$ the $^1n\pi^*(A) \rightarrow ^3\pi\pi^*(A)$ ISC may still be considered ultrafast. Because the $^1n\pi^*(A) \rightarrow ^3n\pi^*(A)$ transition is El-Sayed forbidden, its ISC rate constant is very small in Condon approximation. Spin-vibrational interactions increase the ISC rate constant to $1.6 \times 10^{10} \text{ s}^{-1}$ ($\tau \approx 62 \text{ ps}$). Applying BuCN solvent shifts to the potentials, the $^1n\pi^*(A) \rightarrow ^3n\pi^*(A)$ ISC rate constant changes to $2.5 \times 10^{10} \text{ s}^{-1}$ ($\tau \approx 41 \text{ ps}$). Hence, both deexcitation pathways allow an efficient local singlet-triplet ISC on the A moiety on a time scale which fits the kinetic scheme proposed by the experimentalists.

An unambiguous assignment of the intermediate triplet state is possible, however, when the calculated ESA spectra are compared with the TA spectrum recorded for a short delay time of 0.5 ps in BuCN (Fig. 5a). The band with the highest intensity in this TA spectrum has a maximum around 29500 cm^{-1} . In addition, a weaker band with several maxima in the $22000\text{--}25000 \text{ cm}^{-1}$ regime can be made out. Both features are nearly perfectly matched by the calculated ESA spectrum of the $^3\pi\pi^*(A)$ state. An additional low-energy peak around 19500 cm^{-1} is also visible in the unrestricted DFT ESA spectrum presented by Dobkowski et al.,¹⁵ but has not been observed in the TA experiment for unknown reasons. For comparison, we computed the ESA spectra of the $^3n\pi^*(A)$ and $^1n\pi^*(A)$ states at the DFT/MRCI level of theory as well. Both possess spectral profiles which differ markedly from the measured TA spectrum (Fig. 5a). At variance with Dobkowski et al.,¹⁵ we therefore conclude that the intermediate state populated predominantly after 0.5 ps in the experiment in BuCN solution is the $^3\pi\pi^*(A)$ state and not the $^3n\pi^*(A)$ state.

This conclusion is corroborated by our calculated TEET rate constants. In weakly coupled systems, the rate constant of an EET between a donor and an acceptor molecule is conveniently evaluated according to a Fermi golden rule expression.⁴⁴

$$(2) \quad k_{\text{EET}} = \frac{2\pi}{\hbar} |V_{\text{DA}}^{(el-el)}|^2 \text{FCWDOS}$$

The FCWDOS contains all information about the population of the donor vibrational states at a given temperature and their overlaps with the acceptor vibrational states at the energy of the initial donor state. The electronic coupling matrix element $V_{\text{DA}}^{(el-el)}$ is composed of a Coulomb part $J_{\text{DA}}^{(el-el)}$ which gives rise to Förster resonance energy transfer (FRET)⁴⁵ in case of a dipole-allowed transition and an exchange part $K_{\text{DA}}^{(el-el)}$ which is the origin of Dexter energy transfer.⁴⁶ Due to spin selection rules, only the latter contributes to TEET.

The monomer transition density approach determines an estimate for $V_{\text{DA}}^{(el-el)}$ from the ground- and excited-state properties of separate donor and acceptor molecules, i.e., the monomers. It was originally devised for computing the Coulomb coupling between the FRET partners beyond the ideal dipole approximation.^{47,48} An extension of this method, which includes Dexter terms in addition to Förster terms, was successfully applied to model intramolecular EET as well.⁴⁹ In the framework of this approach, the exchange part of the electronic coupling between the donor and acceptor subunits of the EET systems can be approximated by

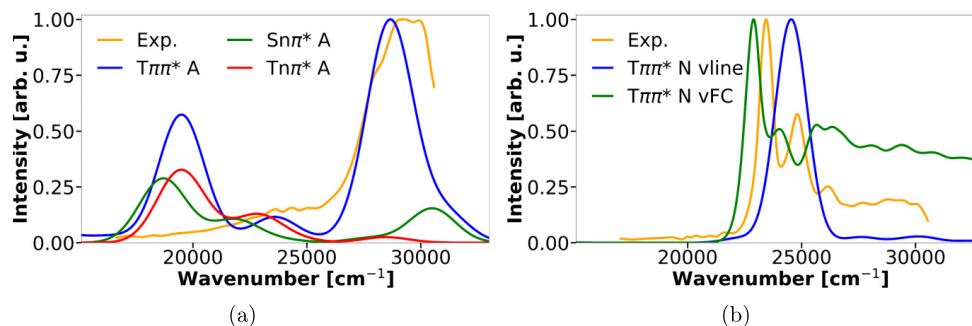
$$(3) \quad K_{\text{DA}}^{(el-el)} = -\frac{1}{2} \sum_{ijkl} \rho_{ij}^{(A)} (il|kj) \rho_{kl}^{(D)}$$

where $\rho_{ij}^{(A)}$ denotes an element of the transition density matrix between the ground and the excited states of the acceptor subunit in the MO basis, $\rho_{kl}^{(D)}$ a transition density matrix element of the donor subunit, and $(il|kj)$ an electronic repulsion integral in Mulliken convention

$$(4) \quad (il|kj) \equiv \langle i(r_1)k(r_2) | r_{12}^{-1} | l(r_1)j(r_2) \rangle .$$

In the particular case of the intramolecular TEET in the AN molecule, all electronic coupling matrix elements employing either $^3n\pi^*(A)$ or $^3\pi\pi^*(A)$ as the initial state and $^3\pi\pi^*(N)$ as the final state vanish in C_{2v} symmetry. To see this, we focus on the leading configurations of the respective wavefunction expansion (Tables S3–S10 and Figs. S7–S10 of the SM). The $^3\pi\pi^*(N)$ acceptor state results mainly from an excitation involving the highest occupied MO (HOMO) and the second lowest unoccupied MO (LUMO+1). (For MO plots, see Fig. S5 of the SM.) These MOs transform according to the a_2

Fig. 5. (a) Short-time and (b) long-time DFT/MRCI triplet and singlet ESA spectra in BuCN in comparison to digitized experimental TA spectra with time delays of (a) 0.5 ps and (b) 5000 ps read from reference.¹⁵ The computed short-time line spectra were normalized with respect to the intensity of the highest peak of the ${}^3\pi\pi^*(A)$ ESA spectrum and were broadened by Gaussians with 1500 cm^{-1} FWHM. In addition to the Gaussian-broadened line spectrum of the long-time ESA spectrum, a vibrationally resolved ESA spectrum computed within the Vertical Hessian Franck–Condon scheme is shown.



and b_1 irreducible representations (irreps), respectively, and can be equated with the MOs i and j in eqs. 3 and 4. The ${}^3n\pi^*(A)$ excitation involves HOMO-6 and LUMO. In this case, the donor MOs k and l transform according to the b_2 and b_1 irreps, respectively. The electron repulsion integral ($il|kj$) can adopt values different from zero only, if the direct products of the four MO irreps contain the totally symmetric representation a_1 , but $a_2 \otimes b_1 \otimes b_2 \otimes b_1 = b_1 \neq a_1$. Therefore, the ${}^3n\pi^*(A) \rightarrow {}^3\pi\pi^*(N)$ Dexter TEET is forbidden in Condon approximation. If we start the Dexter TEET from the ${}^3\pi\pi^*(A)$ state instead, HOMO-5 and LUMO are involved, both transforming according to the b_1 irrep. Even in this case, the direct product representation, $a_2 \otimes b_1 \otimes b_1 \otimes b_1 = b_2$, is not totally symmetric and the integral vanishes. For obtaining a TEET rate different from zero it is therefore mandatory to go beyond the Condon approximation.

Lowering the molecular symmetry to the kinked structure, shown in Fig. S1 of the SM, transfers the acceptor orbitals to the a'' (HOMO) and a' (LUMO+1) irreps of the C_s point group, respectively. The donor orbitals exhibit a' (HOMO-6), a'' (HOMO-5), and a'' (LUMO), respectively. Therefore, while the ${}^3n\pi^*(A) \rightarrow {}^3\pi\pi^*(N)$ TEET becomes symmetry-allowed upon deflection of the anthracenone moiety, the ${}^3\pi\pi^*(A) \rightarrow {}^3\pi\pi^*(N)$ TEET remains symmetry forbidden.

Instead of expanding the Dexter coupling term in an HT-like series, we computed NACMEs between the triplet donor and acceptor states using a finite difference approach recently developed in our group.³⁸ Many, but small NACMEs associated with b_1 -symmetric coupling modes are found which enable the ${}^3n\pi^*(A) \rightarrow {}^3\pi\pi^*(N)$ transition. In the ${}^3\pi\pi^*(A) \rightarrow {}^3\pi\pi^*(N)$, five prominent derivative couplings involving b_2 -symmetric vibrational modes, shown in Fig. S11 of the SM, promote the TEET.

With room temperature rate constants of approximately $k_{IC} = 1.5 \times 10^9\text{ s}^{-1}$ in vacuum and of $k_{IC} = 1.6 \times 10^9\text{ s}^{-1}$ in BuCN, the ${}^3n\pi^*(A) \rightarrow {}^3\pi\pi^*(N)$ transition is much too slow to explain the experimentally observed rise times of the ${}^3\pi\pi^*(N)$ ESA. In contrast to the ${}^3n\pi^*(A) \rightarrow {}^3\pi\pi^*(N)$ TEET, the ${}^3\pi\pi^*(A) \rightarrow {}^3\pi\pi^*(N)$ TEET experiences a substantial impact of the solvent environment.

The energetic proximity of the three triplet states at the relaxed ${}^3\pi\pi^*(A)$ geometry in BuCN and the nearby crossing between the ${}^3\pi\pi^*(A)$ and ${}^3\pi\pi^*(N)$ PEs promotes their nonadiabatic coupling and accelerates the TEET between the ${}^3\pi\pi^*(A)$ and ${}^3\pi\pi^*(N)$ states of AN for which we obtain a rate constant of $k_{IC} = 3.2 \times 10^{11}\text{ s}^{-1}$ in BuCN compared to $k_{IC} = 4.9 \times 10^9\text{ s}^{-1}$ in vacuum. Note that the NACMEs and hence the IC rate constants are very sensitive with respect to the energetic splittings of the triplet states at the ${}^3\pi\pi^*(A)$ minimum geometry and thus prone to uncertainties. The values of computed rate constants might vary depending on the computational setup, but they are expected to be in the right ballpark. The consecutive ${}^1n\pi^*(A) \rightarrow {}^3\pi\pi^*(A)$ ISC (time constant of about 5 ps in BuCN) and ${}^3\pi\pi^*(A) \rightarrow {}^3\pi\pi^*(N)$ TEET (time constant of about 3 ps in BuCN) processes represent the only ${}^1n\pi^*(A) \rightarrow {}^3\pi\pi^*(N)$ pathway whose time constant falls within the experimentally determined risetime of the ${}^3\pi\pi^*(N)$ ESA of 35 ps.¹⁵

For a delay time of 5000 ps after the primary excitation the lowest triplet state, ${}^3\pi\pi^*(N)$, is supposed to be populated. The experimental TA spectrum exhibits a band with several maxima and minima between ca. 23 000 and 26 000 cm^{-1} . The DFT/MRCI calculations find only one strong electronic transition ($1^3B_2 \rightarrow 4^3B_2$) in this wavenumber regime. To prove that the experimentally observed fine structure of this band has a vibrational origin, we computed an FC spectrum of this transition using the VH approach. The good agreement between this spectrum and the experimental TA spectrum (Fig. 5b) is obvious and corroborates our assumption that the peaks do not stem from multiple electronic transitions but can be explained by vibrational progressions of the intense $T_{20}(N) \leftarrow T_1(N)$ ESA.

A vibrationally resolved phosphorescence emission spectrum of the ${}^3\pi\pi^*(N)$ state is displayed in Fig. 6a together with the experimental spectrum measured at 77 K. Save for an overall shift by about 1000 cm^{-1} , the spectra match very well. The vibrational spacing of about 1550 cm^{-1} is attributed

Fig. 6. (a) Phosphorescence spectra of AN in BuCN at 77 K. Blue: computed FC spectra with origin at the DFT/MRCI adiabatic energy (solid line) and shifted by 1000 cm^{-1} (dashed line). Green: digitized spectrum read from reference.¹⁵ (b) Totally symmetric vibrational mode in the electronic ground state causing the visible vibrational progression in the phosphorescence spectrum.

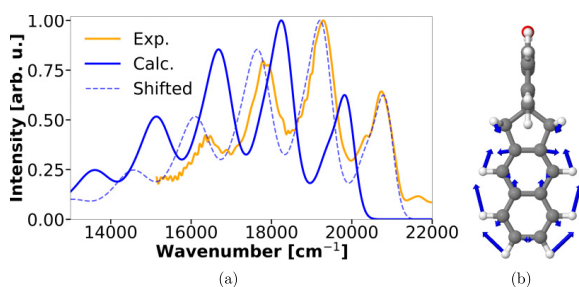
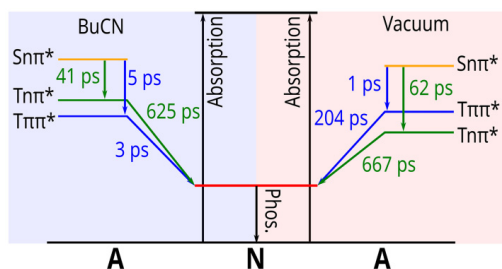


Fig. 7. Proposed kinetic scheme of the ISC and TEET processes following the photoexcitation of AN in BuCN solution and in vacuum at room temperature.



to the totally symmetric deformation mode of the N subunit with wavenumber 1556 cm^{-1} in the electronic ground state (Fig. 6b).

4. Summary and conclusions

In this paper, we investigated the electronic structures of the low-lying electronic states of AN and their intramolecular transition probabilities with the objective to clarify inconsistencies in the excited-state energy dissipation mechanism proposed in recent work by Dobkowski et al.¹⁵ The main results of our computational study are summarized in Fig. 7. We have been able to locate the $^3\pi\pi^*$ (A) state of AN. In BuCN solution, it represents the lowest excited triplet state of the anthracenone moiety, energetically very close to the $^3n\pi^*$ (A) and $^1n\pi^*$ (A) states. The $^3\pi\pi^*$ (A) state is readily populated via ISC from the $^1n\pi^*$ (A) state on the picosecond time scale. A conical intersection close to the $^3\pi\pi^*$ (A) minimum enables efficient TEET to the $^3\pi\pi^*$ (N). This excited-state energy dissipation pathway is much faster than the one proposed by Dobkowski et al.¹⁵ in BuCN solution, namely $^1n\pi^*(A) \rightarrow ^3n\pi^*(A) \rightarrow ^3\pi\pi^*(N)$, which entails an El-Sayed-

forbidden ISC process. The rate-determining step in the latter pathway is the TEET which proceeds at the timescale of several hundred picoseconds according to our calculations and therefore does not represent the favored energy dissipation route. The MRCI methods used in this work allow to compute ESA spectra of all possible intermediate states. Comparison with the experimentally determined TA spectra of Dobkowski et al.¹⁵ clearly identify the $^3\pi\pi^*$ (A) state as the origin of the TA spectrum at short time delay.

Supporting information

Further technical details of the computations, handling of symmetry-broken solutions, conformational effects on the absorption and phosphorescence spectra; MO plots; DFT/MRCI excitation energies of low-lying singlet and triplet states of all complexes at selected minimum geometries, Theodore analyses of the wavefunction characteristics of low-lying states in BuCN.

Acknowledgements

This research was funded by the Deutsche Forschungsgemeinschaft (DFG, German Research Foundation) - 396890929/GRK 2482.

Article information

History dates

Received: 30 September 2022

Accepted: 9 November 2022

Accepted manuscript online: 22 December 2022

Notes

This paper is one of a selection of papers from the 12th Triennial Congress of the World Association of Theoretical and Computational Chemists (WATOC 2020).

Copyright

© 2022 The Author(s). Permission for reuse (free in most cases) can be obtained from copyright.com.

Data availability

The corresponding author can provide further data upon request.

Author information

Author ORCIDs

Christel M. Marian <https://orcid.org/0000-0001-7148-0900>

Author contributions

Investigation: SM

Visualization: SM, TB

Writing – original draft: SM, TB, CM

Methodology: TB

Software: TB

Investigation: BR

Conceptualization: CM
Funding acquisition: CM
Project administration: CM
Supervision: CM

Competing interests

The authors declare there are no competing interests.

Supplementary material

Supplementary data are available with the article at <https://doi.org/10.1139/cjc-2022-0259>.

References

- (1) Dormán, G.; Nakamura, H.; Pulsipher, A.; Prestwich, G. D., *Chem. Rev.* **2016**, *116*, 15284–15398. doi:10.1021/acs.chemrev.6b00342.
- (2) Bharmoria, P.; Bildirir, H., *Chem. Soc. Rev.* **2020**, *49*, 6529–6554. doi:10.1039/D0CS00257G.
- (3) Keller, R. A., *J. Am. Chem. Soc.* **1968**, *90*, 1940–1944. doi:10.1021/ja01010a002.
- (4) Cowan, D. O.; Baum, A. A., *J. Am. Chem. Soc.* **1971**, *93*, 1153–1162. doi:10.1021/ja00734a021.
- (5) Amrein, W.; Schaffner, K., *Helvet. Chim. Acta* **1975**, *58*, 397–415. doi:10.1002/hlca.19750580209.
- (6) Sigman, M. E.; Closs, G. L., *J. Phys. Chem.* **1991**, *95*, 5012–5017. doi:10.1021/j100166a022.
- (7) Wagner, P. J.; Klán, P., *J. Am. Chem. Soc.* **1999**, *121*, 9626–9635. doi:10.1021/ja9902241.
- (8) Wöll, D.; Laimgruber, S.; Galetskaya, M.; Smirnova, J.; Pfeleiderer, W.; Heinz, B.; Gilch, P.; Steiner, U. E., *J. Am. Chem. Soc.* **2007**, *129*, 12148–12158. doi:10.1021/ja072355p.
- (9) Elliott, L. D.; Kayal, S.; George, M. W.; Booker-Milburn, K., *J. Am. Chem. Soc.* **2020**, *142*, 14947–14956. doi:10.1021/jacs.0c05069.
- (10) El-Sayed, M. A.; Tinti, D. S.; Owens, D. V., *Chem. Phys. Lett.* **1969**, *3*, 339–342. doi:10.1016/0009-2614(69)80248-4.
- (11) Marian, C. M., *Annu. Rev. Phys. Chem.* **2021**, *72*, 616–640. doi:10.1146/annurev-physchem-061020-053433.
- (12) Marian, C. M.; Gilka, N., *J. Chem. Theory Comput.* **2008**, *4*, 1501–1515. doi:10.1021/ct8001738.
- (13) Hajgató, B.; Szieberth, D.; Geerlings, P.; De Proft, F.; Deleuze, M. S., *J. Chem. Phys.* **2009**, *131*, 224321. doi:10.1063/1.3270190.
- (14) Maki, A. H.; Weers, J. G.; Hilinski, E. F.; Milton, S. V.; Rentzepis, P. M., *J. Chem. Phys.* **1984**, *80*, 2288–2297. doi:10.1063/1.447016.
- (15) Dobkowski, J.; Gorski, A.; Kijak, M.; Pietrzak, M.; Redeckas, K.; Ven-gris, M., *J. Phys. Chem. A* **2019**, *123*, 6978–6985. doi:10.1021/acs.jpca.9b03414.
- (16) Metz, S.; Marian, C. M., *ChemPhotoChem* **2022**, e202200098.
- (17) Kobayashi, T.; Nagakura, S., *Chem. Phys. Lett.* **1976**, *43*, 429–434. doi:10.1016/0009-2614(76)80593-3.
- (18) Frisch, M. J.; et al., *Gaussian 16 Revision C.01* **2016**, Gaussian Inc., Wallingford, CT.
- (19) Perdew, J. P.; Burke, K.; Ernzerhof, M., *Phys. Rev. Lett.* **1996**, *77*, 3865–3868. doi:10.1103/PhysRevLett.77.3865.
- (20) Adamo, C.; Barone, V., *J. Chem. Phys.* **1999**, *110*, 6158–6170. doi:10.1063/1.478522.
- (21) Schäfer, A.; Horn, H.; Ahlrichs, R., *J. Chem. Phys.* **1992**, *97*, 2571–2577. doi:10.1063/1.463096.
- (22) Cancès, E.; Mennucci, B.; Tomasi, J., *J. Chem. Phys.* **1997**, *107*, 3032. doi:10.1063/1.474659.
- (23) Etinski, M.; Tatchen, J.; Marian, C. M., *J. Chem. Phys.* **2011**, *134*, 154105. doi:10.1063/1.3575582.
- (24) Etinski, M.; Rai-Constapel, V.; Marian, C. M., *J. Chem. Phys.* **2014**, *140*, 114104. doi:10.1063/1.4868484.
- (25) *Computational Strategies for Spectroscopy: from Small Molecules to Nano Systems*; John Wiley & Sons, **2012**, pp. 361–389.
- (26) Götze, J. P.; Karasulu, B.; Thiel, W., *J. Chem. Phys.* **2013**, *139*, 234108. doi:10.1063/1.4844055.
- (27) Ferrer, A.; José, F.; Santoro, F., *Phys. Chem. Chem. Phys.* **2012**, *14*, 13549–13563. doi:10.1039/c2cp41169e.
- (28) Lyskov, I.; Kleinschmidt, M.; Marian, C. M., *J. Chem. Phys.* **2016**, *144*, 034104. doi:10.1063/1.4940036.
- (29) Grimme, S.; Waletzke, M., *J. Chem. Phys.* **1999**, *111*, 5645–5655. doi:10.1063/1.479866.
- (30) Marian, C. M.; Heil, A.; Kleinschmidt, M., *WIREs Comput. Mol. Sci.* **2019**, *9*, e1394. doi:10.1002/wcms.1394.
- (31) Lee, C.; Yang, W.; Parr, R. G., *Phys. Rev. B* **1988**, *37*, 785–789. doi:10.1103/PhysRevB.37.785.
- (32) Becke, A. D., *J. Chem. Phys.* **1993**, *98*, 1372–1377. doi:10.1063/1.464304.
- (33) TURBOMOLE GmbH. **2019**
- (34) Weigend, F.; Häser, M.; Patzelt, H.; Ahlrichs, R., *Chem. Phys. Lett.* **1998**, *294*, 143–152. doi:10.1016/S0009-2614(98)00862-8.
- (35) Plasser, F., *J. Chem. Phys.* **2020**, *152*, 084108. doi:10.1063/1.5143076.
- (36) Kleinschmidt, M.; Tatchen, J.; Marian, C. M., *J. Comput. Chem.* **2002**, *23*, 824–833. doi:10.1002/jcc.10064.
- (37) Kleinschmidt, M.; Tatchen, J.; Marian, C. M., *J. Chem. Phys.* **2006**, *124*, 124101. doi:10.1063/1.2173246.
- (38) Bracker, M.; Marian, C. M.; Kleinschmidt, M., *J. Chem. Phys.* **2021**, *155*, 014102. doi:10.1063/5.0056182.
- (39) Dinkelbach, F.; Marian, C. M., *J. Serb. Chem. Soc.* **2019**, *84*, 819–836. doi:10.2298/JSC190510048D.
- (40) Bracker, M.; Dinkelbach, F.; Weingart, O.; Kleinschmidt, M., *Phys. Chem. Chem. Phys.* **2019**, *21*, 9912–9923. doi:10.1039/C9CP00805E.
- (41) Dinkelbach, F.; Bracker, M.; Kleinschmidt, M.; Marian, C. M., *J. Phys. Chem. A* **2021**, *125*, 10044–10051. doi:10.1021/acs.jpca.1c09150.
- (42) Platt, J. R., *J. Chem. Phys.* **1949**, *17*, 484–495. doi:10.1063/1.1747293.
- (43) Vosskötter, S.; Konieczny, P.; Marian, C. M.; Weinkauff, R., *Phys. Chem. Chem. Phys.* **2015**, *17*, 23573–23581. doi:10.1039/C5CP01826A.
- (44) Hennebicq, E.; Pourtois, G.; Scholes, G. D.; Herz, L. M.; Russell, D. M.; Silva, C.; Setayesh, S.; Grimsdale, A. C.; Müllen, K.; Brédas, J.-L.; Beljonne, D., *J. Am. Chem. Soc.* **2005**, *127*, 4744–4762. doi:10.1021/ja0488784.
- (45) Förster, T., *Ann. Phys. (Berlin)* **1948**, *437*, 55–75. doi:10.1002/andp.19484370105.
- (46) Dexter, D. L., *J. Chem. Phys.* **1953**, *21*, 836–850. doi:10.1063/1.1699044.
- (47) Fink, R.; Pfister, J.; Schneider, A.; Zhao, H.; Engels, B., *Chem. Phys.* **2008**, *343*, 353–361. doi:10.1016/j.chemphys.2007.08.021.
- (48) Fink, R. F.; Pfister, J.; Zhao, H. M.; Engels, B., *Chem. Phys.* **2008**, *346*, 275–285. doi:10.1016/j.chemphys.2008.03.014.
- (49) Spiegel, J. D.; Kleinschmidt, M.; Larbig, A.; Tatchen, J.; Marian, C. M., *J. Chem. Theory Comput.* **2015**, *11*, 4316–4327. doi:10.1021/acs.jctc.5b00501.

Supplementary Material for
Intersystem Crossing and Intramolecular
Triplet Excitation Energy Transfer in
Spiro[9,10-dihydro-9-oxoanthracene-10,2'-
5',6'-benzindan] Investigated by DFT/MRCI
Methods

Simon Metz, Tobias Böhmer, Ben Raunitschke, and Christel M. Marian*

*Institute of Theoretical and Computational Chemistry, Heinrich-Heine-University
Düsseldorf, Universitätsstr. 1, 40225 Düsseldorf, Germany*

E-mail: Christel.Marian@hhu.de

September 30, 2022

Technical Details of the Computations

MRCI: 21 singlet, 20 triplet roots; standard parameter set; esel = 1.0 E_h

TTA: 64 triplet roots; short parameter set; esel = 0.8 E_h

HT expansion of ISC: 21 singlet, 20 triplet roots; short parameter set; esel = 0.8 E_h

NACMEs: 10 triplet roots; short parameter set; esel = 0.8 E_h ; renorm parameter = 10^{-8}

FC spectra: 16000 grid points, integration interval 3000 fs, damping parameter $\eta = 200 \text{ cm}^{-1}$

ISC and IC rate constants: 65536 grid points, integration interval 3000 fs, damping parameter $\eta = 10 \text{ cm}^{-1}$

Handling of Symmetry-Broken Solutions

In order to calculate Franck–Condon spectra, the eigenvalue of the imaginary frequency of the symmetry-constrained saddle-point has to be corrected. To this end, a (TD)DFT scan is carried out along the normal mode. The curvature of the outer part (red encircled points in Figure S1) is used to fit a harmonic frequency to this energy profile, as done in previous works.^{1,2} The fit, shown in Figure S1, yields a harmonic frequency of 13 cm^{-1} , which is close to the absolute value of the imaginary frequencies of -14.58 cm^{-1} . This is also true for the ground-state geometry in BuCN and the $^1n\pi^*$ **A** vacuum geometry. As a result, all other imaginary frequencies for this kind of normal mode were used as absolute values. To test how strongly the Franck–Condon overlaps depend on the eigenvalue of this low-frequency mode, a few calculations with different values were performed which yielded almost identical rate constants and spectra.

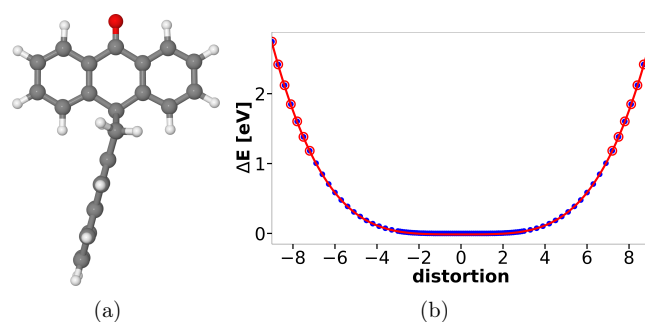


Figure S1: DFT (PBE0/def2-TZVP) minimum structure of the electronic ground state in BuCN an scan along the dimensionless normal coordinate of the imaginary vibrational mode at the C_{2v} -symmetric ground state geometry. Red encircled points are used for the fit of the harmonic potential (red line).

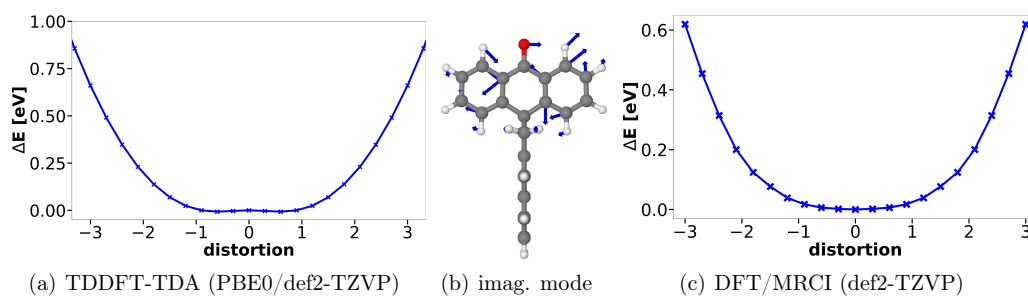


Figure S2: Scan along the dimensionless normal coordinate of the imaginary vibrational mode at the C_{2v} -symmetric ${}^3\pi\pi^*$ (**A**) state geometry. The energy profile of the TDDFT-TDA (PBE0/def2-TZVP) calculations show a shallow double minimum structure whereas the DFT/MRCI energy profile has a minimum at the symmetry point.

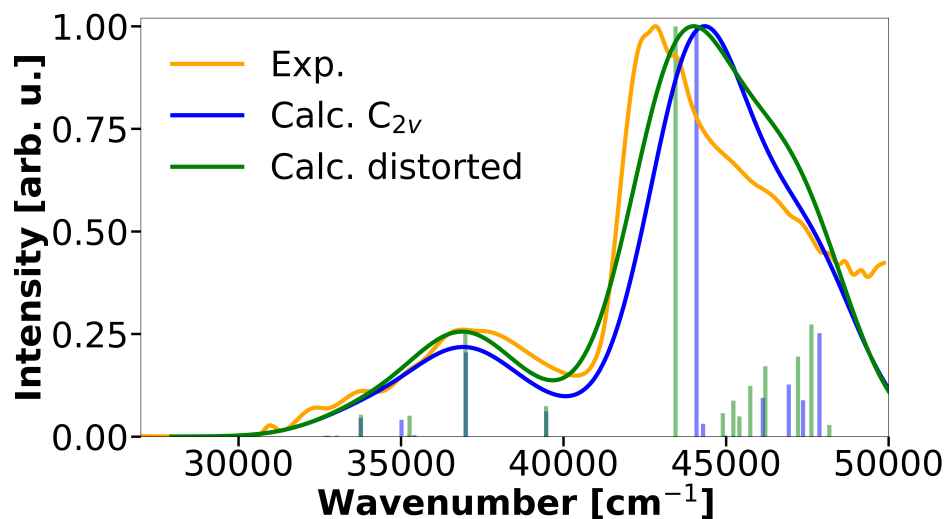


Figure S3: Calculated stationary absorption spectra in BuCN. The bars represent the transitions with their normalized oscillator strength. Blue: C_{2v} symmetric ground state; green: distorted ground-state geometry; orange: digitized spectrum read from Figure 6 of Ref.³

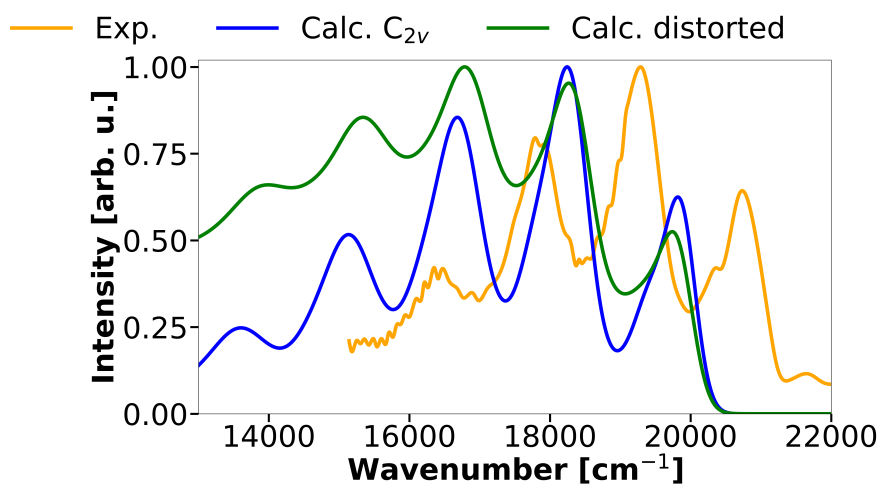


Figure S4: Calculated phosphorescence spectra in BuCN at 77K in comparison to experimental spectra. Blue: C_{2v} symmetric ground state; green: distorted ground-state geometry; orange: digitized spectrum read from Figure 3 of Ref.³

Molecular Orbitals

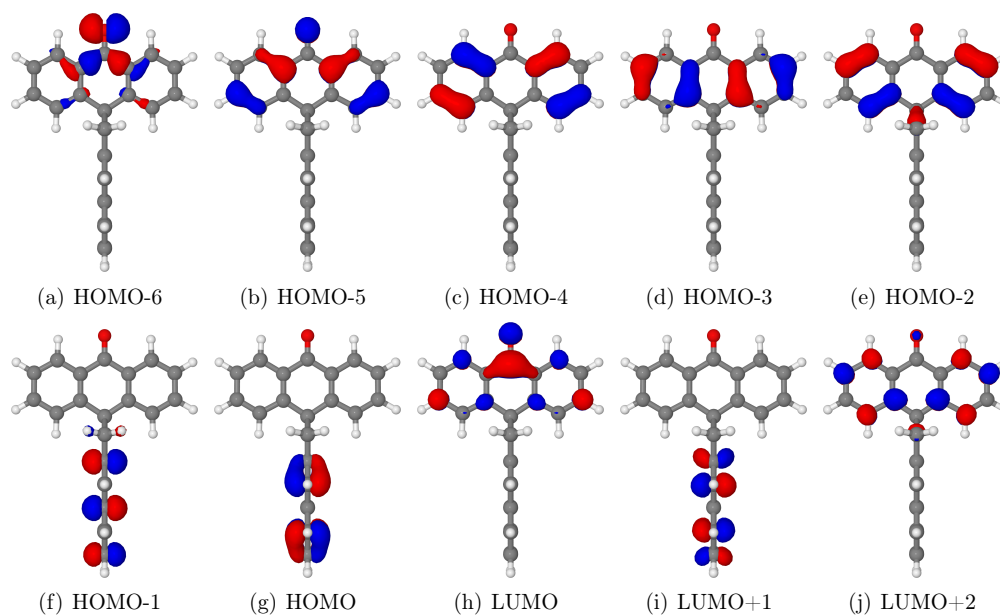


Figure S5: BH-LYP frontier molecular orbitals at the C_{2v} symmetrical ground state geometry in BuCN.

Excited-State Characteristics

Table S1: DFT/MRCI vertical excitation energies of low lying singlet and triplet states of the C_{2v} symmetrical ground state in vacuum.

State	ΔE	Transition	% weight
S ₁ ($^1n\pi^*$ A)	3.58	HOMO-6→LUMO	77.5
S ₂	4.07	HOMO-1→LUMO+1	46.2
		HOMO →LUMO+2	24.2
S ₃	4.20	HOMO →LUMO	41.6
		HOMO-3→LUMO	29.9
T ₁ ($^3\pi\pi^*$ N)	2.95	HOMO →LUMO+1	83.9
T ₂ ($^3n\pi^*$ A)	3.37	HOMO-6→LUMO	77.7
T ₃ ($^3\pi\pi^*$ A)	3.52	HOMO-5→LUMO	66.2
T ₄	3.66	HOMO-4→LUMO	41.7
		HOMO-3→LUMO	19.8

Table S2: DFT/MRCI vertical excitation energies of low lying singlet and triplet states of the C_{2v} symmetrical ground state in BuCN.

State	ΔE	Transition	% weight
S ₁ ($^1n\pi^*$ A)	3.71	HOMO-6→LUMO	78.1
S ₂	4.05	HOMO →LUMO	57.1
		HOMO-3→LUMO	21.7
S ₃	4.06	HOMO-1→LUMO+1	45.1
		HOMO →LUMO+2	21.0
T ₁ ($^3\pi\pi^*$ N)	2.96	HOMO →LUMO+1	84.2
T ₂ ($^3n\pi^*$ A)	3.51	HOMO-6→LUMO	78.5
T ₃ ($^3\pi\pi^*$ A)	3.51	HOMO-5→LUMO	67.3
T ₄	3.60	HOMO-4→LUMO	41.5
		HOMO-3→LUMO	24.5

Table S3: DFT/MRCI vertical excitation energies of low lying singlet and triplet states of the C_{2v} symmetrical ${}^1n\pi^*$ **A** in BuCN.

State	ΔE	Transition	% weight
S ₁ (${}^1n\pi^*$ A)	3.19	HOMO-6→LUMO	79.2
S ₂	3.78	HOMO →LUMO	66.6
		HOMO-3→LUMO	9.7
S ₃	3.97	HOMO-2→LUMO	72.2
T ₁ (${}^3\pi\pi^*$ N)	2.97	HOMO →LUMO+1	83.9
T ₂ (${}^3n\pi^*$ A)	3.03	HOMO-6→LUMO	80.1
T ₃ (${}^3\pi\pi^*$ A)	3.04	HOMO-5→LUMO	76.9
T ₄	3.36	HOMO-3→LUMO	52.2
		HOMO-4→LUMO	20.6

Table S4: DFT/MRCI vertical excitation energies of low lying singlet and triplet states of the C_{2v} symmetrical ${}^1n\pi^*$ **A** in vacuum.

State	ΔE	Transition	% weight
S ₁ (${}^1n\pi^*$ A)	2.93	HOMO-6→LUMO	78.2
S ₂	3.96	HOMO →LUMO	51.0
		HOMO-5→LUMO	16.7
		HOMO-4→LUMO	11.6
S ₃	4.06	HOMO-2→LUMO	59.9
T ₁ (${}^3n\pi^*$ A)	2.77	HOMO-6→LUMO	79.2
T ₂ (${}^3\pi\pi^*$ A)	2.94	HOMO-3→LUMO	77.0
T ₃ (${}^3\pi\pi^*$ N)	2.96	HOMO →LUMO+1	83.6
T ₄	3.42	HOMO-4→LUMO	56.2
		HOMO-5→LUMO	13.0

Table S5: DFT/MRCI vertical excitation energies of low lying singlet and triplet states of the C_{2v} symmetrical ${}^3n\pi^*$ **A** in BuCN.

State	ΔE	Transition	% weight
S ₁ (${}^1n\pi^*$ A)	3.20	HOMO-6→LUMO	79.2
S ₂	3.79	HOMO →LUMO	66.1
		HOMO-3→LUMO	12.2
S ₃	3.98	HOMO-2→LUMO	72.2
T ₁ (${}^3\pi\pi^*$ N)	2.97	HOMO →LUMO+1	83.9
T ₂ (${}^3n\pi^*$ A)	3.04	HOMO-6→LUMO	80.0
T ₃ (${}^3\pi\pi^*$ A)	3.07	HOMO-5→LUMO	76.7
T ₄	3.38	HOMO-3→LUMO	42.4
		HOMO-4→LUMO	29.9

Table S6: DFT/MRCI vertical excitation energies of low lying singlet and triplet states of the C_{2v} symmetrical ${}^3n\pi^*$ **A** in vacuum.

State	ΔE	Transition	% weight
S ₁ (${}^1n\pi^*$ A)	2.92	HOMO-6→LUMO	78.1
S ₂	3.96	HOMO →LUMO	50.6
		HOMO-4→LUMO	15.4
		HOMO-5→LUMO	15.3
S ₃	4.06	HOMO-2→LUMO	56.8
T ₁ (${}^3n\pi^*$ A)	2.76	HOMO-6→LUMO	79.1
T ₂ (${}^3\pi\pi^*$ A)	2.94	HOMO-3→LUMO	76.7
T ₃ (${}^3\pi\pi^*$ N)	2.95	HOMO →LUMO+1	83.5
T ₄	3.43	HOMO-4→LUMO	47.8
		HOMO-5→LUMO	21.0

Table S7: DFT/MRCI vertical excitation energies of low lying singlet and triplet states of the C_{2v} symmetrical ${}^3\pi\pi^*$ **A** in BuCN.

State	ΔE	Transition	% weight
S ₁ (${}^1n\pi^*$ A)	3.11	HOMO-6→LUMO	79.3
S ₂	3.68	HOMO →LUMO	69.1
		HOMO-5→LUMO	9.3
S ₃	3.91	HOMO-3→LUMO	71.5
T ₁ (${}^3\pi\pi^*$ A)	2.91	HOMO-4→LUMO	78.2
T ₂ (${}^3n\pi^*$ A)	2.97	HOMO-6→LUMO	80.3
T ₃ (${}^3\pi\pi^*$ N)	2.97	HOMO →LUMO+1	83.9
T ₄	3.22	HOMO-2→LUMO	71.0

Table S8: DFT/MRCI vertical excitation energies of low lying singlet and triplet states of the C_{2v} symmetrical ${}^3\pi\pi^*$ **A** in Vacuum.

State	ΔE	Transition	% weight
S ₁ (${}^1n\pi^*$ A)	2.84	HOMO-6→LUMO	78.2
S ₂	3.88	HOMO →LUMO	54.3
		HOMO-5→LUMO	18.2
S ₃	4.01	HOMO-4→LUMO	68.2
T ₁ (${}^3n\pi^*$ A)	2.69	HOMO-6→LUMO	79.2
T ₂ (${}^3\pi\pi^*$ A)	2.78	HOMO-2→LUMO	77.6
T ₃ (${}^3\pi\pi^*$ N)	2.95	HOMO →LUMO+1	83.4
T ₄	3.28	HOMO-3→LUMO	68.7

Table S9: DFT/MRCI vertical excitation energies of low lying singlet and triplet states of the C_{2v} symmetrical ${}^3\pi\pi^*$ **N** in BuCN.

State	ΔE	Transition	% weight
S ₁ (${}^1n\pi^*$ A)	3.73	HOMO-6→LUMO	77.5
S ₂	3.76	HOMO →LUMO+1	87.1
S ₃	3.83	HOMO →LUMO	80.7
T ₁ (${}^3\pi\pi^*$ N)	2.26	HOMO →LUMO+1	87.7
T ₂ (${}^3\pi\pi^*$ A)	3.53	HOMO-5→LUMO	67.0
T ₃ (${}^3n\pi^*$ A)	3.53	HOMO-6→LUMO	77.9
T ₄	3.61	HOMO-4→LUMO	40.2
		HOMO-3→LUMO	24.7

Table S10: DFT/MRCI vertical excitation energies of low lying singlet and triplet states of the C_{2v} symmetrical ${}^3\pi\pi^*$ **N** in vacuum.

State	ΔE	Transition	% weight
S_1 (${}^1n\pi^*$ A)	3.60	HOMO-6 \rightarrow LUMO	76.9
S_2	3.74	HOMO \rightarrow LUMO+1	86.9
S_3	3.82	HOMO-1 \rightarrow LUMO+1	44.2
		HOMO \rightarrow LUMO+3	17.7
		HOMO \rightarrow LUMO+4	13.9
T_1 (${}^3\pi\pi^*$ N)	2.25	HOMO \rightarrow LUMO+1	87.5
T_2 (${}^3n\pi^*$ A)	3.39	HOMO-6 \rightarrow LUMO	77.3
T_3 (${}^3\pi\pi^*$ A)	3.53	HOMO-5 \rightarrow LUMO	65.7
T_4	3.64	HOMO-1 \rightarrow LUMO+1	50.7
		HOMO \rightarrow LUMO+3	15.6
		HOMO \rightarrow LUMO+4	12.7

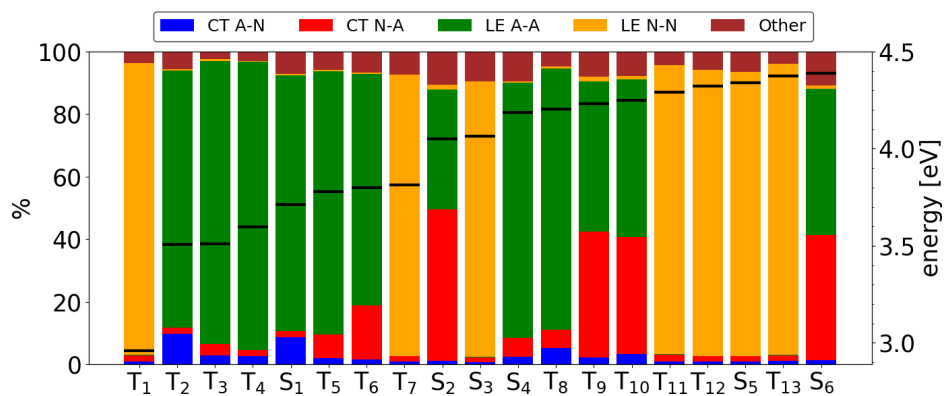


Figure S6: Theodore analysis at the ground state geometry in BuCN for excited states with a vertical excitation energy below 4.5 eV. Orange: local excitation on the naphthalene, green: local excitation on the anthracenone, blue: charge-transfer from the anthracenone to the naphthalene, red: charge-transfer from the naphthalene to the anthracenone, brown: other contribution such as 2-electron excitations.

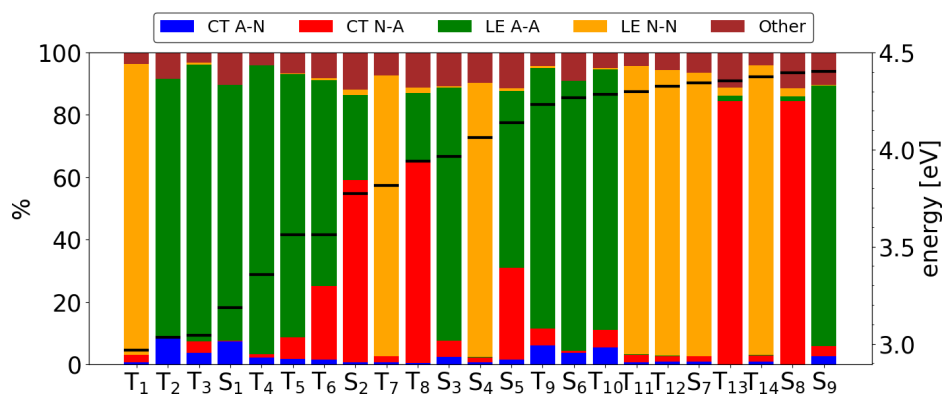


Figure S7: Theodore analysis at the $^1n\pi^*$ geometry in BuCN for excited states with a vertical excitation energy below 4.5 eV. Orange: local excitation on the naphthalene, green: local excitation on the anthracenone, blue: charge-transfer from the anthracenone to the naphthalene, red: charge-transfer from the naphthalene to the anthracenone, brown: other contribution such as 2-electron excitations.

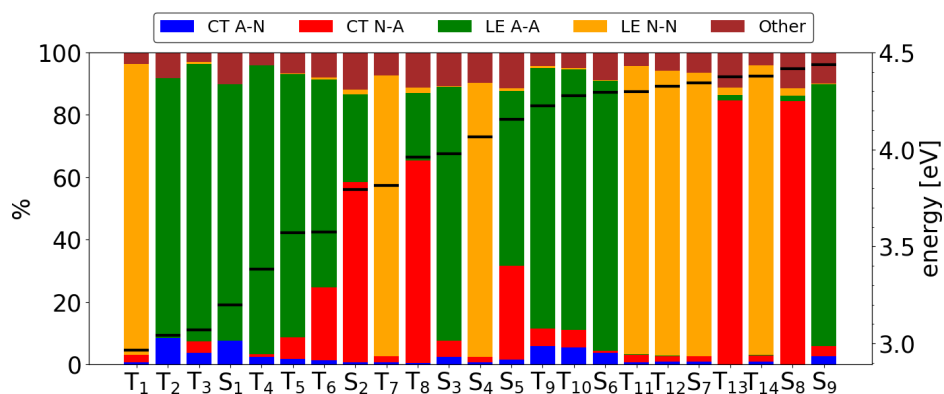


Figure S8: Theodore analysis at the $^3n\pi^*$ geometry in BuCN for excited states with a vertical excitation energy below 4.5 eV. Orange: local excitation on the naphthalene, green: local excitation on the anthracenone, blue: charge-transfer from the anthracenone to the naphthalene, red: charge-transfer from the naphthalene to the anthracenone, brown: other contribution such as 2-electron excitations.

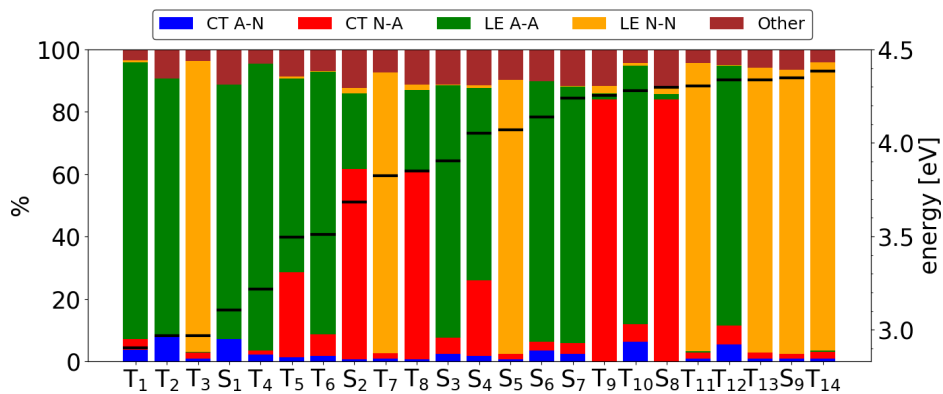


Figure S9: Theodore analysis at the ${}^3\pi\pi^*$ (A) geometry in BuCN for excited states with a vertical excitation energy below 4.5 eV. Orange: local excitation on the naphthalene, green: local excitation on the anthracenone, blue: charge-transfer from the anthracenone to the naphthalene, red: charge-transfer from the naphthalene to the anthracenone, brown: other contribution such as 2-electron excitations.

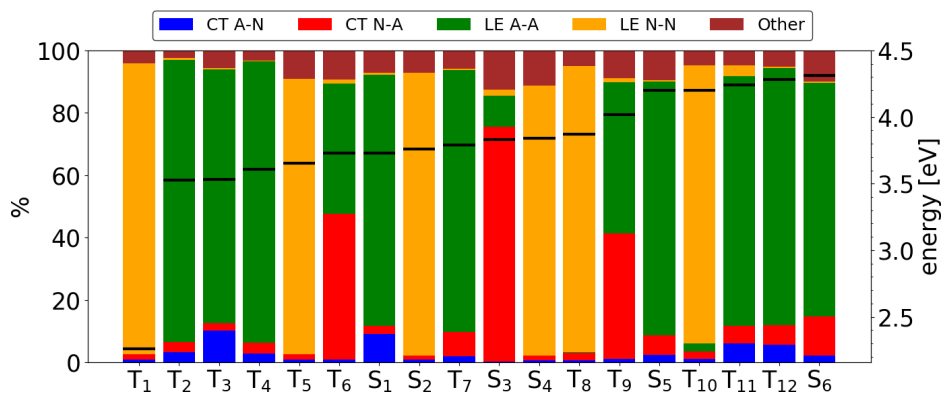


Figure S10: Theodore analysis at the ${}^3\pi\pi^*$ (N) geometry in BuCN for excited states with a vertical excitation energy below 4.5 eV. Orange: local excitation on the naphthalene, green: local excitation on the anthracenone, blue: charge-transfer from the anthracenone to the naphthalene, red: charge-transfer from the naphthalene to the anthracenone, brown: other contribution such as 2-electron excitations.

Vibrational Coupling Modes

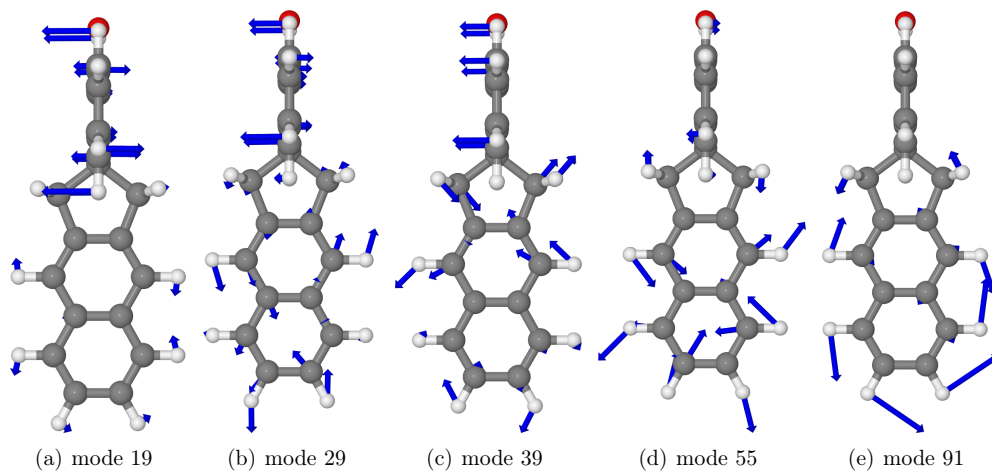


Figure S11: B_2 symmetric coupling vibrational modes promoting the TEET between the ${}^3\pi\pi^*$ (**A**) and ${}^3\pi\pi^*$ (**N**) of AN in BuCN.

References

- (1) Bracker, M.; Dinkelbach, F.; Weingart, O.; Kleinschmidt, M. Impact of fluorination on the photophysics of the flavin chromophore: a quantum chemical perspective. *Phys. Chem. Chem. Phys.* **2019**, *21*, 9912–9923.
- (2) Dinkelbach, F.; Bracker, M.; Kleinschmidt, M.; Marian, C. M. Large inverted singlet–triplet energy gaps are not always favorable for triplet harvesting: Vibronic coupling drives the (reverse) intersystem crossing in heptazine derivatives. *J. Phys. Chem. A* **2021**, *125*, 10044–10051.
- (3) Dobkowski, J.; Gorski, A.; Kijak, M.; Pietrzak, M.; Redeckas, K.; Vengris, M. Combined picosecond time-resolved UV-Vis and NMR techniques used for investigation of the excited state intramolecular triplet-triplet energy transfer. *J. Phys. Chem. A* **2019**, *123*, 6978–6985.

Paper 2

Electron affinities and lowest triplet and singlet state properties of para-oligophenylenes (n=3–5): Theory and experiment

J. Phys. Chem. A, **127**, 8073–8082 (2023)

Timo Schulz, Paul Konieczny, Dennis R. Dombrowski, Simon Metz, Christel M. Marian, Rainer Weinkauff

Contribution: Implementation of Dyson orbitals and their respective norms (DENSOMAT); writing part about Dyson orbitals; revision of the manuscript


 Cite this: *Phys. Chem. Chem. Phys.*, 2023, 25, 29850

Electron affinities and lowest triplet and singlet state properties of *para*-oligophenylenes ($n = 3-5$): theory and experiment†

 Timo Schulz,^{‡a} Paul Konieczny,^{‡b} Dennis R. Dombrowski,^a Simon Metz,^a Christel M. Marian^{ID} *^a and Rainer Weinkauf^{ID} *^b

We apply photodetachment–photoelectron spectroscopy to measure the electron affinities and the energetics of the lowest excited electronic states of the neutral molecules *para*-terphenyl (p3P), *para*-quaterphenyl (p4P) and *para*-quinquephenyl (p5P), including especially the triplet states below S_1 . The interpretation of the experimental data is based on the comparison to calculated 0–0 energies and Dyson norms, using density functional theory and multireference configuration interaction methods, as well as Franck–Condon patterns. The comparison between calculated and experimental vibrational fine-structures reveals a twisted benzoid-like molecular structure of the S_0 ground state and nearly planar quinoid-like nuclear arrangements in the S_1 and T_1 excited states as well as in the D_0 anion ground state. For all *para*-oligophenylenes (ppPs) in this series, at least two triplet states have been identified in the energy regime below the S_1 state. The large optical S_0 – S_1 cross sections of the ppPs are rationalised by the nodal structure of the molecular orbitals involved in the transition. The measured electron affinities range from 380 meV (p3P) over 620 meV (p4P) to 805 meV (p5P). A saturation of the electron binding energy with the increasing number of phenyl units is thus not yet in sight.

 Received 4th July 2023,
 Accepted 4th October 2023

DOI: 10.1039/d3cp03153e

rsc.li/pccp

1 Introduction

The chemical structures of the *para*-terphenyl (p3P), *para*-quaterphenyl (p4P) and *para*-quinquephenyl (p5P) molecules are shown in Fig. 1.

Because of their high fluorescence quantum yields *para*-oligophenylenes (ppPs) are used as UV-laser dyes. For example, p3P was the gain medium in one of the first tunable UV dye lasers.^{1–4} In the search for higher laser efficiencies, broader wavelengths tunabilities and new wavelength ranges it was found that modified p3P chromophores⁵ and longer ppPs can be also used as laser dyes.⁶ Already in 1976, a fluorescence

quantum yield of 0.93 was measured for p3P in solution, although its S_1 lifetime was found to be rather short (1.2 ns).³

In 1982, a resonant multi-photon ionisation (REMPI) gas phase spectrum of the $S_0 \rightarrow S_1$ transition of cold p3P molecules was reported by Murakami *et al.*⁷ In their spectrum, two long progressions of low-frequency vibrations are built upon the origin transition at 4.024 eV. These modes have been assigned to the in-phase and out-of-phase torsional twist modes around the C–C bonds which connect the phenyl rings. As explanation for the occurrence of the long progressions, the authors propose that in the S_0 state the benzene rings are twisted against each other, but lie in one plane in the S_1 state. Other experimental and theoretical publications dealing with the twisted S_0

^a Institute of Theoretical and Computational Chemistry, Heinrich-Heine-University Düsseldorf, Universitätsstr. 1, 40225 Düsseldorf, Germany. E-mail: Christel.Marian@hhu.de; Tel: +49 211 8113209

^b Institute of Physical Chemistry, Heinrich-Heine-University Düsseldorf, Universitätsstr. 1, 40225 Düsseldorf, Germany. E-mail: Rainer.Weinkauf@hhu.de; Tel: +49 211 8111729

† Electronic supplementary information (ESI) available: xyz coordinates of all optimised structures, torsional angles of ground and excited state structures, electron density differences, energies and calculated spectra of conformers, displacement vectors of selected normal mode vibrations, additional computational details, qualitative simulation of “peak-attraction” effect in T_1 of p3P. See DOI: <https://doi.org/10.1039/d3cp03153e>

‡ These authors contributed equally to this work.

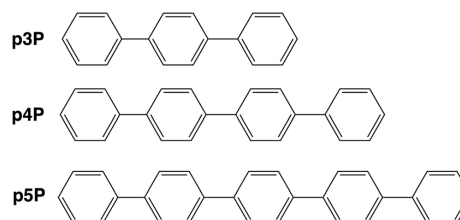


Fig. 1 Chemical structures of *para*-terphenyl (p3P), *para*-quaterphenyl (p4P) and *para*-quinquephenyl (p5P).

geometry of p3P have been reviewed by Baraldi and Pontorini.⁸ Using semiempirical calculations, they found for p3P two nearly isoenergetic conformers: (1) a C_{2h} symmetric conformer with alternating signs of the inter-ring twist angles and (2) a helical conformer with D_2 symmetry. For p3P the angles of the inter-ring twist were calculated to be 35° . The barrier separating the two minima was predicted to be low enough to allow a thermal equilibration of the rotamer populations at room temperature. Interestingly, in the above-mentioned REMPI S_0 - S_1 gas phase spectrum of p3P, despite of the high spectral resolution, no evidence for a second conformer can be found.⁷ This means that either only one conformer is thermally populated or, more plausible, that the two conformers have identical $S_0 \rightarrow S_1$ transition energies.

The role of the inter-ring twist modes on the absorption and emission spectra of p3P were further investigated by Schneider *et al.*⁵ They investigated p3P derivatives with and without additional bridges between the rings and confirmed that the S_0 - S_1 Stokes shifts are relatively large for the non-bridged compounds but considerably smaller if the torsional angle between the phenyl rings is reduced due to the presence of the bridges.⁵ Employing a combination of Hartree-Fock theory and configuration interaction singles Heimel *et al.*⁹ calculated twist angles between 30 and 40 degrees for the S_0 state of p3P. However, the large Stokes shift and the observed violation of the mirror-image-rule in p3P could be only explained when they included the anharmonicities of the torsional potentials in the S_0 and the S_1 states in their Franck-Condon (FC) simulations. Heimel *et al.*⁹ also find in their S_0 - S_1 FC spectrum four members of a sequence of the inter-ring stretch vibration (spacing $\sim 1400 \text{ cm}^{-1}$). This sequence and its combination bands with the torsion modes then explain, why in solution the emission spectrum of p3P is so broad and completely structure-less. Investigations by Lukeš *et al.*¹⁰ performed later with time-dependent density functional theory (TDDFT) came to the conclusion that the π system of the S_1 state adopts a quinoid double-bond structure in p3P.

In a more recent experimental investigation of p3P, p4P, p5P and *para*-sexiphenyl (p6P) by Nijegorodov *et al.*¹¹ the fluorescence quantum efficiencies were measured to be 0.84 (p3P), 0.81 (p4P); 0.89 (p5P) and 0.93 (p6P) and the corresponding fluorescence lifetimes are 1.0 ns (p3P), 0.85 ns (p4P), 0.82 ns (p5P) and 0.78 ns (p6P). Note that in this work no error bars were given despite the small differences between the values. If we assume that the small differences are correct, both series of data follow roughly the same line: the optical S_1 - S_0 transition cross section, being already high for p3P, still increases with chain length and is directly responsible for the increase in the fluorescence quantum efficiencies and the shortening of the S_1 lifetimes.

The larger the molecules become, the more non-radiative decay channels should be accessible. Typically, only the electronic ground state and triplet states are situated below S_1 . The experimental determination of the energetic position of triplet states by conventional methods is difficult in pure hydrocarbons because the electronic singlet-triplet coupling is weak.

The T_1 triplet state energies of p3P (3.1 eV) and p4P (2.3 eV) were measured for the first time by electron energy loss spectroscopy (EELS),¹² a method which competes with photodetachment-photoelectron spectroscopy (PD-PES), used in our investigation. Both methods can access triplet and singlet states of the neutral molecules on an equal footing. Strangely, by EELS no triplet states above T_1 have been found, although the energy range of the EELS spectra includes the S_1 (p3P: 4.9 eV; p4P: 4.6 eV), S_2 and even higher singlet states. Also by transient triplet absorption spectroscopy, no further triplet state was found below S_1 for p3P.¹³

To answer the open questions for the ppPs, we apply PD-PES to intact parent radical ppP anions. The fact that triplet states of the neutral molecule can be directly probed by removal of an electron from an intact radical anion has been known for a long time¹⁴⁻¹⁷ and was applied by us to anthracene,¹⁸ azulene,¹⁹ *N*-methylacridone and *N,N*-dimethylquinacridone.²⁰ With the same method, the electron affinities (EAs) of p3P and p4P were determined by Nakamura *et al.* in 2006.²¹ They also presented theoretical EA values, which agree reasonably well with their experimental values. By using UV lasers, we measure the lowest electronic excited states including S_1 and especially the T_1 and the T_2 states in this work. Finally, we compare calculated FC spectra with the shape of the measured spectra with the aim to gain new insights into the energetics as well as the geometric and electronic structures of the observed electronic states.

2 Methods

2.1 Anion photodetachment-photoelectron spectroscopy: the experimental setup

The sample molecules have been purchased from TCI. The apparatus used in this work for conducting photodetachment-photoelectron spectroscopy (PD-PES) has been described elsewhere.^{19,20} In short, the apparatus consists of four vacuum chambers in a sequence to stepwise reduce the vacuum pressure from the inlet chamber (chamber 1) to the photoelectron spectrometer (chamber 4). At the beginning of each measurement cycle, a heated and pulsed stainless steel gas nozzle releases a short gas pulse of argon (20 bar back pressure) with a small percentage of thermally evaporated sample molecules. As a result a pulsed expansion takes place through the small orifice (diameter 300 μm) into the first vacuum chamber (pressure in average better than 5×10^{-5} mbar). During expansion, radical anion formation by electron attachment to the sample molecules is performed. During the ongoing expansion, the initially hot radical anions then quickly undergo many collisions with the dense Ar gas. By this, the anions are energetically stabilised and strongly cooled. The slow neutral atoms and molecules as well as all the negative sample anions and the positive Ar ions contained in the centre of the expansion pass after about 10 mm through a skimmer orifice into the second vacuum chamber. The latter is used for vacuum pressure reduction between the chambers.

Despite that most of the sample radical anions are intact parent anions, mass selection is required before the

photodetachment, because many aggregates are formed. In chamber number two, for this reason, the ions enter a pulsed linear time-of-flight mass spectrometer (ToF-MS) which includes chambers 3 and 4. After passing several ion focussing lenses and several deflection plates in chamber 3, the anion cloud of interest crosses the PE spectrometer in chamber 4 and is detected at the rear side of chamber 4 on a micro-channel-plate (MCP) ion detector. The mass resolution is at this stage about 200. When crossing chamber 4, in the middle of the perpendicular μ -metal-shielded and therefore field-free PE spectrometer the anions interact with the pulsed detachment laser beam, which comes from above, perpendicular to the ion beam and the PE-spectrometer. Only these electrons which are emitted perpendicular to the ion and the laser beams are detected on a MCP-detector. The energy of the electrons is then determined by a start-stop ToF measurement. To achieve a high accuracy in the time measurement, the slightly focussed detachment laser has a pulse width below 1 ns (fundamental and higher harmonics of a post-amplified Piccolo laser, Innolas, Germany, pulse width 800 ps).

In order to be able to hit as many anions as possible with the laser beam, after mass identification and selection by a mass gate, the anions of interest are post-accelerated before chamber 4 and by this compressed in time and space.²² Photoelectron spectra are recorded by measuring the ToF which the electrons take for the 60 cm long field-free drift tube from the detachment site to the MCP electron detector. The advantage of such a ToF-energy analyser is, that for each cycle the PE spectrum covers always the full electron energy range, which depends on the molecular EA and the photon energy. The disadvantages are (i) a low transmission and (ii) the fact that the smallest peak width (best energy resolution) is only achieved for relatively low-energetic electrons ($E \leq 200$ meV).

To present a good energy resolution, for most of the accessible electronic states of the neutral sample molecule the overview anion PD-PE spectra are composed of sections of sub-spectra recorded with different detachment wavelengths. The disadvantage of this procedure is unfortunately that the relative electronic state intensities in the sub-spectra are different due to Wigner's threshold law²³ and difficult to adjust to each other. However, since we are especially interested in the energetics, such as electron affinities and triplet state energies, a comparison of the intensities is of minor importance.

In the ideal case, a photo excitation of a radical anion would excite into the detachment continuum and the intensities of the vibronic transitions of the final neutral electronic state would be exclusively given by the FC factors between the anion ground state and the neutral electronic state to which the detachment process leads. Unfortunately, anions can have anion-excited states even above the electron detachment threshold. These states, if accidentally resonantly photoexcited, can autoionise. Since in this case the resonant anion excited electronic state is involved, it can (i) either disturb the anion-to-neutral FC factors,²⁴⁻²⁶ or (ii) lead to a vibronically induced delayed autodetachment.²⁷

To avoid surface effects as much as possible, the inner spectrometer wall is heated to 340 K and the PE spectrometer

is energy-calibrated from time to time with the two spin-orbit transitions of atomic iodide.²⁸⁻³⁰ We found that the experimental accuracy concerning the absolute energy is ± 5 meV for electrons with energies below 300 meV, but the relative accuracy is much better than this. The accuracy to determine the energy of the adiabatic origin of an electronic state may, however, be less than the experimental accuracy because the shape of the observed spectral structures might be weak or/and broad and thus make an assignment of the exact origin transition of an electronic state difficult. This is especially the case for the adiabatic positions of the S_0 ground states of the ppPs (see Section 3.1).

2.2 Theoretical methods and computational details

All geometry optimisations and frequency analyses were performed with the Gaussian 16 program³¹ using the PBE0 density functional,^{32,33} which is known to give accurate ground- and excited-state geometries for this class of compounds,³⁴ and a valence triple-zeta basis set with polarisation functions (TZVP)³⁵ for carbon and hydrogen. The geometries of the anionic ground states (D_0) were optimised at the level of unrestricted Kohn-Sham density functional theory (KS-DFT) whereas closed-shell KS-DFT was employed for the neutral ground states (S_0). The minima of the excited singlet states were determined with time-dependent density functional theory (TDDFT), those of the triplet states with TDDFT in the Tamm-Dancoff approximation. Unless stated otherwise, all electronic excitation energies and molecular wavefunctions at the optimised geometries were calculated with the combined DFT and multireference configuration interaction (DFT/MRCI) method^{36,37} employing the recently presented R2022 Hamiltonian³⁸ which is particularly well suited for extended π -systems. DFT/MRCI is a semi-empirical multireference configuration interaction ansatz based on KS orbitals and orbital energies of a closed-shell BH-LYP functional^{39,40} determinant. For the construction of the two-electron integrals in the resolution-of-the-identity approximation, the auxiliary basis sets from the Turbomole library^{41,42} were employed. Computational details concerning the DFT/MRCI parameter set, the selection thresholds for including configuration in the variational space and the number of roots determined in the Davidson diagonalisation procedure can be found in the ESI.† FC spectra were calculated *via* a fast Fourier transformation ansatz employing the Vibes program.^{43,44} Besides adiabatic energies and FC patterns of the excitation, photoionisation cross sections are especially valuable for assigning closely spaced electronic states. To obtain an estimate for the photoionisation probabilities, often Dyson orbitals ϕ_{IF}^{Dyson} and their respective squared norms σ_{IF} are used, disregarding the overlap between the outgoing electron and the ionisation continuum states.⁴⁵⁻⁴⁸ In the context of PES, Dyson orbitals are defined as the overlap between an initial N -electron state and a final $N - 1$ -electron state.

$$\phi_{IF}^{\text{Dyson}}(x_1) = \sqrt{N} \int \psi_F^{N-1}(x_2, x_3, \dots, x_N) \psi_I^N \times (x_1, x_2, x_3, \dots, x_N) dx_2, dx_3, \dots, dx_N \quad (1)$$

Dyson orbitals can also be written as a linear combination of the molecular orbital set of the initial wave function $\{\phi_p\}$:

$$\phi_{\text{IF}}^{\text{Dyson}}(x_1) = \sum_p \gamma_p \phi_p(x_1) \quad (2)$$

where the expansion coefficients, also called Dyson amplitudes, are defined as:

$$\gamma_p = \langle \psi_{\text{F}}^{N-1} | a_p | \psi_{\text{I}}^N \rangle \quad (3)$$

Possible values range between 0 for states that cannot be described by a one-electron transition and 1 for two states that differ exactly by the occupation of one spin orbital. Note, that a value of 1 is only possible if the electron is detached from a singly occupied molecular orbital of the anion. If the electron is removed from a doubly occupied shell, at most a Dyson amplitude of 0.5 can be expected. (For further explanations, see the ESI.†) The squared Dyson norm can be described as the sum over the squared coefficients

$$\sigma_{\text{IF}} = \left\| \phi_{\text{IF}}^{\text{Dyson}} \right\|^2 = \sum_p \gamma_p^2 \quad (4)$$

and is a measure for the probability of a photoionisation. In this work, DFT/MRCI wavefunctions of the anionic ground state and the ground and excited states of the respective neutral molecules have been used to determine the pole strengths.

3 Results and discussion

In the following section, we present the experimental PD–PE overview spectra of p3P, p4P and p5P, explain their specialities and propose first assignments. Subsequently, we report on the results of our quantum chemical calculations before we compare them with the experimental data and discuss the resulting consequences.

3.1 Photodetachment–photoelectron overview spectra

The overview PD–PE spectra of p3P, p4P and p5P (Fig. 2) show the transitions from the anion ground states to the S_0 and to the excited electronic states of the neutral molecules. Note that they are composed of sub-spectra recorded with different detachment wavelengths in order to show spectra with the best possible electron energy resolution and to avoid strange vibrational FC effects as caused by the resonance of the detachment laser with an anion-excited electronic state. Labels with the detachment wavelengths are included in Fig. 2. The relative intensities of the subspectra have been adapted to each other according to graphical aspects. Between two electronic states they can be only interpreted if their spectral structures have been recorded with the same wavelength and if the two states lie rather close in energy. The estimated origin positions of the S_0 states are set to the zero position of the energy scale which is—as a consequence—the energy scale of the neutral molecules. As a result of the definition of the energy axis, the anion ground states lie to the left of the zero point of the x -axis (S_0)

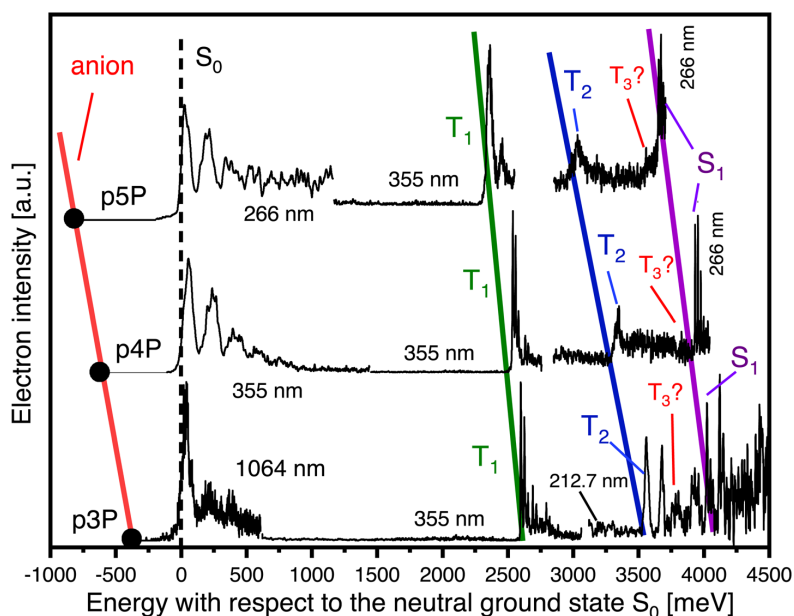


Fig. 2 Composed PD–PE overview spectra of p3P, p4P and p5P illustrating the energetic trends. The coloured lines are only meant to guide the eye. For a better comparison to the spectroscopy of the neutral molecules the energies are given with respect to the neutral S_0 ground state. The positions of the anion D_0 ground states are marked by bullets (for values, see Table 1). The EA increases with increasing size of the molecules, the S_1 and T_1 bands shift slightly to lower energies whereas a stronger shift is observed for T_2 . The assignment of the T_3 band is tentative only.

and the electronically excited states of the neutral molecules to the right side. As expected, the EAs increase and the electronic excited state energies decrease with the increase of the number of phenyl rings.

The assignments included in Fig. 2 are based on simple spectroscopic principles and literature data. The lowest-energetic transition from the radical anion to the neutral molecule leads to the S_0 state. The assignment of the next spectral PE structures is also obvious: in a closed-shell molecule, the T_1 state is usually the first excited state above S_0 and does not appear in UV-VIS spectra. The assignment of the S_1 states can be performed on the basis of their energetics which agree with S_0 - S_1 transition energies known from literature (see Table 1). Since the isolated transitions which are located between T_1 and S_1 have not been observed in the UV-VIS spectra,⁵ they are attributed to T_2 . In addition, further peaks are assigned tentatively to the T_3 state.

The EA values and the excited-state energies of all three molecules are summarised in Table 1 and compared to experimental literature data. In all investigated ppPs, definitively the T_2 states and possibly even the T_3 states lie below the respective S_1 states and the S_1 - T_2 energy gap is relatively small. In Fig. 2 one can see that the vibrational structures of the individual electronic states are rather different. For example, in p3P the first transition to S_0 is much broader (this sub-spectrum was recorded with 1064 nm, providing the best experimental resolution) than the peaks of the transitions to T_1 , T_2 and S_1 . If autodetachment effects were absent, these individual vibrational patterns should be correlated with structural changes between the molecular anion geometry and the geometries of the individual electronic states of the neutral molecules. In Section 3.3, expanded PD-PE spectra of most of the transitions to the individual electronic states of the neutral molecules are shown and compared to corresponding theoretical spectra.

3.2 Quantum chemical results

According to former investigations,^{7-9,21} the changes of the torsional angles, which are allocated between the phenyl rings, play an important role for the interpretation of the electronic and vibronic spectra of the ppPs. Moreover, these twist angles seem to be correlated with C-C bond length alterations. Lukeš *et al.* postulated that ppPs exhibit a quinoid structure in the first excited singlet state and that the double-bond character of

the C-C bond between the phenyl rings causes the planarity in S_1 .¹⁰ We here take these statements as a motivation for a more general investigation on the equilibrium geometry changes in the ground and excited electronic states of the neutral ppPs with regard to the anion ground state. In the following, the trends will be discussed in a qualitative manner.

As mentioned earlier, for the neutral *para*-phenylenes two or more stable rotamers exist which differ in the relative orientation of the phenyl rings, *i.e.*, alternating or helical. Within the error bars of our experiment and our quantum chemical calculations we do not find energetic differences between the two (p3P) and multiple (p4P and p5P) possible conformers of the investigated ppPs, neither in the anions nor in the neutral electronic states. Inter-conformer transitions have very similar transition energies as intra-conformer transitions but have typically broader vibrational structures due to the larger geometry changes. To simplify the complex discussions, we only present the results for the conformers alternating in the sign of the torsion angles.

3.2.1 Quantum chemical results on p3P. The analysis of the twist angles in the equilibrium structures (Fig. 3) shows that D_0 , S_1 , S_2 and T_1 are nearly planar and that S_0 is strongly non-planar. For the S_0 and S_1 states these findings agree well with the results of Lukeš *et al.*¹⁰ and explain the large and irregular S_0 - S_1 Stokes shifts determined in optical spectroscopy.⁵ The minimum structure of the T_3 state could not be determined because the geometry optimisation converges towards a conical intersection with the T_2 potential energy surface.

In Fig. 4, the calculated bond length changes with respect to the anion ground state D_0 are shown. These changes will be rationalised based on the leading configurations of the wavefunctions. To avoid confusion, we designate the molecular orbitals (MOs) according to their occupations in the ground state of the neutral molecule: the highest occupied molecular orbital (HOMO, H) is doubly occupied in both, S_0 and D_0 , whereas the lowest unoccupied molecular orbital (LUMO, L) is empty in S_0 and singly occupied in D_0 .

The leading term of the totally symmetric S_0 state is related to the D_0 state by the ejection of the LUMO electron. The LUMO has bonding character with regard to the inter-ring C-C bonds 4 and 8 (see Fig. 5), where we have used the bond labelling introduced in Fig. 4. Also the C-C bond 6 in the central phenyl

Table 1 Electron affinities and electronic state energies of p3P, p4P and p5P with respect to the neutral ground state S_0 . Experimental data from this work and literature data. All values are given in meV. Note that the energy error in this work is given by the accuracy with which the origin of the S_0 state can be determined (about ± 50 meV)

State	p3P		p4P		p5P	
	Lit.	This work	Lit.	This work	Lit.	This work
EA/ S_0	390 ^a	379	660 ^a	620	—	805
S_1	4024 ^b , 3962 ^c , 4900 ^d	4024	3731 ^c , 4600 ^d	3872	3602 ^c	3688
S_2	6500 ^d	—	4029 ^c , 6400 ^d	—	3967 ^c	—
T_1	2541 ^c , 3100 ^d , 2529 ^e	2598	2392 ^c , 2300 ^d	2478	2318 ^c	2375
T_2	—	3558	—	3260	—	3073
T_3	—	3930 (?)	—	3771 (?)	—	3597 (?)

^a Ref. 21 PD-PES. ^b Ref. 7 REMPI, gas phase. ^c Ref. 11 solution phase. ^d Ref. 12 electron beam, gas phase. ^e Ref. 49 crystal.

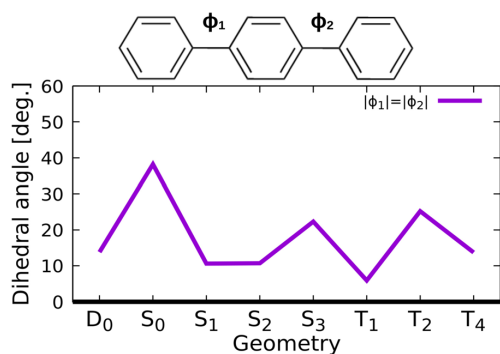


Fig. 3 Calculated torsional angles in the equilibrium geometries of selected anionic and neutral electronic states of p3P.

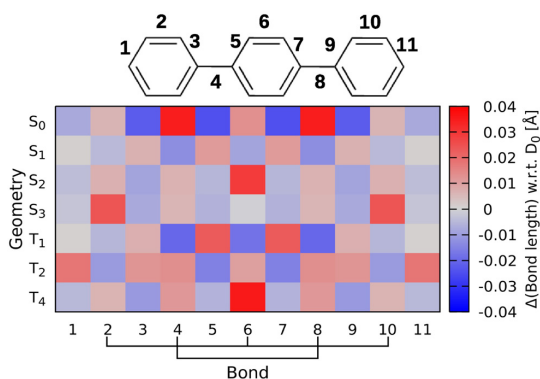


Fig. 4 Bond length differences between the respective neutral states and the D_0 anion state of p3P. The colour bar at the right side gives the correlation between the colours and the bond length changes (in Å).

ring and, to a minor extent, the C–C bonds 2 and 10 in the terminal phenyl rings experience bonding interactions in LUMO. All other C–C bonds of p3P are intersected by nodal planes in the LUMO and therefore have antibonding character. The pattern of the bond length alterations, shown in Fig. 4, exactly follows the expected trends: if one electron is removed from the LUMO, the inter-ring C–C bonds 4 and 8 lose their double-bond character. Accordingly, the steric strain caused by the repulsion between the hydrogen atoms of two neighbouring phenyl rings prevails over the bonding forces and leads to an out-of-plane twist, as may be seen when comparing the torsional angles of the D_0 and the S_0 states in Fig. 3. Also the central bond 6 is strongly elongated in S_0 with respect to D_0 while the bonds carrying odd labels are shortened, but these bond length changes do not have a major impact on the dihedral angles.

If instead an electron is removed from the HOMO, the A_u -symmetric T_1 or S_1 states are reached, depending on the spin orientation of the outgoing electron. Although both states are well represented by the $(H)^1(L)^1$ configuration, the bonding

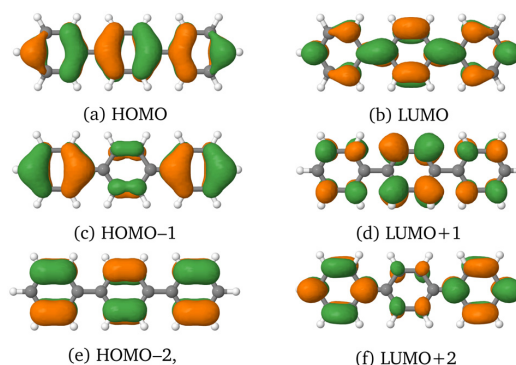


Fig. 5 Important MOs of p3P at the anion ground state geometry. Images of further MOs may be found in the ESI.†

patterns (Fig. 4) are not identical. We notice stronger bond length alterations in the triplet state, a phenomenon already observed for the $(H)^1(L)^1$ states of polyene chains.⁵⁰ Nodal planes intersect the even numbered bonds whereas high electron density is found between the carbon atoms connected by odd numbered bonds (see Fig. 4). In the S_1 and T_1 states, therefore the inter-ring C–C bonds are strengthened and shortened whereas the neighbouring bonds are elongated. Even the bonds 2, 6 and 10 acquire partial double bond character, thus giving the three phenyl rings a quinoid structure.

The geometry changes of the higher-lying electronic states are not as easily deduced because they have multiconfigurational character. The wavefunction of the T_2 state exhibits A_g symmetry and is dominated by an almost equal mixture of $(H-1)^1(L)^1$ and $(H)^1(L+2)^1$ configurations. HOMO–1 and LUMO+2 have larger amplitudes on the terminal phenyl rings than on the central one (see Fig. 5c and f). Ejection of an electron from HOMO–1 and occupation of LUMO+2 both lead to a pronounced elongation of the terminal C–C bonds 1 and 11, other geometry changes are less obvious. Inter-ring twist angles intermediate between the D_0 and S_0 are found for the equilibrium geometry of this state. S_2 and T_4 transform according to the B_u irreducible representation with leading $(H)^1(L+1)^1$ and $(H-2)^1(L)^1$ terms. LUMO+1 and HOMO–2 do not involve the carbon atoms connecting the phenyl rings (see Fig. 5d and e). Therefore, the small twist angles (Fig. 3) are mainly caused by the removal of a HOMO electron in the first case and the remaining electron in the LUMO in the second case. The most pronounced bond length change involves the central C–C bond 6 which is markedly weakened with respect to the anion ground state (Fig. 4).

3.2.2 Quantum chemical results on p4P. The structural differences between the electronic states of p4P show similar patterns as those of p3P (Fig. 6 and 7), save for a few distinct peculiarities concerning the central C–C bond and the related torsional angle Φ_2 . In the anionic ground state, the torsional angles vary between 15° for Φ_2 and -20° for Φ_1 and Φ_3 . The S_0 minimum geometry is again strongly non-planar and the inter-ring bonds are elongated with regard to the D_0 structure.

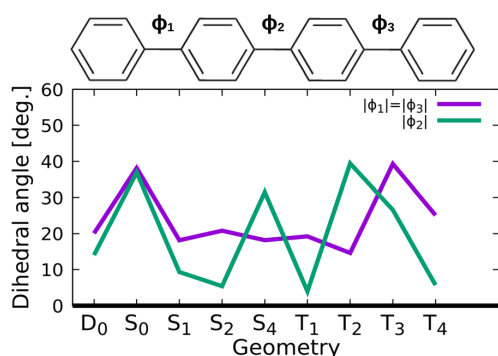


Fig. 6 Torsional angles in the different electronic states of p4P. Note the different behaviour of the outer angles ϕ_1 and ϕ_3 in comparison to ϕ_2 .

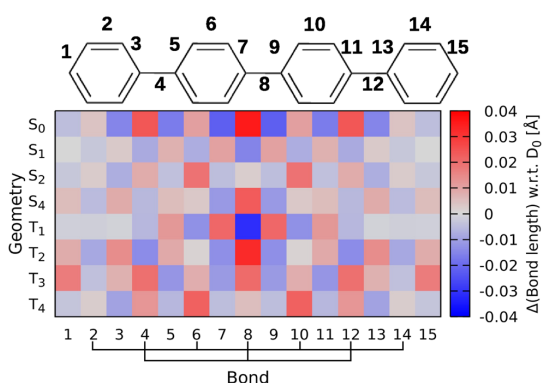


Fig. 7 Bond length differences between the neutral states of p4P with respect to D_0 . For further explanations, see Fig. 4.

The effect is more pronounced for the central bond 8 because the electron density in the LUMO (Fig. 8b), from which the electron is ejected, is higher than for the terminal inter-ring bonds 4 and 12. The S_1 and T_1 states of p4P adopt a quinoidal structure, again with stronger alterations for the central bond and the related twist angle due to the larger orbital amplitudes of the HOMO (Fig. 8a) in that spatial region.

T_2 and S_4 are interesting cases because here opposite tendencies are observed for the outer and inner phenyl rings and the related geometry parameters (Fig. 6 and 7) which can be traced back to the electron density distribution in the involved MOs. Like in p3P, T_2 and S_4 are multiconfigurational wavefunctions with the $(H-1)^1(L)^1$ and $(H)^1(L+1)^1$ configurations as leading terms. Inspection of Fig. 8c reveals bonding character for 8 and antibonding character for 4 and 12 in HOMO-1. Annihilation of an electron in HOMO-1 therefore weakens the central inter-ring bond and strengthens the outer ones. The second configuration cannot be reached from D_0 by a single electron excitation, but requires the removal of an electron from HOMO accompanied by an excitation from LUMO to LUMO+1. While the geometric effects caused by the

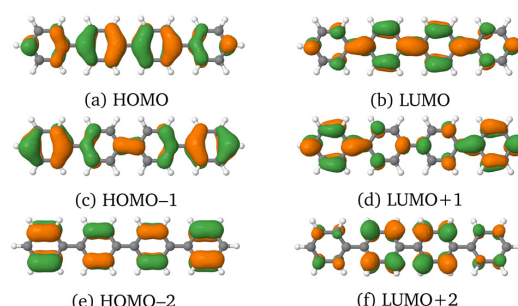


Fig. 8 Important MOs of p4P at the anion ground state geometry. Images of further MOs may be found in the ESI.†

lowering of the HOMO and LUMO populations nearly cancel, occupation of LUMO+1 (Fig. 8d) results in an elongation of the central C-C bond. While the electronic states of neutral p4P, discussed so far, are symmetric with respect to a rotation through 180° about the long C_2 axis (z axis), S_2 and T_4 are antisymmetric. To reach their leading $(H)^1(L+2)^1$ configuration from the D_0 state, again a two-electron process is necessary. Their secondary configuration, $(H-2)^1(L)^1$, is generated by PES through the ejection of an electron from HOMO-2. Neither HOMO-2 (Fig. 8e) nor LUMO+2 (Fig. 8f) exhibit notable amplitudes on the inter-ring C-C bonds. Ejection of an electron from HOMO-2 and occupation of LUMO+2 rather lead to a weakening of the bonds 6 and 10 (Fig. 7) without essentially changing the torsional angles with regard to the anion ground state (Fig. 6).

3.2.3 Quantum chemical results on p5P. Without repeating this kind of detailed discussion for p5P, we notice that for some electronic states the outer ($\phi_1 = \phi_4$) and the inner torsional angles ($\phi_2 = \phi_3$) differ considerably (Fig. 9). In the D_0 anion ground state, all twist angles are around 20° while the S_0 state of p5P is strongly twisted, with all torsional angles close to 40° . In S_1 (configuration $(H)^1(L)^1$), the inner two twist angles are smaller than the outer ones, an effect which is even more pronounced in the T_1 state. The degree of torsion finds its direct correspondence in the inter-ring C-C bond distance (Fig. 10).

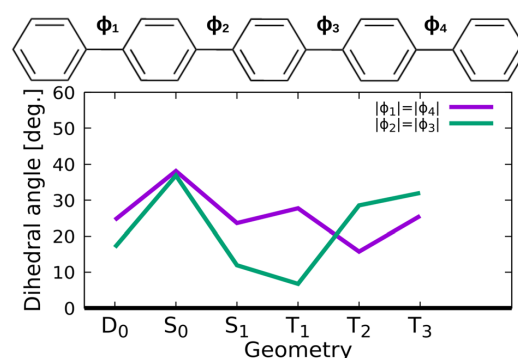


Fig. 9 Torsional angles in the different electronic states of p5P.

Paper

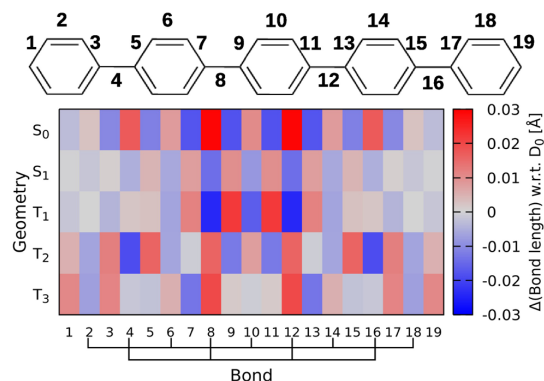


Fig. 10 Bond length differences between the neutral states of p5P with respect to D_0 . For further explanations, see Fig. 4.

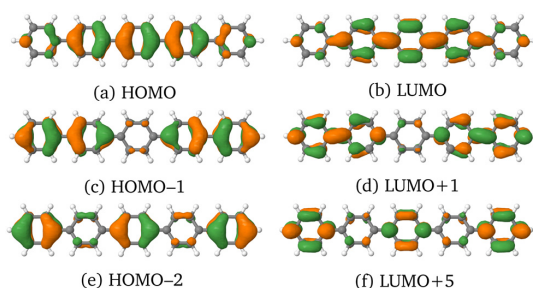


Fig. 11 Important MOs of p5P at the anion ground state geometry. Images of further MOs may be found in the ESI.†

The quinoidal structure appears to extend over the three innermost phenyl rings only. These trends are related to the observation that the electron densities in the HOMO (Fig. 11a) and LUMO (Fig. 11b) orbitals are mainly localised in this part of the molecule. In contrast, HOMO-1 (Fig. 11c) and LUMO+1 (Fig. 11d) have large amplitudes on the outermost phenyl rings and their neighbours and almost zero coefficients on the central phenyl ring. For that reason, the inner inter-ring bonds No. 8 and 12 are weakened whereas the outer inter-ring bonds (No. 4 and 16) are strengthened at the T_2 minimum where the $(H-1)^1(L)^1$ and $(H)^1(L+1)^1$ configurations have nearly equal weights. As a consequence, the outer twist angles are smaller than the inner ones, essentially reversed to the situation in the T_1 state. Also T_3 is not planar. It exhibits a nearly equal mixture of $(H-2)^1(L)^1$, $(H-1)^1(L+1)^1$ and $(H)^1(L+5)^1$ configurations (for orbitals see Fig. 11). Like in T_2 , its inter-ring bonds 8 and 12 are elongated with respect to the D_0 structure, but the bond length alterations in the central ring nearly level out.

In conclusion of this section, with increasing chain length of the ppP, more and more local effects are observed where the inner and outer molecular sections behave differently in individual electronic states. The tendency that a nearly planar quinoidal structure in the S_1 state is restricted to the central parts of the molecule has been reported even for longer

para-phenylene oligomers.⁵¹ While trends for the first excited singlet state were discussed in detail by Lukeš *et al.*,¹⁰ we extended our investigation of the structural changes to several low-lying triplet states.

3.3 Comparison of the experimental and computed spectra

In this chapter we present our theoretical results based on the DFT/MRCI method and compare them to the experimental data. The absolute error for the experimental electronic state energies with respect to the S_0 state is determined by the error with which the exact position of the transition to the S_0 origin can be determined. Due to the broad unresolved structure of this transition, the S_0 origin position may have only an accuracy of roughly 50 meV. Root mean square deviations of the DFT/MRCI method are typically in the 200 meV range for organic molecules with a closed-shell ground state when the R2022 Hamiltonian is employed.³⁸

3.3.1 *para*-Terphenyl (p3P). The agreement between the calculated and measured 0-0 energies is relatively good (Table 2). This applies even to the EA, computed as Δ SCF value at the PBE0/TZVP level of theory, whereas DFT/MRCI underestimates the EA. With the exception of T_1 , which matches the experimental value perfectly, the calculations appear to underestimate the experimental 0-0 energies by about 0.1 eV, whereas adiabatic DFT/MRCI energies which do not include ZPVE corrections are a bit too high. The theoretical value of the T_3 energy, provided in Table 2, has been obtained for a C_s -symmetric saddlepoint structure with a small imaginary frequency (-13 cm^{-1}). Despite many attempts, a proper minimum could not be determined for the T_3 potential energy surface because it undergoes a conical intersection with the T_2 potential. According to the calculations, this saddlepoint lies energetically below the S_1 minimum if ZPVE corrections are taken into consideration. The strong vibronic coupling between two triplet states is held responsible for the irregular vibrational pattern observed between T_2 and S_1 in the overview spectrum.

The very different vibrational substructures of the individual transitions in the experimental p3P PD-PE spectrum shown in Fig. 2 indicate that some electronic states of the neutral molecule exhibit strong structural differences with respect to the anion ground state, an effect which is worth to be further investigated by calculations of FC patterns. As discussed in Sections 3.2.1, p3P is almost planar in the anion ground state, strongly twisted in the neutral ground state S_0 and nearly planar in the S_1 state. A quick look at the overview spectrum of p3P (see Fig. 2) confirms qualitatively these theoretical results: in contrast to the broad anion to S_0 transition, the transitions to excited electronic states, such as T_1 and S_1 , contain intense origin transitions and relatively small intensities for the low-frequency vibrations.

For a more detailed analysis, individual expanded experimental spectra and the corresponding theoretical calculated FC transition spectra have been juxtaposed. Displacement vectors of the most important normal coordinates are visualised in the ESI.†

Table 2 Theoretical and experimental results for p3P: coefficients (absolute values) of leading MO configurations, calculated vertical transition energies ΔE_{vert} at the S_0 geometry, calculated adiabatic transition energies ΔE_{adiab} , and ZPVE corrected transition energies ΔE_{0-0} with respect to S_0 , experimental energies ΔE_{exp} (this work only), oscillator strengths f , calculated vertical electron detachment energies ΔE_{det} and Dyson intensities σ at the D_0 geometry. All energies in eV. In the first row of the table body, the experimental and the ZPVE corrected theoretical EAs are displayed. Experimentally not observed transitions are labelled as 'n.o.'

State	Configurations	ΔE_{vert}	ΔE_{adiab}	ΔE_{0-0}	ΔE_{exp}	f	ΔE_{det}^b	ΔE_{det}^c	σ
S_0	1^1A_g 0.97 GS			EA: 0.42 ^b	EA: 0.380	—	0.53	0.53	0.95
S_1	1^1A_u 0.95 (H) ¹ (L) ¹	4.61	4.03	3.91	4.024	1.15	4.27	4.36	0.46
S_2	1^1B_u 0.67 (H) ¹ (L+1) ¹ 0.50 (H-2) ¹ (L) ¹ 0.28 (H-4) ¹ (L) ¹	4.54	4.21	4.09	n.o.	0.00	4.87	4.59	0.17
S_3	1^1B_g 0.60 (H-3) ¹ (L) ¹ 0.54 (H) ¹ (L+3) ¹	4.63	4.50	4.34	n.o.	0.00	5.19	4.85	0.18
T_1	1^3A_u 0.91 (H) ¹ (L) ¹	3.36	2.74	2.60	2.598	—	3.08	3.12	0.43
T_2	1^3A_g 0.65 (H-1) ¹ (L) ¹ 0.60 (H) ¹ (L+2) ¹	3.83	3.64	3.45	3.558	—	4.13	3.03	0.21
T_3	2^3A_u 0.47 (H-3) ¹ (L+3) ¹ 0.41 (H-5) ¹ (L) ¹	4.17	4.04 ^a	3.81 ^a	3.93 (?)	—	4.88	4.75	0.09
T_4	1^3B_u 0.69 (H) ¹ (L+1) ¹ 0.50 (H-2) ¹ (L) ¹ 0.24 (H-4) ¹ (L) ¹	4.27	4.01	3.95	n.o.	—	4.44	4.40	0.16

^a No minimum was found. In C_s symmetry, still a small imaginary frequency with -13 cm^{-1} is present at the saddlepoint. ^b Computed at the (TD)PBE0/TZVP level of theory. ^c DFT/MRCI energies at the D_0 geometry, shifted by 0.38 eV, the difference between the PBE0/TZVP and DFT/MRCI computed vertical detachment energy of the S_0 state.

The experimental spectrum in Fig. 12a shows at the low-energetic side a smooth onset, then a steep rise at about 400 meV followed by some distinct peaks with spacings of about 54 cm^{-1} before the signal declines again. The width at half height of a fictive envelope of the complete S_0 structure would be about 50 meV. The important question now is where does the S_0 origin transition lie? Remember that the exact position of the S_0 origin affects the determination of the electron affinity and the derived energetic positions with respect to the neutral S_0 state. The first observed weak transition of the S_0 - S_1 spectrum of Murakami *et al.* has been determined by laser spectroscopy (4.024 eV).⁷ We can use this value to qualitatively locate the S_0 origin at about 380 meV above the anion ground state. This position is marked with a black vertical line in Fig. 12a. Since the theoretical spectrum in Fig. 12b essentially predicts a very low intensity for the D_0 - S_0 0-0 transition, the exact position of the experimental origin should lie considerably to the left of the distinct sharp first peak indicated as " S_0 ?" in Fig. 12a. Because the exact determination of the S_0 origin position is impossible on the basis of the presently available information, we set our error bars to $\pm 50 \text{ meV}$.

If one compares the experimental with the calculated FC spectrum (see Fig. 12b), the peak spacings are roughly similar, however, the agreement of the peak intensities is rather poor: (i) in the theoretical FC spectrum the width of the envelope over the vibrational fine structure is about 100 meV and therefore much broader than that of the experimental spectrum (50 meV) and (ii) there are also no sudden intensity-changes in the calculated spectrum as observed in the experimental spectrum. Possible reasons for the deviations between experiment and theory could lie on the experimental or theoretical side. As mentioned in Section 1, resonant anion excited states could manipulate the anion-to-neutral FC factors. The absorption

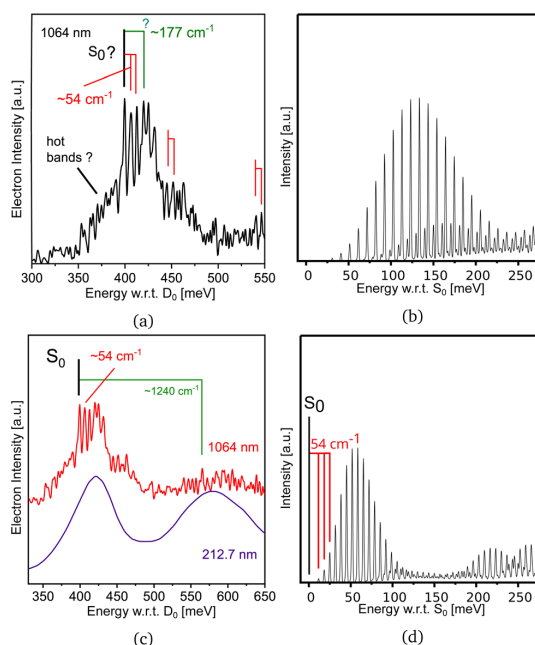


Fig. 12 p3P: experimental and calculated spectra of the transition from D_0 to S_0 . (a) Experimental spectrum recorded with PD wavelength 1064 nm. The vertical black line indicates the expected position of the D_0 - S_0 origin position as derived from the difference between our D_0 - S_1 origin and the S_0 - S_1 origin position by Murakami *et al.*⁷ (b) Simulated FC spectrum (c) PD-PE spectra recorded with 1064 and for comparison with 212.7 nm. (d) Simulated FC-spectrum with the torsional potential scaled to the experimental value of 54 cm^{-1} . For further discussion, see text.

spectrum of p3P anions published by Shida⁵² shows only very small to vanishing absorption at 1064 nm, the wavelength used

for photodetachment, which makes a strong influence on the vibronic intensities very improbable. This indicates that the theoretical treatment of the low-frequency torsional modes is inaccurate. To explain the deviation of the calculated FC spectra from the experiment, it should be noted that the harmonic oscillator model used to determine the FC spectra is not well suited for describing large-amplitude motions. Due to the large displacements in the torsional coordinates by about 30° , a long vibrational progression can be expected. Because the low-frequency torsion modes at 83 cm^{-1} (observed at 54 cm^{-1}) and 217 cm^{-1} (observed at 177 cm^{-1}), exhibit too high wavenumbers, the envelopes of the torsional potentials are too wide. If the potential of the torsional mode in S_1 is adjusted by using the experimental vibrational frequency of 54 cm^{-1} in the FC calculation (Fig. 12d), the vibrational structure is not only compressed because of the lower vibrational frequency, but also the FC factors for the quantum numbers change.

Since the equilibrium structures of the D_0 anionic ground state and the T_1 state of the neutral molecule both are quasi planar, the calculated FC spectra are supposed to be more reliable. Indeed, Fig. 13 shows that the agreement between experiment (left side) and theory (right side) is quite good. The peak observed with a spacing of 225 cm^{-1} above the origin (see green line) can be identified with the calculated inter-ring vibration of 231 cm^{-1} . The next vibration identified in the experimental spectrum lies at 742 cm^{-1} and corresponds nicely to the calculated collective phenyl-ring breathing mode with an energy of 767 cm^{-1} . The first two main peaks in the experimental spectrum have each two satellite peaks somewhat shifted to higher energies (red and orange lines), one directly in the shoulder of the first highest peak (peak position: 24 cm^{-1}) and another one at a distance of about 89 cm^{-1} . Because the first main peak and its neighbouring satellite peak overlap, it is difficult to derive the exact underlying energetic spacing between the molecular vibronic states. Our FC simulations reveal that the three-fold structure might be attributed to a symmetric torsional mode with a calculated frequency of 41 cm^{-1} . To explain this discrepancy of computation and experiment, especially considering the third peak (89 cm^{-1}) we carried out a qualitative simulation (Fig. S12 in the ESI[†]) of a potential peak attraction effect caused by overlapping peaks.

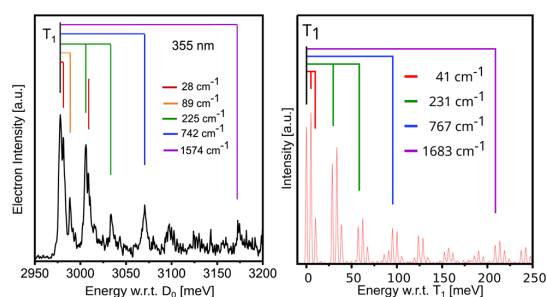


Fig. 13 Experimental (left side) and calculated (right side) spectra of the transition to the T_1 state of p3P.

This resulted in a correction for the experimental 28 cm^{-1} value to 32 cm^{-1} . Obviously, even this fitted frequency of 89 cm^{-1} does not fit into a regular progression. As we did not find another FC active mode in our computations, tentatively matching this frequency, its origin remains inconclusive. However, it is reasonable to assume that anharmonicities are responsible for the observed peak structures.

In Fig. 14 the expanded experimental PD-PES recorded with 212.7 nm and the corresponding calculated FC spectra of the spectral range covering the transition to T_2 up to the transition to S_1 is displayed. The experimental spectrum in Fig. 14 is a good example for the effect that the resolution of ToF PES strongly depends on the electron excess energy: the closer the spectrum comes to the low-energy electron range (from left to right) the better the energy resolution becomes. Wigner's threshold law for photodetachment²³ predicts an intensity loss for structures close to the detachment threshold. This holds especially true for the excitation to the S_1 state.

The experimental transition spectrum to T_2 essentially consists of two equally strong broad peaks with a spacing of 960 cm^{-1} followed by two bunches of threefold structures. This peak pattern is unexpected. As the first two peaks are intense, one would expect a third member of the vibrational progression to follow. Instead, an irregular pattern is observed. In our calculations, we find an intersection between the T_2 and T_3 potential energy surfaces in this energy range which might explain these irregularities. As a consequence, we are not able to locate the minimum geometry of the T_3 state which is why no FC spectrum is plotted for this state in Fig. 14 (right). We first concentrate on the two strong broad peaks in the experimental spectrum. They are both asymmetric and the second peak has clearly a second close side-peak. This indicates that also the first peak has a weak underlying satellite peak shifted slightly to the blue. On the left side, the calculated FC spectrum shows a comb-like structure with a small energy spacing of 83 cm^{-1} corresponding to a torsional mode. Note, however, that the resolution of the computed spectrum depends on the width of the Gaussian damping function (here 5 cm^{-1} full width a half maximum) used in the Fourier transformation of the

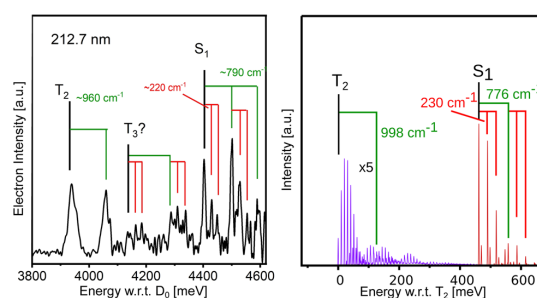


Fig. 14 Experimental (left side) and calculated (right side) spectra of the transitions to the T_2 and the S_1 states in p3P. Note that the T_3 state was omitted from the calculated spectrum because its origin position was not found. For further explanations see text.

correlation function. The small satellite peaks presumably arise from the excitation of a concertina-like stretching motion of the molecule along the C_2 symmetry axis with a frequency of 222 cm^{-1} in the computed spectrum (Fig. 14 right). The comb of peaks starting 998 cm^{-1} above the 0–0 transition in the theoretical spectrum possibly corresponds to the second peak in the experimental spectrum, but has a much too low intensity in comparison to the spectrum on the left side. Obviously, the harmonic force calculations do not properly describe the properties of the T_2 state in this energy range due to the conical intersection.

The agreement between the experimental and the theoretical S_1 spectra is very good. The first three peaks in the experimental S_1 spectrum (spacing about 220 cm^{-1}) nicely correspond to the first three intense peaks in the theoretical spectrum (spacing 230 cm^{-1}). Note that the anion ground state and the S_1 state are nearly planar. The repetition of this threefold structure shifted by 790 cm^{-1} to the blue (experimental value) is somewhat too weak in intensity in the theoretical spectrum (found at 776 cm^{-1} above the origin). It corresponds to an inter-ring C–C stretch vibration, which appears here as a result of the quinoidal reconstruction of the nuclear frame in the S_1 state. Interestingly, in the optical $S_0 \rightarrow S_1$ spectrum of Murakami *et al.*⁷ the symmetric (62 cm^{-1}) and asymmetric (89 cm^{-1}) inter-ring torsion modes have been observed with long progressions. Both vibrations are not observed by us in the $D_0 \rightarrow S_1$ spectrum of Fig. 14 because the displacements in the torsional coordinates between the anion and the S_1 states are very small and the excitation of these modes hence does not gain much intensity.

The tentative assignment of the T_3 transitions needs a detailed explanation. Since the energy spacing between the two three-fold comb-like structures roughly fits in position and spacing in a series with the two strong peaks of T_2 , one could argue that they correspond to T_2 and continue its peak progression. This explanation seems, however, implausible since the structures in T_2 and in the tentatively assigned T_3 are too different for this. Interestingly, the small spacings of their close-lying sub-structures are similar to the distances of the peaks corresponding to the low-energy vibration in S_1 , only the intensities of the substructures are different. Note that also their spacings are such, that they seem to be part of a progression of the S_1 state. However, they cannot correspond to the transition to S_1 , since the energy of the $S_0 \rightarrow S_1$ transition is accurately known from a gas phase experiment⁷ and even then the FC-intensities would not fit. Even assuming a large inaccuracy in the determination of the S_0 origin of 50 meV or more would not bring the S_1 origin in the neighbourhood of the peaks attributed by us to T_3 . Also hot bands can be excluded as explanation because (i) the other hot band transition we observe are usually weak in intensity and (ii) they should lie in the direct vicinity of the origin peak of S_1 and not hundreds of meV away. In conclusion we tentatively attribute them – on the basis of spectroscopic reasons alone – to the transitions to T_3 . Indeed, according to theory (see Table 2), T_3 is expected to lie below the S_1 origin and even the T_4 transition is close-by.

The Dyson intensity for the photodetachment to T_3 is considerably weaker (0.09) than for the transition to T_2 (0.21), which is in qualitative agreement with the small intensity of the observed complex structure above T_2 (see Fig. 14). The PD–PE spectrum of the T_4 state (Dyson norm 0.16) is presumably buried beneath the S_1 bands because the two states are near degenerate according to the calculations. Unfortunately, the identity of these tridental structures between T_2 and S_1 cannot be unambiguously clarified with the help of FC calculations, because T_3 undergoes a conical intersection with T_2 upon geometry optimisation and the true minimum of its potential energy surface could not be located. The strong vibronic coupling in the neighbourhood of the intersection impedes a meaningful computation of spectral envelopes in a static approach and would require a quantum dynamical treatment which is, however, far beyond the scope of this work.

3.3.2 para-Quaterphenyl (p4P). In the PD–PE overview spectrum of p4P in Fig. 2, there is at first glance considerably less peak activity in the energy range between T_1 and S_1 than in the spectrum of p3P. In the high-energetic range again the transitions to T_1 (neutral energy: $2478 \pm 50\text{ meV}$), T_2 (neutral energy: $3260 \pm 50\text{ meV}$) and S_1 (neutral energy: $3872 \pm 50\text{ meV}$) are observed. Only a small peak in front of S_1 might be due to the transition to T_3 , an assignment which, however, needs further support by computational data.

In Table 3 the theoretical results are presented and compared to the experimental data. The calculated electron affinity is somewhat too high (703 meV, compared to $\sim 620\text{ meV}$ in the experiment), which is unexpected from a theoretical point of view, but has been observed for oligothiophenes⁵³ and other compounds²⁰ as well. The Dyson norm for the photodetachment of an electron from the singly occupied anion MO (LUMO in the nomenclature used here) has a value close to 1. The ratio of the Dyson intensities for the transitions to T_1 and to T_2 are about 2 : 1, in nice agreement with the spectrum recorded with 266 nm (not shown as a complete spectrum here). The transition to T_3 has a very low Dyson intensity of 0.12 (for comparison: the neighbouring transition to S_1 has a Dyson intensity of 0.44), which would qualitatively agree with the very small intensity of these peaks in the overview spectrum. The 0–0 transition energy of 3.55 eV, determined in the DFT/MRCI calculations, supports the tentative assignment of T_3 closely below S_1 .

In p4P, the singlet-coupled HOMO–LUMO excitation forms the first excited singlet state. The computed oscillator strength f of its optical $S_0 \rightarrow S_1$ transition is 1.67 and thus has considerably increased in comparison to p3P ($f = 1.15$). The nodal structure of the MOs involved in the $S_0 \rightarrow S_1$ transition is similar in both molecules (cp. Fig. 5 and 8). HOMO and LUMO both exhibit b symmetry with regard to the $C_2(z)$ symmetry axis. Hence, the transition moment for the $S_0 \rightarrow S_1$ transition lies, as in p3P, parallel to the long axis. As in p3P, the oscillator strengths for the transitions to the multiconfigurational S_2 and S_3 states are close to zero.

On the left side of Fig. 15, the PD–PE spectra of the transition to S_0 , recorded with the wavelengths 1064, 355 and

Table 3 Theoretical and experimental results for p4P: coefficients (absolute values) of leading MO configurations, calculated vertical transition energies ΔE_{vert} at the S_0 geometry, calculated adiabatic transition energies ΔE_{adiab} , and ZPVE corrected transition energies ΔE_{0-0} with respect to S_0 , experimental energies ΔE_{exp} (this work only), oscillator strengths f , calculated vertical electron detachment energies ΔE_{det} and Dyson intensities σ at the D_0 geometry. All energies in eV. In the first row of the table body, the experimental and the ZPVE corrected theoretical EAs are displayed. Experimentally not observed transitions are labelled as 'n.o.'

State	Configurations	ΔE_{vert}	ΔE_{adiab}	ΔE_{0-0}	ΔE_{exp}	f	ΔE_{det}^b	ΔE_{det}^c	σ	
S_0	1^1A	0.96 $H^2(L)^0$	—	EA: 0.70 ^b	EA: 0.620	—	0.82	0.82	0.93	
S_1	1^1B_1	0.94 $(H)^1(L)^1$	4.31	3.75	3.65	3.872	1.67	4.25	4.44	
S_2	1^1B_2	0.66 $(H)^1(L+2)^1$ 0.41 $(H-2)^1(L)^1$ 0.35 $(H-4)^1(L)^1$	4.46	4.14	3.98	n.o.	0.00	5.06	4.79	
S_3	1^1B_3	0.52 $(H)^1(L+3)^1$ 0.42 $(H-3)^1(L)^1$ 0.38 $(H-5)^1(L)^1$ 0.43 $(H)^1(L+1)^1$	4.49	^a	^a	n.o.	0.00	5.31	5.00	0.16
S_4	2^1A	0.66 $(H-1)^1(L)^1$ 0.89 $(H)^1(L)^1$ 0.43 $(H)^1(L+1)^1$	4.99	4.69	4.56	n.o.	0.00	5.15	5.17	0.23
T_1	1^3B_1	0.64 $(H-1)^1(L)^1$ 0.60 $(H)^1(L+1)^1$	3.20	2.63	2.51	2.478	—	3.24	3.31	0.41
T_2	1^3A	0.64 $(H-1)^1(L)^1$ 0.60 $(H)^1(L+1)^1$	3.54	3.24	3.13	3.260	—	4.03	3.95	0.21
T_3	2^3B_1	0.51 $(H-6)^1(L)^1$ 0.48 $(H-1)^1(L+1)^1$ 0.44 $(H)^1(L+6)^1$	3.94	3.86	3.55	3.771 (?)	—	4.74	4.62	0.12
T_4	1^3B_2	0.68 $(H)^1(L+2)^1$ 0.40 $(H-2)^1(L)^1$ 0.32 $(H-4)^1(L)^1$	4.19	3.94	3.79	n.o.	—	4.65	4.71	0.13

^a No minimum was found in the calculations. At the converged structure still an imaginary frequency is present. ^b Computed at the (TD-)PBE0/TZVP level of theory. ^c DFT/MRCI energies at the D_0 geometry, shifted by the difference between the PBE0/TZVP and DFT/MRCI computed vertical detachment energy of the S_0 state.

266 nm, are presented. The fact that the spectrum recorded with 266 nm looks very similar in vibrational intensity to the spectrum recorded with 355 nm proves that the wavelength 1064 nm performs a resonant excitation of an anion-excited state which then decays *via* autodetachment. The p4P anion absorption spectrum of Shida in tetrahydrofuran⁵² shows strong absorptions at 1220 nm and 1115 nm. Our detachment wavelength of 1064 nm then would be overlapping with Shida's second broad peak at 1115 nm. The 355 nm spectrum, displayed in Fig. 15 (left side), shows a strong first peak followed by two or more peaks with spacings of about 1475 cm^{-1} . The corresponding calculated FC spectrum is displayed in Fig. 15 (right side). It shows a dense peak structure with very small spacings of 88 cm^{-1} (inter-ring twist mode) which has a nearly Gaussian envelope. The width at half height of the envelope is

about 100 meV and only slightly broader than the first peak in the experimental spectrum. A second comb of low-energetic vibrations shifted by about 1535 cm^{-1} follows. These are combination bands with a high-energetic vibration (experiment: 1475 cm^{-1} , collective inter-ring stretch mode). The broader envelopes of the two structures in the FC spectrum in comparison to the experiment are—as in p3P—presumably also due to the overestimation of the force constant of the twist potential.

In Fig. 16, two experimental spectra and one calculated FC spectrum of the transition to T_1 are displayed. If the theoretical spectrum would be broadened the two spectra would agree well in shape and relative energetic positions and only slightly differ in intensities. This is an example showing that typically the spectra recorded with high excitation energies are not or not much influenced by anion-excited states. The observed mode with a frequency of 170 cm^{-1} can be assigned to a global stretching mode (calculated frequency: 174 cm^{-1}). The next observed mode with 766 cm^{-1} can be assigned to a collective breathing mode with a calculated frequency of 787 cm^{-1} . The most displaced mode, an antisymmetric torsional mode with a frequency of 30 cm^{-1} , which appears as a progression with three strong and two smaller peaks in the calculated spectrum, is not identified in the experimental spectrum due to lack in energy resolution.

In Fig. 17, the experimental and theoretical FC spectra of the transition to the S_1 state are juxtaposed. The first observed mode has an energy of 160 cm^{-1} in the experimental spectrum (left side) and can be identified with the calculated symmetric collective stretching mode along the molecular axis (calculated frequency: 175 cm^{-1}). The weakly observed mode with a

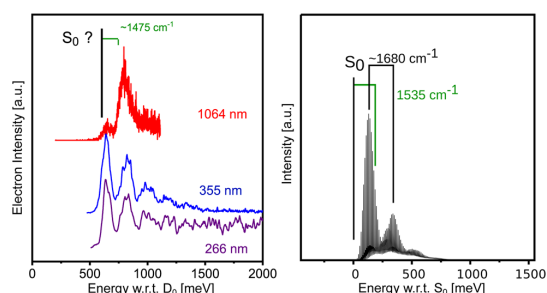


Fig. 15 p4P: experimental (left side, detachment wavelengths 1064 nm, 355 nm and 266 nm) and calculated (right side) spectra of the transition to the S_0 state.

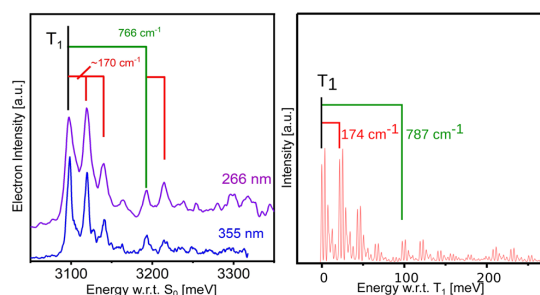


Fig. 16 Experimental spectra recorded with 355 nm and 266 nm (left side) and calculated (right side) FC spectra of the transition to the T_1 state in p4P. For discussion see text.

frequency of 766 cm^{-1} presumably corresponds to the mode with the calculated frequency of 795 cm^{-1} , which is a collective inter-ring breathing mode, at which especially the two inner phenyl rings participate. The intensity of the latter transition is presumably only so extremely small, because it may be affected by Wigner's threshold law.²³ This would mean that the calculated intensity of this transition is somewhat too small. The low-energetic torsion mode with a calculated energy of 78 cm^{-1} appears in the calculated spectrum as a very weak progression of 4 peaks. The transitions of this mode cannot be identified and assigned in the experimental spectrum. They presumably are buried in the background socket behind and between the strong transitions. Overall, for the transition to the S_1 the agreement between experiment and theory can be considered very good.

3.3.3 para-Quinquephenyl (p5P). Except for the very broad transition to the S_0 , the appearance of the spectrum of p5P (Fig. 2) is very similar to that of p4P. The right side of the spectrum is rather simple to explain. The transitions to T_1 (neutral energy: $2340 \pm 50\text{ meV}$), T_2 (neutral energy: $3038 \pm 50\text{ meV}$) and S_1 (neutral energy: $3653 \pm 50\text{ meV}$) are observed. A very small additional structure in front of S_1 is found which could be tentatively assigned to T_3 because its energetic position is in agreement with the calculations. The ratio of the Dyson intensities of the transitions to T_3 and to S_1 are

$0.13/0.44 = 0.29$. This small value can explain why the intensity of the observed T_3 structure is so small (Table 4).

In Fig. 18 we present expanded experimental PD–PE spectra (detachment wavelengths 1064 nm (red), 532 nm (green) and 266 nm (violet)) of p5P. The vibrational peak patterns are very different. The strong rise of the second peak in the PD–PE spectrum recorded with 1064 nm and the many intense peaks in the spectrum recorded with 532 nm are obviously—similar as in p4P—due to resonant photoabsorption channels for the detachment wavelengths 1064 nm and 532 nm in the anionic species of p5P. Unfortunately, no anion absorption spectrum exists for p5P. In the following, we tentatively take the first strong transition in the 266 nm spectrum as the S_0 origin (EA = $805 \pm 50\text{ meV}$).

The calculated transition spectrum to S_0 (Fig. 18) shows very dense combs of peaks with a spacing which corresponds to a symmetric twist mode (calculated energy: 90 cm^{-1}). The envelopes of these twist mode peaks reproduce roughly the structures of the first three peaks in the experimental spectrum recorded with 266 nm. As in p3P and p4P, also here the envelope in the theoretical spectrum is somewhat broader than the peak width in the 266 nm spectrum. The high-energetic spacing between the two comb of peaks in the experimental spectrum is about 1420 cm^{-1} which best agrees with a collective stretching mode (calculated energy: 1338 cm^{-1}).

In Fig. 19, the experimental spectrum of the transition to T_1 of p5P, recorded with 355 nm (left side), and the calculated FC spectrum (right side) are displayed. Note that the origin transition seems to be not the highest peak. Besides a comb of small peaks with a spacing of 40 cm^{-1} in the first part of the experimental spectrum at the blue side, some peaks with spacings of 85 cm^{-1} are observed. In addition, a vibration with an energy of about 742 cm^{-1} is present. A look at the FC simulation shows that a low-frequency mode of 55 cm^{-1} has the highest displacement and forms a comb of nine vibronic close-lying transitions. It should correspond to the observed peak spacing of about 40 cm^{-1} at the rise of the hump. If one takes the envelopes of the peaks in the calculated spectrum, it roughly fits the experimental features. The measured peak spacings of 85 cm^{-1} appearing on the blue side of the hump in the experimental spectrum remain unclear. The observed mode at about 742 cm^{-1} (measured between two well identified combination band peaks) is in an astonishing agreement with the calculated FC-active mode at 741 cm^{-1} . In conclusion, the calculated FC spectrum reasonably well agrees with the experimental spectrum.

One remaining question is, however, why in p5P—in contrast to the corresponding p3P and p4P spectra—the transition to T_1 is relatively broad. A resonant excitation to an anion-excited state with 355 nm seems not to apply here since the spectrum recorded with 266 nm (not shown here) is also broad. In Section 3.2 we had noticed for p5P that the inner three and the outer two torsional angles of equilibrium structures can differ considerably (Fig. 9). Indeed, in the T_1 state, the quinoidal structure appears to be confined to the three innermost phenyl rings, resulting in an almost co-planar orientation of the

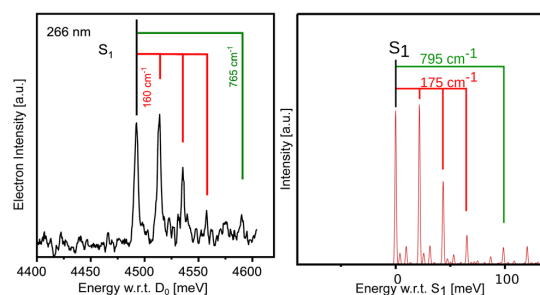


Fig. 17 p4P: experimental (left side) and calculated (right side) spectrum of the transition to S_1 .

Table 4 Theoretical and experimental results for p5P: coefficients (absolute values) of leading MO configurations, calculated vertical transition energies ΔE_{vert} at the S_0 geometry, calculated adiabatic transition energies ΔE_{adiab} , and ZPVE corrected transition energies ΔE_{0-0} with respect to S_0 , experimental energies ΔE_{exp} (this work only), oscillator strengths f , calculated vertical electron detachment energies ΔE_{det} and Dyson intensities σ at the D_0 geometry. All energies in eV. In the first row of the table body, the experimental and the ZPVE corrected theoretical EAs are displayed

State	Configurations	ΔE_{vert}	ΔE_{adiab}	ΔE_{0-0}	ΔE_{exp}	f	ΔE_{det}^a	ΔE_{det}^b	σ	
S_0	1^1A_g	0.95 GS								
S_1	1^1A_u	0.92 (H) ¹ (L) ¹	4.13	3.59	3.49	2.17	4.26	4.41	0.44	
T_1	1^3A_u	0.86 (H) ¹ (L) ¹	3.10	2.56	2.40	2.38	—	3.37	0.39	
T_2	1^3A_g	0.63 (H-1) ¹ (L) ¹	3.33	3.02	2.94	3.07	—	3.97	0.20	
T_3	2^3A_u	0.60 (H) ¹ (L+1) ¹	3.70	3.58	3.41	3.60 (?)	—	4.57	4.45	0.13
		0.51 (H-2) ¹ (L) ¹								
		0.50 (H-1) ¹ (L+1) ¹								
		0.46 (H) ¹ (L+5) ¹								

^a Computed at the (TD-)PBE0/TZVP level of theory. ^b DFT/MRCI energies at the D_0 geometry, shifted by the difference between the PBE0/TZVP and DFT/MRCI computed vertical detachment energy of the S_0 state.

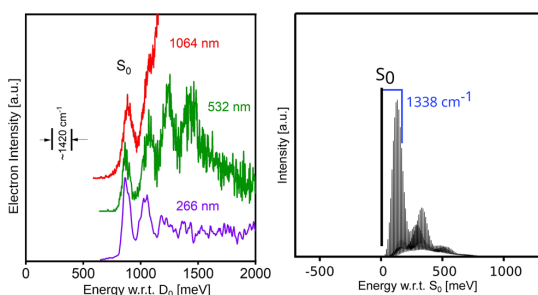


Fig. 18 p5P: experimental (left side) and calculated (right side) spectra of the transition to S_0 . For discussion of the different intensities of the three experimental spectra, see text.

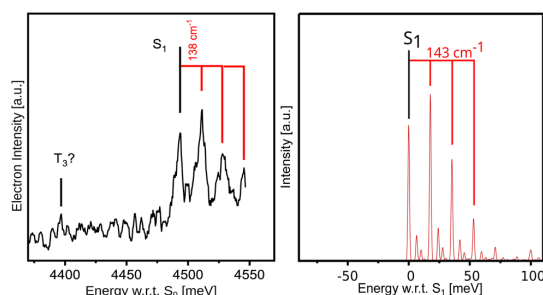


Fig. 20 p5P: experimental (left side) and calculated (right side) spectrum of the transition to S_1 . For assignments see text.

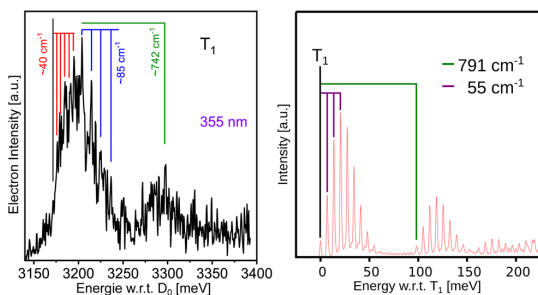


Fig. 19 p5P: experimental (left side) and calculated (right side) spectrum of the transition to T_1 . For explanations see text.

rings (twist angles around 7°), whereas the outer two twist angles are considerably larger (about 24°). Interestingly, in the equilibrium geometry of the D_0 anion ground state the outer twist angles are almost the same as in T_1 (about 22°). However, the two inner twist angles in the anion ground state (about 17°) are much larger than in T_1 . It is therefore not unlikely that, in addition to global stretch modes, also torsional modes are excited, as observed in the photodetachment spectrum of the T_1 state in p5P.

In the S_1 state, the geometry difference with respect to the D_0 structure are less pronounced than in the T_1 state. In the sharp PD-PE spectrum of S_1 (Fig. 20) four quanta of a progression of a vibration with an energy of about 138 cm^{-1} are observed. Since the S_1 state lies very close to the detachment energy of the laser wavelength 266 nm, the intensities of the latter peaks may be affected by Wigner's threshold law²³ and may be smaller than given by the FC factors. The observed mode with an energy of 138 cm^{-1} agrees well with a global stretch mode calculated to have an energy of 143 cm^{-1} . Also the agreement between the intensities in the experimental and the calculated spectrum is very good.

4 Summary and conclusions

In this work, it was possible to record and assign PD-PE spectra of p3P, p4P and p5P. The experimental PD-PE spectra are partly vibrationally resolved and provide—in combination with calculated FC spectra—valuable information on the geometrical structures of the investigated ppPs in their lowest electronic states. No indications for spectral differences between the different possible rotamers in the ppPs have been found in the experimental spectra. The EA values, the oscillator strengths and the energetic positions of the electronic states follow the expectations for an increase in the π -conjugation

length. For most of the electronic states, the calculated energies and structures are qualitatively confirmed by the experimental results, thus strengthening the credibility of these theoretical data, which cannot be directly derived from the experimental data. For example, the calculations provide an understanding why in most of the electronic states bond length changes as well as twist angle changes occur. Surprisingly, for some electronic states in p4P and p5P these displacements are localised on the inner and for others on the outer parts of the molecules. Dyson norms have been evaluated at the DFT/MRCI level of theory to estimate the individual photodetachment probabilities, which are especially interesting for the assignments of the structures attributed to the T_2 states. For high kinetic energies of the photoelectron, the ratios of the Dyson norms compare well with measured photodetachment intensities, but the agreement is less satisfactory for slow photoelectrons due to Wigner's threshold law for photodetachment.²³ To include the latter effect in the model, the overlap between the wavefunction of the outgoing photoelectron and the ionisation continuum would have to be taken into account, which is, however, beyond the scope of this work.

The calculations show that the character of the optical $S_0 \rightarrow S_1$ transition is the same in all molecules: the electric dipole transition moment is parallel to the long molecular axis. The calculated oscillator strengths increase almost linearly with increasing molecular length: p3P: $f = 1.15$, p4P: $f = 1.67$ and p5P: $f = 2.17$ but are somewhat smaller than the values calculated from experimental data (p3P: $f_{\text{exp}} = 2.060$; p4P: $f_{\text{exp}} = 2.360$; p5P: $f_{\text{exp}} = 2.600$).¹¹ Interestingly, a saturation of f with the molecular length does not occur. The MOs involved in the $S_0 \rightarrow S_1$ transition are similar in shape in all investigated ppPs (compare Fig. 5, 8 and 11): the HOMO exhibits along the long axis $2n - 1$ nodal planes (aligned perpendicular to the long molecular axis), $n - 1$ of them cutting the inter-ring C–C bonds (n is here the number of phenyl rings in the molecule). The LUMO has exactly one additional node plane, thus shifting the pattern of double and single bonds by one unit along the C_2 symmetry axis. Both HOMO and LUMO orbitals have in each benzene unit essentially the same density and the same sign concerning the plane formed by the long molecular axis and the axis perpendicular to the benzene ring. This pattern complies with the $\Delta n = \pm 1$ preferences for electric dipole transitions in the quasi-one-dimensional particle-in-the-box model and explains the very high oscillator strengths. As our calculations show and the experiment tentatively confirms, in all investigated ppP molecules definitively two or even possibly three triplet states lie below S_1 . Typically, in a molecule with such an electronic state energy scheme, one would expect high rates for intersystem crossing (ISC) transitions from the S_1 state to the triplet manifold. However, due to the absence of heteroatoms in the molecules, spin–orbit coupling between the excited states is obviously so small that ISC cannot compete against the rapid radiative deactivation on the nanosecond time scale. Our theoretical analysis thus supports the explanation given by Godard and de Witte³ and by Nijegorodov *et al.*¹¹ that the S_1 lifetimes in ppPs are primarily determined by the high oscillator strengths of the $S_1 \rightarrow S_0$ transitions.

In a former paper, we investigated the size of the singlet–triplet splittings in azulene and found that the energy separation between singlet and triplet states of the same spatial MO configuration strongly depends on the overlap between the electron densities in the involved semi-occupied MOs.¹⁹ In the investigated ppPs, S_1 and T_1 both originate from a HOMO–LUMO transition. Since the oscillator strengths of their S_1 – S_0 transitions are very high—which is only possible if the HOMO–LUMO orbital densities strongly overlap¹⁹—their S_1 – T_1 energy gap should be large. In addition, it is expected that the gap decreases in longer molecular chains where the two unpaired electrons are more and more efficiently able to avoid each other. Indeed, the experimentally observed S_1 – T_1 splitting in the ppPs is large and – interestingly – decreases very slowly in this molecular series (1.43 eV (p3P) over 1.39 eV (p4P) to 1.31 eV (p5P)). The quantum chemical calculations predict much faster decreases of the 0–0 energy splittings (1.31 eV (p3P) over 1.14 eV (p4P) to 1.09 eV (p5P)). A similar trend results if the vertical S_1 – T_1 DFT/MRCI energy differences at the respective ground state geometries are compared. Hence, a strong impact of the molecular geometry on the S_1 – T_1 splitting can be excluded. The fact that the S_1 – T_1 energy separation is increasingly underestimated as the chain length grows, rather points towards a more general problem of the applied quantum chemical methods. While the energetic positions of the T_1 0–0 transitions match the experimental values almost perfectly, the 0–0 energies of the S_1 states appear to be underestimated by about 0.1–0.2 eV. The number of samples (3 in this case) is, however, too small for a valid analysis. Forthcoming studies investigating the performance of the DFT/MRCI R2022 Hamiltonian³⁸ on excitation energies of other molecules with extended π -systems will have to prove whether the observed deviation is systematic or coincidental.

In this work, we could show that the twist angles between the phenyl moieties and the bond lengths of the inter-ring C–C bonds are correlated. While the anion ground state, as well as S_1 and T_1 of the neutral molecule are practically planar in p3P, the quinoidal structure in the S_1 and T_1 states of p5P is essentially confined to the innermost three phenyl rings. The twist angles between the terminal rings are considerably larger than those of the central rings in the S_1 and T_1 states of this compound. We interpret these findings in terms of competing forces: while in general the H–H repulsion between neighbouring phenyl units stays the same, the effect of an electron in an orbital with strong bonding contributions in the inter-ring C–C bonds (here LUMO) washes out, because in a large-sized molecule the electron density is distributed over more atoms and bonds, thus less affecting individual bonds.

If one lists the EA values of the ppPs, still no saturation effect with regard to the number of phenyl rings (n) is found: EA(p3P) = 380 ± 50 meV, EA(p4P) = 620 ± 50 meV and EA(p5P) = 805 ± 50 meV. Obviously, the increment, which has to be added to the EA if an additional phenyl ring is attached, decreases but the EA would still considerably increase for longer ppPs. Remembering that the ppP anions are nearly planar and that the neutral ppP molecules are twisted in the S_0 ground state,

such a high EA for long ppPs could provide an alternative explanation for the interesting experimental findings of Yuan *et al.*⁵⁴ By AFM and STM methods, these authors observed twisted (benzoid) and planar (quinoid) structures in long ppPs on metal surfaces and proposed a proton tunneling mechanism for the observed benzoid-to-quinoid transitions. Having in mind the high EAs of longer ppP chains or segments, as proposed in our work, an alternative explanation suggests itself, namely, the involvement of a “surface-to-molecule” charge transfer (CT) state. In such a case, the charge separation takes place only over a very small distance d (≈ 3.2 Å) so that the work function of the metal has to be reduced by the Coulomb integral from infinity to d ,⁵⁵ totalling in a very low or even negative CT state energy with respect to the benzoid neutral ground state.

Conflicts of interest

There are no conflicts to declare.

Acknowledgements

The authors gratefully acknowledge financial support by the Deutsche Forschungsgemeinschaft (DFG, German Research Foundation) through MA 1051/20-1 and 396890929/GRK 2482.

References

- 1 K. Kato, *Jpn. J. Appl. Phys.*, 1972, **11**, 912–913.
- 2 G. A. Abakumov, V. V. Padeev, R. V. Khokhlov and A. P. Simonov, *Spectrosc. Lett.*, 1975, **8**, 651–667.
- 3 B. Godard and O. de Witte, *Opt. Commun.*, 1976, **19**, 325–328.
- 4 H. Bücher and W. Chow, *Appl. Phys.*, 1977, **13**, 267–269.
- 5 D. J. Schneider, D. A. Landis, P. A. Fleitz, J. M. Kauffman and R. N. Steppel, *Laser Chem.*, 1991, **11**, 49–62.
- 6 C. J. Seliskar, D. A. Landis, J. M. Kauffman, R. N. Aziz, M. A. Steppel, C. J. Kelly, Y. Qin and A. Chiorghis, *Laser Chem.*, 1993, **13**, 9–28.
- 7 J. Murakami, M. Okuyama and K. Ito, *Bull. Chem. Soc. Jpn.*, 1982, **55**, 3422–3423.
- 8 I. Baraldi and G. Ponterini, *THEOCHEM*, 1985, **122**, 287–298.
- 9 G. Heimel, M. Daghofer, J. Gierschner, E. J. W. List, A. C. Grimdale, K. Müllen, D. Beljonne, J.-L. Brédas and E. Zojer, *J. Chem. Phys.*, 2005, **122**, 054501.
- 10 V. Lukeš, A. J. A. Aquino, H. Lischka and H.-F. Kauffmann, *J. Phys. Chem. B*, 2007, **111**, 7954–7962.
- 11 N. Nijegorodov, W. Downey and M. Danilov, *Spectrochim. Acta, Part A*, 2000, **56**, 783–793.
- 12 N. A. Borisevich, S. M. Kazakov, É. É. Kolesnik, A. V. Kukhto, A. I. Mit'kovets, D. V. Murtazaliev and O. V. Khristoforov, *J. Appl. Spectrosc.*, 2001, **68**, 447–454.
- 13 X. Cai, M. Sakamoto, M. Hara, S. Tojo, K. Kawai, M. Endo, M. Fujitsuka and T. Majima, *J. Phys. Chem. A*, 2004, **108**, 9361–9364.
- 14 P. G. Wendthold, J. Hu, R. R. Squires and W. C. Lineberger, *J. Am. Chem. Soc.*, 1996, **118**, 475–476.
- 15 T. R. Taylor, R. T. Bise, K. R. Asmis and D. M. Neumark, *Chem. Phys. Lett.*, 1999, **301**, 413–416.
- 16 R. Busani, M. Folkers and O. Cheshnovsky, *Phys. Rev. Lett.*, 1998, **81**, 3836–3839.
- 17 M. Kohno, S. Suzuki, H. Shiromaru and Y. Achiba, *J. Chem. Phys.*, 1999, **110**, 3781–3784.
- 18 J. Schiedt and R. Weinkauff, *Chem. Phys. Lett.*, 1997, **266**, 201–205.
- 19 S. Vosskötter, P. Konieczny, C. M. Marian and R. Weinkauff, *Phys. Chem. Chem. Phys.*, 2015, **17**, 23573–23581.
- 20 J. Meissner, B. Kasper, C. M. Marian and R. Weinkauff, *J. Phys. Chem. A*, 2021, **125**, 8777–8790.
- 21 T. Nakamura, N. Ando, Y. Matsumoto, S. Furuse, M. Mitsui and A. Nakajima, *Chem. Lett.*, 2006, **35**, 888–889.
- 22 G. R. Kinsel and M. V. Johnston, *Int. J. Mass Spectrom. Ion Processes*, 1989, **91**, 157–176.
- 23 E. P. Wigner, *Phys. Rev.*, 1948, 1002–1009.
- 24 J. Schiedt and R. Weinkauff, *J. Chem. Phys.*, 1999, 304–314.
- 25 C. R. Sagan, C. S. Anstöter, M. Thodika, S. Wilson and K. D. Matsika, *J. Phys. Chem. Lett.*, 2022, **13**, 10245–10252.
- 26 A. Jalehdoost and B. von Issendorff, *J. Chem. Phys.*, 2023, **158**, 194302.
- 27 L. G. Christophorou, J. G. Carter and A. A. Christodoulides, *Chem. Phys. Lett.*, 1969, **3**, 237–240.
- 28 E. Luc-Koenig, C. Morillon and J. Vergès, *Phys. Scr.*, 1975, **12**, 199–219.
- 29 D. Hanstorp and M. Gustafsson, *J. Phys. B: At. Mol. Opt. Phys.*, 1992, **25**, 1773–1783.
- 30 R. Peláez, C. Blondel, C. Delsart and C. Drag, *J. Phys. B: At. Mol. Opt. Phys.*, 2009, **42**, 125001.
- 31 M. J. Frisch, G. W. Trucks, H. B. Schlegel, G. E. Scuseria, M. A. Robb, J. R. Cheeseman, G. Scalmani, V. Barone, G. A. Petersson, H. Nakatsuji, X. Li, M. Caricato, A. V. Marenich, J. Bloino, B. G. Janesko, R. Gomperts, B. Mennucci, H. P. Hratchian, J. V. Ortiz, A. F. Izmaylov, J. L. Sonnenberg, D. Williams-Young, F. Ding, F. Lipparini, F. Egidi, J. Goings, B. Peng, A. Petrone, T. Henderson, D. Ranasinghe, V. G. Zakrzewski, J. Gao, N. Rega, G. Zheng, W. Liang, M. Hada, M. Ehara, K. Toyota, R. Fukuda, J. Hasegawa, M. Ishida, T. Nakajima, Y. Honda, O. Kitao, H. Nakai, T. Vreven, K. Throssell, J. A. Montgomery, Jr., J. E. Peralta, F. Ogliaro, M. J. Bearpark, J. J. Heyd, E. N. Brothers, K. N. Kudin, V. N. Staroverov, T. A. Keith, R. Kobayashi, J. Normand, K. Raghavachari, A. P. Rendell, J. C. Burant, S. S. Iyengar, J. Tomasi, M. Cossi, J. M. Millam, M. Klene, C. Adamo, R. Cammi, J. W. Ochterski, R. L. Martin, K. Morokuma, O. Farkas, J. B. Foresman and D. J. Fox, *Gaussian 16, Revision A.03*, Gaussian Inc., Wallingford CT, 2016.
- 32 J. P. Perdew, K. Burke and M. Ernzerhof, *Phys. Rev. Lett.*, 1996, **77**, 3865–3868.
- 33 C. Adamo and V. Barone, *J. Chem. Phys.*, 1999, **110**, 6158–6170.
- 34 E. Brémond, M. Savarese, C. Adamo and D. Jacquemin, *J. Chem. Theory Comput.*, 2018, **14**, 3715–3727.
- 35 A. Schäfer, H. Horn and R. Ahlrichs, *J. Chem. Phys.*, 1992, **97**, 2571–2577.

- 36 S. Grimme and M. Waletzke, *J. Chem. Phys.*, 1999, **111**, 5645–5655.
- 37 C. M. Marian, A. Heil and M. Kleinschmidt, *Wiley Interdiscip. Rev.: Comput. Mol. Sci.*, 2019, **9**, e1394.
- 38 D. Dombrowski, T. Schulz, M. Kleinschmidt and C. M. Marian, *J. Phys. Chem. A*, 2023, **1127**, 2011–2025.
- 39 C. Lee, W. Yang and R. G. Parr, *Phys. Rev. B: Condens. Matter Mater. Phys.*, 1988, **37**, 785–789.
- 40 A. D. Becke, *J. Chem. Phys.*, 1993, **98**, 1372–1377.
- 41 TURBOMOLE V7.5.1 2021, a development of University of Karlsruhe and Forschungszentrum Karlsruhe GmbH, 1989–2007, TURBOMOLE GmbH, since 2007; available from <https://www.turbomole.com>.
- 42 F. Weigend, M. Häser, H. Patzelt and R. Ahlrichs, *Chem. Phys. Lett.*, 1998, **294**, 143–152.
- 43 M. Etinski, J. Tatchen and C. M. Marian, *J. Chem. Phys.*, 2011, **134**, 154105.
- 44 M. Etinski, J. Tatchen and C. M. Marian, *Phys. Chem. Chem. Phys.*, 2014, **16**, 4740–4751.
- 45 M. Spanner, S. Patchkovskii, C. Zhou, S. Matsika, M. Kotur and T. C. Weinacht, *Phys. Rev. A: At., Mol., Opt. Phys.*, 2012, **86**, 053406.
- 46 W. Arbelo-González, R. Crespo-Otero and M. Barbatti, *J. Chem. Theory Comput.*, 2016, **12**, 5037–5049.
- 47 M. L. Vidal, A. I. Krylov and S. Coriani, *Phys. Chem. Chem. Phys.*, 2020, **22**, 2693–2703.
- 48 B. N. C. Tenorio, A. Ponzi, S. Coriani and P. Decleva, *Molecules*, 2022, **27**, 1203.
- 49 E. Morikawa and M. Kotani, *Z. Naturforsch.*, 1980, **35a**, 823–827.
- 50 C. M. Marian and N. Gilka, *J. Chem. Theory Comput.*, 2008, **4**, 1501–1515.
- 51 E. Artacho, M. Rohlfing, M. Côté, P. D. Haynes, R. J. Needs and C. Molteni, *Phys. Rev. Lett.*, 2004, **93**, 116401.
- 52 T. Shida, *Phys. Sci. Data*, 1988, **34**, 1–308.
- 53 R. Weinkauff, L. Lehr, E. W. Schlag, S. Salzmann and C. M. Marian, *Phys. Chem. Chem. Phys.*, 2008, **10**, 393–404.
- 54 B. Yuan, C. Li, Y. Zhao, O. Gröning, X. Zhou, P. Zhang, D. Guan, Y. Li, H. Zheng, C. Liu, Y. Mai, P. Liu, W. Ji, J. Jia and S. Wang, *J. Am. Chem. Soc.*, 2020, **142**, 10034–10041.
- 55 R. Weinkauff and J. Schiedt, *Photochem. Photobiol.*, 1997, **66**, 569–575.

Electronic Supplementary Material (ESI) for PCCP:
**Electron affinities and lowest triplet and singlet state
properties of *para*-oligophenylenes (n=3-5): Theory and
experiment**

Timo Schulz^{‡,a}, Paul Konieczny^{‡,a}, Dennis R. Dombrowski,^b Simon Metz,^a Rainer Weinkauff*,^{b¶}
and Christel M. Marian*^{a¶}

Contents

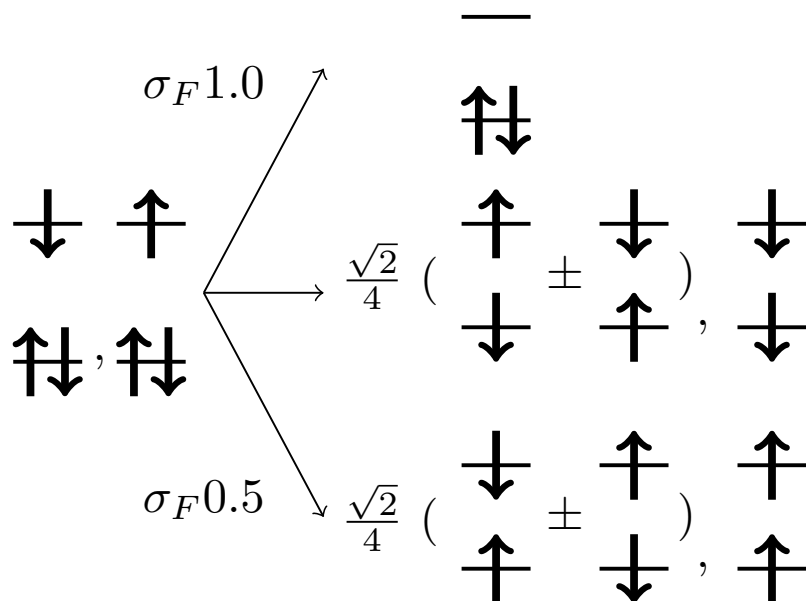
S1	Further Computational Details	S1
S2	Dyson Norm	S2
S3	p3P	S3
S4	p4P	S11
S5	p5P	S14
S6	Dihedral Angles	S16
S7	Geometries	S16
	S7.1 p3P	S17
	S7.2 p4P	S29
	S7.3 p5P	S39

S1 Further Computational Details

- If not noted otherwise, all geometries were optimised on the PBE0/TZVP level of theory.
- The Tamm-Dancoff approximation was used in the optimisation of excited triplet state geometries.
- For all DFT/MRCI calculations the one-particle basis was generated with BHLYP/TZVP and the R2022 Hamiltonian with the standard parameter set was used. For p3P and p-quinquephenyl 6 roots in the totally symmetric and 5 in every other irreducible representation were solved. For p4P 11 roots in the totally symmetric and 10 in every other roots were solved.
- For the first run, a selection threshold of $0.8 E_H$ was used to truncate the CI-expansion.
- For the second run, the selection threshold was increased to $1.0 E_H$.
- The VIBES calculations were done in internal coordinates, 65536 grid points and a time interval of 3000 fs. The temperature was set to 10 K. Before integration, the correlation function was damped with a Gaussian of 100 cm^{-1} full width at half maximum.
- For the VIBES calculations with less damping 1048576 grid points and a time interval of 10000 fs were used. The damping function was reduced to a Gaussian with 5 cm^{-1} full width at half maximum.
- Normal mode vibrations, displayed in Figures S9-S11, S14-S16 and S19-S21 were selected according to the size of the displacements in the Duschinsky transformation.

S2 Dyson Norm

Figure S1: An one-electron detachment might only yield a dyson norm σ_F of 1 if the detachment is from a singly occupied spin orbital. Otherwise the detachment gives a singlet or triplet configuration with a probability of $\frac{1}{2}$, respectively. Note that in the generation of the anion no spin arrangement is preferred and the probability of alpha or beta occupation in the SOMO is exactly one half.



S3 p3P

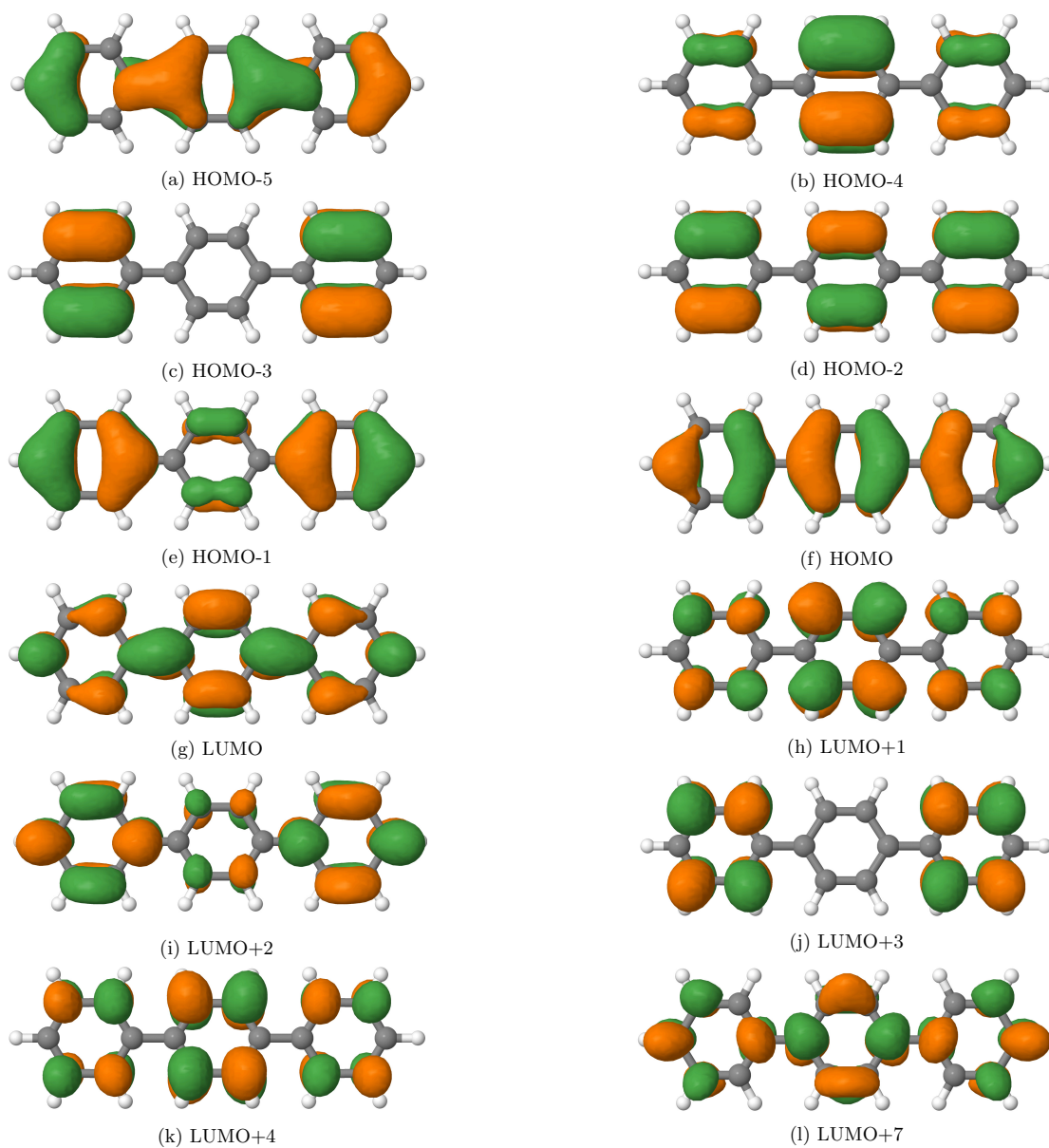


Figure S2: Important molecular orbitals at the anion ground state geometry of p3P.

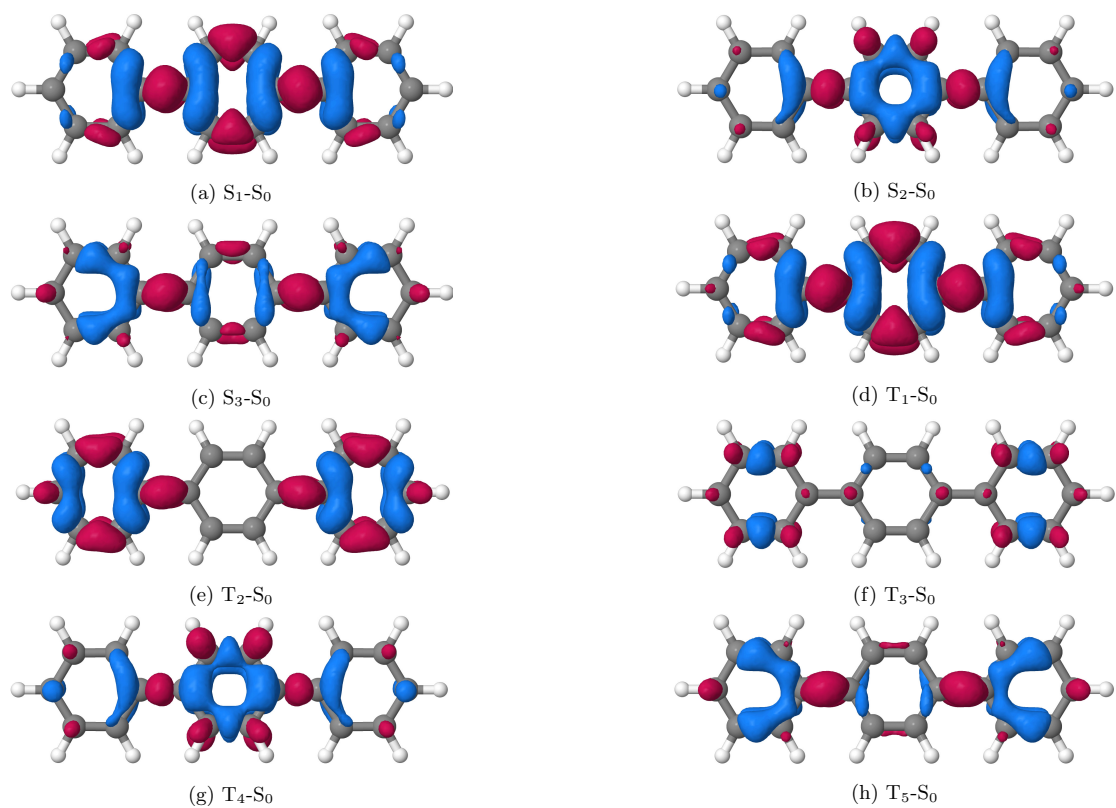


Figure S3: Difference densities (± 0.001) between the excited states and the neutral ground state at the anion ground state geometry of p3P. Blue coloured areas indicate a loss of electron density in the excited state, red coloured areas a gain.

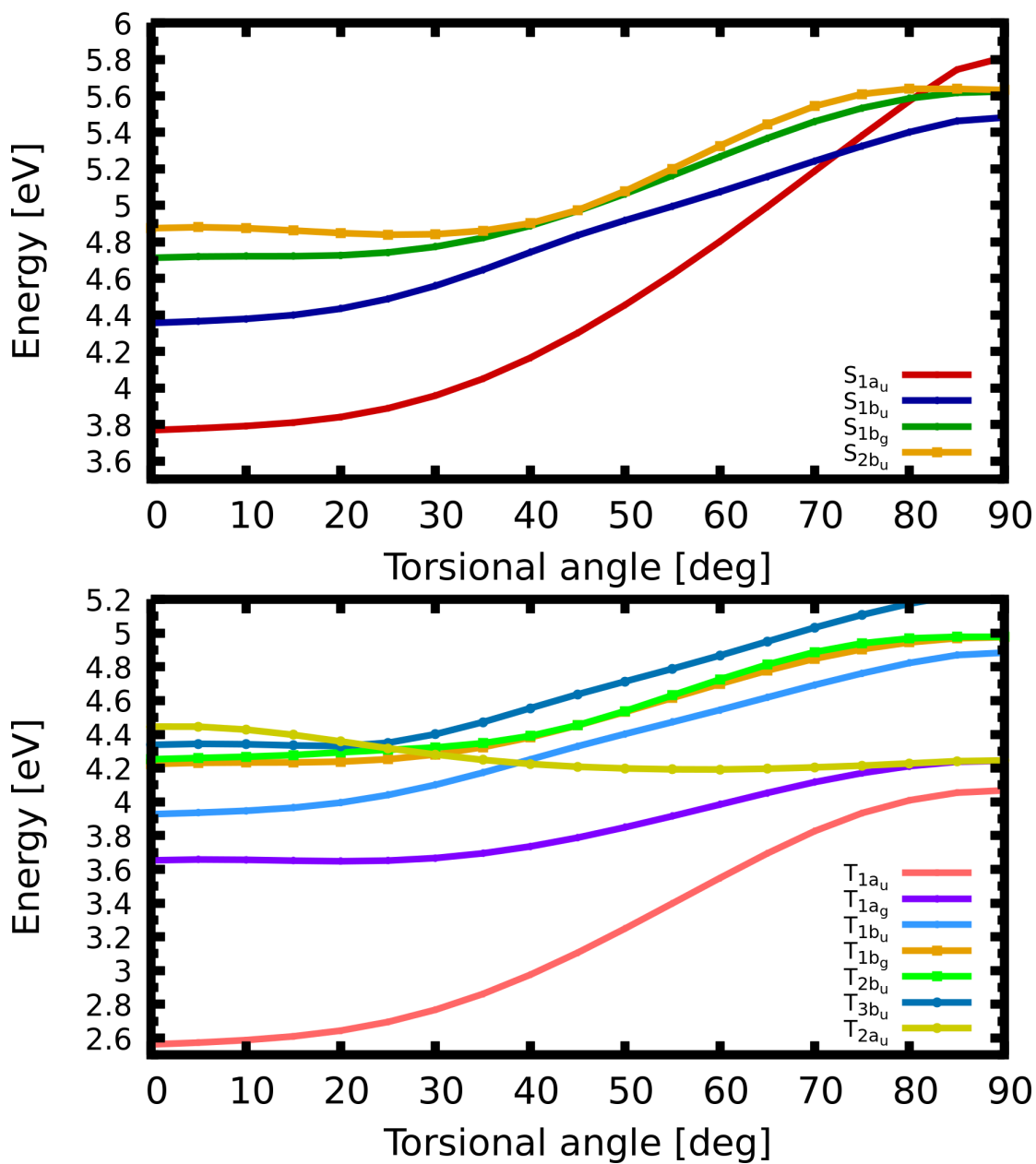


Figure S4: TDDFT scan of the symmetric torsion of singlet (top) and triplet states (bottom) of p3P. The D₀ geometry was used for the unrelaxed scan from 0° to 90°.

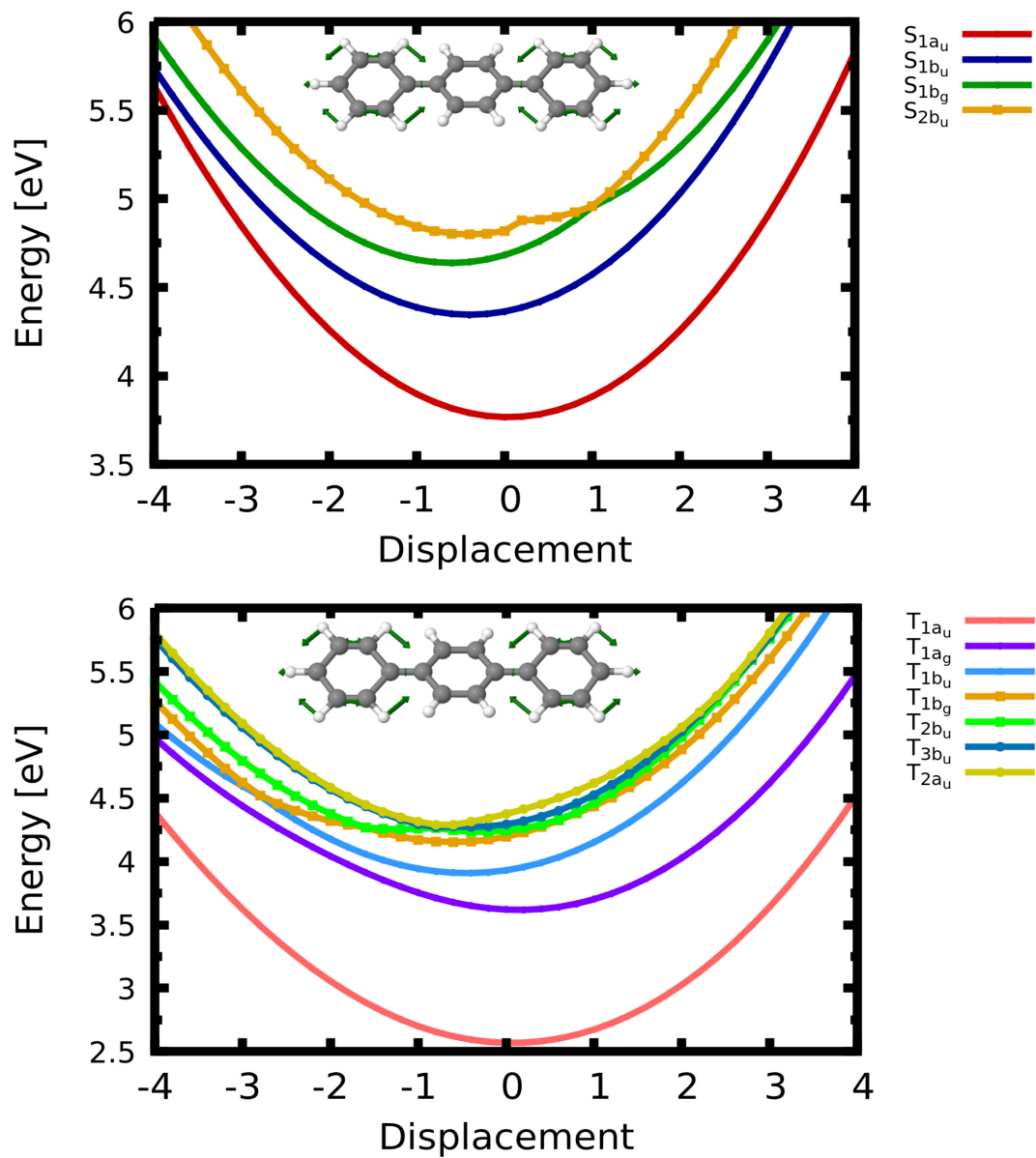


Figure S5: TDDFT scan of singlet (top) and triplet states (bottom) along the symmetric C-C normal mode of p3P. The D_0 geometry was used for the unrelaxed scan.

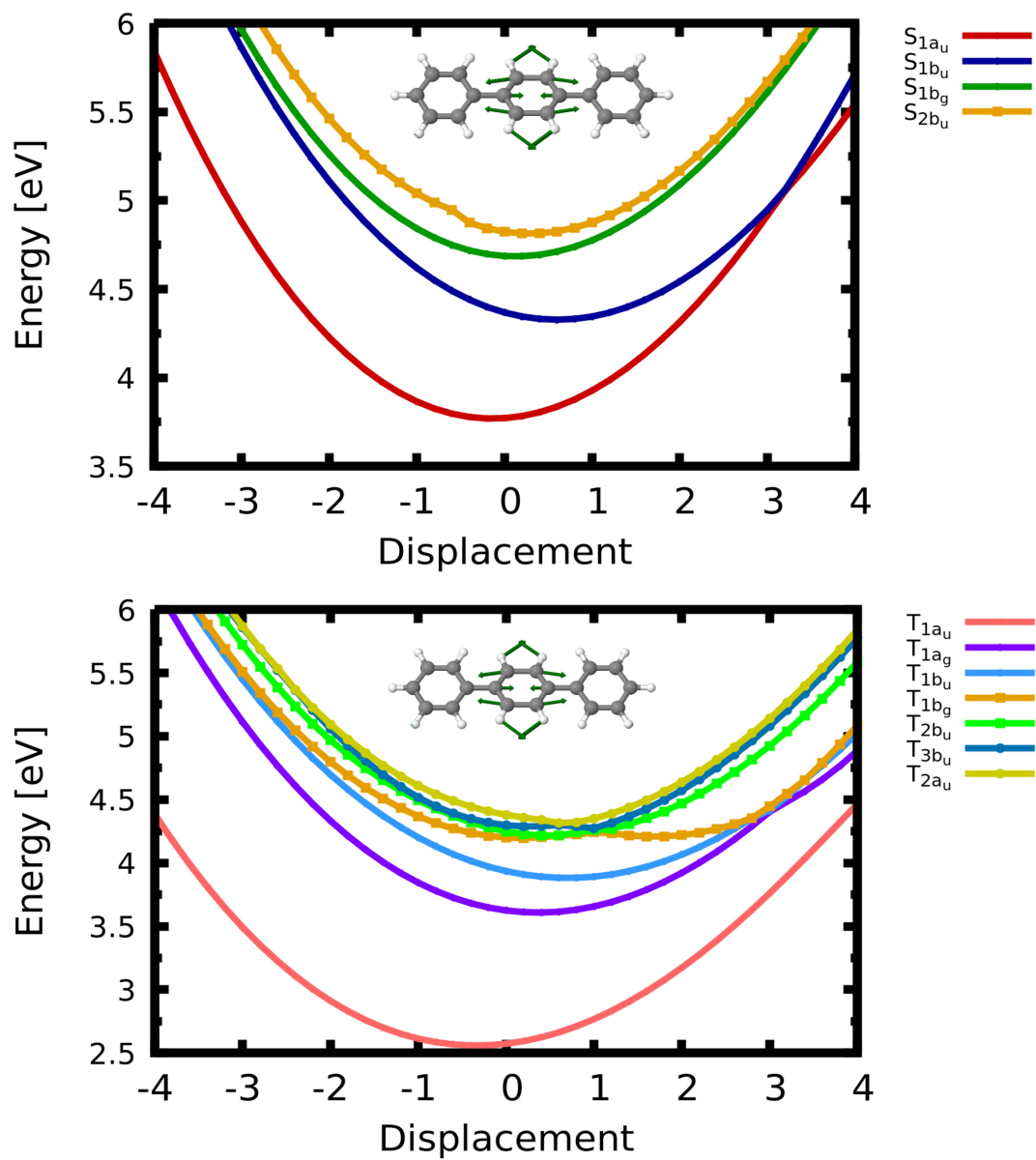
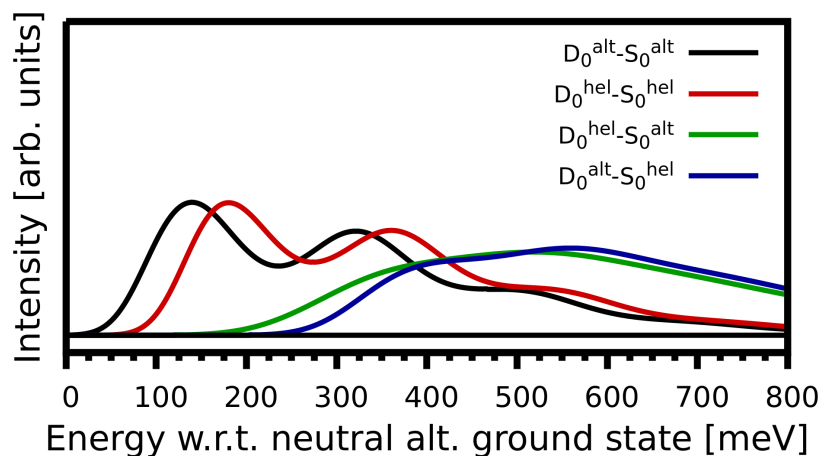
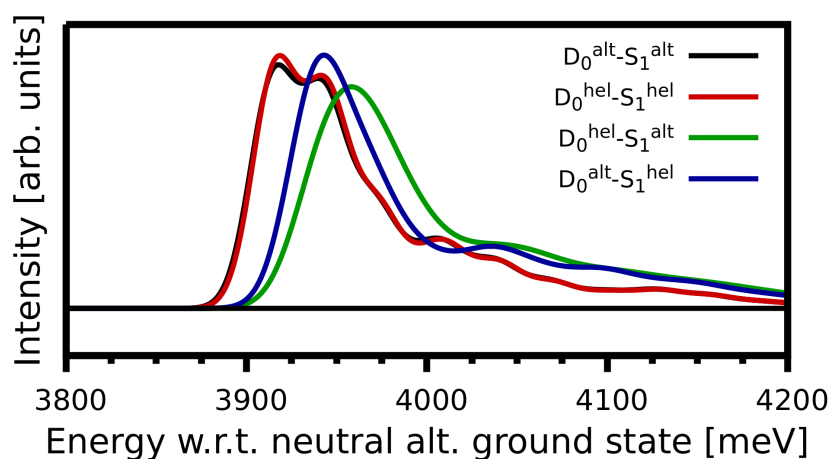


Figure S6: TDDFT scan of singlet (top) and triplet states (bottom) along the symmetric C-C normal mode of p3P. The D_0 geometry was used for the unrelaxed scan.

Table S1: Comparison of adiabatic energies of alternating and helical conformers of p3P. All values in eV

State	Conformer	TDDFT ΔE_{adiab} w.r.t. S_0	DFT/MRCI ΔE_{adiab} w.r.t. S_0
S_0	alternating		
S_0	helical	0.001	0.004
S_1	alternating	3.940	4.027
S_1	helical	3.943	4.028

Figure S7: Comparison of spectra calculated between alternating and helical conformers of the D_0 and S_0 states of p3P. The origin of the spectra was shifted to be the 0-0 transition between the alternating conformers of D_0 and S_0 .Figure S8: Comparison of spectra calculated between alternating and helical conformers of the D_0 and S_1 states of p3P. The origin of the spectra was shifted to be the 0-0 transition between the alternating conformers of D_0 and S_0 .

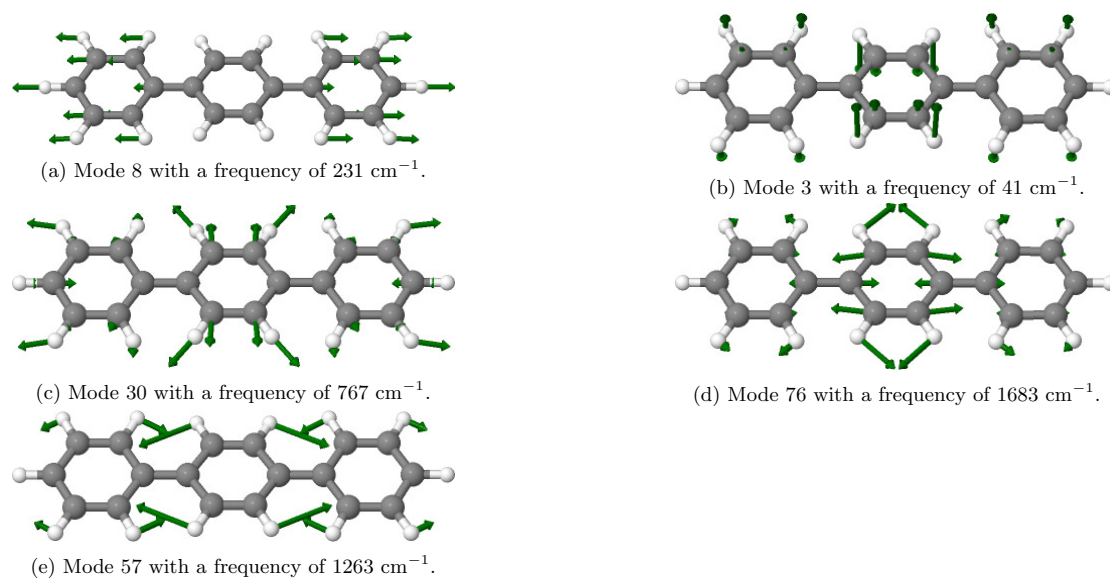


Figure S10: Displacement vectors of selected vibrational modes in the T_1 state of p3P.

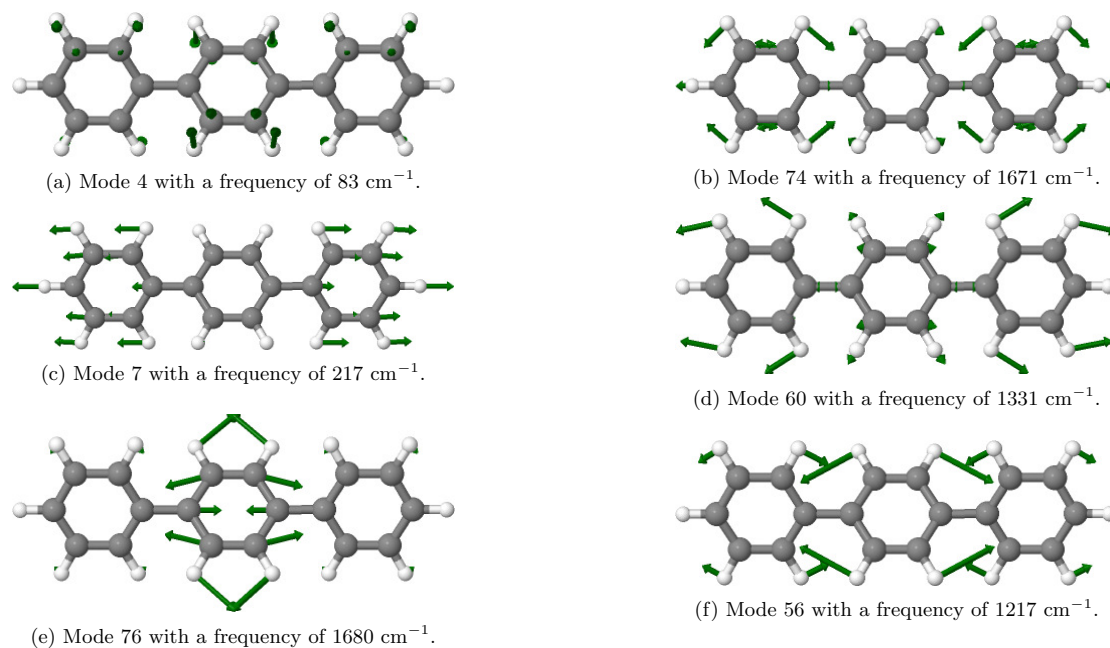
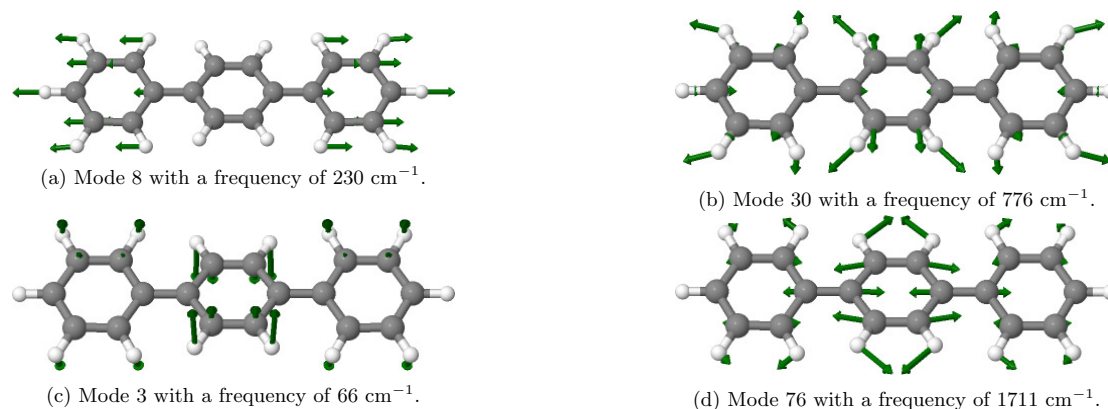
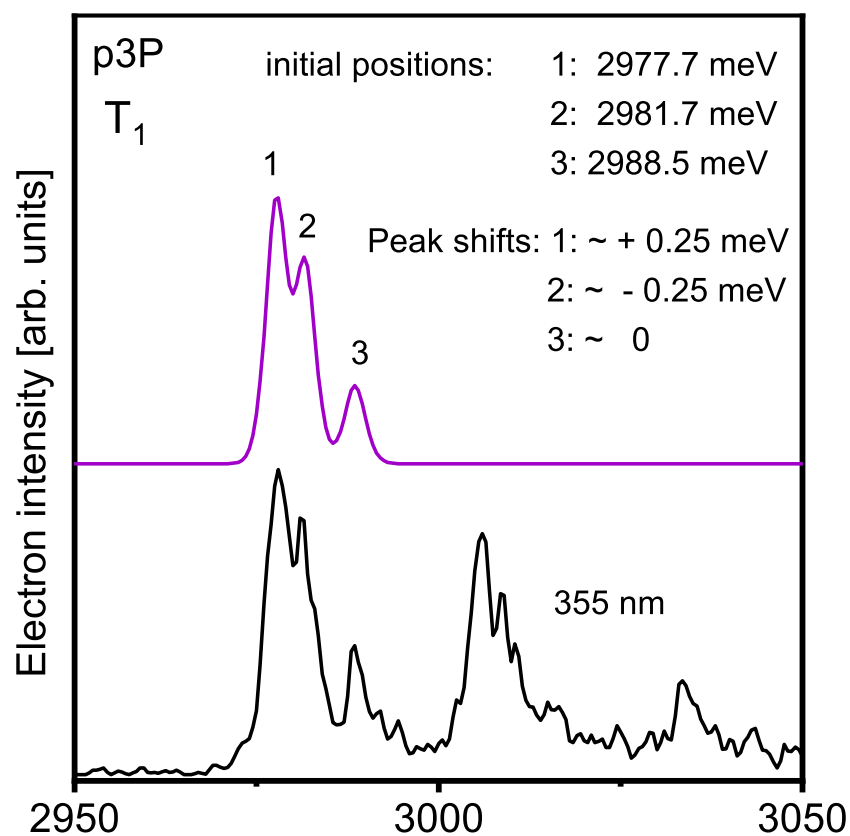


Figure S9: Displacement vectors of selected vibrational modes in the S_0 state of p3P.

Figure S11: Displacement vectors of selected vibrational modes in the S_1 state of p3P.Figure S12: Simulation of the “peak attraction effect” for the vibronic progressions observed in the T_1 state of p3P. The experimental spectrum can be best described by using the initial positions as indicated in the figure. If the individual peaks 1 to 3 at their initial positions are broadened and overlaid the peak maxima shift by about 0.25 meV (peak 1) and -0.25 meV (peak 3), respectively. As the initial peak positions are used to calculate the underlying vibrational frequencies, the value consequently changes from 28 cm^{-1} to 32 cm^{-1} .

S4 p4P

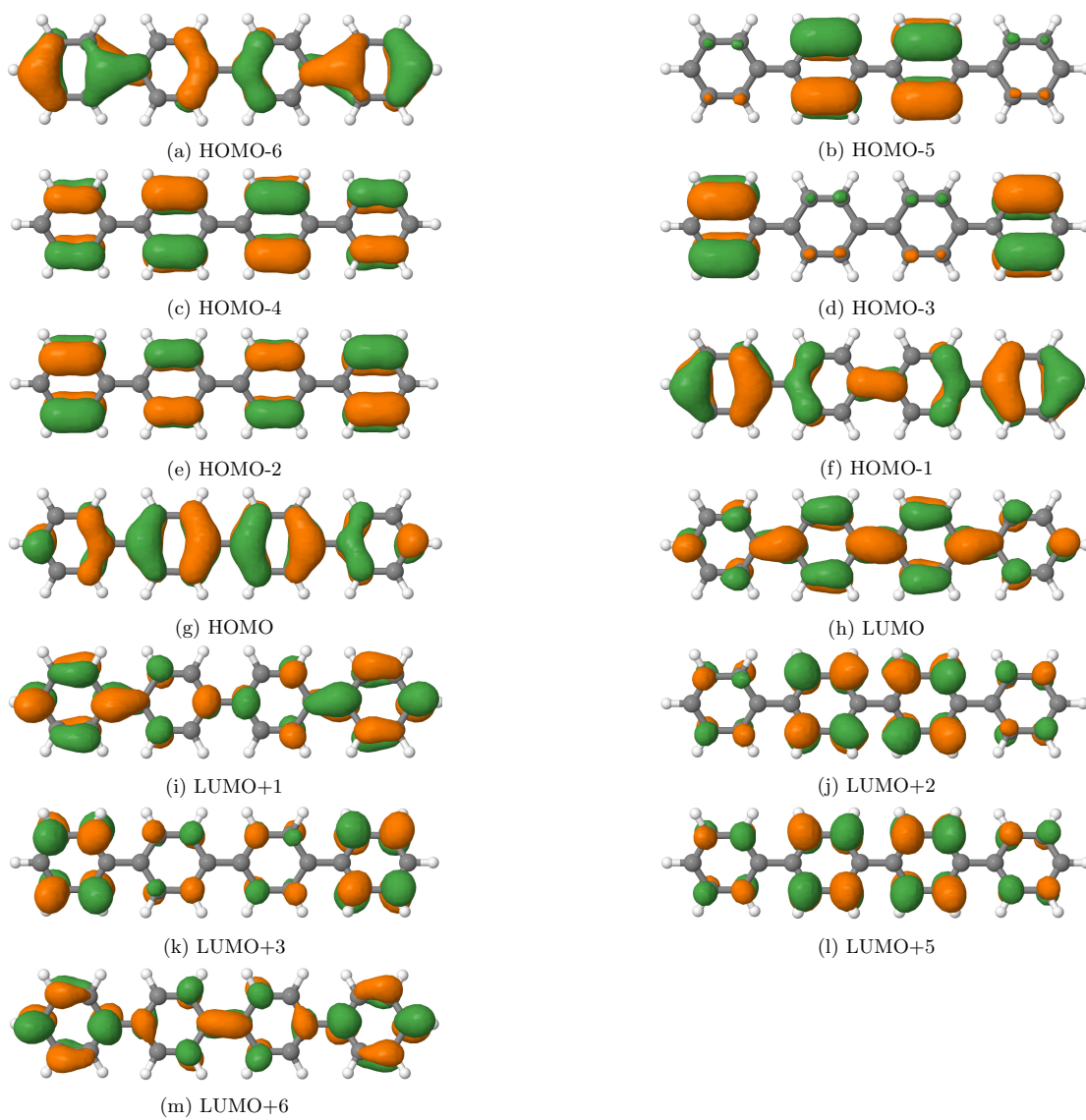


Figure S13: Important molecular orbitals at the anion ground state geometry of p4P.

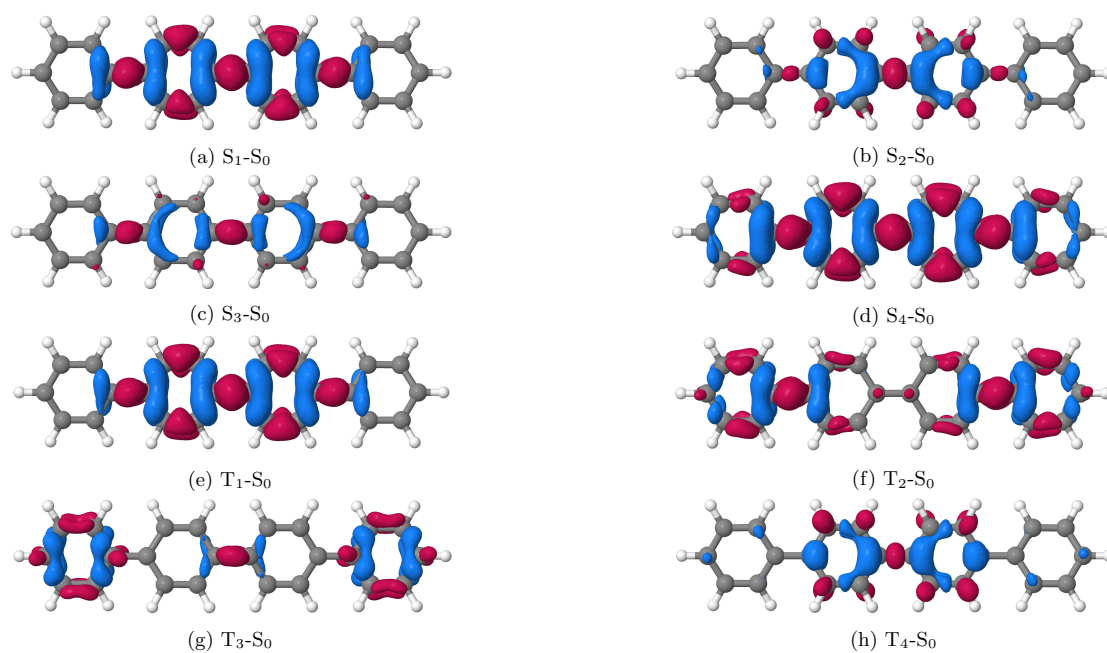


Figure S14: Difference densities (± 0.001) between the excited states and the neutral ground state at the anion ground state geometry of p4P. For colour codes see Fig. S3.

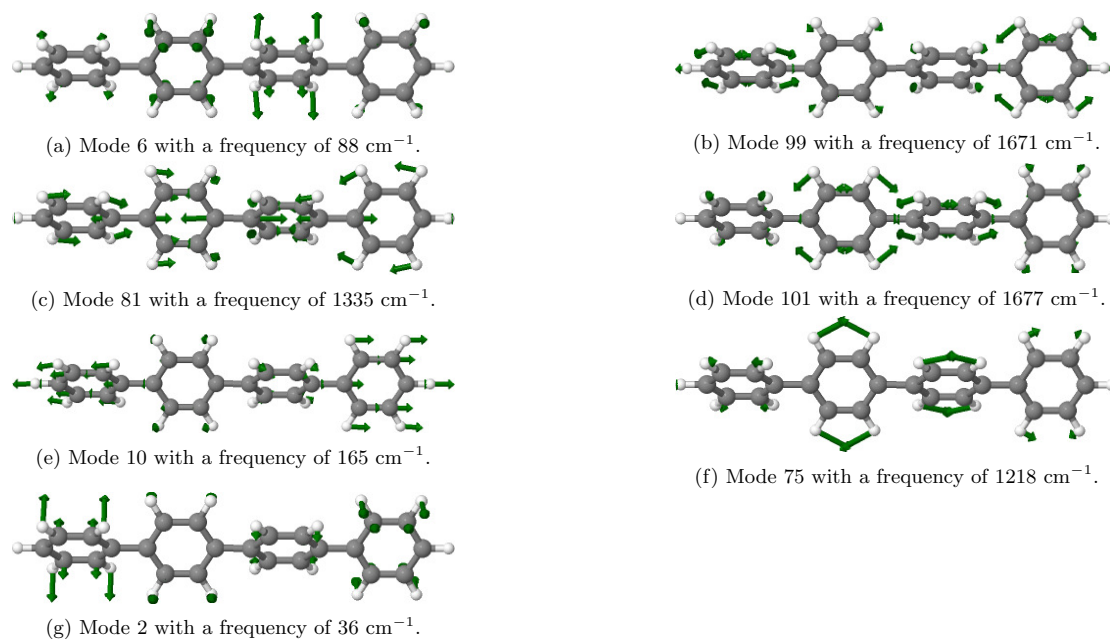


Figure S15: Displacement vectors of selected vibrational modes in the S_0 state of p4P.

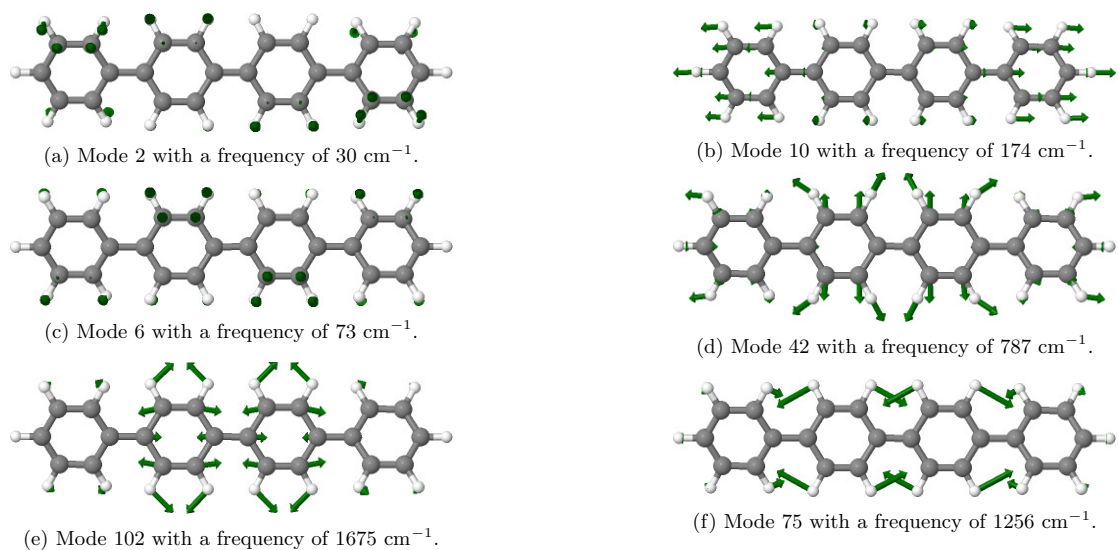


Figure S16: Displacement vectors of selected vibrational modes in the T_1 state of p4P.

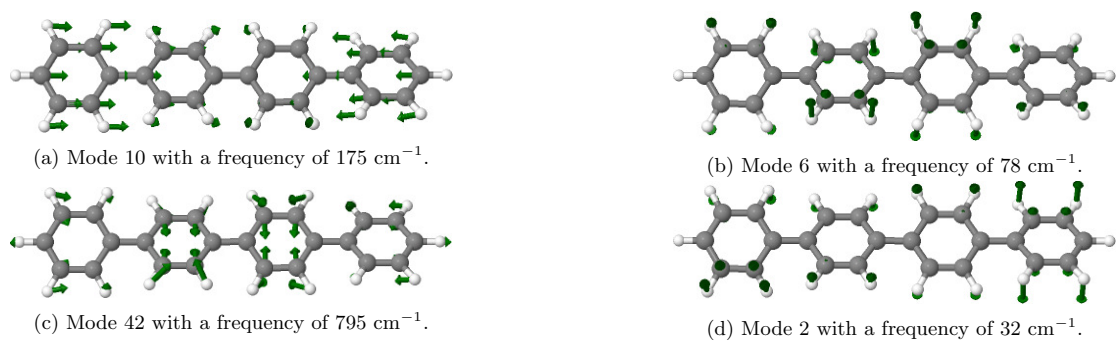


Figure S17: Displacement vectors of selected vibrational modes in the S_1 state of p4P.

S5 p5P

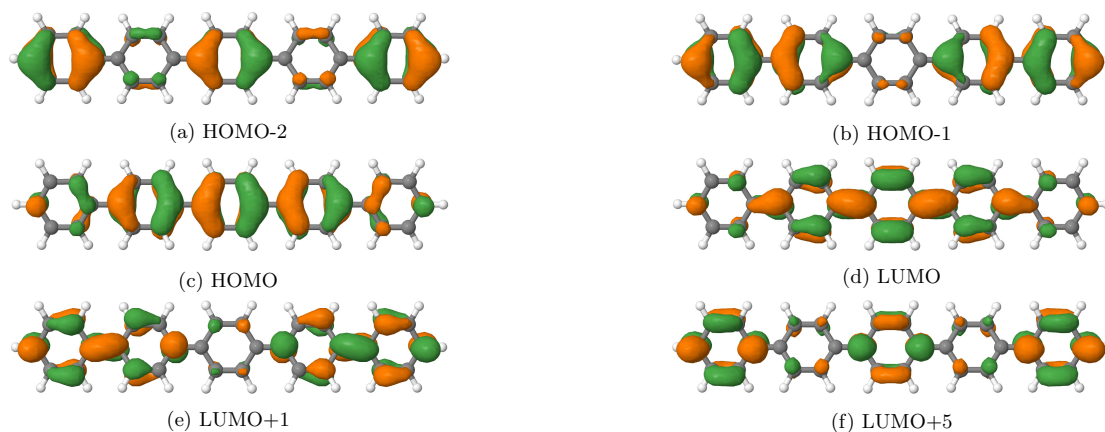


Figure S18: Important molecular orbitals at the anion ground state geometry of p5P.

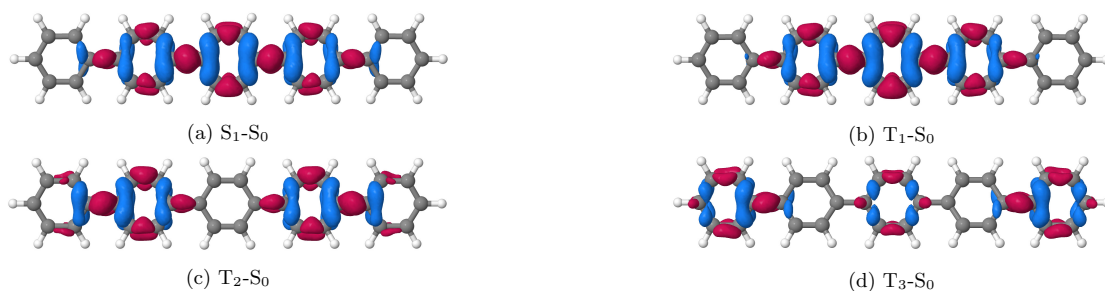


Figure S19: Difference densities (± 0.001) between the excited states and the neutral ground state at the anion ground state geometry of p5P. For colour codes see Fig. S3.

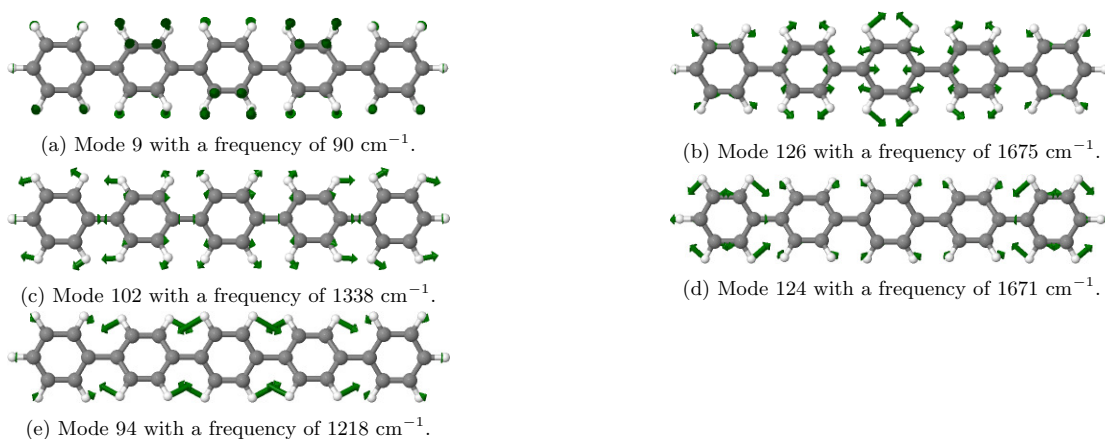


Figure S20: Displacement vectors of selected vibrational modes in the S_0 state of p5P.

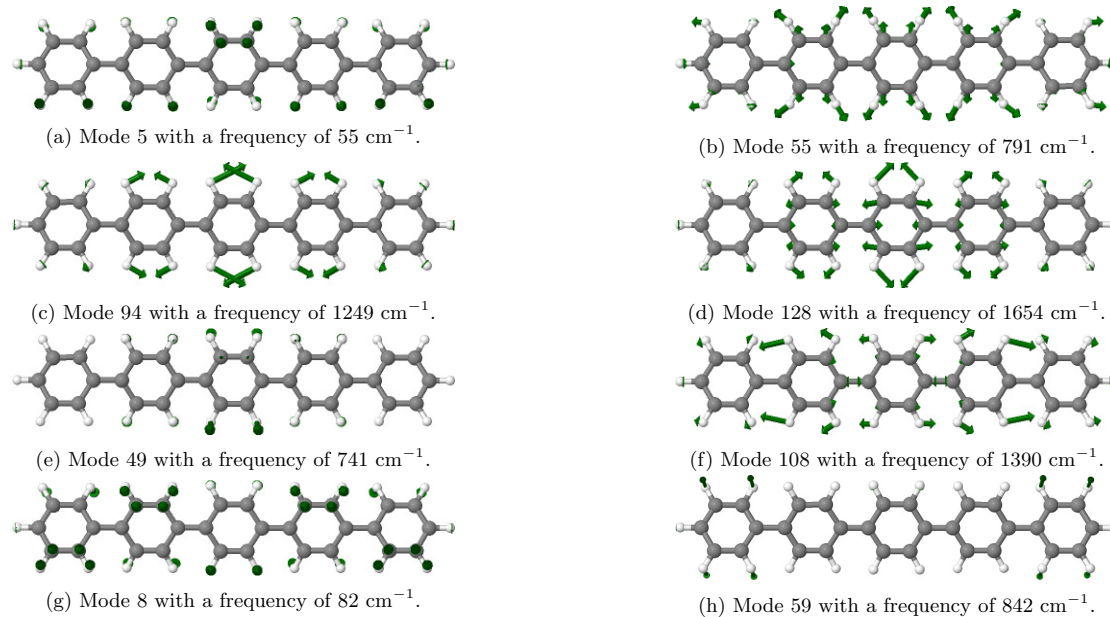


Figure S21: Displacement vectors of selected vibrational modes in the T_1 state of p5P.

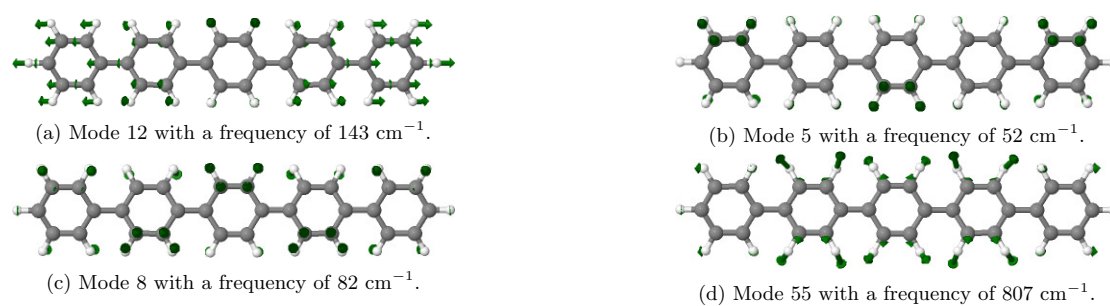


Figure S22: Displacement vectors of selected vibrational modes in the S_1 state of p5P.

S6 Dihedral Angles

Table S2: Dihedral angles of the alternating conformer of p3P

State	Φ_1	Φ_2
D ₀	13.8	-13.8
S ₀	38.2	-38.2
S ₁	10.6	-10.6
S ₂	10.7	-10.7
S ₃	22.3	-22.3
T ₁	5.9	-5.9
T ₂	25.2	-25.2
T ₃	37.9	-39.5
T ₄	13.7	-13.7

Table S3: Dihedral angles of the alternating conformer of p4P

State	Φ_1	Φ_2	Φ_3
D ₀	-20.0	14.0	-20.0
S ₀	-38.1	36.9	-38.1
S ₁	-18.1	9.3	-18.1
S ₂	-20.8	5.4	-20.8
S ₃			
S ₄	-18.2	31.5	-18.2
T ₁	-19.2	4.0	-19.2
T ₂	-14.6	39.4	-14.6
T ₃	-39.3	26.6	-39.3
T ₄	-25.1	5.7	-25.1

Table S4: Dihedral angles of the alternating conformer of p5P

State	Φ_1	Φ_2	Φ_3	Φ_4
D ₀	24.5	-16.9	16.9	-24.5
S ₀	38.1	-36.9	36.9	-38.1
S ₁	23.6	-11.9	11.9	-23.6
T ₁	27.8	-6.8	6.8	-27.8
T ₂	15.7	-28.6	28.6	-15.7
T ₃	25.6	-32.0	32.0	-25.6

S7 Geometries

The cartesian coordinates of all investigated geometries are given below in Å.

S7.1 p3P

D₀ alternating

C	0.0000000	0.0000000	1.4515980
C	0.0000000	0.0000000	2.8913400
C	1.1727840	-0.2503910	3.6498240
C	1.1686500	-0.2501910	5.0298780
C	0.0000000	0.0000000	5.7513340
C	-1.1686500	0.2501910	5.0298780
C	-1.1727840	0.2503910	3.6498240
H	2.1112030	-0.4183150	3.1343470
H	2.0986970	-0.4397840	5.5594460
H	0.0000000	0.0000000	6.8356100
H	-2.0986970	0.4397840	5.5594460
H	-2.1112030	0.4183150	3.1343470
C	1.0764720	-0.5210750	0.6852610
C	1.0764720	-0.5210750	-0.6852610
C	0.0000000	0.0000000	-1.4515980
C	-1.0764720	0.5210750	-0.6852610
C	-1.0764720	0.5210750	0.6852610
H	1.9181440	-0.9797430	1.1934970
H	1.9181440	-0.9797430	-1.1934970
C	0.0000000	0.0000000	-2.8913400
H	-1.9181440	0.9797430	-1.1934970
H	-1.9181440	0.9797430	1.1934970
C	1.1727840	-0.2503910	-3.6498240
C	1.1686500	-0.2501910	-5.0298780
C	0.0000000	0.0000000	-5.7513340
C	-1.1686500	0.2501910	-5.0298780
C	-1.1727840	0.2503910	-3.6498240
H	2.1112030	-0.4183150	-3.1343470
H	2.0986970	-0.4397840	-5.5594460
H	0.0000000	0.0000000	-6.8356100
H	-2.0986970	0.4397840	-5.5594460
H	-2.1112030	0.4183150	-3.1343470

C Included Publications

D₀ helical

H	2.1070350	0.4417650	3.1404395
H	-2.1070350	-0.4417650	3.1404395
H	2.1021320	0.4223150	5.5625305
H	-2.1021320	-0.4223150	5.5625305
H	0.0000000	0.0000000	6.8397325
H	2.1544730	-0.0136170	1.1906505
H	-2.1544730	0.0136170	1.1906505
H	2.1545730	0.0066040	-1.1902965
H	-2.1545730	-0.0066040	-1.1902965
H	2.1078900	-0.4380260	-3.1407495
H	-2.1078900	0.4380260	-3.1407495
H	2.1028450	-0.4187530	-5.5625435
H	-2.1028450	0.4187530	-5.5625435
H	0.0000000	0.0000000	-6.8398785
C	0.0000000	0.0000000	1.4533775
C	0.0000000	0.0000000	2.8936955
C	1.1761710	0.2311910	3.6535065
C	-1.1761710	-0.2311910	3.6535065
C	1.1720830	0.2311770	5.0335245
C	-1.1720830	-0.2311770	5.0335245
C	0.0000000	0.0000000	5.7554735
C	1.1948600	0.0031320	0.6853375
C	-1.1948600	-0.0031320	0.6853375
C	1.1948540	-0.0066050	-0.6851365
C	-1.1948540	0.0066050	-0.6851365
C	0.0000000	0.0000000	-1.4533175
C	0.0000000	0.0000000	-2.8935945
C	1.1765160	-0.2292750	-3.6536005
C	-1.1765160	0.2292750	-3.6536005
C	1.1723980	-0.2293710	-5.0335945
C	-1.1723980	0.2293710	-5.0335945
C	0.0000000	0.0000000	-5.7556245

S₀ alternating

C	0.0000000	0.0000000	1.4121040
C	0.0000000	0.0000000	2.8863880
C	-0.7537970	0.9320700	3.6020900
C	-0.7537990	0.9324770	4.9880100
C	0.0000000	0.0000000	5.6873190
C	0.7537990	-0.9324770	4.9880100
C	0.7537970	-0.9320700	3.6020900
H	-1.3658400	1.6472640	3.0637250
H	-1.3529390	1.6594040	5.5251730
H	0.0000000	0.0000000	6.7713970
H	1.3529390	-1.6594040	5.5251730
H	1.3658400	-1.6472640	3.0637250
C	-0.0158960	1.1952240	0.6916710
C	-0.0158960	1.1952240	-0.6916710
C	0.0000000	0.0000000	-1.4121040
C	0.0158960	-1.1952240	-0.6916710
C	0.0158960	-1.1952240	0.6916710
H	0.0069320	2.1390480	1.2251490
H	0.0069320	2.1390480	-1.2251490
C	0.0000000	0.0000000	-2.8863880
H	-0.0069320	-2.1390480	-1.2251490
H	-0.0069320	-2.1390480	1.2251490
C	-0.7537970	0.9320700	-3.6020900
C	-0.7537990	0.9324770	-4.9880100
C	0.0000000	0.0000000	-5.6873190
C	0.7537990	-0.9324770	-4.9880100
C	0.7537970	-0.9320700	-3.6020900
H	-1.3658400	1.6472640	-3.0637250
H	-1.3529390	1.6594040	-5.5251730
H	0.0000000	0.0000000	-6.7713970
H	1.3529390	-1.6594040	-5.5251730
H	1.3658400	-1.6472640	-3.0637250

C Included Publications

S₀ helical

C	0.0000000	0.0000000	1.4119740
C	0.0000000	0.0000000	2.8863810
C	-0.9367550	-0.7479900	3.6021010
C	-0.9370390	-0.7480560	4.9880360
C	0.0000000	0.0000000	5.6874030
C	0.9370390	0.7480560	4.9880360
C	0.9367550	0.7479900	3.6021010
H	-1.6558230	-1.3555930	3.0638790
H	-1.6676330	-1.3427960	5.5251170
H	0.0000000	0.0000000	6.7714790
H	1.6676330	1.3427960	5.5251170
H	1.6558230	1.3555930	3.0638790
C	-1.1952800	-0.0005660	0.6916710
C	-1.1952890	0.0003690	-0.6917050
C	0.0000000	0.0000000	-1.4119900
C	1.1952890	-0.0003690	-0.6917050
C	1.1952800	0.0005660	0.6916710
H	-2.1391170	0.0152870	1.2254150
H	-2.1390920	-0.0155730	-1.2255020
C	0.0000000	0.0000000	-2.8864180
H	2.1390920	0.0155730	-1.2255020
H	2.1391170	-0.0152870	1.2254150
C	-0.9365300	0.7483110	-3.6020860
C	-0.9368140	0.7483630	-4.9880250
C	0.0000000	0.0000000	-5.6873590
C	0.9368140	-0.7483630	-4.9880250
C	0.9365300	-0.7483110	-3.6020860
H	-1.6553690	1.3561060	-3.0637780
H	-1.6672410	1.3432780	-5.5251400
H	0.0000000	0.0000000	-6.7714360
H	1.6672410	-1.3432780	-5.5251400
H	1.6553690	-1.3561060	-3.0637780

S₁ alternating

C	0.0000000	0.0000000	1.4406780
C	0.0000000	0.0000000	2.8673640
C	1.1796710	-0.2779700	3.6175790
C	1.1728310	-0.2722080	4.9927890
C	0.0000000	0.0000000	5.7008310
C	-1.1728310	0.2722080	4.9927890
C	-1.1796710	0.2779700	3.6175790
H	2.1123680	-0.4668680	3.1022050
H	2.0916740	-0.4771820	5.5313350
H	0.0000000	0.0000000	6.7845140
H	-2.0916740	0.4771820	5.5313350
H	-2.1123680	0.4668680	3.1022050
C	1.1090350	-0.4911470	0.6807740
C	1.1090350	-0.4911470	-0.6807740
C	0.0000000	0.0000000	-1.4406780
C	-1.1090350	0.4911470	-0.6807740
C	-1.1090350	0.4911470	0.6807740
H	1.9614420	-0.9152420	1.1951350
H	1.9614420	-0.9152420	-1.1951350
C	0.0000000	0.0000000	-2.8673640
H	-1.9614420	0.9152420	-1.1951350
H	-1.9614420	0.9152420	1.1951350
C	1.1796710	-0.2779700	-3.6175790
C	1.1728310	-0.2722080	-4.9927890
C	0.0000000	0.0000000	-5.7008310
C	-1.1728310	0.2722080	-4.9927890
C	-1.1796710	0.2779700	-3.6175790
H	2.1123680	-0.4668680	-3.1022050
H	2.0916740	-0.4771820	-5.5313350
H	0.0000000	0.0000000	-6.7845140
H	-2.0916740	0.4771820	-5.5313350
H	-2.1123680	0.4668680	-3.1022050

C Included Publications

S₁ helical

C	0.0000000	0.0000000	1.4417709
C	0.0000000	0.0000000	2.8688569
C	-0.4075240	1.1410420	3.6199649
C	-0.4083040	1.1323630	4.9951649
C	0.0000000	0.0000000	5.7034729
C	0.4083040	-1.1323630	4.9951649
C	0.4075240	-1.1410420	3.6199649
H	-0.7524320	2.0287130	3.1062109
H	-0.7341790	2.0157780	5.5334039
H	0.0000000	0.0000000	6.7871499
H	0.7341790	-2.0157780	5.5334039
H	0.7524320	-2.0287130	3.1062109
C	-0.2307930	1.1900100	0.6807699
C	-0.2175420	1.1924970	-0.6807781
C	0.0000000	0.0000000	-1.4417571
C	0.2175420	-1.1924970	-0.6807781
C	0.2307930	-1.1900100	0.6807699
H	-0.3950280	2.1286090	1.1932059
H	-0.4057320	2.1265970	-1.1931961
C	0.0000000	0.0000000	-2.8688711
H	0.4057320	-2.1265970	-1.1931961
H	0.3950280	-2.1286090	1.1932059
C	-0.0352950	1.2111070	-3.6199571
C	-0.0313920	1.2033140	-4.9951661
C	0.0000000	0.0000000	-5.7034721
C	0.0313920	-1.2033140	-4.9951661
C	0.0352950	-1.2111070	-3.6199571
H	-0.0368450	2.1634430	-3.1062281
H	-0.0489970	2.1447570	-5.5333951
H	0.0000000	0.0000000	-6.7871501
H	0.0489970	-2.1447570	-5.5333951
H	0.0368450	-2.1634430	-3.1062281

S₂ alternating

C	0.000000	0.000000	1.4298380
C	0.000000	0.000000	2.8758580
C	1.1758870	-0.2722900	3.6049720
C	1.1745950	-0.2662450	4.9915980
C	0.0000000	0.0000000	5.6893960
C	-1.1745950	0.2662450	4.9915980
C	-1.1758870	0.2722900	3.6049720
H	2.1043100	-0.4566550	3.0826810
H	2.0922030	-0.4702210	5.5309340
H	0.0000000	0.0000000	6.7735970
H	-2.0922030	0.4702210	5.5309340
H	-2.1043100	0.4566550	3.0826810
C	1.1093120	-0.4879550	0.6996950
C	1.1093120	-0.4879550	-0.6996950
C	0.0000000	0.0000000	-1.4298380
C	-1.1093120	0.4879550	-0.6996950
C	-1.1093120	0.4879550	0.6996950
H	1.9560800	-0.9150670	1.2166650
H	1.9560800	-0.9150670	-1.2166650
C	0.0000000	0.0000000	-2.8758580
H	-1.9560800	0.9150670	-1.2166650
H	-1.9560800	0.9150670	1.2166650
C	1.1758870	-0.2722900	-3.6049720
C	1.1745950	-0.2662450	-4.9915980
C	0.0000000	0.0000000	-5.6893960
C	-1.1745950	0.2662450	-4.9915980
C	-1.1758870	0.2722900	-3.6049720
H	2.1043100	-0.4566550	-3.0826810
H	2.0922030	-0.4702210	-5.5309340
H	0.0000000	0.0000000	-6.7735970
H	-2.0922030	0.4702210	-5.5309340
H	-2.1043100	0.4566550	-3.0826810

C Included Publications

S₃ alternating

C	0.0000000	0.0000000	1.4276480
C	0.0000000	0.0000000	2.8730540
C	-0.6677290	1.0064990	3.6023030
C	-0.6659820	1.0037520	5.0062800
C	0.0000000	0.0000000	5.7061950
C	0.6659820	-1.0037520	5.0062800
C	0.6677290	-1.0064990	3.6023030
H	-1.2332750	1.7657850	3.0778600
H	-1.1968870	1.7812170	5.5425550
H	0.0000000	0.0000000	6.7899230
H	1.1968870	-1.7812170	5.5425550
H	1.2332750	-1.7657850	3.0778600
C	-0.2355380	1.1799530	0.6848550
C	-0.2355380	1.1799530	-0.6848550
C	0.0000000	0.0000000	-1.4276480
C	0.2355380	-1.1799530	-0.6848550
C	0.2355380	-1.1799530	0.6848550
H	-0.3702130	2.1185900	1.2087240
H	-0.3702130	2.1185900	-1.2087240
C	0.0000000	0.0000000	-2.8730540
H	0.3702130	-2.1185900	-1.2087240
H	0.3702130	-2.1185900	1.2087240
C	-0.6677290	1.0064990	-3.6023030
C	-0.6659820	1.0037520	-5.0062800
C	0.0000000	0.0000000	-5.7061950
C	0.6659820	-1.0037520	-5.0062800
C	0.6677290	-1.0064990	-3.6023030
H	-1.2332750	1.7657850	-3.0778600
H	-1.1968870	1.7812170	-5.5425550
H	0.0000000	0.0000000	-6.7899230
H	1.1968870	-1.7812170	-5.5425550
H	1.2332750	-1.7657850	-3.0778600

T₁ alternating

C	0.0000000	0.0000000	1.4494320
C	0.0000000	0.0000000	2.8687540
C	1.1692760	-0.3120750	3.6225990
C	1.1628820	-0.3078810	4.9970620
C	0.0000000	0.0000000	5.7064320
C	-1.1628820	0.3078810	4.9970620
C	-1.1692760	0.3120750	3.6225990
H	2.0944460	-0.5414380	3.1116330
H	2.0747760	-0.5444540	5.5342710
H	0.0000000	0.0000000	6.7897370
H	-2.0747760	0.5444540	5.5342710
H	-2.0944460	0.5414380	3.1116330
C	1.1387790	-0.4335820	0.6761620
C	1.1387790	-0.4335820	-0.6761620
C	0.0000000	0.0000000	-1.4494320
C	-1.1387790	0.4335820	-0.6761620
C	-1.1387790	0.4335820	0.6761620
H	2.0206140	-0.7973920	1.1861440
H	2.0206140	-0.7973920	-1.1861440
C	0.0000000	0.0000000	-2.8687540
H	-2.0206140	0.7973920	-1.1861440
H	-2.0206140	0.7973920	1.1861440
C	1.1692760	-0.3120750	-3.6225990
C	1.1628820	-0.3078810	-4.9970620
C	0.0000000	0.0000000	-5.7064320
C	-1.1628820	0.3078810	-4.9970620
C	-1.1692760	0.3120750	-3.6225990
H	2.0944460	-0.5414380	-3.1116330
H	2.0747760	-0.5444540	-5.5342710
H	0.0000000	0.0000000	-6.7897370
H	-2.0747760	0.5444540	-5.5342710
H	-2.0944460	0.5414380	-3.1116330

C Included Publications

T₂ alternating

C	0.0000000	0.0000000	1.4256650
C	0.0000000	0.0000000	2.8784670
C	1.2079600	-0.1822670	3.6231860
C	1.2051790	-0.1779630	4.9924250
C	0.0000000	0.0000000	5.7094920
C	-1.2051790	0.1779630	4.9924250
C	-1.2079600	0.1822670	3.6231860
H	2.1457330	-0.2875730	3.0914290
H	2.1366410	-0.3014780	5.5333300
H	0.0000000	0.0000000	6.7920920
H	-2.1366410	0.3014780	5.5333300
H	-2.1457330	0.2875730	3.0914290
C	0.9948760	-0.6657250	0.6901830
C	0.9948760	-0.6657250	-0.6901830
C	0.0000000	0.0000000	-1.4256650
C	-0.9948760	0.6657250	-0.6901830
C	-0.9948760	0.6657250	0.6901830
H	1.7619330	-1.2258020	1.2117800
H	1.7619330	-1.2258020	-1.2117800
C	0.0000000	0.0000000	-2.8784670
H	-1.7619330	1.2258020	-1.2117800
H	-1.7619330	1.2258020	1.2117800
C	1.2079600	-0.1822670	-3.6231860
C	1.2051790	-0.1779630	-4.9924250
C	0.0000000	0.0000000	-5.7094920
C	-1.2051790	0.1779630	-4.9924250
C	-1.2079600	0.1822670	-3.6231860
H	2.1457330	-0.2875730	-3.0914290
H	2.1366410	-0.3014780	-5.5333300
H	0.0000000	0.0000000	-6.7920920
H	-2.1366410	0.3014780	-5.5333300
H	-2.1457330	0.2875730	-3.0914290

T₃ alternating

C	0.0021057	0.0185111	1.4155400
C	-0.0102033	0.0169831	2.8882730
C	-0.7807543	0.9117981	3.5985520
C	-0.7827943	0.9067751	5.0200110
C	0.0017277	-0.0273869	5.7177140
C	0.7711357	-0.9295029	5.0231750
C	0.7783727	-0.9194249	3.6036220
H	-1.4146733	1.6139531	3.0692340
H	-1.3946643	1.6193081	5.5590980
H	-0.0016473	-0.0317079	6.8017670
H	1.3859457	-1.6483669	5.5522480
H	1.4192587	-1.6040479	3.0620560
C	-0.0325473	1.2211781	0.6908190
C	-0.0325473	1.2211781	-0.6908190
C	0.0021057	0.0185111	-1.4155400
C	0.0423837	-1.1840999	-0.6909160
C	0.0423837	-1.1840999	0.6909160
H	-0.0238373	2.1629651	1.2279040
H	-0.0238373	2.1629651	-1.2279040
C	-0.0102033	0.0169831	-2.8882730
H	0.0401907	-2.1269349	-1.2263740
H	0.0401907	-2.1269349	1.2263740
C	-0.7807543	0.9117981	-3.5985520
C	-0.7827943	0.9067751	-5.0200110
C	0.0017277	-0.0273869	-5.7177140
C	0.7711357	-0.9295029	-5.0231750
C	0.7783727	-0.9194249	-3.6036220
H	-1.4146733	1.6139531	-3.0692340
H	-1.3946643	1.6193081	-5.5590980
H	-0.0016473	-0.0317079	-6.8017670
H	1.3859457	-1.6483669	-5.5522480
H	1.4192587	-1.6040479	-3.0620560

C Included Publications

T₄ alternating

C	0.0000000	0.0000000	1.4200670
C	0.0000000	0.0000000	2.8712290
C	1.1802580	-0.2496350	3.5969920
C	1.1801950	-0.2418260	4.9831180
C	0.0000000	0.0000000	5.6782240
C	-1.1801950	0.2418260	4.9831180
C	-1.1802580	0.2496350	3.5969920
H	2.1097900	-0.4144050	3.0700520
H	2.1012760	-0.4261680	5.5234330
H	0.0000000	0.0000000	6.7626980
H	-2.1012760	0.4261680	5.5234330
H	-2.1097900	0.4144050	3.0700520
C	1.0985050	-0.5282030	0.7028950
C	1.0985050	-0.5282030	-0.7028950
C	0.0000000	0.0000000	-1.4200670
C	-1.0985050	0.5282030	-0.7028950
C	-1.0985050	0.5282030	0.7028950
H	1.9178570	-0.9968680	1.2270040
H	1.9178570	-0.9968680	-1.2270040
C	0.0000000	0.0000000	-2.8712290
H	-1.9178570	0.9968680	-1.2270040
H	-1.9178570	0.9968680	1.2270040
C	1.1802580	-0.2496350	-3.5969920
C	1.1801950	-0.2418260	-4.9831180
C	0.0000000	0.0000000	-5.6782240
C	-1.1801950	0.2418260	-4.9831180
C	-1.1802580	0.2496350	-3.5969920
H	2.1097900	-0.4144050	-3.0700520
H	2.1012760	-0.4261680	-5.5234330
H	0.0000000	0.0000000	-6.7626980
H	-2.1012760	0.4261680	-5.5234330
H	-2.1097900	0.4144050	-3.0700520

S7.2 p4P

D₀ alternating

C	0.7806110	0.9082350	5.8062540
C	0.0000000	-0.0000000	5.0592930
C	-0.7806110	-0.9082350	5.8062540
C	-0.7770680	-0.9084050	7.1883870
C	0.0000000	-0.0000000	7.9034120
C	0.7770680	0.9084050	7.1883870
C	0.0000000	-0.0000000	3.6091760
C	-0.4206990	-1.1173320	2.8541870
C	-0.4189390	-1.1200580	1.4814770
C	0.0000000	-0.0000000	0.7187820
C	0.4189390	1.1200580	1.4814770
C	0.4206990	1.1173320	2.8541870
C	0.0000000	-0.0000000	-0.7187820
C	-0.6778190	-0.9851910	-1.4814770
C	-0.6745760	-0.9850710	-2.8541870
C	0.0000000	-0.0000000	-3.6091760
C	0.6745760	0.9850710	-2.8541870
C	0.6778190	0.9851910	-1.4814770
C	0.0000000	-0.0000000	-5.0592930
C	0.2969660	1.1601960	-5.8062540
C	0.2991360	1.1573900	-7.1883870
C	0.0000000	-0.0000000	-7.9034120
C	-0.2991360	-1.1573900	-7.1883870
C	-0.2969660	-1.1601960	-5.8062540
H	1.4249810	1.6057570	5.2837790
H	1.4009910	1.6213220	7.7197070
H	0.0000000	-0.0000000	8.9877030
H	-1.4009910	-1.6213220	7.7197070
H	-1.4249810	-1.6057570	5.2837790
H	-0.7127600	-2.0271880	3.3685410
H	-0.7096120	-2.0314240	0.9712230
H	0.7096120	2.0314240	0.9712230
H	0.7127600	2.0271880	3.3685410
H	1.2581170	1.7456730	-0.9712230
H	1.2528420	1.7458250	-3.3685410
H	-1.2528420	-1.7458250	-3.3685410
H	-1.2581170	-1.7456730	-0.9712230
H	-0.4993250	-2.0879890	-5.2837790
H	-0.5258290	-2.0772490	-7.7197070
H	0.0000000	-0.0000000	-8.9877030
H	0.5258290	2.0772490	-7.7197070
H	0.4993250	2.0879890	-5.2837790

C Included Publications

S₀ alternating

C	0.8795760	0.8144520	5.7510770
C	0.0000000	0.0000000	5.0353420
C	-0.8795760	-0.8144520	5.7510770
C	-0.8796100	-0.8148620	7.1369860
C	0.0000000	0.0000000	7.8363060
C	0.8796100	0.8148620	7.1369860
C	0.0000000	0.0000000	3.5611650
C	-0.1883300	-1.1803710	2.8405490
C	-0.1880870	-1.1804740	1.4573630
C	0.0000000	0.0000000	0.7363860
C	0.1880870	1.1804740	1.4573630
C	0.1883300	1.1803710	2.8405490
C	0.0000000	0.0000000	-0.7363860
C	-0.8596390	-0.8306120	-1.4573630
C	-0.8594150	-0.8307530	-2.8405490
C	0.0000000	0.0000000	-3.5611650
C	0.8594150	0.8307530	-2.8405490
C	0.8596390	0.8306120	-1.4573630
C	0.0000000	0.0000000	-5.0353420
C	0.1634190	1.1875520	-5.7510770
C	0.1637350	1.1878150	-7.1369860
C	0.0000000	0.0000000	-7.8363060
C	-0.1637350	-1.1878150	-7.1369860
C	-0.1634190	-1.1875520	-5.7510770
H	1.5879400	1.4344680	5.2128190
H	1.5767510	1.4484170	7.6741390
H	0.0000000	0.0000000	8.9203800
H	-1.5767510	-1.4484170	7.6741390
H	-1.5879400	-1.4344680	5.2128190
H	-0.3018830	-2.1176590	3.3739400
H	-0.3007970	-2.1181450	0.9244990
H	0.3007970	2.1181450	0.9244990
H	0.3018830	2.1176590	3.3739400
H	1.5634900	1.4603130	-0.9244990
H	1.5624700	1.4609250	-3.3739400
H	-1.5624700	-1.4609250	-3.3739400
H	-1.5634900	-1.4603130	-0.9244990
H	-0.2656050	-2.1233710	-5.2128190
H	-0.2834490	-2.1221950	-7.6741390
H	0.0000000	0.0000000	-8.9203800
H	0.2834490	2.1221950	-7.6741390
H	0.2656050	2.1233710	-5.2128190

S₁ alternating

C	0.7924300	0.9082380	5.7668040
C	-0.0000000	0.0000000	5.0272370
C	-0.7924300	-0.9082380	5.7668040
C	-0.7918470	-0.9030350	7.1458170
C	-0.0000000	0.0000000	7.8516470
C	0.7918470	0.9030350	7.1458170
C	-0.0000000	0.0000000	3.5855390
C	-0.4703320	-1.1099330	2.8356370
C	-0.4702680	-1.1143980	1.4706740
C	-0.0000000	0.0000000	0.7110070
C	0.4702680	1.1143980	1.4706740
C	0.4703320	1.1099330	2.8356370
C	-0.0000000	0.0000000	-0.7110070
C	-0.6443440	-1.0236490	-1.4706740
C	-0.6406470	-1.0211440	-2.8356370
C	-0.0000000	0.0000000	-3.5855390
C	0.6406470	1.0211440	-2.8356370
C	0.6443440	1.0236490	-1.4706740
C	-0.0000000	0.0000000	-5.0272370
C	0.2908590	1.1697190	-5.7668040
C	0.2869270	1.1662610	-7.1458170
C	-0.0000000	0.0000000	-7.8516470
C	-0.2869270	-1.1662610	-7.1458170
C	-0.2908590	-1.1697190	-5.7668040
H	1.4428280	1.5999130	5.2460210
H	1.4211410	1.6045190	7.6826410
H	-0.0000000	0.0000000	8.9354360
H	-1.4211410	-1.6045190	7.6826410
H	-1.4428280	-1.5999130	5.2460210
H	-0.7996870	-2.0013870	3.3548360
H	-0.8009330	-2.0091520	0.9595870
H	0.8009330	2.0091520	0.9595870
H	0.7996870	2.0013870	3.3548360
H	1.1885530	1.8070770	-0.9595870
H	1.1829000	1.8016090	-3.3548350
H	-1.1829000	-1.8016090	-3.3548350
H	-1.1885530	-1.8070770	-0.9595870
H	-0.4854990	-2.0989910	-5.2460220
H	-0.5016940	-2.0838490	-7.6826410
H	-0.0000000	0.0000000	-8.9354360
H	0.5016940	2.0838490	-7.6826410
H	0.4854990	2.0989910	-5.2460220

C Included Publications

S₂ alternating

C	0.3461190	-1.1512730	5.7516580
C	0.0000000	-0.0000000	5.0266860
C	-0.3461190	1.1512730	5.7516580
C	-0.3403400	1.1518780	7.1359980
C	0.0000000	-0.0000000	7.8353260
C	0.3403400	-1.1518780	7.1359980
C	0.0000000	-0.0000000	3.5684430
C	-0.7351640	0.9573620	2.8430910
C	-0.7388320	0.9571740	1.4515590
C	0.0000000	-0.0000000	0.7196920
C	0.7388320	-0.9571740	1.4515590
C	0.7351640	-0.9573620	2.8430910
C	0.0000000	-0.0000000	-0.7196910
C	-0.6457730	1.0222680	-1.4515590
C	-0.6472080	1.0188880	-2.8430910
C	0.0000000	-0.0000000	-3.5684430
C	0.6472080	-1.0188880	-2.8430910
C	0.6457730	-1.0222680	-1.4515590
C	0.0000000	-0.0000000	-5.0266860
C	0.9627720	-0.7199280	-5.7516580
C	0.9653230	-0.7147080	-7.1359980
C	0.0000000	-0.0000000	-7.8353260
C	-0.9653230	0.7147080	-7.1359980
C	-0.9627720	0.7199280	-5.7516580
H	0.5867850	-2.0649050	5.2229150
H	0.6001660	-2.0566240	7.6737430
H	0.0000000	-0.0000000	8.9194340
H	-0.6001660	2.0566240	7.6737430
H	-0.5867850	2.0649050	5.2229150
H	-1.3482030	1.6777390	3.3680010
H	-1.3475790	1.6853030	0.9362870
H	1.3475790	-1.6853030	0.9362870
H	1.3482030	-1.6777390	3.3680010
H	1.1209990	-1.8437950	-0.9362870
H	1.1136790	-1.8417870	-3.3680010
H	-1.1136790	1.8417870	-3.3680010
H	-1.1209990	1.8437950	-0.9362870
H	-1.7384760	1.2593050	-5.2229150
H	-1.7261080	1.2690360	-7.6737430
H	0.0000000	-0.0000000	-8.9194340
H	1.7261080	-1.2690360	-7.6737430
H	1.7384760	-1.2593050	-5.2229150

S_4 alternating

C	0.6069690	1.0493430	5.7647140
C	0.0000000	0.0000000	5.0256130
C	-0.6069690	-1.0493430	5.7647140
C	-0.6096780	-1.0410090	7.1415530
C	0.0000000	0.0000000	7.8481720
C	0.6096780	1.0410090	7.1415530
C	0.0000000	0.0000000	3.5813070
C	-0.2486290	-1.1807970	2.8372420
C	-0.2455620	-1.1762170	1.4617650
C	0.0000000	0.0000000	0.7304210
C	0.2455620	1.1762170	1.4617650
C	0.2486290	1.1807970	2.8372420
C	0.0000000	0.0000000	-0.7304230
C	-0.8236710	-0.8748450	-1.4617660
C	-0.8256690	-0.8799830	-2.8372430
C	0.0000000	0.0000000	-3.5813070
C	0.8256690	0.8799830	-2.8372430
C	0.8236710	0.8748450	-1.4617660
C	0.0000000	0.0000000	-5.0256130
C	0.5126670	1.0985010	-5.7647130
C	0.5042830	1.0959510	-7.1415520
C	0.0000000	0.0000000	-7.8481710
C	-0.5042830	-1.0959510	-7.1415520
C	-0.5126670	-1.0985010	-5.7647130
H	1.1128070	1.8506130	5.2401730
H	1.0943710	1.8471110	7.6810790
H	0.0000000	0.0000000	8.9317400
H	-1.0943710	-1.8471110	7.6810790
H	-1.1128070	-1.8506130	5.2401730
H	-0.3983910	-2.1191130	3.3569720
H	-0.3988110	-2.1087600	0.9305020
H	0.3988110	2.1087600	0.9305020
H	0.3983910	2.1191130	3.3569720
H	1.5004340	1.5344770	-0.9305030
H	1.5091610	1.5400600	-3.3569760
H	-1.5091610	-1.5400600	-3.3569760
H	-1.5004340	-1.5344770	-0.9305030
H	-0.8798760	-1.9720350	-5.2401700
H	-0.8875610	-1.9549170	-7.6810780
H	0.0000000	0.0000000	-8.9317390
H	0.8875610	1.9549170	-7.6810780
H	0.8798760	1.9720350	-5.2401700

C Included Publications

T₁ alternating

C	-1.1475270	0.3606200	5.7673450
C	0.0000000	0.0000000	5.0310780
C	1.1475270	-0.3606200	5.7673450
C	1.1437460	-0.3623540	7.1477840
C	0.0000000	0.0000000	7.8525030
C	-1.1437460	0.3623540	7.1477840
C	0.0000000	0.0000000	3.5871180
C	1.2080340	0.0374120	2.8335880
C	1.2142750	0.0418590	1.4742370
C	0.0000000	0.0000000	0.7029880
C	-1.2142750	-0.0418590	1.4742370
C	-1.2080340	-0.0374120	2.8335880
C	0.0000000	0.0000000	-0.7029880
C	1.2142740	-0.0418930	-1.4742370
C	1.2080330	-0.0374440	-2.8335880
C	0.0000000	0.0000000	-3.5871180
C	-1.2080330	0.0374440	-2.8335880
C	-1.2142740	0.0418930	-1.4742370
C	0.0000000	0.0000000	-5.0310780
C	-1.1475380	-0.3605870	-5.7673450
C	-1.1437560	-0.3623220	-7.1477830
C	0.0000000	0.0000000	-7.8525030
C	1.1437560	0.3623220	-7.1477830
C	1.1475380	0.3605870	-5.7673450
H	-2.0424930	0.6760220	5.2456790
H	-2.0392180	0.6566910	7.6839800
H	0.0000000	0.0000000	8.9361860
H	2.0392180	-0.6566910	7.6839800
H	2.0424930	-0.6760220	5.2456790
H	2.1551830	0.1056840	3.3544890
H	2.1676000	0.1049530	0.9674000
H	-2.1676000	-0.1049530	0.9674000
H	-2.1551830	-0.1056840	3.3544890
H	-2.1675970	0.1050130	-0.9674000
H	-2.1551800	0.1057410	-3.3544890
H	2.1551800	-0.1057410	-3.3544890
H	2.1675970	-0.1050130	-0.9674000
H	2.0425130	0.6759640	-5.2456790
H	2.0392360	0.6566350	-7.6839800
H	0.0000000	0.0000000	-8.9361860
H	-2.0392360	-0.6566350	-7.6839800
H	-2.0425130	-0.6759640	-5.2456790

T₂ alternating

C	-1.2083900	-0.1024650	5.7729604
C	0.0000000	0.0000000	5.0241274
C	1.2083900	0.1024650	5.7729604
C	1.2031180	0.0978450	7.1462874
C	0.0000000	0.0000000	7.8572974
C	-1.2031180	-0.0978450	7.1462874
C	0.0000000	0.0000000	3.5881054
C	1.1376900	0.4018770	2.8373254
C	1.1307610	0.4049010	1.4637674
C	0.0000000	0.0000000	0.7348894
C	-1.1307610	-0.4049010	1.4637674
C	-1.1376900	-0.4018770	2.8373254
C	0.0000000	0.0000000	-0.7348886
C	1.1307450	-0.4049440	-1.4637676
C	1.1376750	-0.4019200	-2.8373256
C	0.0000000	0.0000000	-3.5881056
C	-1.1376750	0.4019200	-2.8373256
C	-1.1307450	0.4049440	-1.4637676
C	0.0000000	0.0000000	-5.0241276
C	-1.2083860	0.1025130	-5.7729606
C	-1.2031140	0.0978940	-7.1462876
C	0.0000000	0.0000000	-7.8572976
C	1.2031140	-0.0978940	-7.1462876
C	1.2083860	-0.1025130	-5.7729606
H	-2.1570730	-0.1506710	5.2544144
H	-2.1421820	-0.1635250	7.6845834
H	0.0000000	0.0000000	8.9404374
H	2.1421820	0.1635250	7.6845834
H	2.1570730	0.1506710	5.2544144
H	2.0222250	0.7558520	3.3508194
H	2.0071390	0.7540900	0.9287204
H	-2.0071390	-0.7540900	0.9287204
H	-2.0222250	-0.7558520	3.3508194
H	-2.0071100	0.7541670	-0.9287206
H	-2.0221960	0.7559290	-3.3508186
H	2.0221960	-0.7559290	-3.3508186
H	2.0071100	-0.7541670	-0.9287206
H	2.1570670	-0.1507570	-5.2544146
H	2.1421750	-0.1636120	-7.6845836
H	0.0000000	0.0000000	-8.9404376
H	-2.1421750	0.1636120	-7.6845836
H	-2.1570670	0.1507570	-5.2544146

C Included Publications

T₃ alternating

C	-1.0953480	0.5299630	5.7659680
C	0.0000000	0.0000000	5.0371010
C	1.0953480	-0.5299630	5.7659680
C	1.0952280	-0.5295040	7.1437290
C	0.0000000	0.0000000	7.8561680
C	-1.0952280	0.5295040	7.1437290
C	0.0000000	0.0000000	3.5677430
C	1.1652740	0.2788230	2.8431650
C	1.1683600	0.2757770	1.4627240
C	0.0000000	0.0000000	0.7287830
C	-1.1683600	-0.2757770	1.4627240
C	-1.1652740	-0.2788230	2.8431650
C	0.0000000	0.0000000	-0.7287850
C	1.1683330	-0.2758970	-1.4627270
C	1.1652500	-0.2789310	-2.8431670
C	0.0000000	0.0000000	-3.5677470
C	-1.1652500	0.2789310	-2.8431670
C	-1.1683330	0.2758970	-1.4627270
C	0.0000000	0.0000000	-5.0370990
C	-1.0953320	-0.5300080	-5.7659660
C	-1.0952110	-0.5295490	-7.1437250
C	0.0000000	0.0000000	-7.8561670
C	1.0952110	0.5295490	-7.1437250
C	1.0953320	0.5300080	-5.7659660
H	-1.9287200	0.9622280	5.2239030
H	-1.9373050	0.9467440	7.6840460
H	0.0000000	0.0000000	8.9390520
H	1.9373050	-0.9467440	7.6840460
H	1.9287200	-0.9622280	5.2239030
H	2.0749780	0.5310880	3.3769110
H	2.0813350	0.5314300	0.9380110
H	-2.0813350	-0.5314300	0.9380110
H	-2.0749780	-0.5310880	3.3769110
H	-2.0812820	0.5316420	-0.9380140
H	-2.0749290	0.5312780	-3.3769170
H	2.0749290	-0.5312780	-3.3769170
H	2.0812820	-0.5316420	-0.9380140
H	1.9286830	0.9623050	-5.2238960
H	1.9372700	0.9468230	-7.6840450
H	0.0000000	0.0000000	-8.9390510
H	-1.9372700	-0.9468230	-7.6840450
H	-1.9286830	-0.9623050	-5.2238960

T₄ alternating

C	-1.1113640	0.4570660	5.7413175
C	0.0000000	0.0000000	5.0200115
C	1.1113640	-0.4570660	5.7413175
C	1.1080770	-0.4632920	7.1255045
C	0.0000000	0.0000000	7.8237785
C	-1.1080770	0.4632920	7.1255045
C	0.0000000	0.0000000	3.5575885
C	1.2093940	0.0581720	2.8417365
C	1.2112120	0.0600810	1.4470695
C	0.0000000	0.0000000	0.7211375
C	-1.2112120	-0.0600810	1.4470695
C	-1.2093940	-0.0581720	2.8417365
C	0.0000000	0.0000000	-0.7211165
C	1.2112110	-0.0600080	-1.4470595
C	1.2093880	-0.0581350	-2.8417165
C	0.0000000	0.0000000	-3.5575845
C	-1.2093880	0.0581350	-2.8417165
C	-1.2112110	0.0600080	-1.4470595
C	0.0000000	0.0000000	-5.0200205
C	-1.1115470	-0.4565830	-5.7413295
C	-1.1082790	-0.4627830	-7.1255195
C	0.0000000	0.0000000	-7.8237915
C	1.1082790	0.4627830	-7.1255195
C	1.1115470	0.4565830	-5.7413295
H	-1.9709550	0.8438560	5.2080245
H	-1.9732670	0.8335720	7.6636515
H	0.0000000	0.0000000	8.9079515
H	1.9732670	-0.8335720	7.6636515
H	1.9709550	-0.8438560	5.2080245
H	2.1466240	0.1542520	3.3732055
H	2.1538280	0.1469940	0.9284955
H	-2.1538280	-0.1469940	0.9284955
H	-2.1466240	-0.1542520	3.3732055
H	-2.1538370	0.1468250	-0.9284895
H	-2.1466330	0.1541730	-3.3731645
H	2.1466330	-0.1541730	-3.3731645
H	2.1538370	-0.1468250	-0.9284895
H	1.9713170	0.8430010	-5.2080585
H	1.9736490	0.8326460	-7.6636615
H	0.0000000	0.0000000	-8.9079645
H	-1.9736490	-0.8326460	-7.6636615
H	-1.9713170	-0.8430010	-5.2080585

S7.3 p5P

D₀ alternating

C	-1.1738910	0.2351780	7.9603890
C	0.0000000	-0.0000000	7.2214840
C	1.1738910	-0.2351780	7.9603890
C	1.1734760	-0.2314770	9.3437310
C	0.0000000	-0.0000000	10.0545230
C	-1.1734760	0.2314770	9.3437310
C	0.0000000	-0.0000000	5.7644800
C	1.1617870	0.2718210	5.0179380
C	1.1627960	0.2756740	3.6427440
C	0.0000000	-0.0000000	2.8867880
C	-1.1627960	-0.2756740	3.6427440
C	-1.1617870	-0.2718210	5.0179380
C	0.0000000	-0.0000000	1.4433890
C	1.1923890	-0.0749440	0.6863580
C	1.1923890	-0.0749440	-0.6863580
C	0.0000000	-0.0000000	-1.4433890
C	-1.1923890	0.0749440	-0.6863580
C	-1.1923890	0.0749440	0.6863580
H	2.1419820	-0.1817010	1.1992170
H	2.1419820	-0.1817010	-1.1992170
C	0.0000000	-0.0000000	-2.8867880
H	-2.1419820	0.1817010	-1.1992170
H	-2.1419820	0.1817010	1.1992170
H	2.0791510	0.5421570	3.1287330
H	2.0780420	0.5344980	5.5368180
H	-2.0780420	-0.5344980	5.5368180
H	-2.0791510	-0.5421570	3.1287330
H	2.0952640	-0.4541850	7.4330060
H	2.0994810	-0.4252470	9.8764660
H	0.0000000	-0.0000000	11.1388150
H	-2.0994810	0.4252470	9.8764660
H	-2.0952640	0.4541850	7.4330060
C	1.1627960	0.2756740	-3.6427440
C	1.1617870	0.2718210	-5.0179380
C	0.0000000	-0.0000000	-5.7644800
C	-1.1617870	-0.2718210	-5.0179380
C	-1.1627960	-0.2756740	-3.6427440
H	2.0791510	0.5421570	-3.1287330
H	2.0780420	0.5344980	-5.5368180
C	0.0000000	-0.0000000	-7.2214840
H	-2.0780420	-0.5344980	-5.5368180
H	-2.0791510	-0.5421570	-3.1287330
C	1.1738910	-0.2351780	-7.9603890
C	1.1734760	-0.2314770	-9.3437310
C	0.0000000	-0.0000000	-10.0545230
C	-1.1734760	0.2314770	-9.3437310
C	-1.1738910	0.2351780	-7.9603890
H	2.0952640	-0.4541850	-7.4330060
H	2.0994810	-0.4252470	-9.8764660
H	0.0000000	-0.0000000	-11.1388150
H	-2.0994810	0.4252470	-9.8764660
H	-2.0952640	0.4541850	-7.4330060

C Included Publications

S₀ alternating

C	-1.1588400	0.3067680	7.8999070
C	-0.0000000	0.0000000	7.1841980
C	1.1588400	-0.3067680	7.8999070
C	1.1591950	-0.3065990	9.2858160
C	-0.0000000	0.0000000	9.9851180
C	-1.1591950	0.3065990	9.2858160
C	-0.0000000	0.0000000	5.7100280
C	1.0977740	0.4729520	4.9894260
C	1.0977510	0.4732030	3.6062600
C	-0.0000000	0.0000000	2.8852930
C	-1.0977510	-0.4732030	3.6062600
C	-1.0977740	-0.4729520	4.9894260
C	-0.0000000	0.0000000	1.4126330
C	1.1620570	-0.2801980	0.6915110
C	1.1620570	-0.2801980	-0.6915110
C	-0.0000000	0.0000000	-1.4126330
C	-1.1620570	0.2801980	-0.6915110
C	-1.1620570	0.2801980	0.6915110
H	2.0709620	-0.5367340	1.2243720
H	2.0709620	-0.5367340	-1.2243720
C	-0.0000000	0.0000000	-2.8852930
H	-2.0709620	0.5367340	-1.2243720
H	-2.0709620	0.5367340	1.2243720
H	1.9500370	0.8800660	3.0733900
H	1.9501860	0.8788440	5.5228640
H	-1.9501860	-0.8788440	5.5228640
H	-1.9500370	-0.8800660	3.0733900
H	2.0617720	-0.5730350	7.3616370
H	2.0675410	-0.5561730	9.8229800
H	-0.0000000	0.0000000	11.0691910
H	-2.0675410	0.5561730	9.8229800
H	-2.0617720	0.5730350	7.3616370
C	1.0977510	0.4732030	-3.6062600
C	1.0977740	0.4729520	-4.9894260
C	-0.0000000	0.0000000	-5.7100280
C	-1.0977740	-0.4729520	-4.9894260
C	-1.0977510	-0.4732030	-3.6062600
H	1.9500370	0.8800660	-3.0733900
H	1.9501860	0.8788440	-5.5228640
C	-0.0000000	0.0000000	-7.1841980
H	-1.9501860	-0.8788440	-5.5228640
H	-1.9500370	-0.8800660	-3.0733900
C	1.1588400	-0.3067680	-7.8999070
C	1.1591950	-0.3065990	-9.2858160
C	-0.0000000	0.0000000	-9.9851180
C	-1.1591950	0.3065990	-9.2858160
C	-1.1588400	0.3067680	-7.8999070
H	2.0617720	-0.5730350	-7.3616370
H	2.0675410	-0.5561730	-9.8229800
H	-0.0000000	0.0000000	-11.0691910
H	-2.0675410	0.5561730	-9.8229800
H	-2.0617720	0.5730350	-7.3616370

S₁ alternating

C	-1.1768970	0.2462770	7.9169150
C	0.0000000	0.0000000	7.1851960
C	1.1768970	-0.2462770	7.9169150
C	1.1741040	-0.2477160	9.2983320
C	0.0000000	0.0000000	10.0021110
C	-1.1741040	0.2477160	9.2983320
C	0.0000000	0.0000000	5.7333170
C	1.1754900	0.2459740	4.9910220
C	1.1792330	0.2479450	3.6219230
C	0.0000000	0.0000000	2.8675890
C	-1.1792330	-0.2479450	3.6219230
C	-1.1754900	-0.2459740	4.9910220
C	0.0000000	0.0000000	1.4385610
C	1.2067710	-0.0011280	0.6820820
C	1.2067710	-0.0011280	-0.6820820
C	0.0000000	0.0000000	-1.4385610
C	-1.2067710	0.0011280	-0.6820820
C	-1.2067710	0.0011280	0.6820820
H	2.1587990	-0.0437660	1.1953300
H	2.1587990	-0.0437660	-1.1953300
C	0.0000000	0.0000000	-2.8675890
H	-2.1587990	0.0437660	-1.1953300
H	-2.1587990	0.0437660	1.1953300
H	2.1022290	0.4888040	3.1103420
H	2.0941350	0.4843460	5.5137580
H	-2.0941350	-0.4843460	5.5137580
H	-2.1022290	-0.4888040	3.1103420
H	2.0960160	-0.4748330	7.3908610
H	2.0939040	-0.4532140	9.8349030
H	0.0000000	0.0000000	11.0859860
H	-2.0939040	0.4532140	9.8349030
H	-2.0960160	0.4748330	7.3908610
C	1.1792330	0.2479450	-3.6219230
C	1.1754900	0.2459740	-4.9910220
C	0.0000000	0.0000000	-5.7333170
C	-1.1754900	-0.2459740	-4.9910220
C	-1.1792330	-0.2479450	-3.6219230
H	2.1022290	0.4888040	-3.1103420
H	2.0941350	0.4843460	-5.5137580
C	0.0000000	0.0000000	-7.1851960
H	-2.0941350	-0.4843460	-5.5137580
H	-2.1022290	-0.4888040	-3.1103420
C	1.1768970	-0.2462770	-7.9169150
C	1.1741040	-0.2477160	-9.2983320
C	0.0000000	0.0000000	-10.0021110
C	-1.1741040	0.2477160	-9.2983320
C	-1.1768970	0.2462770	-7.9169150
H	2.0960160	-0.4748330	-7.3908610
H	2.0939040	-0.4532140	-9.8349030
H	0.0000000	0.0000000	-11.0859860
H	-2.0939040	0.4532140	-9.8349030
H	-2.0960160	0.4748330	-7.3908610

C Included Publications

T₁ alternating

C	-1.1564420	0.3213850	7.9172570
C	0.0000000	-0.0000000	7.1917800
C	1.1564420	-0.3213850	7.9172570
C	1.1549520	-0.3224310	9.3006770
C	0.0000000	-0.0000000	10.0025160
C	-1.1549520	0.3224310	9.3006770
C	0.0000000	-0.0000000	5.7328100
C	1.1734770	0.2541330	4.9933550
C	1.1787340	0.2569760	3.6249780
C	0.0000000	-0.0000000	2.8654380
C	-1.1787340	-0.2569760	3.6249780
C	-1.1734770	-0.2541330	4.9933550
C	0.0000000	-0.0000000	1.4464490
C	1.2076560	0.1172700	0.6779530
C	1.2076560	0.1172700	-0.6779530
C	0.0000000	-0.0000000	-1.4464490
C	-1.2076560	-0.1172700	-0.6779530
C	-1.2076560	-0.1172700	0.6779530
H	2.1597300	0.1813150	1.1878480
H	2.1597300	0.1813150	-1.1878480
C	0.0000000	-0.0000000	-2.8654380
H	-2.1597300	-0.1813150	-1.1878480
H	-2.1597300	-0.1813150	1.1878480
H	2.1042470	0.4941640	3.1176130
H	2.0904710	0.4924360	5.5197940
H	-2.0904710	-0.4924360	5.5197940
H	-2.1042470	-0.4941640	3.1176130
H	2.0579730	-0.6055570	7.3872450
H	2.0597710	-0.5858830	9.8371920
H	0.0000000	-0.0000000	11.0864050
H	-2.0597710	0.5858830	9.8371920
H	-2.0579730	0.6055570	7.3872450
C	1.1787340	0.2569760	-3.6249780
C	1.1734770	0.2541330	-4.9933550
C	0.0000000	-0.0000000	-5.7328100
C	-1.1734770	-0.2541330	-4.9933550
C	-1.1787340	-0.2569760	-3.6249780
H	2.1042470	0.4941640	-3.1176130
H	2.0904710	0.4924360	-5.5197940
C	0.0000000	-0.0000000	-7.1917800
H	-2.0904710	-0.4924360	-5.5197940
H	-2.1042470	-0.4941640	-3.1176130
C	1.1564420	-0.3213850	-7.9172570
C	1.1549520	-0.3224310	-9.3006770
C	0.0000000	-0.0000000	-10.0025160
C	-1.1549520	0.3224310	-9.3006770
C	-1.1564420	0.3213850	-7.9172570
H	2.0579730	-0.6055570	-7.3872450
H	2.0597710	-0.5858830	-9.8371920
H	0.0000000	-0.0000000	-11.0864050
H	-2.0597710	0.5858830	-9.8371920
H	-2.0579730	0.6055570	-7.3872450

T₂ alternating

C	-1.2054540	0.0807890	7.9221800
C	0.0000000	0.0000000	7.1782810
C	1.2054540	-0.0807890	7.9221800
C	1.2005160	-0.0841430	9.2986560
C	0.0000000	0.0000000	10.0067470
C	-1.2005160	0.0841430	9.2986560
C	0.0000000	0.0000000	5.7402940
C	1.1819550	0.2490220	4.9874500
C	1.1780430	0.2499260	3.6187720
C	0.0000000	0.0000000	2.8795670
C	-1.1780430	-0.2499260	3.6187720
C	-1.1819550	-0.2490220	4.9874500
C	0.0000000	0.0000000	1.4203910
C	1.1466610	-0.3414270	0.6900980
C	1.1466610	-0.3414270	-0.6900980
C	0.0000000	0.0000000	-1.4203910
C	-1.1466610	0.3414270	-0.6900980
C	-1.1466610	0.3414270	0.6900980
H	2.0425820	-0.6505790	1.2159990
H	2.0425820	-0.6505790	-1.2159990
C	0.0000000	0.0000000	-2.8795670
H	-2.0425820	0.6505790	-1.2159990
H	-2.0425820	0.6505790	1.2159990
H	2.0937440	0.4894150	3.0905530
H	2.1027930	0.4909830	5.5024880
H	-2.1027930	-0.4909830	5.5024880
H	-2.0937440	-0.4894150	3.0905530
H	2.1505030	-0.1761050	7.4030890
H	2.1394140	-0.1601730	9.8359320
H	0.0000000	0.0000000	11.0901380
H	-2.1394140	0.1601730	9.8359320
H	-2.1505030	0.1761050	7.4030890
C	1.1780430	0.2499260	-3.6187720
C	1.1819550	0.2490220	-4.9874500
C	0.0000000	0.0000000	-5.7402940
C	-1.1819550	-0.2490220	-4.9874500
C	-1.1780430	-0.2499260	-3.6187720
H	2.0937440	0.4894150	-3.0905530
H	2.1027930	0.4909830	-5.5024880
C	0.0000000	0.0000000	-7.1782810
H	-2.1027930	-0.4909830	-5.5024880
H	-2.0937440	-0.4894150	-3.0905530
C	1.2054540	-0.0807890	-7.9221800
C	1.2005160	-0.0841430	-9.2986560
C	0.0000000	0.0000000	-10.0067470
C	-1.2005160	0.0841430	-9.2986560
C	-1.2054540	0.0807890	-7.9221800
H	2.1505030	-0.1761050	-7.4030890
H	2.1394140	-0.1601730	-9.8359320
H	0.0000000	0.0000000	-11.0901380
H	-2.1394140	0.1601730	-9.8359320
H	-2.1505030	0.1761050	-7.4030890

C Included Publications

T₃ alternating

C	-1.1980150	0.1818510	7.9200220
C	-0.0000000	0.0000000	7.1832130
C	1.1980150	-0.1818510	7.9200220
C	1.1948860	-0.1844870	9.2960330
C	-0.0000000	0.0000000	10.0059680
C	-1.1948860	0.1844870	9.2960330
C	-0.0000000	0.0000000	5.7281180
C	1.1456550	0.3499150	4.9938280
C	1.1437140	0.3516200	3.6135670
C	-0.0000000	0.0000000	2.8852790
C	-1.1437140	-0.3516200	3.6135670
C	-1.1456550	-0.3499150	4.9938280
C	-0.0000000	0.0000000	1.4222340
C	1.1684910	-0.3116910	0.6858880
C	1.1684910	-0.3116910	-0.6858880
C	-0.0000000	0.0000000	-1.4222340
C	-1.1684910	0.3116910	-0.6858880
C	-1.1684910	0.3116910	0.6858880
H	2.0688830	-0.5959830	1.2182340
H	2.0688830	-0.5959830	-1.2182340
C	-0.0000000	0.0000000	-2.8852790
H	-2.0688830	0.5959830	-1.2182340
H	-2.0688830	0.5959830	1.2182340
H	2.0365920	0.6660570	3.0850540
H	2.0406940	0.6656180	5.5166140
H	-2.0406940	-0.6656180	5.5166140
H	-2.0365920	-0.6660570	3.0850540
H	2.1262060	-0.3582770	7.3899790
H	2.1227720	-0.3406770	9.8348260
H	-0.0000000	0.0000000	11.0891430
H	-2.1227720	0.3406770	9.8348260
H	-2.1262060	0.3582770	7.3899790
C	1.1437140	0.3516200	-3.6135670
C	1.1456550	0.3499150	-4.9938280
C	-0.0000000	0.0000000	-5.7281180
C	-1.1456550	-0.3499150	-4.9938280
C	-1.1437140	-0.3516200	-3.6135670
H	2.0365920	0.6660570	-3.0850540
H	2.0406940	0.6656180	-5.5166140
C	-0.0000000	0.0000000	-7.1832130
H	-2.0406940	-0.6656180	-5.5166140
H	-2.0365920	-0.6660570	-3.0850540
C	1.1980150	-0.1818510	-7.9200220
C	1.1948860	-0.1844870	-9.2960330
C	-0.0000000	0.0000000	-10.0059680
C	-1.1948860	0.1844870	-9.2960330
C	-1.1980150	0.1818510	-7.9200220
H	2.1262060	-0.3582770	-7.3899790
H	2.1227720	-0.3406770	-9.8348260
H	-0.0000000	0.0000000	-11.0891430
H	-2.1227720	0.3406770	-9.8348260
H	-2.1262060	0.3582770	-7.3899790

Excitonic Coupling of a TADF Assistant Dopant and a Multi-Resonance TADF Emitter

Adv. Opt. Mater., 2402241 (2024)

Simon Metz, Christel M. Marian

Contribution: All quantum chemical calculations; preparation of all figures;
writing and revision of manuscript



Excitonic Coupling of a TADF Assistant Dopant and a Multi-Resonance TADF Emitter

Simon Metz and Christel M. Marian*

The excitation energy transfer (EET) between two conformers of the deep-blue thermally activated delayed fluorescence emitter DBA-BTICz and the multi-resonance fluorescence emitter ν -DABNA is studied by means of quantum chemistry according to Fermi's Golden Rule. Excitation energies, fluorescence and intersystem crossing rate constants of the individual EET donor and acceptor molecules, determined by a combination of density functional theory and a multireference configuration interaction approach, match the experimental data very well. Interestingly, two different conformers of DBA-BTICz with similar absorption, but distinct emission and transfer properties are found. The vibronic envelopes of the DBA-BTICz emission and the ν -DABNA absorption spectra are computed by means of a vertical Hessian approach. Their overall shapes and peak positions agree well with the experimental data but the widths of the computed vibronic spectra remain a critical factor in the evaluation of the spectral overlap integral. The distance and orientation dependencies of the excitonic coupling matrix elements, evaluated in the ideal dipole approximation (IDA), are carefully assessed by means of the monomer transition density (MTD) approach. Deviations between the IDA and MTD results of at most 20% at typical Förster radii justify the use of the computationally much less demanding IDA for estimating environmental and orientation effects on the EET rate.

high intensities.^[2] Their main disadvantage is the low internal quantum efficiency (IQE) which is limited to 25%.^[3] To reach an IQE of 100%, the electrically generated triplet excitons must be integrated into the light-emitting process. One approach to accomplish this goal is to utilize phosphorescent dyes.^[4] Drawbacks are environmental concerns and the high costs of the heavy-metal complexes as well as the low photochemical stability especially of the blue emitters.^[5–7] The third generation of OLEDs seeks to address these issues while maintaining 100% IQE. A mechanism known as thermally activated delayed fluorescence (TADF) is employed, whereby triplet excitons are up-converted to the singlet manifold through reverse intersystem crossing (rISC). One of the prerequisites for this process to take place is a small energy gap between the lowest-lying singlet and triplet states.^[8] To this end, typically charge-transfer (CT) character is introduced into the excited states. On the one hand, the small overlap of the hole and particle densities in donor–acceptor systems with spatially well

separated highest occupied molecular orbital (HOMO) and lowest unoccupied molecular orbital (LUMO) reduces the exchange interaction and hence the singlet–triplet splitting (ΔE_{ST}) as desired. On the other hand, it impairs the emissive properties of these dyes which tend to have low color purity and long exciton lifetimes. Multi-resonance (MR) TADF emitters, which are characterized by alternating HOMO and LUMO amplitudes on neighboring centers, are better off in this respect. While ΔE_{ST} remains small, their emission spectra are typically much narrower.^[9–14] The latest generation strives to combine the most advantageous properties of the previous OLED generations, namely 100% IQE and clear colors. Here, TADF molecules are used as assistant dopants to a fluorescence or MR-TADF emitter. The TADF molecules harvest singlet as well as triplet excitons. While the singlet excitons can be conveyed directly to the lowest excited singlet state on the fluorescent emitter by Förster resonance energy transfer (FRET), the triplet excitons have to undergo a rISC process first. Such systems are referred to as hyperfluorescent (HF) systems.^[15]

Excitation energy transfer (EET) processes in HF systems are particularly interesting from a theoretical point of view. Compared to typical FRET pairs consisting of two fluorophores, transition dipole moments of TADF molecules and hence EET rate constants are much smaller. Moreover, intersystem crossing (ISC)

1. Introduction

Organic light-emitting diodes (OLEDs) play a pivotal role in the contemporary display market, offering a number of advantages over other display technologies, such as true black and ultra-thin flexible screens.^[1] In the first OLED generation, fluorescent molecules were employed. These dyes exhibit excellent emission properties, high color purity (narrow emission spectrum) and

S. Metz, C. M. Marian
Institute of Theoretical and Computational Chemistry
Faculty of Mathematics and Natural Sciences
Heinrich Heine University Düsseldorf
40204 Düsseldorf, Germany
E-mail: Christel.Marian@hhu.de

The ORCID identification number(s) for the author(s) of this article can be found under <https://doi.org/10.1002/adom.202402241>

© 2024 The Author(s). Advanced Optical Materials published by Wiley-VCH GmbH. This is an open access article under the terms of the [Creative Commons Attribution-NonCommercial-NoDerivs](https://creativecommons.org/licenses/by-nc-nd/4.0/) License, which permits use and distribution in any medium, provided the original work is properly cited, the use is non-commercial and no modifications or adaptations are made.

DOI: [10.1002/adom.202402241](https://doi.org/10.1002/adom.202402241)

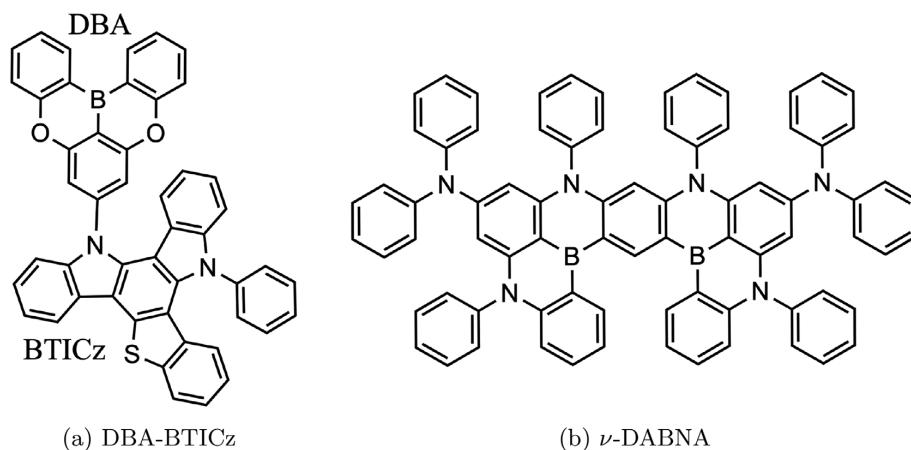


Figure 1. Chemical structures of the molecules investigated in this work. In the HF OLED, DBA-BTICz plays the role of the exciton harvester and FRET donor while ν -DABNA is the FRET acceptor and final emitter.

is an important competing process and has to be included in the modeling. While it is clear that the spectral overlap between the donor emission and acceptor absorption has to be large, little is known about the optimal ratio between fluorescence and ISC/rISC rate constants of the TADF donor. In view of further nonradiative deactivation channels such as internal conversion to the electronic ground state, a high FRET rate appears desirable.

Classical FRET theory is based on the ideal dipole approximation (IDA) describing the process as a long-range interaction between two transition dipoles located on the donor and the acceptor moiety, respectively.^[16,17] Since the IDA is known to fail at small donor–acceptor distances,^[18,19] more accurate, but at the same time computationally more demanding approaches were developed for modeling of the excitonic coupling matrix element (ECME) between the donor and acceptor. Among them are the transition density cube (TDC)^[20,21] and the monomer transition density (MTD)^[22–25] methods. Instead of transition dipole vectors with origin at the barycenter of the respective molecule, these methods employ delocalized transition density matrices. As the dopants used in HF devices are typically very large, the evaluation of the ECME by means of the MTD method poses a significant challenge. Striving for computational efficiency raises the question, how accurate the much less demanding IDA is in case of weak EET couplings.

To our knowledge, we here present the first application of the MTD method to a HF system. The FRET pair consists of the deep-blue TADF emitter DBA-BTICz as the assistant dopant and the MR-type TADF emitter ν -DABNA as the final fluorescence emitter (Figure 1) that were used by Braveenth et al.^[26] to fabricate a HF OLED device. The authors of this experimental study provide detailed information on the energetic position and kinetic constants of the involved states that can be used as reference data for the assessment of the theoretical models.

2. Theoretical Models

2.1. Excitation Energy Transfer Rate

In a weakly coupled system, the rate constant of an EET between a donor and acceptor molecule can be calculated according to Fermi's golden rule approach:

$$k_{\text{EET}} = \frac{2\pi}{\hbar} |V_{DA}|^2 \text{FCWDOS} \quad (1)$$

where V_{DA} is the excitonic coupling matrix element and FCWDOS represents the Franck–Condon weighted density of states. The latter is typically approximated by the spectral overlap integral, which is calculated as the integral of the product function of the donor's emission spectrum $E_D(\omega)$ and the acceptor's absorption spectrum $A_A(\omega)$. Both spectra have to be normalized to unit area. This approximation results in the following expression for the EET rate:

$$k_{\text{EET}} = \frac{2\pi}{\hbar} |V_{DA}|^2 \int_0^\infty A_A(\omega) E_D(\omega) d\omega \quad (2)$$

For the computation of vibrationally resolved electronic, i.e., vibronic spectra $A_A(\omega)$ and $E_D(\omega)$, various approaches can be employed. In the ideal case, in which the nuclei perform infinitesimal motions about their equilibrium positions, the choice of coordinates (Cartesian vs internal, e.g.) does not have significant impact on the resulting spectral shape. This changes when large-amplitude vibrational motions such as torsions or out-of-plane bending vibrations are excited upon an electronic transitions. In this case, typically internal coordinates are preferable as they represent the curvilinear displacements of the nuclei closer than the rectilinear Cartesian coordinates.^[27,28] Likewise, using adiabatic Hessian (AH) or vertical Hessian (VH) approaches for computing FC factors makes no difference as long as the potential energy surfaces (PESs) are strictly harmonic. In reality, this condition is

rarely fulfilled, however. The AH method simulates vibronic transitions using harmonic potentials of the initial and final states at their respective equilibrium positions and is therefore supposed to provide a good representation of the spectral origin and the wavelength regime close to the 0–0 transition.^[29–31] In contrast, the VH method extrapolates the final state PES from the gradients and Hessian at the FC point. The VH method is therefore expected to provide a better description of the peak maxima and short-time spectra where the nuclei have not fully adjusted to the electronic potential of the final state.

The computationally more demanding part to evaluate is the ECME. Several approaches were developed to calculate this term. For systems where the intramolecular distance is large compared to the molecular extensions of donor and acceptor, the coupling can be described by the IDA.^[16,17] The coupling is estimated as the long-range electrostatic interaction between the electric transition dipole moments μ

$$V_{DA}^{\text{IDA}} = \kappa \frac{|\mu_D||\mu_A|}{n^2 |R_{DA}|^3} \quad (3)$$

where $\mu_D = e \int \Psi_{0,D}^* \sum_n r_n \Psi_{1,D} dr_n$ refers to the donor emission and $\mu_A = e \int \Psi_{1,A}^* \sum_n r_n \Psi_{0,A} dr_n$ to the acceptor absorption. R_{DA} is the position vector connecting the barycenters of donor and acceptor, n the refractive index of the medium and κ describes the relative orientation between the transition dipole moments μ :

$$\kappa = n_D n_A - 3(e_{DA} n_D)(e_{DA} n_A) \quad (4)$$

Here, n_D and n_A are the unit vectors of the transition dipole moments and e_{DA} is the unit vector of the connection between the barycenters of the donor and acceptor.

A more sophisticated method is the monomer transition density approach elaborated by Fink et al.^[22,23] and later extended in our laboratory to include exchange contributions.^[24] Here, the ECME is described with the help of the spinless reduced one-electron transition density matrices (1-TDM) ρ_D and ρ_A :

$$V_{DA}^{\text{MTD}} = \sum_{i,j \in D} \sum_{k,l \in A} \rho_{ij}^D \rho_{kl}^A ((ij|kl) - \frac{1}{2} (il|kj)) \quad (5)$$

Here, i and j represent donor MOs, k and l acceptor MOs and $(ij|kl)$ is the electronic repulsion integral in Mulliken convention:

$$(ij|kl) = \int \psi_i^*(r_1) \psi_j(r_1) \frac{1}{r_{12}} \psi_k^*(r_2) \psi_l(r_2) dr_1 dr_2 \quad (6)$$

The construction of the dimer four-index two-electron integrals (Equation 6) is the computationally most demanding part. For being able to investigate dimer systems of the size presented in this work, a resolution-of-the-identity (RI) approximation in the Coulomb metric^[32,33] is made employing auxiliary basis sets.

$$(ij|kl) \approx (ij|kl)_{\text{RI}} = \sum_P B_{ij}^P B_{kl}^P \quad (7)$$

where B_{ij}^P are three-index two-electron integrals defined as

$$B_{ij}^P = \sum_Q (ij|Q)(Q|P)^{-1/2} \quad (8)$$

P and Q denote auxiliary basis functions and $(Q|P)$ is a two-index two-electron integral. Only the three-index two-electron integrals (Equation 8) are stored on disk from which the required four-index two-electron integrals are constructed later on-the-fly.

3. Computational Details

All geometry optimizations and vibrational frequency analyses were conducted using the Gaussian 16 program package.^[34] For the geometry optimizations of ground states, density functional theory (DFT) in combination with an optimally tuned range-separated hybrid functional LC- ω HPBE^[35,36] and the def2-SVP(P)^[37] basis set was employed. To reach a balanced description of CT and valence excitations, the range-separation parameter ω was tuned separately for both molecules (Figure S16, Supporting Information). Time-dependent DFT was employed for the optimization of singlet excited states. To avoid triplet instability problems,^[38] the Tamm–Dancoff approximation was used for excited triplet states. Note that TDDFT and TDDFT-TDA energies are not directly comparable. These methods are used here solely for geometry optimizations and vibrational frequency analyses. In order to converge the frequency analysis of ν -DABNA, the two-electron integral accuracy was decreased to 10^{-11} (default: 10^{-12}). Toluene solvation effects were accounted for by the polarizable continuum model (PCM).^[39–41] The point charges generated by the self-consistent reaction field in the geometry optimization step were then exported and reused in subsequent multireference configuration interaction (MRCI) and ECME calculations.

Excitation energies and 1-TDM were calculated with the semiempirical DFT/MRCI method^[42,43] working with the TURBOMOLE package^[44,45] for generating MOs and two-electron integrals. MOs were optimized employing the BH-LYP functional^[46] as the DFT/MRCI Hamiltonians are parameterized for this hybrid functional. Two-electron integrals were computed in the RI approximation using the MP2 optimized auxiliary basis sets^[47] for the resolution of the identity. The redesigned R2016 Hamiltonian^[48] in conjunction with a configuration selection threshold of $0.8 E_h$ was used in the DFT/MRCI calculations. In the singlet and triplet manifolds, 15 roots were considered for DBA-BTICz and 10 roots for ν -DABNA. Fragment-based characterization of the DFT/MRCI wave function was performed with the TheoDRE program,^[49] while transition densities were computed using ORBKIT.^[50] Electronic spin–orbit coupling matrix elements (SOCMEs) between DFT/MRCI wave functions were determined with Spock^[51,52] employing the Breit–Pauli Hamiltonian in atomic mean-field approximation. All plots of molecular orbitals and densities were created with Jmol.^[53] Overlays of ground- and excited-state minimum geometrical structures were visualized with VMD.^[54] Temperature dependent intersystem crossing rate constants and vibronic spectra were calculated with a recent extension^[31] of the VIBES program. Unless noted otherwise, emission spectra were computed^[55,56] in internal coordinates using the VH approach. Before the

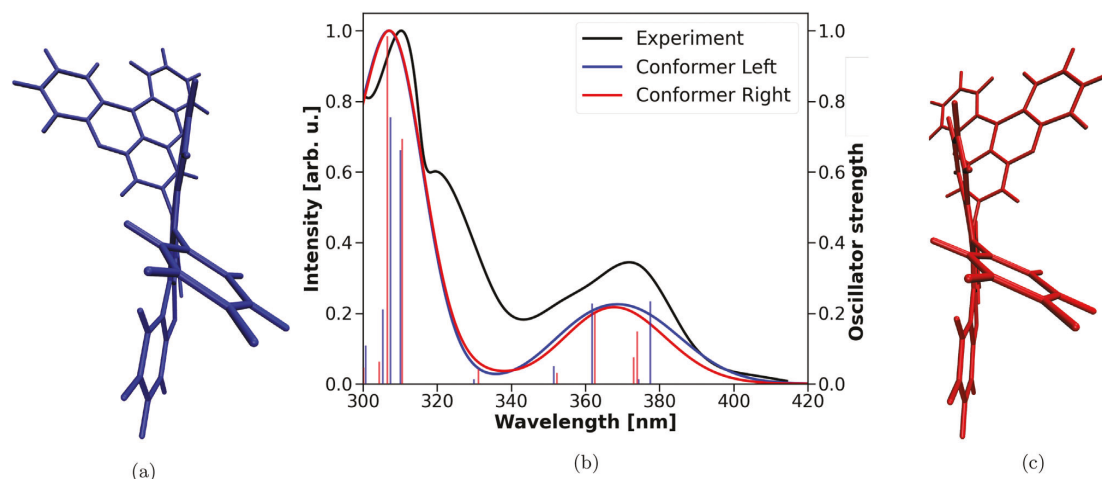


Figure 2. a) Left conformer of DBABTICz. b) Calculated Gaussian-broadened absorption spectra of the two DBA-BTICz conformers (FWHM: 2000 cm^{-1}) together with an experimental spectrum in toluene.^[26] c) Right conformer of DBABTICz.

Fourier transformation, the autocorrelation function was multiplied by a Gaussian damping function of 200 cm^{-1} full width at half-maximum (FWHM). Integration was performed on a time interval of 300 fs using a grid of 16384 (2^{14}) points. The MTD calculations were carried out with the singlet and triplet excitation energy transfer (STREET) program developed in our group. Required input files are the donor and acceptor monomer 1-TDM from preceding DFT/MRCI calculations as well as the monomer MOs and control and basis set files in TURBOMOLE format. From these, a new set of TURBOMOLE files for the dimer is created. While orthogonalization corrections might become necessary for short monomer separations.^[57] During the merge step, the molecules can be translated and rotated. To avoid a recalculation of the one-electron (transition) density matrices and MOs for every arrangement of the monomers in space, these can be transformed to the new set of coordinates.^[19] The generation of the two-electron integrals according to Equation (7) is the computationally most expensive step and determines the speed of the MTD calculation. In the RI expansion of the dimer four-index two-electron integrals, the same atom-centered auxiliary basis sets are used as for the monomer calculations. To reduce the computational demands, a frozen core and anticore can be defined. A test calculation has shown that MOs with energies below $-3.0 E_h$ and above $+2.0 E_h$ can be frozen in this step without significant loss of accuracy (Table S27, Supporting Information). To further speed up the subsequent computation of the ECME, a threshold can be applied to the transition density matrices to omit the integral contraction for negligible density contributions.

For the calculation of the spectral overlap, a polynomial spline is fitted to the donor emission and acceptor absorption spectrum to construct the product and integrate it. The spline is constructed in an adaptive manner, with additional segments being added in regions that require greater flexibility. In order to guarantee a good fit between the original data and the polynomial spline, the normalized root-mean-squared deviation

(NRMSD) is minimized until a convergence criterion of 10^{-4} is met.

4. Results and Discussion

4.1. Assistant Dopant—DBA-BTICz

The assistant dopant for the hyperfluorescent system is a reported TADF molecule with a dihydrobenzo-thieno-indolo-carbazol (BTICz) donor and an oxygen-bridged boron (DBA) acceptor moiety (Figure 1a).^[26] For this molecule, two ground-state conformers were found (Figure 2a,c), which differ mainly in the orientation of the DBA moiety with respect to the BTICz. The blue-colored structure in Figure 2 is named left conformer, because the acceptor is in this view located left of the donor. Correspondingly, the other conformer is labeled the right conformer. The right conformer was found when we started the geometry optimization from the B3LYP/6-31G ground-state structure published by Braveenth et al.^[26] An extensive search for the T_{CT} excited-state minimum led to a structure resembling the left conformer. The two conformers are basically isoenergetic and are separated by a small energy barrier of 10 kJ mol^{-1} at most in the electronic ground state (Figure S1, Supporting Information).

Despite their structural differences, the conformers exhibit very similar absorption behaviors. A comparison of the calculated spectra with the experimental spectrum in toluene^[26] (Figure 2b) may serve as a first quality check to ascertain the suitability of the applied quantum chemical methods. Especially the first absorption band between 340 and 400 nm is very well described by the calculations. A closer look reveals that not only the absorption of the first excited singlet state but up to four singlet states have a significant contribution to this absorption band. Despite being mostly of CT character, the S_1 state (S_{CT}) has appreciable oscillator strength in both conformers (Table S1, Supporting Information). Their wave function compositions are dominated by HOMO-1 \rightarrow LUMO and HOMO \rightarrow LUMO excitations, with a

preference for the former in the left conformer (Table S2, Supporting Information) and for the latter in the right conformer (Table S3, Supporting Information). The LUMO is localized on the DBA moiety, with the largest amplitude for the empty boron π orbital (Figures S2d and S3e, Supporting Information). HOMO-1 and HOMO are π orbitals localized on the BTICz moiety. In addition to the trivial nodes in the BTICz molecular plane, the HOMO-1 orbital exhibits a structure with nodal planes at nearly right angles with the donor–acceptor linkage (Figures S2b and S3c, Supporting Information) whereas the nodal planes are nearly parallel to this bond in the HOMO (Figures S2c and S3d, Supporting Information). It is this nodal structure that determines the transition dipole moment. With a value of $f=0.234$, the oscillator strength of the $S_1 \leftarrow S_0$ absorption is higher in the left conformer than in the right conformer ($f=0.148$). In exchange, the right conformer has a more intense absorption into the S_2 state (left: $f=0.013$, right: $f=0.076$), which leads to nearly identical absorption envelopes for both conformers in total.

The triplet wave functions of both conformers have very similar compositions at the S_0 geometry (Figure S4, Supporting Information). T_1 and T_2 have mostly locally excited (LE) character, where T_1 exhibits a local transition on the BTICz unit (T_{BTICz}) and T_2 a transition on the DBA moiety (T_{DBA}). In the FC region, these states are followed by three further triplet states with mixed LE and CT character.

To determine the EET capabilities of DBA-BTICz, geometry-relaxed nuclear structures of the lowest-excited electronic states are required. For both conformers, the lowest excited singlet state (S_{CT}) and the two lowest triplets states (T_{BTICz} , T_{DBA}) were optimized. Due to PES crossings in the triplet manifold during the optimization, the minimum on the T_{CT} PES could not be found. We therefore use its energetic position at the corresponding S_{CT} minimum geometry as proxy to its true minimum energy. The structural differences between the optimized geometries of the excited states can be seen in Figure S5 (Supporting Information). For S_{CT} and T_{DBA} , the main adjustment in comparison with the ground state refers to the relative orientation of the DBA and BTICz moieties. For T_{BTICz} , this orientation is more similar to the ground state and the biggest displacements happen at the indole and benzothiophene nuclear frames.

The calculated adiabatic S_{CT} energy (3.23 eV in both conformers) is 0.1 eV higher than the onset of the experimental room-temperature luminescence spectrum (3.13 eV) in toluene, as reported by Braveenth et al.^[26] Zero-point vibrational energy (ZPVE) corrections lower the computed emission energies, resulting in 0-0 transition energies of 3.09 and 3.10 eV for the left and right conformers, respectively. The experimental fluorescence spectrum of DBA-BTICz is very well reproduced by the calculated vertical Hessian spectra of the two conformers (Figure 3). The onset and the maximum are nearly perfectly matched. Solely the band width is somewhat too high in comparison to the experiment. Due to large-amplitude displacements of the S_{CT} and S_0 nuclear frames in a shearing coordinate (cp. Figure S5, Supporting Information), the more commonly used adiabatic Hessian approach^[55] is not applicable in this case (Figure S7, Supporting Information).

The S_{CT} states of both conformers originate predominantly from HOMO→LUMO transitions at their respective minimum geometries, but the respective HOMOs have different shapes.

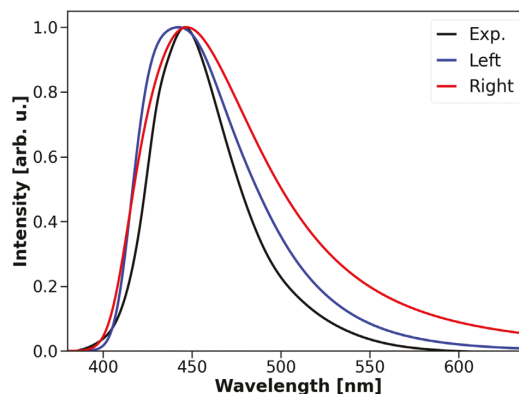


Figure 3. Calculated fluorescence spectra of DBA-BTICz with the VH approach at 300 K in comparison to a experimental spectrum in toluene solution.^[26]

The HOMO of the left conformer (Figure S8a, Supporting Information) closely resembles the HOMO-1 orbital at the ground-state minimum (Figure S2b, Supporting Information). It has a non-negligible amplitude at the carbazole nitrogen atom connecting the donor to the acceptor moiety and exhibits nodal planes at nearly right angles with this C–N bond. In contrast, the HOMO of the right conformer (Figure S8b, Supporting Information) corresponds to the HOMO at the ground-state minimum (Figure S3c, Supporting Information). It has higher contributions of the sulfur p-orbital and exhibits nodal planes nearly parallel to the donor–acceptor linkage. These differences in the orbital nodal structures lead to different directions of the transition dipole moment vectors (TDMVs). They are easily spotted when the transition densities (Figure 4, bottom) of the excitations are compared. The corresponding difference densities (Figure 4, top) reflect the charge flow upon excitation and are less informative with regard to the orientation of the TDMVs. The calculated fluorescence rate constant of the right conformer amounts to $k_{\text{F}} = 6.2 \times 10^6 \text{ s}^{-1}$, in excellent agreement with the radiative rate constant $k_{\text{r},\text{S}} = 7.5 \times 10^6 \text{ s}^{-1}$ of the excited singlet state derived from time-resolved measurements in DBFPO film.^[26] The fluorescence rate constant of the left conformer ($k_{\text{F}} = 6.5 \times 10^7 \text{ s}^{-1}$) is one order magnitude higher. According to Förster theory, the FRET rate of a fluorophore is roughly proportional to its radiative rate constant.^[16,17] We therefore expect the rate constant k_{EET} for the EET from the S_{CT} state of the left conformer to ν -DABNA to be higher than from the right conformer. However, the FRET efficiency of a TADF molecule, Φ_{FRET} , in addition strongly depends on its ISC rate constant (see below, Equation 9). The question thus arises how the different electronic structures of the two S_{CT} states affect the ISC probabilities.

Adiabatic ΔE_{ST} values of TADF emitters that are required for computing ISC and rISC rate constants are notoriously difficult to model.^[58] In particular, spectral shifts of CT transitions in toluene are much larger than may be expected from the relative permittivity $\epsilon = 2.38$ of that solvent. A recent computational study on the photophysical properties of a donor–acceptor TADF compound in the presence of two explicitly treated toluene molecules

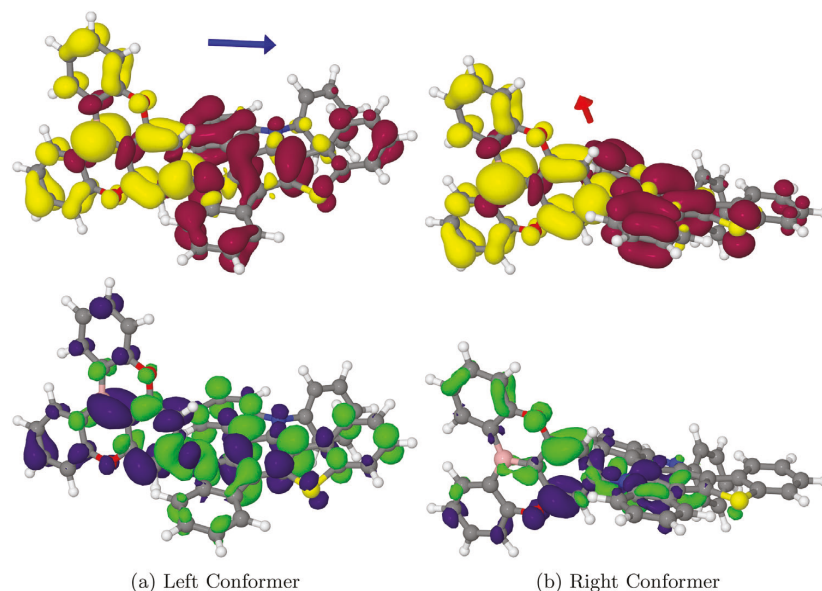


Figure 4. Top: Difference densities (isosurface ± 0.001) and the TDMV of the $S_0 \rightarrow S_{CT}$ transition of both DBA-BTICz conformers at the optimized S_{CT} geometry. Red-colored areas indicate a loss of electron density, yellow-colored areas again with respect to the ground-state density. Bottom: Corresponding transition densities (isosurface ± 0.0003) of the $S_0 \rightarrow S_{CT}$ excitation. Positive values are colored purple and negative values green. Note that the sign of the transition dipole moment is arbitrary.

revealed that the S_{CT} state was especially susceptible to excitonic coupling between the solute and the solvent, in addition to the electrostatic interaction mimicked by the PCM.^[59]

The adiabatic excitation energies and the characters of the excited states at their optimized geometries are given in Table 1 and visualized in Figure 5. The lowest triplet state of DBA-BTICz is the T_{BTICz} state, with predominantly LE character on the BTICz moiety. With a value of 2.83 eV, its adiabatic excitation energy in the right conformer is in perfect agreement with the onset of the experimental low-temperature photoluminescence spectra in toluene.^[26] Correspondingly, the adiabatic ΔE_{ST} value of 0.40 eV overestimates the experimental value of 0.29 eV, determined as the difference between the onsets of the room-temperature and low-temperature luminescence spectra,^[26] by 0.11 eV. To test the influence of the singlet–triplet energy gap on the ISC and rISC rate constants, we performed rate constant calculations in FC approximation using the adiabatic Hessian approach implemented in the VIBES program^[55] with two different setups: The

first was based on ΔE_{ST} values as obtained by the DFT/MRCI method, the second used vertically shifted potentials matching the experimental energy gap. The shift changes the vibrational density of states of the final state at the energy of the initial state, while the SOCME, which enters the Fermi golden rule expression quadratically,^[60] is unaltered. Comparing the results for both setups in Table S4 (Supporting Information) shows that the actual value of the energy gap influences the ISC rate constant only moderately. Shifting the energy gap to the experimental value reduces the rate constant for the $S_{CT} \leftrightarrow T_{BTICz}$ ISC from 4.2×10^6 to 3.2×10^6 s⁻¹. At first sight, this reduction of the transition probability appears to contradict the energy gap law. One should keep in mind, however, that an exponential increase of the rate constant with decreasing energy gap can be expected only in the case of nested potentials.^[60,61] In the strong coupling case, in which the potentials are markedly displaced in some vibrational coordinates, a Gaussian-shaped dependence of the rate constant on the energy separation is usually observed. Obviously, the $S_{CT} \leftrightarrow$

Table 1. Computed adiabatic and 0–0 excitation energies [eV] and excited-state character [%] of the optimized DBA-BTICz states.

State	Left					Right				
	Adiabatic	0–0	CT	LE _{BTICz}	LE _{DBA}	Adiabatic	0–0	CT	LE _{BTICz}	LE _{DBA}
S_{CT}	3.23	3.09	75.3	8.1	6.4	3.23	3.10	80.6	3.3	6.0
T_{CT} ^{a)}	3.19		33.5	40.1	19.4	3.22		60.7	3.8	26.6
T_{DBA}	2.97	2.85	8.2	31.0	54.6	2.93	2.82	4.1	0.6	88.2
T_{BTICz}	2.72	2.59	9.3	84.1	0.8	2.83	2.66	2.2	93.5	0.1

^{a)} Data taken from the S_{CT} geometries.

T_{BTICz} transition is located in the inverted energy regime of the latter coupling case where the rate constant increases with increasing energy separation of the potentials. Together with the $S_{\text{CT}} \rightarrow T_{\text{DBA}}$ transition to the second triplet state, a LE state localized on the DBA acceptor, the deactivation of the S_{CT} population of the right conformer by ISC reaches rate constants of the same size ($\approx 10^7 \text{ s}^{-1}$) as the radiative deactivation by fluorescence. The reverse transition, $T_{\text{BTICz}} \leftarrow S_{\text{CT}}$, needs thermal activation. This process therefore benefits appreciably from a reduced energy gap. Nevertheless, with a rate constant of about 10^2 s^{-1} at an assumed energy gap of 0.29 eV, rISC from T_{BTICz} to S_{CT} appears to be quite inefficient in the right conformer, unless a spin-vibronic mechanism^[62] involving the intermediate T_{DBA} and T_{CT} states is operative in the rISC process.

In the left conformer, the computed adiabatic ΔE_{ST} separation between the S_{CT} and T_{BTICz} state is even larger (0.51 eV). This difference may be explained by the fact that the T_{BTICz} states of the conformers originate from LEs on different parts of the BTICz unit. For the left conformer (Figure S6c, Supporting Information), the benzothiophen subunit is more involved in the LE while for the right conformer (Figure S6f, Supporting Information) the excitation is shifted toward one of the indole subunits. The different charge distributions have direct consequences for the SOC between T_{BTICz} and S_{CT} which is significantly higher in the left conformer at the S_{CT} geometry than its counterpart in the right conformer (Table S4, Supporting Information). Moreover, our VIBES calculations yield larger FCWDS values for this relative orientation of the BTICz and DBA units, resulting in ISC rate constants of about $10^7 - 10^8 \text{ s}^{-1}$ for the left conformer. While the computed $T_{\text{BTICz}} \leftarrow S_{\text{CT}}$ rISC rate constant at an assumed energy gap of 0.29 eV ($2 \times 10^2 \text{ s}^{-1}$) is much larger for this conformer (Table S4, Supporting Information), the transition is too slow to explain the experimentally observed delayed fluorescence decay time of 6.5 μs .^[26] Again, spin-vibronic interactions involving the intermediate T_{DBA} and T_{CT} states are supposed to speed up the rISC process.^[62] We have refrained from performing such calculations as they are computationally very resource extensive and because they have little relevance for the EET process as such.

4.2. Fluorescent Emitter - ν -DABNA

The fluorescent emitter of the HF-OLED ν -DABNA (Figure 1b) is a reported MR TADF molecule with a very narrow emission band in the pure-blue region.^[11,13] For this molecule two ground-state conformers were found (Figure S11, Supporting Information), which differ by the orientation of the peripheral phenyl rings of the diphenylamine substituents. Because the conformers have almost identical ground-state and excited-state energies and the excitations are mainly located on the core unit, only one of the conformers is discussed.

The ground-state and all calculated excited-state geometries have C_2 symmetry. The first two excited singlet and triplet states have multiresonance character where the hole and particle densities are located on alternating atoms (Figure 6). S_1 and T_1 are corresponding B -symmetric states with the TDMV of the singlet state parallel to the long axis, while S_2 and T_2 are A -symmetric where the TDMV of the S_2 state is orientated along the short axis which coincides with the symmetry axis. For a better understand-

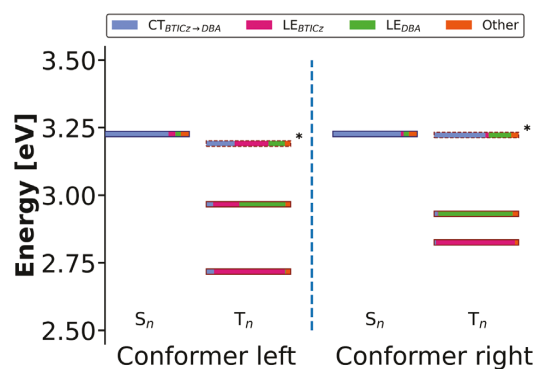


Figure 5. Adiabatic DFT/MRCI energies of the low-lying DBA-BTICz excited states and TheoDORE analysis results at their respective minimum geometries. *State could not be optimized, data are taken from the S_{CT} geometry.

ing of the difference between the S_1 and S_2 excitations, we refer to the shapes of the MOs involved in these transitions (Figure S13, Supporting Information).

In Figure S9, an experimental absorption spectrum in toluene is compared to a Gaussian-broadened line spectrum and an overlay of the adiabatic vibronic spectra of the $S_1 \leftarrow S_0$ and $S_2 \leftarrow S_0$ transitions. The peak maximum of the $S_1 \leftarrow S_0$ band in the Gaussian-broadened line spectrum is markedly blue shifted to the first experimental peak. The blue shift of the $S_2 \leftarrow S_0$ transition is less severe. The S_1 peak position and shape of the computed FC spectrum match their experimental counterparts very well, whereas the second peak is red shifted. In both calculated spectra, the intensity ratio of the second and first peaks is overestimated in comparison to the experiment. In this case, an AH approach was chosen for the calculation of the absorption spectrum of ν -DABNA (Figure 7). The DABNA core is relatively rigid, with the largest geometric change between the bond lengths of the S_0 and S_1 structures being below 0.01 Å (Table S7, Supporting Information). This leads to very similar shapes of AH and VH spectra (Figure S10, Supporting Information), but slightly shifted origins (ca. 400 cm^{-1}).

The calculated adiabatic S_1 energy of 2.81 eV is in proximity of the experimental onset of the fluorescence spectra of 2.75 eV.^[13] Stavrou et al. determined a singlet–triplet energy gap of ≤ 70 meV from spectral origins in different media at 20 K which increases to about 120 meV at 80 K.^[13] A similar ΔE_{ST} value of ca. 70 meV was deduced by Kondo et al. from an Arrhenius plot of the rISC activity.^[11] The B -symmetric T_1 exhibits an adiabatic excitation energy of 2.60 eV, 0.09 eV lower than the experimentally determined onset of the phosphorescence at 20 K (2.69 eV).^[13] With a value of about 200 meV, the calculated energy difference between S_1 and T_1 is therefore higher than the experimentally determined ΔE_{ST} value. We find the A -symmetric T_2 state adiabatically at 2.68 eV, about 120 meV below the S_1 state, which supports the assumption that this state is involved in the rISC process of ν -DABNA.^[11,13] This statement also fits with the theoretical work done on the smaller but similar molecule DABNA-1.^[63,64]

The calculated fluorescence rate constant (k_f) of 2.3×10^8 matches the experimental value of 2.4×10^8 in a 0.25 μM toluene

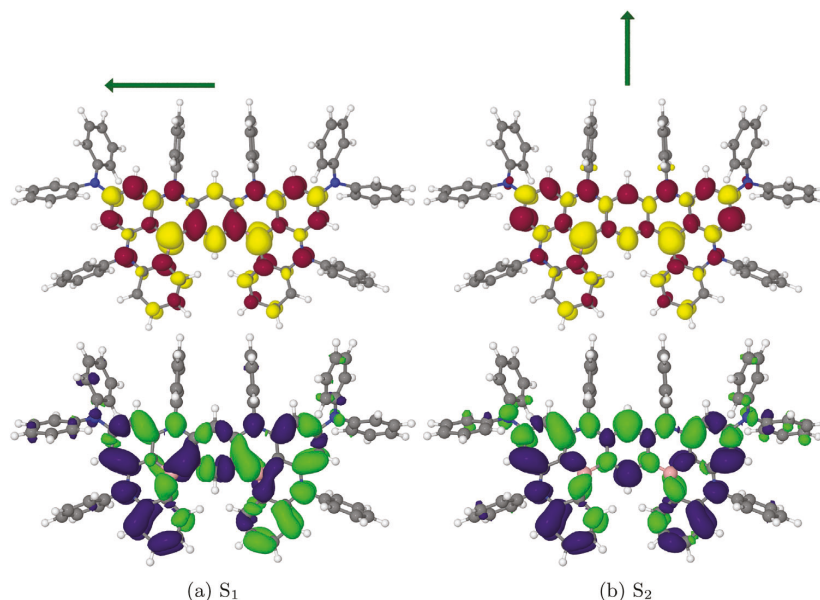


Figure 6. Top: Difference density (isovalue ± 0.001) and direction of transition dipole moment of the S_1 and S_2 state at the ground-state minimum geometry of ν -DABNA. Bottom: Transition densities (isosurface ± 0.0003) of the $S_0 \rightarrow S_1$ and $S_0 \rightarrow S_2$ transition of ν -DABNA. For color codes, see Figure 4.

solution very well.^[13] The calculated adiabatic fluorescence spectrum is a little bit too broad but otherwise in good agreement with the experimental one (Figure 8).

4.3. Excitation Energy Transfer

This section deals with the EET calculations on the two previously elaborated molecules. The rate constant is calculated according to Equation 2, which consists of an electronic part, i.e., the squared ECME, and the spectral overlap integral.

First, the dependence of the EET rate constant on the spectral overlap is discussed. In Figure 9, the overlaps between the

normalized emission spectra of the S_{CT} state of DBA-BTICz molecule and the normalized absorption spectra of the S_1 state of ν -DABNA are visualized. For each setup, the spectral overlap integral (in inverse wavenumber units) is listed as well. As mentioned before, the computed FC spectra are a little bit too broad in comparison to the experimental ones (Figure 9a). As a consequence, the corresponding overlap integrals of the FC spectra substantially are larger than the one obtained when the experimental spectrum of DBA-BTIC in toluene solution is employed instead. Note, however, that the experimental emission spectrum of DBA-BTIC in film (Figure 9d) is red-shifted with respect to the corresponding spectrum in toluene solution (Figure 9a) by about 900 cm^{-1} . This shift of the DBA-BTIC emission further

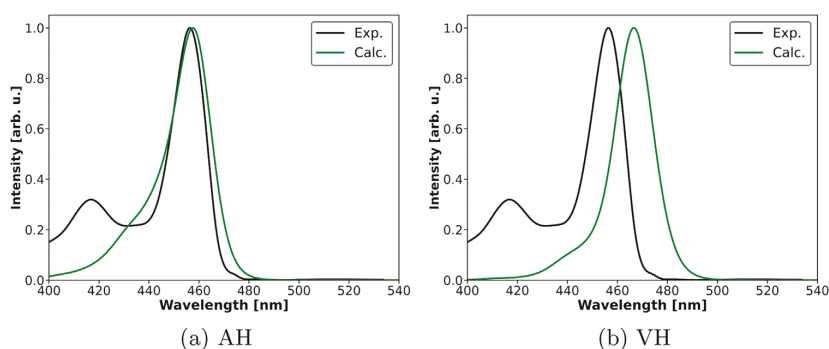


Figure 7. Calculated room-temperature S_1 absorption spectra of ν -DABNA in AH and VH approximation compared to an experimental spectrum in toluene.^[13]

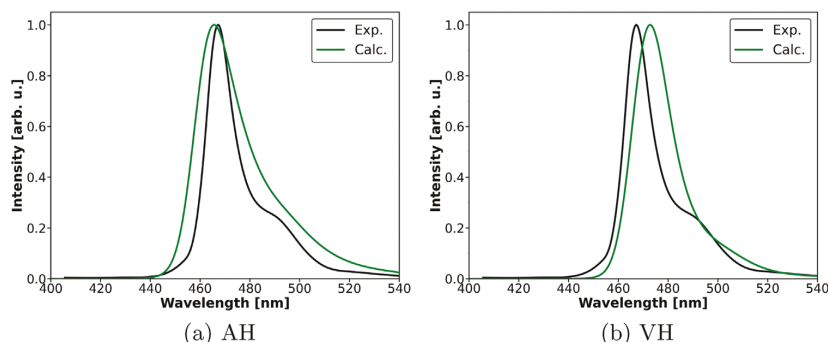


Figure 8. Experimental fluorescence spectrum of ν -DABNA in toluene at room temperature^[13] compared to calculated AH and VH spectra.

reduces the spectral overlap with the ν -DABNA absorption from its value of 5.9×10^{-5} cm in toluene to 4.3×10^{-5} cm in film. These examples clearly demonstrate how sensitive the spectral overlap integral—and hence the EET rate constant—can be with regard to even small variations of the spectral width.

The second factor entering Equation (2) is the squared ECME. Because the molecules are already large by themselves with 140 (ν -DABNA) and 81 (DBA-BTICz) atoms, respectively, it is not feasible to examine them in a supermolecular picture. Therefore, monomer-based approaches were used to determine the ECME. As described in Section 2.1, the IDA rests on the dipole-dipole

interaction of the transition moments while the MTD approach utilizes spinless reduced one-electron transition density matrices and two-electron integrals. The 1-TDMs are calculated with the DFT/MRCI method, a very cost efficient approach for such big molecules.

The ECME is strongly dependent on the distance and the relative orientation of donor and acceptor. In the IDA, the orientation factor κ^2 is a measure for how effective the energy transfer can be. It describes the relative orientation between the TDMVs of donor and acceptor (see Equation 4). The κ^2 values range between 0 for a perfectly perpendicular orientation of the TDMVs and 4

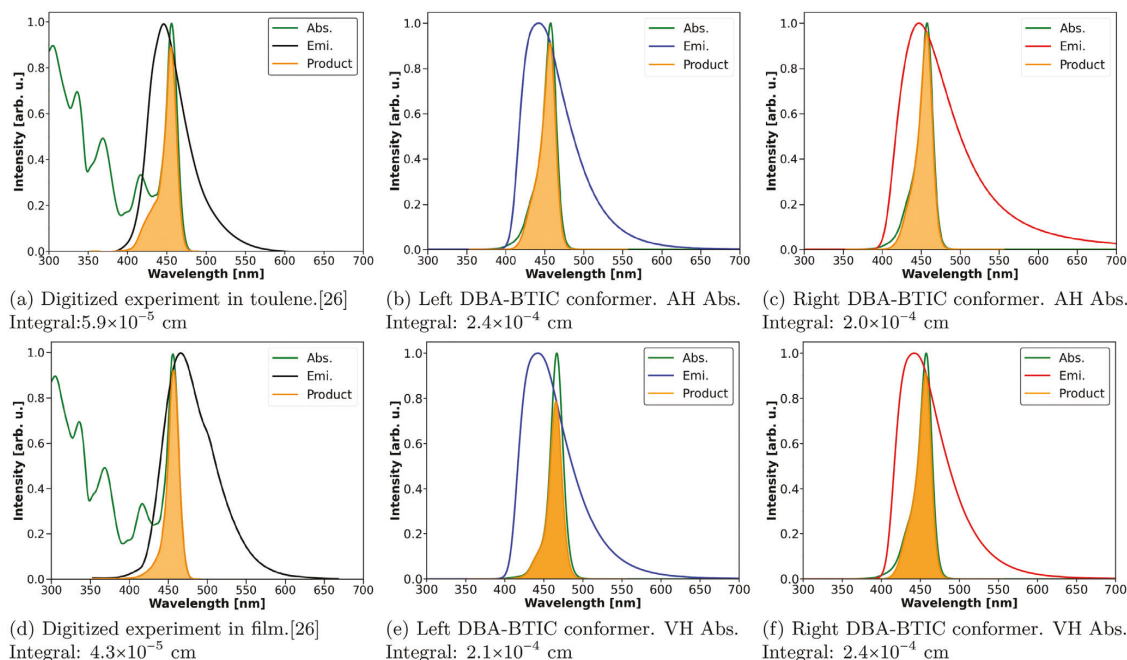


Figure 9. Spectral overlap between the DBA-BTICz fluorescence and ν -DABNA absorption spectra for the two DBA-BTICz conformers in toluene solution and the corresponding digitized experimental spectra.^[26]

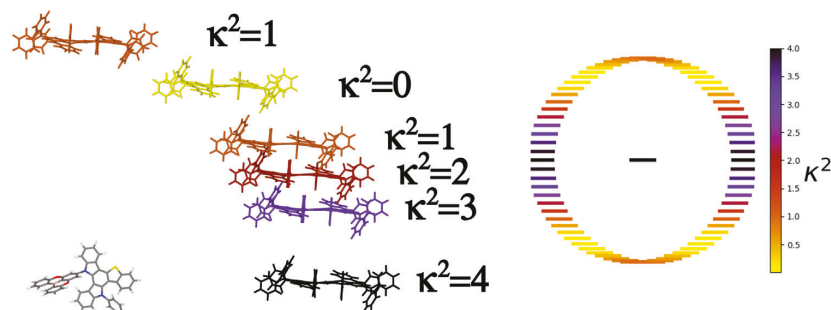


Figure 10. Left: κ^2 -values for relative orientations of DBA-BTICz (left conformer) and *v*-DABNA monomers where the TDMVs are pointing in the same direction. Right: Circular distribution of κ^2 values when the TDMVs are pointing in the same direction. The donor is located in the origin, the acceptor on the circumference of the circle.

for a collinear arrangement of the TDMVs. **Figure 10** shows the circular distribution of the κ^2 values when the TDMVs are pointing in the same direction. In solutions, where the two molecules can freely rotate, the orientation factor is often approximated to $2/3$.^[16] For random but rigid orientations, it was estimated to be lower ($\kappa^2 = 0.714 \times 2/3$).^[65]

To assess the performance of the IDA with regard to the MTD approach for the HF system under investigation, we carried out two series of test calculations. In the first series, the validity of the IDA was tested for a fixed distance R_{DA} between the barycenters of the donor and acceptor molecules but varying κ^2 values. Ideally, the ratio between the MTD values and κ^2 should be constant. The actual R_{DA} value is not essential for this test of the IDA. We chose a distance between the molecular barycenters of $R_{DA} = 40 \text{ \AA}$ that is close to the expected average R_{DA} value in the device (see below). This series of test calculations was carried out for the left conformer of the DBA-BTICz donor. In a second series of calculations, κ^2 was chosen to be maximal (collinear arrangement of the transition dipoles) and the distance R_{DA} was varied. This second series of test calculations was performed for both conformers of the EET donor.

In preparation of the first series of ECME calculations, the nuclear frames of both molecules were rotated such that their TDMVs are aligned to the *x*-axis. Then the barycenter of the acceptor was arranged along the circumference of a circle in the *xy*-plane with radius $R_{DA} = 40 \text{ \AA}$ to account for different values of κ^2 (Figure 10). In **Table 2**, the κ values and the MTD ECMEs as well as the closest distance between atoms of the donor and the

acceptor are listed. While the magnitudes of the MTD ECMEs qualitatively follow the trend predicted by the κ values, their ratio is not perfectly constant. The inline alignment of the TDMVs (**Figure 11a**) yields the highest ECME. At the other extreme, where the TDMVs are perpendicular to one another (**Figure 11b**), the coupling is close to zero. However, for this orientation a coupling to the S_2 state of the *v*-DABNA could happen. As the TDMV of this state is orientated along the short axis of the molecule, it would be inline with that of the donor state. There is only a small energetic overlap between the S_1 emission of DBA-BTICz and the S_2 absorption of *v*-DABNA, however (Figure 9d). Consequently, this process would be slow. Interestingly, a κ^2 value of 0 can also be reached for a slip-stacked parallel alignment of the TDMVs when the angle between the line connecting the barycenters of the monomers and their TDMVs adopt a value of 54.7356° (yellow structure in Figure 10).

The distance dependence of the MTD and IDA ECMEs for both DBA-BTICz conformers can be seen in **Figure 12**. In this second test series, ECMEs were calculated for an inline orientation of the donor and acceptor TDMVs at different barycenter distances. Both conformers show a similar behavior with a very quickly descending curve. On an absolute scale, the ECME at a given intermolecular distance is much smaller for the right conformer, however. This finding agrees with the observation (Section 4.1) that the transition dipole moment and hence the radiative rate constant of the DBA-BTICz $S_1 \rightarrow S_0$ is reduced in comparison to the values found for the left conformer. Figure 12a shows that the IDA values of the left conformer match the corresponding MTD values very well in the entire distance regime considered, spanning from 30 to 120 \AA . In contrast, the IDA and MTD results for the right conformer (Figure 12b) start to deviate when the separation of the barycenters drops below approximately 60 \AA . While the deviation between MTD and IDA is 11% at a distance of 60 \AA it increases to 18% at 40 \AA and 23% at 30 \AA .

The Förster radius is the distance at which the EET efficiency Φ_{FRET}

$$\Phi_{\text{FRET}} = \frac{k_{\text{EET}}}{k_{\text{EET}} + k_{\text{ISC}} - k_{\text{ISC}} + k_{\text{F}} + k_{\text{IC}}} \quad (9)$$

reaches 50%.^[16,17] In other words, it is the distance at which k_{EET} has the same size as the sum of all other donor deactivation

Table 2. MTD ECMEs for the left conformer. Barycenter distance: 40 \AA .

Orientation ^{a)}	Min. Dist. [\AA]	$ \kappa $	MTD ECME [cm^{-1}]	MTD ECME/ $ \kappa $ [cm^{-1}]
Parallel	19.256	2	4.715276	2.357638
Parallel	20.139	$\sqrt{3}$	3.939731	2.274605
Parallel	21.314	$\sqrt{2}$	3.138551	2.219291
Parallel	23.111	1	2.239849	2.239849
Parallel	25.675	0	0.112298	–
Parallel	28.942	1	2.139160	2.139160
Orthogonal	24.553	0	0.045766	–

^{a)} The order of the table entries follow the geometrical arrangements in Figure 10.

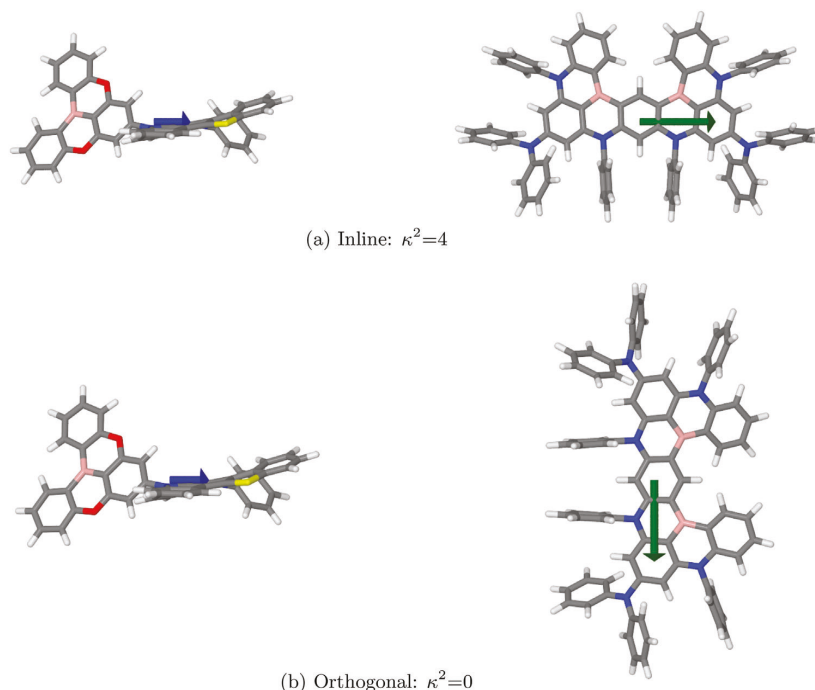


Figure 11. Inline and perpendicular orientation of the left conformer of DBA-BTICz and *v*-DABNA. The respective transition dipole moment vectors are indicated by arrows.

processes. The experimentally evaluated Förster radius is 46.77 Å.^[26] Based on this value, Braveenth et al. deduced an average intermolecular distance between donor and acceptor of 40.77 Å in the device.

As shown above, the relative orientation of the donor and acceptor molecules has huge impact on the EET coupling strength. Since we may assume a random distribution of orientations in OLED stacks, we here discuss the upper limit of our theoretical results and subsequently adjust the orientation factor to the value $\kappa^2 = 0.714 \times 2/3 = 0.476$, recommended by Maksimov

and Rozman^[65] for randomly placed donors and acceptors in the solid state. At 40 Å, the inline orientation results in a rate constant of $6.2 \times 10^9 \text{ s}^{-1}$ for the left and $8.1 \times 10^8 \text{ s}^{-1}$ for the right conformer using the MTD approach. These values are by far higher than the experimental rate constant of $7.48 \times 10^7 \text{ s}^{-1}$.^[26] Randomization of the relative donor and acceptor orientations then would lead to k_{EET} rate constants of $7.4 \times 10^8 \text{ s}^{-1}$ (left) and $9.6 \times 10^7 \text{ s}^{-1}$ (right).

Another factor that has not been accounted for so far in the MTD calculations, is the damping effect of the medium on the

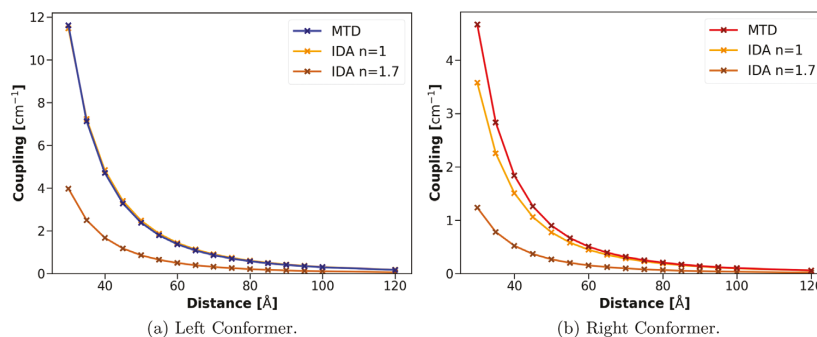


Figure 12. Comparison of MTD and IDA ECMEs for an inline orientation of the TDMVs, dependent of the barycenter distance and the refractive index n .

EET. The damping of the EET by the surrounding medium can be estimated with the help of the IDA (Equation 3), where the ECME is divided by the square of the refractive index of the surrounding medium. The refractive index of DBFPO layer is close to $n = 1.7$ in the considered wavelength regime.^[26] Taking both, randomization and damping, into consideration brings the MTD rate constants down to $k_{\text{EET}} \approx 8.9 \times 10^7 \text{ s}^{-1}$ (left) and $k_{\text{EET}} \approx 1.2 \times 10^7 \text{ s}^{-1}$ (right) for a random distribution of donors and acceptors at a barycenter distance of 40 Å, in fair agreement with the experimental value of $7.48 \times 10^7 \text{ s}^{-1}$ as determined by Braveenth et al.^[26] Employing the spectral overlap integral determined by us on the basis of the experimental spectra in film instead of the quantum chemically derived ones, yields EET rate constants that are much smaller, i.e., $k_{\text{EET}} \approx 1.6 \times 10^7 \text{ s}^{-1}$ (left) and $k_{\text{EET}} \approx 2.6 \times 10^6 \text{ s}^{-1}$ (right).

To get an upper limit for the calculated Förster radii of the DBA-BTICz conformers, we compared the sum of the fluorescence and ISC rate constants of both conformers with the corresponding EET rate constants for the respective inline orientations of the TDMVs in vacuum ($\kappa^2 = 4$, $n = 1$), neglecting all other nonradiative processes. This estimate yields maximal theoretical Förster radii of approximately 65–70 Å for the left conformer (Table S8, Supporting Information) and 55–65 Å for the right conformer (Table S9, Supporting Information). While these values help with the assessment of the computational methods, they are not directly comparable with experimental data. Taking the above described scaling factors for damping by the medium and randomization of the donor–acceptor orientation into account, reduces the Förster radii to approximately 30–35 Å for the left conformer and to 40–45 Å for the right conformer. Our finding that the Förster radius of the left conformer is smaller than the one for the right conformer despite its larger EET rate constant is related to the other rate constants entering the expression for Φ_{FRET} (Equation 9). In particular, the high fluorescence and ISC rate constants, which are not affected by damping or randomization factors, reduce the FRET efficiency and thus the Förster radius of that conformer.

5. Conclusion

In this work, we have investigated the performance of various quantum chemical methods to calculate the excitonic coupling of a reported hyperfluorescent system. In this system, the TADF molecule DBA-BTICz acts as the assistant dopant, while *v*-DABNA is the MR-fluorescence emitter. The DFT/MRCI method provides excitation energies and transition dipole moments of the monomers in excellent agreement with experimental values, even though the molecules are sizeable. A further strength of this multiconfiguration method is that the orientation of the TDMVs can be determined with high confidence, even for CT- and MR-type molecules. The emission spectra were calculated in FC approximation by a vertical Hessian approach which yields band shapes matching the experimental ones very well. Nevertheless, due to the underlying harmonic oscillator model, the computed FC spectra are somewhat too broad.

Interestingly, for DBA-BTICz two stable conformers were found, which exhibit distinct emission properties with TDMVs pointing in different directions. The S_1 state of the left conformer possesses a nearly 10 times higher radiative rate constant but also

a much higher ISC rate constant than the right conformer. In both conformers, the adiabatic energy splitting between the S_1 and T_1 states, ΔE_{ST} , is overestimated with respect to the experimental value. Test calculations show that the ISC rate constant does not critically depend on the actual ΔE_{ST} value. This is different for the rISC process. In this case, significantly too small rate constants are obtained in FC approximation. Note, however, that three triplet states are located below the S_1 state. A proper modeling of the rISC process would therefore require the inclusion of vibronic coupling effects which is beyond the scope of the present study. For *v*-DABNA, two conformers were found which differ only in the dihedral angles of peripheral phenyl rings. Because they have very similar spectral characteristics, it was considered sufficient to focus on one of them. In this case, the orientation of the TDMV is determined by symmetry. Due to the rigidity of the nuclear frame, the room-temperature VH and AH FC spectra have very similar shapes. Both exhibit slightly higher widths than the first peak of the experimental absorption spectrum. The maximum of the AH spectrum perfectly matches the experimental peak maximum while the VH spectrum is energetically slightly (400 cm^{-1}) red shifted in comparison to the experiment.

To compute the rate constant of the energy transfer process, Fermi's golden rule approach was chosen. Here, the squared excitonic coupling matrix element and the spectral overlap integral are utilized. We assessed the validity of the ideal dipole approximation by means of MTD calculations. The IDA is a very simple method for estimating the ECME, whereas the MTD method is much more sophisticated but also computationally more demanding due to the calculation of two-electron Coulomb and exchange integrals, which not only takes a long time (ca. 12 h), but also requires a lot of memory (about 20 GB). For the left conformer of DBA-BTICz, distance dependent calculations of the ECME showed very good agreement between IDA and MTD over the entire range. For the right conformer, the IDA values deviate from the MTD reference data by up to 20%. Irrespective of these differences, the environmental damping can be estimated by the IDA. The ECMEs, computed for different relative orientations of the monomers, follow the trend predicted by $|\kappa|$ -values in the IDA quite well.

The most critical ingredients of the rate constant evaluation refer to the spectral overlap integral and the relative orientation of the donor and acceptor molecules in space. We assumed here a random orientation in the solid state giving rise to a κ^2 value of 0.476. Despite the good agreement of the individual monomer spectra with their experimental counterparts, the spectral overlap integral is overestimated. The *v*-DABNA absorption peak is almost completely enclosed by the DBA-BTICz emission band. Therefore, even small deviations of its spectral width lead to marked variations of the spectral overlap integral. Using our computed ECMEs together with spectral overlap integrals resulting from the VH approach yield EET rate constants in fair agreement with the experimental values if the damping of the interaction by the DBFPO medium is included and a random orientation is assumed (Table 3). Interestingly, we obtain a shorter Förster radius (30–35 Å) for the left conformer of DBA-BTICz than for the right conformer (40–45 Å) despite its larger EET rate constant. We attribute this finding to the much larger ISC rate constant of the left conformer which indirectly reduces the EET probability in relation to the prompt fluorescence.

Table 3. Comparison of the key characteristics of the hyperfluorescent system consisting of the left or right conformers of the DBA-BTICz assistant dopant as the FRET donor and the ν -DABNA acceptor calculated at the MTD level with experimental values.

Property		Experiment ^{a)}	DBA-BTICz (left)	DBA-BTICz (right)
Radiative rate constant (donor)	k_F^D	$7.5 \times 10^6 \text{ s}^{-1}$	$6.5 \times 10^7 \text{ s}^{-1}$	$6.2 \times 10^6 \text{ s}^{-1}$
ISC rate constant (donor)	k_{ISC}^D	$2.5 \times 10^7 \text{ s}^{-1}$	$1.7 \times 10^8 \text{ s}^{-1}$	$7.2 \times 10^6 \text{ s}^{-1}$
EET rate constant (in DBFPO)	k_{EET}	$7.5 \times 10^7 \text{ s}^{-1}$	$8.9 \times 10^7 \text{ s}^{-1}$ ^b	$6.2 \times 10^6 \text{ s}^{-1}$ ^b
Förster radius	R_F	46.77 Å	30-35 Å	40-45 Å

^{a)} Ref. [26]; ^{b)} Barycenter distance $|R_{DA}| = 40 \text{ Å}$, random relative orientation.

Supporting Information

Supporting Information is available from the Wiley Online Library or from the author.

Acknowledgements

The authors thank the Deutsche Forschungsgemeinschaft (DFG, German Research Foundation) for financial support through GRK 2482, project number 396890929.

Open access funding enabled and organized by Projekt DEAL.

Conflict of Interest

The authors declare no conflict of interest.

Data Availability Statement

The data that support the findings of this study are available in the supplementary material of this article.

Keywords

DFT/MRCI, excitonic coupling matrix element, fermi golden rule, hyperfluorescence, ideal dipole approximation, monomer transition density approach, spectral overlap

Received: August 20, 2024

Revised: December 17, 2024

Published online:

- [1] H.-W. Chen, J.-H. Lee, B.-Y. Lin, S. Chen, S.-T. Wu, *Light: Sci. Appl.* **2018**, *7*, 17168.
- [2] G. Hong, X. Gan, C. Leonhardt, Z. Zhang, J. Seibert, J. M. Busch, S. Bräse, *Adv. Mater.* **2021**, *33*, 2005630.
- [3] M. A. Baldo, D. O'Brien, M. Thompson, S. Forrest, *Phys. Rev. B* **1999**, *60*, 14422.
- [4] M. A. Baldo, D. F. O'Brien, Y. You, A. Shoustikov, S. Sibley, M. E. Thompson, S. R. Forrest, *Nature* **1998**, *395*, 151.
- [5] D. Volz, M. Wallesch, C. Fléchon, M. Danz, A. Verma, J. Navarro, D. Zink, S. Bräse, T. Baumann, *Green Chem.* **2015**, *17*, 1988.
- [6] E. Tankelevičiūtė, I. D. Samuel, E. Zysman-Colman, *J. Phys. Chem. Lett.* **2024**, *15*, 1034.
- [7] J.-H. Lee, C.-H. Chen, P.-H. Lee, H.-Y. Lin, M.-k. Leung, T.-L. Chiu, C.-F. Lin, *J. Mater. Chem. C* **2019**, *7*, 5874.
- [8] A. Endo, K. Sato, K. Yoshimura, T. Kai, A. Kawada, H. Miyazaki, C. Adachi, *Appl. Phys. Lett.* **2011**, *98*.

- [9] T. Hatakeyama, K. Shiren, K. Nakajima, S. Nomura, S. Nakatsuka, K. Kinoshita, J. Ni, Y. Ono, T. Ikuta, *Adv. Mater.* **2016**, *28*, 2777.
- [10] H. Hirai, K. Nakajima, S. Nakatsuka, K. Shiren, J. Ni, S. Nomura, T. Ikuta, T. Hatakeyama, *Angew. Chem.* **2015**, *127*, 13785.
- [11] Y. Kondo, K. Yoshiura, S. Kitera, H. Nishi, S. Oda, H. Gotoh, Y. Sasada, M. Yanai, T. Hatakeyama, *Nat. Photonics* **2019**, *13*, 678.
- [12] S. Madayanad Suresh, D. Hall, D. Beljonne, Y. Olivier, E. Zysman-Colman, *Adv. Funct. Mater.* **2020**, *30*, 1908677.
- [13] K. Stavrou, A. Danos, T. Hama, T. Hatakeyama, A. Monkman, *ACS Appl. Mater. Interfaces* **2021**, *13*, 8643.
- [14] H. Jiang, J. Jin, W.-Y. Wong, *Adv. Funct. Mater.* **2023**, *33*, 2306880.
- [15] H. Nakanotani, T. Higuchi, T. Furukawa, K. Masui, K. Morimoto, M. Numata, H. Tanaka, Y. Sagara, T. Yasuda, C. Adachi, *Nat. Commun.* **2014**, *5*, 4016.
- [16] T. Förster, *Ann. Physik* **1948**, *437*, 55.
- [17] T. Förster, *Discuss. Faraday Soc.* **1959**, *27*, 7.
- [18] C. Y. Wong, C. Curutchet, S. Tretiak, G. D. Scholes, *J. Chem. Phys.* **2009**, *130*, 081104.
- [19] J. D. Spiegel, S. Fulle, M. Kleinschmidt, H. Gohlke, C. M. Marian, *J. Phys. Chem. B* **2016**, *120*, 8845.
- [20] B. P. Krueger, G. D. Scholes, R. Jimenez, G. R. Fleming, *J. Phys. Chem. B* **1998**, *102*, 2284.
- [21] B. P. Krueger, G. D. Scholes, G. R. Fleming, *J. Phys. Chem. B* **1998**, *102*, 5378.
- [22] R. F. Fink, J. Pfister, A. Schneider, H. Zhao, B. Engels, *Chem. Phys.* **2008**, *343*, 353.
- [23] R. F. Fink, J. Pfister, H. M. Zhao, B. Engels, *Chem. Phys.* **2008**, *346*, 275.
- [24] J. D. Spiegel, M. Kleinschmidt, A. Larbig, J. Tatchen, C. M. Marian, *J. Chem. Theory Comput.* **2015**, *11*, 4316.
- [25] J. D. Spiegel, I. Lyskov, M. Kleinschmidt, C. M. Marian, *Chem. Phys.* **2017**, *482*, 265.
- [26] R. Braveenth, H. Lee, J. D. Park, K. J. Yang, S. J. Hwang, K. R. Naveen, R. Lampande, J. H. Kwon, *Adv. Funct. Mater.* **2021**, *31*, 2105805.
- [27] J. R. Reimers, *J. Chem. Phys.* **2001**, *115*, 9103.
- [28] A. Baiardi, J. Bloino, V. Barone, *J. Chem. Theory Comput.* **2015**, *11*, 3267.
- [29] A. Hazra, H. H. Chang, M. Nooijen, *J. Chem. Phys.* **2004**, *121*, 2125.
- [30] J. P. Götze, B. Karasulu, W. Thiel, *J. Chem. Phys.* **2013**, *139*, 234108.
- [31] T. Böhmer, M. Kleinschmidt, C. M. Marian, *J. Chem. Phys.* **2024**, *161*, 094114.
- [32] O. Vahtras, J. Almlöf, M. Feyereisen, *Chem. Phys. Lett.* **1993**, *213*, 514.
- [33] F. Weigend, M. Häser, *Theor. Chim. Acta* **1997**, *97*, 331.
- [34] M. J. Frisch, G. W. Trucks, H. B. Schlegel, G. E. Scuseria, M. A. Robb, J. R. Cheeseman, G. Scalmani, V. Barone, G. A. Petersson, H. Nakatsuji, X. Li, M. Caricato, A. V. Marenich, J. Bloino, B. G. Janesko, R. Gomperts, B. Mennucci, H. P. Hratchian, J. V. Ortiz, A. F. Izmaylov, J. L. Sonnenberg, D. Williams-Young, F. Ding, F. Lipparini, F. Egidi, J. Goings, B. Peng, A. Petrone, T. Henderson, D. Ranasinghe, et al., Gaussian 16 Revision C.01, **2016**, Gaussian Inc. Wallingford CT.
- [35] O. A. Vydrov, G. E. Scuseria, *J. Chem. Phys.* **2006**, *125*.

- [36] T. M. Henderson, A. F. Izmaylov, G. Scalmani, G. E. Scuseria, *J. Chem. Phys.* **2009**, 131.
- [37] A. Schäfer, H. Horn, R. Ahlrichs, *J. Chem. Phys.* **1992**, 97, 2571.
- [38] M. Peach, D. Tozer, *J. Phys. Chem. A* **2012**, 9783.
- [39] E. Cancès, B. Mennucci, J. Tomasi, *J. Chem. Phys.* **1997**, 107, 3032.
- [40] R. Cammi, S. Corni, B. Mennucci, J. Tomasi, *J. Chem. Phys.* **2005**, 122.
- [41] G. Scalmani, M. J. Frisch, B. Mennucci, J. Tomasi, R. Cammi, V. Barone, *J. Chem. Phys.* **2006**, 124.
- [42] S. Grimme, M. Waletzke, *J. Chem. Phys.* **1999**, 111, 5645.
- [43] C. M. Marian, A. Heil, M. Kleinschmidt, *Wiley Interdiscip. Rev. Comput. Mol. Sci.* **2019**, 9, e1394.
- [44] TURBOMOLE V7.5.0 2020, a development of University of Karlsruhe and Forschungszentrum Karlsruhe GmbH, 1989-2007, TURBOMOLE GmbH, since 2007; available from <http://www.turbomole.com> (accessed: December 2024).
- [45] S. G. Balasubramani, G. P. Chen, S. Coriani, M. Diedenhofen, M. S. Frank, Y. J. Franzke, F. Furche, R. Grotjahn, M. E. Harding, C. Hättig, A. Hellweg, B. Helmich-Paris, C. Holzer, U. Huniar, M. Kaupp, A. Marefat Khah, S. Karbalaei Khani, T. Müller, F. Mack, B. D. Nguyen, S. M. Parker, E. Perlt, D. Rappoport, K. Reiter, S. Roy, M. Rückert, G. Schmitz, M. Sierka, E. Tapavicza, D. P. Tew, et al., *J. Chem. Phys.* **2020**, 152, 184107.
- [46] A. D. Becke, *J. Chem. Phys.* **1993**, 98, 1372.
- [47] F. Weigend, M. Häser, H. Patzelt, R. Ahlrichs, *Chem. Phys. Lett.* **1998**, 294, 143.
- [48] I. Lyskov, M. Kleinschmidt, C. M. Marian, *J. Chem. Phys.* **2016**, 144.
- [49] F. Plasser, *J. Chem. Phys.* **2020**, 152.
- [50] G. Hermann, V. Pohl, J. C. Tremblay, B. Paulus, H. Hege, A. Schild, *J. Comp. Chem.* **2016**, 37, 1511.
- [51] M. Kleinschmidt, J. Tatchen, C. M. Marian, *J. Comput. Chem.* **2002**, 23, 824.
- [52] M. Kleinschmidt, C. M. Marian, *J. Chem. Phys.* **2005**, 311, 71.
- [53] Jmol: an open-source Java viewer for chemical structures in 3d. <http://www.jmol.org/> (accessed: December 2024).
- [54] W. Humphrey, A. Dalke, K. Schulten, *J. Mol. Graph.* **1996**, 14, 33. see also <http://www.ks.uiuc.edu/Research/vmd/> (accessed: December 2024).
- [55] M. Etinski, V. Rai-Constapel, C. M. Marian, *J. Chem. Phys.* **2014**, 140.
- [56] M. Etinski, J. Tatchen, C. M. Marian, *J. Chem. Phys.* **2011**, 134.
- [57] F. Meitza, Phd thesis, Heinrich Heine University, Düsseldorf, Germany **2023**, <https://docserv.uni-duesseldorf.de/servlets/DocumentServlet?id=62953> (accessed: December 2024).
- [58] T. Froitzheim, S. Grimme, J.-M. Mewes, *J. Chem. Theory Comput.* **2022**, 18, 7702.
- [59] J. M. Kaminski, T. Böhmer, C. M. Marian, *J. Phys. Chem. C* **2024**, 128, 13711.
- [60] C. M. Marian, *Annu. Rev. Phys. Chem.* **2021**, 72, 617.
- [61] R. Englman, J. Jortner, *Mol. Phys.* **1970**, 18, 145.
- [62] T. J. Penfold, E. Gindensperger, C. Daniel, C. M. Marian, *Chem. Rev.* **2018**, 118, 6975.
- [63] T. Northey, T. Penfold, *Org. Electron.* **2018**, 59, 45.
- [64] K. Shizu, H. Kaji, *Commun. Chem.* **2022**, 5, 53.
- [65] M. Z. Maksimov, I. M. Rozman, *Opt. Spectrosc.* **1962**, 12, 337.

ADVANCED OPTICAL MATERIALS

Supporting Information

for *Adv. Optical Mater.*, DOI 10.1002/adom.202402241

Excitonic Coupling of a TADF Assistant Dopant and a Multi-Resonance TADF Emitter

*Simon Metz and Christel M. Marian**

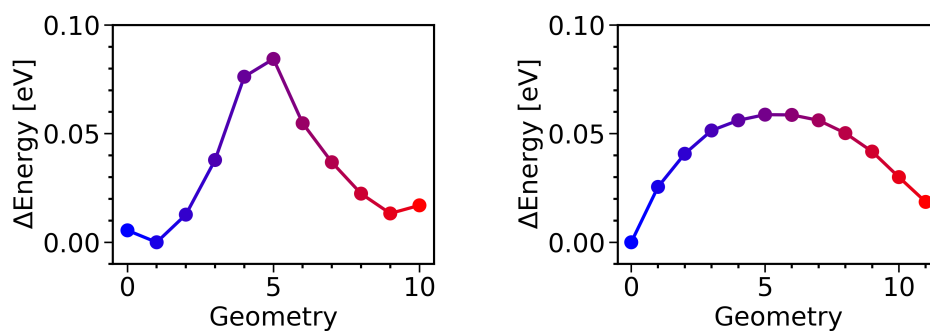
Supporting Information for :
Excitonic Coupling of a TADF Assistant Dopant
and a Multi-resonance TADF Emitter

Simon Metz and Christel M. Marian*

*Institute of Theoretical and Computational Chemistry, Faculty of Mathematics and Natural
Sciences, Heinrich Heine University Düsseldorf, 40204 Düsseldorf, Germany*

E-mail: Christel.Marian@hhu.de

S1 Assistant Dopant - DBA-BTICz



(a) DFT/MRCI energies along a linearly interpolated path in vacuum.

(b) DFT (BH-LYP) energies of a minimum energy path calculated with the nudged elastic band method implemented in Orca.¹ Start and endpoint were also optimized with BH-LYP.

Figure S1: Estimates of the energy barrier separating the ground states of right and left conformers of the assistant dopant DBA-BTICz.

Table S1: Singlet excitation wavelengths λ_{ex} above 300 nm and oscillator strengths (f) of the left and right conformers of the assistant dopant DBA-BTICz at the respective ground-state geometry.

Transition	Left		Right	
	λ_{ex} [nm]	f	λ_{ex} [nm]	f
$S_0 \rightarrow S_1$	377	0.234	374	0.148
$S_0 \rightarrow S_2$	374	0.013	373	0.076
$S_0 \rightarrow S_3$	362	0.228	363	0.199
$S_0 \rightarrow S_4$	352	0.050	352	0.031
$S_0 \rightarrow S_5$	330	0.013	331	0.042
$S_0 \rightarrow S_6$	310	0.661	311	0.694
$S_0 \rightarrow S_7$	307	0.755	307	0.984
$S_0 \rightarrow S_8$	305	0.211	304	0.063
$S_0 \rightarrow S_9$	301	0.108	300	0.046

Table S2: Contributions to the wavefunctions of the first four excited singlets with a higher percentage than 3% at the S_0 geometry of the left DBA-BTICz conformer.

State	MOs	%	Type
S_1	HOMO-1 \rightarrow LUMO	46.7	CT
	HOMO \rightarrow LUMO	29.9	CT
	HOMO-1 \rightarrow LUMO+1	3.1	LE _{BTICz}
S_2	HOMO \rightarrow LUMO	36.5	CT
	HOMO-1 \rightarrow LUMO	19.8	CT
	HOMO \rightarrow LUMO+1	14.6	LE _{BTICz}
	HOMO-1 \rightarrow LUMO+2	7.8	LE _{BTICz}
	HOMO-2 \rightarrow LUMO	3.9	LE _{DBA}
S_3	HOMO-2 \rightarrow LUMO	71.0	LE _{DBA}
	HOMO \rightarrow LUMO+1	4.1	LE _{BTICz}
S_4	HOMO \rightarrow LUMO+1	26.5	LE _{BTICz}
	HOMO \rightarrow LUMO	16.3	CT
	HOMO-1 \rightarrow LUMO+2	15.0	LE _{BTICz}
	HOMO-1 \rightarrow LUMO	9.9	CT
	HOMO \rightarrow LUMO+2	5.8	LE _{BTICz}
	HOMO-2 \rightarrow LUMO	3.1	LE _{DBA}

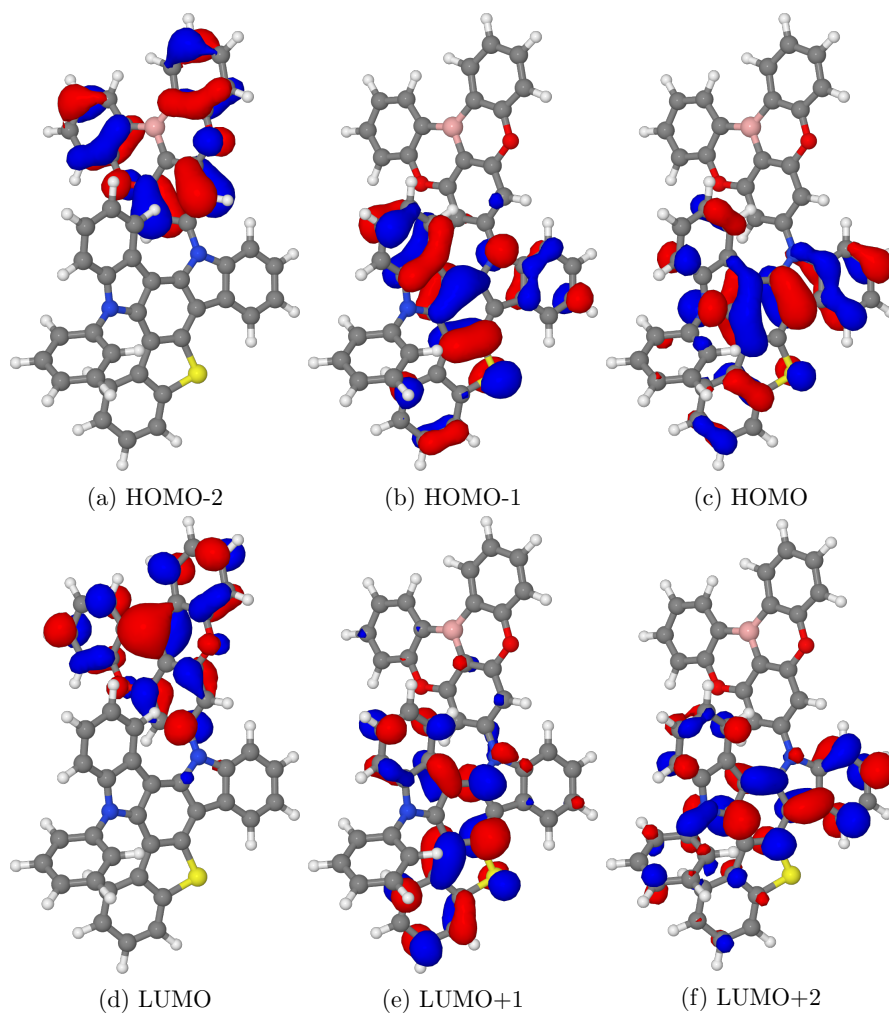


Figure S2: Molecular orbitals of DBA-BTICz (isovalue 0.03) at the ground-state minimum geometry of the left conformer.

Table S3: Contributions to the wavefunctions of the first four excited singlets with a higher percentage than 3% at the S_0 geometry of the right DBA-BTICz conformer.

State	MOs	%	Type
S ₁	HOMO →LUMO	71.4	CT
	HOMO-1→LUMO	22.3	CT
S ₂	HOMO-1→LUMO	47.5	CT
	HOMO-2→LUMO	11.2	LE _{DBA}
	HOMO →LUMO	10.7	CT
	HOMO →LUMO+1	7.2	LE _{BTICz}
	HOMO-1→LUMO+2	6.7	LE _{BTICz}
S ₃	HOMO-2→LUMO	55.9	LE _{DBA}
	HOMO →LUMO+1	10.0	CT
	HOMO-1→LUMO+2	6.7	LE _{BTICz}
	HOMO-3→LUMO	5.3	CT
S ₄	HOMO →LUMO+1	26.7	LE _{BTICz}
	HOMO →LUMO	19.8	CT
	HOMO-1→LUMO+2	16.1	LE _{BTICz}
	HOMO-1→LUMO	6.7	CT
	HOMO-2→LUMO	5.1	LE _{DBA}

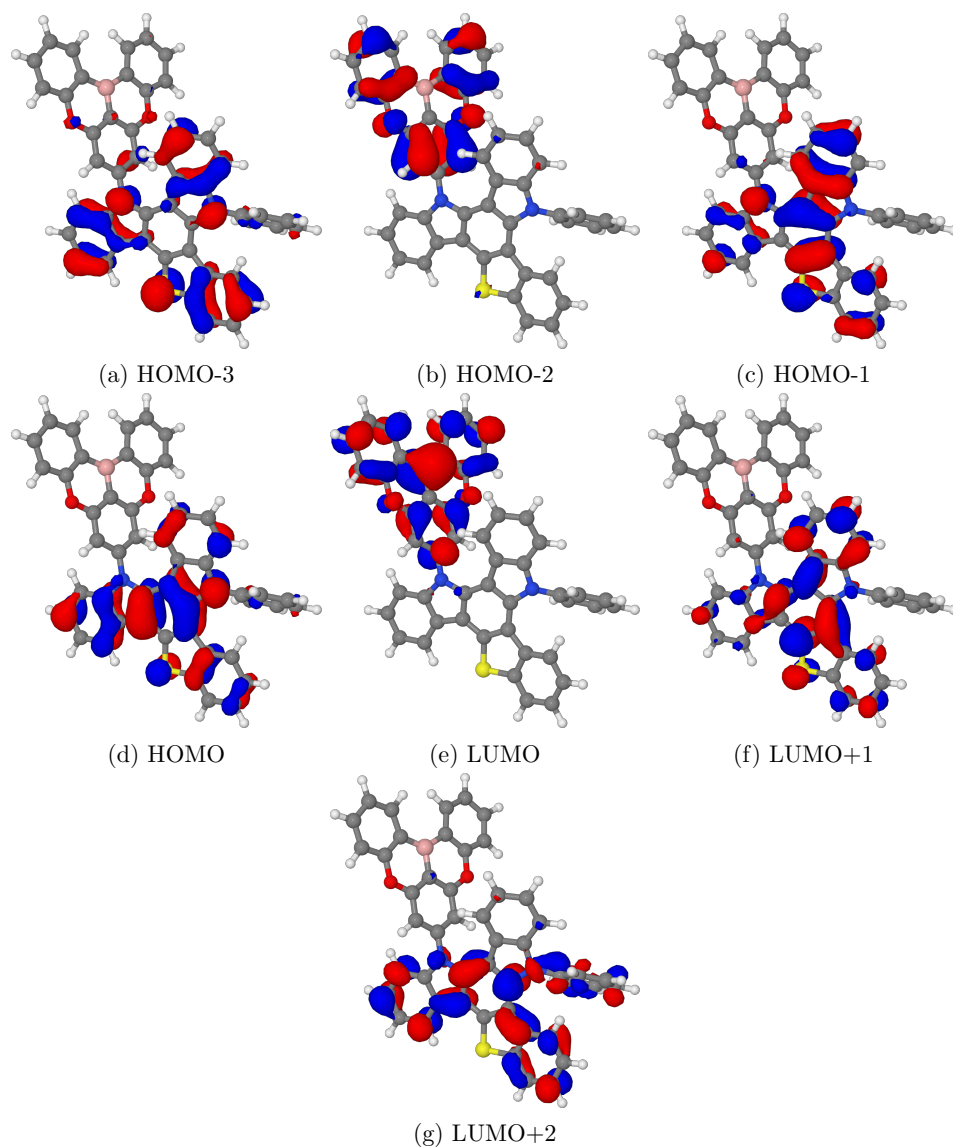


Figure S3: Molecular orbitals of DBA-BTICz (isovalue 0.03) at the ground-state minimum geometry of the right conformer.

Table S4: Computed adiabatic energy differences ΔE [eV], radiative rate constants k_r [s^{-1}], spin-orbit couplings [cm^{-1}], ISC and rISC rate constants $k_{(r)ISC}$ [cm^{-1}] of the DBA-BTICz conformers at room temperature in toluene.

Initial	Final	Left				Right			
		ΔE	k_r	SOC	$k_{(r)ISC}$	ΔE	k_r	SOC	$k_{(r)ISC}$
S _{CT}	S ₀	3.23	6.5×10^7			3.23	6.2×10^6		
	T _{CT}	0.04 ^a		0.306		0.01 ^a		0.167	
	T _{DBA}	0.26		0.538	8.8×10^7	0.30		0.112	3.0×10^6
	T _{BTICz}	0.51		0.701	8.7×10^7	0.40		0.201	4.2×10^6
	T _{BTICz}	0.29 ^b		0.701	5.3×10^7	0.29 ^b		0.201	3.2×10^6
T _{DBA}	S ₀	2.97	0.9×10^0			2.93	0.8×10^0		
	S _{CT}	-0.26		0.448	2.4×10^4	-0.30		0.032	5.4×10^0
T _{BTICz}	S ₀	2.72	1.2×10^0			2.83	1.1×10^0		
	S _{CT}	-0.51		0.521	0.6×10^0	-0.40		0.569	1.5×10^0
	S _{CT}	-0.29 ^b		0.521	2.0×10^3	-0.29 ^b		0.569	5.6×10^1

^aAt the optimized S_{CT} geometry.

^bPotential energy surfaces shifted to experimental ΔE_{ST} value.²

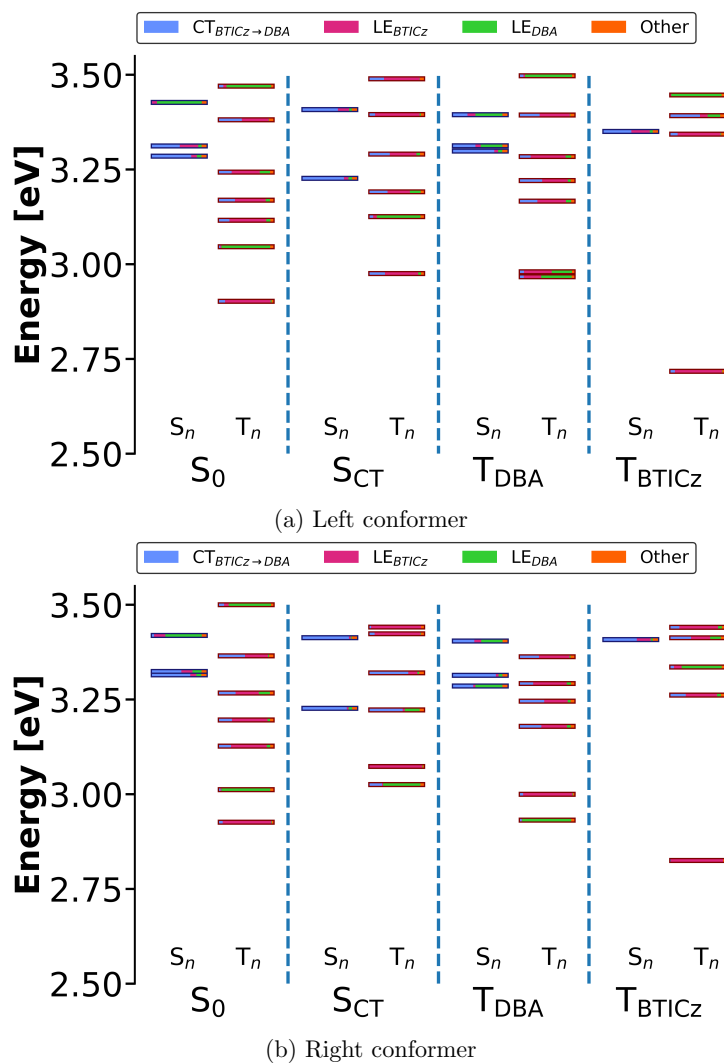


Figure S4: DFT/MRCI energies of DBA-BTICz at the optimized geometries and TheoDORE analysis results of the transitions. All excitation energies are given with reference to the ground-state energy at the respective S_0 minimum.

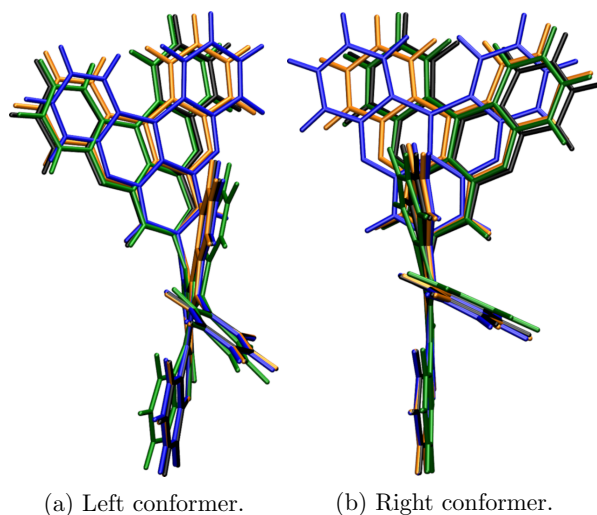


Figure S5: Overlay of the molecular structures of DBA-BTICz in the ground state and optimized excited states. Black: S_0 , Blue: S_{CT} , Orange: T_{DBA} , Green: T_{BTICz} . The structures are aligned to maximize the overlap between the carbazole units of the BTICz moiety.

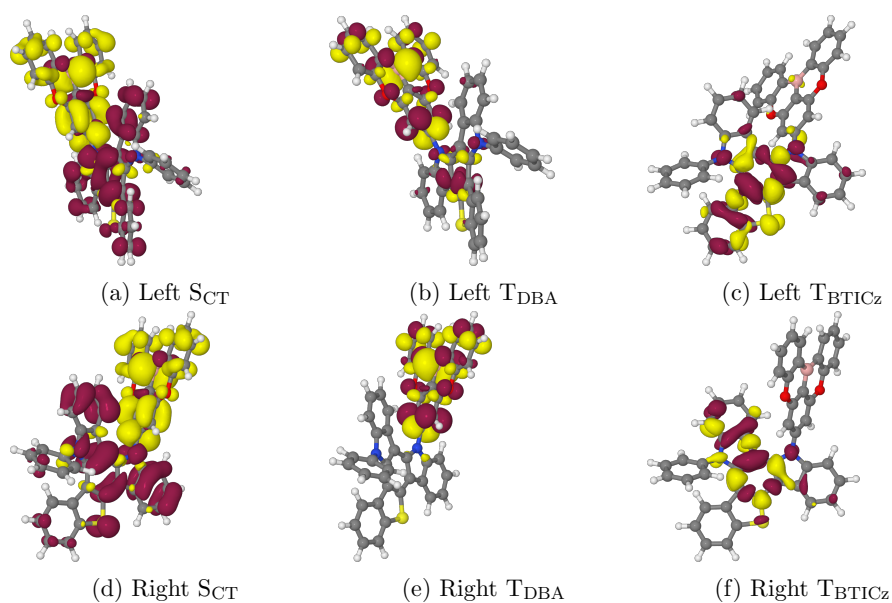


Figure S6: Difference densities of the excited states of DBA-BTICz (isovalue ± 0.001) at their optimized geometries. Red-colored areas indicate a loss of electron density, yellow-colored areas a gain of electron density with regard to the electronic ground state.

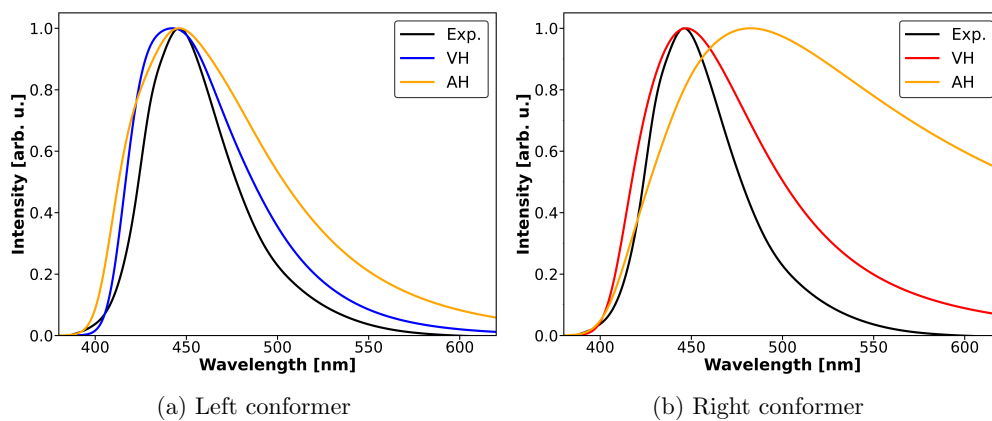


Figure S7: Comparison of the emission spectra of the S_{CT} state of DBA-BTICz calculated in internal coordinates with the adiabatic Hessian (AH) and vertical Hessian (VH) approaches.

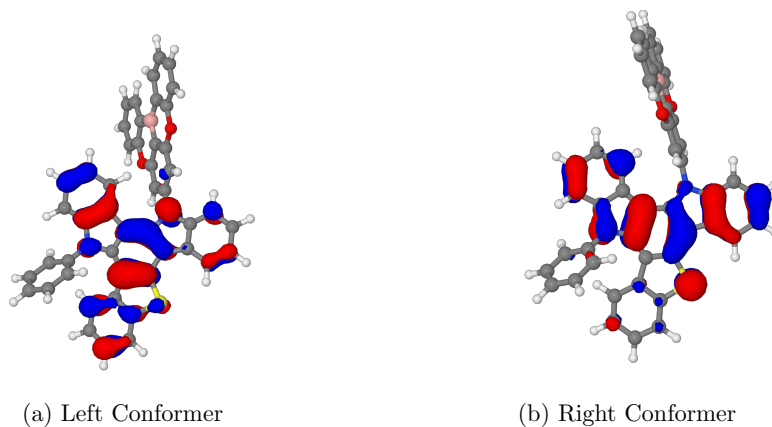


Figure S8: HOMO at the S_{CT} geometry of both DBA-BTICz conformers (cutoff 0.03).

S2 Fluorescent Emitter - ν -DABNA

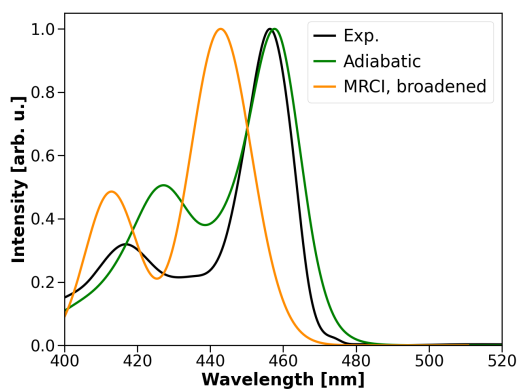


Figure S9: Calculated absorption spectra of ν -DABNA compared to an experimental spectrum in toluene.³ The Gaussian broadened (FWHM: 1000 cm^{-1}) line spectrum is based on DFT/MRCI excitation energies and oscillator strengths. The adiabatic FC spectrum is the sum of the absorption spectra of the S_1 and S_2 states.

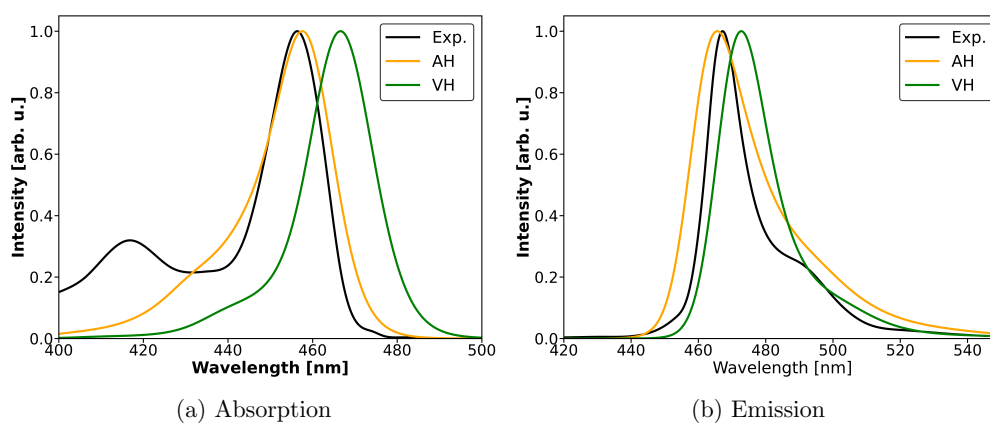


Figure S10: Comparison of ν -DABNA absorption and emission spectra calculated in internal coordinates (adiabatic) and with the vertical hessian approach (vertical).

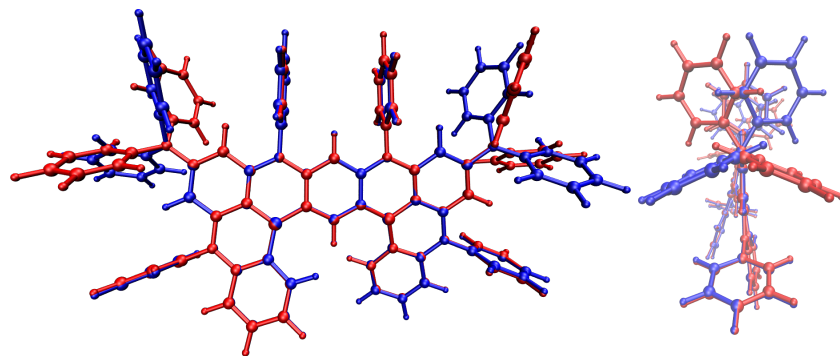


Figure S11: Structural differences between the two ν -DABNA conformers.

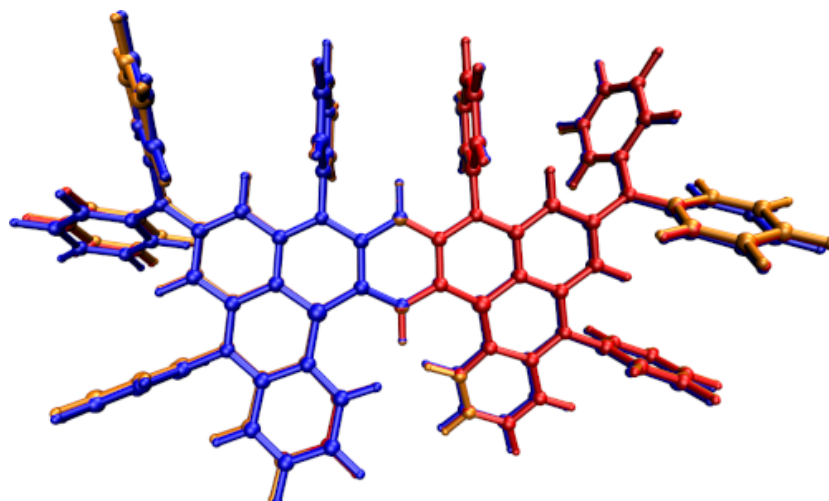


Figure S12: Comparison of the excited state geometries of ν -DABNA with the ground state structure. Blue: Ground State, Red: S_1 , Orange: T_1 . All geometries have C_2 symmetry.

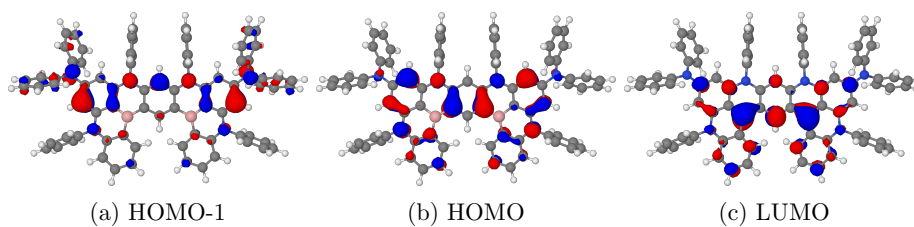


Figure S13: MOs (cutoff 0.03) of ν -DABNA at the ground state geometry. The S_1 state is a HOMO–LUMO transition, while the S_2 is a HOMO-1–LUMO transition.

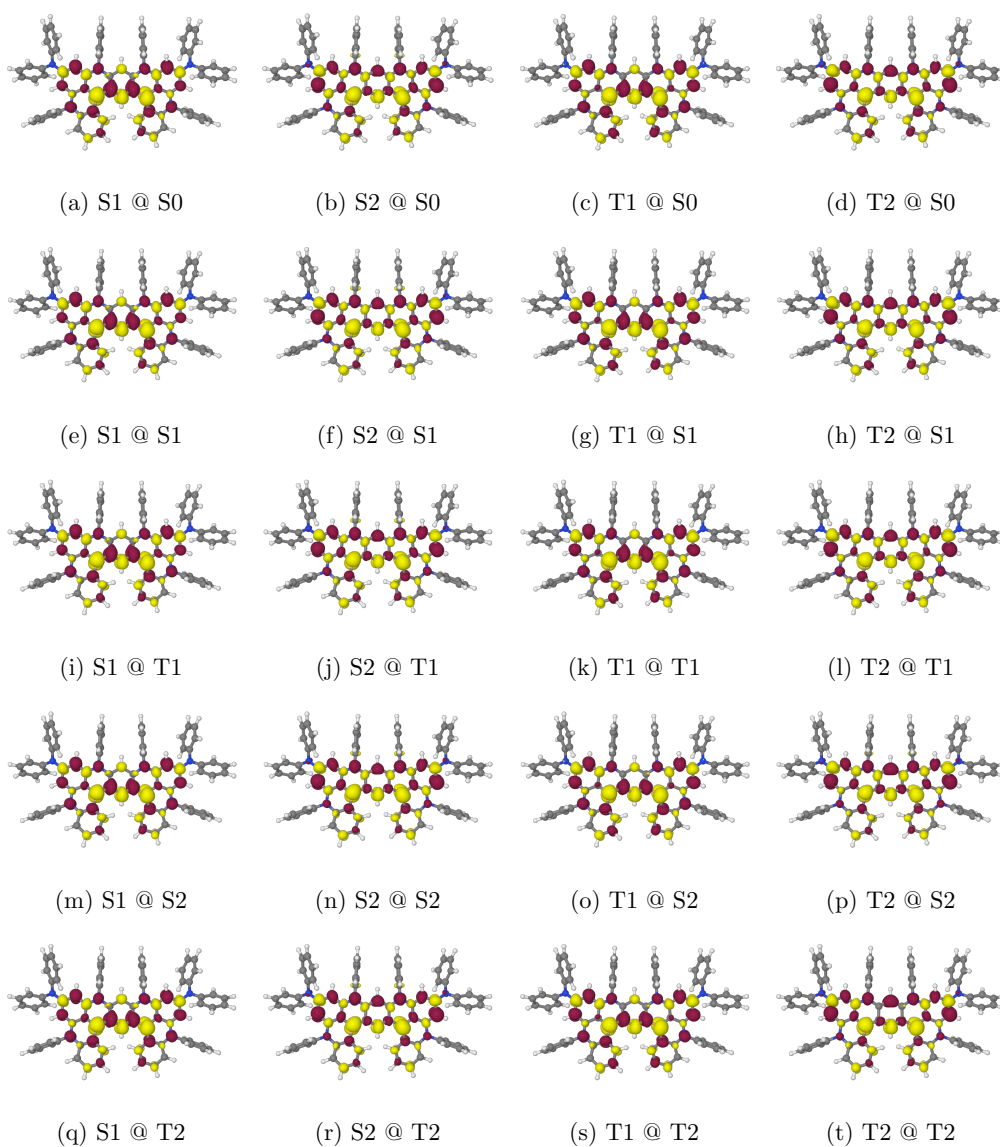


Figure S14: Difference densities for the excited states of ν -DABNA. For color codes, see Figure S6.

Table S5: Adiabatic and 0-0 energies [eV] of the optimized excited states of ν -DABNA.

State	Adiabatic	0-0
S ₁	2.81	2.71
S ₂	3.00	2.91
T ₁	2.60	2.49
T ₂	2.68	2.59

Table S6: Singlet excitation energies and oscillator strength of ν -DABNA at the ground-state geometry

Transition	Energy [nm]	[eV]	f
S ₀ → S ₁	442	2.81	0.687
S ₀ → S ₂	412	3.01	0.331
S ₀ → S ₃	379	3.27	0.000
S ₀ → S ₄	377	3.29	0.599
S ₀ → S ₅	355	3.49	0.289
S ₀ → S ₆	332	3.74	0.673
S ₀ → S ₇	329	3.77	0.002
S ₀ → S ₈	327	3.79	0.044
S ₀ → S ₉	321	3.86	0.039
S ₀ → S ₁₀	321	3.86	0.058

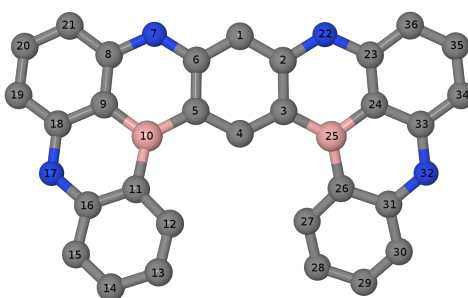
Figure S15: Numbering of the ν -DABNA core atoms.

Table S7: Bond length difference (ΔB) between the geometries of S_0 and S_1 of ν -DABNA. For atom numbering see Figure S15

Atom 1	Atom 2	ΔB [\AA]
C2 (C6)	C3 (C5)	0.0084
C4 (C4)	C5 (C3)	0.0073
C6 (C2)	N7 (N22)	-0.0062
C8 (C23)	C9 (C24)	-0.0050
C11 (C26)	C16 (C31)	0.0046
C14 (C29)	C15 (C30)	0.0045
C16 (C31)	N17 (N32)	0.0041
C12 (C27)	C13 (C28)	0.0039
N7 (N22)	C8 (C23)	0.0038
C18 (C33)	C19 (C34)	0.0032
C15 (C30)	C16 (C31)	-0.0029
C8 (C23)	C21 (C36)	0.0026
C20 (C35)	C21 (C36)	0.0025
C13 (C28)	C14 (C29)	-0.0024
C1 (C1)	C6 (C2)	0.0024
N17 (N32)	C18 (C33)	-0.0008
C19 (C34)	C20 (C35)	0.0007
C9 (C24)	C18 (C33)	-0.0005
B10 (B25)	C11 (C26)	-0.0005
C5 (C3)	B10 (B25)	-0.0005
C11 (C26)	C12 (C27)	0.0003
C9 (C24)	B10 (B25)	-0.0001

S3 Excitation Energy Transfer between DBA-BTICz and ν -DABNA

Table S8: EET rate constant and Förster radii (R_F) between the left conformer of DBA-BTICz and ν -DABNA for different orientation factors (κ^2) and refractive indices (n). Different spectral overlaps are used, the experimental one (Exp.), VH emission and AH absorption spectra (VHAH) and VH emission and VH absorption spectra (VHVH).

	κ^2	n	Coupling [cm ⁻¹]	k_{EET}			R_F in Å		
				Exp.	VHAH	VHVH	Exp.	VHAH	VHVH
MTD	4	1	4.7153	1.1×10^9	6.2×10^9	5.6×10^9	50-55	65-70	65-70
	4	1.7	1.6316	1.4×10^8	7.5×10^8	6.7×10^8	35-40	45-50	45-50
	0.476	1	1.6266	1.3×10^8	7.4×10^8	6.7×10^8	35-40	45-50	45-50
	0.476	1.7	0.5628	1.6×10^7	8.9×10^7	8.0×10^7	<30	30-35	30-35
IDA	4	1	4.8443	1.2×10^9	6.6×10^9	5.9×10^9	50-55	65-70	65-70
	4	1.7	1.6762	1.4×10^8	7.9×10^8	7.1×10^8	35-40	45-50	45-50
	0.476	1	1.6711	1.4×10^8	7.8×10^8	7.0×10^8	35-40	45-50	45-50
	0.476	1.7	0.5782	1.7×10^7	9.4×10^7	8.4×10^7	<30	30-35	30-35

Table S9: EET rate constant and Förster radii (R_F) between the right conformer of DBA-BTICz and ν -DABNA for different orientation factors (κ^2) and refractive indices (n). Different spectral overlaps are used, the experimental one (Exp.), VH emission and AH absorption spectra (VHAH) and VH emission and VH absorption spectra (VHVH).

	κ^2	n	Coupling [cm ⁻¹]	k_{EET}			R_F		
				Exp.	VHAH	VHVH	Exp.	VHAH	VHVH
MTD	4	1	1.8376	1.7×10^8	8.1×10^8	9.5×10^8	45-50	55-60	60-65
	4	1.7	0.6359	2.0×10^7	9.7×10^7	1.1×10^8	30-35	40-45	40-45
	0.476	1	0.6339	2.0×10^7	9.7×10^7	1.1×10^8	30-35	40-45	40-45
	0.476	1.7	0.2193	2.4×10^6	1.2×10^7	1.3×10^7	30-35	40-45	40-45
IDA	4	1	1.5085	1.2×10^8	5.5×10^8	6.4×10^8	40-45	55-60	55-60
	4	1.7	0.5220	1.4×10^7	6.5×10^7	7.6×10^7	30-35	35-40	40-45
	0.476	1	0.5204	1.4×10^7	6.5×10^7	7.6×10^7	30-35	35-40	40-45
	0.476	1.7	0.1801	1.6×10^6	7.8×10^6	9.1×10^6	30-35	40-45	40-45

Table S10: EET rate constants between the left conformer of DBA-BTICz and ν -DABNA. Coupling calculated with the MTD approach, a refractive index of 1 and a κ^2 of 4. Different spectral overlaps are used, the experimental one (Exp.), VH emission and AH absorption spectra (VHAH) and VH emission and VH absorption spectra (VHVH).

Distance Å	Coupling [cm ⁻¹]	Exp.	k _{EET}	
			VHAH	VHVH
30	11.6148	6.8×10 ⁹	3.8×10 ¹⁰	3.4×10 ¹⁰
35	7.1340	2.6×10 ⁹	1.4×10 ¹⁰	1.3×10 ¹⁰
40	4.7153	1.1×10 ⁹	6.2×10 ⁹	5.6×10 ⁹
45	3.2862	5.5×10 ⁸	3.0×10 ⁹	2.7×10 ⁹
50	2.3845	2.9×10 ⁸	1.6×10 ⁹	1.4×10 ⁹
55	1.7868	1.6×10 ⁸	8.9×10 ⁸	8.1×10 ⁸
60	1.3740	9.6×10 ⁷	5.3×10 ⁸	4.8×10 ⁸
65	1.0797	5.9×10 ⁷	3.3×10 ⁸	2.9×10 ⁸
70	0.8641	3.8×10 ⁷	2.1×10 ⁸	1.9×10 ⁸
75	0.7024	2.5×10 ⁷	1.4×10 ⁸	1.2×10 ⁸
80	0.5788	1.7×10 ⁷	9.4×10 ⁷	8.5×10 ⁷
85	0.4826	1.2×10 ⁷	6.5×10 ⁷	5.9×10 ⁷
90	0.4066	8.4×10 ⁶	4.6×10 ⁷	4.2×10 ⁷
95	0.3458	6.1×10 ⁶	3.4×10 ⁷	3.0×10 ⁷
100	0.2966	4.5×10 ⁶	2.5×10 ⁷	2.2×10 ⁷
120	0.1719	1.5×10 ⁶	8.3×10 ⁶	7.5×10 ⁶

Table S11: EET rate constants between the left conformer of DBA-BTICz and ν -DABNA. Coupling calculated with IDA, a refractive index of 1 and a κ^2 of 4. Different spectral overlaps are used, the experimental one (Exp.), VH emission and AH absorption spectra (VHAH) and VH emission and VH absorption spectra (VHVH).

Distance Å	Coupling [cm ⁻¹]	Exp.	k _{EET}	
			VHAH	VHVH
30	11.4828	6.7×10 ⁹	3.7×10 ¹⁰	3.3×10 ¹⁰
35	7.2312	2.7×10 ⁹	1.5×10 ¹⁰	1.3×10 ¹⁰
40	4.8443	1.2×10 ⁹	6.6×10 ⁹	5.9×10 ⁹
45	3.4023	5.9×10 ⁸	3.2×10 ⁹	2.9×10 ⁹
50	2.4803	3.1×10 ⁸	1.7×10 ⁹	1.6×10 ⁹
55	1.8635	1.8×10 ⁸	9.7×10 ⁸	8.8×10 ⁸
60	1.4354	1.0×10 ⁸	5.8×10 ⁸	5.2×10 ⁸
65	1.1290	6.5×10 ⁷	3.6×10 ⁸	3.2×10 ⁸
70	0.9039	4.1×10 ⁷	2.3×10 ⁸	2.1×10 ⁸
75	0.7349	2.7×10 ⁷	1.5×10 ⁸	1.4×10 ⁸
80	0.6055	1.9×10 ⁷	1.0×10 ⁸	9.3×10 ⁷
85	0.5048	1.3×10 ⁷	7.1×10 ⁷	6.4×10 ⁷
90	0.4253	9.2×10 ⁶	5.1×10 ⁷	4.6×10 ⁷
95	0.3616	6.6×10 ⁶	3.7×10 ⁷	3.3×10 ⁷
100	0.3100	4.9×10 ⁶	2.7×10 ⁷	2.4×10 ⁷
120	0.1794	1.6×10 ⁶	9.0×10 ⁶	8.1×10 ⁶

Table S12: EET rate constants between the left conformer of DBA-BTICz and ν -DABNA. Coupling calculated with the MTD approach, a refractive index of 1 and a κ^2 of 0.476. Different spectral overlaps are used, the experimental one (Exp.), VH emission and AH absorption spectra (VHAH) and VH emission and VH absorption spectra (VHVH).

Distance Å	Coupling [cm ⁻¹]	k _{EET}		
		Exp.	VHAH	VHVH
30	4.0067	8.1×10 ⁸	4.5×10 ⁹	4.0×10 ⁹
35	2.4610	3.1×10 ⁸	1.7×10 ⁹	1.5×10 ⁹
40	1.6266	1.3×10 ⁸	7.4×10 ⁸	6.7×10 ⁸
45	1.1336	6.5×10 ⁷	3.6×10 ⁸	3.2×10 ⁸
50	0.8227	3.4×10 ⁷	1.9×10 ⁸	1.7×10 ⁸
55	0.6164	1.9×10 ⁷	1.1×10 ⁸	9.6×10 ⁷
60	0.4740	1.1×10 ⁷	6.3×10 ⁷	5.7×10 ⁷
65	0.3725	7.0×10 ⁶	3.9×10 ⁷	3.5×10 ⁷
70	0.2981	4.5×10 ⁶	2.5×10 ⁷	2.2×10 ⁷
75	0.2423	3.0×10 ⁶	1.6×10 ⁷	1.5×10 ⁷
80	0.1996	2.0×10 ⁶	1.1×10 ⁷	1.0×10 ⁷
85	0.1665	1.4×10 ⁶	7.8×10 ⁶	7.0×10 ⁶
90	0.1403	1.0×10 ⁶	5.5×10 ⁶	5.0×10 ⁶
95	0.1193	7.2×10 ⁵	4.0×10 ⁶	3.6×10 ⁶
100	0.1023	5.3×10 ⁵	2.9×10 ⁶	2.6×10 ⁶
120	0.0593	1.8×10 ⁵	9.8×10 ⁵	8.9×10 ⁵

Table S14: Left Conformer, IDA, Vacuum, $\kappa^2 = 0.476$

Distance Å	Coupling [cm ⁻¹]	Exp.	k _{EET}	
			VHAH	VHVV
30	3.9611	8.0×10 ⁸	4.4×10 ⁹	4.0×10 ⁹
35	2.4945	3.2×10 ⁸	1.7×10 ⁹	1.6×10 ⁹
40	1.6711	1.4×10 ⁸	7.8×10 ⁸	7.0×10 ⁸
45	1.1737	7.0×10 ⁷	3.9×10 ⁸	3.5×10 ⁸
50	0.8556	3.7×10 ⁷	2.0×10 ⁸	1.8×10 ⁸
55	0.6428	2.1×10 ⁷	1.2×10 ⁸	1.0×10 ⁸
60	0.4951	1.2×10 ⁷	6.9×10 ⁷	6.2×10 ⁷
65	0.3894	7.7×10 ⁶	4.2×10 ⁷	3.8×10 ⁷
70	0.3118	4.9×10 ⁶	2.7×10 ⁷	2.5×10 ⁷
75	0.2535	3.3×10 ⁶	1.8×10 ⁷	1.6×10 ⁷
80	0.2089	2.2×10 ⁶	1.2×10 ⁷	1.1×10 ⁷
85	0.1742	1.5×10 ⁶	8.5×10 ⁶	7.7×10 ⁶
90	0.1467	1.1×10 ⁶	6.0×10 ⁶	5.4×10 ⁶
95	0.1247	7.9×10 ⁵	4.4×10 ⁶	3.9×10 ⁶
100	0.1070	5.8×10 ⁵	3.2×10 ⁶	2.9×10 ⁶
120	0.0619	1.9×10 ⁵	1.1×10 ⁶	9.7×10 ⁵

Table S15: EET rate constants between the left conformer of DBA-BTICz and ν -DABNA. Coupling calculated with the MTD approach, a refractive index of 1.7 and a κ^2 of 4. Different spectral overlaps are used, the experimental one (Exp.), VH emission and AH absorption spectra (VHAH) and VH emission and VH absorption spectra (VHVH).

Distance Å	Coupling [cm ⁻¹]	Exp.	k _{EET}	
			VHAH	VHVH
30	4.0189	8.2×10 ⁸	4.5×10 ⁹	4.1×10 ⁹
35	2.4685	3.1×10 ⁸	1.7×10 ⁹	1.5×10 ⁹
40	1.6316	1.3×10 ⁸	7.5×10 ⁸	6.7×10 ⁸
45	1.1371	6.6×10 ⁷	3.6×10 ⁸	3.3×10 ⁸
50	0.8252	3.5×10 ⁷	1.9×10 ⁸	1.7×10 ⁸
55	0.6183	1.9×10 ⁷	1.1×10 ⁸	9.6×10 ⁷
60	0.4754	1.1×10 ⁷	6.3×10 ⁷	5.7×10 ⁷
65	0.3736	7.1×10 ⁶	3.9×10 ⁷	3.5×10 ⁷
70	0.2990	4.5×10 ⁶	2.5×10 ⁷	2.3×10 ⁷
75	0.2430	3.0×10 ⁶	1.7×10 ⁷	1.5×10 ⁷
80	0.2003	2.0×10 ⁶	1.1×10 ⁷	1.0×10 ⁷
85	0.1670	1.4×10 ⁶	7.8×10 ⁶	7.0×10 ⁶
90	0.1407	1.0×10 ⁶	5.5×10 ⁶	5.0×10 ⁶
95	0.1197	7.3×10 ⁵	4.0×10 ⁶	3.6×10 ⁶
100	0.1026	5.3×10 ⁵	2.9×10 ⁶	2.7×10 ⁶
120	0.0595	1.8×10 ⁵	9.9×10 ⁵	8.9×10 ⁵

Table S16: EET rate constants between the left conformer of DBA-BTICz and ν -DABNA. Coupling calculated with IDA, a refractive index of 1.7 and a κ^2 of 4. Different spectral overlaps are used, the experimental one (Exp.), VH emission and AH absorption spectra (VHAH) and VH emission and VH absorption spectra (VHVH).

Distance Å	Coupling [cm ⁻¹]	k _{EET}		
		Exp.	VHAH	VHVH
30	3.9733	8.0×10 ⁸	4.4×10 ⁹	4.0×10 ⁹
35	2.5021	3.2×10 ⁸	1.8×10 ⁹	1.6×10 ⁹
40	1.6762	1.4×10 ⁷	3.9×10 ⁸	3.5×10 ⁸
50	0.8582	3.7×10 ⁷	2.1×10 ⁸	1.9×10 ⁸
55	0.6448	2.1×10 ⁷	1.2×10 ⁸	1.0×10 ⁸
60	0.4967	1.3×10 ⁷	6.9×10 ⁷	6.2×10 ⁷
65	0.3906	7.7×10 ⁶	4.3×10 ⁷	3.8×10 ⁷
70	0.3128	5.0×10 ⁶	2.7×10 ⁷	2.5×10 ⁷
75	0.2543	3.3×10 ⁶	1.8×10 ⁷	1.6×10 ⁷
80	0.2095	2.2×10 ⁶	1.2×10 ⁷	1.1×10 ⁷
85	0.1747	1.5×10 ⁶	8.5×10 ⁶	7.7×10 ⁶
90	0.1472	1.1×10 ⁶	6.1×10 ⁶	5.5×10 ⁶
95	0.1251	7.9×10 ⁵	4.4×10 ⁶	3.9×10 ⁶
100	0.1073	5.8×10 ⁵	3.2×10 ⁶	2.9×10 ⁶
120	0.0621	2.0×10 ⁵	1.1×10 ⁶	9.7×10 ⁵

Table S17: EET rate constants between the left conformer of DBA-BTICz and ν -DABNA. Coupling calculated with the MTD approach, a refractive index of 1.7 and a κ^2 of 0.476. Different spectral overlaps are used, the experimental one (Exp.), VH emission and AH absorption spectra (VHAH) and VH emission and VH absorption spectra (VHVH).

Distance Å	Coupling [cm ⁻¹]	k _{EET}		
		Exp.	VHAH	VHVH
30	1.3864	9.7×10 ⁷	5.4×10 ⁸	4.8×10 ⁸
35	0.8515	3.7×10 ⁷	2.0×10 ⁸	1.8×10 ⁸
40	0.5628	1.6×10 ⁷	8.9×10 ⁷	8.0×10 ⁷
45	0.3923	7.8×10 ⁶	4.3×10 ⁷	3.9×10 ⁷
50	0.2847	4.1×10 ⁶	2.3×10 ⁷	2.0×10 ⁷
55	0.2133	2.3×10 ⁶	1.3×10 ⁷	1.1×10 ⁷
60	0.1640	1.4×10 ⁶	7.5×10 ⁶	6.8×10 ⁶
65	0.1289	8.4×10 ⁵	4.6×10 ⁶	4.2×10 ⁶
70	0.1031	5.4×10 ⁵	3.0×10 ⁶	2.7×10 ⁶
75	0.0838	3.6×10 ⁵	2.0×10 ⁶	1.8×10 ⁶
80	0.0691	2.4×10 ⁵	1.3×10 ⁶	1.2×10 ⁶
85	0.0576	1.7×10 ⁵	9.3×10 ⁵	8.4×10 ⁵
90	0.0485	1.2×10 ⁵	6.6×10 ⁵	5.9×10 ⁵
95	0.0413	8.6×10 ⁴	4.8×10 ⁵	4.3×10 ⁵
100	0.0354	6.4×10 ⁴	3.5×10 ⁵	3.2×10 ⁵
120	0.0205	2.1×10 ⁴	1.2×10 ⁵	1.1×10 ⁵

Table S18: EET rate constants between the left conformer of DBA-BTICz and ν -DABNA. Coupling calculated with IDA, a refractive index of 1.7 and a κ^2 of 0.476. Different spectral overlaps are used, the experimental one (Exp.), VH emission and AH absorption spectra (VHAH) and VH emission and VH absorption spectra (VHVH).

Distance Å	Coupling [cm ⁻¹]	Exp.	k _{EET}	
			VHAH	VHVH
30	1.3706	9.5×10 ⁷	5.3×10 ⁸	4.7×10 ⁸
35	0.8631	3.8×10 ⁷	2.1×10 ⁸	1.9×10 ⁸
40	0.5782	1.7×10 ⁷	9.4×10 ⁷	8.4×10 ⁷
45	0.4061	8.4×10 ⁶	4.6×10 ⁷	4.2×10 ⁷
50	0.2961	4.4×10 ⁶	2.5×10 ⁷	2.2×10 ⁷
55	0.2224	2.5×10 ⁶	1.4×10 ⁷	1.2×10 ⁷
60	0.1713	1.5×10 ⁶	8.2×10 ⁶	7.4×10 ⁶
65	0.1348	9.2×10 ⁵	5.1×10 ⁶	4.6×10 ⁶
70	0.1079	5.9×10 ⁵	3.3×10 ⁶	2.9×10 ⁶
75	0.0877	3.9×10 ⁵	2.2×10 ⁶	1.9×10 ⁶
80	0.0723	2.6×10 ⁵	1.5×10 ⁶	1.3×10 ⁶
85	0.0603	1.8×10 ⁵	1.0×10 ⁶	9.2×10 ⁵
90	0.0508	1.3×10 ⁵	7.2×10 ⁵	6.5×10 ⁵
95	0.0432	9.4×10 ⁴	5.2×10 ⁵	4.7×10 ⁵
100	0.0370	6.9×10 ⁴	3.8×10 ⁵	3.5×10 ⁵
120	0.0214	2.3×10 ⁴	1.3×10 ⁵	1.2×10 ⁵

Table S19: EET rate constants between the right conformer of DBA-BTICz and ν -DABNA. Coupling calculated with the MTD approach, a refractive index of 1 and a κ^2 of 4. Different spectral overlaps are used, the experimental one (Exp.), VH emission and AH absorption spectra (VHAH) and VH emission and VH absorption spectra (VHVH).

Distance Å	Coupling [cm ⁻¹]	k _{EET}		
		Exp.	VHAH	VHVH
30	4.6698	1.1×10 ⁹	5.2×10 ⁹	6.1×10 ⁹
35	2.8281	4.1×10 ⁸	1.9×10 ⁹	2.2×10 ⁹
40	1.8376	1.7×10 ⁸	8.1×10 ⁸	9.5×10 ⁸
45	1.2596	8.0×10 ⁷	3.8×10 ⁸	4.4×10 ⁸
50	0.9003	4.1×10 ⁷	1.9×10 ⁸	2.3×10 ⁸
55	0.6654	2.2×10 ⁷	1.1×10 ⁸	1.2×10 ⁸
60	0.5056	1.3×10 ⁷	6.1×10 ⁷	7.2×10 ⁷
65	0.3930	7.8×10 ⁶	3.7×10 ⁷	4.3×10 ⁷
70	0.3115	4.9×10 ⁶	2.3×10 ⁷	2.7×10 ⁷
75	0.2511	3.2×10 ⁶	1.5×10 ⁷	1.8×10 ⁷
80	0.2053	2.1×10 ⁶	1.0×10 ⁷	1.2×10 ⁷
85	0.1700	1.5×10 ⁶	6.9×10 ⁶	8.1×10 ⁶
90	0.1424	1.0×10 ⁶	4.9×10 ⁶	5.7×10 ⁶
95	0.1204	7.3×10 ⁵	3.5×10 ⁶	4.1×10 ⁶
100	0.1027	5.3×10 ⁵	2.5×10 ⁶	3.0×10 ⁶
120	0.0585	1.7×10 ⁵	8.2×10 ⁵	9.6×10 ⁵

Table S20: EET rate constants between the right conformer of DBA-BTICz and ν -DABNA. Coupling calculated with IDA, a refractive index of 1 and a κ^2 of 4. Different spectral overlaps are used, the experimental one (Exp.), VH emission and AH absorption spectra (VHAH) and VH emission and VH absorption spectra (VHVH).

Distance Å	Coupling [cm ⁻¹]	Exp.	k _{EET}	
			VHAH	VHVH
30	3.5757	6.5×10 ⁸	3.1×10 ⁹	3.6×10 ⁹
35	2.2517	2.6×10 ⁸	1.2×10 ⁹	1.4×10 ⁹
40	1.5085	1.2×10 ⁸	5.5×10 ⁸	6.4×10 ⁸
45	1.0595	5.7×10 ⁷	2.7×10 ⁸	3.1×10 ⁸
50	0.7723	3.0×10 ⁷	1.4×10 ⁸	1.7×10 ⁸
55	0.5803	1.7×10 ⁷	8.1×10 ⁷	9.4×10 ⁷
60	0.4470	1.0×10 ⁷	4.8×10 ⁷	5.6×10 ⁷
65	0.3515	6.3×10 ⁶	3.0×10 ⁷	3.5×10 ⁷
70	0.2815	4.0×10 ⁶	1.9×10 ⁷	2.2×10 ⁷
75	0.2288	2.7×10 ⁶	1.3×10 ⁷	1.5×10 ⁷
80	0.1886	1.8×10 ⁶	8.5×10 ⁶	1.0×10 ⁷
85	0.1572	1.3×10 ⁶	5.9×10 ⁶	6.9×10 ⁶
90	0.1324	8.9×10 ⁵	4.2×10 ⁶	4.9×10 ⁶
95	0.1126	6.4×10 ⁵	3.0×10 ⁶	3.5×10 ⁶
100	0.0965	4.7×10 ⁵	2.2×10 ⁶	2.6×10 ⁶
120	0.0559	1.6×10 ⁵	7.5×10 ⁵	8.7×10 ⁵

Table S21: EET rate constants between the right conformer of DBA-BTICz and ν -DABNA. Coupling calculated with MTD, a refractive index of 1 and a κ^2 of 0.476. Different spectral overlaps are used, the experimental one (Exp.), VH emission and AH absorption spectra (VHAH) and VH emission and VH absorption spectra (VHVH).

Distance Å	Coupling [cm ⁻¹]	k _{EET}		
		Exp.	VHAH	VHVH
30	1.6109	1.3×10 ⁸	6.2×10 ⁸	7.3×10 ⁸
35	0.9756	4.8×10 ⁷	2.3×10 ⁸	2.7×10 ⁸
40	0.6339	2.0×10 ⁷	9.7×10 ⁷	1.1×10 ⁸
45	0.4345	9.6×10 ⁶	4.5×10 ⁷	5.3×10 ⁷
50	0.3106	4.9×10 ⁶	2.3×10 ⁷	2.7×10 ⁷
55	0.2295	2.7×10 ⁶	1.3×10 ⁷	1.5×10 ⁷
60	0.1744	1.5×10 ⁶	7.3×10 ⁶	8.5×10 ⁶
65	0.1356	9.3×10 ⁵	4.4×10 ⁶	5.1×10 ⁶
70	0.1075	5.9×10 ⁵	2.8×10 ⁶	3.2×10 ⁶
75	0.0866	3.8×10 ⁵	1.8×10 ⁶	2.1×10 ⁶
80	0.0708	2.5×10 ⁵	1.2×10 ⁶	1.4×10 ⁶
85	0.0587	1.7×10 ⁵	8.3×10 ⁵	9.6×10 ⁵
90	0.0491	1.2×10 ⁵	5.8×10 ⁵	6.8×10 ⁵
95	0.0415	8.7×10 ⁴	4.1×10 ⁵	4.8×10 ⁵
100	0.0354	6.4×10 ⁴	3.0×10 ⁵	3.5×10 ⁵
120	0.0202	2.1×10 ⁴	9.8×10 ⁴	1.1×10 ⁵

Table S22: EET rate constants between the right conformer of DBA-BTICz and ν -DABNA. Coupling calculated with IDA, a refractive index of 1 and a κ^2 of 0.476. Different spectral overlaps are used, the experimental one (Exp.), VH emission and AH absorption spectra (VHAH) and VH emission and VH absorption spectra (VHVH).

Distance Å	Coupling [cm ⁻¹]	k _{EET}		
		Exp.	VHAH	VHVH
30	1.2335	7.7×10 ⁷	3.7×10 ⁸	4.3×10 ⁸
35	0.7768	3.1×10 ⁷	1.4×10 ⁸	1.7×10 ⁸
40	0.5204	1.4×10 ⁷	6.5×10 ⁷	7.6×10 ⁷
45	0.3655	6.8×10 ⁶	3.2×10 ⁷	3.7×10 ⁷
50	0.2664	3.6×10 ⁶	1.7×10 ⁷	2.0×10 ⁷
55	0.2002	2.0×10 ⁶	9.6×10 ⁶	1.1×10 ⁷
60	0.1542	1.2×10 ⁶	5.7×10 ⁶	6.7×10 ⁶
65	0.1213	7.5×10 ⁵	3.5×10 ⁶	4.1×10 ⁶
70	0.0971	4.8×10 ⁵	2.3×10 ⁶	2.6×10 ⁶
75	0.0789	3.2×10 ⁵	1.5×10 ⁶	1.7×10 ⁶
80	0.0650	2.1×10 ⁵	1.0×10 ⁶	1.2×10 ⁶
85	0.0542	1.5×10 ⁵	7.1×10 ⁵	8.2×10 ⁵
90	0.0457	1.1×10 ⁵	5.0×10 ⁵	5.8×10 ⁵
95	0.0388	7.6×10 ⁴	3.6×10 ⁵	4.2×10 ⁵
100	0.0333	5.6×10 ⁴	2.7×10 ⁵	3.1×10 ⁵
120	0.0193	1.9×10 ⁴	8.9×10 ⁴	1.0×10 ⁵

Table S23: EET rate constants between the right conformer of DBA-BTICz and ν -DABNA. Coupling calculated with the MTD approach, a refractive index of 1.7 and a κ^2 of 4. Different spectral overlaps are used, the experimental one (Exp.), VH emission and AH absorption spectra (VHAH) and VH emission and VH absorption spectra (VHVH).

Distance Å	Coupling [cm ⁻¹]	Exp.	k _{EET}	
			VHAH	VHVH
30	1.6158	1.3×10 ⁸	6.3×10 ⁸	7.3×10 ⁸
35	0.9786	4.9×10 ⁷	2.3×10 ⁸	2.7×10 ⁸
40	0.6359	2.0×10 ⁷	9.7×10 ⁷	1.1×10 ⁸
45	0.4358	9.6×10 ⁶	4.6×10 ⁷	5.3×10 ⁷
50	0.3115	4.9×10 ⁶	2.3×10 ⁷	2.7×10 ⁷
55	0.2303	2.7×10 ⁶	1.3×10 ⁷	1.5×10 ⁷
60	0.1749	1.6×10 ⁶	7.4×10 ⁶	8.6×10 ⁶
65	0.1360	9.4×10 ⁵	4.4×10 ⁶	5.2×10 ⁶
70	0.1078	5.9×10 ⁵	2.8×10 ⁶	3.3×10 ⁶
75	0.0869	3.8×10 ⁵	1.8×10 ⁶	2.1×10 ⁶
80	0.0710	2.6×10 ⁵	1.2×10 ⁶	1.4×10 ⁶
85	0.0588	1.8×10 ⁵	8.3×10 ⁵	9.7×10 ⁵
90	0.0493	1.2×10 ⁵	5.8×10 ⁵	6.8×10 ⁵
95	0.0417	8.8×10 ⁴	4.2×10 ⁵	4.9×10 ⁵
100	0.0355	6.4×10 ⁴	3.0×10 ⁵	3.5×10 ⁵
120	0.0203	2.1×10 ⁴	9.9×10 ⁴	1.1×10 ⁵

Table S24: EET rate constants between the right conformer of DBA-BTICz and ν -DABNA. Coupling calculated with IDA, a refractive index of 1.7 and a κ^2 of 4. Different spectral overlaps are used, the experimental one (Exp.), VH emission and AH absorption spectra (VHAH) and VH emission and VH absorption spectra (VHVH).

Distance Å	Coupling [cm ⁻¹]	Exp.	k _{EET}	
			VHAH	VHVH
30	1.2373	7.8×10 ⁷	3.7×10 ⁸	4.3×10 ⁸
35	0.7791	3.1×10 ⁷	1.5×10 ⁸	1.7×10 ⁸
40	0.5220	1.4×10 ⁷	6.5×10 ⁷	7.6×10 ⁷
45	0.3666	6.8×10 ⁶	3.2×10 ⁷	3.8×10 ⁷
50	0.2672	3.6×10 ⁶	1.7×10 ⁷	2.0×10 ⁷
55	0.2008	2.0×10 ⁶	9.7×10 ⁶	1.1×10 ⁷
60	0.1547	1.2×10 ⁶	5.7×10 ⁶	6.7×10 ⁶
65	0.1216	7.5×10 ⁵	3.6×10 ⁶	4.1×10 ⁶
70	0.0974	4.8×10 ⁵	2.3×10 ⁶	2.7×10 ⁶
75	0.0792	3.2×10 ⁵	1.5×10 ⁶	1.8×10 ⁶
80	0.0652	2.2×10 ⁵	1.0×10 ⁶	1.2×10 ⁶
85	0.0544	1.5×10 ⁵	7.1×10 ⁵	8.3×10 ⁵
90	0.0458	1.1×10 ⁵	5.0×10 ⁵	5.9×10 ⁵
95	0.0390	7.7×10 ⁴	3.6×10 ⁵	4.2×10 ⁵
100	0.0334	5.7×10 ⁴	2.7×10 ⁵	3.1×10 ⁵
120	0.0193	1.9×10 ⁴	9.0×10 ⁴	1.0×10 ⁵

Table S25: EET rate constants between the right conformer of DBA-BTICz and ν -DABNA. Coupling calculated with the MTD approach, a refractive index of 1.7 and a κ^2 of 0.476. Different spectral overlaps are used, the experimental one (Exp.), VH emission and AH absorption spectra (VHAH) and VH emission and VH absorption spectra (VHVH).

Distance Å	Coupling [cm ⁻¹]	k _{EET}		
		Exp.	VHAH	VHVH
30	0.5574	1.6×10 ⁷	7.5×10 ⁷	8.7×10 ⁷
35	0.3376	5.8×10 ⁶	2.7×10 ⁷	3.2×10 ⁷
40	0.2193	2.4×10 ⁶	1.2×10 ⁷	1.3×10 ⁷
45	0.1503	1.1×10 ⁶	5.4×10 ⁶	6.3×10 ⁶
50	0.1075	5.9×10 ⁵	2.8×10 ⁶	3.2×10 ⁶
55	0.0794	3.2×10 ⁵	1.5×10 ⁶	1.8×10 ⁶
60	0.0603	1.8×10 ⁵	8.7×10 ⁵	1.0×10 ⁶
65	0.0469	1.1×10 ⁵	5.3×10 ⁵	6.2×10 ⁵
70	0.0372	7.0×10 ⁴	3.3×10 ⁵	3.9×10 ⁵
75	0.0300	4.6×10 ⁴	2.2×10 ⁵	2.5×10 ⁵
80	0.0245	3.0×10 ⁴	1.4×10 ⁵	1.7×10 ⁵
85	0.0203	2.1×10 ⁴	9.9×10 ⁴	1.2×10 ⁵
90	0.0170	1.5×10 ⁴	6.9×10 ⁴	8.1×10 ⁴
95	0.0144	1.0×10 ⁴	5.0×10 ⁴	5.8×10 ⁴
100	0.0123	7.6×10 ³	3.6×10 ⁴	4.2×10 ⁴
120	0.0070	2.5×10 ³	1.2×10 ⁴	1.4×10 ⁴

Table S26: EET rate constants between the right conformer of DBA-BTICz and ν -DABNA. Coupling calculated with IDA, a refractive index of 1.7 and a κ^2 of 0.476. Different spectral overlaps are used, the experimental one (Exp.), VH emission and AH absorption spectra (VHAH) and VH emission and VH absorption spectra (VHVH).

Distance Å	Coupling [cm ⁻¹]	Exp.	k _{EET}	
			VHAH	VHVH
30	0.4268	9.2×10 ⁶	4.4×10 ⁷	5.1×10 ⁷
35	0.2688	3.7×10 ⁶	1.7×10 ⁷	2.0×10 ⁷
40	0.1801	1.6×10 ⁶	7.8×10 ⁶	9.1×10 ⁶
45	0.1265	8.1×10 ⁵	3.8×10 ⁶	4.5×10 ⁶
50	0.0922	4.3×10 ⁵	2.0×10 ⁶	2.4×10 ⁶
55	0.0693	2.4×10 ⁵	1.2×10 ⁶	1.3×10 ⁶
60	0.0534	1.4×10 ⁵	6.8×10 ⁵	8.0×10 ⁵
65	0.0420	8.9×10 ⁴	4.2×10 ⁵	4.9×10 ⁵
70	0.0336	5.7×10 ⁴	2.7×10 ⁵	3.2×10 ⁵
75	0.0273	3.8×10 ⁴	1.8×10 ⁵	2.1×10 ⁵
80	0.0225	2.6×10 ⁴	1.2×10 ⁵	1.4×10 ⁵
85	0.0188	1.8×10 ⁴	8.5×10 ⁴	9.9×10 ⁴
90	0.0158	1.3×10 ⁴	6.0×10 ⁴	7.0×10 ⁴
95	0.0134	9.2×10 ³	4.3×10 ⁴	5.1×10 ⁴
100	0.0115	6.7×10 ³	3.2×10 ⁴	3.7×10 ⁴
120	0.0067	2.3×10 ³	1.1×10 ⁴	1.2×10 ⁴

S4 Further Computational Details

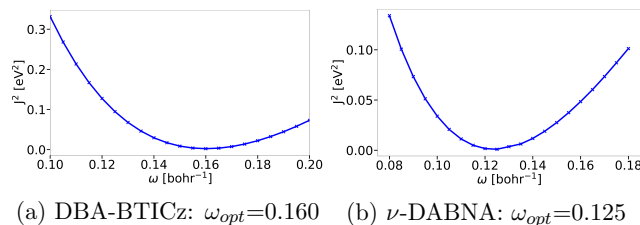


Figure S16: Scan of the range separation parameter ω for both molecules.

Table S27: Comparison between MTD calculation with a freeze of orbitals and without. Calculations were done with the right conformer of DBA-BTICz and ν -DABNA.

	MTD ECME [cm^{-1}]	Comput. time
Freeze	1.656531	10h 17m 2s
NoFreeze	1.673928	17h 12m 25s

Table S36: XYZ coordinates in Å of the S_0 geometry of ν -DABNA.

C	0.160013	1.246903	1.067099
B	0.364508	2.610828	1.780585
C	0.204568	3.835613	0.889519
C	0.062888	3.701246	-0.526530
N	0.076970	2.421272	-1.104327
C	0.077746	1.227247	-0.364330
C	0.704581	2.915665	3.269389
C	0.620790	4.272087	3.720033
N	0.319952	5.318470	2.828944
C	0.183339	5.152196	1.443514
C	-0.065916	4.835776	-1.351539
C	-0.109648	6.118600	-0.772854
C	0.000000	6.282268	0.619362
C	0.000000	0.000000	-1.054837
N	-0.265193	7.258179	-1.604125
C	0.860651	4.583516	5.086347
C	0.000000	0.000000	1.707232
C	1.122028	1.947929	4.221696
C	0.014322	2.334524	-2.542058
H	-0.139259	4.740171	-2.441143
H	-0.053667	7.291603	1.043686
C	0.206448	6.655109	3.357453
C	1.230417	3.586662	5.987815
C	1.385691	2.256741	5.556309
H	0.771321	5.619284	5.441082
H	1.417610	3.856874	7.040240
H	1.709705	1.472303	6.258567
H	1.266967	0.909494	3.889165
C	-0.077746	-1.227247	-0.364330
N	-0.076970	-2.421272	-1.104327
C	-0.062888	-3.701246	-0.526530
C	-0.204568	-3.835613	0.889519
B	-0.364508	-2.610828	1.780585
C	-0.160013	-1.246903	1.067099
C	-0.014322	-2.334524	-2.542058
C	0.065916	-4.835776	-1.351539
C	-0.183339	-5.152196	1.443514
C	-0.704581	-2.915665	3.269389
C	-1.122028	-1.947929	4.221696
C	-1.385691	-2.256741	5.556309
C	-1.230417	-3.586662	5.987815
C	-0.860651	-4.583516	5.086347
C	-0.620790	-4.272087	3.720033

C Included Publications

H	-1.266967	-0.909494	3.889165
H	-1.709705	-1.472303	6.258567
H	-1.417610	-3.856874	7.040240
H	-0.771321	-5.619284	5.441082
N	-0.319952	-5.318470	2.828944
C	0.000000	-6.282268	0.619362
C	0.109648	-6.118600	-0.772854
N	0.265193	-7.258179	-1.604125
C	1.231354	-2.287191	-3.190447
C	1.286610	-2.209871	-4.589601
C	0.100953	-2.177739	-5.340756
C	-1.142231	-2.225289	-4.690527
C	-1.202040	-2.304527	-3.291222
H	2.152843	-2.313732	-2.588437
H	2.264134	-2.176055	-5.096728
H	0.146328	-2.117427	-6.440006
H	-2.074829	-2.201537	-5.276827
H	-2.169415	-2.343631	-2.766873
C	1.202040	2.304527	-3.291222
C	1.142231	2.225289	-4.690527
C	-0.100953	2.177739	-5.340756
C	-1.286610	2.209871	-4.589601
C	-1.231354	2.287191	-3.190447
H	2.169415	2.343631	-2.766873
H	2.074829	2.201537	-5.276827
H	-0.146328	2.117427	-6.440006
H	-2.264134	2.176055	-5.096728
H	-2.152843	2.313732	-2.588437
C	-0.206448	-6.655109	3.357453
C	1.042601	-7.128157	3.792173
C	1.156584	-8.429996	4.302532
C	0.026126	-9.259188	4.376031
C	-1.220937	-8.784526	3.938978
C	-1.339621	-7.482892	3.430229
H	1.920491	-6.466865	3.726557
H	2.137077	-8.799409	4.643489
H	0.117591	-10.282238	4.774812
H	-2.109725	-9.433439	3.992486
H	-2.311061	-7.097789	3.083236
C	-1.042601	7.128157	3.792173
C	-1.156584	8.429996	4.302532
C	-0.026126	9.259188	4.376031
C	1.220937	8.784526	3.938978
C	1.339621	7.482892	3.430229
H	-1.920491	6.466865	3.726557
H	-2.137077	8.799409	4.643489
H	-0.117591	10.282238	4.774812
H	2.109725	9.433439	3.992486
H	2.311061	7.097789	3.083236
H	0.000000	0.000000	2.804066
H	0.053667	-7.291603	1.043686
H	0.139259	-4.740171	-2.441143
H	0.000000	0.000000	-2.149804
C	1.111934	-7.203223	-2.744672
C	-0.422412	-8.464966	-1.300007
C	2.363461	-6.551958	-2.681025

Table S37: XYZ coordinates in Å of the S₁ geometry of ν-DABNA.

C	-0.084002	-1.260759	1.104338
B	-0.228649	-2.638545	1.804676
C	-0.022602	-3.848781	0.903491
C	0.131721	-3.704677	-0.505218
N	0.076548	-2.417212	-1.073150
C	0.000000	-1.231637	-0.335201
C	-0.545448	-2.964755	3.293592
C	-0.437285	-4.328707	3.730863
N	-0.112316	-5.355638	2.819409
C	0.040074	-5.171222	1.438704
C	0.317551	-4.825498	-1.342383
C	0.406488	-6.116987	-0.782293
C	0.279896	-6.289887	0.608077
C	0.000000	0.000000	-1.027134
N	0.614823	-7.237962	-1.627940
C	-0.669821	-4.671826	5.087779
C	0.000000	0.000000	1.747915
C	-0.966294	-2.022325	4.269912
C	0.158489	-2.319985	-2.510844
H	0.397172	-4.714059	-2.430674
H	0.364080	-7.299530	1.027486
C	0.018056	-6.698226	3.331069
C	-1.049604	-3.695476	6.014151
C	-1.217125	-2.363063	5.603294

H	-0.565289	-5.712901	5.421729
H	-1.227072	-3.986079	7.062491
H	-1.539385	-1.591781	6.321450
H	-1.123641	-0.978493	3.962465
C	0.000000	1.231637	-0.335201
N	-0.076548	2.417212	-1.073150
C	-0.131721	3.704677	-0.505218
C	0.022602	3.848781	0.903491
B	0.228649	2.638545	1.804676
C	0.084002	1.260759	1.104338
C	-0.158489	2.319985	-2.510844
C	-0.317551	4.825498	-1.342383
C	-0.040074	5.171222	1.438704
C	0.545448	2.964755	3.293592
C	0.966294	2.022325	4.269912
C	1.217125	2.363063	5.603294
C	1.049604	3.695476	6.014151
C	0.669821	4.671826	5.087779
C	0.437285	4.328707	3.730863
H	1.123641	0.978493	3.962465
H	1.539385	1.591781	6.321450
H	1.227072	3.986079	7.062491
H	0.565289	5.712901	5.421729
N	0.112316	5.355638	2.819409
C	-0.279896	6.289887	0.608077
C	-0.406488	6.116987	-0.782293
N	-0.614823	7.237962	-1.627940
C	-1.411257	2.202097	-3.135046
C	-1.486229	2.120901	-4.533065
C	-0.314013	2.154501	-5.304977
C	0.936032	2.270669	-4.676886
C	1.016667	2.353834	-3.278903
H	-2.321708	2.178093	-2.516582
H	-2.469276	2.033631	-5.022715
H	-0.375395	2.092012	-6.403272
H	1.857995	2.298632	-5.279467
H	1.989381	2.446462	-2.771595
C	-1.016667	-2.353834	-3.278903
C	-0.936032	-2.270669	-4.676886
C	0.314013	-2.154501	-5.304977
C	1.486229	-2.120901	-4.533065
C	1.411257	-2.202097	-3.135046
H	-1.989381	-2.446462	-2.771595
H	-1.857995	-2.298632	-5.279467
H	0.375395	-2.092012	-6.403272
H	2.469276	-2.033631	-5.022715
H	2.321708	-2.178093	-2.516582
C	-0.018056	6.698226	3.331069
C	-1.268734	7.152591	3.780300
C	-1.398134	8.459705	4.272992
C	-0.282428	9.310816	4.314774
C	0.965882	8.853075	3.863565
C	1.101120	7.546477	3.372090
H	-2.134629	6.473787	3.740174
H	-2.379578	8.815753	4.625135
H	-0.386519	10.337830	4.699914
H	1.843077	9.519057	3.892223
H	2.073621	7.173960	3.014776
C	1.268734	-7.152591	3.780300
C	1.398134	-8.459705	4.272992
C	0.282428	-9.310816	4.314774
C	-0.965882	-8.853075	3.863565
C	-1.101120	-7.546477	3.372090
H	2.134629	-6.473787	3.740174
H	2.379578	-8.815753	4.625135
H	0.386519	-10.337830	4.699914
H	-1.843077	-9.519057	3.892223
H	-2.073621	-7.173960	3.014776
H	0.000000	0.000000	2.842896
H	-0.364080	7.299530	1.027486
H	-0.397172	4.714059	-2.430674
H	0.000000	0.000000	-2.121323
C	-1.535014	7.148868	-2.705161
C	0.083711	8.450890	-1.384355
C	-2.753309	6.449094	-2.553477

Table S38: XYZ coordinates in Å of the T_1 geometry of ν -DABNA.

C	-0.082427	-1.260827	1.106913
B	-0.220547	-2.640152	1.806888
C	-0.017631	-3.847708	0.905264
C	0.131406	-3.703612	-0.506088
N	0.075610	-2.416747	-1.072686

C Included Publications

C	0.000000	-1.230979	-0.332071
C	-0.531820	-2.969738	3.295652
C	-0.424329	-4.334908	3.731682
N	-0.102313	-5.360625	2.819141
C	0.045376	-5.172047	1.437451
C	0.310904	-4.824764	-1.344048
C	0.400175	-6.116012	-0.787407
C	0.280021	-6.289249	0.604503
C	0.000000	0.000000	-1.022976
N	0.607650	-7.240548	-1.632500
C	-0.654617	-4.681024	5.088590
C	0.000000	0.000000	1.749077
C	-0.950130	-2.029756	4.275955
C	0.154991	-2.318116	-2.510545
H	0.390235	-4.712469	-2.432493
H	0.365206	-7.299921	1.021767
C	0.032099	-6.704484	3.327982
C	-1.030917	-3.707303	6.017982
C	-1.197921	-2.373687	5.608230
H	-0.550678	-5.723261	5.419044
H	-1.206909	-3.999198	7.066018
H	-1.518864	-1.603628	6.328332
H	-1.107632	-0.985061	3.971985
C	0.000000	1.230979	-0.332071
N	-0.075610	2.416747	-1.072686
C	-0.131406	3.703612	-0.506088
C	0.017631	3.847708	0.905264
B	0.220547	2.640152	1.806888
C	0.082427	1.260827	1.106913
C	-0.154991	2.318116	-2.510545
C	-0.310904	4.824764	-1.344048
C	-0.045376	5.172047	1.437451
C	0.531820	2.969738	3.295652
C	0.950130	2.029756	4.275955
C	1.197921	2.373687	5.608230
C	1.030917	3.707303	6.017982
C	0.654617	4.681024	5.088590
C	0.424329	4.334908	3.731682
H	1.107632	0.985061	3.971985
H	1.518864	1.603628	6.328332
H	1.206909	3.999198	7.066018
H	0.550678	5.723261	5.419044
N	0.102313	5.360625	2.819141
C	-0.280021	6.289249	0.604503
C	-0.400175	6.116012	-0.787407
N	-0.607650	7.240548	-1.632500
C	-1.406915	2.203154	-3.136928
C	-1.479370	2.120405	-4.534995
C	-0.305585	2.149806	-5.304643
C	0.943582	2.263543	-4.674311
C	1.021735	2.348292	-3.276309
H	-2.318698	2.182779	-2.520307
H	-2.461712	2.035325	-5.026418
H	-0.365022	2.086097	-6.402969
H	1.866759	2.288371	-5.275151
H	1.993742	2.439078	-2.767308
C	-1.021735	-2.348292	-3.276309
C	-0.943582	-2.263543	-4.674311
C	0.305585	-2.149806	-5.304643
C	1.479370	-2.120405	-4.534995
C	1.406915	-2.203154	-3.136928
H	-1.993742	-2.439078	-2.767308
H	-1.866759	-2.288371	-5.275151
H	0.365022	-2.086097	-6.402969
H	2.461712	-2.035325	-5.026418
H	2.318698	-2.182779	-2.520307
C	-0.032099	6.704484	3.327982
C	-1.285101	7.156572	3.772514
C	-1.418613	8.464423	4.262102
C	-0.304826	9.317950	4.305185
C	0.945717	8.862110	3.858352
C	1.085262	7.554799	3.369992
H	-2.149471	6.475917	3.731283
H	-2.401801	8.819093	4.610627
H	-0.412235	10.345554	4.687759
H	1.821306	9.530089	3.887719
H	2.059470	7.184019	3.015601
C	1.285101	-7.156572	3.772514
C	1.418613	-8.464423	4.262102
C	0.304826	-9.317950	4.305185
C	-0.945717	-8.862110	3.858352
C	-1.085262	-7.554799	3.369992
H	2.149471	-6.475917	3.731283
H	2.401801	-8.819093	4.610627
H	0.412235	-10.345554	4.687759
H	-1.821306	-9.530089	3.887719

H	-2.059470	-7.184019	3.015601
H	0.000000	0.000000	2.844114
H	-0.365206	7.299921	1.021767
H	-0.390235	4.712469	-2.432493
H	0.000000	0.000000	-2.117269
C	-1.564217	7.167054	-2.677861
C	0.136476	8.429930	-1.417259
C	-2.784364	6.479792	-2.487131

Table S39: XYZ coordinates in Å of the T₂ geometry of ν -DABNA.

C	-0.062657	-1.265869	1.136338
B	-0.158178	-2.651108	1.835739
C	0.037800	-3.850678	0.922259
C	0.145248	-3.701806	-0.499109
N	0.065980	-2.417619	-1.051300
C	0.000000	-1.236917	-0.288477
C	-0.424677	-2.999182	3.331197
C	-0.281892	-4.362575	3.756432
N	0.032410	-5.379525	2.830114
C	0.131898	-5.175860	1.446632
C	0.306699	-4.819256	-1.354545
C	0.421540	-6.104027	-0.808361
C	0.348719	-6.281001	0.596814
C	0.000000	0.000000	-0.982813
N	0.626063	-7.233010	-1.645494
C	-0.467127	-4.717024	5.117604
C	0.000000	0.000000	1.774628
C	-0.830056	-2.070101	4.326649
C	0.096039	-2.305506	-2.490927
H	0.358468	-4.696473	-2.443201
H	0.463669	-7.292741	1.004770
C	0.203938	-6.723182	3.324683
C	-0.832171	-3.753463	6.062309
C	-1.033836	-2.421439	5.664553
H	-0.336012	-5.758762	5.440409
H	-0.973027	-4.053339	7.113538
H	-1.347965	-1.659667	6.396346
H	-1.012803	-1.026852	4.031718
C	0.000000	1.236917	-0.288477
N	-0.065980	2.417619	-1.051300
C	-0.145248	3.701806	-0.499109
C	-0.037800	3.850678	0.922259
B	0.158178	2.651108	1.835739
C	0.062657	1.265869	1.136338
C	-0.096039	2.305506	-2.490927
C	-0.306699	4.819256	-1.354545
C	-0.131898	5.175860	1.446632
C	0.424677	2.999182	3.331197
C	0.830056	2.070101	4.326649
C	1.033836	2.421439	5.664553
C	0.832171	3.753463	6.062309
C	0.467127	4.717024	5.117604
C	0.281892	4.362575	3.756432
H	1.012803	1.026852	4.031718
H	1.347965	1.659667	6.396346
H	0.973027	4.053339	7.113538
H	0.336012	5.758762	5.440409
N	-0.032410	5.379525	2.830114
C	-0.348719	6.281001	0.596814
C	-0.421540	6.104027	-0.808361
N	-0.626063	7.233010	-1.645494
C	-1.325210	2.187800	-3.160186
C	-1.347072	2.090137	-4.559034
C	-0.146215	2.108558	-5.286001
C	1.079728	2.227101	-4.612451
C	1.107738	2.327199	-3.213638
H	-2.258720	2.176262	-2.576745
H	-2.311217	2.001082	-5.084493
H	-0.166234	2.032737	-6.384955
H	2.024074	2.243682	-5.179669
H	2.060807	2.422526	-2.670826
C	-1.107738	-2.327199	-3.213638
C	-1.079728	-2.227101	-4.612451
C	0.146215	-2.108558	-5.286001
C	1.347072	-2.090137	-4.559034
C	1.325210	-2.187800	-3.160186
H	-2.060807	-2.422526	-2.670826
H	-2.024074	-2.243682	-5.179669
H	0.166234	-2.032737	-6.384955
H	2.311217	-2.001082	-5.084493
H	2.258720	-2.176262	-2.576745
C	-0.203938	6.723182	3.324683

C Included Publications

C	-1.477395	7.160081	3.725159
C	-1.647182	8.468610	4.201734
C	-0.548560	9.339506	4.276062
C	0.722839	8.900108	3.873774
C	0.897856	7.592062	3.398843
H	-2.329459	6.465790	3.660435
H	-2.646554	8.810176	4.515751
H	-0.684142	10.367572	4.648413
H	1.586820	9.581574	3.928118
H	1.889062	7.233941	3.080150
C	1.477395	-7.160081	3.725159
C	1.647182	-8.468610	4.201734
C	0.548560	-9.339506	4.276062
C	-0.722839	-8.900108	3.873774
C	-0.897856	-7.592062	3.398843
H	2.329459	-6.465790	3.660435
H	2.646554	-8.810176	4.515751
H	0.684142	-10.367572	4.648413
H	-1.586820	-9.581574	3.928118
H	-1.889062	-7.233941	3.080150
H	0.000000	0.000000	2.869899
H	-0.463669	7.292741	1.004770
H	-0.358468	4.696473	-2.443201
H	0.000000	0.000000	-2.077300
C	-1.521471	7.145085	-2.744526
C	0.094704	8.429778	-1.399481
C	-2.750769	6.460744	-2.613893

Table S28: XYZ coordinates in Å of the S₀ geometry of the left DBA-BTICz conformer.

C	0.756243	0.888035	-3.197742
C	0.833406	-0.294624	-2.444260
C	-0.196074	-1.235993	-2.574325
C	-1.289478	-1.044618	-3.448035
C	-1.312806	0.153864	-4.194976
C	-0.311852	1.128432	-4.079515
B	-2.400151	-2.087744	-3.577736
C	-3.525482	-1.680882	-4.576772
C	-3.386193	-0.434536	-5.243567
O	-2.328168	0.421161	-5.057195
O	-0.092659	-2.361223	-1.821359
C	-1.021098	-3.371395	-1.867002
C	-2.181861	-3.346250	-2.685435
C	-4.693721	-2.423209	-4.898963
C	-5.645821	-1.970433	-5.810830
C	-5.462788	-0.729040	-6.450527
C	-4.336514	0.039931	-6.169005
C	-0.716958	-4.453314	-1.017348
C	-1.574949	-5.548801	-0.968166
C	-2.736290	-5.570535	-1.765031
C	-3.020842	-4.490157	-2.598326
N	1.797400	1.852077	-3.086851
C	2.689364	2.111474	-4.142174
C	3.833036	2.779535	-3.626295
C	3.621676	2.905005	-2.197782
C	2.352723	2.349513	-1.901733
C	2.586095	1.768176	-5.498992
C	3.637625	2.136425	-6.346658
C	4.768401	2.822311	-5.856155
C	4.876995	3.142077	-4.498800
C	4.433656	3.367672	-1.140276
C	4.036344	3.307893	0.219569
C	2.670371	2.933772	0.452651
C	1.820720	2.433441	-0.584625
C	5.160607	3.635755	1.106576
C	6.305538	4.054343	0.370095
S	6.060731	3.973845	-1.362044
C	0.507861	2.210422	0.006514
C	0.621700	2.569226	1.377462
N	1.928828	2.999472	1.638737
C	-0.475996	2.544875	2.254389
C	-1.712337	2.139490	1.745812
C	-1.854187	1.790996	0.387054
C	-0.761483	1.831990	-0.482977
C	7.511828	4.424695	0.985215
C	7.606649	4.342778	2.376207
C	6.513368	3.871131	3.127236
C	5.311189	3.519552	2.507874
C	2.210280	3.797628	2.789655
C	2.499676	5.164808	2.647332
C	2.756682	5.942842	3.783398
C	2.705600	5.368054	5.061894
C	2.399683	4.006241	5.202533
C	2.157356	3.217776	4.069456
H	1.674248	-0.481771	-1.763509
H	-0.381625	2.065132	-4.647969
H	-4.860614	-3.393799	-4.411141
H	-6.536200	-2.579815	-6.029287
H	-6.208077	-0.360987	-7.173349
H	-4.164399	1.014473	-6.649209
H	0.198577	-4.405180	-0.409599
H	-1.339979	-6.396441	-0.305062
H	-3.415426	-6.436244	-1.730197
H	-3.931605	-4.532219	-3.212058
H	1.712516	1.225919	-5.887850
H	3.576750	1.883530	-7.416955
H	5.577116	3.103553	-6.548514
H	5.768231	3.667251	-4.123051
H	-0.371159	2.848852	3.305309
H	-2.587369	2.108283	2.414070
H	-2.841035	1.493220	-0.000213
H	-0.910375	1.592083	-1.542541
H	8.369331	4.752711	0.377832
H	8.545443	4.623673	2.878789
H	6.602483	3.769981	4.220168
H	4.492931	3.132265	3.125397
H	2.529490	5.611025	1.642028
H	2.993667	7.011925	3.667013
H	2.904598	5.984126	5.952654
H	2.359701	3.548158	6.203287
H	1.944664	2.142442	4.167774

Table S29: XYZ coordinates in Å of the S_{CT} geometry of the left DBA-BTICz conformer.

C	0.969787	0.745670	-3.289598
C	1.020634	-0.472920	-2.555121
C	-0.062196	-1.336929	-2.630383
C	-1.233607	-1.061899	-3.407863
C	-1.220443	0.164740	-4.141616
C	-0.157893	1.059526	-4.108671
B	-2.401370	-2.008343	-3.455774
C	-3.586312	-1.515751	-4.358717
C	-3.416938	-0.276139	-5.035906
O	-2.288578	0.506217	-4.930242
O	0.024418	-2.500658	-1.913898
C	-0.978176	-3.446683	-1.898244
C	-2.203522	-3.312507	-2.606638
C	-4.826369	-2.165086	-4.587654
C	-5.820303	-1.640057	-5.422173
C	-5.605290	-0.416041	-6.075545
C	-4.400289	0.266707	-5.881291
C	-0.678515	-4.569469	-1.108331
C	-1.606017	-5.611173	-0.997535
C	-2.828691	-5.523916	-1.680832
C	-3.106656	-4.396458	-2.463511
N	2.025527	1.687986	-3.154286
C	2.916862	1.999494	-4.194210
C	3.982267	2.785987	-3.679515
C	3.721343	2.924094	-2.254791
C	2.473600	2.281589	-1.990506
C	2.855406	1.594888	-5.534135
C	3.881874	2.032884	-6.383066
C	4.934653	2.830745	-5.896334
C	5.000857	3.208488	-4.543442
C	4.468021	3.422135	-1.188794
C	4.027379	3.331224	0.185045
C	2.688008	2.908696	0.382983
C	1.884580	2.350244	-0.686268
C	5.107600	3.718185	1.097412
C	6.238723	4.218576	0.393445
S	6.046036	4.143301	-1.354519
C	0.585112	2.071205	-0.140772
C	0.634592	2.459664	1.236437
N	1.904085	2.951596	1.539462
C	-0.489602	2.393180	2.071395
C	-1.681153	1.915220	1.518594
C	-1.760913	1.531914	0.159177
C	-0.649034	1.608751	-0.672328
C	7.399418	4.659226	1.038611
C	7.462890	4.566925	2.434367
C	6.388132	4.015961	3.153527
C	5.226863	3.592154	2.500243
C	2.121049	3.743624	2.712039
C	2.339970	5.125597	2.596680
C	2.535869	5.893657	3.751799
C	2.492927	5.291172	5.017686
C	2.255491	3.912973	5.128764
C	2.074172	3.134399	3.977734
H	1.890616	-0.731076	-1.935839
H	-0.213400	2.001521	-4.671764
H	-5.023242	-3.125014	-4.088411
H	-6.765799	-2.187028	-5.564785
H	-6.376596	0.010138	-6.736884
H	-4.195627	1.229407	-6.373825
H	0.291871	-4.602460	-0.590166
H	-1.370550	-6.491361	-0.378064
H	-3.567220	-6.337705	-1.604754
H	-4.070902	-4.357768	-2.991039
H	2.035434	0.958750	-5.895501
H	3.865560	1.741643	-7.444375
H	5.727361	3.159603	-6.585917
H	5.839174	3.822907	-4.182361
H	-0.441611	2.714911	3.120608
H	-2.576948	1.845869	2.155383
H	-2.715290	1.168284	-0.249736
H	-0.735645	1.329705	-1.728117
H	8.249636	5.048861	0.458868
H	8.368758	4.902850	2.962277
H	6.458301	3.907157	4.246625
H	4.421417	3.140496	3.089989
H	2.361363	5.593294	1.600878
H	2.716781	6.975846	3.660193
H	2.642843	5.899492	5.923084
H	2.220080	3.434999	6.120086
H	1.913160	2.048215	4.052649

Table S30: XYZ coordinates in Å of the T_{DBA} geometry of the left DBA-BTICz conformer.

C	0.805980	0.819973	-3.166575
C	0.856809	-0.423241	-2.492752
C	-0.208544	-1.335291	-2.638660
C	-1.333826	-1.096722	-3.458101
C	-1.330755	0.144200	-4.131486
C	-0.299950	1.099336	-4.000051
B	-2.459906	-2.100246	-3.606681
C	-3.590435	-1.626501	-4.568180
C	-3.443273	-0.339378	-5.178749
O	-2.357657	0.482790	-4.952399
O	-0.099171	-2.497449	-1.946073
C	-1.054193	-3.491619	-1.985799
C	-2.250293	-3.396350	-2.768689
C	-4.775634	-2.315925	-4.931336
C	-5.724682	-1.780803	-5.813768
C	-5.534858	-0.510552	-6.387163
C	-4.382551	0.214187	-6.065016
C	-0.733814	-4.600548	-1.183903
C	-1.614158	-5.686143	-1.127865
C	-2.802829	-5.639616	-1.878453
C	-3.104795	-4.523996	-2.672864
N	1.870945	1.750158	-3.046423
C	2.768380	1.995517	-4.097301
C	3.886844	2.713885	-3.595968
C	3.656357	2.879239	-2.175030
C	2.398000	2.299813	-1.871262
C	2.680721	1.605413	-5.442523
C	3.726394	1.975077	-6.296448
C	4.834857	2.707603	-5.821069
C	4.926194	3.076029	-4.474669
C	4.451749	3.390957	-1.127914
C	4.051914	3.357084	0.251454
C	2.697572	2.945415	0.470424
C	1.864089	2.392315	-0.554179
C	5.164289	3.739680	1.112140
C	6.299501	4.169491	0.366904
S	6.062393	4.034444	-1.362832
C	0.565429	2.122421	0.051624
C	0.670544	2.516345	1.414122
N	1.958303	3.008849	1.657897
C	-0.418557	2.461025	2.300170
C	-1.637529	1.982207	1.813995
C	-1.770995	1.591305	0.466527
C	-0.688166	1.667475	-0.413753
C	7.493525	4.590053	0.973427
C	7.587562	4.548984	2.366279
C	6.505920	4.067754	3.127799
C	5.315337	3.666248	2.516298
C	2.209916	3.847293	2.786995
C	2.447664	5.220053	2.607774
C	2.676185	6.037267	3.722232
C	2.647687	5.495473	5.015724
C	2.393413	4.127347	5.193126
C	2.180178	3.300279	4.081970
H	1.708609	-0.681837	-1.848045
H	-0.377548	2.057124	-4.533775
H	-4.964349	-3.312570	-4.507094
H	-6.627230	-2.363066	-6.058797
H	-6.278751	-0.088529	-7.079795
H	-4.186026	1.211326	-6.486200
H	0.208301	-4.585327	-0.616116
H	-1.375885	-6.560863	-0.503996
H	-3.505766	-6.487199	-1.843815
H	-4.045353	-4.530819	-3.242152
H	1.823510	1.026413	-5.816295
H	3.680721	1.685699	-7.358224
H	5.640287	2.987687	-6.517728
H	5.800042	3.639092	-4.113196
H	-0.320667	2.796015	3.342247
H	-2.504524	1.924582	2.490812
H	-2.743115	1.232083	0.094603
H	-0.834812	1.392053	-1.463566
H	8.342812	4.925046	0.358336
H	8.516973	4.869546	2.862497
H	6.594903	3.998884	4.223255
H	4.507327	3.273456	3.143479
H	2.460095	5.640097	1.590897
H	2.872824	7.110973	3.576854
H	2.824101	6.142163	5.889367
H	2.371767	3.694914	6.205777
H	2.009483	2.220558	4.209718

Table S31: XYZ coordinates in Å of the T_{BTICz} geometry of the left DBA-BTICz conformer.

C	0.754491	0.942739	-3.233319
C	0.817851	-0.180822	-2.386891
C	-0.181912	-1.153391	-2.492618
C	-1.243575	-1.053461	-3.421282
C	-1.260056	0.089193	-4.252963
C	-0.286062	1.091938	-4.172058
B	-2.323074	-2.128328	-3.519328
C	-3.424244	-1.814233	-4.578145
C	-3.284725	-0.615586	-5.327186
O	-2.247625	0.271209	-5.169570
O	-0.084456	-2.221995	-1.658632
C	-0.980544	-3.261842	-1.678170
C	-2.106266	-3.323688	-2.542403
C	-4.571043	-2.597156	-4.879094
C	-5.502128	-2.227735	-5.848946
C	-5.318192	-1.033170	-6.571612
C	-4.213051	-0.226026	-6.312476
C	-0.681267	-4.279713	-0.751292
C	-1.507121	-5.398097	-0.669535
C	-2.630795	-5.506667	-1.511582
C	-2.911871	-4.487871	-2.420822
N	1.754999	1.940037	-3.132560
C	2.615107	2.288647	-4.202612
C	3.727800	3.007610	-3.688250
C	3.556010	3.078553	-2.242142
C	2.286818	2.440063	-1.946626
C	2.515310	1.972626	-5.561942
C	3.535901	2.423820	-6.416476
C	4.628497	3.160013	-5.927502
C	4.735116	3.450568	-4.557967
C	4.350268	3.533683	-1.211214
C	3.976230	3.297538	0.202537
C	2.570248	2.971684	0.418551
C	1.724933	2.519079	-0.618844
C	5.096900	3.406839	1.062530
C	6.260027	3.931799	0.382608
S	5.965352	4.228695	-1.342901
C	0.398352	2.391087	-0.060617
C	0.499037	2.773082	1.313809
N	1.819667	3.124377	1.585140
C	-0.618657	2.826762	2.166073
C	-1.859671	2.476532	1.634208
C	-1.986771	2.098848	0.275320
C	-0.880779	2.060187	-0.571756
C	7.461392	4.164295	1.035423
C	7.564204	3.852645	2.414909
C	6.468603	3.285198	3.094008
C	5.257221	3.053028	2.443968
C	2.197892	3.819964	2.774048
C	2.667460	5.141565	2.694040
C	3.036803	5.816855	3.863895
C	2.919578	5.187529	5.112058
C	2.431289	3.874669	5.189236
C	2.075004	3.185613	4.022477
H	1.633021	-0.299204	-1.661093
H	-0.363948	1.986257	-4.803839
H	-4.739145	-3.531519	-4.325259
H	-6.376557	-2.866268	-6.047937
H	-6.046299	-0.730997	-7.341028
H	-4.041843	0.714900	-6.855999
H	0.205811	-4.165288	-0.111009
H	-1.275275	-6.195854	0.053856
H	-3.283391	-6.391335	-1.452789
H	-3.791748	-4.598184	-3.070279
H	1.675044	1.385429	-5.957126
H	3.472186	2.191542	-7.491210
H	5.410642	3.504760	-6.621274
H	5.600447	4.011362	-4.173399
H	-0.520384	3.147048	3.213049
H	-2.752638	2.506604	2.277962
H	-2.980412	1.841063	-0.123547
H	-1.013462	1.791663	-1.628030
H	8.325992	4.573696	0.490762
H	8.510450	4.039263	2.945481
H	6.569811	3.009347	4.155601
H	4.430167	2.577608	2.986582
H	2.746020	5.631347	1.712189
H	3.414123	6.849262	3.798431
H	3.207768	5.723829	6.029605
H	2.336964	3.375342	6.166276
H	1.717985	2.145645	4.070513

Table S32: XYZ coordinates in Å of the S_0 geometry of the right DBA-BTICz conformer.

C	1.332452	0.002658	-2.792243
C	1.258454	-1.389135	-2.971202
C	0.006867	-1.959890	-3.242585
C	-1.172158	-1.186900	-3.328232
C	-1.042561	0.207132	-3.140624
C	0.192596	0.816890	-2.883983
B	-2.530349	-1.831566	-3.609924
C	-3.702953	-0.808525	-3.686872
C	-3.388681	0.560285	-3.473565
O	-2.124282	1.024834	-3.209547
O	-0.026460	-3.307685	-3.409459
C	-1.190700	-3.995771	-3.648828
C	-2.466175	-3.381382	-3.763694
C	-5.069891	-1.091352	-3.954352
C	-6.048251	-0.099843	-4.002035
C	-5.689717	1.244036	-3.778966
C	-4.363558	1.576554	-3.515746
C	-1.006031	-5.386950	-3.771923
C	-2.106169	-6.206057	-4.012172
C	-3.391725	-5.642482	-4.128872
C	-3.553862	-4.263539	-4.005602
N	2.600647	0.604065	-2.546677
C	3.568501	0.711616	-3.559546
C	4.525481	1.691955	-3.183195
C	4.100122	2.200811	-1.894085
C	2.922944	1.504086	-1.523459
C	3.641542	0.041521	-4.790350
C	4.716430	0.345221	-5.634078
C	5.689569	1.298074	-5.266327
C	5.599733	1.978421	-4.047453
C	4.638287	3.165216	-1.017367
C	4.041912	3.502818	0.224612
C	2.805419	2.838249	0.524463
C	2.287777	1.773234	-0.279689
C	4.897780	4.433738	0.976421
C	6.034702	4.832145	0.215991
S	6.115466	4.044417	-1.344698
C	1.152844	1.210399	0.440815
C	0.955065	2.033402	1.583139
N	1.951984	3.017634	1.623463
C	-0.113096	1.830799	2.473260
C	-0.950310	0.733543	2.254148
C	-0.721474	-0.146009	1.176527
C	0.316850	0.085742	0.270385
C	7.007272	5.718469	0.704902
C	6.875808	6.205656	2.006916
C	5.795676	5.785223	2.805067
C	4.824864	4.913210	2.304966
C	1.771029	4.218052	2.374530
C	1.622923	5.447675	1.710620
C	1.435517	6.621301	2.451794
C	1.373416	6.572743	3.852242
C	1.507281	5.342414	4.512647
C	1.712992	4.166144	3.779077
H	2.150902	-2.022348	-2.880786
H	0.258381	1.904845	-2.751763
H	-5.374212	-2.131917	-4.134628
H	-7.095468	-0.365577	-4.213192
H	-6.454357	2.036230	-3.812964
H	-4.049639	2.615818	-3.338969
H	0.010614	-5.795070	-3.672754
H	-1.965512	-7.294339	-4.108300
H	-4.263999	-6.287472	-4.315908
H	-4.567372	-3.848517	-4.097578
H	2.882318	-0.697025	-5.085250
H	4.800357	-0.171744	-6.603066
H	6.525914	1.513117	-5.949538
H	6.357039	2.729380	-3.775880
H	-0.284082	2.506285	3.322869
H	-1.787975	0.548002	2.944871
H	-1.369523	-1.026065	1.042162
H	0.481128	-0.620842	-0.552509
H	7.864217	6.006136	0.076649
H	7.629673	6.898760	2.411987
H	5.710513	6.141201	3.843683
H	4.015553	4.594138	2.969862
H	1.663806	5.478274	0.611484
H	1.330708	7.583652	1.926781
H	1.221896	7.497067	4.431192
H	1.465564	5.296954	5.612254
H	1.857557	3.203862	4.292653

Table S33: XYZ coordinates in Å of the S_{CT} geometry of the right DBA-BTICz conformer.

C	1.260626	0.251701	-3.089065
C	1.234979	-1.167055	-2.945361
C	0.019765	-1.827671	-3.088256
C	-1.209378	-1.156178	-3.382004
C	-1.114202	0.262364	-3.553511
C	0.074930	0.968241	-3.422726
B	-2.511843	-1.891689	-3.510123
C	-3.735904	-0.972441	-3.859951
C	-3.479433	0.417969	-4.016622
O	-2.234049	0.988861	-3.866391
O	0.035939	-3.191327	-2.938438
C	-1.100327	-3.965910	-3.023564
C	-2.396252	-3.442239	-3.289455
C	-5.085350	-1.362206	-4.051195
C	-6.105172	-0.455975	-4.371403
C	-5.804476	0.906596	-4.516985
C	-4.486410	1.343249	-4.339797
C	-0.863171	-5.336231	-2.820127
C	-1.927795	-6.243175	-2.870180
C	-3.224794	-5.771817	-3.124415
C	-3.438732	-4.402054	-3.327497
N	2.473259	0.967499	-2.854818
C	3.440859	1.128624	-3.821102
C	4.468853	2.001060	-3.337233
C	4.066448	2.379238	-2.011347
C	2.840559	1.717450	-1.729865
C	3.474118	0.570011	-5.117876
C	4.566423	0.885109	-5.916956
C	5.602692	1.739443	-5.448945
C	5.565567	2.301335	-4.173599
C	4.661353	3.203414	-1.025403
C	4.080362	3.439757	0.252539
C	2.787976	2.867868	0.453699
C	2.186561	1.915030	-0.489876
C	4.993302	4.216879	1.106910
C	6.153194	4.622622	0.390295
S	6.178853	4.011053	-1.253408
C	0.962786	1.444211	0.121392
C	0.795035	2.191286	1.319229
N	1.903212	3.047819	1.494277
C	-0.329979	2.063823	2.130866
C	-1.297343	1.107451	1.764823
C	-1.127507	0.309424	0.625234
C	-0.009893	0.471438	-0.206972
C	7.187762	5.373757	0.965229
C	7.090745	5.713095	2.316993
C	5.986161	5.276597	3.069794
C	4.954905	4.537206	2.482486
C	1.860750	4.124971	2.436145
C	1.846525	5.450535	1.975103
C	1.784255	6.501228	2.899479
C	1.717418	6.230844	4.273961
C	1.716565	4.903233	4.727769
C	1.791892	3.845566	3.811873
H	2.144786	-1.732425	-2.699855
H	0.085762	2.058794	-3.556922
H	-5.351204	-2.424461	-3.947472
H	-7.137520	-0.815021	-4.509285
H	-6.593817	1.632490	-4.769786
H	-4.209879	2.403164	-4.446782
H	0.167981	-5.666330	-2.622435
H	-1.741640	-7.317213	-2.709891
H	-4.072832	-6.473785	-3.165802
H	-4.466054	-4.062478	-3.525018
H	2.662472	-0.085507	-5.462529
H	4.632863	0.468012	-6.933550
H	6.451439	1.963899	-6.113342
H	6.375838	2.964660	-3.836759
H	-0.464659	2.683270	3.028116
H	-2.192088	0.984089	2.394170
H	-1.879739	-0.449933	0.365566
H	0.109128	-0.168668	-1.085606
H	8.061905	5.671789	0.366876
H	7.891044	6.299877	2.793534
H	5.928536	5.512076	4.143676
H	4.130043	4.194631	3.115600
H	1.887411	5.653568	0.894519
H	1.781438	7.541423	2.539084
H	1.664292	7.059855	4.996471
H	1.666616	4.686352	5.806006
H	1.821057	2.802084	4.159980

Table S34: XYZ coordinates in Å of the T_{DBA} geometry of the right DBA-BTICz conformer.

C	1.267929	0.106631	-2.844648
C	1.206993	-1.301827	-2.930648
C	-0.030712	-1.930208	-3.187279
C	-1.241616	-1.224228	-3.362467
C	-1.132238	0.181799	-3.278647
C	0.083427	0.855697	-3.041954
B	-2.559824	-1.923007	-3.625732
C	-3.761000	-0.943529	-3.784520
C	-3.489530	0.458345	-3.674683
O	-2.228745	0.965193	-3.437675
O	-0.010604	-3.285815	-3.254519
C	-1.139458	-4.045131	-3.489846
C	-2.438447	-3.475538	-3.685382
C	-5.121460	-1.259861	-4.029110
C	-6.117703	-0.280649	-4.153722
C	-5.800465	1.084702	-4.038452
C	-4.473377	1.454715	-3.796530
C	-0.882833	-5.426253	-3.517418
C	-1.936551	-6.317256	-3.746942
C	-3.231611	-5.806337	-3.945803
C	-3.467109	-4.424475	-3.914597
N	2.508658	0.760486	-2.621226
C	3.464509	0.890311	-3.638929
C	4.460062	1.816249	-3.228774
C	4.066150	2.272869	-1.911280
C	2.868193	1.598823	-1.558279
C	3.498356	0.271619	-4.898176
C	4.572826	0.575464	-5.741993
C	5.582173	1.478329	-5.344587
C	5.532561	2.105170	-4.094913
C	4.649067	3.176263	-0.998787
C	4.076192	3.481465	0.261284
C	2.808638	2.866094	0.534665
C	2.240296	1.855952	-0.306394
C	4.977194	4.334748	1.050625
C	6.125785	4.719411	0.300839
S	6.160292	4.006467	-1.297472
C	1.060020	1.347550	0.383459
C	0.898981	2.149165	1.547417
N	1.956320	3.063890	1.630105
C	-0.194848	1.997203	2.416004
C	-1.106094	0.970938	2.152666
C	-0.922670	0.109958	1.052402
C	0.146302	0.292073	0.170260
C	7.141197	5.534346	0.825395
C	7.040864	5.959465	2.151803
C	5.948463	5.547515	2.937690
C	4.935442	4.747143	2.402748
C	1.847068	4.245674	2.423970
C	1.782015	5.505674	1.805577
C	1.662957	6.660602	2.589132
C	1.587100	6.564273	3.986399
C	1.638199	5.304455	4.601175
C	1.775131	4.145528	3.825215
H	2.107466	-1.915187	-2.784652
H	0.096292	1.953920	-3.000015
H	-5.415089	-2.314961	-4.125744
H	-7.158740	-0.586857	-4.343857
H	-6.581042	1.854369	-4.135804
H	-4.171732	2.507933	-3.696850
H	0.148289	-5.774309	-3.356372
H	-1.749258	-7.401521	-3.770605
H	-4.070894	-6.496296	-4.128011
H	-4.494941	-4.068770	-4.075538
H	2.708911	-0.426643	-5.213022
H	4.627844	0.101162	-6.734590
H	6.416269	1.696357	-6.029622
H	6.319954	2.815836	-3.801261
H	-0.330349	2.659047	3.282580
H	-1.966377	0.826939	2.825142
H	-1.629122	-0.716829	0.879912
H	0.271769	-0.402652	-0.667207
H	8.006560	5.814083	0.205143
H	7.828421	6.595888	2.584815
H	5.887342	5.852702	3.994021
H	4.117162	4.429854	3.057719
H	1.833363	5.574303	0.708623
H	1.622909	7.646388	2.099916
H	1.489373	7.474312	4.598590
H	1.584934	5.221129	5.698052
H	1.854020	3.157562	4.303187

Table S35: XYZ coordinates in Å of the T_{BTICz} geometry of the right DBA-BTICz conformer.

C	1.354978	0.015482	-2.827732
C	1.271406	-1.367434	-3.063297
C	0.007825	-1.924313	-3.305735
C	-1.171661	-1.147528	-3.307350
C	-1.030627	0.237548	-3.066352
C	0.215090	0.835068	-2.836406
B	-2.541979	-1.778436	-3.558554
C	-3.713800	-0.751603	-3.546503
C	-3.387562	0.606493	-3.287767
O	-2.112131	1.058118	-3.055320
O	-0.035823	-3.263630	-3.528235
C	-1.211348	-3.940628	-3.743759
C	-2.488953	-3.320969	-3.776791
C	-5.090813	-1.021100	-3.772542
C	-6.067614	-0.027392	-3.738794
C	-5.697003	1.305081	-3.471756
C	-4.360489	1.624580	-3.247244
C	-1.035803	-5.325701	-3.931424
C	-2.147728	-6.133641	-4.154882
C	-3.435782	-5.564898	-4.190175
C	-3.588722	-4.191901	-4.004181
N	2.631774	0.602990	-2.594586
C	3.610562	0.687563	-3.585903
C	4.605935	1.622359	-3.159709
C	4.185267	2.116437	-1.877693
C	2.985778	1.460740	-1.547647
C	3.674866	0.051470	-4.836830
C	4.775700	0.330993	-5.651041
C	5.788240	1.231579	-5.234921
C	5.712301	1.880790	-4.004218
C	4.739169	3.081064	-0.969842
C	4.072210	3.460730	0.267355
C	2.839868	2.851920	0.525985
C	2.332845	1.706800	-0.283147
C	4.903304	4.412213	1.021251
C	6.075893	4.780341	0.302012
S	6.217065	3.952487	-1.246148
C	1.285468	1.103485	0.451635
C	1.016997	1.949540	1.588129
N	1.942910	3.022090	1.592816
C	-0.030926	1.698273	2.459909
C	-0.821912	0.531574	2.245472
C	-0.534610	-0.350771	1.192236
C	0.506251	-0.087955	0.294444
C	7.030482	5.669082	0.808740
C	6.838852	6.201476	2.091876
C	5.717830	5.821596	2.845200
C	4.762816	4.936899	2.323923
C	1.675282	4.250594	2.257738
C	1.582966	5.445305	1.519249
C	1.319507	6.654429	2.173437
C	1.130259	6.684026	3.563559
C	1.216674	5.493124	4.299228
C	1.495538	4.280298	3.654702
H	2.164134	-2.006045	-3.035210
H	0.289517	1.916240	-2.661330
H	-5.404719	-2.052412	-3.986482
H	-7.122987	-0.282627	-3.920181
H	-6.460223	2.098773	-3.441074
H	-4.037009	2.654925	-3.038400
H	-0.016779	-5.738256	-3.894491
H	-2.014330	-7.217228	-4.301259
H	-4.317294	-6.201216	-4.363049
H	-4.604385	-3.772901	-4.032378
H	2.888154	-0.642321	-5.166105
H	4.856049	-0.158701	-6.634115
H	6.644474	1.425320	-5.899888
H	6.499153	2.587197	-3.699083
H	-0.260976	2.372777	3.295088
H	-1.657363	0.319727	2.930396
H	-1.135122	-1.265635	1.068168
H	0.728272	-0.798319	-0.511889
H	7.919778	5.932118	0.215755
H	7.579254	6.901429	2.509624
H	5.580567	6.217449	3.863536
H	3.912695	4.648975	2.952530
H	1.725286	5.417613	0.428438
H	1.254332	7.584382	1.586915
H	0.919605	7.636648	4.073975
H	1.080406	5.506856	5.392161
H	1.608689	3.354598	4.237934

References

- (1) Ásgeirsson, V.; Birgisson, B. O.; Bjornsson, R.; Becker, U.; Neese, F.; Riplinger, C.; Jónsson, H. Nudged elastic band method for molecular reactions using energy-weighted springs combined with eigenvector following. *J. Chem. Theory Comput.* **2021**, *17*, 4929–4945.
- (2) Braveenth, R.; Lee, H.; Park, J. D.; Yang, K. J.; Hwang, S. J.; Naveen, K. R.; Lampande, R.; Kwon, J. H. Achieving Narrow FWHM and High EQE Over 38% in Blue OLEDs Using Rigid Heteroatom-Based Deep Blue TADF Sensitized Host. *Adv. Funct. Mater.* **2021**, *31*, 2105805.
- (3) Stavrou, K.; Danos, A.; Hama, T.; Hatakeyama, T.; Monkman, A. Hot Vibrational States in a High-Performance Multiple Resonance Emitter and the Effect of Excimer Quenching on Organic Light-Emitting Diodes. *ACS Appl. Mater. Interfaces* **2021**, *13*, 8643–8655.

**Computational Approach to Phosphor-Sensitized
Fluorescence Based on Monomer Transition
Densities**

J. Chem. Theory Comput., **21**, 2569-2581 (2024)

Simon Metz, Christel M. Marian

Contribution: Implementation of triplet–singlet EET (STrEET); All quantum chemical calculations; preparation of all figures; writing first draft; revision of manuscript

Computational Approach to Phosphor-Sensitized Fluorescence Based on Monomer Transition Densities

Simon Metz and Christel M. Marian*

Cite This: *J. Chem. Theory Comput.* 2025, 21, 2569–2581

Read Online

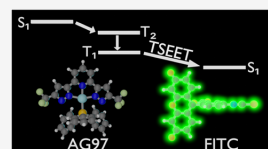
ACCESS |

Metrics & More

Article Recommendations

Supporting Information

ABSTRACT: We present here an extension of the monomer transition density approach to spin multiplicity-altering excitation energy transfer (EET) processes. It builds upon complex-valued wave functions of the density functional theory-based multireference spin–orbit coupling configuration interaction method for generating the one-particle transition density matrices of the donor and acceptor molecules, which are then contracted with two-electron Coulomb and exchange integrals of the dimer. Due to the extensive use of symmetry relations between tensor components, the computation of triplet–singlet coupling remains technically feasible. As a proof-of-principle application, we have chosen an EET system, consisting of the phosphorescent platinum complex AG97 as the donor and the fluorescein derivative FITC as the acceptor. Taking experimental conditions into account, we estimate a Förster radius of about 35 Å. For intermolecular donor–acceptor separations close to the Förster radius and beyond, the error introduced by the ideal dipole approximation is rather small.



1. INTRODUCTION

Intermolecular excitation energy transfer (EET) plays an important role in natural and artificial light-harvesting systems,^{1–3} organic light-emitting devices (OLEDs),^{4–7} and for biomolecular structure analysis.^{8–11} There are two major mechanisms for through-space EET from an electronically excited donor molecule D to an acceptor molecule A, Förster resonance energy transfer (FRET)¹² and Dexter EET.¹³ Commonly, EET is assumed to conserve the electron spin multiplicity. Closer inspection reveals, however, that this is not always the case. In addition to singlet–singlet EET (SSEET) and triplet–triplet EET (TTEET), EET between electronic states of different spin multiplicity has been observed.¹⁴

FRET may be thought of as a virtual photon exchange between D and A,^{12,14} conveying the excitation energy nonradiatively over long distances, with typical Förster radii ranging between 20 and 100 Å. The coupling is brought about by long-range dipole–dipole interaction of the molecular transition moments. One might therefore be tempted to believe that FRET is limited to SSEET between fluorescent dyes. As early as 1959, Förster predicted that FRET from triplet to singlet excited states (triplet–singlet EET, TSEET) is possible if the donor is sufficiently phosphorescent while the acceptor is strongly absorbing.¹⁵ This prediction rested on the following considerations. The FRET efficiency (η_{EET}) is given by

$$\eta_{\text{EET}} = \frac{k_{\text{EET}}}{k_{\text{EET}} + k_{\text{rad}} + k_{\text{nr}}} \quad (1)$$

Here, k_{EET} is the rate of Förster EET from the donor molecule to the acceptor molecule and k_{rad} and k_{nr} are the intrinsic radiative and nonradiative rates on the donor, respectively.

According to Förster theory, k_{EET} is proportional to k_{rad} . As long as nonradiative decay does not dominate the deactivation process, i.e., as long as $k_{\text{rad}} > k_{\text{nr}}$, FRET can be efficient even if the optical transition is (nearly) forbidden in the donor while the acceptor is a strongly absorbing dye. FRET between an excited triplet state of the donor and a singlet state of the acceptor may be slow but can still be a dominant decay pathway, because the competing intramolecular de-excitation processes are forbidden as well.¹⁶ Experimentally, Förster's hypothesis was initially confirmed by Ermolaev and Sveshnikova¹⁷ as well as Bennett et al.,¹⁸ who observed FRET between phosphorescent donors and fluorescent acceptors in the solid state with Förster radii around 50 Å. The Förster radius is defined as the distance at which the FRET efficiency η_{EET} is 50%.

In contrast to FRET, Dexter EET is a short-range process, dependent on the exchange interaction between the donor and acceptor states and thus decreasing exponentially with decreasing overlap between their electron densities.¹³ Dexter EET preserves the spin symmetry of a donor–acceptor pair unless strong spin–orbit coupling is involved. Because of the exchange mechanism, it is the major origin of TTEET. Triplet states of fluorescent emitters typically represent energy sinks which are nonradiatively deactivated and therefore lost for luminescence. In the worst case, they are photochemically

Received: December 10, 2024

Revised: February 5, 2025

Accepted: February 6, 2025

Published: February 19, 2025



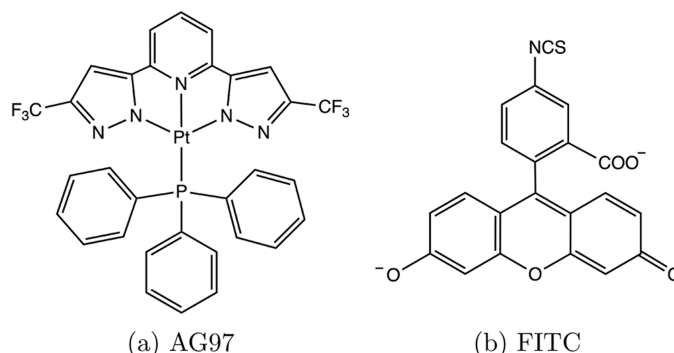


Figure 1. Chemical structures of the phosphorescent Pt^{II}-complex AG97 and the dianionic fluorescent label fluorescein isothiocyanate (FITC) investigated in this work.

active and lead to the degradation of the dye. In phosphor-sensitized fluorescent systems, Dexter TTEET should therefore be avoided as far as possible.

In material sciences, the concept of phosphor-sensitized fluorescence has been applied to improve the emission efficiency and color purity of OLEDs. For example, the green phosphor Ir(ppy)₃ was employed as a sensitizing agent to increase the internal quantum efficiency of red or yellow fluorescence in OLEDs.^{4,19} Unicolored phosphor-sensitized fluorescence was exploited to construct stable deep blue OLEDs.²⁰ By combining phosphorescent and fluorescent emitters with strongly overlapping emission bands, the initial color of the phosphorescence could be preserved. High efficiencies were reached by charge-recombination on the phosphorescent emitter while realizing short emissive lifetimes by fast energy transfer to the fluorescent emitter. Other groups utilized phosphor sensitization as a means to build efficient fluorescent white OLEDs.^{21–25}

In the context of biomolecular imaging, phosphor-sensitized fluorescence is a valuable tool as well. Biomolecular imaging holds the potential to monitor the structure of living cells and tissue at the molecular level.^{26,27} Fluorescence lifetime imaging microscopy (FLIM) plays a crucial role in these studies.²⁸ Here, often the autofluorescence, i.e., the fluorescence of naturally occurring endogenous molecules is measured as its lifetime depends on the environment of the fluorophore. Another possibility is to use exogenous molecules to determine changes in the temperature, viscosity and pH.²⁹ In these cases, the autofluorescence can interfere with the emission of the fluorescent probes as their lifetimes are on the same time scale (0.1–10 ns). Phosphorescence lifetime imaging microscopy (PLIM) circumvents this problem. Here, transition metal complexes with a lifetime in the range of 100 ns to 10 μs are utilized to separate time scales by transferring their excitation energy to fluorescent reporters which in turn emit delayed fluorescence that can be read out by time-gated spectroscopy.³⁰

Recently, Delcanale et al.³¹ investigated a Pt^{II}-complex (AG97 - Figure 1a) for its capability in time-gated detection. While its luminescence is quenched in solution, phosphorescence can be observed for aggregates of this complex. Due to the substantial Pt–Pt distance (5.757 Å in the crystalline state), intermetallic interactions are not notable, but rotovibrational degrees of freedom that could lead to a quick nonradiative decay of the emission appear to be suppressed

in the aggregates.³¹ In addition to the phosphorescence of AG97 physisorbed onto the surface of a protein (bovine serum albumin - BSA), the authors observed delayed fluorescence on the microsecond time scale from the fluorescein isothiocyanate (FITC - Figure 1b) reporter which is covalently bound to this protein. While these observations and the slight shortening of the AG97 lifetime components in the presence of BSAFITC are consistent with resonant TSEET, other processes such as uncorrelated emission-absorption or Dexter-like EET were not excluded by Delcanale et al.³¹

Owing to the large importance of EET in natural and artificial light-harvesting systems, material science, and for biomolecular structure analysis, several quantum chemical methods for calculating excitonic coupling matrix elements (ECMEs) between a donor in an electronically excited state and an acceptor in the electronic ground state were devised.^{14,32–39} To our knowledge, so far none of them targeted spin-forbidden EET, however. In the present work, we will show how the monomer transition density (MTD) approach for SSEET, as implemented in our laboratory for density functional theory based multireference configuration interaction (DFT/MRCI) wave functions,^{40,41} can be extended to TTEET and, in particular, to TSEET. As perturbational sum-overstates expressions of phosphorescence probabilities are known to converge very slowly with the number of intermediate states, we opt for a variational approach to generate the spin-orbit coupled wave functions, i.e., the density functional-based multireference spin-orbit configuration interaction (DFT/MRSOCI) method.⁴² DFT/MRSOCI has been applied successfully for studying phosphorescence rate constants of Ir- and Pt-complexes.^{43–46} In addition to averaged quantities, the method allows to compute fine-structure resolved electric transition moment vectors and can thus provide concrete clues with regard to favorable relative orientation(s) of the donor and acceptor molecules. ECMEs, evaluated by means of the extended MTD approach, will furthermore allow to check the validity of Förster's ideal dipole approximation (IDA) involving the transition dipoles, an orientation factor and the distance R_{DA} between the donor and acceptor centroids. A proof-of-principle application of the extended MTD approach to TSEET from the phosphorescent AG97 complex to the fluorescence label FITC (cp. Figure 1) will address technical issues as well.

2. THEORY

2.1. EET Rate Constants. Except for cases of coherent superpositions of donor and acceptor states, where quantum dynamics methods are required for the modeling of the EET process,³⁶ the weak coupling limit is applicable and EET rate constants may be calculated using Fermi's golden rule approximation.^{47–49}

$$k_{\text{EET}} = \frac{2\pi}{\hbar} \sum_{\text{MN}} \sum_{\text{KL}} f(E_{\text{D}^*\text{M}}) f(E_{\text{AL}}) \times |\langle \Psi_{\text{DN}} \Psi_{\text{A}^*\text{K}} | \hat{V}_{\text{DA}}^{(\text{el-el})} | \Psi_{\text{D}^*\text{M}} \Psi_{\text{AL}} \rangle|^2 \times \delta(E_{\text{D}^*\text{M}} + E_{\text{AL}} - E_{\text{DN}} - E_{\text{A}^*\text{K}}) \quad (2)$$

Here, $f(E_{\text{D}^*\text{M}})$ represents the thermal occupation of the vibrational state M of the electronically excited donor molecule with vibronic wave function $\Psi_{\text{D}^*\text{M}}$ and energy $E_{\text{D}^*\text{M}}$. Likewise, $f(E_{\text{AL}})$ denotes the thermal occupation of the vibrational state L of the acceptor molecule in the electronic ground state with vibronic wave function Ψ_{AL} and energy E_{AL} . The delta distribution term ensures that only energy-conserving processes contribute to the EET rate. Note that the δ -term is given in inverse energy units.

Assuming that the electronic part of the coupling does not depend strongly on the intramolecular nuclear coordinates (Condon approximation), the coupling between D and A can be approximated as

$$\langle \Psi_{\text{A}^*\text{K}} \Psi_{\text{DN}} | \hat{V}_{\text{DA}}^{(\text{el-el})} | \Psi_{\text{D}^*\text{M}} \Psi_{\text{AL}} \rangle \approx V_{\text{DA}} \langle \chi_{\text{AL}} | \chi_{\text{A}^*\text{K}} \rangle \langle \chi_{\text{D}^*\text{M}} | \chi_{\text{DN}} \rangle \quad (3)$$

where the χ denote purely vibrational wave functions of the donor and acceptor in the electronic ground and excited states, respectively. The EET rate constant is then given by

$$k_{\text{EET}}^{\text{FC}} = \frac{2\pi}{\hbar} |V_{\text{DA}}|^2 \sum_{\text{MN}} \sum_{\text{KL}} f(E_{\text{AL}}) f(E_{\text{D}^*\text{M}}) \langle \chi_{\text{AL}} | \chi_{\text{A}^*\text{K}} \rangle^2 \langle \chi_{\text{D}^*\text{M}} | \chi_{\text{DN}} \rangle^2 \times \delta(E_{\text{D}^*\text{M}} + E_{\text{AL}} - E_{\text{A}^*\text{K}} - E_{\text{DN}}) \quad (4)$$

In Condon approximation, the determination of the EET rate constant thus reduces to the evaluation of the overlap between the vibrationally resolved emission spectrum of the donor and the absorption spectrum of the acceptor in addition to the computation of their ECMES. To avoid the explicit summation over the vibrational states, a generating function formalism in multimode harmonic oscillator approximation including a Duschinsky transformation is employed for computing the Franck–Condon spectra.⁵⁰ In the VIBES program, temperature effects are accounted for by assuming a Boltzmann population of the initial states.⁵¹

The Franck–Condon weighted density of states (FCWDOS) is typically approximated as the spectral overlap of the normalized donor emission $F_{\text{D}}(\omega)$ and the normalized acceptor absorption spectrum $A_{\text{A}}(\omega)$. In this case, the EET rate is given by^{36,47}

$$k_{\text{EET}}^{\text{FC}} = \frac{2\pi}{\hbar} |V_{\text{DA}}|^2 \int_0^\infty F_{\text{D}}(\omega) A_{\text{A}}(\omega) d\omega \quad (5)$$

2.2. MTD Approach for Spin Multiplicity-Conserving EET. In the framework of the monomer transition density (MTD) approach,^{35,40} the ECME $V_{\text{DA}}^{\text{SS}}$ for the SSEET between two molecules with singlet electronic ground states is evaluated by contracting the one-electron transition density matrices (1-TDMs) $\rho_{\text{D},ij}^{\text{SS}}$ of the donor D and $\rho_{\text{A},kl}^{\text{SS}}$ of the acceptor A with

two-electron Coulomb and exchange integrals. Here, the two electron integrals are denoted in Mulliken convention.

$$V_{\text{DA}}^{\text{SS}} = \sum_{ijkl} \left[(\phi_i \phi_j | \phi_k \phi_l) - \frac{1}{2} (\phi_i \phi_l | \phi_k \phi_j) \right] \rho_{\text{D},ij}^{\text{SS}} \rho_{\text{A},kl}^{\text{SS}} \quad (6)$$

Exchange contributions to EET were first introduced by Fujimoto in the transition-density-fragment interaction approach.⁵²

In our implementation, the four-index two-electron integrals are approximated by a product of three-index integrals employing a resolution-of-the-identity approximation⁵³

$$(\phi_i \phi_j | \phi_k \phi_l) \approx \sum_{P,Q} (\phi_i \phi_j | P) \cdot (P | Q)^{-1} \cdot (Q | \phi_k \phi_l) \quad (7)$$

where the P and Q are auxiliary basis sets optimized for correlated wave functions.⁵⁴

TTEET conserves the M_S quantum number of the wave function. Therefore, only three terms contribute to the ECME of two triplet states, located on the donor and acceptor molecules, respectively. For compounds with singlet electronic ground states, $V_{\text{DA}}^{\text{TT}}$ is given by

$$V_{\text{DA}}^{\text{TT}} = - \sum_{ijkl} (\phi_i \phi_j | \phi_k \phi_l) \left[\rho_{\text{D},ij}^{\text{ST}^+} \rho_{\text{A},kl}^{\text{T}^+ \text{S}} + \rho_{\text{D},ij}^{\text{ST}^-} \rho_{\text{A},kl}^{\text{T}^- \text{S}} + \frac{1}{2} \rho_{\text{D},ij}^{\text{ST}^0} \rho_{\text{A},kl}^{\text{T}^0 \text{S}} \right] \quad (8)$$

in MTD approximation. Herein, T^+ , T^- and T^0 denominate the $M_S = +1$, $M_S = -1$ and $M_S = 0$ sublevels of the respective triplet states. Due to the spin flip excitations with regard to the electronic ground state, only exchange-type integrals enter eq 8. Dipole–dipole coupling terms therefore do not contribute to TTEET at this level of theory.

In the absence of spin–orbit coupling (SOC), the 1-TDMs of the individual triplet sublevels in eq 8 are related via the Wigner-Eckart theorem (WET). The WET states that matrix elements of irreducible tensor operators consist of a physical part, i.e., the reduced matrix element (RME), and a geometrical part. The RME is system specific and further depends on the rank of the operator and the spin or spatial angular momentum of the interacting states but not on the tensor components. The geometrical part relates the matrix elements of all components by vector coupling coefficients that are not system specific. One-electron spin operators can be expressed as first-rank tensor operators. In the present context, this means that the singlet–triplet 1-TDMs in eq 8 need to be evaluated explicitly for one triplet sublevel only while all other 1-TDMs can be generated via the WET.

Spin–orbit free DFT/MRCI wave functions are always expanded in a basis of configuration state functions (CSFs) with maximal M_S quantum number. The CSFs are eigenfunctions of the total spin operator, \hat{S}^2 , and the projection of \hat{S} onto the z axis, \hat{S}_z . This means that, unlike the entries in $\rho_{\text{D},ij}^{\text{ST}^0}$ and $\rho_{\text{A},kl}^{\text{T}^0 \text{S}}$, the elements of the $\rho_{\text{D},ij}^{\text{ST}^+}$ and $\rho_{\text{A},kl}^{\text{T}^+ \text{S}}$ 1-TDMs are different for α and β spin electrons. At first sight, it appears technically unfavorable to employ DFT/MRCI wave functions with $M_S = 1$ instead of the $M_S = 0$ components for the computation of TTEET matrix elements. The choice of an $M_S \neq 0$ component is mandatory, however, for the evaluation of SOC matrix elements between two triplet states, because the

mutual SOC of two $M_S = 0$ triplet components vanishes by symmetry and would therefore falsely yield zero RMEs.⁵⁵

2.3. Extended MTD Approach for Spin Multiplicity-Altering EET. The computation of ECMEs for phosphoresensitized fluorescence requires the use of spin-orbit mixed wave functions for the donor and acceptor. The ability to determine the spectroscopic properties of phosphorescent and fluorescent dyes with good accuracy by means of quantum chemical methods is an important prerequisite for a meaningful computation of excitonic coupling constants. As the donor and acceptor molecules are sizable, most *ab initio* methods for generating multiplicity-mixed wave functions are not applicable. Here, we employ the DFT/MRSOCI approach,⁴² that is derived from the spin-orbit free semi-empirical DFT/MRCI method,^{56,57} for that purpose. The advantage of this variational ansatz is that it treats electron correlation and SOC on the same footing. Therefore, it does not suffer from problems of slow convergence with respect to the number of *LS*-coupled basis states which are typical for sum-over-states perturbation theory approaches.^{43,44} To determine the phosphorescence rate constants of a transition metal complex, for example, it is sufficient to solve for just four roots of the complex eigenvalue problem in DFT/MRSOCI, i.e., one root for the S_0 electronic ground state and three roots comprising the T_1 fine-structure sublevels.

SOC does not only mix singlet and triplet multiplicities, it also couples states of equal multiplicity but different spatial symmetry or M_S values. For an optimal use of symmetry properties in the evaluation of Hamiltonian matrix elements, the MRSOCI expansion is set up in a basis of CSFs. Without spatial symmetry being present, a multiplicity-mixed wave function of a system with an even number of electrons therefore consists of a singlet block, three triplet blocks of CSFs with $M_S = +1$, $M_S = 0$, and $M_S = -1$ quantum numbers, respectively, and possibly further blocks for higher multiplicity states.

The DFT/MRSOCI wave functions of the donor can be written as linear combinations of CSFs with complex-valued coefficients. For each fine-structure component of the triplet-excited donor, a separate wave function is generated. For sublevel T_a , e.g., the spin-orbit mixed donor wave function reads

$$\langle T_a | = \sum_{S=S_{\min}}^{S_{\max}} \sum_{M_S=-S}^S \sum_{\{\Gamma\}} \sum_{\{\mathbf{n}\}} \sum_{w(\mathbf{n})} t_{a,S,M_S,\Gamma,\mathbf{n},w(\mathbf{n})}^* \times \langle S, M_S, \Gamma, \mathbf{n}, w(\mathbf{n}) | \quad (9)$$

The sums in eq 9 run over all possible spin quantum numbers S and M_S , the irreducible representations Γ of the molecular point group, all configurations \mathbf{n} , and all associated CSF indices $w(\mathbf{n})$. In the present example, S is limited to 0 and 1 because low-lying quintets are not to be expected in d^8 transition metal systems. A similar notation is used for the electronic ground state wave function $|S_0\rangle$ of the donor.

$$|S_0\rangle = \sum_{S=S_{\min}}^{S_{\max}} \sum_{M_S=-S}^S \sum_{\{\Gamma\}} \sum_{\{\mathbf{n}\}} \sum_{w(\mathbf{n})} g_{S,M_S,\Gamma,\mathbf{n},w(\mathbf{n})} \times |S, M_S, \Gamma, \mathbf{n}, w(\mathbf{n})\rangle \quad (10)$$

It can be shown that the spin-free length form of the electric dipole operator is an appropriate transition operator in the presence of SOC.^{58,59} To obtain the 1-TDMs, it is therefore

sufficient to couple the spin-orbit mixed ground and excited wave functions by the spin-free one-electron excitation operator $\hat{E}_{ij} = \sum_{\sigma} \hat{a}_{i\sigma}^\dagger \hat{a}_{j\sigma}$.⁴² Hence, only terms with $S' = S$ and $M_{S'} = M_S$ contribute to the 1-TDM and the spin-free CSF-coupling coefficients η of Wetmore and Segal⁶⁰ can be used.

$$\begin{aligned} \rho_{D,ij}^{S_0T_a} &= \langle T_a | \hat{E}_{ij} | S_0 \rangle \\ &= \sum_{S=S_{\min}}^{S_{\max}} \sum_{\{\Gamma\}} \sum_{\{\mathbf{n}\}} \sum_{w(\mathbf{n})} \eta(S, \mathbf{n}, w(\mathbf{n}), \mathbf{n}', w'(\mathbf{n}')) \\ &\times \sum_{M_S=-S}^S t_{a,S,M_S,\Gamma,\mathbf{n},w(\mathbf{n})}^* g_{S,M_S,\Gamma,\mathbf{n}',w'(\mathbf{n}')} \end{aligned} \quad (11)$$

For each of the triplet fine-structure levels T_a , T_b and T_c of the donor D, individual ECMEs have to be evaluated. Not only the length but also the orientation of transition dipole varies among the fine-structure levels. For sublevel T_a , e.g., the ECME is given by

$$V_{DA}^{T_aS} \approx \sum_{ijkl} \left[(\phi_i \phi_j | \phi_k \phi_l) - \frac{1}{2} (\phi_i \phi_j | \phi_k \phi_l) \right] \rho_{D,ij}^{S_0T_a} \rho_{A,kl}^{SS} \quad (12)$$

where $\rho_{A,ij}^{SS}$ denotes the 1-TDM between the DFT/MRSOCI wave functions of the ground and excited singlet states of the acceptor A. As the CSF expansion coefficients are complex-valued, so are $\rho_{D,ij}^{S_0T_a}$, $\rho_{A,kl}^{SS}$ and $V_{DA}^{T_aS}$. In addition to the intricacy of the task, the sheer size of the problem requires elaborate programming and screening techniques.

The contribution of each triplet sublevel to the total EET rate constant depends on the ISC rates with which the triplet sublevels are populated from the primarily excited state, the spin relaxation time, the zero-field splitting (ZFS) and the temperature. If one assumes that spin relaxation between the sublevels occurs on a shorter time scale than phosphorescence or FRET, the sublevel population adopts a Boltzmann distribution. Notwithstanding this assumption, individual rate constants are reported here for the fine-structure sublevels in addition to the sublevel-averaged values.

Although the formulas in this section have been worked out explicitly for the common case of singlet-triplet coupling, the method is not restricted to this case. The formalism may be applied equally well to doublet-quartet couplings, for example.

3. COMPUTATIONAL DETAILS

The Gaussian 16 program package⁶¹ was used for geometry optimizations and vibrational frequency analyses. For the ground-state calculations, Kohn-Sham density functional theory (KS-DFT) in conjunction with the PBE0 hybrid functional⁶² was utilized. The def2-SVP basis set^{63,64} and a scalar relativistic effective core potential (ECP)⁶⁵ for the platinum atom were chosen. The excited-state optimizations were carried out using time-dependent DFT (TDDFT) for the singlet states and the Tamm-Dancoff approximation (TDA) for the triplet states. It should be noted that these two methods have only been used for geometry optimization and vibrational frequency analysis. Solvent environments were described implicitly by the polarizable continuum model (PCM)⁶⁶⁻⁶⁸ implemented into Gaussian 16. Due to the dianionic protonation state of the FITC label, we also tested the performance of a long-range-corrected hybrid functional with varying amounts of Hartree-Fock exchange in the geometry

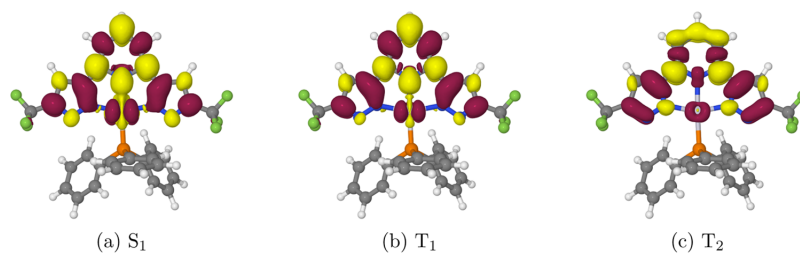


Figure 2. Difference of the electron density distribution in the S_1 , T_1 and T_2 states of AG97 with respect to the ground-state electron density (difference density, isovalues ± 0.001) at the S_0 geometry in DCM. Red-colored areas indicate a loss, yellow-colored areas a gain of electron density in the excited state.

optimization step. We opted here for the CAM-B3LYP⁶⁹ functional with the range-separation parameter ω set to its default value of $\omega = 0.33$. As the molecular minimum geometries and vibrational frequencies did not differ substantially between the two functionals, all DFT/MRCI calculations were performed using the PBE0-optimized structures.

The (TD)DFT-generated PCM point charges were exported for subsequent DFT/MRCI^{56,57} calculations of the excitation energies working with the TURBOMOLE package.⁷⁰ Here, the R2018 Hamiltonian⁷¹ with parameters optimized for a configuration selection threshold of $0.8 E_h$ was used. The molecular orbitals (MOs) of the ground-state determinant were generated with the BH-LYP functional.⁷² For the construction of the two-electron integrals in the resolution-of-identity (RI) approximation, the auxiliary basis sets from the TURBOMOLE library⁵⁴ were utilized. In the DFT/MRCI calculations, 10 roots were considered in the singlet and triplet manifolds, respectively. Fragment-based characterization of the DFT/MRCI wave function was performed with the TheoDORE program.⁷³ Plots of molecular orbitals and difference densities were created with Jmol.⁷⁴ Electronic spin-orbit coupling matrix elements (SOCMEs) and phosphorescence lifetimes were determined with the SpOCK program.^{42,75,76} Herein, a SOC-ECP⁶⁵ on the platinum and an atomic mean-field approximation of the Breit–Pauli spin-orbit operator^{77,78} on all other centers was employed. In most applications, at least five DFT/MRSOCI roots were determined to enable the computation of the S_1 transitions in addition to T_1 phosphorescence. To describe SOC effects on the absorption spectrum of the platinum complex the quasi-degenerate perturbation theory (SOC-QDPT)⁵⁵ was employed for the calculation of the excitation energies and the transition dipole moments.

Franck–Condon (FC) factors and FCWDOS for determining spectral profiles and rate constants were computed with the vertical Hessian (VH) approach recently implemented in the VIBES program.^{50,51,79} To ease the Fourier transformation, the time correlation function was multiplied by a Gaussian damping function. For FC spectra, a damping function of 200 cm^{-1} full width at half-maximum (fwhm) was chosen and the integration was performed on a time interval of 300 fs with a grid of $16384 (2^{14})$ points, while for intersystem crossing (ISC) rate constants a damping function of 10 cm^{-1} fwhm, a time interval of 3000 fs and $65536 (2^{16})$ points was used. ECMEs between the donor and acceptor molecules were computed in MTD approximation with an extended version of our Singlet and Triplet Excitation Energy Transfer (STrEET)

program⁴¹ which generates and processes complex-valued transition density matrices based on DFT/MRSOCI wave functions as outlined in Section 2.3. To reduce the number of two-electron Coulomb and exchange integrals required for the computation of the ECME in MTD approximation (eq 12), molecular orbitals of the donor and acceptor with orbital energies below $-3.0 E_h$ and above $+2.0 E_h$ were discarded, in line with the typical thresholds applied in DFT/MRCI calculations.

4. PROOF-OF-PRINCIPLE APPLICATION TO A PLIM SYSTEM

4.1. EET Donor: AG97. AG97 exhibits a quasi-square-planar coordination of the platinum center which carries a tridentate ligand on one side and triphenylphosphine on the other side. Experiments were carried out by the Strasser group³¹ in phosphate-buffered saline (PBS), where AG97 forms aggregates, in deaerated dichloromethane (DCM) and dimethyl sulfoxide (DMSO) solutions as well as in frozen glassy matrices of 1:1 mixtures of MeOH/CH₂Cl₂. Our computations were performed for monomeric complexes, embedded in a polarizable continuum model of either DCM or DMSO. The optimized ground-state structures in DCM and DMSO are very similar and agree well with the crystal structure (where AG97 forms dimers)³¹ save for the rotation of the phenyl groups of the triphenylphosphine ligand.

The three lowest-lying excited states, S_1 , T_1 and T_2 , are mainly of ligand-centered (LC) type with portions of metal-to-ligand charge transfer (MLCT) character mixed into the wave function, as becomes evident from the difference densities (Figure 2) and a TheoDORE fragment analysis of the 1-TDM (Figure S1). S_1 and T_1 are dominated by transitions from the highest occupied molecular orbital (HOMO) to the lowest unoccupied molecular orbital (LUMO). With a value of about 1400 cm^{-1} , the energy gap between the S_1 and T_1 states is quite small at the DFT/MRCI level of theory, despite the fact that both originate from the same local $\pi - \pi^*$ excitation on the tridentate ligand. Small singlet–triplet splittings are typical of CT states where the hole and particle densities are spatially well separated, but they are encountered as well in π -systems in which the singly occupied MOs peak at neighboring centers.^{80,81} The MO plots of AG97 in Figure S3 reveal that the electron distributions in HOMO and LUMO are nearly disjoint, indeed. As the exchange interaction, which causes the singlet–triplet pair to split, decays exponentially with the distance between the electrons, the energy gap of such systems is rather small. The situation is different for the T_2 and S_4 states which mainly result from HOMO to LUMO + 1

excitations. The MO plots in Figure S3 show that the electron densities in the singly occupied HOMO and LUMO+1 orbitals strongly overlap, resulting in a large exchange splitting of more than 7000 cm^{-1} . In the context of PLIM, the S_4 state is irrelevant whereas the T_2 state is located in close energetic proximity of the S_1 state at the scalar relativistic level (Table S1) and interacts with S_1 via strong SOC (see below).

As may be expected for LC states, the calculated vertical excitation energies of the S_1 , T_1 and T_2 states experience only mild changes in the different environments (Table S1). In particular, they are nearly the same for AG97 in DCM and DMSO solution, just as in the experimental spectrum.³¹ In the following, therefore only computational results of AG97 in a DCM environment are discussed.

To model the photophysical decay processes following the S_1 absorption, geometry optimizations of the lowest three excited states (S_1 , T_1 , T_2) were carried out. Minimum structures could be located for the S_1 and T_1 states whereas all attempts to find a minimum of the T_2 potential energy surface (PES) failed as the optimization paths ended in crossings with the T_1 PES. To determine ISC rate constants, therefore the FCWDOS was computed with the recently introduced vertical Hessian approach.⁷⁹ This approach allows the calculation of the FCWDOS between S_1 and T_2 even without the knowledge of the minimum structure of the T_2 state. To this end, the PES is parabolically extrapolated by using the energy, gradients and the Hessian of the T_2 state at the S_1 minimum geometry. The adiabatic DFT/MRCI energies and the corresponding 0–0 energies are displayed in Table S3.

At the S_1 minimum structure, the difference densities of the S_1 and T_1 are almost identical to those at the ground state geometry (cp. Figure S6 and 2). Since the leading configurations of the S_1 and T_1 states are the same, their mutual SOCMEs are quite small (Table S4). The difference densities in Figure S6 reveal that the orientation of the d hole on the Pt atom changes when going from S_1 (d_{xz}) to T_2 (d_{z^2} with the z axis approximately perpendicular to the plane of the tridentate ligand). Hence, SOC between S_1 and T_2 is orbital-allowed⁸⁷ and yields large SOCMEs. The resulting ISC rate constants are listed in Table 1. Despite the moderate size of

Table 1. ISC Rate Constants k_{ISC} as Determined at the S_1 Geometry of AG97 in DCM

transition	$\sum \text{SOCMEs}^2 [\text{cm}^{-2}]$	FCWDOS [$\text{cm}^2 \text{s}^{-1}$]	$k_{\text{ISC}} [\text{s}^{-1}]$
$S_1 \rightarrow T_1$	1.93	2.0×10^7	3.8×10^7
$S_1 \rightarrow T_2$	305777.67	1.4×10^7	4.3×10^{12}

the SOCMEs, the $S_1 \rightarrow T_1$ ISC rate constant is 1 order of magnitude larger than the computed fluorescence rate constant (cp. Table S5). Both processes can, however, not compete with the much faster $S_1 \rightarrow T_2$ ISC which exhibits a rate constant in the order of 10^{12} s^{-1} . These results suggest a preferred excited-state energy dissipation pathway in which the S_1 state transfers its population intermediately to the T_2 state. Due to the presence of a conical intersection between the T_1 and T_2 PESs in the energetic proximity of the T_2 minimum, internal conversion to the T_1 state is expected to be very fast and efficient.

A distinctive feature of the T_1 geometry is that the tridentate ligand is no longer symmetrical with respect to the central Pt–N bond (Figure S7). While the electron density distribution remains nearly unchanged in the S_1 state in comparison to the

S_1 minimum geometry, it localizes in the T_1 and T_2 states at the T_1 minimum (Figure S8). The onset and the peak maxima of the VH phosphorescence spectrum, calculated for a temperature of 300 K in DCM (Figure 3), are only slightly

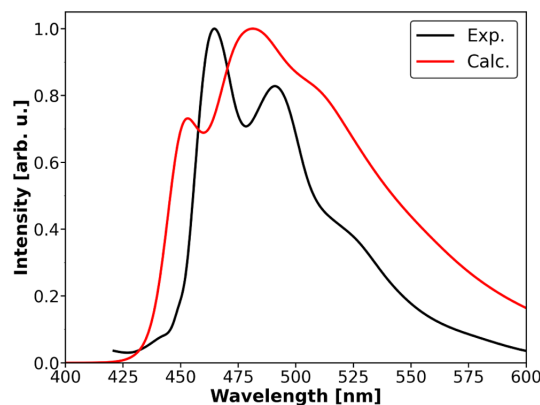


Figure 3. Calculated phosphorescence spectrum of AG97 in DCM at 300 K compared to a digitized experimental emission spectrum in deaerated DCM at room temperature, read from Figure S9 of ref 31.

blue-shifted with respect to their experimental counterparts at room temperature. However, while the vibrational progressions of both spectra are similar, the lower-energy parts of the FC spectrum are overestimated in intensity. We attribute this deviation to the harmonic oscillator approximation which does not properly represent the torsional vibrations of the CF_3 and $\text{P}(\text{Ph})_3$ residues. Delcanale et al.³¹ report a luminescence decay time of $19\ \mu\text{s}$ in a glassy $\text{MeOH}/\text{CH}_2\text{Cl}_2$ (1:1) matrix at 77 K. The Boltzmann-averaged radiative lifetime of $\tau = 33\ \mu\text{s}$ ($k_r = 3.0 \times 10^4 \text{ s}^{-1}$), calculated for a temperature of 77 K in DCM, is somewhat longer and fits very well considering that the experimentally determined lifetime contains nonradiative decay components in addition to the pure phosphorescence decay.

For analyzing the TSEET process, the transition dipole moment vector (TDMV) of each fine-structure level of the T_1 state has to be considered individually. In Table 2, therefore

Table 2. Individual and Averaged DFT/MRSOCI Properties of the T_1 Fine-Structure Sublevels of AG97 in DCM

state	MRSOCI energy [eV]	TDMV [D]	phosphorescence rate constant [s^{-1}]		
			sublevel	mean	Boltzmann
T_a	2.7084	0.0376628	4628.9	3.5×10^4	3.4×10^4 (300 K)
T_b	2.7100	0.1311328	56016.8		
T_c	2.7151	0.1163539	44461.9		3.0×10^4 (77 K)

the properties of the T_a , T_b and T_c substates of T_1 , as determined at the DFT/MRSOCI level of theory, are listed separately. The substates differ only slightly in energy, but the transition dipole strength, i.e., the length of the TDMV, is an order of magnitude lower for T_a compared to T_b and T_c . In addition to the length, the direction of the TDMV is a very important factor in the EET process. Details about the composition of the DFT/MRSOCI wave functions in terms of

spin-orbit-free LS basis states are available in Table S6. While the contributions of singlet states to the T_a wave function (root 2) are below 1%, $T_b \rightarrow S_0$ (root 3) borrows mainly intensity from the spin-allowed $S_3 \rightarrow S_0$ and $S_2 \rightarrow S_0$ transitions. Its TDMV points out of the plane of the tridentate ligand, roughly in z direction (Figure 4a). The T_c state (root 4) is dominated

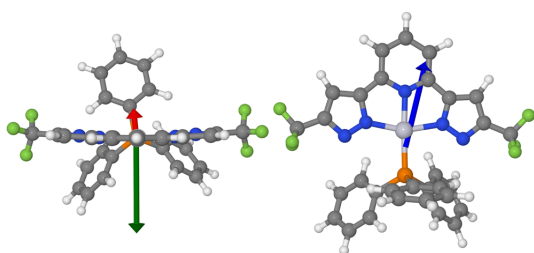


Figure 4. Arrows show the direction of the TDMVs of the three T_1 fine-structure levels of AG97 as computed with DFT/MRSOCI at the T_1 geometry in DCM. T_a (root 2): red, T_b (root 3): green, T_c (root 4): blue.

by the T^0 component and mixes in small amounts of S_1 character. The $T_c \rightarrow S_0$ transition therefore largely shares the direction of its TDMV (Figure 4b) with the $S_1 \rightarrow S_0$ transition which lies in the plane of the ligand nearly parallel to the central Pt–N axis (approximately in y direction).

4.2. EET Acceptor FITC. Fluorescein is a commonly used and well studied fluorescent probe. Depending on the pH value of the environment, it can exist in different tautomeric and prototropic forms. In its neutral state, a quinoid-like structure, a lactone form and a zwitterion are possible. Additionally, a cationic structure, two monoanionic structures and a dianionic structure are known.^{82–84} Delcanale et al.³¹ used FITC in PBS with a pH value of 7.4 for their EET experiments. The dominant species in this setting should be the dianion, which can be confirmed by comparing the absorption and emission spectra to spectra recorded at pH 10.5.⁸³ In the PLIM experiment, the fluorescent FITC reporter

is bound to BSA by a reaction between the isothiocyanate and a primary amine of the protein forming covalent thiourea bonds, which results in a small red shift of its absorption and emission spectra.^{31,85}

We performed calculations on the dianionic form of FITC in a water environment described implicitly by a PCM model. The S_1 state originates from an optically bright $\pi\pi^*$ excitation located on the xantheno core (Figure 5a). It is energetically very well separated from other singlet and triplet excited states. Figure 5b shows the experimental absorption spectrum of BSAFITC and the calculated VH absorption spectrum of the S_1 state. The spectral shape is perfectly reproduced while the computed spectrum is red-shifted by about 500 cm^{-1} .

4.3. Triplet–Singlet EET from AG97 to FITC. The ECME between the donor and acceptor molecules is strongly dependent on the distance and the relative orientation of their nuclear frames. In Förster's IDA, the coupling is estimated as the electrostatic dipole–dipole interaction between the transition dipole moments $\vec{\mu}_D$ and $\vec{\mu}_A$ of the donor and acceptor, respectively, which decreases with the third power of the distance R_{DA} between the barycenters of donor and acceptor.

$$V_{DA}^{IDA} = \kappa \frac{|\vec{\mu}_D||\vec{\mu}_A|}{n^2 R_{DA}^3} \quad (13)$$

In solution, the interaction is damped by n^2 where n is the refractive index of the medium. The factor κ is a scalar describing the relative orientation of the respective TDMVs with regard to the vector \vec{R}_{DA} connecting the barycenters of the donor and acceptor.

$$\kappa = \vec{n}_D \vec{n}_A - 3(\vec{e}_{DA} \vec{n}_D)(\vec{e}_{DA} \vec{n}_A) \quad (14)$$

The entities \vec{n}_D , \vec{n}_A and \vec{e}_{DA} appearing in eq 14 are the corresponding unit vectors. The orientation factor κ^2 can adopt values between 4 (in-line arrangement) and 0 (perpendicular arrangement).

The graphs in Figure 6 show the typical distance dependence of ECMEs. In producing Figure 6a, the TDMV

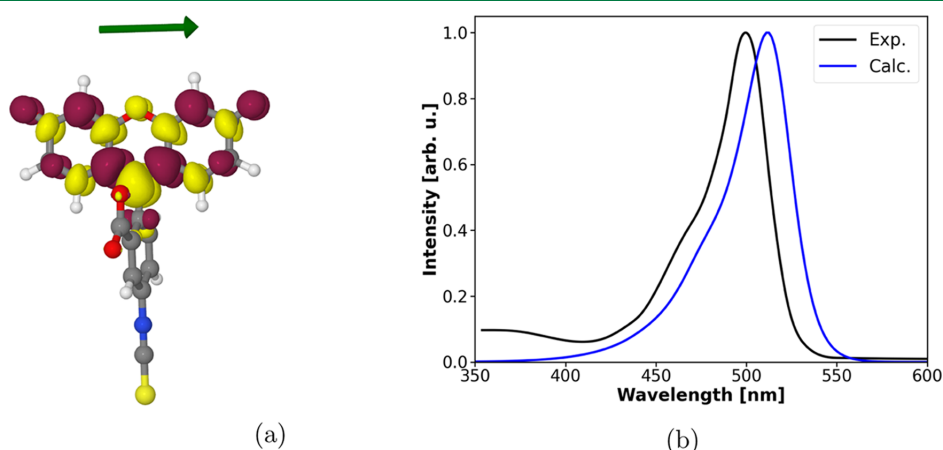


Figure 5. Absorption of the dianionic FITC in water. (a) Difference densities of the S_1 state at the ground state geometry with the direction of the $S_1 \leftarrow S_0$ TDMV. (b) Calculated VH absorption spectrum in implicit water environment compared to a digitized experimental absorption spectrum of BSAFITC in PBS buffer, read from Figure 6 of ref 31.

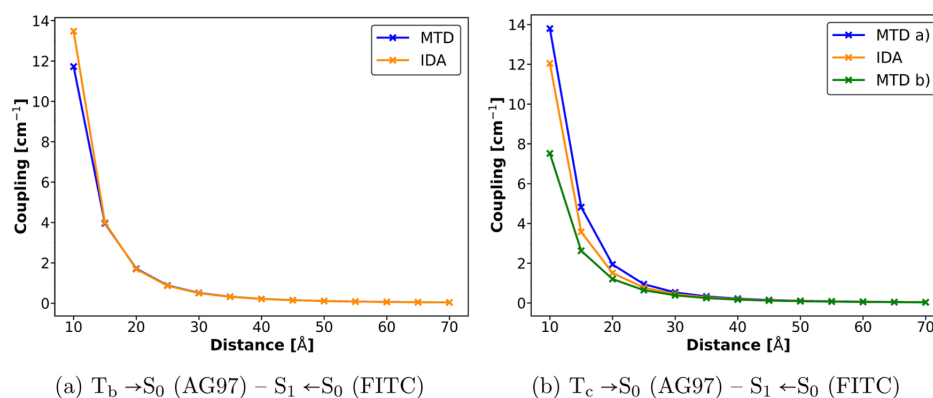


Figure 6. Distance dependence of the ECME between AG97 and FITC in IDA and MTD approximation for in-line arrangements of the donor and acceptor TDMVs, $\vec{\mu}_D$ and $\vec{\mu}_A$. The relative orientations of the donor and acceptor molecules are displayed in Figures 7 and 8, respectively.

of the $T_b \rightarrow S_0$ (AG97) emission was aligned to the TDMV of the $S_1 \leftarrow S_0$ (FITC) absorption (Figure 7). In this scenario,

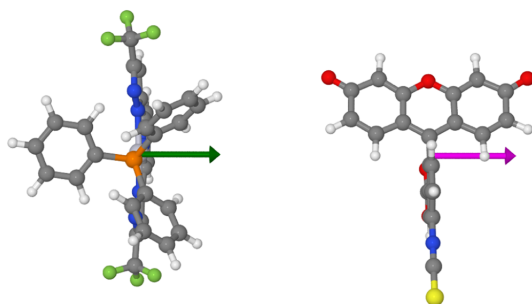


Figure 7. Donor–acceptor arrangement in which the TDMV of the T_b sublevel of AG97 is aligned in line with the singlet TDMV (pink) of FITC.

where the TDMVs are perpendicular to the molecular plane of the tridentate Pt-ligand, the ECMEs computed with the MTD and IDA methods match almost perfectly. However, the IDA starts to deviate markedly from the MTD values when the barycenter distance drops below 20 Å. When the molecules are rotated such that the TDMV of the $T_c \rightarrow S_0$ (AG97) emission and the TDMV of the $S_1 \leftarrow S_0$ (FITC) absorption are arranged in line (Figure 8), the IDA apparently deviates from the MTD values even for longer distances. In this case, the TDMVs lie approximately in the molecular plane of the tridentate ligand. Within the IDA, it makes no difference whether the FITC molecule is positioned on the same or opposite side of this ligand because only the modulus of the transition dipole moment enters the expression for the ECME (eq 13). In the MTD approach, the transition density matrices are convoluted with the intermolecular two-electron integrals (eq 12). Note that the exchange contributions vanish for barycenters distances larger than 10 Å (Table S7). While the barycenter of AG97 is located close to the Pt atom, the 1-TDM of the $T_1 \rightarrow S_0$ phosphorescence is mainly localized on the tridentate ligand. As a result, the ECME value is larger than the IDA value for case (a) where FITC and the tridentate ligand are located on the same side of the Pt atom (Figure 8a)

whereas it is smaller for case (b) where they are on opposite sides (Figure 8b). The distance R_{DA} between the barycenters of the donor and acceptor molecules is therefore not an appropriate measure for determining the dipole–dipole coupling in these cases.

The ECMEs in Table 3 were obtained for a fixed distance of 30 Å but different alignments of the TDMVs. For the collinear alignments of the TDMVs of the first and second triplet sublevels of AG97 with the TDMV of FITC, very similar results are obtained because $T_a \rightarrow S_0$ and $T_b \rightarrow S_0$ almost point in the same direction, save for the inverted sign (red and green arrows in Figure 4). In accord with the lengths of their TDMVs, the ECME of sublevel T_b is more than 3 times larger than that of sublevel T_a (Table 3 top and middle). As the ECME enters the expression for the EET rate constant (eq 5) quadratically, this results in a ten times larger k_{EET} value. Because of the low κ^2 values, the ECMEs of the third sublevel are close to zero in these nuclear arrangements. Correspondingly, if the TDMVs of the third sublevel is aligned collinearly with the TDMV of FITC, the ECMEs of the other two sublevels almost vanish while the ECME of the third sublevel is at its maximum (Table 3 bottom). Note, however, that the IDA is not a good approximation in this case. As seen from the entries of Table 3, it makes a pronounced difference whether the FITC molecule and the tridentate ligand reside on the same or opposite sides of the Pt atom.

The donor capabilities of the AG97 benefit from the fact that the T_1 sublevels are thermally accessible at room temperature (ZFS = 44 cm⁻¹ according to the DFT/MRSOCI calculations) and that the TDMVs of the second and third triplet sublevels are almost perpendicular. Therefore, only a few molecular arrangements lead to an almost complete suppression of the energy transfer. One of them is shown in Figure S10.

To get an estimate of the TSEET rate constant and the Förster radius, the squared ECMEs have to be multiplied by various factors and the spectral overlap integral. Initially, we were tempted to employ experimental spectra instead of the theoretical ones for determining this integral for two reasons. First, the experimental conditions (PBS solution, BSA-bound labels) are not easily modeled. Second, while our computed excitation energies and radiative rate constants match their experimental counterparts very well, the same does not apply

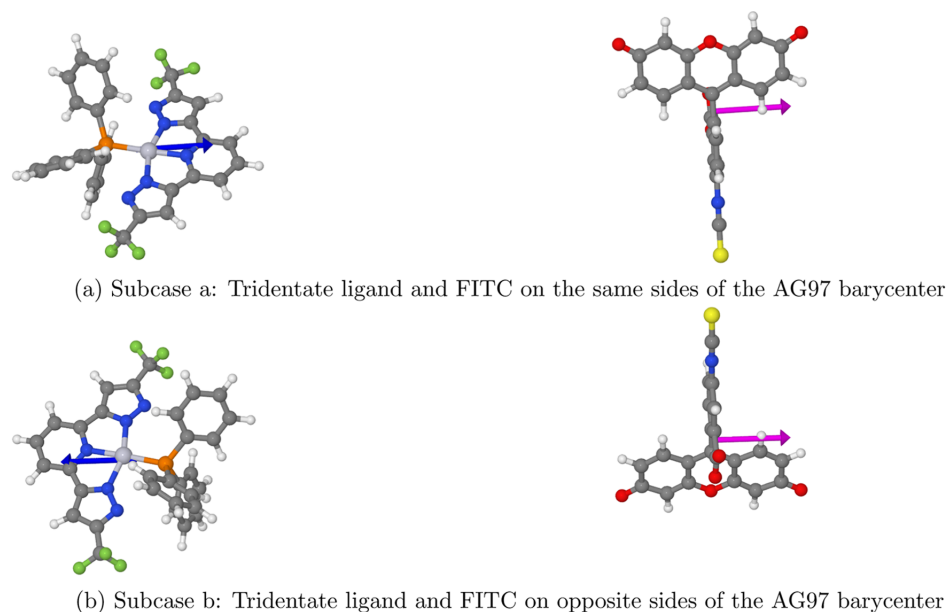


Figure 8. Donor–acceptor arrangements in which the TDMV of the T_c sublevel of AG97 is aligned in line with the singlet TDMV (pink) of FITC.

Table 3. ECMEs (cm^{-1}) for the T_1 (AG97)-Sensitized Fluorescence of FITC Assuming Different Relative Orientations of the Donor and Acceptor Molecules Using the IDA and MTD Approaches^a

TDMV of T_a (AG97) and S_1 (FITC) collinear			
	T_a	T_b	T_c
MTD	0.142	0.493	0.043
IDA	0.144	0.498	0.035
κ^2	4.000	3.946	0.025
TDMV of T_b (AG97) and S_1 (FITC) collinear			
	T_a	T_b	T_c
MTD	0.142	0.508	0.038
IDA	0.143	0.499	0.007
κ^2	3.940	4.000	0.001
TDMV of T_c (AG97) and S_1 (FITC) collinear			
	T_a	T_b	T_c
MTD ^b	0.006	0.092	0.528
MTD ^c	0.009	0.065	0.384
IDA	0.012	0.007	0.446
κ^2	0.028	0.001	4.000

^aIn all cases, the molecular centroids were 30 Å apart. ^bTridentate ligand and FITC on the same side of the AG97 barycenter. ^cTridentate ligand and FITC on opposite sides of the AG97 barycenter.

to the spectral envelopes of the computed room-temperature emission spectrum which is broader than the experimental phosphorescence band (Figure 3). This is a consequence of the harmonic oscillator approximation employed in the vibrational frequency calculations. It causes vibronic transitions involving higher vibrational quanta of the electronic ground state to gain too much intensity in conformationally flexible molecules.⁷⁹ Consequentially, the artificially intense low-

energy tail of the computed AG97 phosphorescence spectrum might overlap too strongly with the absorption spectrum of FITC and could thus spoil the results. It turned out, however, that this is not the case and very similar values for the spectral overlap integrals are obtained when we employ either calculated or experimental spectra for that purpose. The spectral overlap integral of the computed room-temperature phosphorescence spectrum of AG97 in DCM and the absorption spectrum of FITC in water (Figure 9a) adopts a value of 2.0×10^{-4} cm compared to a value of 1.8×10^{-4} cm for the overlap of experimental emission spectrum of AG97 bound to BSAFITC and the absorption spectrum of BSAFITC in PBS (Figure 9b). Multiplication with $2\pi/\hbar$ leads to EET rate constants of $k_{\text{EET}} = |V_{\text{DA}}|^2 2.36 \times 10^8 \text{ cm}^2 \text{ s}^{-1}$ (theo.) vs $k_{\text{EET}} = |V_{\text{DA}}|^2 2.14 \times 10^8 \text{ cm}^2 \text{ s}^{-1}$ (exp.) if the ECME V_{DA} is given in units of wavenumbers. In the following, we employ the theoretically determined value of the spectral overlap integral in the evaluation of the EET rate constant and the Förster radius.

ECMEs and EET rate constants depend strongly on the distance and the relative orientation of the donor and acceptor units. Corresponding values for the individual T_1 sublevels at intermolecular AG97 and FITC separations between 20 and 90 Å and an inline alignment of their TDMVs are displayed in Tables S7, S11 and S14 of the SI. The refractive index n for fluorescein in water is ≈ 1.34 . It enters the denominator of the rate equation in fourth power, resulting in a damping factor of ≈ 3.22 . A large uncertainty refers to the relative orientation of the donor–acceptor pairs in space. Assuming a spherically isotropic distribution of TDMVs leads to an averaged κ^2 -value of $2/3$.⁸⁶ Because of the small ZFS, it may be assumed that the T_1 sublevels of AG97 are populated with nearly equal weights at room temperature. The averaged computed TSEET rate constants over the three triplet components are displayed in Table S18. For obtaining an estimate of the Förster radius, we

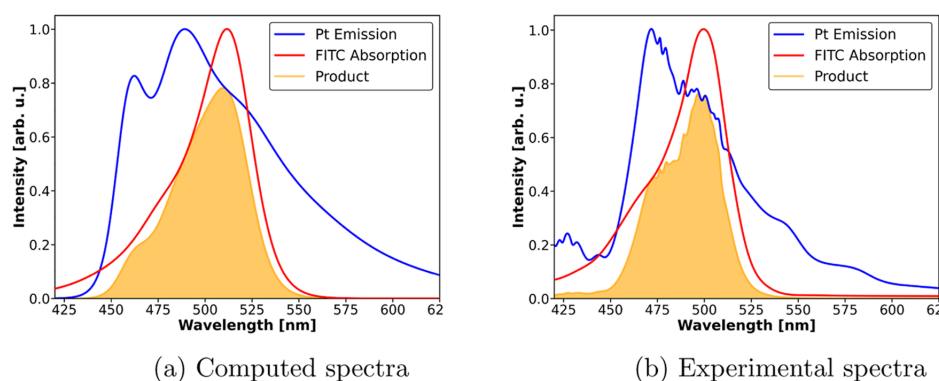


Figure 9. Spectral overlap between (a) the computed emission spectrum of AG97 in DCM and FITC in water (b) the digitized experimental emission spectrum of AG97 bound to BSA and the absorption spectrum of BSAFITC in PBS at room temperature. The experimental spectra were read from Figure 6 of ref 31.

compared the resulting k_{EET} values with the averaged phosphorescence rate constant of $k_{\text{p}} \approx 3.5 \times 10^4 \text{ s}^{-1}$. Assuming that no other nonradiative deactivation channels of the donor excitation have to be taken into consideration, a Förster radius between 55 and 60 Å is obtained. As we will see below, this assumption may not be justified, however.

Delcanale et al.³¹ report that the AG97 photoluminescence is completely quenched in DMSO and is very short-lived in DCM fluid solution due to solvent–solute interactions. Conversely, a clear-structured phosphorescence band (luminescence quantum yield $\Phi_{\text{p}} \approx 0.05$) was obtained from AG97 aggregates in PBS buffer at room temperature. Using a luminescence quantum yield of 5% in the evaluation of the effective phosphorescence lifetime reduces the Förster radius substantially. Furthermore, as AG97 is physisorbed on the surface of BSAFITC in the experiment, a value of the orientation factor of $\kappa^2 = 0.714 \times 2/3$, which was derived for random but rigid orientations,⁸⁷ appears more appropriate. Taking both factors into account, we obtain a Förster radius of about 35 Å as our best estimate. This value does not substantially change, if the IDA is employed in the computation of the ECME instead of the MTD approach (Table S19). In view of the described uncertainties in the computation of the Förster radius, the errors introduced by the IDA in comparison to the full MTD approach appear insignificant.

5. CONCLUSIONS AND OUTLOOK

In this paper, we have presented an extension of the monomer transition density (MTD) approach covering spin multiplicity-altering excitation energy transfer (EET) processes between singlet and triplet states in addition to spin multiplicity-conserving ones. In principle, the method can handle EET processes involving doublet or quartet states as well. The MTD approach was originally developed for computing the excitonic coupling between a singlet-excited donor molecule and an acceptor in the singlet ground state.^{35,40} The STRREET program contracts one-particle transition density matrices based on DFT/MRCI wave functions of the monomers with RI-approximated two-electron Coulomb and exchange integrals of the dimer to compute excitonic coupling matrix elements (ECMEs).⁴¹ The extended MTD approach presented here builds upon complex-valued wave functions of the density

functional theory based multireference spin–orbit coupling configuration interaction (DFT/MRSOCI) method for generating the required one-particle transition density matrices. EET rate constants and Förster radii are then determined according to Fermi's golden rule by multiplying the squared ECMEs by the spectral overlap integral and damping factors taking care of the susceptibility of the surrounding medium and the orientational averaging. We show here that the computation of triplet–singlet EET (TSEET) rate constants is technically feasible even for sizable donor and acceptor molecules. Due to the extensive use of symmetry relations between tensor components, it is not much more resource demanding than for singlet–singlet EET (SSEET). Regarding the vibrationally resolved monomer spectra that form the basis for the calculation of the spectral overlap integral, we advocate the use of a vertical Hessian approach⁷⁹ which typically generates narrower spectral envelopes than adiabatic Hessian approaches and compares better with experimental band shapes of conformationally flexible molecules.

As a proof-of-principle application, we have chosen an EET system consisting of the phosphorescent platinum complex AG97 as the donor and the fluorescence reporter FITC, a fluorescein derivative, as the acceptor. Aggregates of AG97 adsorbed on a protein surface had been used by Delcanale et al.³¹ as phosphorescent labels with luminescence lifetime-based readouts. Our computed excitation energies and transition moments of the monomers match their experimental counterparts very well. Although the width of the computed room-temperature phosphorescence spectrum in solution is somewhat broader than the experimental emission spectrum of the AG97 aggregates, the spectral overlap with the FITC absorption spectrum is nearly identical in both setups. Interestingly, the transition dipole moment vectors of the individual AG97 T₁ sublevels point in different directions. The fact that they cover a large angular range may be considered an advantage over a fluorescent EET donor. A clear disadvantage of a phosphorescent EET donor is its substantially smaller radiative rate constant, which makes TSEET more sensitive to competing nonradiative deactivation processes in comparison to SSEET from a strongly fluorescent donor. In the current sample application, a luminescence quantum yield of merely 5% was measured.³¹ Taking the luminescence quantum yield into consideration and assuming a random orientation of the

donor and acceptor molecules yields a Förster radius of about 35 Å.

The ECMEs generated with the help of the MTD approach have been used as reference data for assessing the validity of the much less involved and hence much less costly ideal dipole approximation (IDA). For intermolecular donor–acceptor separations close to the Förster radius and beyond, the error introduced by the IDA is found to be rather small. Interestingly, the three sublevels of the T_1 state behave differently in this respect. For the first two sublevels, T_{1a} and T_{1b} , there is hardly any difference between the IDA and MTD results, even for barycenter distances as short as 20 Å. Their TDMVs are approximately orthogonal to the plane spanned by the π -system of the tridentate Pt ligand. For the TSEET from the third T_1 component, T_{1c} , whose TDMV lies in the plane of the tridentate ligand, it matters whether this ligand and the FITC acceptor are positioned on the same or opposite sides of the AG97 barycenter. Within the MTD approach, larger ECMEs are obtained for the case in which the FITC acceptor and the tridentate ligand are closer to each other. As only the relative orientations of the TDMVs and the barycenter distance of the donor and acceptor molecules enter the IDA equations, the IDA yields an ECME value intermediate between the two MTD cases.

With regard to applications, the computational tools developed in this work are not restricted to phosphorescence lifetime imaging. In OLEDs, EET from a phosphorescent or thermally activated delayed fluorescence (TADF) assistant dopant to a strongly fluorescent chromophore has been used to improve the intensity and color purity of the emitted light.^{4–7} For achieving high internal quantum efficiencies, it is important that singlet and triplet excitons are harvested alike. Phosphorescent and TADF assistant dopants can earn 100% of the excitons but typically have much lower radiative rate constants than strong fluorophores. In these devices, therefore the advantage of SSEET over TSEET in terms of competitive deactivation processes is leveled out. Our recent theoretical work on a hyperfluorescent system undergoing SSEET from a TADF assistant dopant to a strongly fluorescent multiresonant emitter demonstrated that the MTD method can provide Förster radii and valuable data for assessing the validity of the IDA approach.⁴¹ Application of the extended MTD method to phosphor-sensitized fluorescence involving TSEET from a phosphorescent dopant to a fluorescent OLED emitter will be presented in due course.

■ ASSOCIATED CONTENT

Data Availability Statement

The data that support the findings of this study are available within this article and its [Supporting Information](#). Additional data are available from the corresponding author upon reasonable request.

Supporting Information

The Supporting Information is available free of charge at <https://pubs.acs.org/doi/10.1021/acs.jctc.4c01688>.

TheoDORÉ analysis of the DFT/MRCI wave functions, solvent dependence of the excitation energies of AG97, molecular orbitals and difference densities of AG97, comparison of perturbational and variational inclusion of SOC, FITC tautomers, coupling matrix elements and EET rate constants depending on the intermolecular distance and orientation of the donor and acceptor,

geometry information on the structures (bond distances and xyz coordinates) ([PDF](#))

■ AUTHOR INFORMATION

Corresponding Author

Christel M. Marian – *Institute of Theoretical and Computational Chemistry, Faculty of Mathematics and Natural Sciences, Heinrich Heine University Düsseldorf, Düsseldorf D-40225, Germany*; orcid.org/0000-0001-7148-0900; Email: Christel.Marian@hhu.de

Author

Simon Metz – *Institute of Theoretical and Computational Chemistry, Faculty of Mathematics and Natural Sciences, Heinrich Heine University Düsseldorf, Düsseldorf D-40225, Germany*

Complete contact information is available at: <https://pubs.acs.org/10.1021/acs.jctc.4c01688>

Notes

The authors declare no competing financial interest.

■ ACKNOWLEDGMENTS

The authors thank the Deutsche Forschungsgemeinschaft (DFG, German Research Foundation) for financial support through GRK 2482, project number 396890929.

■ REFERENCES

- (1) Mirkovic, T.; Ostroumov, E. E.; Anna, J. M.; van Grondelle, R.; Govindjee; Scholes, G. D. Light absorption and energy transfer in the antenna complexes of photosynthetic organisms. *Chem. Rev.* **2017**, *117*, 249–293.
- (2) Currie, M. J.; Mapel, J.; Heidel, T.; Goffri, S.; Baldo, M. High-efficiency organic solar concentrators for photovoltaics. *Science* **2008**, *321*, 226–228.
- (3) Frischmann, P. D.; Mahata, K.; Würthner, F. Powering the future of molecular artificial photosynthesis with light-harvesting metallosupramolecular dye assemblies. *Chem. Soc. Rev.* **2013**, *42*, 1847–1870.
- (4) Baldo, M. A.; Thompson, M. E.; Forrest, S. R. High-efficiency fluorescent organic light-emitting devices using a phosphorescent sensitizer. *Nature* **2000**, *403*, 750–753.
- (5) Nakanotani, H.; Higuchi, T.; Furukawa, T.; Masui, K.; Morimoto, K.; Numata, M.; Tanaka, H.; Sagara, Y.; Yasuda, T.; Adachi, C. High-Efficiency Organic Light-Emitting Diodes with Fluorescent Emitters. *Nat. Commun.* **2014**, *5*, No. 4016.
- (6) Tanaka, I.; Tokiti, S. *Highly Efficient OLEDs with Phosphorescent Materials*; Yersin, Ed.; Wiley; Wiley-VCH: Weinheim, 1999, 2008; Vol. 17, pp 283–309.
- (7) Stavrou, K.; Franca, L.; Danos, A.; Monkman, A. Key requirements for ultraefficient sensitization in hyperfluorescence organic light-emitting diodes. *Nat. Photonics* **2024**, *18*, 554–561.
- (8) Stryer, L.; Haugland, R. P. Energy transfer: a spectroscopic ruler. *Proc. Natl. Acad. Sci. U.S.A.* **1967**, *58*, 719–726.
- (9) Jares-Erijman, E. A.; Jovin, T. FRET imaging. *Nat. Biotechnol.* **2003**, *21*, 1387–1395.
- (10) Clegg, R. M.; Holub, O.; Gohlke, C. Methods in Enzymology. In *Biophotonics, Part A*; Academic Press, 2003; Vol. 360, pp 509–542.
- (11) Hell, S. W. Far-Field Optical Nanoscopy. *Science* **2007**, *316*, 1153–1158.
- (12) Förster, T. Zwischenmolekulare Energiewanderung und Fluoreszenz. *Ann. Phys.* **1948**, *437*, 55–75.
- (13) Dexter, D. L. A Theory of Sensitized Luminescence in Solids. *J. Chem. Phys.* **1953**, *21*, 836–850.
- (14) Scholes, G. D. Long-range resonance energy transfer in molecular systems. *Annu. Rev. Phys. Chem.* **2003**, *54*, 57–87.

- (15) Förster, T. 10th Spiers Memorial Lecture. Transfer mechanisms of electronic excitation. *Discuss. Faraday Soc.* **1959**, *27*, 7–17.
- (16) Bennett, R. O.; Kellogg, R. Mechanisms and rates of radiationless energy transfer. *Photochem. Photobiol.* **1968**, *7*, 571–581.
- (17) Ermolaev, V.; Sveshnikova, E. Inductive-Resonance Transfer of Energy from Aromatic Molecules in the Triplet State *Sov. Phys. Dokl.* **1963**; Vol. 8, p 373.
- (18) Bennett, R. G.; Schwenker, R.; Kellogg, R. Radiationless intermolecular energy transfer. II. Triplet→ singlet transfer. *J. Chem. Phys.* **1964**, *41*, 3040–3041.
- (19) D'Andrade, B. W.; Baldo, M. A.; Adachi, C.; Brooks, J.; Thompson, M. E.; Forrest, S. R. High-efficiency yellow double-doped organic light-emitting devices based on phosphor-sensitized fluorescence. *Appl. Phys. Lett.* **2001**, *79*, 1045–1047.
- (20) Heimel, P.; Mondal, A.; May, F.; Kowalsky, W.; Lennartz, C.; Andrienko, D.; Lovrincic, R. Unicolored phosphor-sensitized fluorescence for efficient and stable blue OLEDs. *Nat. Commun.* **2018**, *9*, No. 4990.
- (21) Lei, G.; Wang, L.; Qiu, Y. Blue phosphorescent dye as sensitizer and emitter for white organic light-emitting diodes. *Appl. Phys. Lett.* **2004**, *85*, 5403–5405.
- (22) Cheng, G.; Zhang, Y.; Zhao, Y.; Liu, S.; Ma, Y. Improved efficiency for white organic light-emitting devices based on phosphor sensitized fluorescence. *Appl. Phys. Lett.* **2006**, *88*, No. 083512.
- (23) Kanno, H.; Sun, Y.; Forrest, S. R. White organic light-emitting device based on a compound fluorescent-phosphor-sensitized-fluorescent emission layer. *Appl. Phys. Lett.* **2006**, *89*, No. 143516.
- (24) Yao, J.; Ying, S.; Sun, Q.; Dai, Y.; Qiao, X.; Yang, D.; Chen, J.; Ma, D. High efficiency blue/green/yellow/red fluorescent organic light-emitting diodes sensitized by phosphors: general design rules and electroluminescence performance analysis. *J. Mater. Chem. C* **2019**, *7*, 11293–11302.
- (25) Yao, J.; Chen, Y.; Wu, Y.; Qiao, X.; Yang, D.; Dai, Y.; Sun, Q.; Ma, D. High efficiency and low efficiency roll-off all fluorescent white organic light-emitting diodes based on phosphor sensitization. *J. Mater. Chem. C* **2020**, *8*, 1666–1672.
- (26) Bastiaens, P. I.; Pepperkok, R. Observing proteins in their natural habitat: the living cell. *Trends Biochem. Sci.* **2000**, *25*, 631–637.
- (27) Wouters, F. S.; Verveer, P. J.; Bastiaens, P. I. Imaging biochemistry inside cells. *Trends Cell Biol.* **2001**, *11*, 203–211.
- (28) Suhling, K.; French, P. M.; Phillips, D. Time-resolved fluorescence microscopy. *Photochem. Photobiol. Sci.* **2005**, *4*, 13–22.
- (29) Datta, R.; Heaster, T. M.; Sharick, J. T.; Gillette, A. A.; Skala, M. C. Fluorescence lifetime imaging microscopy: fundamentals and advances in instrumentation, analysis, and applications. *J. Biomed. Opt.* **2020**, *25*, No. 071203.
- (30) Baggaley, E.; Weinstein, J. A.; Williams, J. A. G. *Luminescent and Photoactive Transition Metal Complexes as Biomolecular Probes and Cellular Reagents*; Lo, K. K.-W., Ed.; Springer: Berlin Heidelberg, 2015; pp 205–256.
- (31) Delcanale, P.; Galstyan, A.; Daniliuc, C. G.; Grecco, H. E.; Abbuzzetti, S.; Faust, A.; Viappiani, C.; Strasser, C. A. Oxygen-Insensitive Aggregates of Pt(II) Complexes as Phosphorescent Labels of Proteins with Luminescence Lifetime-Based Readouts. *ACS Appl. Mater. Interfaces* **2018**, *10*, 24361–24369.
- (32) Krueger, B. P.; Scholes, G. D.; Fleming, G. R. Calculation of couplings and energy-transfer pathways between the pigments of LH2 by the ab initio transition density cube method. *J. Phys. Chem. B* **1998**, *102*, 5378–5386.
- (33) Brédas, J.-L.; Beljonne, D.; Coropceanu, V.; Cornil, J. Charge-transfer and energy-transfer processes in π -conjugated oligomers and polymers: a molecular picture. *Chem. Rev.* **2004**, *104*, 4971–5004.
- (34) Madjet, M.; Abdurahman, A.; Renger, T. Interpigment Coulomb couplings from ab-initio transition charges: application to strongly coupled pigments in photosynthetic antennae and reaction centers *J. Phys. Chem. B* **2006**; Vol. 110, p 17268.
- (35) Fink, R.; Pfister, J.; Schneider, A.; Zhao, H.; Engels, B. Ab initio configuration interaction description of excitation energy transfer between closely packed molecules. *Chem. Phys.* **2008**, *343*, 353–361.
- (36) May, V.; Kühn, O. *Charge and Energy Transfer Dynamics in Molecular Systems, 3rd, Revised and Enlarged Edition*; Wiley-VCH: Weinheim, 2011.
- (37) You, Z.-Q.; Hsu, C.-P. Theory and calculation for the electronic coupling in excitation energy transfer. *Int. J. Quantum Chem.* **2014**, *114*, 102–115.
- (38) Fujimoto, K. J. Theoretical Calculations of Excitation Energy Transfer. In *Chemical Science of π -Electron Systems*. Tokyo, 2015; pp 761–777.
- (39) Curutchet, C.; Mennucci, B. Quantum chemical studies of light harvesting. *Chem. Rev.* **2017**, *117*, 294–343.
- (40) Spiegel, J. D.; Kleinschmidt, M.; Larbig, A.; Tatchen, J.; Marian, C. M. Quantum-chemical studies on excitation energy transfer processes in BODIPY-based donor-acceptor systems. *J. Chem. Theory Comput.* **2015**, *11*, 4316–4327.
- (41) Metz, S.; Marian, C. M. Excitonic coupling of a TADF assistant dopant and a multi-resonance TADF emitter. *Adv. Opt. Mater.* **2024**, No. 2402241.
- (42) Kleinschmidt, M.; Tatchen, J.; Marian, C. M. SPOCK. CI: A multireference spin-orbit configuration interaction method for large molecules. *J. Chem. Phys.* **2006**, *124*, No. 124101.
- (43) Kleinschmidt, M.; van Wüllen, C.; Marian, C. M. Intersystem-crossing and phosphorescence rates in fac-Ir^{III}(ppy)₃: A theoretical study involving multi-reference configuration interaction wavefunctions. *J. Chem. Phys.* **2015**, *142*, No. 094301.
- (44) Heil, A.; Gollnisch, K.; Kleinschmidt, M.; Marian, C. M. On the photophysics of four heteroleptic iridium(III) phenylpyridyl complexes investigated by relativistic multi-configuration methods. *Mol. Phys.* **2016**, *114*, 407–422.
- (45) Heil, A.; Marian, C. M. Structure–Emission Property Relationships in Cyclometalated Pt(II) β -Diketonate Complexes. *Inorg. Chem.* **2019**, *58*, 6123–6136.
- (46) Föller, J.; Friese, D. H.; Riese, S.; Kaminski, J. M.; Metz, S.; Schmidt, D.; Würthner, F.; Lambert, C.; Marian, C. M. On the photophysical properties of Ir III, Pt II, and Pd II (phenylpyrazole)-(phenyldipyrrin) complexes. *Phys. Chem. Chem. Phys.* **2020**, *22*, 3217–3233.
- (47) Hennebicq, E.; Pourtois, G.; Scholes, G. D.; Herz, L. M.; Russell, D. M.; Silva, C.; Setayesh, S.; Grimsdale, A. C.; Müllen, K.; Brédas, J.-L.; Beljonne, D. Exciton Migration in Rigid-Rod Conjugated Polymers: An Improved Förster Model. *J. Am. Chem. Soc.* **2005**, *127*, 4744–4762.
- (48) Fückel, B.; Köhn, A.; Harding, M. E.; Diezemann, G.; Hinze, G.; Basché, T.; Gauss, J. Theoretical investigation of electronic excitation energy transfer in chromophoric assemblies. *J. Chem. Phys.* **2008**, *128*, No. 074505.
- (49) Stehr, V.; Fink, R. F.; Tafipolski, M.; Deibel, C.; Engels, B. Comparison of different rate constant expressions for the prediction of charge and energy transport in oligoacenes. *WIREs Comput. Mol. Sci.* **2016**, *6*, 694–720.
- (50) Etinski, M.; Tatchen, J.; Marian, C. M. Time-dependent approaches for the calculation of intersystem crossing rates. *J. Chem. Phys.* **2011**, *134*, No. 154105.
- (51) Etinski, M.; Tatchen, J.; Marian, C. M. Thermal and Solvent Effects on the Triplet Formation in Cinnoline. *Phys. Chem. Chem. Phys.* **2014**, *16*, 4740–4751.
- (52) Fujimoto, K. J. Transition-density-fragment interaction combined with transfer integral approach for excitation-energy transfer via charge-transfer states. *J. Chem. Phys.* **2012**, *137*, No. 034101.
- (53) Vahtras, O.; Almlöf, J.; Feyereisen, M. Integral approximations for LCAO-SCF calculations. *Chem. Phys. Lett.* **1993**, *213*, 514–518.
- (54) Weigend, F.; Häser, M.; Patzelt, H.; Ahlrichs, R. RI-MP2: optimized auxiliary basis sets and demonstration of efficiency. *Chem. Phys. Lett.* **1998**, *294*, 143–152.

- (55) Marian, C. *Reviews In Computational Chemistry*; Lipkowitz, K.; Boyd, D., Eds.; Wiley; Wiley-VCH: Weinheim, 1999, 2001; Vol. 17, pp 99–204.
- (56) Grimme, S.; Waletzke, M. A combination of Kohn–Sham density functional theory and multi-reference configuration interaction methods. *J. Chem. Phys.* **1999**, *111*, 5645–5655.
- (57) Marian, C. M.; Heil, A.; Kleinschmidt, M. The DFT/MRCI method. *WIREs Comput. Mol. Sci.* **2019**, *9*, No. e1394.
- (58) Lohr, L. L., Jr Spin-forbidden electric-dipole transition moments. *J. Chem. Phys.* **1966**, *45*, 1362–1363.
- (59) Goodman, L.; Laurenzi, B. J. Probability of singlet–triplet transitions. *Adv. Quantum Chem.* **1968**, *4*, 153–169.
- (60) Wetmore, R. W.; Segal, G. A. Efficient generation of configuration interaction matrix elements. *Chem. Phys. Lett.* **1975**, *36*, 478–483.
- (61) Frisch, M. J.; Trucks, G. W.; Schlegel, H. B.; Scuseria, G. E.; Robb, M. A.; Cheeseman, J. R.; Scalmani, G.; Barone, V.; Petersson, G. A.; Nakatsuji, H.; Li, X.; Caricato, M.; Marenich, A. V.; Bloino, J.; Janesko, B. G.; Gomperts, R.; Mennucci, B.; Hratchian, H. P.; Ortiz, J. V.; Izmaylov, A. F.; Sonnenberg, J. L.; Williams-Young, D.; Ding, F.; Lipparini, F.; Egidi, F.; Goings, J.; Peng, B.; Petrone, A.; Henderson, T.; Ranasinghe, D.; Zakrzewski, V. G.; Gao, J.; Rega, N.; Zheng, G.; Liang, W.; Hada, M.; Ehara, M.; Toyota, K.; Fukuda, R.; Hasegawa, J.; Ishida, M.; Nakajima, T.; Honda, Y.; Kitao, O.; Nakai, H.; Vreven, T.; Throssell, K.; Montgomery, J. A., Jr.; Peralta, J. E.; Ogliaro, F.; Bearpark, M. J.; Heyd, J. J.; Brothers, E. N.; Kudin, K. N.; Staroverov, V. N.; Keith, T. A.; Kobayashi, R.; Normand, J.; Raghavachari, K.; Rendell, A. P.; Burant, J. C.; Iyengar, S. S.; Tomasi, J.; Cossi, M.; Millam, J. M.; Klene, M.; Adamo, C.; Cammi, R.; Ochterski, J. W.; Martin, R. L.; Morokuma, K.; Farkas, O.; Foresman, J. B.; Fox, D. J. Gaussian 16 Revision C.01 Gaussian Inc.: Wallingford, CT, 2016.
- (62) Adamo, C.; Barone, V. Toward reliable density functional methods without adjustable parameters: The PBE0 model. *J. Chem. Phys.* **1999**, *110*, 6158–6170.
- (63) Schäfer, A.; Horn, H.; Ahlrichs, R. Fully optimized contracted Gaussian basis sets for atoms Li to Kr. *J. Chem. Phys.* **1992**, *97*, 2571–2577.
- (64) Weigend, F.; Ahlrichs, R. Balanced basis sets of split valence, triple zeta valence and quadruple zeta valence quality for H to Rn: Design and assessment of accuracy. *Phys. Chem. Chem. Phys.* **2005**, *7*, 3297.
- (65) Andrae, D.; Häußermann, U.; Dolg, M.; Stoll, H.; Preuß, H. Energy-adjusted ab initio pseudopotentials for the second and third row transition elements. *Theor. Chim. Acta* **1990**, *77*, 123–141.
- (66) Cancès, E.; Mennucci, B.; Tomasi, J. A new integral equation formalism for the polarizable continuum model: Theoretical background and applications to isotropic and anisotropic dielectrics. *J. Chem. Phys.* **1997**, *107*, 3032–3041.
- (67) Cammi, R.; Corni, S.; Mennucci, B.; Tomasi, J. Electronic excitation energies of molecules in solution: State specific and linear response methods for nonequilibrium continuum solvation models. *J. Chem. Phys.* **2005**, *122*, No. 104513.
- (68) Scalmani, G.; Frisch, M. J.; Mennucci, B.; Tomasi, J.; Cammi, R.; Barone, V. Geometries and properties of excited states in the gas phase and in solution: Theory and application of a time-dependent density functional theory polarizable continuum model. *J. Chem. Phys.* **2006**, *124*, No. 094107.
- (69) Yanai, T.; Tew, D. P.; Handy, N. C. A new hybrid exchange–correlation functional using the Coulomb-attenuating method (CAM-B3LYP). *Chem. Phys. Lett.* **2004**, *393*, 51–57.
- (70) TURBOMOLE. TURBOMOLE V7.5.0 2020, a development of University of Karlsruhe and Forschungszentrum Karlsruhe GmbH, 1989–2007, TURBOMOLE GmbH, since 2007 2020 <http://www.turbomole.com>.
- (71) Heil, A.; Kleinschmidt, M.; Marian, C. M. On the performance of DFT/MRCI Hamiltonians for electronic excitations in transition metal complexes: The role of the damping function. *J. Chem. Phys.* **2018**, *149*, No. 164106.
- (72) Becke, A. D. A new mixing of Hartree-Fock and local density-functional theories. *J. Chem. Phys.* **1993**, *98*, 1372–1377.
- (73) Plasser, F. TheoDORE: A toolbox for a detailed and automated analysis of electronic excited state computations. *J. Chem. Phys.* **2020**, *152*, No. 084108.
- (74) Jmol: an open-source Java viewer for chemical structures in 3d. <http://www.jmol.org/>.
- (75) Kleinschmidt, M.; Tatchen, J.; Marian, C. M. Spin-orbit coupling of DFT/MRCI wavefunctions: Method, test calculations, and application to thiophene. *J. Comput. Chem.* **2002**, *23*, 824–833.
- (76) Kleinschmidt, M.; Marian, C. M. Efficient generation of matrix elements for one-electron spin-orbit operators. *Chem. Phys.* **2005**, *311*, 71–79.
- (77) Heß, B. A.; Marian, C. M.; Wahlgren, U.; Gropen, O. A mean-field spin-orbit method applicable to correlated wavefunctions. *Chem. Phys. Lett.* **1996**, *251*, 365–371.
- (78) AMFI is an atomic spin–orbit integral program written by B. Schimmelpfennig, University of Stockholm, 1996.
- (79) Böhmer, T.; Kleinschmidt, M.; Marian, C. M. Toward the improvement of vibronic spectra and non-radiative rate constants using the vertical Hessian method. *J. Chem. Phys.* **2024**, *161*, No. 094114.
- (80) Vosskötter, S.; Konieczny, P.; Marian, C. M.; Weinkauff, R. Towards an understanding of the singlet-triplet splittings in conjugated hydrocarbons: Azulene investigated by anion photoelectron spectroscopy and theoretical calculations. *Phys. Chem. Chem. Phys.* **2015**, *17*, 23573–23581.
- (81) Hatakeyama, T.; Shiren, K.; Nakajima, K.; Nomura, S.; Nakatsuka, S.; Kinoshita, K.; Ni, J.; Ono, Y.; Ikuta, T. Ultrapure Blue Thermally Activated Delayed Fluorescence Molecules: Efficient HOMO–LUMO Separation by the Multiple Resonance Effect. *Adv. Mater.* **2016**, *28*, 2777–2781.
- (82) Martin, M. M.; Lindqvist, L. The pH dependence of fluorescein fluorescence. *J. Lumin.* **1975**, *10*, 381–390.
- (83) Gerasimova, M. A.; Tomilin, F. N.; Malyar, E. Y.; Varganov, S. A.; Fedorov, D. G.; Ovchinnikov, S. G.; Slyusareva, E. A. Fluorescence and photoinduced proton transfer in the protolytic forms of fluorescein: Experimental and computational study. *Dyes Pigm.* **2020**, *173*, No. 107851.
- (84) Klonis, N.; Sawyer, W. H. Spectral properties of the prototropic forms of fluorescein in aqueous solution. *J. Fluoresc.* **1996**, *6*, 147–157.
- (85) Hungerford, G.; Benesch, J.; Mano, J. F.; Reis, R. L. Effect of the labelling ratio on the photophysics of fluorescein isothiocyanate (FITC) conjugated to bovine serum albumin. *Photochem. Photobiol. Sci.* **2007**, *6*, 152–158.
- (86) Loura, L. Simple Estimation of Förster Resonance Energy Transfer (FRET) Orientation Factor Distribution in Membranes. *Int. J. Mol. Sci.* **2012**, *13*, 15252–15270.
- (87) Maksimov, M. Z.; Rozman, I. M. On Energy Transfer in Solid Solutions. *Opt. Spectrosc.* **1962**; Vol. 12, p 337.

Supporting Information for Computational Approach to Phosphor-Sensitized Fluorescence Based on Monomer Transition Densities

Simon Metz and Christel M. Marian*

*Institute of Theoretical and Computational Chemistry, Faculty of Mathematics and Natural
Sciences, Heinrich Heine University Düsseldorf, Universitätsstr. 1, D-40225 Düsseldorf,
Germany*

E-mail: Christel.Marian@hhu.de

Table S1: Vertical excitation energies E_{vert} [cm^{-1}], oscillator strengths f and leading terms of the spin-orbit free DFT/MRCI wave function [%] at the ground state geometry in various environments

Solvent	State	E_{vert}	f	Orbital Transition	Percentage
Vacuum	S ₁	25700	3.5×10^{-2}	HOMO → LUMO	79
	T ₁	24329	—	HOMO → LUMO	83
	T ₂	25882	—	HOMO → LUMO+1	72
DCM	S ₁	26496	3.4×10^{-2}	HOMO → LUMO	78
	T ₁	25071	—	HOMO → LUMO	83
	T ₂	26760	—	HOMO → LUMO+1	59
DMSO	S ₁	26679	3.3×10^{-2}	HOMO → LUMO	78
	T ₁	25247	—	HOMO → LUMO	83
	T ₂	27022	—	HOMO → LUMO+1	61

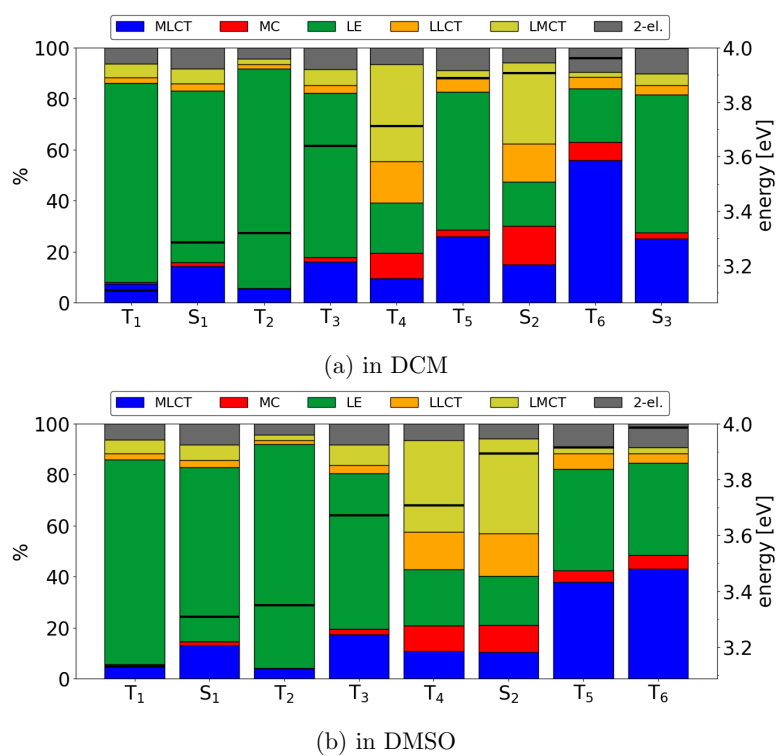
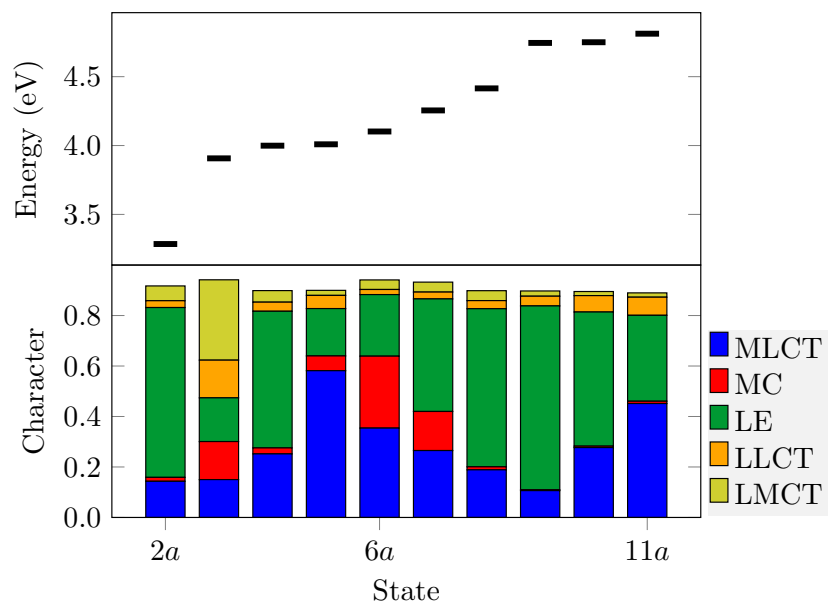
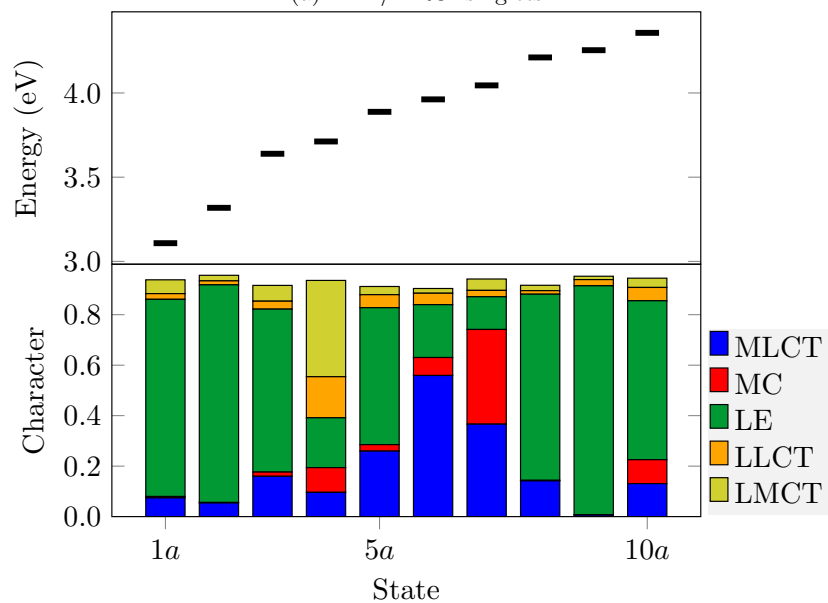


Figure S1: TheoDORE analysis of low-lying DFT/MRCI states with an excitation energy below 4.0 eV at the ground state geometry of AG97 in DCM and DMSO.



(a) DFT/MRCI singlets



(b) DFT/MRCI triplets

Figure S2: TheoDORE analysis of the *LS*-coupled DFT/MRCI basis states of AG97 at the ground state geometry in DCM.

Table S2: Vertical excitation energies E_{vert} [cm^{-1}], oscillator strengths f and projection of the wave function of the spin-orbit mixed states onto the LS -coupled DFT/MRCI basis states for AG97 in DCM at the S_0 minimum

	SOC-QDPT				DFT/MRSOCI			
	E_{vert}	f	LS state	$ c ^2$	E_{vert}	f	LS state	$ c ^2$
Root 1	0		S_0	0.993543	0		S_0	0.975466
			T_4^+	0.002825			T_4^+	0.002499
			T_4^-	0.002825			T_4^-	0.002499
Root 2	25049	2.4×10^{-6}	T_1^+	0.480391	25678	2.0×10^{-6}	T_1^+	0.475605
			T_1^-	0.480391			T_1^-	0.475605
			T_6^0	0.023458			T_6^0	0.020937
			T_5^0	0.006337			T_5^0	0.005513
Root 3	25051	1.1×10^{-5}	T_1^0	0.941760	25693	6.9×10^{-4}	T_1^+	0.474888
			T_6^+	0.011367			T_1^-	0.474888
			T_6^-	0.011367			S_4	0.020536
			T_1^+	0.010085			S_3	0.005832
			T_1^-	0.010085			T_1^0	0.002021
Root 4	25061	7.3×10^{-4}	T_1^+	0.473289	25735	1.2×10^{-4}	T_1^0	0.949938
			T_1^-	0.473289			T_6^+	0.011095
			S_4	0.020293			T_6^-	0.011095
			T_1^0	0.019121			T_1^+	0.001099
			S_3	0.005737			T_1^-	0.001099
Root 5	26125	1.8×10^{-2}	S_1	0.900378	26347	2.0×10^{-2}	S_1	0.904776
			T_6^+	0.031566			T_6^+	0.024612
			T_6^-	0.031566			T_6^-	0.024612
Root 6	26874	9.2×10^{-5}	T_2^+	0.492882	25678	1.9×10^{-4}	T_2^+	0.484990
			T_2^-	0.492882			T_2^-	0.484990
			T_6^0	0.005355			T_4^0	0.005380
			S_2	0.001735			S_4	0.005468
			S_{10}	0.001548			S_3	0.001487
Root 7	26898	5.5×10^{-5}	T_2^0	0.886667	25693	2.0×10^{-5}	T_2^+	0.485654
			T_2^+	0.045340			T_2^-	0.485654
			T_2^-	0.045340			T_6^0	0.005953
			T_6^+	0.004515			T_2^0	0.002784
			T_6^-	0.004515			S_2	0.001849
			T_4^+	0.002709			S_{10}	0.001487
			T_4^-	0.002709			T_5^0	0.001441
			S_1	0.002304				
Root 8	26900	1.5×10^{-4}	T_2^+	0.448442	25735	9.3×10^{-5}	T_2^0	0.960962
			T_2^-	0.448442			T_6^+	0.005114
			T_2^0	0.088419			T_6^-	0.005114
			T_4^0	0.004710			T_4^+	0.003025
			S_4	0.004038			T_4^-	0.003025
							S_1	0.001936

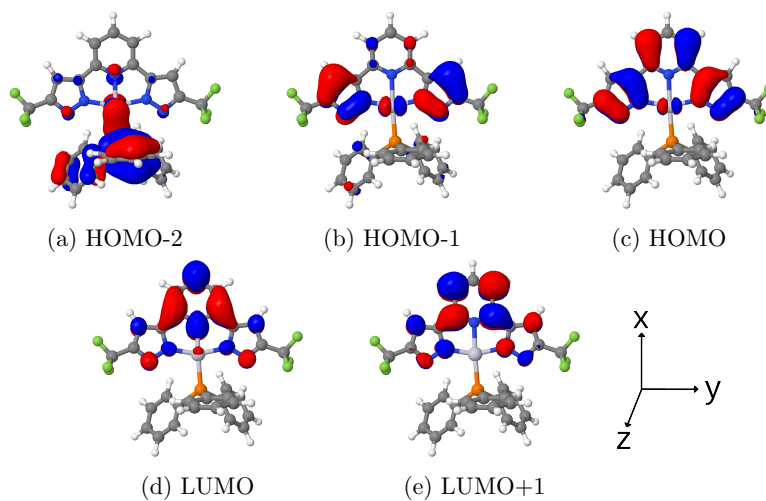


Figure S3: Frontier orbitals of AG97 (cutoff 0.03) at the S_0 geometry in DCM.

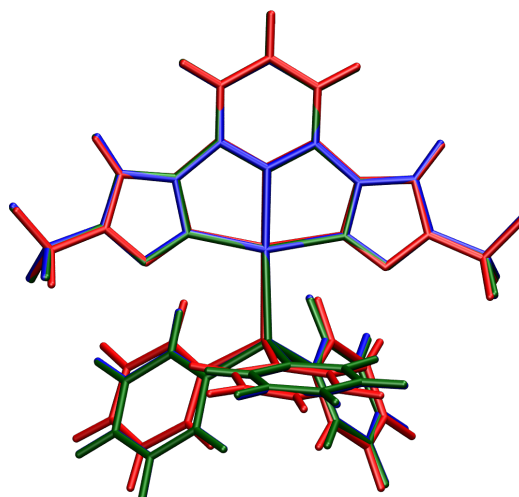


Figure S4: Comparison between the geometrical structures of the three optimized states in DCM. The blue wireframe belongs to the ground state, the red one to the first excited singlet state and the green one to the first triplet state.

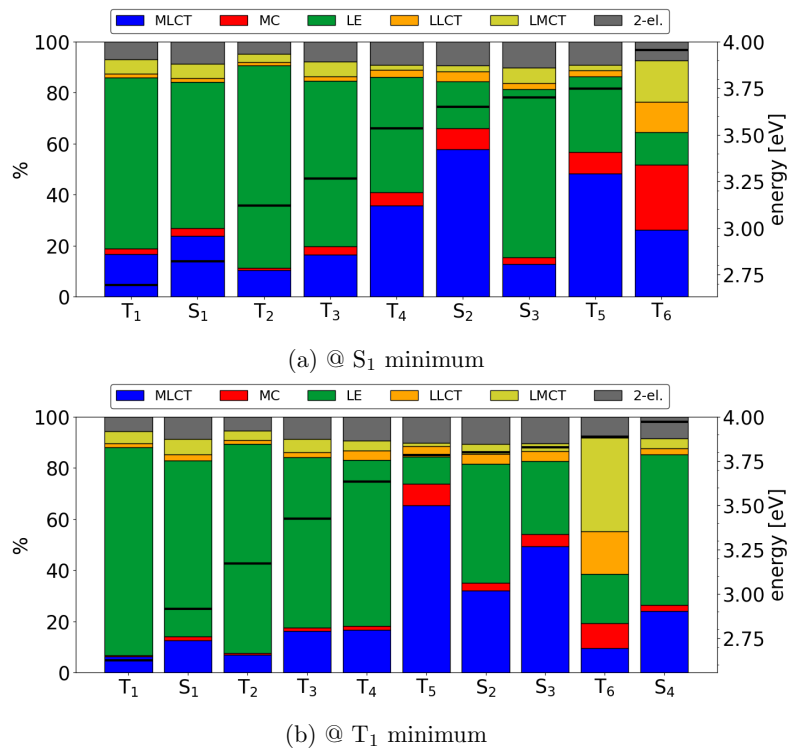


Figure S5: TheoDORE analyses of low-lying DFT/MRCI states at the S_1 and T_1 minimum geometries of AG97 in DCM.

Table S3: Adiabatic DFT/MRCI energies E_{adia} and corresponding 0-0 energies E_{0-0} [eV] of the optimized states of AG97 in DCM.

State	E_{adia}	E_{0-0}
S_1	3.14	3.06
T_1	2.92	2.80
T_2	3.17 ^a	2.98 ^a

^aExtrapolated from data at the S_1 geometry within the VH approach

Table S4: SOCMEs [cm^{-1}] at the S_1 geometry of AG97 in DCM.

Transition	SOCMEs			$\sum \text{SOCMEs}^2$
	x	y	z	
$S_1 \rightarrow T_1$	0.50152	-0.31997	-1.25372	1.92572
$S_1 \rightarrow T_2$	-1.78181	-447.74390	-324.49946	305777.6744

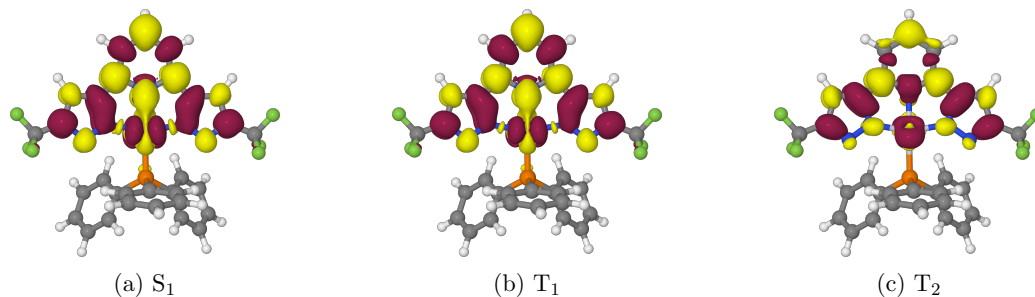


Figure S6: Difference densities of AG97 at the S_1 geometry in DCM (isovalues ± 0.001). Red-colored areas indicate a loss, yellow-colored areas a gain of electron density in the excited state.

Table S5: Vertical excitation energies E_{vert} [cm^{-1}], radiative rate constants k_r [s^{-1}] and projection of the wave function of the spin-orbit mixed states onto the LS -coupled DFT/MRCI basis states for AG97 in DCM at the S_1 minimum

	SOC-QDPT				/DFT/MRSOCI			
	E_{vert}	k_r	LS state	$ c ^2$	E_{vert}	k_r	LS state	$ c ^2$
Root 1	0		S_0	0.995003	0		S_0	0.977212
			T_5^+	0.001811			T_6^+	0.001628
			T_5^-	0.001811			T_6^-	0.001628
Root 2	21510	2.3×10^1	T_1^+	0.470797	22154	6.4×10^2	T_1^+	0.466503
			T_1^-	0.470797			T_1^-	0.466503
			T_4^0	0.019685			T_4^0	0.018261
			T_5^0	0.018262			T_5^0	0.016814
Root 3	21515	8.6×10^3	T_1^0	0.938164	22182	2.0×10^5	T_1^+	0.441235
			T_4^+	0.010217			T_1^-	0.441235
			T_4^-	0.010217			T_1^0	0.060066
			T_5^+	0.009189			S_2	0.027971
			T_5^-	0.009189			S_4	0.004544
Root 4	21550	1.6×10^5	T_1^+	0.477552	22213	6.6×10^4	T_1^0	0.873382
			T_1^-	0.477552			T_1^+	0.032546
			S_2	0.029499			T_1^-	0.032546
			S_4	0.004256			T_5^+	0.009381
							T_5^-	0.009381
Root 5	22314	1.6×10^6	S_1	0.914763	22555	1.9×10^6	S_1	0.913305
			T_5^+	0.015379			T_5^+	0.012687
			T_5^-	0.015379			T_5^-	0.012687
			T_4^+	0.014185			T_4^+	0.011455
			T_4^-	0.014185			T_4^-	0.011455

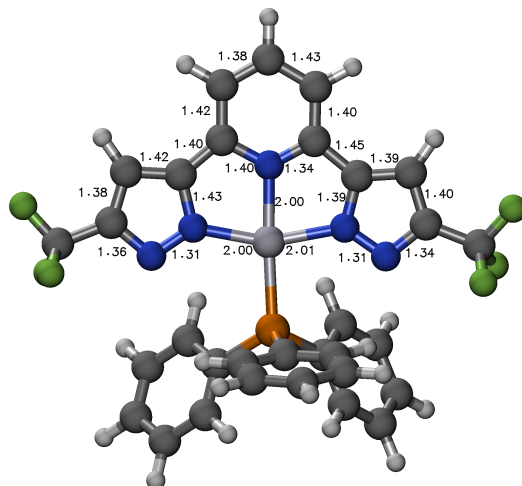


Figure S7: Bond lengths in Å at the T₁ geometry in DCM.

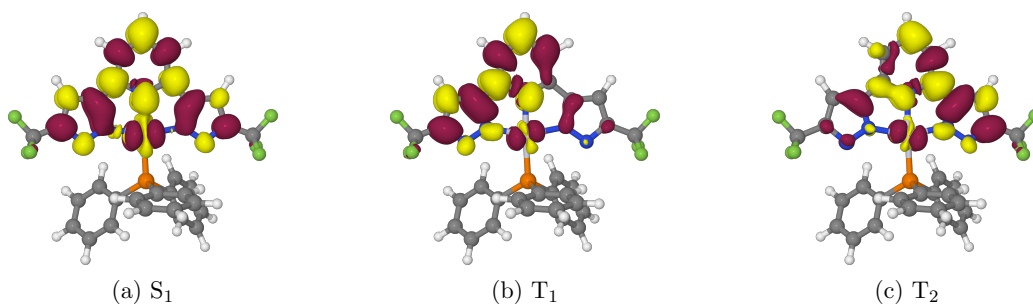


Figure S8: Difference densities of AG97 at the T₁ geometry in DCM (isovalues ± 0.001). Red-colored areas indicate a loss, yellow-colored areas a gain of electron density in the excited state.

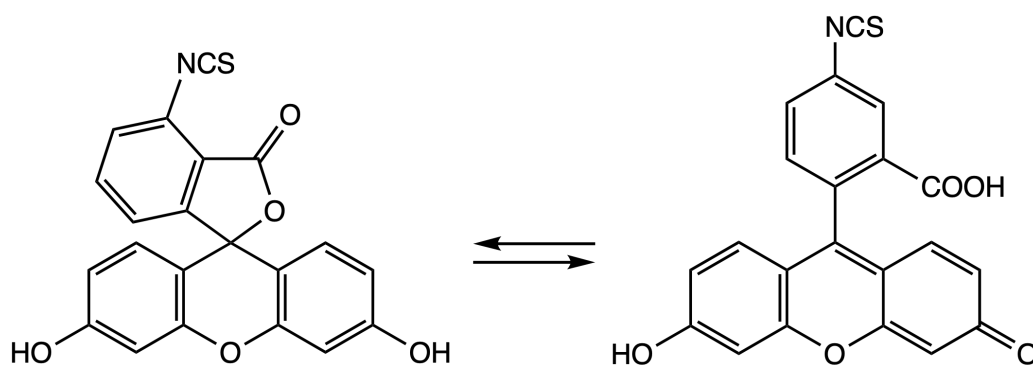


Figure S9: Lactone and quinoid forms of neutral FITC

Table S6: Vertical excitation energies E_{vert} [cm^{-1}], radiative rate constants k_r [s^{-1}] and projection of the wave function of the spin-orbit mixed states onto the LS -coupled DFT/MRCI basis states for AG97 in DCM at the T_1 minimum

	SOC-QDPT				/DFT/MRSOCI			
	E_{vert}	k_r	LS state	$ c ^2$	E_{vert}	k_r	LS state	$ c ^2$
Root 1	0		S_0	0.994678	0		S_0	0.976592
			T_6^+	0.002269			T_6^+	0.002017
Root 2	21200	8.7×10^3	T_6^-	0.002269	21845	4.6×10^3	T_6^-	0.002017
			T_1^+	0.476195			T_1^+	0.487397
			T_1^-	0.476195			T_1^-	0.487397
Root 3	21202	7.2×10^3	T_1^0	0.033651	21858	5.6×10^4	T_5^0	0.008679
			T_1^0	0.928982			T_1^+	0.487240
			T_1^+	0.028353			T_1^-	0.487240
			T_1^-	0.028353			S_3	0.005783
			T_5^+	0.004897			S_2	0.002642
Root 4	21203	5.1×10^4	T_5^-	0.004897	21899	4.4×10^4	T_1^0	0.001103
			T_1^+	0.481937			T_1^0	0.973951
			T_1^-	0.481937			T_5^+	0.004911
			T_1^0	0.022992			T_5^-	0.004911
			S_3	0.005468			S_1	0.001510
			S_2	0.002458				
Root 5	23264	1.5×10^7	S_1	0.942916	23471	1.6×10^7	S_1	0.934549
			T_5^+	0.022707			T_5^+	0.018237
			T_5^-	0.022707			T_5^-	0.018237
			T_4^+	0.002213			T_4^+	0.001736
			T_4^-	0.002213			T_4^-	0.001736

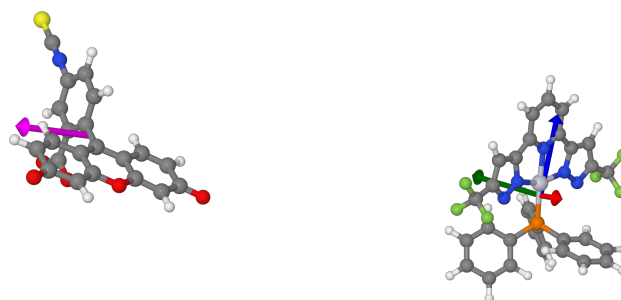


Figure S10: Donor-acceptor arrangement in which the orientation factor κ^2 is close to zero for the dipole-dipole coupling of the TDMVs of all three triplet sublevels of AG97 with the singlet TDMV (pink) of FITC.

Table S7: ECMEs (cm^{-1}) for the T_1 AG97-sensitized fluorescence of FITC assuming different relative orientations of the donor and acceptor molecules using IDA and MTD approaches. The contributions of the exchange integrals are given in the brackets. In all cases, the molecular centroids were 10 Å apart.

TDMV of T_a (AG97) and S_1 (FITC) collinear			
	T_a	T_b	T_c
MTD	3.575 (0.002)	12.409 (0.007)	0.057 (0.000)
IDA	3.888	13.447	0.951
κ^2	4.000	3.946	0.025
TDMV of T_b (AG97) and S_1 (FITC) collinear			
	T_a	T_b	T_c
MTD	3.266 (0.001)	11.722 (0.004)	1.803(0.000)
IDA	3.862	13.479	0.202
κ^2	3.940	4.000	0.001
TDMV of T_c (AG97) and S_1 (FITC) collinear ^a			
	T_a	T_b	T_c
MTD ^b	1.703 (0.032)	7.228 (0.092)	13.798 (0.218)
MTD ^c	1.587 (0.001)	7.018(0.007)	7.518(0.015)
IDA	0.327	0.007	12.047
κ^2	0.028	0.001	4.000

^a Closest intermolecular contact ca. 1.4 Å
^bTridentate ligand and FITC on the same side of the AG97 barycenter
^cTridentate ligand and FITC on opposite sides of the AG97 barycenter

Table S8: Distance dependency of ECMEs (cm^{-1}) and EET rate constants (s^{-1}) between the T_a of AG97 and FITC using the IDA and MTD approaches. Coupling calculated with a refractive index of 1 and a κ^2 value of 4.

Distance [Å]	Coupling		k_{EET}	
	MTD	IDA	MTD	IDA
10	3.5748	3.8883	3.0×10^9	3.6×10^9
15	1.1463	1.1521	3.1×10^8	3.1×10^8
20	0.4910	0.4860	5.7×10^7	5.6×10^7
25	0.2521	0.2489	1.5×10^7	1.5×10^7
30	0.1459	0.1440	5.0×10^6	4.9×10^6
35	0.0918	0.0907	2.0×10^6	1.9×10^6
40	0.0614	0.0608	8.9×10^5	8.7×10^5
45	0.0431	0.0427	4.4×10^5	4.3×10^5
50	0.0314	0.0311	2.3×10^5	2.3×10^5
55	0.0236	0.0234	1.3×10^5	1.3×10^5
60	0.0182	0.0180	7.8×10^4	7.7×10^4
65	0.0143	0.0142	4.8×10^4	4.7×10^4
70	0.0114	0.0113	3.1×10^4	3.0×10^4
75	0.0093	0.0092	2.0×10^4	2.0×10^4
80	0.0076	0.0076	1.4×10^4	1.4×10^4
85	0.0064	0.0063	9.6×10^3	9.5×10^3
90	0.0054	0.0053	6.8×10^3	6.7×10^3

Table S9: Distance dependency of ECMEs (cm^{-1}) and EET rate constants (s^{-1}) between the T_a of AG97 and FITC using the IDA and MTD approaches. Coupling calculated with a refractive index of 1.34 and a κ^2 value of 4.

Distance [Å]	Coupling		k_{EET}	
	MTD	IDA	MTD	IDA
10	1.9909	2.1655	9.4×10^8	1.1×10^9
15	0.6384	0.6416	9.6×10^7	9.7×10^7
20	0.2735	0.2707	1.8×10^7	1.7×10^7
25	0.1404	0.1386	4.7×10^6	4.5×10^6
30	0.0813	0.0802	1.6×10^6	1.5×10^6
35	0.0511	0.0505	6.2×10^5	6.0×10^5
40	0.0342	0.0338	2.8×10^5	2.7×10^5
45	0.0240	0.0238	1.4×10^5	1.3×10^5
50	0.0175	0.0173	7.2×10^4	7.1×10^4
55	0.0131	0.0130	4.1×10^4	4.0×10^4
60	0.0101	0.0100	2.4×10^4	2.4×10^4
65	0.0079	0.0079	1.5×10^4	1.5×10^4
70	0.0064	0.0063	9.6×10^3	9.4×10^3
75	0.0052	0.0051	6.3×10^3	6.2×10^3
80	0.0043	0.0042	4.3×10^3	4.2×10^3
85	0.0035	0.0035	3.0×10^3	2.9×10^3
90	0.0030	0.0030	2.1×10^3	2.1×10^3

Table S11: Root2 (T_a) $n=1.34$, $\kappa^2=2/3$

Distance [Å]	Coupling		k_{EET}	
	MTD	IDA	MTD	IDA
10	0.8128	0.8840	1.6×10^8	1.8×10^8
15	0.2606	0.2619	1.6×10^7	1.6×10^7
20	0.1116	0.1105	2.9×10^6	2.9×10^6
25	0.0573	0.0566	7.8×10^5	7.6×10^5
30	0.0332	0.0327	2.6×10^5	2.5×10^5
35	0.0209	0.0206	1.0×10^5	1.0×10^5
40	0.0140	0.0138	4.6×10^4	4.5×10^4
45	0.0098	0.0097	2.3×10^4	2.2×10^4
50	0.0071	0.0071	1.2×10^4	1.2×10^4
55	0.0054	0.0053	6.8×10^3	6.7×10^3
60	0.0041	0.0041	4.0×10^3	4.0×10^3
65	0.0032	0.0032	2.5×10^3	2.4×10^3
70	0.0026	0.0026	1.6×10^3	1.6×10^3
75	0.0021	0.0021	1.1×10^3	1.0×10^3
80	0.0017	0.0017	7.1×10^2	7.0×10^2
85	0.0014	0.0014	5.0×10^2	4.9×10^2
90	0.0012	0.0012	3.5×10^2	3.5×10^2

Table S12: Distance dependency of ECMEs (cm^{-1}) and EET rate constants (s^{-1}) between the T_b of AG97 and FITC using the IDA and MTD approaches. Coupling calculated with a refractive index of 1 and a κ^2 value of 4.

Distance [Å]	Coupling		k_{EET}	
	MTD	IDA	MTD	IDA
10	11.7215	13.4793	3.2×10^{10}	4.3×10^{10}
15	3.9566	3.9939	3.7×10^9	3.8×10^9
20	1.7084	1.6849	6.9×10^8	6.7×10^8
25	0.8783	0.8627	1.8×10^8	1.8×10^8
30	0.5082	0.4992	6.1×10^7	5.9×10^7
35	0.3196	0.3144	2.4×10^7	2.3×10^7
40	0.2139	0.2106	1.1×10^7	1.0×10^7
45	0.1500	0.1479	5.3×10^6	5.2×10^6
50	0.1092	0.1078	2.8×10^6	2.7×10^6
55	0.0820	0.0810	1.6×10^6	1.6×10^6
60	0.0631	0.0624	9.4×10^5	9.2×10^5
65	0.0496	0.0491	5.8×10^5	5.7×10^5
70	0.0397	0.0393	3.7×10^5	3.6×10^5
75	0.0322	0.0320	2.5×10^5	2.4×10^5
80	0.0266	0.0263	1.7×10^5	1.6×10^5
85	0.0221	0.0219	1.2×10^5	1.1×10^5
90	0.0186	0.0185	8.2×10^4	8.1×10^4

Table S13: Distance dependency of ECMEs (cm^{-1}) and EET rate constants (s^{-1}) between the T_b of AG97 and FITC using the IDA and MTD approaches. Coupling calculated with a refractive index of 1.34 and a κ^2 value of 4.

Distance [Å]	Coupling		k_{EET}	
	MTD	IDA	MTD	IDA
10	6.5279	7.5069	1.0×10^{10}	1.3×10^{10}
15	2.2035	2.2243	1.1×10^9	1.2×10^9
20	0.9514	0.9384	2.1×10^8	2.1×10^8
25	0.4891	0.4804	5.7×10^7	5.5×10^7
30	0.2830	0.2780	1.9×10^7	1.8×10^7
35	0.1780	0.1751	7.5×10^6	7.2×10^6
40	0.1191	0.1173	3.4×10^6	3.3×10^6
45	0.0835	0.0824	1.6×10^6	1.6×10^6
50	0.0608	0.0601	8.7×10^5	8.5×10^5
55	0.0457	0.0451	4.9×10^5	4.8×10^5
60	0.0351	0.0348	2.9×10^5	2.9×10^5
65	0.0276	0.0273	1.8×10^5	1.8×10^5
70	0.0221	0.0219	1.2×10^5	1.1×10^5
75	0.0180	0.0178	7.6×10^4	7.5×10^4
80	0.0148	0.0147	5.2×10^4	5.1×10^4
85	0.0123	0.0122	3.6×10^4	3.5×10^4
90	0.0104	0.0103	2.5×10^4	2.5×10^4

Table S14: Distance dependency of ECMEs (cm^{-1}) and EET rate constants (s^{-1}) between the T_b of AG97 and FITC using the IDA and MTD approaches. Coupling calculated with a refractive index of 1.34 and a κ^2 value of $2/3$.

Distance [Å]	Coupling		k_{EET}	
	MTD	IDA	MTD	IDA
10	2.6650	3.0647	1.7×10^9	2.2×10^9
15	0.8996	0.9081	1.9×10^8	1.9×10^8
20	0.3884	0.3831	3.6×10^7	3.5×10^7
25	0.1997	0.1961	9.4×10^6	9.1×10^6
30	0.1155	0.1135	3.2×10^6	3.0×10^6
35	0.0727	0.0715	1.2×10^6	1.2×10^6
40	0.0486	0.0479	5.6×10^5	5.4×10^5
45	0.0341	0.0336	2.7×10^5	2.7×10^5
50	0.0248	0.0245	1.5×10^5	1.4×10^5
55	0.0186	0.0184	8.2×10^4	8.0×10^4
60	0.0143	0.0142	4.9×10^4	4.8×10^4
65	0.0113	0.0112	3.0×10^4	2.9×10^4
70	0.0090	0.0089	1.9×10^4	1.9×10^4
75	0.0073	0.0073	1.3×10^4	1.2×10^4
80	0.0060	0.0060	8.6×10^3	8.5×10^3
85	0.0050	0.0050	6.0×10^3	5.9×10^3
90	0.0042	0.0042	4.2×10^3	4.2×10^3

Table S15: Distance dependency of ECMEs (cm^{-1}) and EET rate constants (s^{-1}) between the T_c of AG97 and FITC using the IDA and MTD approaches. Coupling calculated with a refractive index of 1 and a κ^2 value of 4.

Distance [Å]	Coupling			k_{EET}		
	MTD ^a	MTD ^b	IDA	MTD ^a	MTD ^b	IDA
10	13.7983	7.5177	12.0465	4.5×10^{10}	1.3×10^{10}	3.4×10^{10}
15	4.8169	2.6219	3.5693	5.5×10^9	1.6×10^9	3.0×10^9
20	1.9345	1.2013	1.5058	8.8×10^8	3.4×10^8	5.4×10^8
25	0.9447	0.6439	0.7710	2.1×10^8	9.8×10^7	1.4×10^8
30	0.5284	0.3838	0.4462	6.6×10^7	3.5×10^7	4.7×10^7
35	0.3246	0.2468	0.2810	2.5×10^7	1.4×10^7	1.9×10^7
40	0.2134	0.1679	0.1882	1.1×10^7	6.7×10^6	8.4×10^6
45	0.1477	0.1194	0.1322	5.2×10^6	3.4×10^6	4.1×10^6
50	0.1065	0.0879	0.0964	2.7×10^6	1.8×10^6	2.2×10^6
55	0.0793	0.0666	0.0724	1.5×10^6	1.0×10^6	1.2×10^6
60	0.0606	0.0516	0.0558	8.7×10^5	6.3×10^5	7.4×10^5
65	0.0473	0.0408	0.0439	5.3×10^5	3.9×10^5	4.5×10^5
70	0.0377	0.0329	0.0351	3.4×10^5	2.6×10^5	2.9×10^5
75	0.0305	0.0268	0.0286	2.2×10^5	1.7×10^5	1.9×10^5
80	0.0250	0.0222	0.0235	1.5×10^5	1.2×10^5	1.3×10^5
85	0.0208	0.0186	0.0196	1.0×10^5	8.1×10^4	9.1×10^4
90	0.0175	0.0157	0.0165	7.2×10^4	5.8×10^4	6.5×10^4

^aTridentate ligand and FITC on the same side of the AG97 barycenter

^bTridentate ligand and FITC on opposite sides of the AG97 barycenter

Table S16: Distance dependency of ECMEs (cm^{-1}) and EET rate constants (s^{-1}) between the T_c of AG97 and FITC using the IDA and MTD approaches. Coupling calculated with a refractive index of 1.34 and a κ^2 value of 4.

Distance [Å]	Coupling			k_{EET}		
	MTD ^a	MTD ^b	IDA	MTD ^a	MTD ^b	IDA
10	7.6845	4.1867	6.7089	1.4×10^{10}	4.1×10^9	1.1×10^{10}
15	2.6826	1.4602	1.9878	1.7×10^9	5.0×10^8	9.3×10^8
20	1.0774	0.6690	0.8386	2.7×10^8	1.1×10^8	1.7×10^8
25	0.5261	0.3586	0.4294	6.5×10^7	3.0×10^7	4.4×10^7
30	0.2942	0.2137	0.2485	2.0×10^7	1.1×10^7	1.5×10^7
35	0.1808	0.1374	0.1565	7.7×10^6	4.5×10^6	5.8×10^6
40	0.1189	0.0935	0.1048	3.3×10^6	2.1×10^6	2.6×10^6
45	0.0823	0.0665	0.0736	1.6×10^6	1.0×10^6	1.3×10^6
50	0.0593	0.0490	0.0537	8.3×10^5	5.7×10^5	6.8×10^5
55	0.0441	0.0371	0.0403	4.6×10^5	3.2×10^5	3.8×10^5
60	0.0337	0.0288	0.0311	2.7×10^5	2.0×10^5	2.3×10^5
65	0.0264	0.0227	0.0244	1.6×10^5	1.2×10^5	1.4×10^5
70	0.0210	0.0183	0.0196	1.0×10^5	7.9×10^4	9.0×10^4
75	0.0170	0.0149	0.0159	6.8×10^4	5.3×10^4	6.0×10^4
80	0.0139	0.0124	0.0131	4.6×10^4	3.6×10^4	4.1×10^4
85	0.0116	0.0103	0.0109	3.2×10^4	2.5×10^4	2.8×10^4
90	0.0097	0.0087	0.0092	2.2×10^4	1.8×10^4	2.0×10^4

^aTridentate ligand and FITC on the same side of the AG97 barycenter

^bTridentate ligand and FITC on opposite sides of the AG97 barycenter

Table S17: Distance dependency of ECMEs (cm^{-1}) and EET rate constants (s^{-1}) between the T_c of AG97 and FITC using the IDA and MTD approaches. Coupling calculated with a refractive index of 1.34 and a κ^2 value of 2/3.

Distance [Å]	Coupling			k_{EET}		
	MTD ^a	MTD ^b	IDA	MTD ^a	MTD ^b	IDA
10	3.1372	1.7092	2.7389	2.3×10^9	6.9×10^8	1.8×10^9
15	1.0952	0.5961	0.8115	2.8×10^8	8.4×10^7	1.6×10^8
20	0.4398	0.2731	0.3424	4.6×10^7	1.8×10^7	2.8×10^7
25	0.2148	0.1464	0.1753	1.1×10^7	5.1×10^6	7.3×10^6
30	0.1201	0.0873	0.1014	3.4×10^6	1.8×10^6	2.4×10^6
35	0.0738	0.0561	0.0639	1.3×10^6	7.4×10^5	9.6×10^5
40	0.0485	0.0382	0.0428	5.6×10^5	3.5×10^5	4.3×10^5
45	0.0336	0.0271	0.0301	2.7×10^5	1.7×10^5	2.1×10^5
50	0.0242	0.0200	0.0219	1.4×10^5	9.4×10^4	1.1×10^5
55	0.0180	0.0151	0.0165	7.7×10^4	5.4×10^4	6.4×10^4
60	0.0138	0.0117	0.0127	4.5×10^4	3.3×10^4	3.8×10^4
65	0.0108	0.0093	0.0100	2.7×10^4	2.0×10^4	2.4×10^4
70	0.0086	0.0075	0.0080	1.7×10^4	1.3×10^4	1.5×10^4
75	0.0069	0.0061	0.0065	1.1×10^4	8.8×10^3	1.0×10^4
80	0.0057	0.0050	0.0053	7.7×10^3	6.0×10^3	6.8×10^3
85	0.0047	0.0042	0.0045	5.3×10^3	4.2×10^3	4.7×10^3
90	0.0040	0.0036	0.0038	3.7×10^3	3.0×10^3	3.3×10^3

^aTridentate ligand and FITC on the same side of the AG97 barycenter

^bTridentate ligand and FITC on opposite sides of the AG97 barycenter

Table S18: EET rate constants (s^{-1}) between AG97 and FITC using the MTD and IDA approaches. Coupling calculated with a refractive index of 1.34 and a κ^2 value of $2/3$. Rate constants for individual triplet sublevel have been added and averaged.

Distance [\AA]	MTD		IDA
	$\frac{T_a+T_b+T_c^a}{3}$	$\frac{T_a+T_b+T_c^b}{3}$	$\frac{T_a+T_b+T_c}{3}$
10	1.4×10^9	8.4×10^8	1.4×10^9
15	1.6×10^8	9.7×10^7	1.2×10^8
20	2.8×10^7	1.9×10^7	2.2×10^7
25	7.0×10^6	5.1×10^6	5.7×10^6
30	2.3×10^6	1.7×10^6	1.9×10^6
35	8.8×10^5	7.0×10^5	7.6×10^5
40	3.9×10^5	3.2×10^5	3.4×10^5
45	1.9×10^5	1.6×10^5	1.7×10^5
50	9.9×10^4	8.4×10^4	8.9×10^4
55	5.5×10^4	4.8×10^4	5.0×10^4
60	3.2×10^4	2.8×10^4	3.0×10^4
65	2.0×10^4	1.8×10^4	1.9×10^4
70	1.3×10^4	1.1×10^4	1.2×10^4
75	8.4×10^3	7.5×10^3	7.8×10^3
80	5.7×10^3	5.1×10^3	5.3×10^3
85	3.9×10^3	3.6×10^3	3.7×10^3
90	2.8×10^3	2.5×10^3	2.6×10^3

^aTridentate ligand and FITC on the same side of the AG97 barycenter

^bTridentate ligand and FITC on opposite sides of the AG97 barycenter

Table S19: EET rate constants (s^{-1}) between AG97 and FITC using the MTD approaches. Coupling calculated with a refractive index of 1.34 and a κ^2 value of $2/3 \times 0.714$. Rate constants for individual triplet sublevel are added and averaged.

Distance [\AA]	MTD		IDA
	$\frac{T_a+T_b+T_c^a}{3}$	$\frac{T_a+T_b+T_c^b}{3}$	$\frac{T_a+T_b+T_c}{3}$
10	9.9×10^8	6.0×10^8	9.9×10^8
15	1.2×10^8	6.9×10^7	8.7×10^7
20	2.0×10^7	1.3×10^7	1.6×10^7
25	5.0×10^6	3.6×10^6	4.1×10^6
30	1.6×10^6	1.2×10^6	1.4×10^6
35	6.3×10^5	5.0×10^5	5.4×10^5
40	2.8×10^5	2.3×10^5	2.4×10^5
45	1.3×10^5	1.1×10^5	1.2×10^5
50	7.1×10^4	6.0×10^4	6.4×10^4
55	3.9×10^4	3.4×10^4	3.6×10^4
60	2.3×10^4	2.0×10^4	2.1×10^4
65	1.4×10^4	1.3×10^4	1.3×10^4
70	9.1×10^3	8.1×10^3	8.4×10^3
75	6.0×10^3	5.4×10^3	5.6×10^3
80	4.0×10^3	3.7×10^3	3.8×10^3
85	2.8×10^3	2.5×10^3	2.6×10^3
90	2.0×10^3	1.8×10^3	1.9×10^3

^aTridentate ligand and FITC on the same side of the AG97 barycenter
^bTridentate ligand and FITC on opposite sides of the AG97 barycenter

Table S20: XYZ coordinates in Å of the S_0 geometry of AG97 in Vacuum.

Pt	-0.097919	0.745004	-0.117528
P	0.076874	-1.539227	-0.006615
N	-2.094918	1.077183	-0.064065
N	-3.153817	0.318504	0.057748
N	-0.150647	2.770007	-0.172592
N	1.873203	1.173249	-0.102265
N	2.963773	0.459609	0.014782
F	-6.498409	1.563592	0.147405
F	-5.874624	-0.268423	-0.806364
F	-5.778632	-0.088710	1.330922
F	6.224901	1.831270	0.423143
F	5.524190	-0.096880	1.100560
F	5.808743	0.266897	-0.996675
C	-4.212239	1.137882	0.075812
C	-3.832431	2.480977	-0.028424
H	-4.471066	3.360042	-0.035360
C	-2.444047	2.406205	-0.112889
C	-1.357371	3.365402	-0.186696
C	-1.415250	4.761138	-0.248286
H	-2.377846	5.272721	-0.262332
C	-0.214796	5.470267	-0.286979
H	-0.240687	6.561528	-0.335115
C	1.018663	4.818148	-0.262171
H	1.955837	5.374553	-0.287170
C	1.027193	3.421970	-0.200981
C	2.161117	2.515618	-0.141726
C	3.544857	2.650960	-0.051887
H	4.143307	3.557898	-0.044193
C	3.984291	1.325142	0.045822
C	-5.591675	0.578764	0.189107
C	5.387001	0.825141	0.143808
C	-1.368098	-2.536799	-0.508260
C	-2.188714	-2.058215	-1.534683
H	-2.009485	-1.067927	-1.957046
C	-3.244047	-2.833713	-2.007602
H	-3.890449	-2.442605	-2.796272
C	-3.486038	-4.092208	-1.460892
H	-4.320301	-4.696095	-1.826218
C	-2.665290	-4.579531	-0.444130
H	-2.850217	-5.566889	-0.014267
C	-1.607182	-3.807948	0.030275
H	-0.971286	-4.198865	0.828051
C	0.462999	-1.974168	1.721712
C	-0.576499	-2.156035	2.644808
H	-1.617932	-2.117793	2.314531
C	-0.282675	-2.376515	3.988536
H	-1.096885	-2.522947	4.702273
C	1.043173	-2.402874	4.420599
H	1.270872	-2.576735	5.475228
C	2.076810	-2.192444	3.508790
H	3.115992	-2.190487	3.846256
C	1.793750	-1.971508	2.162188
H	2.604271	-1.764016	1.458488
C	1.406753	-2.241486	-1.046091
C	1.829672	-1.549416	-2.184953
H	1.423429	-0.557794	-2.398317
C	2.777651	-2.113738	-3.035432
H	3.108415	-1.562747	-3.918796
C	3.311256	-3.369363	-2.752477
H	4.060980	-3.807560	-3.415778
C	2.890766	-4.065162	-1.619109
H	3.307520	-5.049529	-1.392975
C	1.938138	-3.507439	-0.770412
H	1.615018	-4.060534	0.115017

Table S21: XYZ coordinates in Å of the S₀ geometry of AG97 in DMSO.

Pt	-0.086886	0.748475	-0.087202
P	0.087910	-1.535970	0.026932
N	-2.089769	1.075199	-0.033819
N	-3.150623	0.317692	0.109918
N	-0.149103	2.773662	-0.170815
N	1.885665	1.188686	-0.082029
N	2.985327	0.484965	0.039103
F	-6.500651	1.549103	0.199589
F	-5.870297	-0.304122	-0.707121
F	-5.754039	-0.062422	1.421825
F	6.246879	1.880818	0.375358
F	5.558191	-0.023757	1.125274
F	5.809642	0.270392	-0.985834
C	-4.207689	1.140229	0.116992
C	-3.828343	2.481430	-0.017027
H	-4.459788	3.365742	-0.039314
C	-2.441326	2.401357	-0.106322
C	-1.356192	3.365982	-0.199699
C	-1.423098	4.757970	-0.290338
H	-2.387355	5.265968	-0.315181
C	-0.226090	5.473167	-0.345527
H	-0.257124	6.562475	-0.417182
C	1.010180	4.826071	-0.309129
H	1.943787	5.387516	-0.349729
C	1.023234	3.433025	-0.217863
C	2.163942	2.531456	-0.145467
C	3.546022	2.683002	-0.068526
H	4.129968	3.599505	-0.083911
C	3.997418	1.362100	0.048323
C	-5.580951	0.580262	0.258092
C	5.400975	0.871829	0.142321
C	-1.355436	-2.524133	-0.504291
C	-2.125225	-2.048145	-1.572495
H	-1.913237	-1.065664	-1.999956
C	-3.165314	-2.819968	-2.085682
H	-3.764835	-2.437857	-2.915224
C	-3.446006	-4.070405	-1.534647
H	-4.266102	-4.672651	-1.933276
C	-2.677632	-4.552668	-0.474759
H	-2.890654	-5.533303	-0.042723
C	-1.631200	-3.786650	0.037187
H	-1.032787	-4.180072	0.862115
C	0.458624	-1.991959	1.753910
C	-0.587197	-2.162094	2.672789
H	-1.627333	-2.109896	2.341305
C	-0.304684	-2.395682	4.017314
H	-1.125032	-2.534455	4.725366
C	1.018563	-2.449145	4.456524
H	1.237809	-2.634824	5.510757
C	2.060585	-2.255234	3.549652
H	3.097883	-2.281519	3.891899
C	1.786477	-2.021285	2.202873
H	2.605051	-1.835876	1.503410
C	1.408955	-2.244070	-1.021224
C	1.795235	-1.562131	-2.180519
H	1.373549	-0.576896	-2.394681
C	2.720449	-2.132448	-3.053264
H	3.018438	-1.592681	-3.955225
C	3.267966	-3.383847	-2.771539
H	3.997259	-3.828205	-3.453286
C	2.883103	-4.069155	-1.618200
H	3.308132	-5.050593	-1.394901
C	1.951647	-3.506429	-0.747511
H	1.653078	-4.056520	0.148446

Table S22: XYZ coordinates in Å of the S_0 geometry of AG97 in DCM.

Pt	-0.090876	0.747217	-0.091520
P	0.080976	-1.538073	0.023669
N	-2.091996	1.081140	-0.034418
N	-3.154647	0.326769	0.107649
N	-0.145969	2.772716	-0.173650
N	1.883086	1.180160	-0.089842
N	2.979614	0.472382	0.030869
F	-6.499048	1.572548	0.210344
F	-5.881246	-0.267207	-0.731175
F	-5.760461	-0.065544	1.401923
F	6.242556	1.858666	0.386446
F	5.548717	-0.052699	1.114206
F	5.812012	0.262237	-0.992715
C	-4.209312	1.151894	0.116619
C	-3.826063	2.492287	-0.014473
H	-4.455855	3.377798	-0.034564
C	-2.439242	2.408779	-0.104395
C	-1.351225	3.369177	-0.197964
C	-1.412938	4.761825	-0.285615
H	-2.375563	5.273061	-0.307027
C	-0.213491	5.472643	-0.341824
H	-0.240758	6.562286	-0.411061
C	1.020495	4.821146	-0.309021
H	1.956188	5.379164	-0.349875
C	1.028970	3.427606	-0.220593
C	2.166114	2.522189	-0.150787
C	3.548747	2.667922	-0.072047
H	4.136865	3.581743	-0.084134
C	3.995091	1.345184	0.042927
C	-5.585343	0.595988	0.250384
C	5.397628	0.851299	0.138924
C	-1.358787	-2.530731	-0.507378
C	-2.154012	-2.043781	-1.551016
H	-1.962398	-1.050730	-1.962474
C	-3.194890	-2.817789	-2.059310
H	-3.816146	-2.425383	-2.867690
C	-3.449124	-4.082303	-1.529272
H	-4.269984	-4.686261	-1.923737
C	-2.653905	-4.576714	-0.494991
H	-2.846437	-5.568709	-0.079543
C	-1.608263	-3.807768	0.012854
H	-0.989563	-4.209402	0.818686
C	0.451595	-1.989384	1.751761
C	-0.592773	-2.196673	2.664195
H	-1.632288	-2.173890	2.327680
C	-0.308894	-2.427999	4.008909
H	-1.127803	-2.595256	4.712503
C	1.013210	-2.442163	4.453897
H	1.233360	-2.626018	5.508315
C	2.052773	-2.209813	3.553200
H	3.088742	-2.203266	3.900422
C	1.778032	-1.977364	2.206496
H	2.593051	-1.758660	1.511942
C	1.407811	-2.241625	-1.019688
C	1.779255	-1.568732	-2.188827
H	1.343101	-0.591917	-2.412889
C	2.709503	-2.135690	-3.057901
H	2.996859	-1.602295	-3.967051
C	3.277201	-3.374733	-2.762606
H	4.011243	-3.816128	-3.441175
C	2.907935	-4.050559	-1.598941
H	3.349988	-5.021786	-1.364234
C	1.971690	-3.491013	-0.731582
H	1.686836	-4.032422	0.174023

Table S23: XYZ coordinates in Å of the S_1 geometry of AG97 in DCM.

Pt	-0.045085	0.787671	-0.184844
P	0.109099	-1.524617	-0.007044
N	-1.989789	1.048998	0.051230
N	-2.997072	0.253541	0.332623
N	-0.150061	2.765312	-0.405195
N	1.879760	1.225223	-0.209445
N	2.980911	0.521577	-0.070491
F	-6.350112	1.364772	0.822543
F	-5.802967	-0.380124	-0.317988
F	-5.402904	-0.313668	1.791674
F	6.249715	1.922800	0.110629
F	5.571347	0.064788	0.974387
F	5.759901	0.252362	-1.157629
C	-4.078191	1.039319	0.404547
C	-3.786566	2.394544	0.179244
H	-4.471063	3.238016	0.187095
C	-2.414690	2.395095	-0.036325
C	-1.378011	3.368718	-0.244386
C	-1.452126	4.756348	-0.245071
H	-2.421238	5.247111	-0.136774
C	-0.271038	5.516163	-0.356516
H	-0.320344	6.605108	-0.357673
C	0.977795	4.866174	-0.404725
H	1.904911	5.442310	-0.422102
C	1.029550	3.477531	-0.402049
C	2.168259	2.602654	-0.338088
C	3.551205	2.724388	-0.300085
H	4.153277	3.625921	-0.369530
C	3.988501	1.400444	-0.128547
C	-5.413083	0.424106	0.677908
C	5.397247	0.906682	-0.047454
C	-1.332251	-2.465570	-0.623911
C	-2.069512	-1.938922	-1.690883
H	-1.833528	-0.944326	-2.077924
C	-3.107031	-2.675913	-2.257316
H	-3.680618	-2.254585	-3.086177
C	-3.417080	-3.942086	-1.761419
H	-4.234991	-4.517234	-2.202224
C	-2.682081	-4.473797	-0.701675
H	-2.919488	-5.466420	-0.311741
C	-1.639358	-3.741975	-0.135689
H	-1.068685	-4.171956	0.690879
C	0.354813	-1.977787	1.740378
C	-0.754487	-2.129749	2.584713
H	-1.767607	-2.059317	2.180424
C	-0.566483	-2.358411	3.946498
H	-1.434817	-2.483061	4.597702
C	0.722818	-2.423922	4.475703
H	0.866999	-2.606282	5.543374
C	1.827247	-2.245948	3.642351
H	2.838138	-2.281553	4.055283
C	1.648723	-2.017364	2.278929
H	2.516618	-1.852347	1.635601
C	1.470575	-2.281768	-0.966047
C	1.915774	-1.646622	-2.130743
H	1.511168	-0.669345	-2.405740
C	2.875704	-2.254221	-2.937521
H	3.220166	-1.749143	-3.842954
C	3.399447	-3.497701	-2.585311
H	4.156344	-3.971156	-3.215418
C	2.955862	-4.137205	-1.427302
H	3.361436	-5.112730	-1.148775
C	1.990983	-3.535839	-0.621247
H	1.648012	-4.049665	0.280103

Table S24: XYZ coordinates in Å of the T₁ geometry of AG97 in DCM.

Pt	-0.090159	0.757957	-0.113398
P	0.081284	-1.537727	0.020305
N	-2.065500	1.071387	-0.036189
N	-3.123697	0.320639	0.115280
N	-0.134934	2.753490	-0.200829
N	1.878085	1.184834	-0.108820
N	2.971217	0.478323	0.004435
F	-6.491913	1.537097	0.218261
F	-5.833539	-0.284675	-0.729689
F	-5.709992	-0.083495	1.405860
F	6.247965	1.860897	0.303933
F	5.549513	-0.015868	1.111507
F	5.780058	0.219511	-1.009975
C	-4.191699	1.159144	0.117712
C	-3.842469	2.490591	-0.019533
H	-4.490777	3.361619	-0.041391
C	-2.430390	2.448881	-0.108576
C	-1.384089	3.380159	-0.200331
C	-1.416222	4.800155	-0.258572
H	-2.380292	5.312792	-0.264009
C	-0.236345	5.512895	-0.302675
H	-0.252234	6.602131	-0.347229
C	1.018810	4.824670	-0.279867
H	1.961029	5.372976	-0.302793
C	1.024105	3.424660	-0.223868
C	2.165988	2.538682	-0.165961
C	3.552286	2.675421	-0.094128
H	4.144947	3.586079	-0.106451
C	3.991343	1.354235	0.013500
C	-5.562141	0.579500	0.254573
C	5.392524	0.852661	0.105833
C	-1.358301	-2.530692	-0.513914
C	-2.152162	-2.041614	-1.557728
H	-1.956575	-1.049142	-1.969587
C	-3.194360	-2.813082	-2.067257
H	-3.813773	-2.419300	-2.876418
C	-3.451947	-4.077265	-1.537869
H	-4.273732	-4.679313	-1.933341
C	-2.658708	-4.573603	-0.503053
H	-2.853669	-5.565355	-0.088125
C	-1.611670	-3.807006	0.005790
H	-0.994536	-4.210187	0.812071
C	0.445672	-1.990607	1.749870
C	-0.600739	-2.196152	2.660431
H	-1.639384	-2.175585	2.321032
C	-0.320648	-2.422362	4.006822
H	-1.141518	-2.588368	4.708471
C	1.000043	-2.433144	4.456158
H	1.217255	-2.612909	5.511882
C	2.041882	-2.203055	3.557493
H	3.076890	-2.194481	3.907587
C	1.770639	-1.976065	2.209148
H	2.588065	-1.761191	1.516187
C	1.410280	-2.252726	-1.014480
C	1.789923	-1.586441	-2.184721
H	1.356666	-0.609926	-2.415999
C	2.723128	-2.159775	-3.046504
H	3.016563	-1.631217	-3.956559
C	3.285813	-3.399054	-2.742897
H	4.022001	-3.845619	-3.415753
C	2.908619	-4.068504	-1.578052
H	3.346564	-5.039995	-1.336751
C	1.969778	-3.502140	-0.717917
H	1.679125	-4.038398	0.188908

Table S25: XYZ coordinates in Å of the S_0 geometry (PBE0) of FITC in Water.

S	-2.446934	-5.809448	-5.044812
O	-2.333431	1.255556	-0.211430
O	1.293507	2.080156	1.989280
O	-3.771060	0.306268	-1.647623
O	-0.221060	-0.308436	5.745310
O	2.999111	4.663279	-1.549733
N	-1.583646	-3.826638	-3.309854
C	0.114626	0.257887	0.227220
C	-0.400609	-0.782337	-0.708707
C	0.017069	0.066380	1.617217
C	0.848852	1.350716	-0.267614
C	-1.677204	-0.744737	-1.298362
C	0.619358	1.017463	2.497416
C	1.432995	2.274127	0.653208
C	-2.692371	0.382619	-1.026376
C	0.460690	-1.850093	-1.007751
C	-0.675203	-1.018826	2.235723
C	1.046123	1.629306	-1.654192
C	-2.054984	-1.769525	-2.166093
C	0.551479	0.907821	3.866196
C	2.149411	3.374597	0.245775
C	0.082711	-2.870549	-1.870125
C	-0.755548	-1.145753	3.592603
C	1.752786	2.716955	-2.080163
C	-1.190799	-2.829758	-2.456343
C	-0.143736	-0.184781	4.507328
C	2.355851	3.671801	-1.153189
C	-1.954552	-4.670036	-4.049633
H	1.453302	-1.879786	-0.551223
H	-1.151691	-1.758527	1.586885
H	0.607721	0.941357	-2.382030
H	-3.050512	-1.710819	-2.609046
H	1.032857	1.663168	4.491424
H	2.576483	4.046251	0.993885
H	0.760417	-3.696041	-2.094482
H	-1.290601	-1.984397	4.047250
H	1.891991	2.912558	-3.147278

Table S26: XYZ coordinates in Å of the S_0 geometry (CAM-B3LYP) of FITC in Water.

S	-0.65226	7.51453	0.00000
O	2.50207	-0.44636	0.00000
O	-0.35346	-3.69259	0.00000
O	3.35343	1.62559	0.00000
O	-0.38905	-3.86034	4.69521
O	-0.38905	-3.86034	-4.69521
N	-0.50433	4.74839	0.00000
C	-0.14009	-0.91015	0.00000
C	-0.15831	0.58456	0.00000
C	-0.21200	-1.61380	1.21266
C	-0.21200	-1.61380	-1.21266
C	0.99592	1.38351	0.00000
C	-0.31141	-3.03787	1.18949
C	-0.31141	-3.03787	-1.18949
C	2.42217	0.79718	0.00000
C	-1.41710	1.20135	0.00000
C	-0.17217	-1.00584	2.50654
C	-0.17217	-1.00584	-2.50654
C	0.86109	2.77048	0.00000
C	-0.37279	-3.79819	2.33021
C	-0.37279	-3.79819	-2.33021
C	-1.54952	2.58223	0.00000
C	-0.22925	-1.73922	3.65109
C	-0.22925	-1.73922	-3.65109
C	-0.39605	3.37311	0.00000
C	-0.33505	-3.19784	3.64274
C	-0.33505	-3.19784	-3.64274
C	-0.56442	5.92364	0.00000
H	-2.31587	0.58109	0.00000
H	-0.09020	0.08166	2.56042
H	-0.09020	0.08166	-2.56042
H	1.77461	3.36418	0.00000
H	-0.45243	-4.88383	2.25196
H	-0.45243	-4.88383	-2.25196
H	-2.53387	3.05175	0.00000
H	-0.19729	-1.25691	4.63132
H	-0.19729	-1.25691	-4.63132